Development of ruthenium nanoparticles as catalyst models for the splitting of water : combination of experimental and theoretical chemistry approaches

Roberto Gonzalez-Gomez

THÈSE

En vue de l'obtention du
DOCTORAT DE L'UNIVERSITÉ DE TOULOUSE

Délivré par l'Université Toulouse 3 - Paul Sabatier

Présentée et soutenue par

Roberto GONZáLEZ GóMEZ

Le 11 avril 2019

Développement de nanoparticules de ruthénium comme modèles de catalyseurs pour le craquage de l'eau : approches expérimentale et théorique

---

Ecole doctorale : **SDM - SCIENCES DE LA MATIERE - Toulouse**

Spécialité : **Chimie Organométallique et de Coordination**

Unité de recherche :
LCC - Laboratoire de Chimie de Coordination

Thèse dirigée par
Karine PHILIPPOT et Romuald POTEAU

Jury

M. Jean-François HALET, Rapporteur
M. Jean-Yves PIQUEMAL, Rapporteur
Mme Carine MICHEL, Examinatrice
Mme Montserrat GOMEZ SIMON, Examinatrice
Mme Karine PHILIPPOT, Directrice de thèse
M. Romuald POTEAU, Co-directeur de thèse

AKNOWLEDGMENTS

This thesis work was developed thanks to the Mexican financial support of the National Council of Science and Technology (CONACyT). I thus thank greatly to this institution for having awarded me the doctoral grant under the program “Becas de Posgrado en el Extranjero” (CVU: 483283) and thus promoting my postgraduate studies.

I would like to thank Dr. Jean-François Halet, Pr. Jean-Yves Piquemal, Dr. Carine Michel and Pr. Montserrat Gómez Simon for accepting to be the jury members of my thesis.

My deepest and most sincerely gratitude goes to my supervisors Dr. Karine Philippot and Pr. Romuald Poteau who have guided me through the doctoral research. I would like to thank you for giving me support, encouragement and motivation. Special gratitude for your kindness and enthusiasm, and for providing me valuable suggestion during these years. Without your help and wisdom my doctoral scientific formation could not be possible.

Thanks to Pr. Catherine Amiens and Dr. Iker del Rosal for sharing their vast knowledge during scientific discussions. Also, I would like to offer my appreciation for having the opportunity to work with you.

I would like to thank the current and former members of the team “Engineering of Metal Nanoparticles” at the Laboratory of Coordination Chemistry (LCC) and of the team “Physical and Chemical Modelization” at the Laboratory of Physics and Chemistry of Nano-objects (LPCNO).

I would like to extend my gratitude to Dr. Pierre Lecante for X-ray analyses, to Vincent Collière for electron microscopy experiments and to Dr. Yannick Coppel and Dr. Christian Bijani for nuclear magnetic resonance experiments. Thanks for the scientific discussions that were a valuable contribution for the characterization of the nanoparticles systems presented in this thesis. Without your collaboration this work could have not been completed.

AKNOWLEDGMENTS

My special thanks to my friends and co-workers Laize Zaramello, Elena Martín Morales, Jordi Creus Casanovas, Samuel Drouet, Carlos Álvares Lamsfus, Chen Zhang, Alvaro Fernández Álvarez, Carlos Pinheiro, Luca Digianantonio, Luis Miguel Martínez Prieto, Israel Cano, Julian Crespo Gutiérrez, Andreas Sergides and David Poirot for their valuable time that we shared together in this adventure.

Thank you to my teammates Lorraine, Mai-Phuong, Yan, Laura, Lea, Thiquyen, Elisa, Jorge, Ionut, Mahmoud, Lluìs, Laurent, Paul, Iskander, Adrien B., Adrien S., Karl, Thomas and François, for their friendship.

Special thanks to my friends in Mexico Itzel, Hamlet, Hiroshi, Miguel, Fernando A., Diego, Fernando L. and Is-boset, for always giving me a good reason to laugh.

I would like to thank my parents Gabriela and Roberto for giving me their love and guidance through all my life. To my sister Jimena for always being with me even in the worst moments and for giving me the cutest nephew, Santi. To my uncles José and Joaquín for always being there for me. To my aunt Guillermina for being the light in my road. Also, I would like to thank to my grandmother Marina and my aunts Malena and Miriam for being so supportive. To my cousin Juan for sharing many adventures. To my grandma Consuelo who always will be in my heart.

Finally, I would like to thank my wife Ana who was and will be always by my side in this journey.

TABLE OF CONTENTS

TABLE OF CONTENTS

LIST OF FIGURES

LIST OF FIGURES

LIST OF FIGURES

LIST OF FIGURES

LIST OF SCHEMES

LIST OF TABLES

LIST OF TABLES

LIST OF TABLES

ABBREVIATIONS

- **Å:** Angstrom
- **AIM:** Atoms in Molecule
- **AO:** Atomic Orbital
- **ATR-FTIR:** Attenuated Total Reflectance Fourier-Transform Infrared
- **BDE:** Bond-Dissociation Energy
- **BEP:** Brønsted-Evans-Polanyi (BEP) Relations**.**
- **bpy:** Bipyridine
- **cc-pvdz:** Correlation-Consistent Polarized Valance Double Zeta Basis Set
- **cc-pvtz:** Correlation-Consistent Polarized Valance Triple Zeta Basis Set
- **CINEB:** Climbing Image Nudge Elastic Band
- **^{13}CO:** ^{13}C Labeled Carbon monoxide
- **COD:** 1,5-Cyclooctadiene (C_8H_{12})
- **COT:** 1,3,5-Cyclooctatriene (C_8H_{10})
- **CP-MAS:** Cross Polarization - Magic Angle Spinning
- **DFT:** Density Functional Theory
- **DOSY:** Diffusion-Ordered Spectroscopy
- **dppb:** bis-(diphenylphosphino)butane ($C_{28}H_{28}P_2$)
- **EA:** Elemental Analysis
- **EDX:** Energy-Disperse X-Ray Spectroscopy
- **EtAc:** Ethanoic acid (CH_3COOH)
- **FFT:** Fast-Fourier Transform
- **FTIR:** Fourier-Transform Infrared
- **FTS:** Fisher-Tropsch Synthesis
- **GC:** Gas Chromatography
- **GGA:** Generalized Gradient Approach
- **GIAO:** Gauge Including Atomic Orbital
- **GIPAW:** Gauge Including Projected Augmented Wave
- **hcp:** Hexagonal Close Pack
- **HDA:** Hexadecylamine ($CH_3(CH_2)_{15}NH_2$)
- **HEC:** Hydrogen Evolution Catalyst
- **HER:** Hydrogen Evolution Reaction
- **Hz:** Hertz
- **ICP-AES:** Inductively Coupled Plasma Atomic Emission Spectroscopy
- **IEFPCM:** Integral Equation Formalism Polarizable Continuum Model
- **MAS:** Magic Angle Spinning
- **MEP:** Minimum Energy Pathway
- **MNPs:** Metal Nanoparticles
- **MPA:** Mulliken Population Analysis
- **MS:** Mass Spectrometry
- **nm:** Nanometer

- **NMR:** Nuclear Magnetic Resonance
- **NOESY:** Nuclear Overhauser Effect Spectroscopy
- **NPA:** Natural Populations
- **NPs:** Nanoparticles
- **OcAc:** Octanoic acid ($C_7H_{15}COOH$)
- **PAW:** Projector Augmented Waves Method
- **PBE:** Perdew-Burke-Ernzerhof Functional
- ***p*COHP:** Projected Crystal Orbital Hamilton Populations
- ***p*DOS:** Projected Density of States
- **PDT:** Photodynamic Therapy
- **PentAc:** Pentanoic acid (C_4H_9COOH)
- ***p*MPA:** Projected Mulliken Population Analysis
- **PS:** Photosensitizer
- **PTA:** 1,3,5-Triaza-7-phosphaadamantane ($C_6H_{12}N_3P$)
- **QSE:** Quantum Size Effects
- **r.t.:** Room Temperature
- **RDF:** Radial Distribution Function
- **RuNPs:** Ruthenium Nanoparticles
- **SDD-ECP:** Stuttgart-Dresden Relativistic Effective Core Potential
- **SMD:** Solvation Model Density
- **TEM:** Transmission Electron Microscopy
- **THF:** Tetrahydrofuran (C_4H_8O)
- **TFA:** Trifluoroacetic acid (CF_3COOH)
- **TMS:** Tetramethylsilane ($Si(CH_3)_4$)
- **TS:** Transition State
- **TST:** Transition State Tool
- **VASP:** Vienna *Ab initio* Simulation Package
- **WAXS:** Wide-Angle X-ray Scattering
- **WOC:** Water Oxidation Catalyst
- **WOR:** Water Oxidation Reaction
- **ZPE:** Zero-Point Energy

GENERAL INTRODUCTION

The search for renewable energy is one the greatest challenges of our modern society. Even when sunlight can be considered as an almost inexhaustible source of energy, that could bring our world to adopt a new paradigm of sustainable development, harnessing it requires its conversion to storable fuels, such as hydrogen (H_2).[[1],[2]] Having this in mind, this PhD manuscript is an upstream study in the general context of the solar hydrogen production *via* photocatalytic water splitting, as illustrated in the image hereafter.

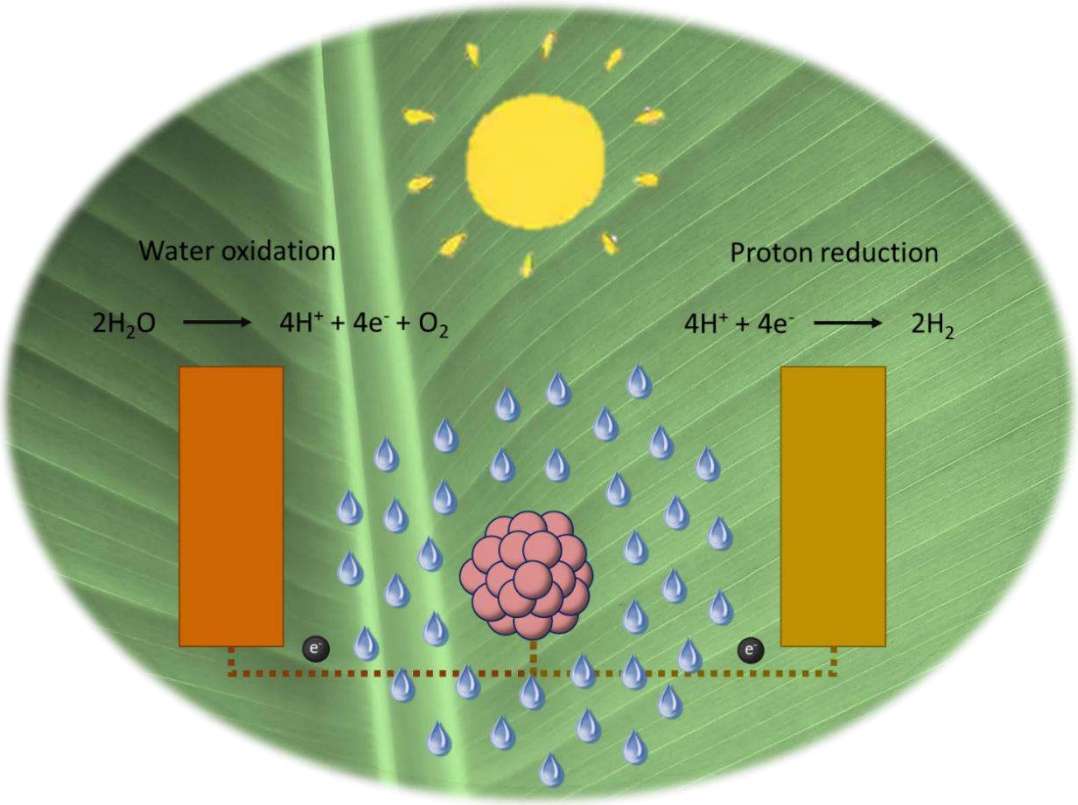

Two combined catalytic reactions are involved in the photoproduction of hydrogen from water: hydrogen evolution (HE) and water oxidation (WO). However, each reaction of this green route needs to be improved. The rational design of catalysts,[3,4] as well as the understanding of their photophysical and catalytic properties, are real challenges. Metal nanoparticles (MNPs) have been reported as efficient HE and WO catalysts.[5–7] Such nanomaterials have shown to exhibit high electrocatalytic activities, with respect to WO and HE reactions, with a low overpotential. Among other factors, comparison with bulk materials brings out the importance of using materials that possess a high surface area as catalysts for water splitting process. The main drawback of such catalysts lies in their cost, which is significantly higher than state-of-the-art catalysts. Therefore, it is necessary to develop MNPs that can be used as a better alternative.

Different ruthenium-based nanomaterials with various composition, morphologies, structures and sizes have been reported in the literature as catalyst for water splitting process. In particular, ruthenium nanomaterials have proven to be interesting alternatives to Pt and Pd based catalysts for HER.[8] Improvement of the electrocatalytic performance of ruthenium nanoparticles (RuNPs) compared to that of Ru black powder has been established and attributed to the greater specific area that the RuNPs display. Very recently, the potential of RuNPs stabilized with phenylpyridine or MeOH/THF for the HER has been demonstrated.[5],[9]

Regarding RuNPs, despite their diversity, there is still a need to modify their surface in order to improve their properties and functionality. The physical and chemical properties of RuNPs depend on their structural characteristics like their shape, size, defects, but also on the nature of capping ligands used to stabilize them and on the number of adsorbed species onto the metal surface. Although carboxylic acids are widely used as surfactants in colloidal synthesis, the direct adsorption of carboxylic acids onto ruthenium metal surfaces has received less attention.

This PhD thesis provides a reference study in the aim to design a novel class of nanocatalyst for the HER activated by light. To access nanomaterials that can be activated by light, it is required to elaborate hybrid materials that combine MNPs with a photosensitizing molecules grafted on their surface. This can be done for instance through the use of a polypyridyl ruthenium complex that bears pending carboxylic acids groups that can act as anchoring functions.

For this purpose, we started studying the surface properties of RuNPs stabilized by carboxylic acids as model systems. Alkyl chains with different lengths are considered. On the experimental side, RuNPs were synthesized following the organometallic approach using ethanoic (EtAc), pentanoic (PentAc) and octanoic acid (OcAc) as stabilizers. TEM characterization revealed small NPs with a homogeneous morphology and good dispersion. The surface state of these RuNPs was probed by analytical techniques such as IR, WAXS, NMR, etc., leading to a trustful mapping of their surface. Once the optimal ligand ratio to get RuNPs of similar sizes and their synthetic conditions were established, it was possible to determine the influence of the alkyl chain length of the carboxylic acid ligands on the surface properties of the NPs.

In parallel, density functional theory (DFT) calculations were performed according to a thermodynamic model fed with DFT energies. Also, a systematic analysis of the bond properties and of the electronic states (Density of States, Crystal Orbital Hamilton Population, atomic charges) was carried out.

DFT calculations of the vibrational features of model Ru_{55} NPs and of the chemical shifts of model [Ru_6] clusters also allowed to corroborate the spectroscopic experimental assignations. Spectroscopic data as well as DFT mechanistic studies showed that the carboxylic acids lie on the metal surface as carboxylates, together with hydrogen atoms. The experimental and theoretical titration results are in good agreement, indicating it as a relevant step to build a model to understand the ligand influence on RuNPs properties.

For the optimal surface composition, the hydrogen adsorption Gibbs free energy was found close to the 0 $kcal.mol^{-1}$ criterion which, according to the seminal work of Nørskov *et al.*,[10] makes these RuNPs a promising HEC. As a result, the best nanocatalyst revealed to have both, intermediate crowded metal surface and intermediate alkyl chain length for the capping ligand, indicating the RuNPs stabilized by pentanoic acid as the most promising catalyst.

Since RuNPs are known to be active catalysts for the reduction of arenes, the direct use of a polypyridyl complex as stabilizer during the synthesis of RuNPs under hydrogen atmosphere may lead to the reduction of the bipyridine ligands. To circumvent this potential issue, synthesis PS-modified RuNPs can be envisaged by a ligand exchange method. For this purpose, exchange ligand viability studies have been performed starting from RuNPs pre-stabilized with octanoic acid and exposed to incoming ligands (benzoic and trifluoroacetic acids). Moreover, theoretical studies

on the reliability of this procedure with actual photosensitizers, namely $[Ru(bpy)_x(bpy\text{-}(RCOOH)_x)_{3-x}]^{2+}$, were performed.

This thesis dissertation is divided into six chapters.

The first chapter gives a general overview to situate this work in the current context based on bibliographic data. In general, it presents the interests of metal nanoparticles (MNPs) according with their novel properties. Furthermore, a focus is given on the synthesis and catalytic properties of RuNPs. Also, DFT methods for modelling MNPs are described.

The second chapter is dedicated to the experimental and theoretical description of RuNPs stabilized by ethanoic acid, where it can be found a complete surface mapping of this optimized nanosystem together whit its viability for HER.

Meanwhile, in chapter three the optimal surface coverage of RuNPs stabilized by pentanoic and octanoic acid is described by a combination of experimental and theoretical tools. The viability of these catalysts and the ligand alkyl chain length influence on the formation and activity of RuNPs are deeply discussed.

In the fourth chapter are presented studies of ligand exchange at the surface of preformed RuNPs stabilized by octanoic acid when adding benzoic or trifluoracetic acids. These studies were boarded as prove of content for the viability of this strategy to anchor photosensitizers with carboxylic acid pending groups onto the surface of preformed RuNPs. This approach has been theoretically studied as presented in the chapter five.

The sixth chapter deals with the experimental and theoretical techniques used for the development of this PhD work. At the end of the manuscript, several appendices can be found that include the calculated DFT energies and general information utilized for theoretical calculations.

As a general view, this research work was designed in order to bring a better understanding of the structure/properties relationship at the nanoscale, aiming to explain the surface properties of RuNPs directly stabilized by carboxylic acids and their catalytic viability. The major contribution of this thesis is to closely combine experimental and theoretical studies to access a deep knowledge in the surface properties of the described RuNPs systems.

CHAPTER I

General Background

1.1 Metal Nanoparticles: Interests, Properties and Applications

In the past twenty five years, metal nanoparticles (MNPs) have been strongly attracting the attention of the scientific community and enterprises due to their unique properties located between those of bulk materials and molecules.[[11],[12]] It is well-known that controlling the structure of these nanomaterials can directly influence their physical and chemical properties, that can be of interest for applications in various fields ranging from biology, medicine, optoelectronics, catalysis, energy, etc.[13] Especially, their catalytic reactivity can be tuned by a fine control of their structure,[14] leading to novel characteristics contrasting to that exhibited by molecules and bulk materials.[[15],[16]]

MNPs have a different chemical and physical behaviors due to their electronic change when reaching a critical nanoscale size, [1 – 100 nm]. For example the decrease in its boiling and melting point[17] or the change in its optical properties (color).[18] In comparison to bulk materials, the size reduction towards the nanoscale carries a decrease in the electron mobility (delocalized electrons) that leads to quantum size effects (QSE).[19] As a consequence, the properties of MNPs do not follow the same rules as those of bulk materials because of the appearance of particular nano-effects.

The particular properties of MNPs can be explained in terms of QSE by describing the relationship between the valence and conduction band in these materials. In bulk metals these bands at some point overlap leading to a partial occupation of the conduction band by the valence electrons (*s* & *d*). This lets highly mobile electrons which are responsible for the electrical conductivity of these materials. When the valence and conduction bands are slightly separated by a gap, materials act as semiconductor materials. However, if the observed gap is too large, materials are named as insulators.

The continuum band existing in bulk metals begins to separate when the quantity of metal atoms in the material decreases which is the case in nanomaterials. Meaning that the band overlapping does not longer exist, and the material tends to be a semiconductor. The gap between the valence and the conduction bands increases while the material size decreases till getting a similar situation as for molecular entities where discrete energy levels exist (figure 1.1). At this

point, the properties of bulk metals are replaced for those of quantum dots which follow the quantum mechanical rules. This induces a change in the electronic properties of nanomaterials, making it metal nanoparticles to display intermediate properties comparatively to those of bulk metals and molecular species.[20]

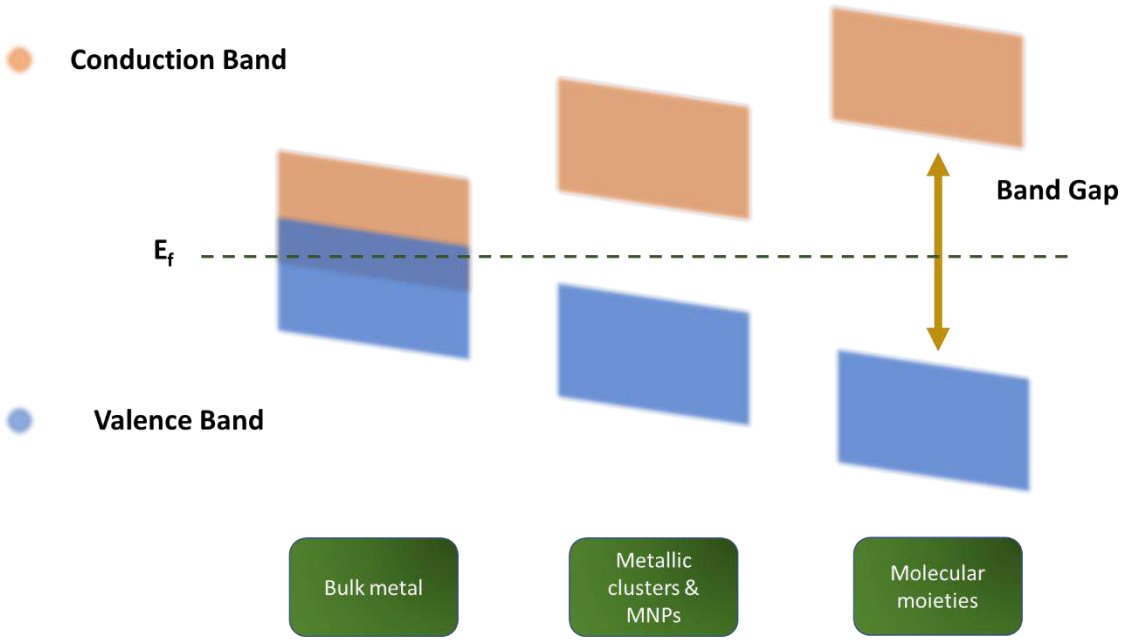

Figure 1.1 Energy level diagram from bulk metal to molecular moieties.

The previous phenomenon is particularly true for metal nanoparticles in the size range [1 - 10 nm] because they are expected to exhibit an intermediate state among bulk metal and molecular moieties. As it was described, in this size range the properties of the material is highly dependent on the number of metal atoms held into the nanocluster, this phenomenon is explained due to the change in the quantized energy levels, the so-called quantum size effect (figure 1.2).

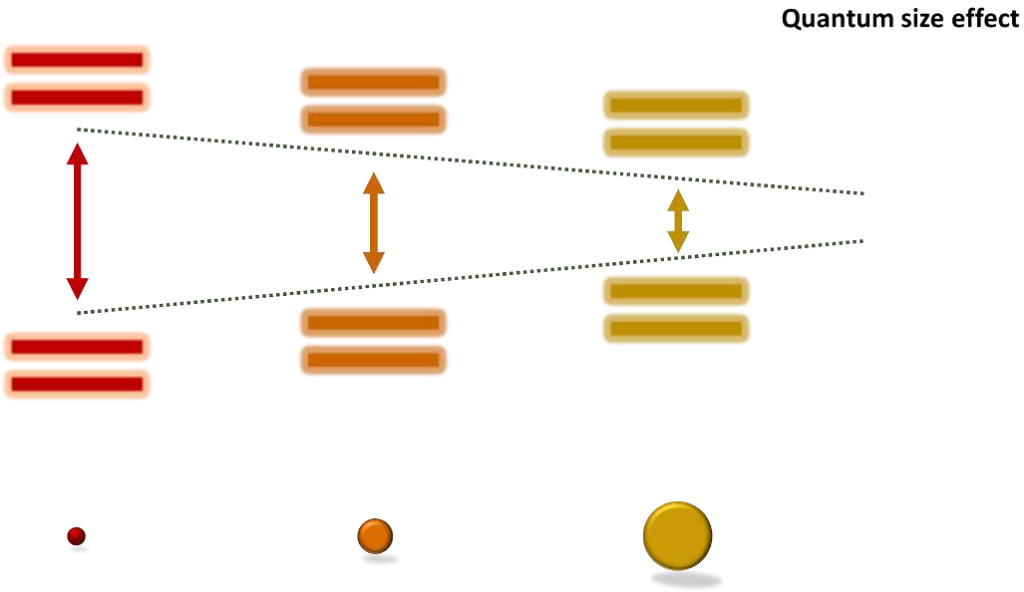

Figure 1.2 Representation of the quantum size effect and discrete electronic energy levels in MNPs.

Additionally, the properties of MNPs are dependent of the number of metal atoms present at their surface compared to the ones of the core. The surface to volume ratio increases with the size reduction of the MNPs, which makes very small NPs to have high quantities of surface atoms. Given their higher surface-to volume ratio compared with bulk metal entities (figure 1.3), MNPs display higher numbers of potentially active surface sites, making them to be highly attractive systems for several applications such, as catalysis.[15]

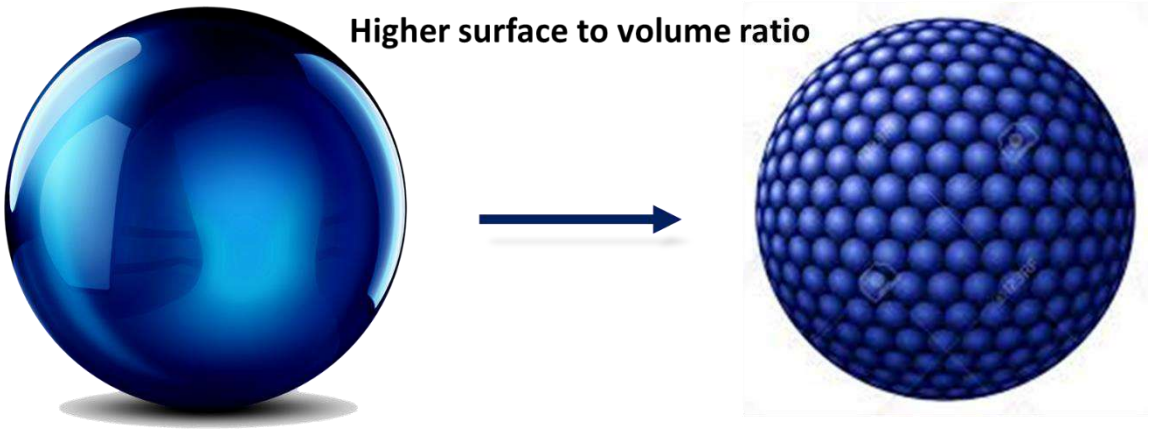

Figure 1.3 Comparison of the surface area in bulk materials and metal nanoparticles.

Furthermore, nanoparticles can be tuned with different shapes (like spheres, cubes, wires, etc.) and diverse crystallographic facets. MNPs can be designed to contain different types of atoms depending on their location in corners, faces or edges, that will present different reactivity properties, which can be of interest for selective catalysis.[21]

Well-crystallized MNPs have close packed structures (bcc, fcc or hcp) where the central atom is surrounded by successive layers of atoms in order to decrease their surface energy. They are considered as full-shell clusters and the magic number rules for them can be applied, allowing to obtain several data on the different atoms presented in the outer and inner shell of the materials.[22] For example, a full-shell cluster containing a total of 13 atoms, which is the smallest possible size, apart from the central atom, the surface layer is made of 12 atoms corresponding to the maximum possible coordination number. Larger clusters will contain a total number of atoms as 55, 147, 309, etc., leading to NPs of *ca.* 1.1, 1.6 and 2.0 respectively, in the case of ruthenium. The ratio of surface metal atoms in NPs is accessible by knowing the NP crystalline structure and the mean size.[23]

In addition, it is possible to calculate the approximate number of metal atoms depending on their location at the surface of the NPs, *i.e.* edges, corners and faces (table 1.1).[24] It can be observed that smaller the NPs are, higher their surface atom numbers are. Some NPs have been reported to be complete full-shell clusters, among them gold NPs, such as $Au_{55}[P(C_6H_5)_{13}]_{12}Cl_6$.[25]

Table 1.1 Close-packed magic number clusters. The rest of the metal surface atoms highlighted in blue are located in the NP faces.

	Number of shells			
	1	2	3	4
General description	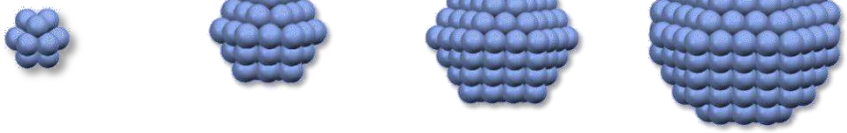			
Size of RuNP (nm)	0.7	1.1	1.6	2.0
Total number of metal atoms	13	55	147	309
Number of surface atoms (%)	92	76	63	52
Edge atoms (%)	0	54	41	29
Corner atoms (%)	92	22	8	2

Thus, at very small sizes ([1.0 - 2.0 nm]) the properties of MNPs can be highly variable due to their difference in metal surface area, size, shape, composition, crystalline structure, etc. Therefore, a precise control of MNPs size, stability and reactivity becomes crucial. Meaning that the synthesis of MNPs has a major impact or a direct correlation in modifying the energy gap, which is part of the novel properties of these materials.

The potential of MNPs in catalysis has been known since decades through the development of heterogeneous catalysts where metal nanoparticles are deposited into a support.[26] In the last 25 years, the field of MNPs has known a renewed interest with numerous efforts devoted to their controlled synthesis, which is a great advantage for an accurate study of their catalytic properties and make them suitable for a target reaction.

The use of MNPs in catalysis (figure 1.4) is based on the assumption of their high metal surface area, where surface active sites may have a direct interaction with the substrates, thus

mimicking homogeneous catalysts. But due to their low solubility in reaction solvents, which depends on the stabilizing agents used for their synthesis, MNPs are often described as a semi-heterogeneous catalyst.[27] Moreover, catalysis is considered as colloidal when MNPs form stable suspensions in the reaction solvent (aqueous or organic). In the other hand, supported catalysis concerns to MNPs deposited onto or in the pores of a support (carbon-based materials, metal oxide materials such as SiO_2, TiO_2, Al_2O_3, etc.).

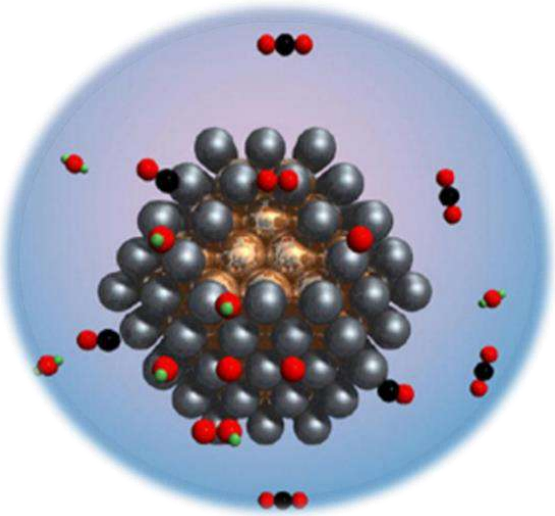

Figure 1.4 Nanocatalyst are claimed to have better activity and selectivity than that of bulk materials.[28]

Published studies have demonstrated that metal nanoparticles are more active than their bulk metal material counterparts for several catalytic reactions ([14],[29],[30]) Some of these reactions are for instance:

- Reforming reaction
- Hydrocracking
- Heck type couplings
- Hydrogenation
- Oxidations
- McMurry couplings
- Hydrosilylation
- Suzuki couplings
- Cycloadditions

Since the last five years, there has been an increased interest in the use of MNPs for the catalytic water splitting reaction. It has been shown by several groups that nanomaterials can be more active than their bulk metals in both hydrogen evolution reaction (HER)[31] and oxygen evolution reaction (OER)[32] (figure 1.5).

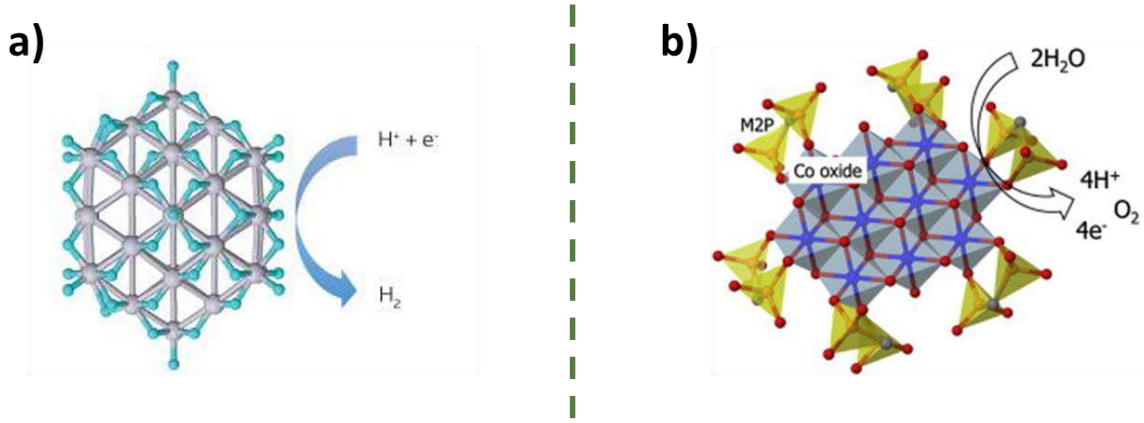

Figure 1.5 MNPs used in the water splitting reaction. a) HER[31] & b) OER.[32]

Since a precise control of the MNPs characteristics (size, shape, crystalline structure, etc.), stability and surface reactivity are crucial for their application in catalysis, different synthesis tools have been developed.

1.2 Synthesis of Metal Nanoparticles

With the noticeable exception of some 11 superatomic clusters that are electron- and atom-precise compounds,[([33]–[35])] nanostructures with well-defined structures (nanoclusters) are not often found in the literature. In most cases, nanosystems presenting a lower crystalline order in their outer and inner structures are reported. This is particularly true for very small NPs which are often less crystallized. In this context the materials are named as nanoparticles, nanostructure, colloids or nanosystems.

There are two main methodologies to synthesize MNPs (figure 1.6). The top-down procedure involves the granulating of bulk materials to reduce their size by different physical methodologies (thermal and mechanical) or chemical grinding and the subsequent stabilization of the generated material by adding a protective agent. Nevertheless, this approach produce irreproducible materials with non-controlled size.[36]

The other technique, bottom-up, is widely used by the scientific community interested in catalysis because it can provide nanoparticles with well-controlled size, structure and surface which is crucial for designing a reliable catalyst. Additionally, this methodology allows to get

reproducible nanosystems that can be deeply analyzed and characterized. This approach is based on the release of metal atoms, followed by their nucleation into seeds or nuclei and then the growth of NPs till certain size is reached. The growth is determined by the reaction medium or/and the presence of protective ligands.[37]

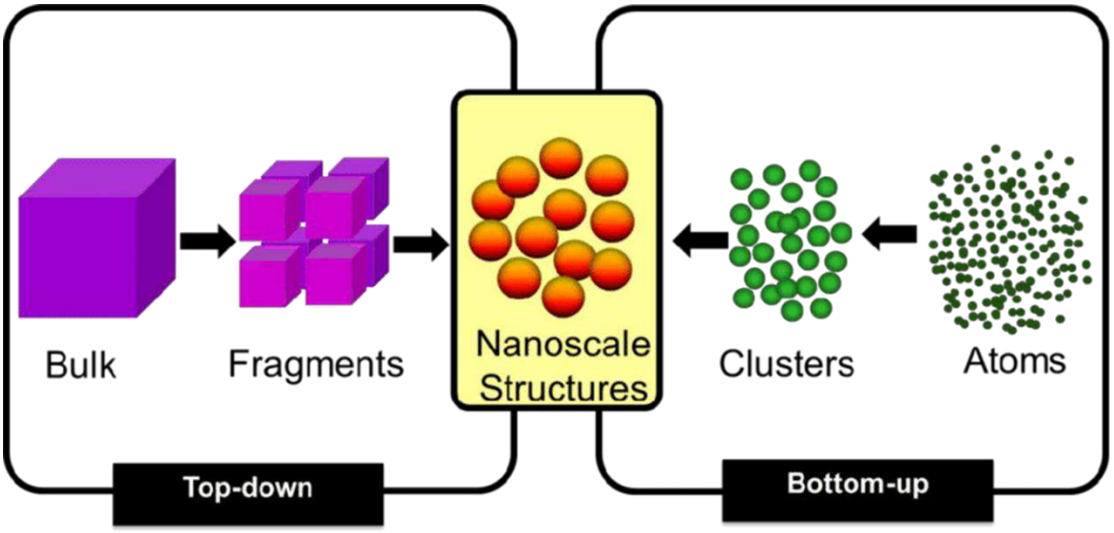

Figure 1.6 Main approaches for the synthesis of MNPs.[38]

1.2.1 Synthesis of MNPs in Solution

Our goal in this work was to synthetize well-defined metal nanoparticles which can be studied by an experimental and theoretical approach. Therefore, a bottom-up type of synthesis was chosen. MNPs can be formed in diverse ways, either in vapor (flame synthesis)[39] or solution. Due to experimental performance, instruments and basically to the difficulties met in the NPs synthesis, solution methodology was selected as the synthesis approach of MNPs.

Various methods for the synthesis of MNPs in solution have been developed, such as:

- Chemical precipitation or salt reduction[40]
- Hydrothermal method[41]
- Photochemical or sonochemical decomposition[42]
- Electrochemical reduction[43]
- Organometallic decomposition[44]
- Sol-Gel method[45]
- Polyol method[46]
- Radiation induced synthesis[47]

Synthesis of MNPs in solution usually offers homogeneous populations with narrow size distributions. However, this depends on the mechanism of NPs formation and consequently on the reaction conditions.

1.2.2 Formation Mechanism of MNPs

The uniformity and reproducibility of MNPs populations depend on the nucleation mechanism and the subsequent growth of them.[27]

Whilst the formation of MNPs has been described by the LaMer mechanism for supersaturate reaction media, however this approach was not accurate enough to describe diluted systems.[48] The gradual formation of nanoparticles is based on a three step process: nucleation, growth and agglomeration.[49] In the past decade, a four-step general mechanism has also been published for the salt reduction method that consist in two autocatalytic surface steps, namely growth and bulk formation stages (scheme 1.1).([50],[51])

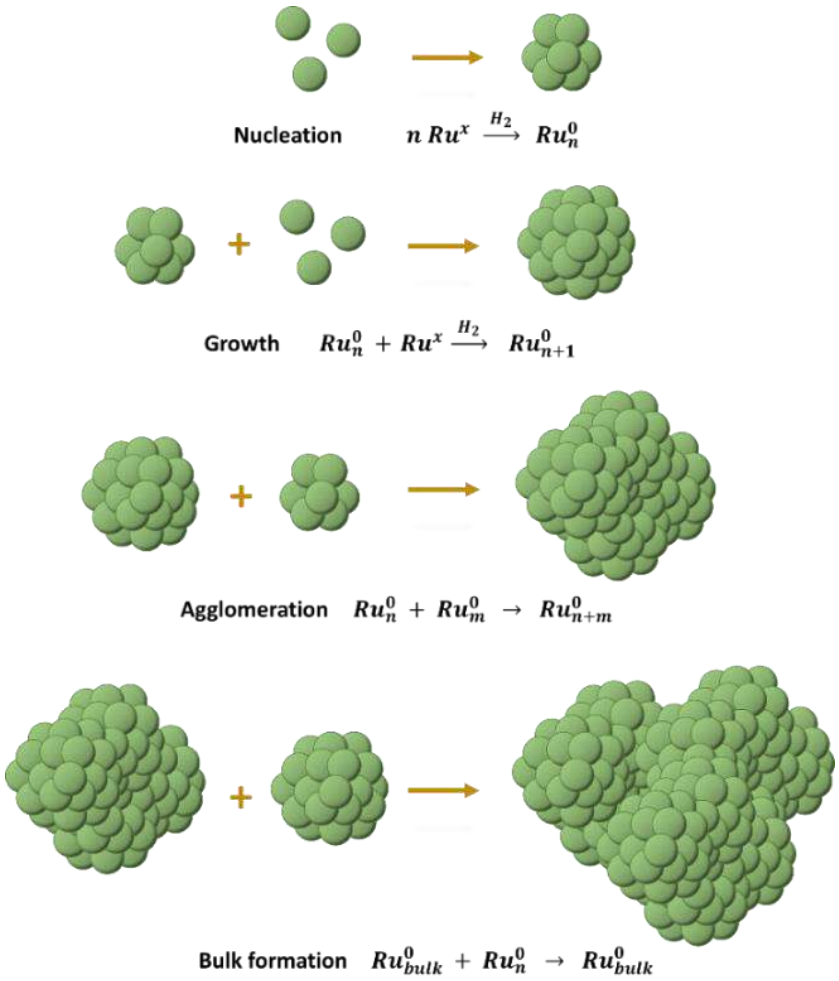

Scheme 1.1 Mechanism of formation of MNPs described for the metal salt reduction method.

When the nucleation step is started with the reduction of the metal salt, the zero-valent atoms approaches to each other to form irreversible metal seeds whose viability depends on the saturation of the solution. Then, the first autocatalytic process (growth) happens through the diffusion of metal nuclei to the preformed seeds. Later, if the previous step does not stop, the formed nanosystems start to get closer and to form aggregates and later on bulk materials. Therefore, the presence of a stabilizer that prevents the two last steps is required in order to obtain MNPs. Thus, the growth process is a crucial step that underlines the importance of the stabilizing agent in order to control the MNPs size and morphology.

Nevertheless, the production of homogeneous nanoparticles in size and morphology depends greatly on the differentiation between nucleation and growth processes. When these

processes are overlapped, the growth procedure will depend on the specific type of seeds formed during the nucleation procedure, so-called Ostwald ripening.[52] If no differentiation is observed, then an heterogeneous nanosystem will be produced. As a counterpart, homogeneous systems population will be observed if the processes can be differentiated (scheme 1.2).

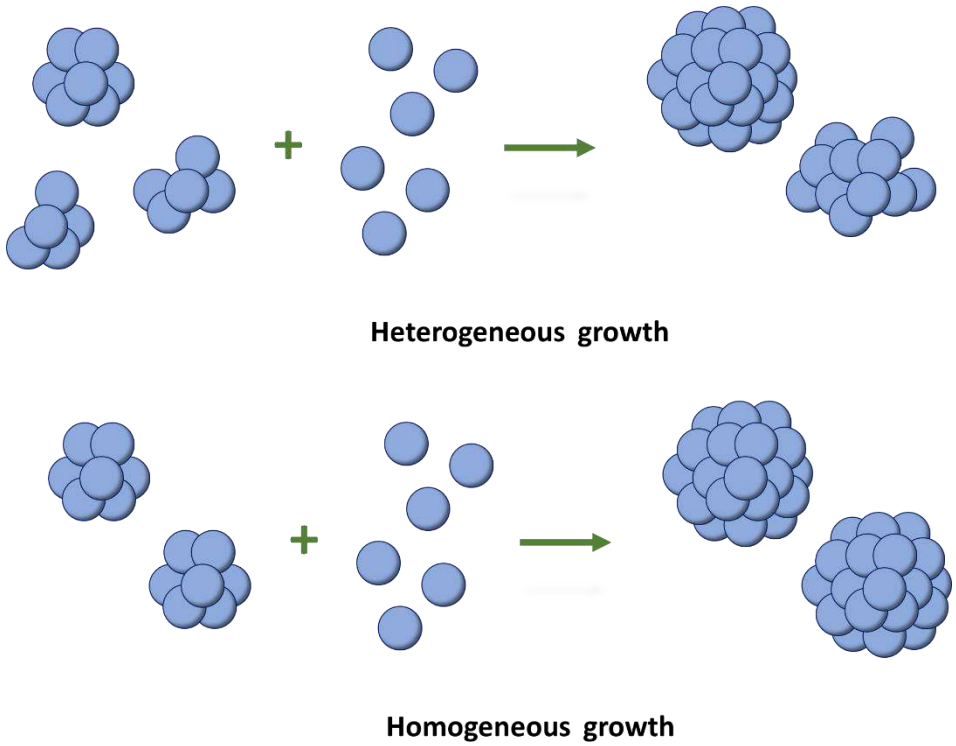

Scheme 1.2 Heterogeneous and homogeneous formation of MNPs according to the growth process.

1.2.3 Stabilization of MNPs

MNPs possess a high quantity of surface energy which makes them thermodynamically unstable. In order to reduce this phenomenon, particles tend to attract each other in the absence of repulsive forces, which leads to their agglomeration and coalescence.[18] Thus, it is necessary to avoid the continuum growth of MNPs to elude the formation of aggregates or bulk materials by adding a ligand barrier, namely as stabilizing agent, aiming to produce homogeneous and well-defined MNPs (figure 1.7).[53]

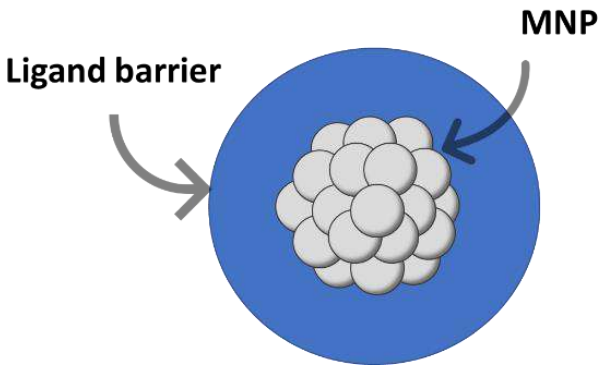

Figure 1.7 Representation of stabilized MNP.

There are mainly four different modes of stabilization (figure 1.8): electrostatic (ammonium salts), steric (polymers, dendrimers, ligands), electrosteric (polyoxoanions) and solid supports (zeolites, silica).[54]

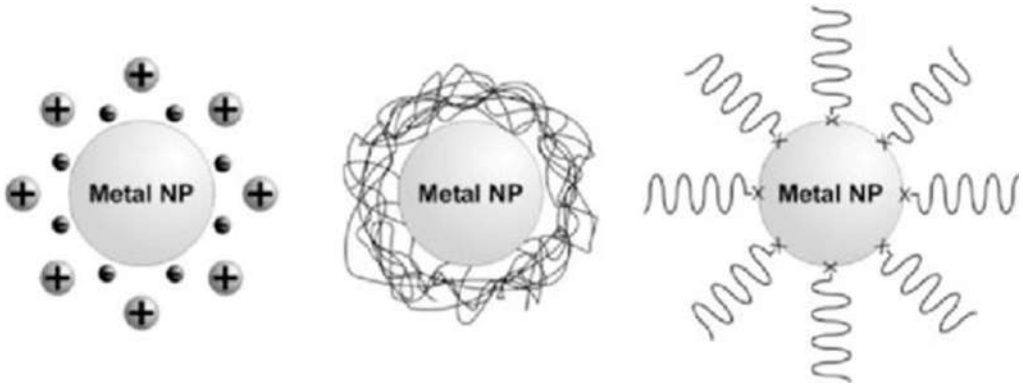

Figure 1.8 Representation of MNPs stabilized by electrostatic interactions, polymers and organic ligands, respectively.[54]

Steric stabilization mode allows to prepare homogeneous MNPs that are surrounded by a protective layer. Polymers and dendrimers, such as PVP[55] or PAMAM[56], are examples of stabilizers, being generally considered to have a low interaction with the metal surface. Ligands can have covalent interactions with MNPs that generally provides well-defined particles. The σ or π donation/back-donation to the metal surface of thiols, amines and phosphines are examples of these ligands which have been widely used. The donor strength of the stabilizing agent influences strongly the size and morphology of the nanosystems.[44]

Polymers or ligands are common stabilizers that can act against MNP continuous growth by forming an efficient barrier and allow obtaining homogeneous populations of well-defined MNPs. They can be used in the organometallic approach which is a well-known procedure to have at disposal well-controlled MNPs.

1.2.4 Synthesis of MNPs by the Organometallic Approach

The organometallic approach is a powerful method to produce homogeneous MNPs in solution. It is based in the use of organometallic complexes which typically have metal-carbon bonds (M-alkyl, M-olefin, etc.) that can be broken, hydrogenated or even displaced in mild reaction conditions (*T*, *p*). Ligands displacement or their decomposition generate uncoordinated metal atoms that thus constituting the metal source for the formation of MNPs.

This approach was first applied to form nickel nanopowders by the decomposition of a nickel organometallic complex ($[Ni(C_5H_5)_2]$) under hydrogen.[57] But later on, the hydrogenation of several metal complexes in the absence of any extra ligands was observed to generate bulk metal materials.[58] Therefore, the addition of a stabilizing agent is crucial to get stable MNPs. Various stabilizers have been used, in particular in the case of RuNPs, which allowed to develop this approach and get a large panel of particles.[59]

The organometallic approach (scheme 1.3) in essence treats with the decomposition in solution of an organometallic complex (or in some cases a metal-organic complex) in the presence of hydrogen (H_2) or carbon monoxide (CO) in mild conditions (low temperature and gas pressure). The minimum amount of stabilizing agent is added in order to limit the quantity of organics at the metal surface, but this depends on the systems. Olefinic complexes are generally preferred because they easily decompose under hydrogen at low temperature. The use of hydrogen allows avoiding the presence of derivatives from strong reductant agents such as $NaBH_4$.[60] Moreover, the release of alkanes that result from ligand hydrogenation is not an issue because they are inert towards the metal surface and can be easily eliminated under high-vacuum. This approach allows thus to limit the presence of pollutants at the metal surface.[44]

The control of the growth of the NPs is possible by the addition of a stabilizing agent which can be a polymer or a ligand. Various ligands have been explored, in particular for RuNPs, being considered as strong or weak ligands depending on their interaction with the metal surface.[61]

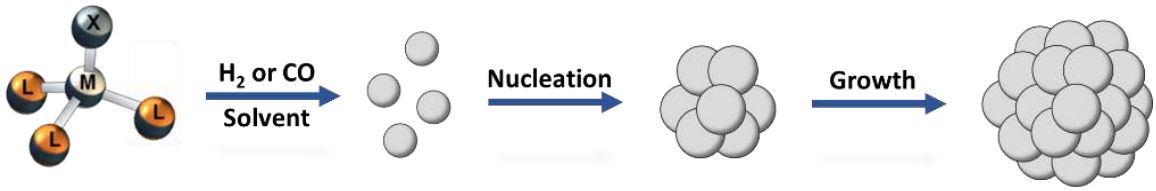

Scheme 1.3 Representation of the synthesis of MNPs by the organometallic approach.

The organometallic approach implies to have adequate metal complexes (which mostly are air or water sensitive and require to be handled under inert atmosphere) as metal source. It presents several advantages that allow to produce MNPs having a clean metal surface and a specific amount of added ligands that protect them from agglomeration and coalescence. The ability to use different types of stabilizers (polymers or organic ligands) is exploited in favor to design specific MNPs sizes and morphologies with tailor-made properties.[62] As it will be seen later, this methodology was used in this work in order to synthesize model RuNPs with the aim to have a better control of the structure/properties relationships and after to design appropriate nanocatalysts for the water-splitting process.

The types of organometallic complexes commonly used for this technique are enlisted hereafter.

- Carbonyl complexes: $[Fe(CO)_5]$; $[Ru_3(CO)_{12}]$
- Olefinic complexes: $[Ni(COD)_2]$; [Ru(COD)(COT)]
- Alkyl complexes: $[Pt(CH_3)_2(COD)]$
- Allyl complexes: $[Co(\eta^3\text{-}C_8H_{13})(\eta^4\text{-}C_8H_{12})]$; $[Rh(\eta^3\text{-}C_3H_5)_3]$

1.3 DFT for Modeling Organometallic Nanocatalysts

Nowadays, several technological and industrial processes are based on the use of catalytic processes, leading to a more efficient industry. This issue produced better life conditions, however it also generated environmental problems. In order to solve these problems, the scientific

community has rulled out the importance of disposing more efficient catalysts and possibly which are environmentally friendly composed of earth abundant materials.[63] This concerns heterogeneous MNPs but also modern nanocatalysts (either in solution or dispersed into a support) which are in general better defined.

Due to the surface interaction of the catalysts with the substrates, their viability and efficiency are determined by their electronic structure which is also intrinsically related to the structure and composition of the catalysts (figure 1.9).[64] Therefore, it is possible to design or choose between several types of catalysts for a specific chemical reaction. Theoretical descriptions of solid catalysts are of high importance because they study the adsorption-desorption phenomena of the substrates onto catalysts, which is a crucial step for knowing their reliability and selectivity.[65]

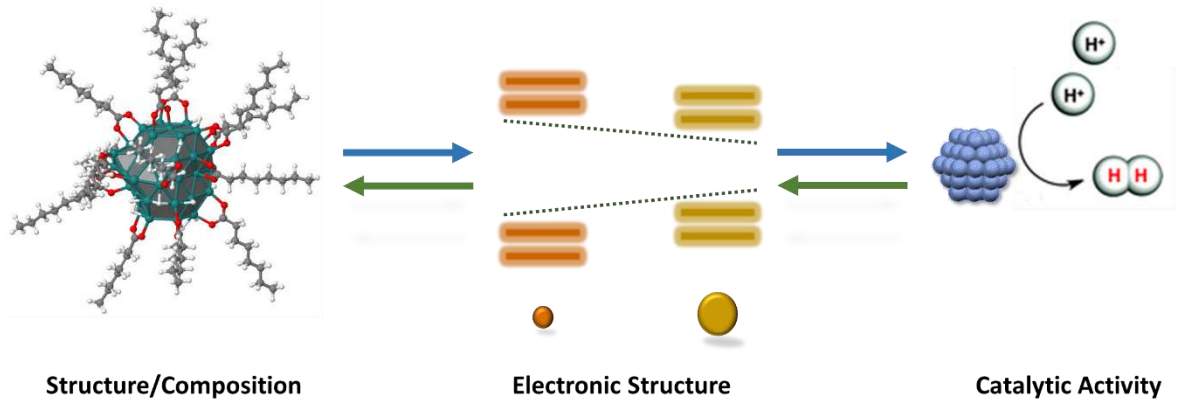

Figure 1.9 Representation of the link between MNPs structure-composition, electronic structure and catalytic activity (e.g. HER).

Since a couple of decades, Density Functional Theory (DFT), despite some weaknesses (such as a bad description dispersive van der Waals interactions) and the unpleasant profusion of functionals, is considered as a tool of choice in the rationalization of the performance of heterogeneous[([66],[67])] and homogeneous catalysis.

Regarding heterogeneous catalysis, the standard strategy consists in the description of the catalysts by slab models and in taking advantage of periodic-DFT calculations. Such methodologies are also designed to efficiently describe the electronic density of metallic systems, *i.e*. they successfully solve the problem of SCF convergence due to the degeneracy of electronic states at

the Fermi level. This is why in the present work, although it was considered finite-size ruthenium nanoparticles, it was used one of the reference periodic DFT software, VASP.[[68],[69]]

Since the seminal work of Thomas and Fermi[[70],[71]] and later on of Kohn and Sham,[72] DFT has revolutionized modern computational chemistry, thanks to the Generalized Gradient Approximation (GGA) functionals, such as PBE.[73] They are fast enough to allow the treatment of extended systems and are more accurate for describing reaction energies or the relative stability of isomers than the Local Density Approximation (LDA).[72] This is the functional used in this work, although in the molecular DFT, GGA functionals are nowadays replaced by the so-called hybrid functionals, which contain a fraction of Hartree-Fock exchange.

Even so, using hybrid functionals in periodic-DFT calculations increases the computational cost by an order of magnitude, and it does not significantly improve the description of metallic systems, although it has been proven that it can slightly change the picture regarding the preferred grafting sites of adsorbates and the associated energies.[74]

However, GGA functionals such as PBE or revised-PBE[66] have proven their ability to successfully address catalytic processes on transition metal surfaces and alloys.[75]

1.3.1 Methods for Describing MNPs

Several methodologies for describing the electronic properties of metal surface have been reported in the literature. Each one of them can be useful for obtain the morphology of MNPs, specify their crystallinity, describe the MNPs core or inner shell or the optimization of geometries due to the relationship between crystalline structure and morphology. These methods are enlisted hereafter.

- Wulff construction theorem[76]
- X-ray diffusion for RDF profiles[77]
- Monte Carlo method[78]
- Reverse Monte Carlo method[79]

1.3.2 Strategy Used to Define the Surface of MNPs

One strategy for modeling MNPs is to consider them as an assembly of the crystallographic planes they exhibit in the synthesized nanoparticles. Each surface is modeled by a metal slab and it is possible to take advantage of this periodicity in order to efficiently solve the Schrödinger equation. For example, in order to account for the possible specificity of the surface chemistry of each crystallographic plane, a 2.0 nm hcp RuNPs should be modelled at least by $(10\bar{1}0)$, $(10\bar{1}1)$ and (0001) planes. On top of that, the steps that have been proven to exist in such NPs must be modeled by high index crystallographic planes, such as the $(10\bar{1}5)$ plane which accounts for the so-called B_5 sites.[80]

This methodology is a well-defined approach for very large NP, but it involves representing the whole nanoparticle by several planes, which makes it a computationally prohibitive method for NPs that have complex shapes. Another hybrid approach, such as the one depicted in figure 1.10 in case of a PtNP deposited on a substrate,[81] consists in describing the exhibited surface of the PtNP by a slab and its corners and lateral walls by an appropriate mid-size NP.

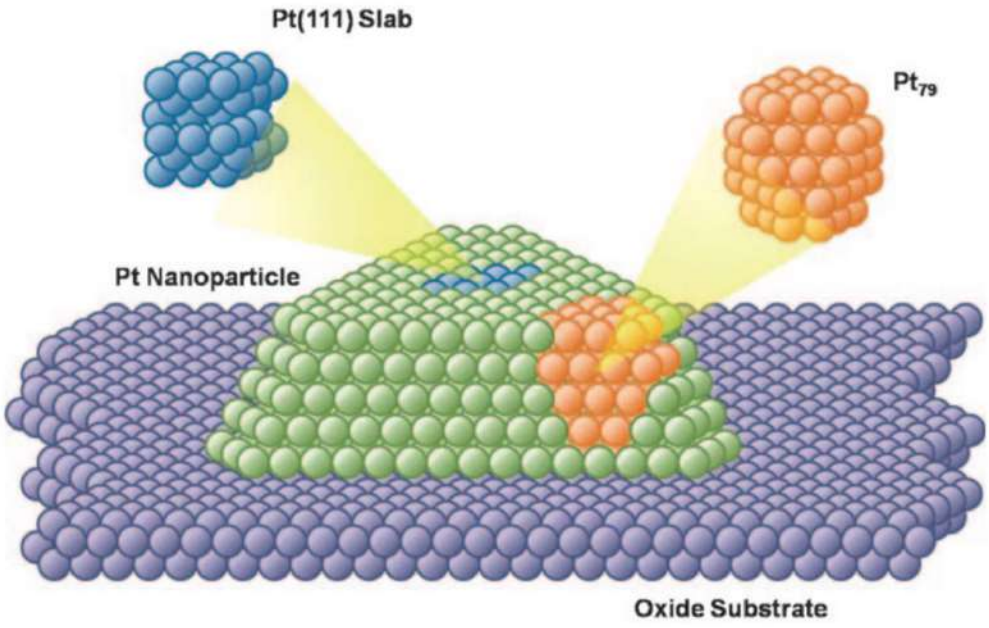

Figure 1.10 Representation of a PtNP supported onto an oxide substrate (support). The PtNP exhibits a combination of a Pt(111) slab layers for the inner facets and Pt_{79} nanoparticles for modeling the edge, corner, and nearby sites.[81]

Although, synthetized nanoparticles may possess different irregularities in their structure, as well as complex shapes, and it is difficult to describe or model them as a superposition of infinite crystalline structures. Therefore, the inclusion of different reactive sites as B_4 or B_5 or of corrugated surfaces makes theoretical calculations more reliable.[80] This methodology was not used in this work because the experimental RuNPs are small ([1 - 2 nm]) and should be considered as a superposition of edges and corners rather than a superposition of infinite crystallographic planes. Leaving aside the fact that finite size effects make their electronic structure different from the bulk metal.

Therefore, the nanosystems considered in this work are modelled by large clusters. This methodology offers the possibility to observe the whole nanoparticle as a single entity considering different types of surface and reactive sites. This provides a better representation of the experimental features. It has been shown with this approach that it is possible to account for several surface properties (IR, surface composition, etc.) observed in experiments.[82]

The model developed in the previous reference (*see* section 6.2.1) is a spherical 1.0 nm hcp crystal, with two (0001) planes, sidewalls reminiscent of $(10\bar{1}1)$ planes, a corrugated surface and a tip that models B_5 and B_4 sites. It is an all-in-one model that represents the diversity of colloidal ([1 - 2 nm]) RuNP. In the framework of periodic-DFT methods, it is described inside a unitcell, with a vacuum large enough to avoid spurious interactions between the cluster and its periodic images (figure 1.11).

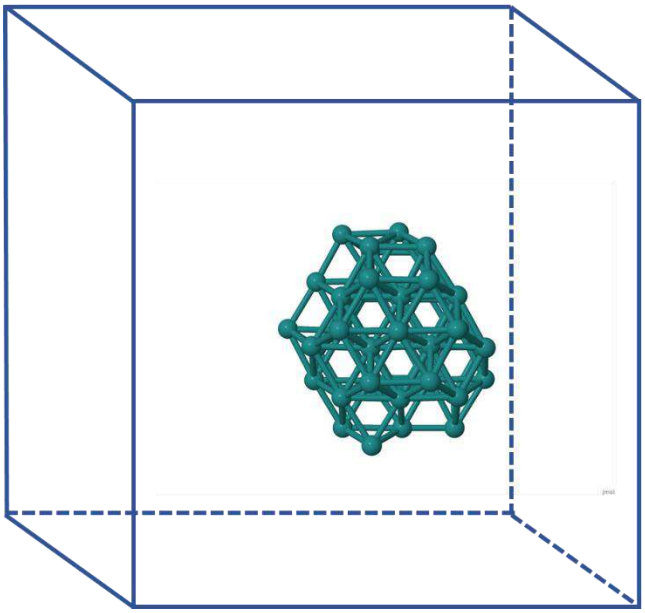

Figure 1.11 Ru_{55} hcp cluster in a unit cell optimized by VASP..

1.4 Ruthenium Nanoparticles

Ruthenium is a d8 transition metal ([Kr] $4d^7$ $5s^1$) with an atomic mass of 101.01 $g.mol^{-1}$. This electron rich metal was discovered in 1843 by the Russian G. Klaus. Ruthenium is isolated from other metals by a series of chemical processes which final stage is the hydrogen reduction of ammonium ruthenium chloride. This metal is not easily oxidized, however under oxygen pressure forms its more stable oxide (RuO_2).[83]

For many years, ruthenium-based catalysts have been used in the industry for a wide range of chemical reactions or even in technological devices. For example, $Ru_3(CO)_{12}$ has been applied as catalyst to produce ammonia[84] or acetic acid.[85] Other ruthenium derivatives are also used for olefin metathesis,[86] oxidations or hydrogenations.[87]

Due to its chemical and physical properties, ruthenium has been used in several catalytic processes. However, in order to increase its profitability, the scientific community focused on extending its activity and selectivity. Owing to their intermediate properties between those of bulk materials and molecular complexes, ruthenium nanoparticles (RuNPs) have been developed with high interest. It is expected from their high surface to volume ratio to get a high active surface.

1.4.1 Synthesis of RuNPs

RuNPs were first synthetized by the reduction of $RuCl_3$ in the presence of borohydrides and surfactants.[88] Then, the nanoparticles were carried on under softener conditions aiming to design better homogeneous nanoparticles. In this way, RuNPs were also produced by the reduction of $RuCl_3$ in polyol.[89] This method, so-called "the polyol method" has the advantage to allow the formation of RuNPs in milder conditions and to provide more homogeneous populations of NPs while using only a polyol as both reducing and stabilizing agent.[90] Also, ligands can be added in order to tune the RuNPs characteristics.

Another efficient approach to produce RuNPs is the organometallic approach which is the method chosen in this PhD work. It is based on the decomposition of a ruthenium organometallic complex under mild reaction conditions and in the presence of a stabilizing agent. As a consequence, monodisperse RuNPs can be obtained with a clean surface (absence of side products).[77]

Different organometallic precursor have been used to synthetize RuNPs (figure 1.12) among them it can be found metal carbonyl complexes ($[Ru_3(CO)_{12}]$) and allyl/olefin complexes such as $[Ru(COD)(\eta^3\text{-}C_3H_5)_2]$.[91] However, the most employed complex is the ruthenium(1,5-cyclooctadiene)(1,3,5-cyclooctriene) ([Ru(COD)(COT)]) which represents an ideal compound due to its fast decomposition at low temperature (≤ r.t.) and low gas pressure ([1 - 3 bar] H_2). Another important advantage is that the hydrogenation of this precursor releases only cyclooctane as side product, which is inert towards the metal surface and can be easily removed under high-vacuum.

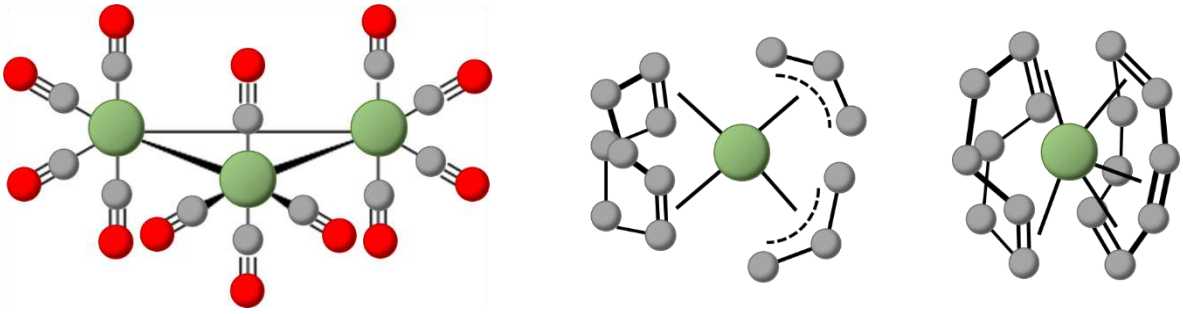

Figure 1.12 Representation of organometallic precursor used to synthetize RuNPs. $[Ru_3(CO)_{12}]$, $[Ru(COD)(\eta^3\text{-}C_3H_5)_2]$, [Ru(COD)(COT)], respectively.

The RuNPs synthetized by the organometallic approach generally present an hcp crystalline structure as for bulk ruthenium, and this even for amorphous RuNPs. But following other synthetic methodologies such as chemical reduction, formation of fcc RuNPs has been observed. It is worth to mention that these fcc RuNPs have presented a different catalytic activity than that of hcp RuNPs.[92]

Therefore, the reproducible control of the synthesis conditions is a crucial point for the study of RuNPs and their possible catalytic applications.

1.4.2 Stabilization of RuNPs

The nature of the stabilizing agent (ligand barrier) employed for preparing RuNPs can be adapted in order to obtain desired chemical and physical properties. This gives RuNPs a wide range of multifunctionality.[93]

The synthesis of RuNPs by following the organometallic approach with [Ru(COD)(COT)] leads to the hydrogenation of the olefins to cyclooctane which present weak interactions with the RuNPs. As a consequence, the particles start to agglomerate and precipitates as bulk material at least in common solvent used in the RuNPs synthesis.

For example, tetrahydrofurane (THF) has been shown that although its coordination ability at metal surface, it does not allow the formation of homogeneous NPs, leading to aggregates. This phenomenon is even worse when using *n*-pentane due to its absence of metal interacting functional groups. However, it has been demonstrated that a combination of an alcohol like methanol with THF, allows the formation of small RuNPs. Alcohols bearing an alkyl chain longer than ethanol are also efficient stabilizers of RuNPs without any extra ligand.[94]

In order to limit the agglomeration of the formed RuNPs, two different strategies have been developed. The first one implies the use of polymers as ligand barrier and the second is based on the addition of organic ligands than directly interact with the metal surface. Cellulose[95] and mainly polyvinylpyrrolidone (PVP) have been widely used to form RuNPs, these polymers

avoid agglomeration of the particles by providing a poor interacting ligand barrier with the RuNPs surface.[96]

On the other hand, organic ligands are very interesting stabilizers because they can modulate better their size and morphology due to its participation in the nucleation and growth processes during the NP synthesis. Given their different chemical nature, ligands offer a large variety of functional groups able to interact with the metal surface which will influence the growth of the particles, as well as the quantity of used ligand in the *in-situ* synthesis.

These variables can have different impact degrees on the RuNPs, depending on the systems either the size, dispersion, surface state or also organization of the particles. For example, RuNPs show smaller sizes when the electron donor strength of the ligand increase (figure 1.13).[93]

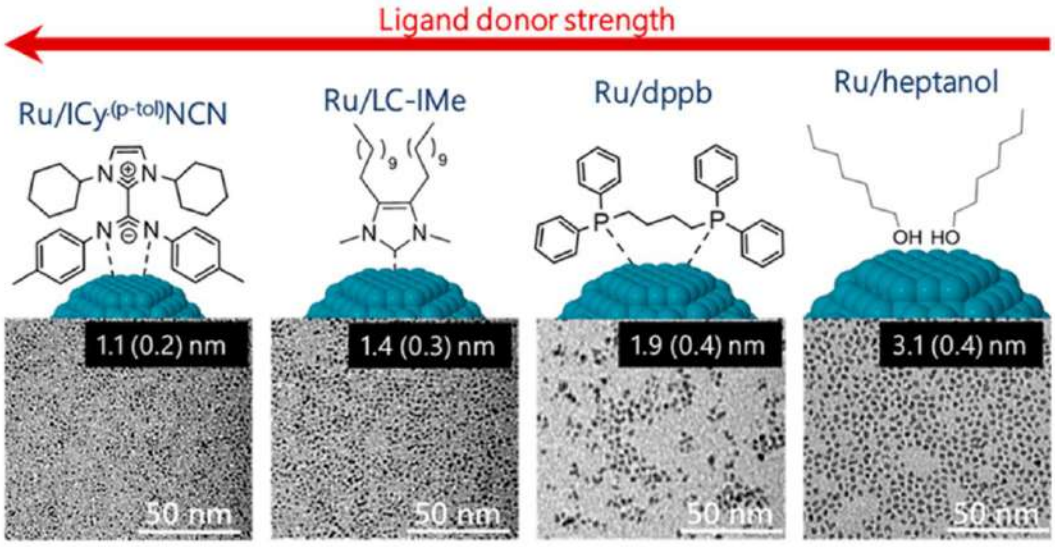

Figure 1.13 Variation of the size of RuNPs synthetized by the organometallic approach in relation with the ligand donor strength of the stabilizers. Ligands: 1,3- dicyclohexylimidazolium-2-di-p-tolylcarbodiimide; 1,3- dimethyl-4,5-diundecyl imidazol-2-ylidene; bis-(diphenylphosphino)butane, heptanol, respectively.[93]

In the last years, RuNPs have been widely synthetize through the organometallic approach by using different kind of ligands. The material reactivity was modulated and tested by changing the type of ligand used for its synthesis. Hereafter are enlisted some examples of the used ligands.

- Alcohols: heptanol, propanol[94]
- Amines: hexadeclamine (HDA), octylamine[97]
- Aminophosphines: 1,3,5-tri-aza-7-phosphaadamantane (PTA)[98]
- Phosphines: bis-(diphenylphosphino)butane (dppb)[99]
- N-heterocycles carbenes (NHCs): *N*,*N*-di(*tert*-butyl)imidazol-2-ylidene[100]
- Pyridines: 4-(3-phenylpropyl) pyridine[101]

RuNPs are widely used as reference because it is possible to shed light on their chemical behavior and on their surface/structure properties due to the absence of magnetic perturbations, such as Knight shift.[102] At least at the range size of [1 – 2 nm],[103] which make the obtained RuNPs suitable to be characterized by solid and liquid NMR studies.([104],[105]) The almost absence of this phenomenon is highlighted when oxygen spacer are present in the interface of the formed hybrid material, such as hydroxyl group.[106] As a result, it has been possible to detect mobile hydrogen species on RuNPs[107] and even get a clear evidence of the interaction between ligands such as phosphines[108] or carbenes[100] with the metal surface. The last findings have opened a new branch for studying the influence of the ligands onto the RuNPs in order to change their reactivity and selectivity in several catalytic reactions.

In the frame of the present work, it was stablished to use different carboxylic acid as ligands to stabilize RuNPs which to our knowledge have not been deeply yet studied. In the literature, is recently reported only one attempt to create RuNPs with organometallic chemistry tools by using hexasubstitued fullerene ($C_{66}(COOH)_{12}$) as stabilizing agent.[109]

1.4.3 Experimental and Theoretical Characterization of RuNPs

Ligand-stabilized RuNPs are hybrid materials that possess a metal core and an organic layer made of ligands capping the metal surface. Since the interaction between metal core and ligands in NPs can be strong, it is difficult to characterize them experimentally, e.g. NMR or IRFT, due to the low mobility of the organic layer.[110]

Therefore, a trustworthy RuNP theoretical model is highly desired in order to describe a synthetized nanosystem, aiming to understand its activity and selectivity properties for a target catalytic reaction for instance. Especially, the relationships between the metal core and the coordinated species in terms of steric and electronic effects are required in order to be able to adjust the synthesis conditions for reaching identified properties. Taking into account the QSE and the degeneracy of the electronic states at the Fermi level, a good approach to modelling the RuNPs is based on periodic-DFT methodologies.[111]

Combining theoretical and experimental tools has been already validated as a powerful approach to describe the electronic structure of MNPs and also the interactions of the metal surface with the capping ligands. Some examples of the findings obtained by the combination of these approaches are enlisted below.

- Hydrogen adsorption sites on an infinite Ru(0001) slab model in different crystalline close packs compared with ^{2}H solid-state MAS-NMR.[112]
- Reactive hydrogen species on ruthenium clusters ([Ru_4] & [Ru_6]) by experimental and DFT NMR.([113],[114])
- Surface composition of RuNPs in equilibrium with syngas.[82]
- Enantiospecific CH activation using ruthenium catalyst corroborated by the Ru_{55} model.[115]

It is possible to establish a fruitful dialog between theory and experiments thanks to a combination of MNPs characterization methods. In this way, the nanosystems can be better described in terms of structure, composition, catalytic activity and selectivity, due to the wider vision that these joint approaches can provide. In the following table a comparison of the different analytical techniques, experimental and theoretical, to determine the RuNPs properties is presented (table 1.2).

Table 1.2 Experimental and theoretical techniques for determining RuNPs properties.

Property	Technique	
	Experimental	Theoretical
Composition	EA ICP EDX	Capping ligands adsorption energies
Shape and structure of the metal core	WAXS SAXS TEM	*Ab initio* thermodynamic + Wulff construction (Gibbs energy) Reverse Monte Carlo (RMC)
Adsorption sites of ligands	Solution or solid-state NMR IR AFM (extended surfaces only)	NMR IR Theoretical AFM
Number of surface ligands	L/[M] ratio Titration	*Ab initio* thermodynamics
Adsorption strength of ligands	Spectroscopy (IR & NMR)	Energies (usually DFT)
Catalytic activity **Reaction mechanisms**	Identification of products Yields TOF	Frontier orbital theory / correlation diagrams / COHP Multi-step reaction studies (QST, NEB)
Electronic density	STM	DOS MOs & COHP

1.4.4 Modification of RuNPs by Ligand Exchange

MNPs multifunctionality can be improved by changing their size, morphology and their capping ligands. All of these characteristics are intrinsically related and determine the stability, activity and selectivity of the nanosystem.[[13],[36]] Initially, MNPs characteristics were modified by changing their synthetic conditions but it is also possible to tune them by modifying preformed nanosystems.

For instance, the stability of MNPs can be improved by exchanging the molecules laying on their surface with the aim to provide new properties and functionality to the MNPs.[116] In almost all cases, the exchanged ligand has lesser interaction with the metal surface than the new capped

ligands. Meaning that a necessary condition to have an efficient ligand exchange is to add a stabilizing agent that will stronger bound to the MNPs surface (figure 1.14).[117]

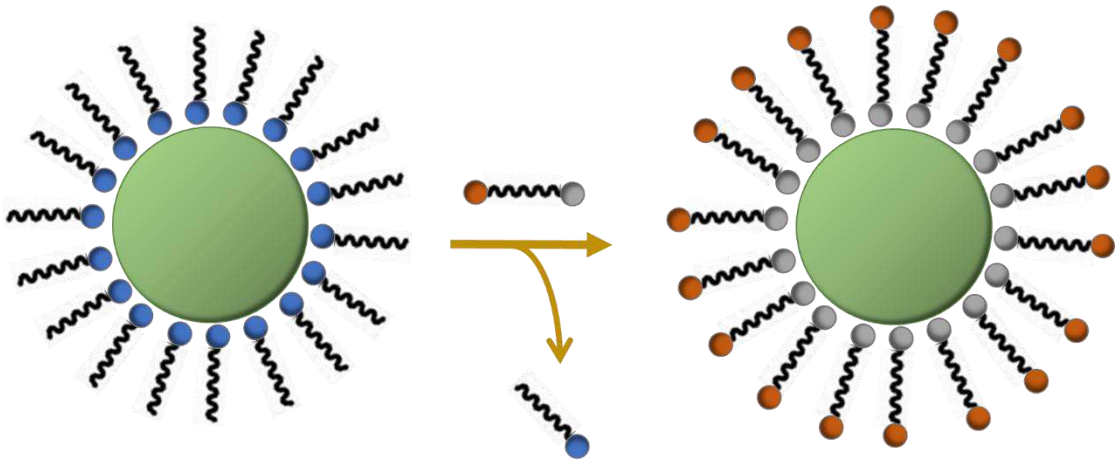

Figure 1.14 Representation of ligand exchange at the surface of MNPs.

For noble metals, it has been reported that thiol derivatives have a high affinity for MNPs surface making them suitable compounds to be incorporated onto the nanosystem, e.g. alkanethiolates for chelating thiols.[118] Nevertheless, it is important to point out that the ligand exchange leads to another type of MNPs stabilization. Therefore, the size, shape, composition and surface-state of the nanoparticles can be modified.[119]

Ligand exchange is often applied for changing the chemical and physical properties of preformed nanoparticles. Since MNPs are usually synthetized in organic solvents, it could be necessary to make them soluble in water by a phase transfer.[120] This can be obtained by making a ligand exchange between hydrophobic and hydrophilic ligands or vice versa (figure 1.15).([121],[122]) This methodology is often followed for increasing the MNPs biocompatibility,[123] however it can be also used for applications in catalysis in neat water or in biphasic conditions.

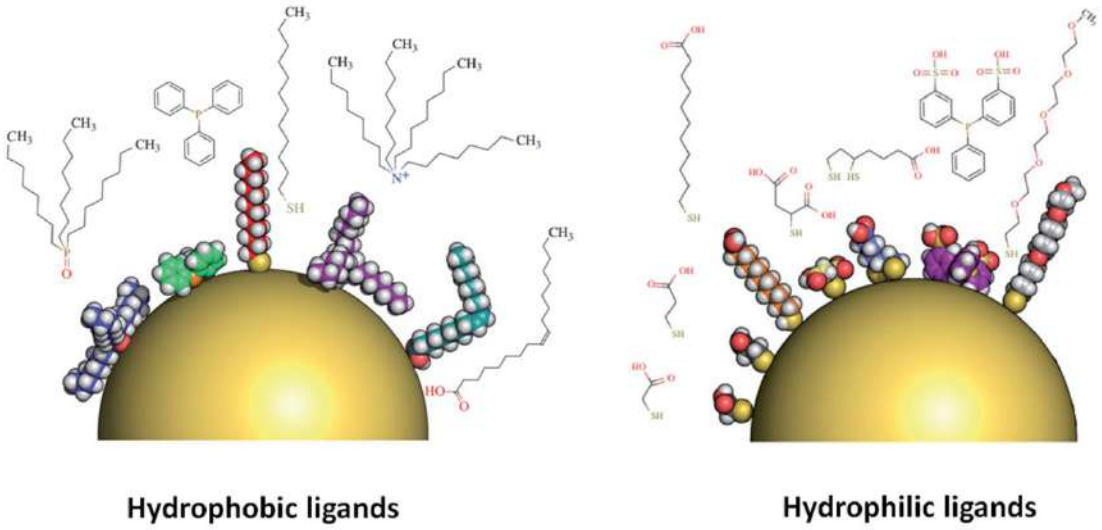

Figure 1.15 Some hydrophobic and hydrophilic capping ligands used for MNPs phase transfer.[121]

This methodology can be also applied for the identification of the real nature and composition of a stabilizing agent onto RuNPs.[124] By taking into account the ligand bond strength, it is possible to remove ligands from the surface of preformed RuNPs and replace it by dodecanethiol. In this way, the RuNPs get poisoned and the exchanged ligand can be characterized.[125]

It is well-known that the hydrogenation of benzene under reductive atmosphere cannot be afforded in normal conditions and it is necessary the use of a catalyst.[126] Ruthenium-based catalysts have been widely used for the olefin or arenes reductions and its potentiality has increase when RuNPs is used. Indeed, the presence of hydrogen atmosphere and RuNPs is favorable to the hydrogenation of these functions present in the skeleton of the ligands.[27] Therefore, the use of ligand exchange is a strategy to circumvent this issue and insert alkyne- or aryl-based ligands onto RuNPs.([127],[128])

In the present work, the technique of ligand exchange was applied as approach in order to introduce carboxylic acids containing aryl substituents onto the issued RuNPs by avoiding their hydrogenation. The main perspective was to insert polypyridyl based photosensitizers (PS) having carboxylic acids as pending groups to anchor them at the surface of preformed RuNPs and obtain hybrid nanomaterials PS-RuNPs.

1.5 Interest of RuNPs in Catalysis

A crucial role for the industry progress has been the development of novel highly active and selective catalysts.[26] During the last decades, catalysts have been the center of attention of many research institutes in order to improve or develop novel heterogenous or homogeneous catalyst. Concerning MNPs they have also attracted a lot of interest from the scientific community owing they combine advantages both from homogeneous and heterogeneous catalyst, such as active surface and electronic configuration, which make them very efficient catalysts in certain catalytic processes.[129] Some authors even point out that MNPs possesses the best catalytic efficiency.[130]

RuNPs have shown high catalytic activity for hydrogenation reactions such as selective reduction of olefins, arenes hydrogenation, etc., under mild conditions.[131] Aromatic ring reduction was obtained in the presence of RuNPs stabilized by diphosphites[132], however the efficiency of RuNPs was improved when the particles were stabilized by carbenes.[129] These studies evidenced the influence of the stabilizing agent into the catalytic properties of RuNPs.

For similar aryl reductive reaction, it was observed that the RuNPs size has also a direct effect on the catalytic performance.[108] By changing the quantity of stabilizing agent introduced during the NPs synthesis, it was possible to change the size of the particles and also their catalytic properties.[133]

The selectivity of the RuNPs for the reduction of styrene has been evaluated according to free active sites located onto their surface and their size.[105] For the aromatic ring reduction it is necessary to have enough free space at the surface of RuNPs. It is generally considered that a minimum of 3 neighboring ruthenium atoms is required to enable reduction an aromatic group, meaning it can be done only on faces. Meanwhile, alkenes can be reduced in the edges or corners of the RuNPs (figure 1.16).[134]

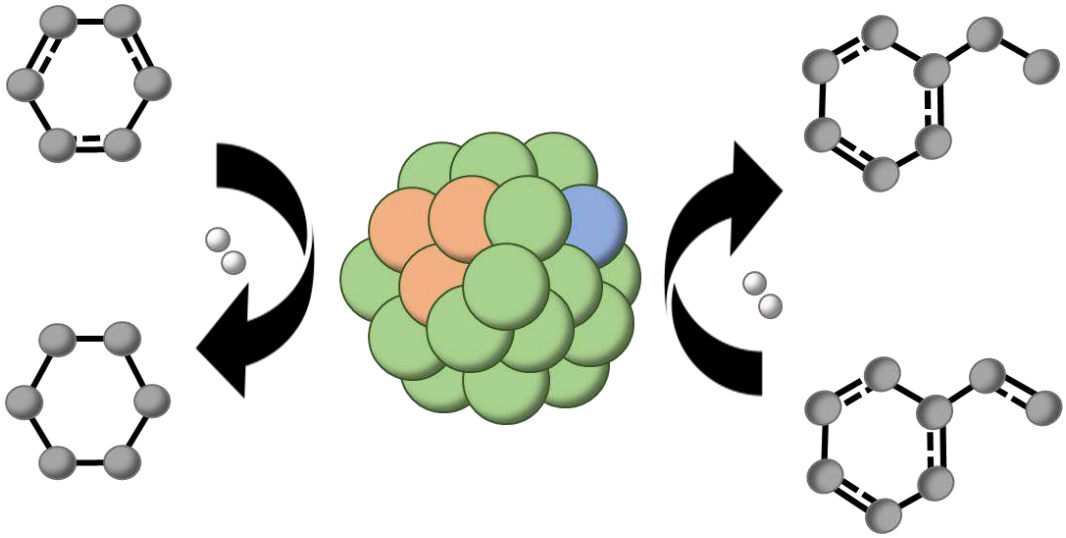

Figure 1.16 Representation of the selective hydrogenation catalysis performed on RuNPs.

There are many other catalytic reactions that can be performed by using RuNPs. Among them, it can be found the hydrogenation of carbon monoxide (CO) into alkanes for the Fisher-Tropsch Synthesis (FTS).[135] In the other hand, RuNPs have also demonstrated to be efficient catalysts for the oxidation of CO into carbon dioxide (CO_2).[136] In this context, it was observed that not only the size and type of capping ligand affect the catalytic performance, but also their morphology and crystalline structure.[92]

RuNPs are also active systems in photocatalysis or electrocatalysis.[9] Recently, studies were published concerning the use of RuNPs prepared by the organometallic approach for the catalytic HER reaction which is involved in the water splitting process.[137] In particular, it was found that RuNPs catalysts show a higher performance than ruthenium black powder, as it has been shown for ruthenium nanosystems functionalized by 4-phenylpyridine ligands. In fact, the latter presents an electrocatalytic activity close to that of platinum based catalysts, which are reported to be the most efficient catalysts for this reaction.[137] This again underlines the strong role of the stabilizing ligand onto NPs properties and reinforces the idea to develop fine comparative studies in order to identify better performing systems for a target reaction.

As it will be described later on, this PhD manuscript lies in this context. It is focused on the synthesis and the full characterization (experimentally and theoretically) of RuNPs stabilized with carboxylic acids. These RuNPs were chosen to serve as models for the future design of efficient

nanocatalysts for water splitting process. This reaction can be electro- or photo-activated, this last mechanism requires to associate a photosensitizing species to the RuNPs which can be performed through the anchoring a polypyridyl ruthenium complex at the surface of the particles by grafting pending groups, like carboxylic acids.

CHAPTER II

Ethanoic Acid-Capped RuNPs: Experimental and Theoretical Studies

2.1 Introduction

Science is in continuous evolution and Chemistry is not the exception, in the last years new branches were explored. The ability to create, characterize and control artificial structures in a nanometer (nm) size range is one of the examples, so-called nanoscale science or nanotechnology. The manipulation of different systems at a nanometer level and its applications, involves the cooperative efforts of many sciences such as molecular biology, physics, materials science, chemistry, etc.

The human necessity to create new materials with novel or improved properties as thermal conductivity, optical response, elasticity, etc., is the driving force to develop nanomaterials. In fact, these materials such as metal nanoparticles (MNPs) present changes in the electronic, chemical and physical properties in comparison with bulk materials or molecular compounds. Also, this branch of materials science has been developed in order to perform more efficient and complex demands like catalysis for the decomposition of contaminants, response-materials with higher sensitive to a specific stimulus, devices for conversion of sunlight into current and even energy storage systems.

Materials build in the nanometer range (figure 2.1) are described as nanocomposites which are performed as continuous assembled objects, molecules or atoms till they arrive to a nanosize. Their novel behavior implies the combination of their individual components properties and their mutual interactions.[138] Therefore nanoscale materials show a behavior intermediate between bulk material and molecular systems.

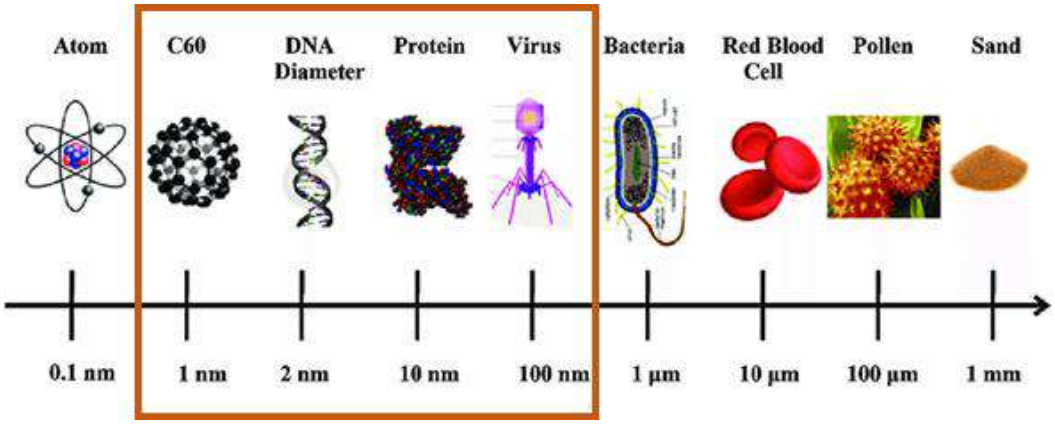

Figure 2.1 Nanomaterials size in comparison with organic and inorganic structures.[139]

The fraction of atoms that are present at the surface of the nanomaterials, [80.0 – 50.0 %] for MNPs ranging from [1.0 - 2.0 nm], is quite bigger than the possible reactive atoms present in a bulk material. Therefore, the nanosystems possess improvement properties, like higher reactivity than the corresponding macro materials did not possess.

Manipulation of materials at the nanometer scale produce nanoparticles and nanostructures with different sizes, morphologies and structures. The nanomaterials have a length size typically between [1.0 – 100.0 nm] at least in one dimension. The size of them are smaller than bulk materials but higher than small molecules.[140]

For example, palladium nanoparticles in size between *ca.* [1 - 2 nm] possess a number of particles ranging between [35 - 290 atoms], meanwhile for ruthenium nanoparticles (RuNPs) it ranges from *ca.* [38 – 310 atoms] at the same NP size in their typically crystalline structure (table 2.1).[141]

Table 2.1 Number of atoms for metal nanoparticle of 1.0 and 2.0 nm in size following their typical crystalline structure.

	Ru	**Au**	**Ni**	**Ag**	**Pd**
Crystalline structure	hcp	fcc	fcc	fcc	fcc
Number of atoms in 1.0 nm NPs (N)	39	31	49	31	36
Number of atoms in 2.0 nm NPs (N)	308	248	389	248	288

Nanoparticles size is quite important because at certain length the nanomaterials follow quantum mechanical rules instead of the classic. This phenomenon is found as a result of their electronic compatibility with atoms or molecules.

The fundamental properties of metal nanoparticles depend on their size, morphology, shape (anisotropy), structure, crystallinity, etc. Thus, these materials can be tune in order to find novel properties by changing the synthesis conditions. It has been reported that drastic changes can be observed if small modifications on the nanoparticles morphology are created. Therefore, it is of highly importance to obtain monodisperse nanoparticles. Indeed for this reason, a synthetic procedure which can provide controlled nanosystems is desired.[142]

Different strategies have been developed in order to build controlled nanoparticles, mainly including protective ligand shells such as organic molecules. Amines, phosphines, thiols and oligomers have been widely used to synthetize MNPs. These moieties do not control just the nanoparticles growthless and morphology, but also changes their solubility.[143]

Despite of the flourishing stapes of nanoscience in the early years of this century, the interest in metal nanoparticles (MNPs) continues to be very strong in both academic and industrial domains due to their several applications in many fields ranging from biology,[144] medicine,[145] catalysis,[146] optoelectronics,[147] to energy[148] (figure 2.2).

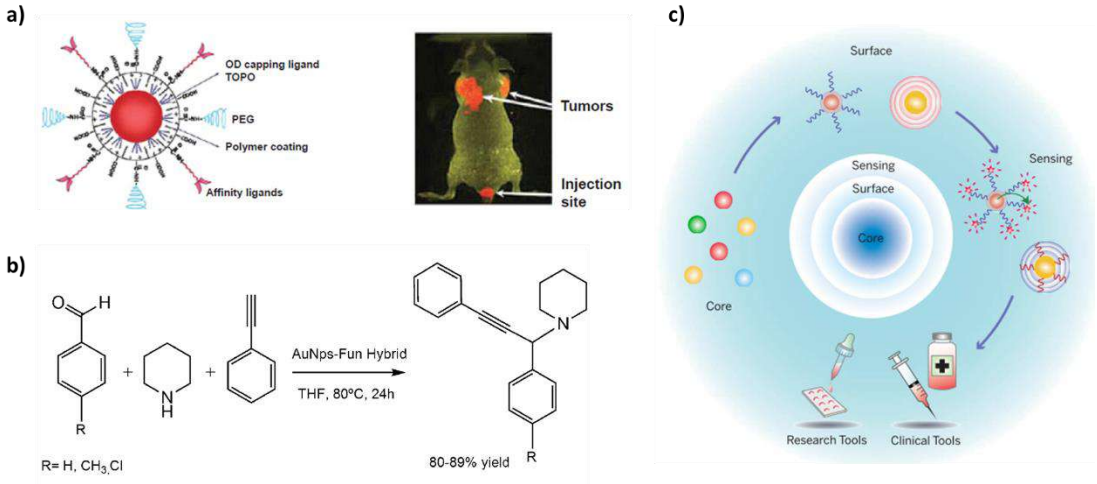

Figure 2.2 Interest on metal nanoparticles in different fields: (a) medicine;[145] (b) catalysis;[146] (c) biology.[144]

A bottom-up synthetic methodology that can provide controlled nanoparticles with homogenous morphology and avoiding the presence of undesired reactions substrates is the organometallic approach.[149] This powerful methodology allows the formation of hybrid nanoparticles constituted of a metal core surrounded by an organic layer from metal-organic complexes as metal sources and polymers or ligands as stabilizing agents (figure 2.3). Together with the coordinating character of the stabilizer, reductive agents used and applied reaction conditions for the decomposition of metal complexes are very important parameters to produce well-controlled zero-valent metal nanoparticles. Thermodynamic and kinetic parameters highly influence the decomposition and growth process, being thus key-points to get precisely controlled NPs in terms of size, shape, composition, surface state and dispersion.

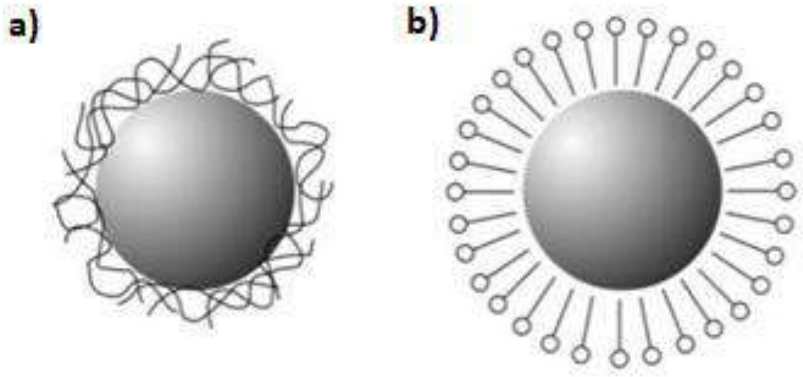

Figure 2.3 Metal nanoparticle protected by: (a) polymer; (b) ligand molecules.[150]

This approach provides MNPs which possess a clean surface due to the practical easy removal of side reaction products such as alkanes, but since they are stabilized by molecules covalently bounded (organic stabilizers), their surface composition is also a key factor that influences the electronic structure of the metal core.

Therefore, in this approach the surface ligands nature can be also tuned to provide different self-assembly properties. Thus, the nanoparticle properties can be adjusted by changing the stabilizing agent and/or the metal source, having even a high impact in their nanosystems solubility.

MNPs have been produced by several research groups but due to its fascinating applications there is still a need to modify their surface in order to improve their properties and extend their multifunctionality.

As mentioned in the previous chapter, the organometallic approach has been largely employed to produce metal ruthenium nanoparticles (RuNPs). For this purpose, various ligands such as amines, pyridines, imines, phosphines, carbenes, alcohols, thiols, betaines, etc., have been used as stabilizing agents[[59],[93],[101],[133]] (figure 2.4 a). However, carboxylic acids have received much less attention because they are identified as proton sources[151] (figure 2.4 b) even when their adsorption on several metallic surfaces has been broadly observed and studied.[152] But the use of simple carboxylic acids can be of interest in order to study the anchoring at a metal surface of more sophisticated molecules having carboxylic pending groups like polypyridyl ruthenium complexes that are used in the water-splitting reaction activated by light for example. ref

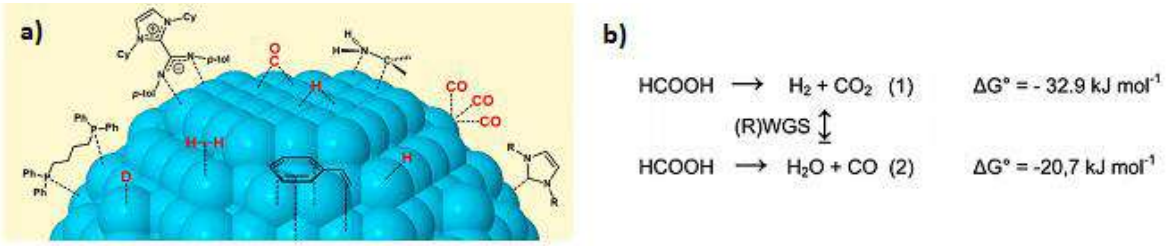

Figure 2.4. (a) Different type of ligands used for stabilizing RuNPs;[93] (b) reaction pathways for the formic acid decomposition.[151]

To our best knowledge the literature reports only one attempt on the stabilization of RuNPs with carboxylic acids following the one-step organometallic approach, using fullerenehexamalonic acid ($C_{66}(COOH)_{12}$) as stabilizer (figure 2.5).[109]

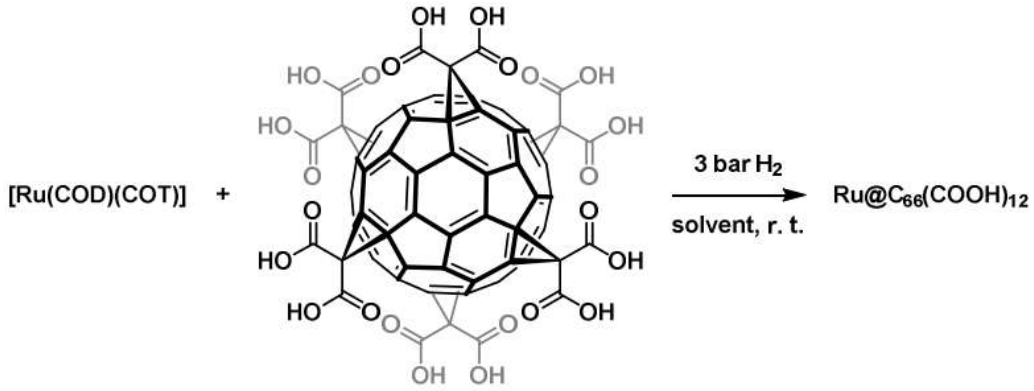

Figure 2.5 Synthesis of $Ru_x(C_{66}(COOH)_{12})_y$ nanoparticles.[109]

In this chapter, it is going to be presented a full-study where computational and experimental chemistry team-up and complement each other, in order to completely characterize ruthenium nanoparticles (RuNPs) functionalized at their surface by ethanoic acid molecules ($Ru_x(CH_3COOH)_y$). This carboxylic acid has been chosen to build a model system due to the simplicity of the acid that allows more accessible theoretical calculations. It was nevertheless necessary to first evaluate the potential of this ligand as RuNPs stabilizer.

As a result of the characterization, a better understanding of the NPs electronic structure and their surface properties will be shown. The combined strategy offers new data about the 3D representation of ultra-small RuNPs, this methodology offered valuable information on the surface chemistry of the nanoparticles, giving a balance between their surface coverage and ligand adsorption energies. By this way, potential interests of the studied particles can be drawn for catalytic application such as HER.

It is important to remark that before performing any theoretical investigation, it is necessary to have a structural model not beyond the reach of the first principle methods which is as close as possible to experimental findings (figure 2.6).[153] This is with the aim to calculate reliable physical or chemical properties, however this goal is not easy to reach and even more complicated when it concerns hybrid and complex systems such as metal nanoparticles.

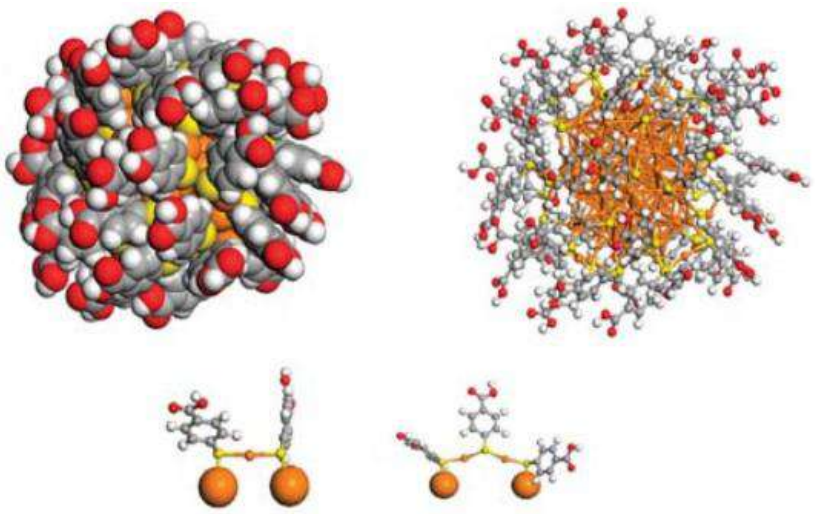

Figure 2.6 Gold model nanoparticle covered by *p*-mercaptobenzoic acid (Au_{102}(*p*-MBA)$_{44}$) and their different coordination modes.[153]

Yet, with the appropriated tools in hand, it is possible to use computational chemistry with the same level of accuracy and relevance as in molecular chemistry in order to describe ultra-small nanoparticles. This PhD work took benefit of previous results obtained.[82]

Thus, the following section will describe the synthesis of RuNPs stabilized with ethanoic acid (CH_3COOH) and their full characterization using several techniques namely, transmission electron microscopy (TEM), high-resolution TEM (HRTEM), wide-angle X-ray scattering (WAXS), proton and 13-carbon nuclear magnetic resonance (NMR) and Fourier transform infrared (FTIR).

These techniques were used in order to get experimental information on the RuNPs morphology (size, shape & crystalline structure) and the composition-surface state (nature and coordination of surface molecules) of the obtained RuNPs. The spectroscopic experimental assignations were corroborated in parallel with DFT calculations of the vibrational normal modes obtained from the optimized RuNPs as well as the chemical shifts found for different carboxylic coordination modes onto a hexanuclear ruthenium cluster [Ru_6].

The surface ligand coverage of these novel RuNPs was also investigated and discussed both experimentally and theoretically with the aim to describe the ruthenium nanoparticle surface chemistry. The RuNPs surface state were obtained with atomic charges and *d*-band centers calculations.

Furthermore, to understand the RuNPs catalytic properties and their possible performance, it was obtained the ligand adsorption energy onto optimize RuNPs. These are fundamental calculations for implement the Sabatier-Balding principle and the Brønsted-Evans-Polanyi (BEP) relations.[154]

Also in this chapter, the RuNPs catalytic efficiency was evaluated for the hydrogen evolution reaction (HER) due to its relationship between the nanoparticles surface composition and the molecular hydrogen (H_2) dissociative adsorption energies.[10]

2.2 Synthesis and Structural Characterization of RuNPs

The ruthenium nanoparticles (RuNPs) presented in this chapter were synthetized at room temperature (r.t.) by following the organometallic approach (scheme 2.1). Where a ruthenium organometallic precursor ([Ru(COD)(COT)]; (COD= 1,5 cyclooctadiene, COT= 1,3,5-cyclooctatriene)) was reduced in a pentane solution under molecular hydrogen (H_2) and in the presence of ethanoic acid as stabilizing agent (*see* section 6.1.2.2).

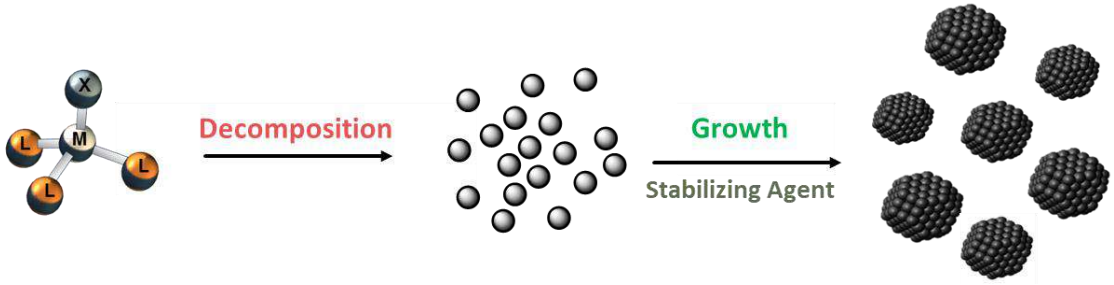

Scheme 2.1 General synthesis pathway of NPs by following the organometallic approach.

2.2.1 Organometallic Ruthenium Precursor

The source of ruthenium metal to synthetize RuNPs could come from different organometallic precursors. Some of them such as [$RuCl_3$] and [Ru(NO)(NO_3)] contains halogens or oxides that can directly interact with the nanoparticles surface, providing a polluted surface. For this reason, is desired to find an organometallic precursor that, when decomposed in a reductive

atmosphere, has secondary substrates molecules unable to interact with the nanoparticle surface. For that purpose, the synthesis of ruthenium nanoparticles was performed by using [Ru(COD)(COT)] as metal source.

[Ru(COD)(COT)] is a yellowish crystalline material that was synthetized and characterized according to a published procedure[155] (*see* section 6.1.2.1). This metal precursor was used for the first time in the 80's decade, when it was exposed to a reductive atmosphere of hydrogen (H_2) in the presence of different phosphines (scheme 2.2).[156]

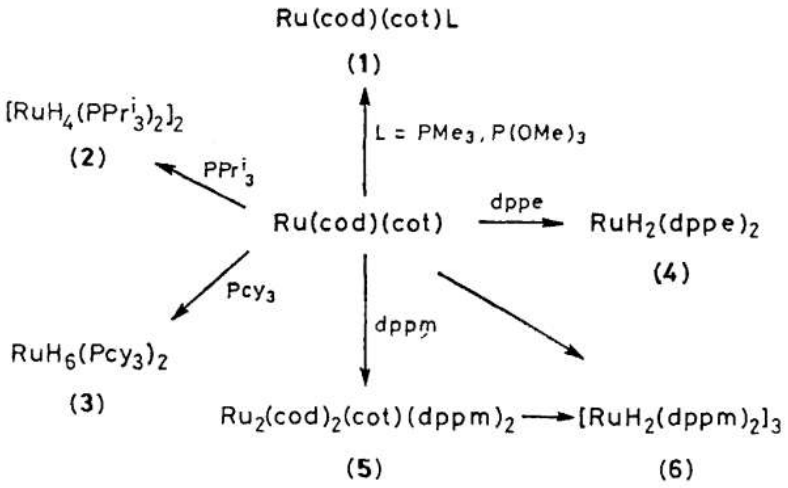

Scheme 2.2 Reactions profile of [Ru(COD)(COT)] with various types of phosphines.[156]

Later, it was found that the double bonds of the cyclooctatrien (COT) can be easily displaced by small cone angle phosphines ligands. After, it was found that the [Ru(COD)(COT)] substituents can be easily removed by the presence of molecular hydrogen. In general, the reduction reaction possesses fast kinetics and, in the absence of any strong coordinated ligand, all the double bonds are reduced forming naked ruthenium atoms, that start to nucleate and coalescence in order to reduce their surface energy.[157]

The previous observations have provided the possibility to prepare RuNPs by decomposing the [Ru(COD)(COT)] in the presence of hydrogen. Considering, as main factor, the addition of a coordinated ligand that prevent the excessive growth of the particles and the formation of RuNPs, avoiding the generation of a bulk metal material.

This methodology has been applied for more than 30 years and therefore several types of ligands have been used as stabilizing agents to form RuNPs. Polymers,[95] weakly[158] or strong coordinated ligands[135] have been utilized to create a wide gamma of RuNPs of different sizes and morphologies, which possesses different physical and chemical properties.

2.2.2 Synthesis of Ethanoic Acid-Capped RuNPs

As a first attempt to prepare monometallic RuNPs using ethanoic acid as stabilizing agent, a [Ligand]/[Ru] ratio of 0.2 molar equivalent (equiv.) compared to the quantity of the ruthenium precursor introduced was used ($Ru_X(CH_3COOH)_{0.2}$). This proportion of ligand was chosen as starting point because it was previously proved to be effective to generate stable and homogenous RuNPs with different ligands.[159]

More precisely, [Ru(COD)(COT] and ethanoic acid (0.2 equiv.) were dissolved in pentane under argon atmosphere inside a Fisher-Porter reactor, forming a yellowish solution. The reactor was evacuated under high-vacuum and then pressurized with molecular hydrogen (3 bar) under vigorous stirring at r.t. After *ca.* 2 minutes, the initial yellow solution turned black. To ensure complete decomposition of the ruthenium organometallic precursor, the reaction mixture was maintained for 30 min (scheme 2.3). Then, the reactor was evacuated under high-vacuum in order to remove the reductive gas excess and the colloidal suspension was concentrated to the half volume.

During the synthetic process a stable colloidal solution was not achieved, indeed, the formation of a precipitate was observed after *ca.* 10 min of reaction.

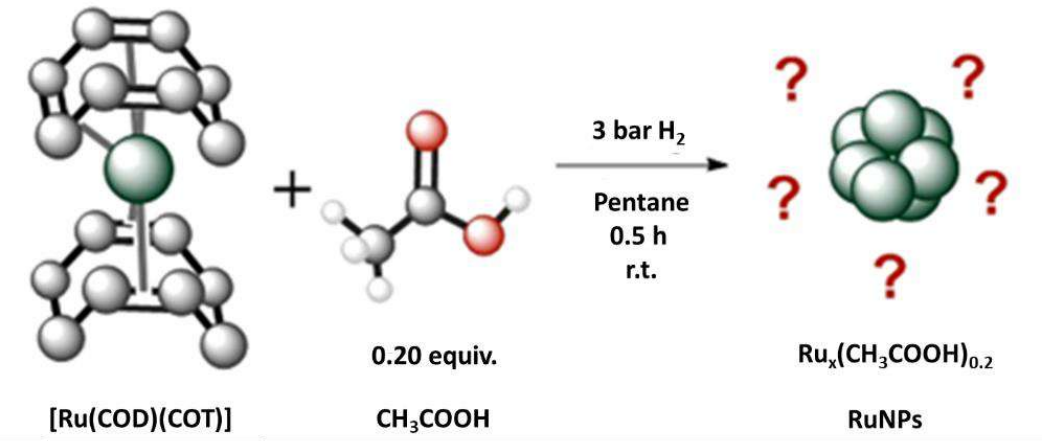

Scheme 2.3 Synthesis of RuNPs stabilized by 0.2 equiv. of ethanoic acid.

2.2.2.1 Structural Characterization of RuNPs Stabilized with 0.2 equiv. of CH_3COOH

A stable colloidal solution was almost obtained by applying vigorous stirring to the concentrated sample, however some precipitates were observed. Transmission Electron Microscopy (TEM) images recorded after deposition of a drop of the crude concentrated colloidal suspension onto a carbon-covered copper grid, revealed the formation of two types of metallic materials. One composed by superstructures or aggregates in a size range between [50.0 – 180.0 nm] (figure 2.7 a) and other consisted of ill-defined ultra-small RuNPs (figure 2.7 b). Thus, as it was expected due to the system precipitation, a non-homogeneous sample was obtained.

The presence of aggregates on the grid can explain the formation of a precipitate during the synthesis procedure. Size measurement of the isolated small NPs evidenced the presence of two different populations of individual RuNPs with a mean diameter of *ca.* 0.82 ± 0.25 nm and *ca.* 1.18 ± 0.32 nm (figure 2.7 c).

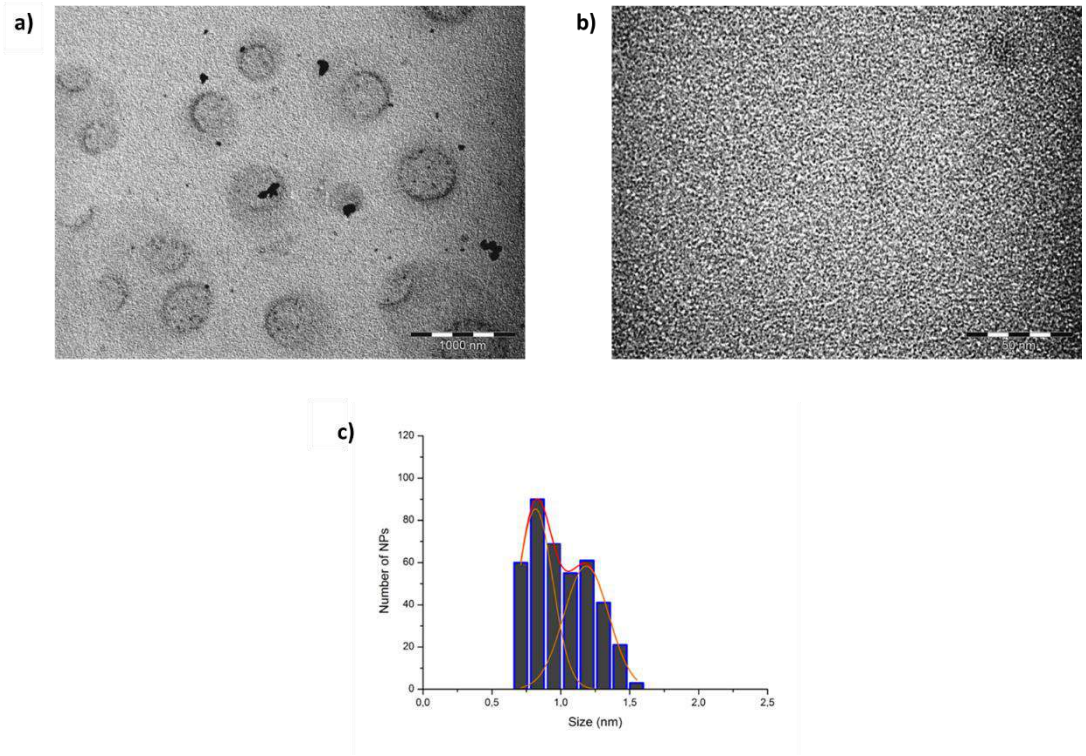

Figure 2.7 TEM micrographs of $Ru_x(CH_3COOH)_{0.2}$ NPs sample; (a) ruthenium superstructures; scale bar: 1000 nm; (b) ultra-small RuNPs; scale bar: 50 nm; (c) size histogram of individual RuNPs.

High-resolution TEM (HRTEM) showed the presence of ultra-small nanoparticles with clearly poor crystallinity. No particle displaying a crystalline compact structure was able to be found for this sample of particles (figure 2.8).

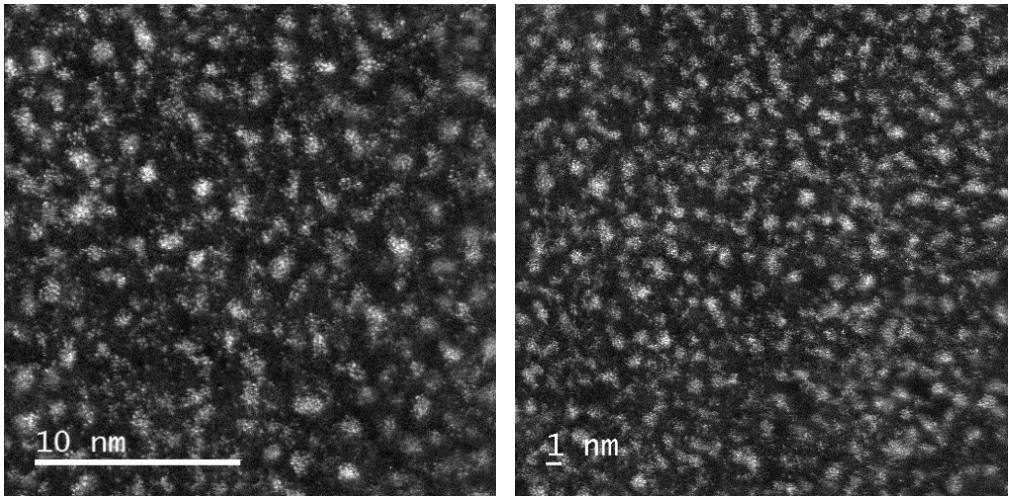

Figure 2.8 HRTEM of $Rux(CH_3COOH)_{0.2}$ individual NPs.

EDX (Energy Dispersive X-ray) analysis confirmed the presence of elemental ruthenium in the zones of the grid covered by the RuNPs deposition (see comparison between spot 002 and spot 001 in figure 2.9). Moreover, agglomeration of the particles under the beam was observed during the analysis.

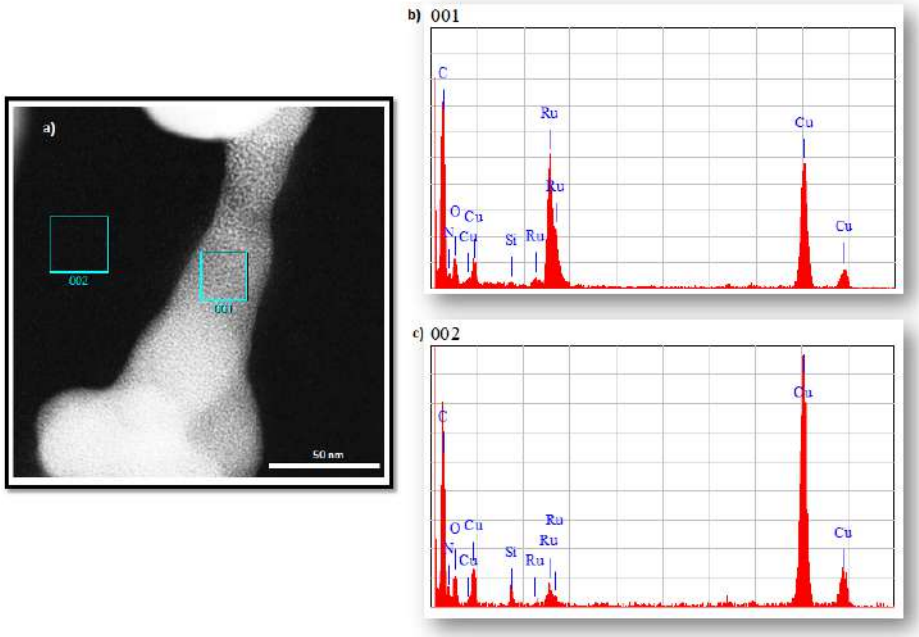

Figure 2.9 (a) Dark field micrograph of $Ru_x(CH_3COOH)_{0.2}$ NPs with two different highlighted spots; EDX spectra analysis of (b) 001 spot corresponding to a zone with RuNPs and (c) 002 spot for the metal free carbon-covered grid.

The EDX analysis for the element quantification was performed for the highlighted spots, on them, it was possible to observe the relation between the oxygen and ruthenium amount found in the sample (table 2.2). This ratio indicates that the spot 001, which has a high concentration of RuNPs, has less quantity of oxygen (*ca.* 0.2) than the expected from the experimental conditions used for the RuNPs synthesis, [O]/[Ru] = 0.4. This result indicates that no oxidation took place and that lower quantity of the 0.2 equiv. of ethanoic acid added for the NPs synthesis is interacting with the nanosystem. Also, it was determined that the RuNPs surrounding area (spot 002) possesses low quantity of ruthenium, which could explain the heterogeneity found in the system.

Table 2.2 EDX analysis for element quantification of oxygen & ruthenium ratio in comparison with the experimental synthesis relation for $Ru_x(CH_3COOH)_{0.2}$ NPs.

	Experimental relation	001 spot	002 spot
[O]/[Ru] ratio	0.40	0.22	2.22

Due to the formation of small RuNPs, it is possible to formulate as a hypothesis that the ethanoic acid can act as a ligand to stabilize RuNPs. However, the lack of homogeneity and stability of the sample obtained could be attributed to a deficiency of capping ligand. Consequently, it was considered to use more ethanoic acid ligand.

2.2.2.2 Structural Characterization of RuNPs Stabilized with 0.4 equiv. of CH_3COOH

Following the observations obtained in the previous experiments, a synthesis of RuNPs was repeated in the same conditions as for $Ru_x(CH_3COOH)_{0.2}$ NPs. But with the particularity of increasing 100.0 % the quantity of stabilizing agent, the ratio $[CH_3COOH]/[Ru]$ was raised to 0.4 equiv. ($Ru_x(CH_3COOH)_{0.4}$; (scheme 2.4)).

In these synthesis conditions, the yellowish initial solution, formed by the dissolution of the [Ru(COD)(COT)] and ethanoic acid in pentane, turned black at the same reaction time as previously observed for $Ru_x(CH_3COOH)_{0.2}$ (*ca.* 2 min), but this time no precipitate was observed under vigorous stirring. However, a semi-stable colloidal solution was obtained since metal product sedimentation appeared when magnetic stirring was stopped for a few hours.

This deposition can be due to a low solubility of the nanoparticles in pentane. Primally, this phenomenon can be explained by the fact that ethanoic acid contains a polar head that can interact with the surface of the RuNPs and a short organic tail thus making the RuNPs less soluble in pentane.[160] Stirring again the sample allowed to get a colloidal suspension that can be better analyzed.

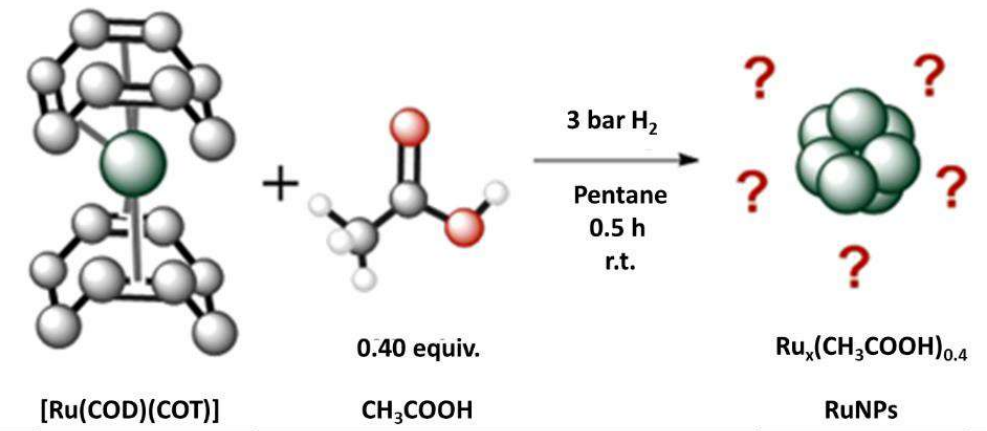

Scheme 2.4 Synthesis of RuNPs stabilized by 0.4 equiv. of ethanoic acid.

Structural characterization of $Ru_x(CH_3COOH)_{0.4}$ NPs was started by analyzing the TEM micrographs recorded from the crude concentrated colloidal suspension. The images evidence the presence of small RuNPs with a mean size of *ca.* 1.51 ± 0.58 nm (figure 2.10) which possess a spheroid morphology. The nanosystems form a semi-homogeneous population with a bit large size distribution but without being able to observe any aggregates.

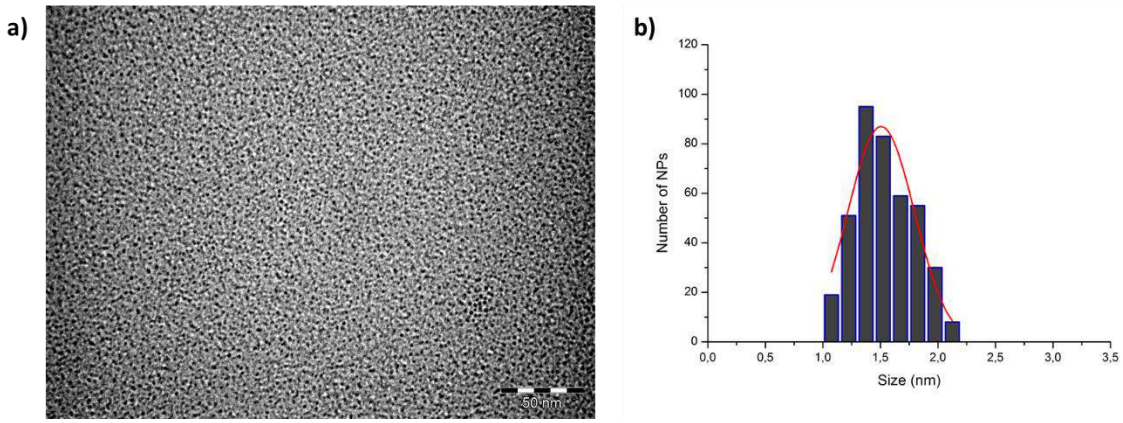

Figure 2.10 (a) TEM micrograph of $Ru_x(CH_3COOH)_{0.4}$ NPs, scale bar: 50nm; (b) corresponding size histogram of RuNPs.

As it can be seen from TEM analysis, the increase of ethanoic acid quantity to a $[CH_3COOH]/[Ru]$ of 0.4 equiv. led to a stable colloidal suspension containing small, semi-homogeneous and well-dispersed RuNPs. Thus, confirming the previous hypothesis planted concerning the use of ethanoic acid as stabilizing agent for forming RuNPs was proved to be true

by increasing the ligand metal ratio. Given the stability and homogeneity of $Ru_x(CH_3COOH)_{0.4}$ system, it was decided to focus on it for the rest of this theoretical and experimental study on ethanoic acid-capped RuNPs.

HRTEM studies performed using the same grid as for TEM analysis, the studio revealed RuNPs with poor crystallinity but higher than that of the $Ru_x(CH_3COOH)_{0.2}$ system (figure 2.11 a). Despite of this factor, some atomic planes were sufficiently visible to be measured to resolve their crystalline structure. Fast Fourier Transformation (FFT) on the red highlighted spot of HRTEM micrograph, indicated the presence of interplanar distances of 0.238 and 0.208 nm that can be attributed to crystalline (100) and (101) plans of the bulk ruthenium hexagonal close packed (*hcp*) structure (figure 2.11 b). Moreover, the isolated particle presents a Miller pattern of $[\bar{1}2\bar{1}3]$ (figure 2.11 c). In general, NPs showed a similar low crystallinity degree, which is another indicative that corroborate the formation of a homogenous system.

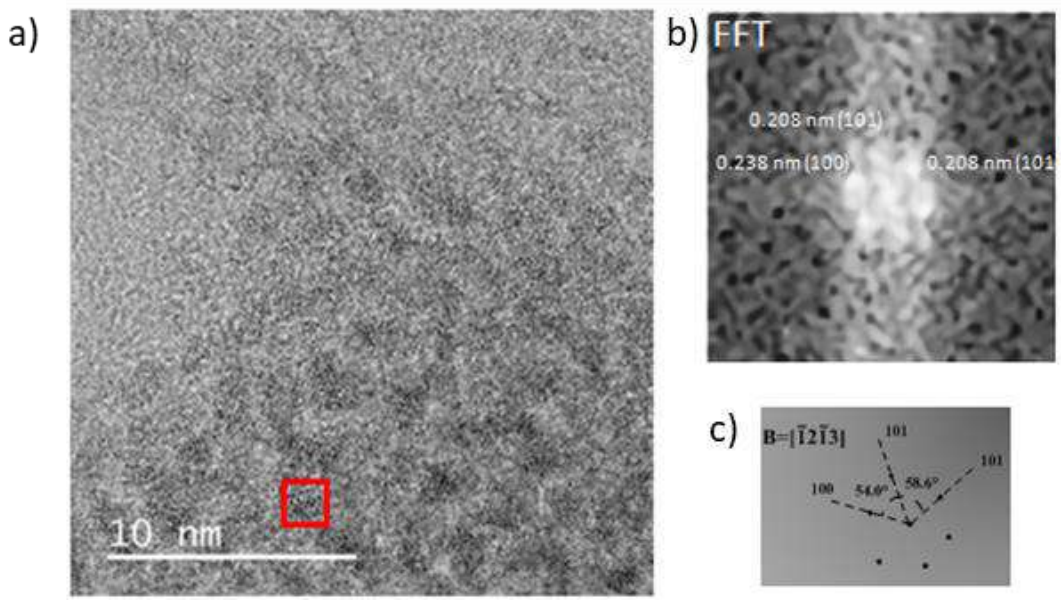

Figure 2.11 HRTEM analysis of $Ru_x(CH_3COOH)_{0.4}$ NPs; (a) micrograph; (b) FFT (c) Miller pattern.

Wide-angle X-ray Scattering (WAXS) is a useful technique to get information on the crystalline structure and size of crystalline domains of small NPs (< 4 nm), data that can be compared to those obtained by TEM and HRTEM. It is worth to point out that WAXS is a statistical technique quite sensitive for small and ultra-small objects no matter the oxidation state or crystallinity.

WAXS data was recorded on sample $Ru_x(CH_3COOH)_{0.4}$ in the solid state under argon atmosphere (inside a sealed capillary). The results did not evidence any crystalline feature for the $Ru_x(CH_3COOH)_{0.4}$. Besides a huge peak at low angle indicative of agglomeration, only very broad features were observed which are not in agreement with any compact structure (figure 2.12 a).

In the RDF pattern in real space (Fig. 2.12 b), it is observed a well-defined function fully consistent with metallic ruthenium, which is poorly resolved and does not allow a clear structure indexation. A coherence length, which corresponds to the size of crystalline domains, can be estimated to *ca.* 0.9 nm. This pattern points to very small amorphous metallic RuNPs.

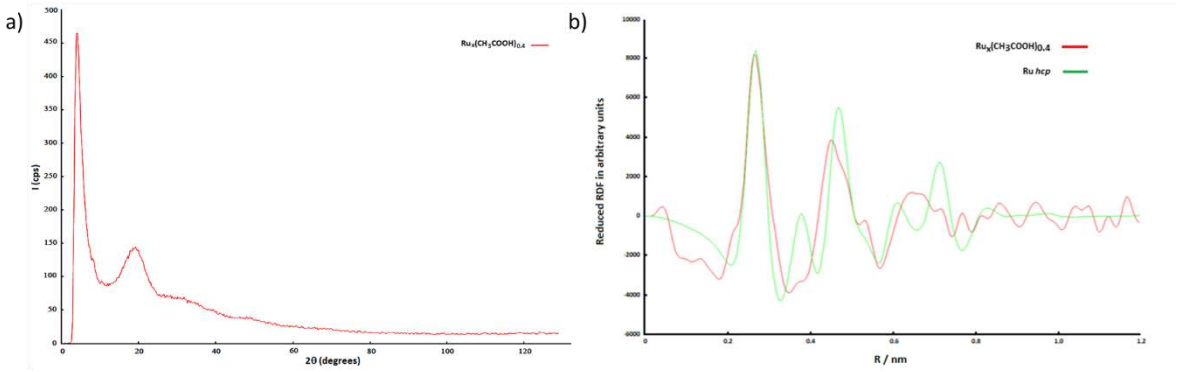

Figure 2.12 (a) WAXS spectrum of $Ru_x(CH_3COOH)_{0.4}$ NPs; (b) RDFs comparison in real space; $Ru_x(CH_3COOH)_{0.4}$ (red) vs Ru *hcp* crystalline structure computed for 30 Ru atoms (green).

The comparison of WAXS and HRTEM data evidenced at first approximation some discrepancy but they are not in contradiction since WAXS is a statistic technique sensitive to very small objects, crystalline or not, whilst HRTEM largely relies on phase contrast and emphasizes the better crystallized fraction of a sample. Indeed, the WAXS RDF indicates an estimated RuNPs coherence length smaller than that of TEM by *ca.* 0.6 nm. Revealing the probable presence of ultra-small nanoparticles or nanoclusters, smaller than < 1.0 nm which are difficult to characterize by HRTEM. One can thus estimate that the *hcp* NPs revealed by HRTEM are likely related to a limited coalescence leading to bigger domains.[161]

Also, WAXS analysis provides useful information about the stability of metal nanoparticles under inert atmosphere with time. Two different measurements have been performed on the same sealed capillary of $Ru_x(CH_3COOH)_{0.4}$ (thus RuNPs kept under argon atmosphere) with a delay time of more than one year between them (figure 2.13). As it can be seen, no modifications were

observed between both measurements, meaning that at least without reductive or oxidative atmosphere, the general structure and composition of the ruthenium particles remained.

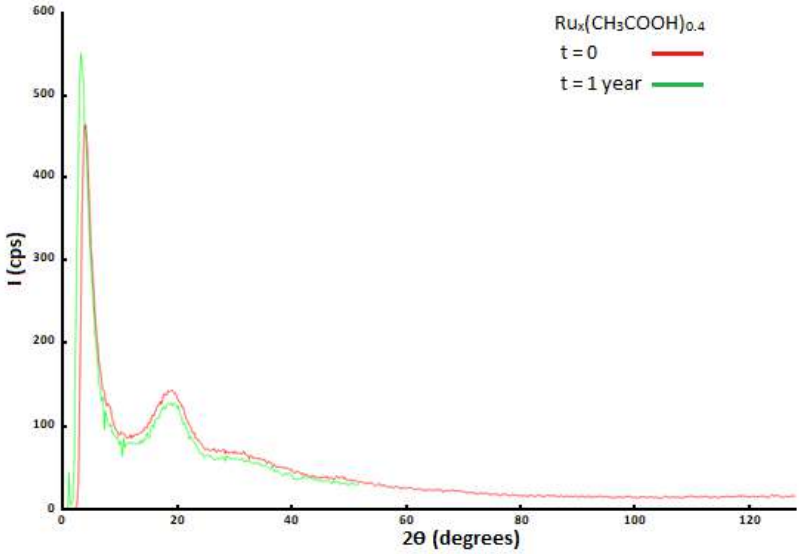

Figure 2.13 WAXS spectra recorded from $Ru_x(CH_3COOH)_{0.4}$ NPs; (red) freshly prepared sample; t = 0; (green) stored for long time; t = 1 year.

EDX analysis performed on $Ru_x(CH_3COOH)_{0.4}$ NPs sample revealed agglomeration phenomenon under the electron beam as previously observed with $Ru_x(CH_3COOH)_{0.2}$ NPs (figure 2.14 a). The EDX data confirmed the presence of strong peaks corresponding to elemental ruthenium on the zones where RuNPs are visible (figure 2.14 c; spot 005)

In addition, it can be seen that the NPs surrounding zone has no metal presence (spot 004), this result is quite different than that obtained for $Ru_x(CH_3COOH)_{0.2}$ NPs where some leftover ruthenium was found in the similar spot (figure 2.14 b). As a brief conclusion, it can be said that for $Ru_x(CH_3COOH)_{0.4}$ NPs system all the metal precursor supplied for the synthesis was decomposed into a semi-homogeneous ruthenium nanostructures, which possess high-sensitivity to the electron beam. This data is another evidence of the importance of the nanoparticles synthesis conditions, as for this study case, the relevance of the quantity of ligand used to stabilize the RuNPs.

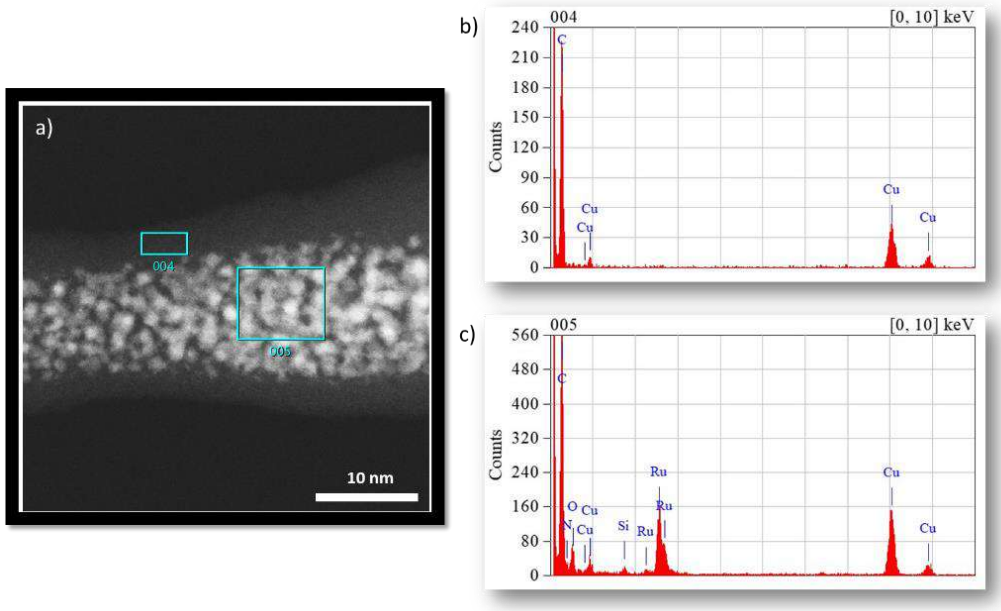

Figure 2.14 (a) Dark field micrograph of $Ru_x(CH_3COOH)_{0.4}$ NPs with two analyzed highlighted spots; EDX spectra analyses of (b) 004 and (c) 005 spot corresponding to free carbon-covered grid zone and to deposited RuNPs, respectively.

Highlighted spots were analyzed to obtain the elemental quantification [O]/[Ru] ratio (table 2.3). The spot 004 showed only signals for the holey carbon-covered copper grid, meaning that no sample was deposed.

Meanwhile, for the 005 spot it was *ca.* 0.5, being this value lower than the expected from the experimental ratio conditions (0.8). Even when this technique is not well-known as a quantitative methodology, it can be said that there is a lower quantity of ligand surrounding the NPs than the added into the synthesis setup, this phenomenon can be attributed to the ligand lost in the washing process. Another observable fact is that no nanoparticles oxidation took place, meaning that as it was seen in WAXS, the RuNPs are stable through time and yet probably in different atmospheres.

Table 2.3 EDX analysis for element quantification of oxygen & ruthenium ratio ratio in comparison with the experimental synthesis relation for $Ru_x(CH_3COOH)_{0.4}$ NPs.

	Experimental relation	**004 spot**	**005 spot**
[O]/[Ru] ratio	0.80	-----	0.47

After the structural characterization of the $Ru_x(CH_3COOH)_{0.4}$ NPs, complementary theoretical and spectroscopy techniques, namely nuclear magnetic resonance (NMR) and infrared (IR) were used to analyze the coordination of the ethanoic acid to the ruthenium surface. Thus, to characterize the surface state of $Ru_x(CH_3COOH)_{0.4}$ NPs. The experimental results will be presented in forthcoming sections, together with DFT-based analysis. The main objective of these studies was to obtain information about the quantity of capping ligands, the nature of the bonding and the surface composition of $Ru_x(CH_3COOH)_{0.4}$ NPs.

2.3 Study of the Ethanoic Acid Interactions with the Surface of RuNPs

Complementary techniques based on nuclear magnetic resonance (NMR) spectroscopy were performed in order to study the interaction strength of ethanoic acid at the surface of RuNPs. In parallel, DFT calculations were carried out to provide theoretical information on the chemical shifts depending on the coordination mode of the ethanoic acid at the particle surface by using a hexanuclear ruthenium cluster [Ru_6] as a model system.

This will be an important step to analyze the surface state of the nanosystem and to prove the formation of a hybrid material. Besides, it will be the first time that the combination of theoretical and experimental results will be presented.

2.3.1 Proton-Liquid NMR Characterization

Small RuNPs are suitable nanomaterials to be analyzed by nuclear magnetic resonance, because they do not present a Knight shift phenomenon or if it is present is considered to be not significant.[[102],[110]] This effect is correlated to a NMR signal displacement due to an additional magnetic field created by an electron cloud as present in metallic systems.[162]

Therefore, a proton-liquid NMR (^{1}H-NMR) spectrum was recorded from the $Ru_x(CH_3COOH)_{0.4}$ NPs (figure 2.15) after several washings with pentane-THF cycles and drying under high-vacuum during half a day. For achieving the NMR measurements, the nanoparticles were re-dispersed in THF-d^8.

The RuNPs experimental ^{1}H-NMR spectrum (figure 2.15 blue) was compared with that of the pure ethanoic acid (figure 2.15 red). It is important to note that this later corresponds to the carboxylic acid dimer and not to the isolated molecule. The ^{1}H-NMR spectrum of the nanoparticles shows signals of the NMR solvent (THF) at *ca*. 3.6 & 1.7 ppm, and a signal attributed to an oxidative impurity, water, at *ca*. 2.5 ppm. It is worthy to notice that no sharp signals at *ca*. 1.93 and 10.59 ppm can be observed as expected for the methyl (-CH_3) and acid proton (RCOOH) of the ethanoic acid, respectively, according to the signals provided by the spectrum recorded for the free ligand.

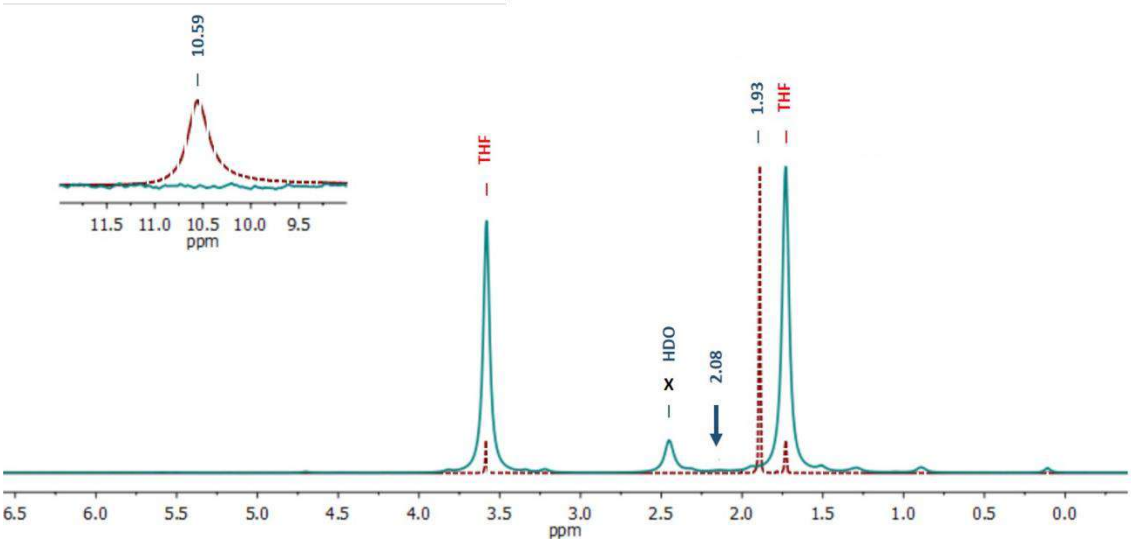

Figure 2.15 ^{1}H-NMR (THF-d^8); (blue) $Ru_x(CH_3COOH)_{0.4}$ NPs; (red) CH_3COOH.

The lack of the characteristic signals of the ethanoic acid in the RuNPs systems, indicates that the sample does not contain free ligand in solution. The absence of any other peak in the low-frequency region suggests that the ethanoic acid ligand is strongly interacting with the RuNPs surface, this phenomenon can be observed due to the reduce of the ligand mobility. Moreover, evidences of another peak which is quite broad is observed at *ca*. 2.08 ppm by DOSY-NMR *vide infra*.

Previous statement is based on reports saying that molecules which have a high degree of freedom (like free CH_3COOH) present sharper signals than rigid compounds. Ligands attached at the nanoparticles surface can thus be expected to have reduced dynamics and therefore to present broad signals. Presence of this type of peaks is often used as a proof or evidence of ligand coordination at the NPs surface.([163],[164])

In the present case, due to its signal position at *ca.* 2.08 ppm and broadness, this lightly shifted signal compared to that of free CH_3COOH can be assumed to correspond to a methyl group close to the surface of the RuNPs coming from ethanoic acid. Thus, it is a direct prove of their interaction and their role in the RuNPs stabilization.

The assignation of this broad signal was confirmed by DFT calculations, where chemical shift of protonated-unprotonated carboxylic acid were calculated as free ligands and as interacting species in several coordination modes and locations onto a hexaruthenium nanocluster [Ru_6] (figure 2.16) by using Gaussian09 software. This strategy to obtain theoretical NMR chemical shifts was previously validated by different research groups (*see* section 6.2.5).([165],[166])

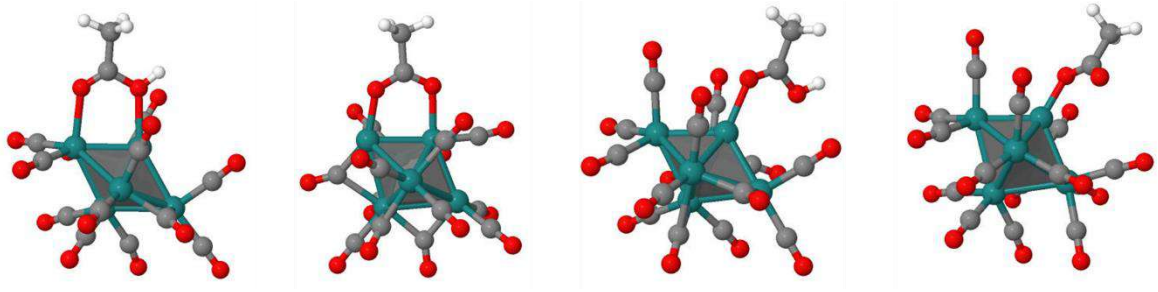

Figure 2.16 [Ru_6] nanoclusters used as model for the DFT chemical shift calculations.

As starting point, the mean chemical shift of the methyl protons of the free ligand species that could interact with the NP (carboxylic acid-carboxylate) was calculated. For the ethanoic acid dimer, the chemical shift was found to be at 1.9 ppm (figure 2.17 a), meanwhile this value changed to 1.3 ppm for the unprotonated ethanoate moiety (figure 2.17 b).

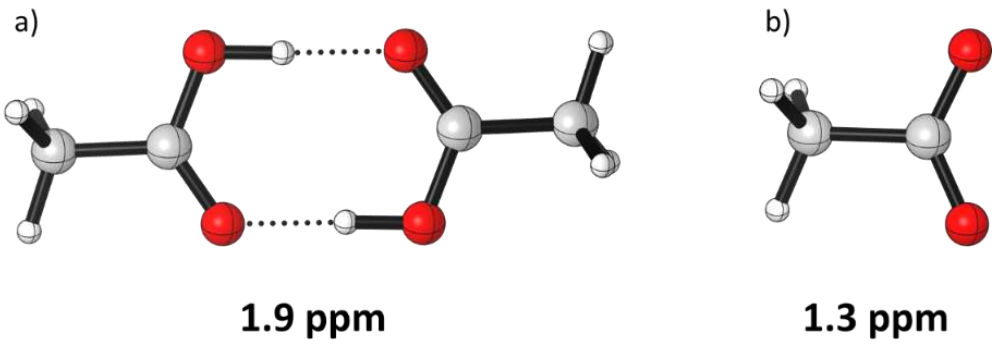

Figure 2.17 DFT mean methyl protons chemical shift of (a) ethanoic acid dimer & (b) ethanoate.

As it can be seen, the calculated methyl proton signal of the free ethanoic acid dimer is quite similar to that of the experimental counterpart (1.93 ppm in THF-d^8). Owing to these results it can be said that no free carboxylic species are present in the deuterated solution and that the broad signal at *ca.* 2.08 ppm found in the experimental spectrum does not correspond to any of the ethanoic acid or ethanoate free entities

Thus, calculations of chemical shifts of methyl protons of ethanoic acid or ethanoate species when interacting with the Ru_6 nanocluster were performed. First it was observed, that the methyl protons are always unshielded compared with the free ethanoic acid dimer. The chemical shift observed for moieties interacting as carboxylic acid were found to be *ca.* [2.6 – 2.9 ppm] depending on the coordination mode (figure 2.18). These values mean that the direct ligand interaction with the nanocluster leads to deshielded signals at least by *ca.* 0.7 ppm. These values are different from the signal at 2.08 ppm observed on the experimental ^{1}H NMR spectrum, thus indicating that the ethanoic acid ligand is probably not coordinated as a carboxylic acid.

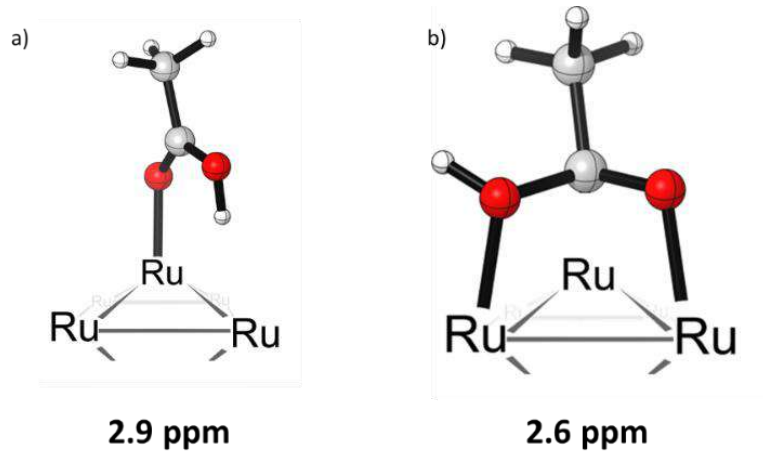

Figure 2.18 DFT mean methyl protons chemical shift of CH_3COOH interacting with $[Ru_6]$ nanocluster in different coordination modes; (a) η; (b) μ.

Similar calculations were then done by focusing on the ethanoate interaction mode. For this case, three different coordination modes were analyzed: chair, monodentate and bidentate (figure 2.19). The results show also a proton deshielding in comparison with the free ligand moieties, but not as high as that found for the ethanoic acid moiety. In fact, the chemical shift of the ethanoate methyl protons coordinated in a bidentate mode (*ca.* [2.0 – 2.2 ppm]) is in the range of the broad signal observed in the experimental spectrum. The other two coordination modes are at higher ppm values (chair *ca.* 2.6 ppm; monodentate *ca.* 2.3 ppm) and do not correspond to the experimental data.

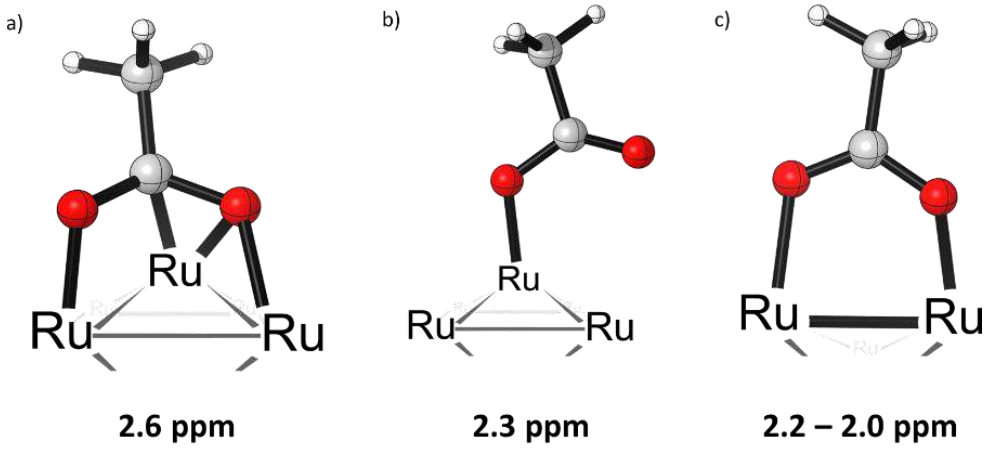

Figure 2.19 DFT mean methyl protons chemical shift of CH_3COO moiety interacting with $[Ru_6]$ nanocluster in different coordination modes; (a) chair: σ carbon, μ^3; (b) monodentate: η; (c) bidentate: μ.

According to the DFT chemical shift results obtained in the [Ru_6] nanocluster, there is no doubt that the signal experimentally observed at *ca.* 2.14 ppm cannot be assigned to free carboxylic moieties nor to ethanoic acid coordinated onto the NPs surface but to chemisorbed ethanoate and probably in a bidentate coordination mode.

Furthermore, to corroborate this data some calculations were performed on small cations (Na^+) instead of the [Ru_6] nanocluster. First of all, as it was shown the ethanoate protons are shielded by *ca.* 0.6 ppm in comparison with that of the ethanoic acid dimer, due to a delocalized charge formed in the system. However, the interaction of the negative moiety with the ruthenium cluster deshields the methyl protons by a similar quantity of ppm (*ca.* [0.7 – 0.9 ppm]). This assertion was supported by calculations performed in sodium ethanoate (CH_3COONa), where the ethanoates protons are found to be at *ca.* 1.9 ppm with a deshielding of *ca.* 0.6 ppm.

As a result, it has been observed a counterbalanced phenomenon, that is why the methyl protons of the ethanoate moiety in interaction with the nanocluster seems to have similar chemical shift than that of the free ethanoic acid dimer. The level of deshielding caused by the metal interaction depends on its nature. For example, calculations performed with another cation (Mg^{2+}) showed a deshielding of *ca.* 0.8 ppm, resulting in a chemical shift of 2.1 ppm (figure 2.20).

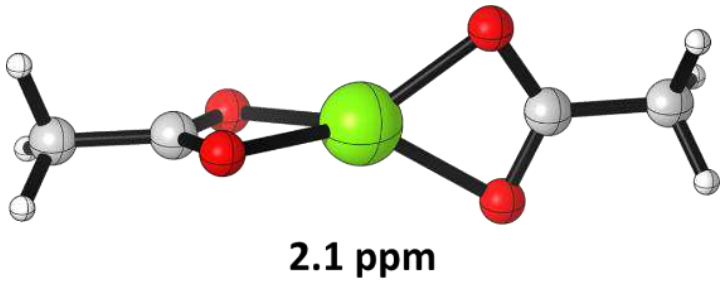

Figure 2.20 DFT mean methyl protons chemical shift of two CH_3COO moieties interacting with Mg^{2+}.

The theoretical and experimental findings are summarized in the figure 2.21. Where it can be seen that signals visible for the free ethanoic acid experimental spectrum (blue) do not correspond to that of the $Ru_x(CH_3COOH)_{0.4}$ NPs system (red), meaning that there is no free ligand. Given the DFT calculations, preliminary hypothesis can be done about the ligand features (ethanoate) and its coordination mode (bidentate). This is the first evidence of the mutual support

importance between experimental findings and theoretical calculations for this complex system of RuNPs. The characterization of the $Ru_x(CH_3COOH)_{0.4}$ NPs was pursued with DOSY NMR studies.

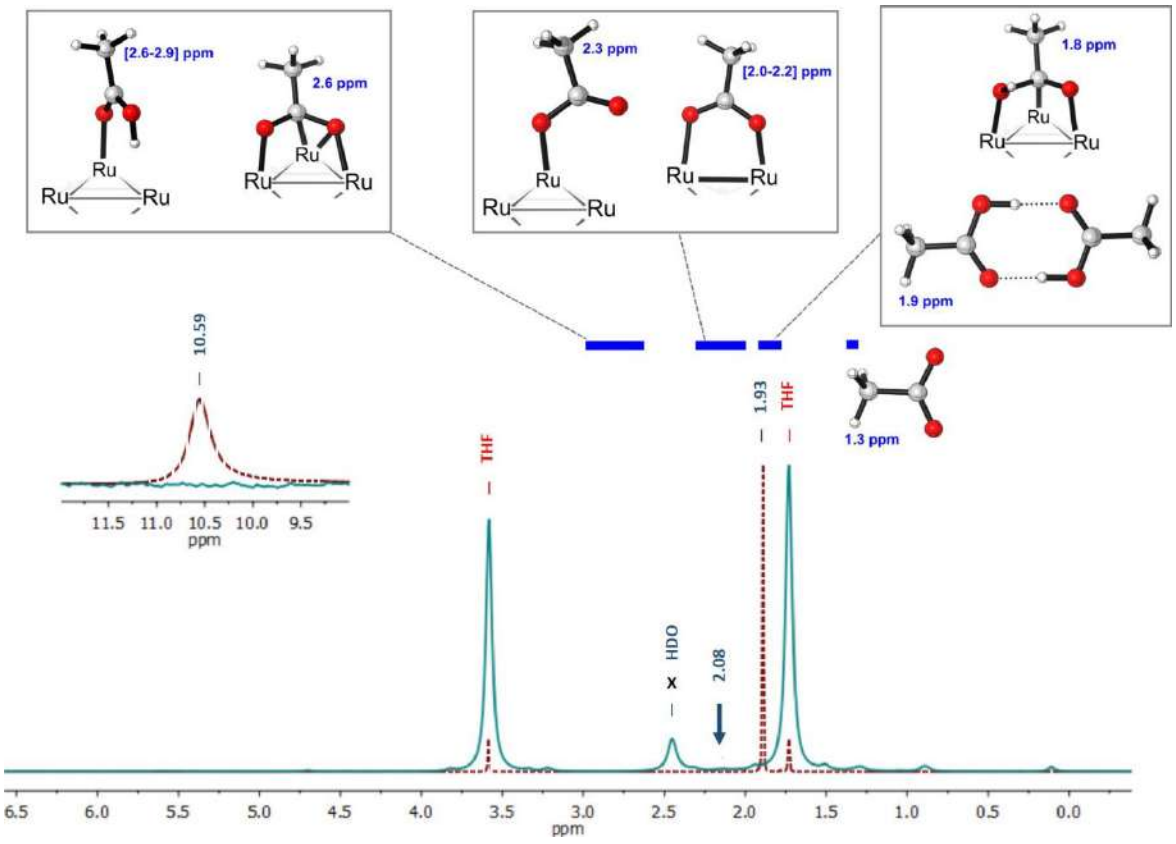

Figure 2.21 Experimental ^{1}H-NMR (THF-d^8) of $Ru_x(CH_3COOH)_{0.4}$ NPs (blue) in comparison with free CH_3COOH (red). DFT ^{1}H-NMR chemical shifts of the methyl group in various models ($(CH_3COOH)_2$, CH_3COO^-, $[Ru_6]$ clusters).

2.3.2 Diffusion-Ordered Proton NMR Experiments

Diffusion-ordered NMR spectroscopy (DOSY-NMR) is a powerful experimental tool that allows to obtain information about the dynamic behavior of chemical compounds dispersed into a liquid environment. By using this technique, it is possible to elucidate the interactions between small species (ligands) and big structures (nanoparticle) in liquid state.

DOSY-NMR can be used as a diffusion-filtered ^{1}H-NMR experiment to eliminate the contribution of free and small molecules with fast diffusion (D = [10^{-8} - 10^{-9} $m^2.s^{-1}$]) like impurities, free ligands or solvents, thereby leaving visible only the signals corresponding to larger species or

systems with lower diffusion coefficients such as ligands interacting with the nanoparticle surface. The DOSY NMR methodology has been already applied by several research groups in order to distinguish the signals corresponding to free ligands in solution from those of interacting ligands with the MNP surface.([98],[167],[168])

Therefore, the DOSY-NMR technique was here used in order to determine the sample purity (presence or absence of free ligand), the hydrodynamic radius of the particles (metal core + ligand layer) and primarily about ethanoic acid interactions with the RuNPs surface. Thus, DOSY (1D and 2D) ^{1}H-NMR experiments were performed on $Ru_x(CH_3COOH)_{0.4}$ NPs dispersed in THF-d^8 at r.t.

The diffusion-filtered ^{1}H-NMR spectrum of $Ru_x(CH_3COOH)_{0.4}$ NPs (figure 2.22) revealed two broad signals at *ca*. 0.14 & [1.0 – 3.0] ppm. The first one is assigned without doubt to grease, meanwhile the second peak can be attributed to different coordination modes and sites (surface heterogeneity) of ethanoic acid at the RuNPs surface. The signal spotted at *ca.* 2.08 ppm was found by a peak deconvolution fitted with a combination of Lorentzian and Gaussian functions (L/G = 1.00).[169]

The higher-field peak provides clearly insights of the ethanoic acid coordination onto the RuNPs surface. Also, it shows how the chemical environment of the ligand change due to its interaction with the RuNPs, this phenomenon can be seen by the methyl protons chemical shift modification and corroborated by previous DFT studies.

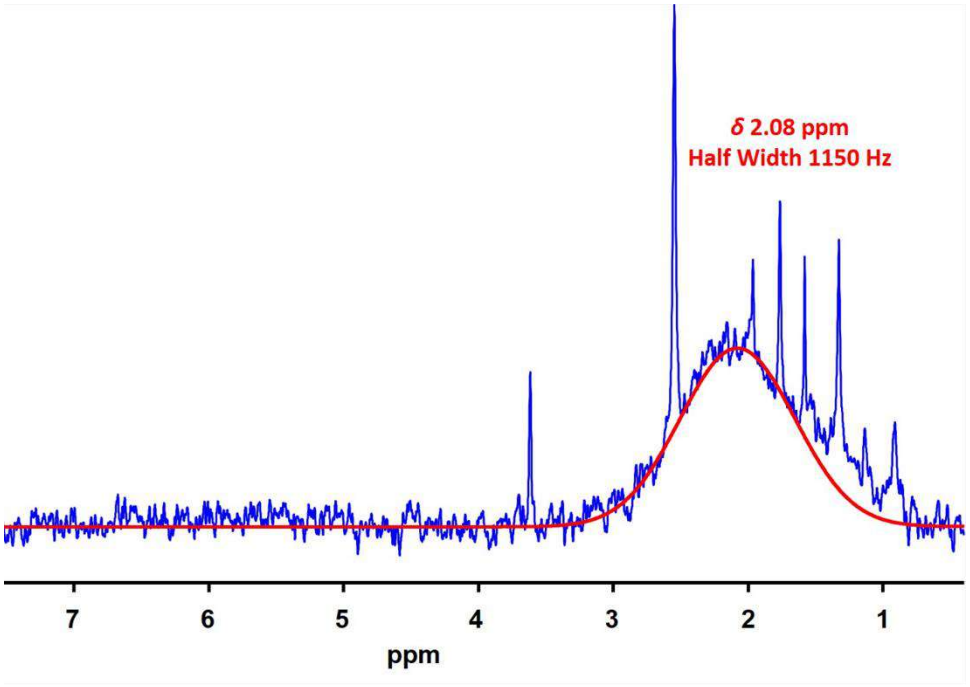

Figure 2.22 Diffusion-filtered DOSY ^{1}H-NMR (THF-d^{8}) spectrum of $Ru_x(CH_3COOH)_{0.4}$ NPs.

The 2D-DOSY NMR experiment allows to distinguish different species by classifying them according to their mobility in the solvent and their hydrodynamic size. Signals of species which possess similar diffusion coefficient will probably belong to the same system or should have highly similar properties between them.[170] The 2D-DOSY NMR experiment for $Ru_x(CH_3COOH)_{0.4}$ NPs (figure 2.23) evidenced signals of species with fast mobility (high diffusion coefficient) that were attributed to water and THF due to their chemical shift.

The 2D-DOSY NMR experiment for $Ru_x(CH_3COOH)_{0.4}$ NPs (figure 2.23) evidenced signals of moieties with fast mobility (high diffusion coefficient) that were attributed to water and THF. However, there is another organic moiety which is heavier and diffuse slower in the deuterate solvent, as it was observed in the diffusion-filtered DOSY ^{1}H-NMR. The overlapping of the broad signal and solvents make the DOSY data difficult to analyze. Nevertheless, interesting results could be obtained by following the evolution of the integration of the [1.9 - 2.2 ppm] area, that contains mostly signals of methyl groups of strongly or weakly bonded ethanoic acid molecules, with the gradient strength.

This diffusional attenuation is shown in figure 2.23 and it was fitted with the classical Stejskal-Tanner equation. The decay could not be fitted with a mono-exponential model and only a bi-exponential analysis least-square fitting leads to a perfectly match of the experimental data. Two different diffusion coefficient (*D*) were extracted from this fitting, one representing 55.0 ± 10.0 % of the signal with D_1 = 2.0 ± 0.3 × 10^{-9} $m^2.s^{-1}$ and the other one representing 45.0 ± 10.0 % of the weight signal with D_2 = 0.5 ± 0.1 × 10^{-9} $m^2.s^{-1}$

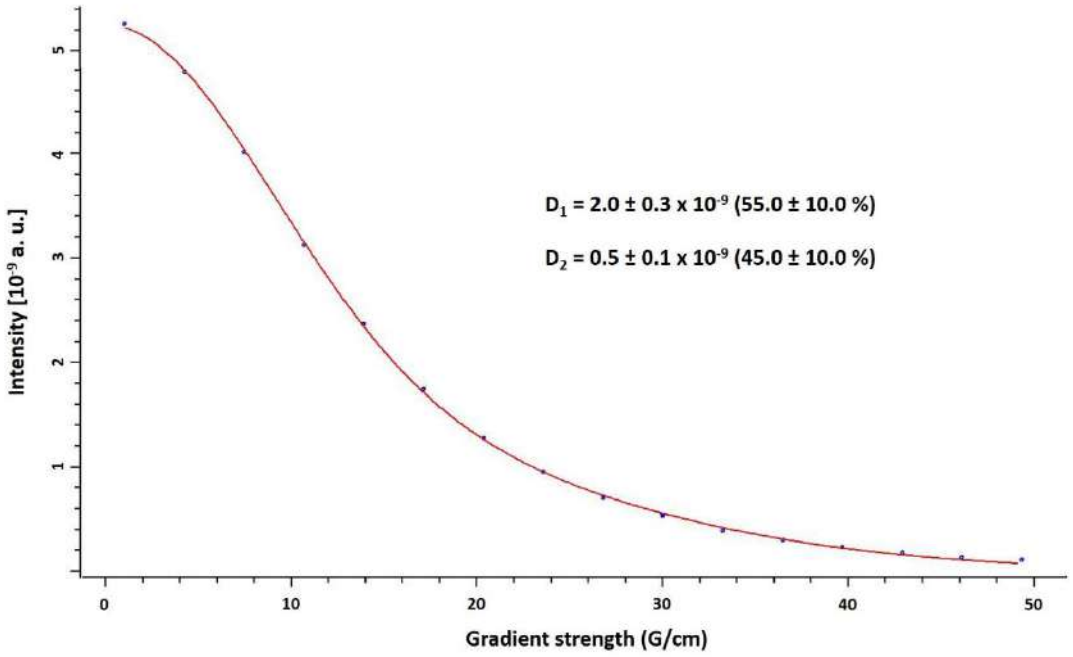

Figure 2.23 Diffusional attenuation of the [1.9 - 2.2 ppm] area for $Ru_x(CH_3COOH)_{0.4}$ NPs dispersed in THF-d^8 at r.t. Data were analyzed with a bi-exponential least-square fitting.

The significant difference between these two diffusion coefficients confirmed the different interaction strength of the capping ligands at the NPs surface, namely a distension between weakly and strongly bonded ligands. The lower diffusion coefficient is attributed to the ligands in strong interaction with the metal surface (*i.e.* direct coordination) and the faster one is assigned to ligands with higher mobility that can be in fast exchange with free ligand in solution (outside the main coordination sphere).

The population of the strongly bonded species (45.0 %) must be considered as a minimal value. Indeed, a significant part of the broad signal weight corresponding to slow diffusion species

detected at *ca.* 2.08 ppm lies outside the [2.2 – 1.9 ppm] range, thus strongly bonded population is probably higher.

At this experimental stage of work, it was not possible to assure that all the ethanoic acid used for the RuNPs synthesis (0.4 equiv.) interacts with the metal system, because there exists the possible ligand removal in the cleaning process applied to the particles for their purification. However, taking as a consideration that all the introduced ligand stays interacting as weakly or strongly bonded onto the RuNPs, it can be estimated from the TEM mean diameter, possible crystalline structure (*hcp*) and DOSY weighted signal averages (*see* section 6.1.3.6.2) that at minimum there are *ca.* 28 carboxylic moieties per ruthenium nanoparticle (28 $CH_3COO(H)/Ru_{NP}$) or *ca.* 0.3 ethanoic ligands per ruthenium surface atom (0.3 $CH_3COO(H)/Ru_{Surf}$).

Hydrodynamic radii were calculated using as a basis the diffusion coefficients observed and solvent viscosity (*see* section 6.1.3.7.1). The radii were found to be *ca*. 0.94 nm for the specie of lower diffusion coefficient and *ca.* 0.23 nm for the faster diffusing specie. From these results, the hydrodynamic diameters of the objects with the lowest coefficient diffusion can be estimated to be *ca*. 1.88 and 0.46 nm (radii x 2), respectively. It is important to remind that the hydrodynamic diameter includes both the metal core and the capping-ligand layer (scheme 2.5 a).

When comparing this value with the NPs mean diameter of *ca*. 1.5 nm obtained from TEM analysis, which represents only the metal core, a difference of *ca*. 0.4 nm is obtained. This difference corresponds to the organic layer thickness of the ethanoic acids surrounding the metal core. For comparison purpose, the hydrodynamic radius of the free ethanoic acid dimer was found to be *ca.* 0.4 nm. Consequently, the metal core calculated by DOSY can be adjusted to *ca.* 1.5 nm when eliminating the contribution of the organic layer, which is in very good agreement with that found by TEM studies. Concerning the calculated hydrodynamic diameter for the carboxylic species with higher diffusion coefficient (*ca.* 0.5 nm), this value is even bigger than that obtained for the free ethanoic acid dimer (ca. 0.4 nm). Therefore the presence of exchanging ligands interacting in a weaker mode with the metal surface and thus making them more dynamics in solution, can be proposed (scheme 2.5 b).[([44],[45])]

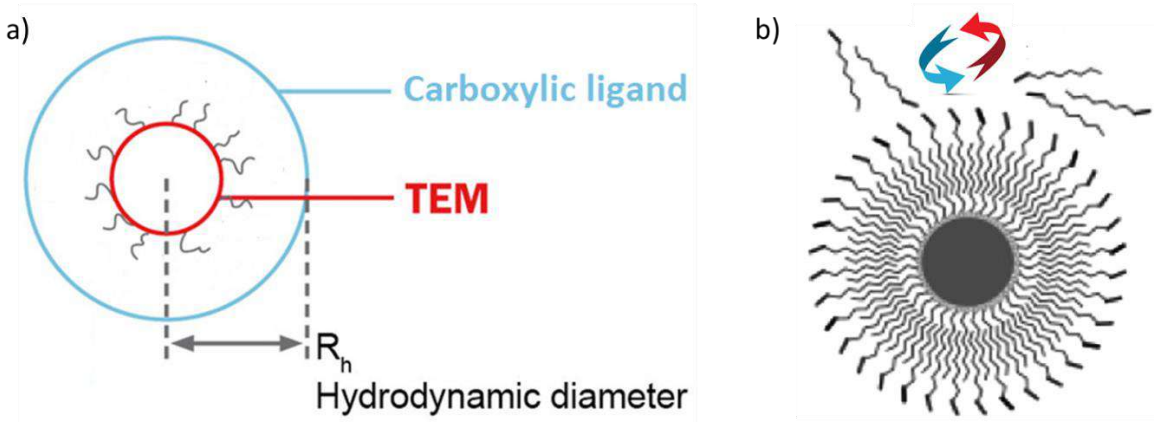

Scheme 2.5 (a) Hydrodynamic diameter representation and (b) fast exchanging ligand proposed.

Liquid NMR techniques (^{1}H and DOSY) allowed to evidence the interaction and coordination of ethanoic moieties onto the RuNPs surface, and the experimental results were corroborated by a DFT-based analysis. Also, information about the ethanoic acid bonding nature, the formation of a hybrid material, the possible quantity of ligand attached directly at the NPs surface and the probable proton acid dissociation were obtained.

In the next section, theoretical studies as well as solid-state NMR and IR spectroscopies, will provide more information on the nature of the coordinated ligand.

2.4 Carboxylic Acid Possible Deprotonation

DFT chemical shift calculations previously described underline that the most probable structure, in agreement to the experimental NMR, found for the carboxylic moiety interacting with the nanoparticle surface is an ethanoate (carboxylate) coordinated in bridging mode (bidentate). In order to answer this question, DFT-based thermodynamic and kinetic studies of the CH_3COO-H bond dissociation were performed. Also, experimental solid-NMR and IR studies with their theoretical counterpart provided useful information that will be presented.

2.4.1 Carboxylic Adsorption Strengths and CH_3COO-H Bond Dissociation

Previous published work had showed calculations regarding the formic acid proton dissociation (HCOO-H) on bare metal (0001) surface. They demonstrated that the process is an exothermic reaction in several transitional metals, for ruthenium it was observed that the value is of *ca.* 129 kcal.mol^{-1}.[171] In another publication, it was reported some evidences of the proton acid bond dissociation in RuNPs stabilized by fullerenehexamalonic acid.[109] Both works point out that the carboxylic acids probably interact as carboxylates with RuNPs surface

Two different models were built and optimized in order to consider the adducts adsorption energies, bond dissociation kinetics and final geometric properties. These models were built from a previously tested Ru_{55} *hcp* NP initial model which is *ca.* 1.0 nm in size (*see* section 6.2.1). The theoretical findings were obtained by performing a series of periodic DFT calculations (*see* section 6.2.2). The mechanism and energy profile were obtained by calculating the adsorption energies of the different adducts in relation with the Ru_{55} NP model (*see* section 6.2.3). The veracity of this methodology was reported in a previous publication.[82]

The first studied model (figure 2.24 a; 1) was based on a bare Ru_{55} NP, thus the calculated energy profile derives from the direct interaction of the carboxylic moiety and the initial Ru_{55} NP model. The second analyzed model (figure 2.24 b; 2) was created from the same base model (Ru_{55} NP) but considering some experimental findings. ^{1}H-NMR provides some insights of the carboxylate presence, in addition of the reductive media (H_2) used for the RuNPs synthesis. Hence, the model was decorated with 15 ethanoates and 32 hydrides. In this last model (2), the ruthenium surface accommodates 0.4 carboxylates and 0.7 hydrides per ruthenium surface atom (CH_3COO/Ru_{surf} & H/Ru_{surf}). Among the 32 hydrides, 15 derive from the carboxylic acid deprotonation meanwhile the rest comes from the reductive media.

The surface composition is close to that determined experimentally by DOSY NMR experiments (28 $CH_3COO(H)/Ru_{NP}$). Indeed, considering that in *ca* 1.5 nm NPs, the number of ruthenium surface atoms is *ca.* 83 Ru_{surf} atoms. It can be inferred that for a 1.0 nm Ru_{55} NP (44

Ru_{surf} atoms) the ethanoates surface coverage should be *ca.* 15 $CH_3COO(H)/Ru_{NP}$. The hydride surface composition in model 2 is slightly beyond the experimental evidence (*see* section 2.5.1).

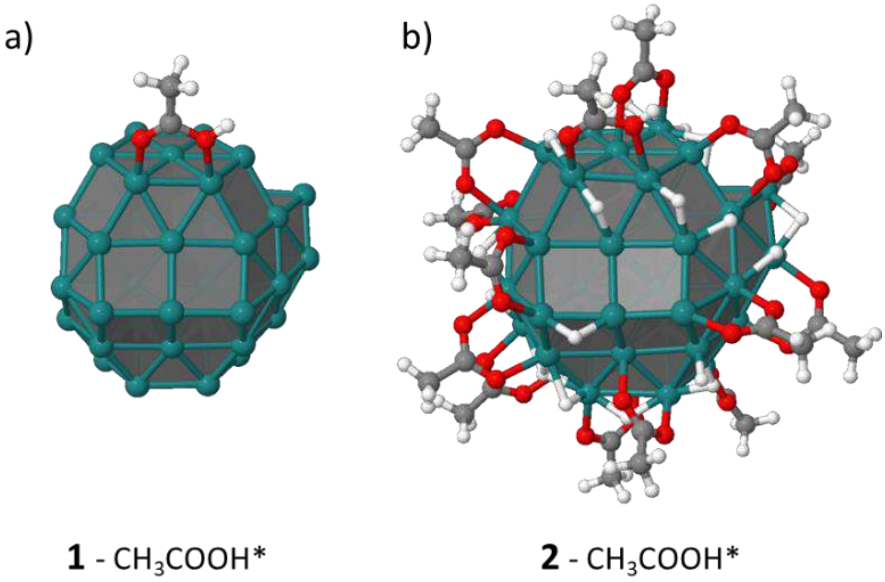

Figure 2.24 Theoretical models used for studying the ethanoic acid interaction with (a) Ru_{55} NP; model 1 & (b) $Ru_{55}(CH_3COO)_{15}H_{32}$ NP; model 2. The faceting of the surface is highlighted with translucent gray planes.

The model 2 that was built as close as possible to the experimental findings provides reference data for an upper limit in terms of surface coverage, meanwhile, the model 1 represents the lowest limit with no surface species. The ethanoic acid ligand was adsorbed on the same site on the 1 and 2 models, *i.e*. edge between the (001) and (101) Ru_{55} NP planes. The ethanoic acid adsorption energy on the bare Ru_{55} NP is about -23.9 $kcal.mol^{-1}$ (figure 2.25; 1 - CH_3COOH*; black profile). When comparing with the adsorption energy of carbon monoxide (CO) on the same model (*ca.* -45.0 $kcal.mol^{-1}$), ethanoic acid can be considered as a ligand moderately chemisorbed.[82] This characteristic becomes less true for the model 2 due to a weaker adsorption energy of the ethanoic acid, -14.0 $kcal.mol^{-1}$, (figure 2.25; 2 - CH_3COOH*; red profile). This value is in the same range to the dissociative adsorption energy of H_2 on bare Ru_{55} NP surface and close to that on crowded hydrogenated Ru_{55} NP, 2H* *ca.* -28.8 & -24.0 $kcal.mol^{-1}$, respectively (*see* section appendix A.1).

Although no steric hindrance impedes the grafting of an ethanoic acid in the model 2, the presence of hydrides and ethanoates in the vicinity of the grafting site, increases the fullness of

the antibonding states, thus reduces the Ru_{55} NP *d*-band center energy and therefore weakens the adsorption strength of the ethanoic acid on the ruthenium metal surface (*see* section 2.6.1).[([172],[173])]

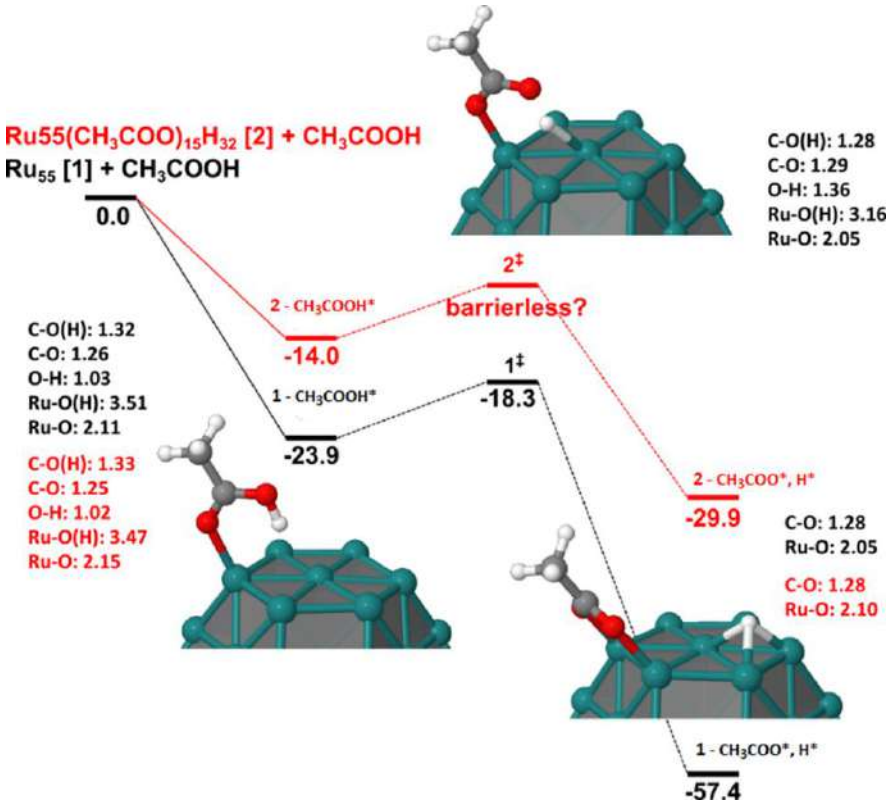

Figure 2.25 Energy profile of the CH_3COO-H bond dissociation. Black profile: O-H activation on the Ru_{55} NP (model 1); red profile: O-H activation on the $Ru_{55}(CH_3COO)_{15}H_{32}$ NP (model 2). Geometries are shown for the model 1, similar parameters were found in model 2. Energies are given in kcal.mol^{-1}. Some characteristic bond lengths are also given, in Å (same color convention as the energy profiles).

The CH_3COO-H bond dissociation on the model 1 (CH_3COOH*) was found to have a small activation barrier, transitional state (TS), of 5.6 kcal.mol^{-1} (figure 2.25; 1 ‡). The procedure is possible due to the adsorption of the dissociated proton (hydride) on the Ru_{55} NP nearest edge, followed by the coordination of the ethanoate in a bridging mode (figure 2.25; 1 - CH_3COO*, H*). The resulting $Ru_{55}(CH_3COO)(H)$ NP is more stable than its carboxylic acid counterpart $Ru_{55}(CH_3COOH)$ NP by 33.5 kcal.mol^{-1}. The CH_3COO-H bond dissociation energy (*ca.* 112 kcal.mol^{-1})[174] is overcompensated by the hydride adsorption and the formation of a five-membered dimetallacycle involving the ethanoate moiety and two ruthenium surface atoms.

Characteristic bond lengths are also given in figure 2.25, similar length trends were found for the naked (1) and crowded Ru_{55} NP model (2). Ongoing from the adsorbed ethanoic acid to its ethanoate counterpart, the O-Ru bond length is reduced by *ca.* 0.06 Å, whereas both C-O bonds have the same length, only *ca.* 0.06 Å larger than a typical $CH_3C{=}O(OH)$ bond length,[175] indicating the conjugation of the dimetallacycle.

Several calculations were performed in order to find the transitional state for the model 2 but it was not detected. This suggests a nearly barrierless CH_3COO-H activation, *i.e*. a very flat energy surface, on ethanoates-stabilized Ru_{55} NP (figure 2.25; 2 ‡).[176] Despite of this phenomenon the ethanoic acid and ethanoate adsorptions energies can be comparable. Like in the model 1, the ethanoate-hydride species in $Ru_{55}(CH_3COO)_{16}(H)_{33}$ NP is thermodynamically more stable than the adsorbed ethanoic form by 15.9 kcal.mol^{-1}.

As it can be concluded from the CH_3COO-H bond dissociation profiles, the grafting of an additional carboxylic group is less favorable in the model 2 than on the bare Ru_{55} NP (1). However, it is also interesting to evaluate the average dissociative adsorption energy of the 16 ethanoic acids.

$$Ru_{55}H_{17} + 16CH_3COOH \rightarrow Ru_{55}(CH_3COO)_{16}H_{33}$$

The adsorption energy for each carboxylate-hydride species is -40.1 kcal.mol^{-1} (*see* section appendix A.4). This value is relatively close to the -29.9 kcal.mol^{-1} energy calculated for the dissociative adsorption energy on model 2 (figure 2.25; 2 - CH_3COO*, H*). The addition of several ligands at the NP surface decreases the surface energy and the adsorption of a new moiety is less energetic,[[177],[178]] thus highlighting the collective effect involved by the simultaneous adsorption of the ethanoic acids.

An attempt to perform a geometry optimization of the carboxylic acid counterpart $Ru_{55}(CH_3COOH)_{16}(H)_{17}$, led to a spontaneous decoordination of five ethanoic acids from the ruthenium metal surface.

$$Ru_{55}H_{17} + 16CH_3COOH \rightarrow Ru_{55}(CH_3COOH)_{11}H_{17} + 5CH_3COOH$$

The thermodynamic and kinetic data offered from the calculated profiles indicate that carboxylic acids interacting with RuNPs will readily form mainly carboxylate species on the metal surface, at least in the explored surface composition [0 H, 0 CH_3COOH - 0.7 H, 0.4

$CH_3COOH]/Ru_{surf}$] and probably beyond. These theoretical data agree with those provided by proton DFT chemical shifts which indicate that the experimental ^{1}H-NMR signal assigned for the ligand -metal interaction can be associated to ethanoates coordinated in a bidentate mode.

2.4.2 Solid-NMR Characterization

Heterogeneity, solubility and motion reduction (associated to dipolar couplings and chemical shift anisotropy) are some of the variables that can cause broad and weak signals in liquid NMR instead of sharp and well-defined ones.[179] In fact, this event is produced because of an increase on the T_2 relaxation time according to the next equation derived from the Heisenberg Uncertainty Principle.[180]

$$\nu_{1/2} = \frac{1}{\pi T_2}$$

By this way, the information obtained from solution NMR is not enough clear for determining the molecular structure or the intermolecular packing of ligands at the NP surface.[181] In particular, this phenomenon is more evident for atoms close to the NP surface and even more importantly for those directly attached. Therefore, they cannot be identified by liquid-state NMR.[164] The application of a high-speed rotation at the magic angle spinning (MAS) allows to reduce this phenomenon, thus leading to visible signals in solid-state NMR that are not accessible by solution NMR.

Thus, information on ligand atoms in close proximity with the metal surface can be reached by solid-state NMR, making this technique a powerful tool to observe the ligand conformation in the metal nanoparticle periphery. For instance, ^{13}C and ^{31}P solid-state NMR allowed to get precise data on the carbon and phosphorous atoms directly attached to the surface of RuNPs stabilized by carbenes[100] or phosphine ligands.[167]

Owing these previous backgrounds, solid-state ^{13}C CP Hahn-MAS NMR was performed on the $Ru_x(CH_3COOH)_{0.4}$ NPs in order to characterize more deeply their surface state. To avoid the formation of electric arcs between the NMR coils and rotor met with the purified RuNPs powder which was due to the high metal content, a THF colloidal suspension of the RuNPs sample was dispersed in mesoporous silica (*see* section 6.1.3.7).

The recorded spectrum is shown in figure 2.26. Two intense peaks are visible at *ca*. 24.2 and 66.8 ppm which are attributed to the carbon atoms from THF used to disperse the particles in silica. The shoulder observed in the foot of the THF signal at *ca*. 24.2 ppm, can be assigned to the methyl carbon of the carboxylic moiety molecular. The chemical shift of the carboxylic group in organic molecules is expected to be found in the region above 170.0 ppm. In the spectrum, the only signal visible over this zone is at *ca*. 186.0 ppm which is downfield shifted compared with the signal of the carboxylic carbon of the free ethanoic acid dimer found in solution NMR (THF-d^8; 171.7 ppm).[182]

The signal marked with an "x" is attributed to the THF degradation as well as the signals found at 126.3 & 142.8 ppm. As it will be observed, these two signals cannot be completely ignored because they could represent a chair coordination mode of the ethanoate onto the RuNPs.

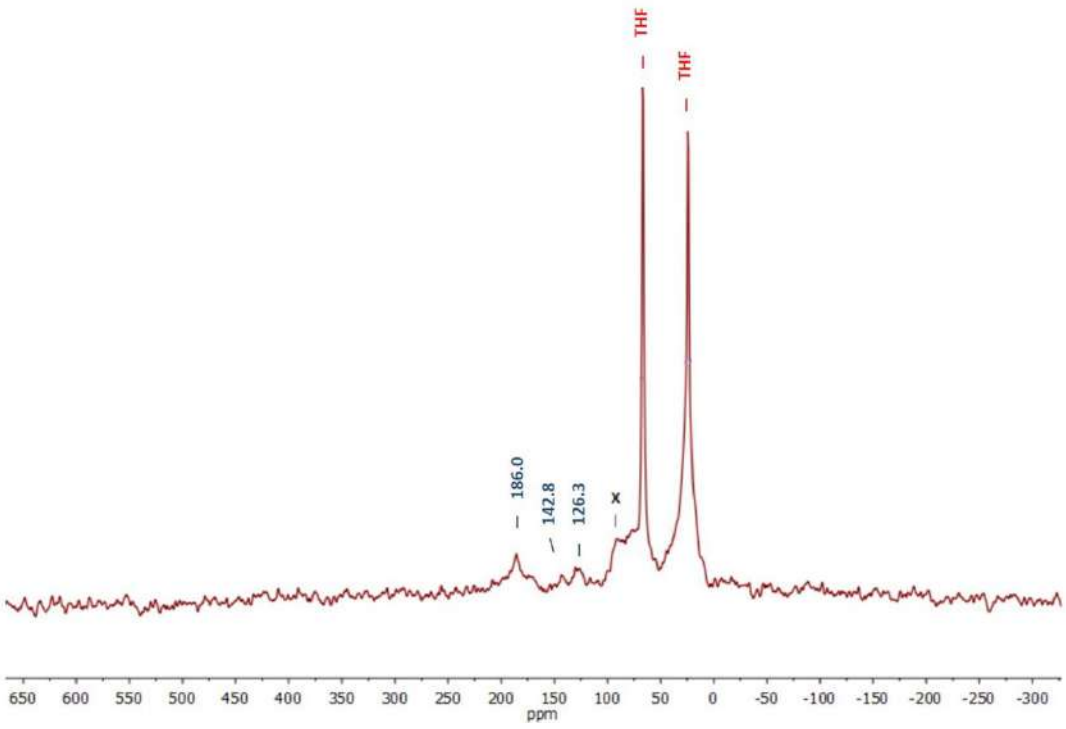

Figure 2.26 ^{13}C CP Hahn-MAS NMR of $Ru_x(CH_3COOH)_{0.4}$ NPs diluted in porous silica.

Taken as a base the same procedure as for ^{1}H-NMR, the assignation of the ^{13}C-NMR signal was corroborated by DFT calculations followed by elucidation of the probable ligand molecular structure. In these calculations, the carbon chemical shifts of protonated-unprotonated carboxylic

acid were obtained as free ligands and as coordinated species onto a [Ru_6] nanocluster (scheme 2.6) by following the previously decribed methodology (*see* section 2.3.1).

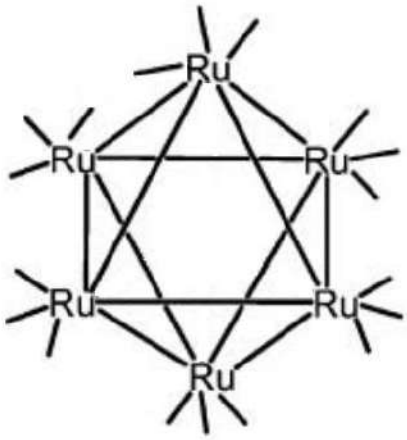

Scheme 2.6 [Ru_6] nanocluster geometrical illustration.

As above mentioned, the carboxylic carbon signal corresponding to the free ethanoic acid dimer was found to be ca. 171.7 ppm in THF-d^8, but it can be shifted depending of the deuterated solvent used for the measurement; *i.e.* 175.8 ppm in benzene-d^6, 176.0 ppm in chloroform-*d* and 177.2 ppm in D_2O.[182] The DFT calculated chemical shift for this specific carbon is 172 ppm (figure 2.27), a value which is in the range of the experimental shift reported and thus accurate enough to evaluate trends. This result points out that the DFT calculations have a good reliability.

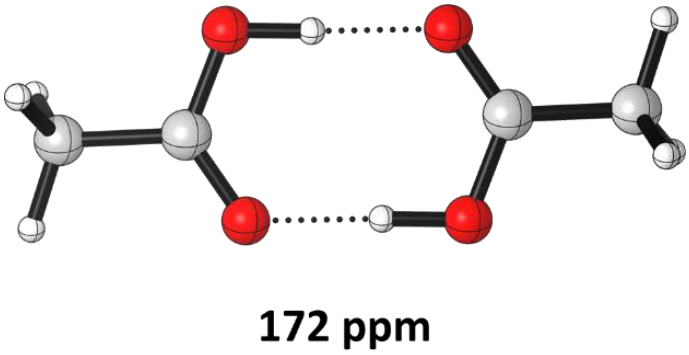

Figure 2.27 DFT mean chemical shift of the carboxylic carbon atoms in the ethanoic acid dimer.

The experimental peak observed as a shoulder in the bottom of the THF signal at *ca*. 24.2 ppm, can be attributed to the carbon of the methyl group of the ethanoic acid due to DFT-NMR

calculations. According to the theoretical model, this signal can be shifted from [20 to 33 ppm] (figure 2.28) thus showing a weak dependence on the coordination mode resonance. But given the broadness of the experimental peak which overlaps with the THF signal, any structure can be assigned.

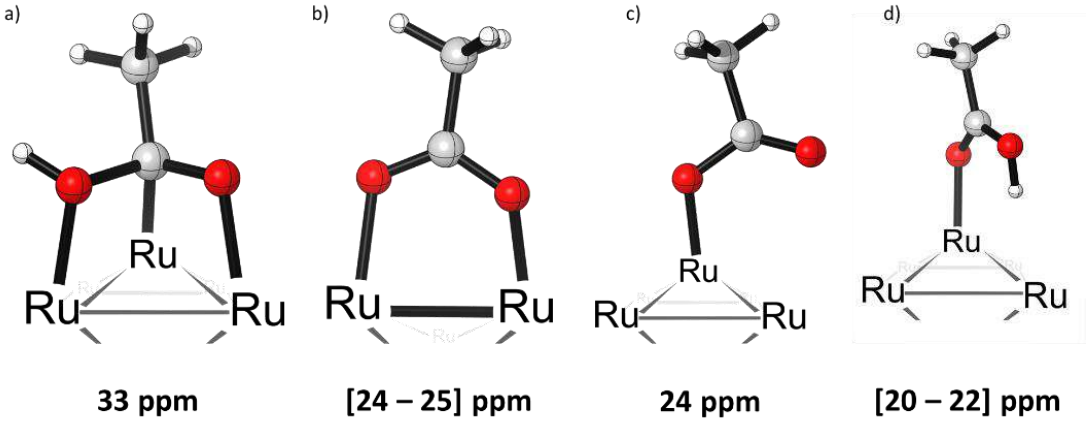

Figure 2.28 Methyl carbon DFT chemical shift of the ethanoic moieties interacting with [Ru_6] nanocluster. Different coordination modes (a) CH_3COOH; σ carbon, μ, (b) CH_3COO; μ, (c) CH_3COO; η & (d) CH_3COOH; η.

Since it was not possible to know any significant data form the methyl carbon, the carboxylic carbon was then evaluated. The obtained values first indicate that there is no free ethanoic acid and nor free ethanoate (figure 2.29 b; 157 ppm) thus corroborating the ^{1}H-NMR findings about the absence of free ligand.

Also, it can be seen that the experimental signal observed at 186.0 ppm does not correspond to π-coordinated carboxylic species that are calculated in low field, at 137 & 147 ppm (figure 2.29 d, c) but it can be assigned to the peaks observed at *ca.* 142.8 & 126.3 ppm.

Thus, the experimental signal observed at *ca.* 186.0 ppm should correspond to a ligand σ-coordination on the ruthenium surface except the ethanoate coordinated as monodentate because its chemical shift is similar to the free ethanoic acid at 170 ppm (figure 2.29 a).

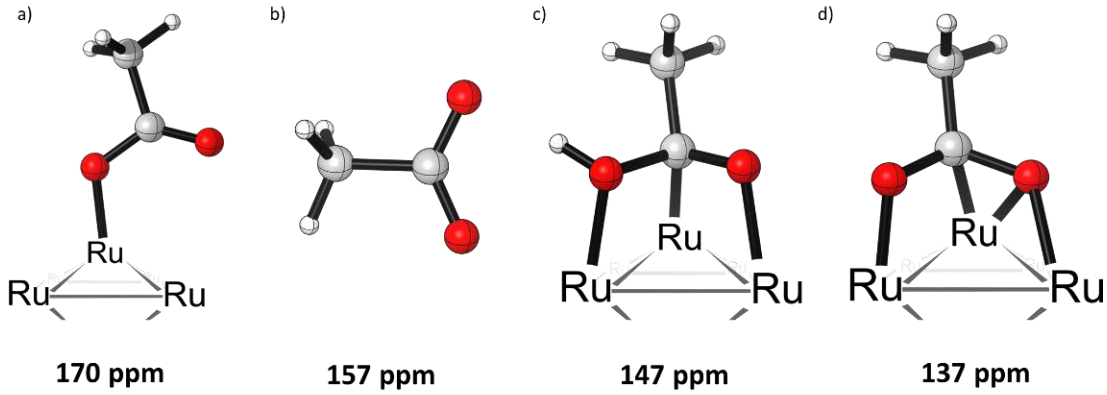

Figure 2.29 Carboxylic carbon DFT chemical shift of the carboxylic moieties free and interacting with [Ru_6] nanocluster. Different coordination modes (a) CH_3COO; η, (c) CH_3COOH; σ carbon, μ, (d) CH_3COO; σ carbon, μ^3 & (b) free CH_3COO.

Hence, the carbon deshielded signal in comparison with free ethanoic acid dimer, can be assigned just to a direct coordination of the ligand onto the RuNPs surface. This data is supported by the broadness of the signal found in the experimental spectrum, the phenomenon is produced for the ligand reduced mobility and the metal surface heterogeneity.

In difference with the ^{1}H-NMR data which indicated the deprotonated species to be favored at the NP surface, the DFT ^{13}C-NMR chemical shifts cannot offer reliable conclusion about the carboxylic moiety molecular structure. It is not easy to distinguish between an ethanoate coordinated in a bringing mode and a σ-bonded coordinated ethanoic acid, because their chemical shifts overlap, [177 - 186 ppm] and [180 - 185 ppm], respectively (figure 2.30). Even it is not possible to rule out the presence of ligand in a π-coordination mode. However, the ^{13}C-DFT-calculations allow to discard the presence of free ligand.

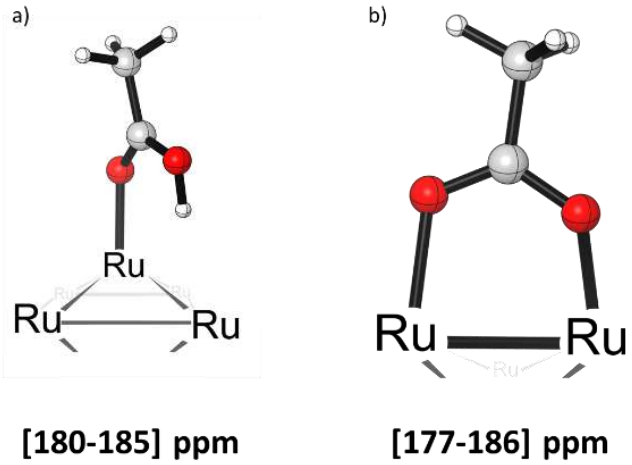

Figure 2.30 Carboxylic carbon DFT chemical shift of the carboxylic moieties interacting with [Ru_6] nanocluster. Different coordination modes (a) CH_3COOH; η & (b) CH_3COO; μ.

These calculations cannot corroborate the CH_3COO-H bond dissociation because there was not a significant difference between the signals observed for the ethanoic acid or ethanoate coordination at the Ru_{55} NP surface

As an outcome of both the ^{1}H and ^{13}C-NMR results and the energy profile, the ligands capping the $Ru_x(CH_3COOH)_{0.4}$ NPs should be interacting as ethanoates. If from the ^{1}H-NMR calculations it was not clear if the ethanoate is coordinated as a dimetallacycle or σ-coordinated through one of its oxygens.

It can be interfered from ^{13}C-NMR calculations and energy profile that ethanoate moiety is formed at the nanoparticle surface and stabilize the system with ethanoates interacting in a bidentate coordination mode. In the figure 2.31, it is summarizing the experimental and theoretical ^{13}C-NMR findings.

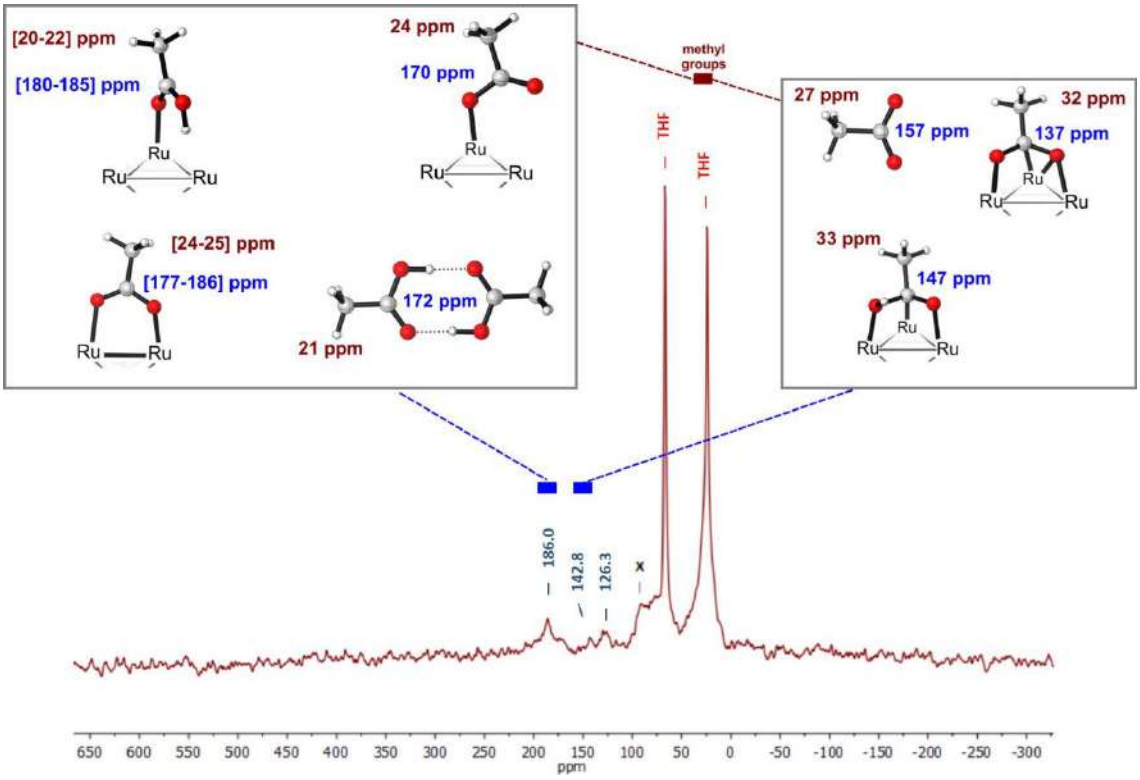

Figure 2.31 Experimental ^{13}C solid-NMR of $Ru_x(CH_3COOH)_{0.4}$ NPs and DFT ^{13}C-NMR chemical shifts of the methyl (red) and carboxylic carbon (blue) in various models ($(CH_3COOH)_2$, CH_3COO^- & $[Ru_6]$ clusters).

2.4.3 Vibrational Properties

Evidences of the free ligand absence and of the ethanoic moiety interaction with the RuNPs surface have been provided in previous sections. Also, insights in favor of the ethanoate coordination against the ethanoic acid have been shown by DFT chemical shift calculation (^1H and ^{13}C-NMR) and by CH_3COO-H bond dissociation profile. However, till now there is no experimental evidence that supports this finding. Thus, to complete this study and answer the question of the molecular structure of the ligand attached onto the metal surface, an FTIR analysis on a solid sample of purified $Ru_x(CH_3COOH)_{0.4}$ NPs was performed in the ATR mode, using a spectrophotometer installed inside a glove box (*see* section 6.1.3.3). The obtained spectrum was first compared with the experimental fundamental peaks of sodium ethanoate in liquid[183] and solid state([184],[185]) (figure 2.32).

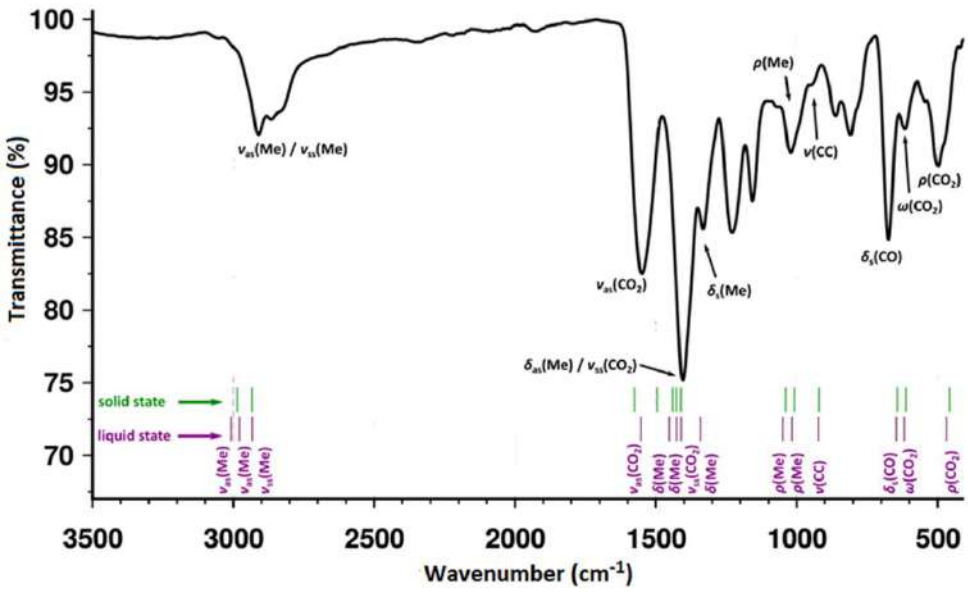

Figure 2.32 Experimental FTIR spectrum of $Ru_x(CH_3COOH)_{0.4}$ NPs and main peaks assignments. The experimental peaks position and assignment of sodium ethanoate (CH_3COONa) are also indicated: in the solid (green) and liquid state (purple). *ν*: stretching; *δ*: bending; *ρ*: rocking; *ω*: wagging; ss or s: symmetric; as: asymmetric.

The experimental FTIR spectrum shows a small broad vibration band at *ca*. 3400 cm^{-1} attributed to the symmetric (ν_s) and asymmetric (ν_{as}) stretching vibration modes of water. The presence of this molecule was previously noticed in the ^{1}H-NMR spectrum but even after long period under high-vacuum it was not possible to totally remove it.

The bands observed at *ca.* 2970 cm^{-1} are attributed to the ν_{as} and ν_{ss} vibration modes of the methyl group of the carboxylic moiety ($(CH_3)COO(H)$). No carboxylic acid ($R(C=O)OH$) stretching vibration bands are visible in the region [1850 - 1600 cm^{-1}], indicating the absence of free or coordinated ethanoic acid for which a vibration band is expected at *ca.* 1800 cm^{-1} in standard conditions.[186]

Instead, a band at *ca.* 1545 cm^{-1} can be found and it is attributed to the ν_{as} vibration mode of a carboxylate ($CH_3(C=O)O$) thanks to its similarities with the sodium ethanoate spectrum.[183] At lower energies, two well separated bands between 1500 and 1300 cm^{-1} can be observed. Compared to the sodium ethanoate spectrum, they can be attributed to three different vibration modes, the asymmetric stretching mode ν_{as} of the carboxylate group ($CH_3(C=O)O$), and the bending asymmetric δ_{as} and symmetric δ_s vibration modes of the methyl group ($(CH_3)COO$). Below 1000 cm^{-1}, five well separated characteristic bands of the ethanoate moiety can be assigned. They

successively correspond to ρ ($(CH_3)COO$), ν ($H_3(CC)OO$), δ_s ($CH_3(CO)O$), ω ($CH_3(C{=}OO)$), ρ ($CH_3(C{=}OO)$) vibration modes, the wavenumber of these signals corresponds with high accuracy to those visible on the sodium ethanoate spectra (1000, 910, 660, 600 & 510 cm^{-1}), meaning no significant shift was found. The FTIR experimental data point out that the coordinated ligand is under an ethanoate form, due to the absence of carboxylic acid vibration mode and the high similitude with the sodium ethanoate spectra

In order to obtain the theoretical counterpart, Ru-H, and Ru-ethanoate normal modes of vibration of the Ru_{55} crowded NP (2 - CH3COO*, H* model) were calculated (*see* section 6.2.2 & 6.2.7). Although this model cannot represent exactly the experimental $Ru_x(CH_3COOH)_{0.4}$ NPs, it is a relevant approach for the purpose of corroborating the assignment of experimental bands (figure 2.33).

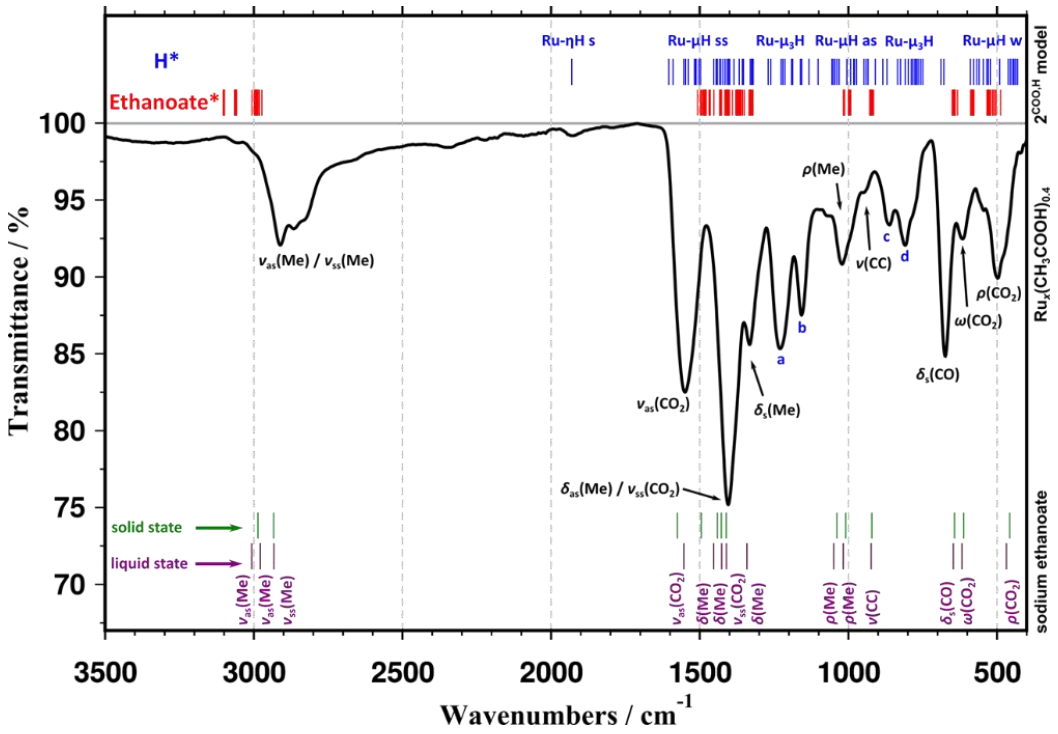

Figure 2.33 Experimental FTIR spectrum of $Ru_x(CH_3COOH)_{0.4}$ NPs and theoretical harmonic frequencies calculated for model 2 CH_3COO*, H* (blue: Ru-H modes; red: Ru-ethanote modes). The signals of CH_3COONa are also shown.

The harmonic frequencies calculated for the ν_{as} and ν_{ss} vibration modes of the ($(CH_3)COO$; figure 2.33 red) are slightly overestimated by 200 cm^{-1} with respect to the experimental spectrum. Meanwhile, the ν_{as} vibration mode of the ethanoate ($CH_3(C{=}OO)$) is slightly underestimated and

they are found between [1500 – 1300 cm^{-1}], this effect can be attributed to the overestimation of the Ru to COO back-donation.[187] The last five bands are in a good agreement with the normal modes of vibration calculated for this model.

Due to the different coordination modes of the hydrides that lie on the studied theoretical model, the Ru-H harmonic frequencies (figure 2.33 blue) can be found in a high range of frequencies from [1600 to 400 cm^{-1}]. Except one mode of vibration that corresponds to the hydride η coordination mode that appears around 1950 cm^{-1}, which could be assigned to a small peak observed in the experimental spectrum at the same frequency range. The theoretical calculations of vibrational bands show a good agreement with the experimental data and present useful trends to elucidate the structure of the ligand coordinated as ethanoate at the RuNPs surface

Four bands (a-d) observed in the experimental spectrum at 1220, 1150, 850 and 800 cm^{-1} cannot be correlated with any ethanoate vibration modes. Also, they do not correspond to any calculation performed on the 2 - CH3COO*, H* model. Similar harmonic frequencies calculations were thus performed in the 2 - CH3COOH* model, where three different normal modes of vibration were found and attributed to a, b and c unassigned signals, namely at 1243, 1155 δ_s (CH_3(COOH)), and 853 cm^{-1} ν (H_3(CC)OOH). However, carboxylic acid vibration mode (CH_3(C=O)OH) was found in in 2 - CH3COOH* model at 1680 cm^{-1}. Since no band were observed around 1700 cm^{-1} in the experimental spectrum, the hypothesis of the presence of a mixture of entities as in the 2 - CH3COOH* model cannot be supported.

But as silicon grease and perfluoropolyeter (PFPE) lubricant were used to maintain inert atmosphere during the $Ru_x(CH_3COOH)_{0.4}$ NPs synthesis, band a can be assigned to the PFPE presence,[188] meanwhile c and d signals are attributed to those of silicon grease.[189] The presence of these pollutants was also observed in the ^{1}H-NMR spectrum.

To finish, THF could be responsible for the peak b and the weak peak close to 1950 cm^{-1}, that were previously noted to possibly correspond to Ru-H η vibration mode, due to its presence during the RuNPs purification process (*see* section 2.5.3). Also, the THF under certain catalytic conditions can be polymerized (PTHF) which has a vibration mode at *ca.* 1110 cm^{-1}.[190] Thus the band b could be assigned to PTHF. Previous published study has proved the THF decarbonylation

in the presence of RuNPs leading to the presence of a carbonyl vibration on FTIR spectra.[133] Thus, the small peak here found at *ca.* 1950 cm^{-1} can be also assigned to the presence of CO.

As a conclusion of this section, the normal modes analysis together with the sodium ethanoate data provide a clear assignment of most of the experimental FTIR bands observed for $Ru_x(CH_3COOH)_{0.4}$ NPs. These results combined with the experimental and theoretical ^{1}H and ^{13}C-NMR and the CH_3COO-H bond dissociation profile point out that all the ligands surrounding the RuNPs are not under the carboxylic acid form but deprotonated as ethanoates.

2.5 Surface Composition

The nanomaterials surface composition has an important influence on their size, solubility and surface state of these metal systems.([191],[192]) The catalytic performance of such systems depend on the surface energy of the nanoparticle, due to adsorption-desorption processes and to the influence of stabilizing ligands on surface energy.([177],[193]) A catalyst will have the best performance when this ratio is fully optimized.[194]

Apart from elucidation of ligand coordination mode at NP surface, the knowledge of the ligands present at the surface and of the surface coverage is an important prerequisite in order to shed light on the possible relationship between these properties and the catalytic activity of such materials.[10] Therefore the surface composition becomes a crucial parameter to be studied.

2.5.1 Experimental Titration of Surface Hydrides

The synthesis of $Ru_x(CH_3COOH)_{0.4}$ NPs has been performed by the decomposition of a ruthenium metal precursor in the presence of reductive atmosphere (H_2). The presence of hydrides at the NPs surface has been demonstrated as a consequence of the synthetic conditions in different metals,([195],[196]) including ruthenium.[59] It has also been seen than these hydrides seem to be highly reactive.[59]

Thus, owing to the synthesis conditions (3 bar H_2, r.t.), the presence of hydrides at the surface of the RuNPs was expected. The titration of surface hydrides was performed by investigating the $Ru_x(CH_3COOH)_{0.4}$ NPs as catalysts in the hydrogenation model reaction of 2-norbornene at r.t. with no extra hydrogen added (*see* section 6.1.4.1). The olefin conversion into norbornane in the presence of $Ru_x(CH_3COOH)_{0.4}$ NPs was observed to be low, but enough for its detection and quantification by GC analysis (scheme 2.7).

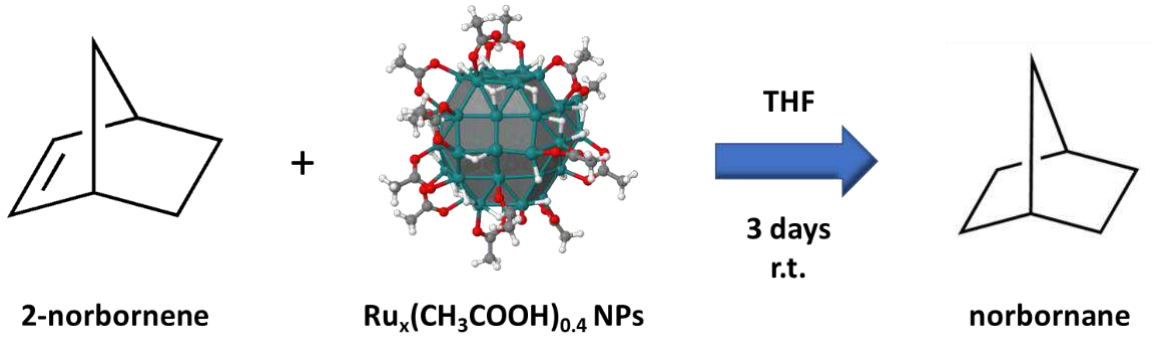

Scheme 2.7 Surface hydrides titration by a catalytic reduction of 2-norbornene in the presence of $Ru_x(CH_3COOH)_{0.4}$ NPs.

The reductive formation of norbornane was measured by GC. Indirectly, the reaction yield allows the determination of reactive hydrides that are responsible for the 2-norbornene reduction. Furthermore, this data permits to calculate the hydrides surface coverage on the $Ru_x(CH_3COOH)_{0.4}$ NPs by considering the nanoparticles mean size obtained by TEM microscopy (*ca.* 1.5 nm) and the estimated crystalline structure observed by HRTEM (*hcp*).

The calculated value was *ca*. 0.3 reactive hydrides per ruthenium surface atom (0.3 H_{reac}/Ru_{surf}). This value means that at room temperature there are at least 25 hydrides per ruthenium nanoparticle (25 H/Ru_{NP}) for these $Ru_x(CH_3COOH)_{0.4}$ NPs.

The hydrides titration for these nanosystems appears a bit low compared to values previously reported for other ligand-stabilized RuNPs that were in the range [1.0 - 1.6 H_{reac}/Ru_{surf}].[93] This result thus shows an important difference in terms of metal surface state of the nanoparticles with less surface hydrides present. Therefore, their evaluation in catalysis is an important goal to be achieved.

2.5.2 DFT Titration of Surface Species

In this section, it will be shown that it is possible as well to theoretically evaluate the number of ethanoates and hydrides at the surface of the $Ru_x(CH_3COOH)_{0.4}$ NPs. As a reminder, the experimental titration of reactive hydrogen atoms at r.t. by an indirect olefin reductive reaction has been shown in the section 2.5.1. However, due to experimental issues a reliable titration of the ethanoates at the Ru NPs surface was not fully accomplished (*see* section 2.3.2). Thus, the DFT titration of surface species can be a complementary and powerful tool to map the surface state of the $Ru_x(CH_3COOH)_{0.4}$ NPs an get information about the quantity of capping-ligands and determine a precise surface composition of the RuNPs.

It is indeed possible to calculate the Gibbs free energy and other thermodynamic functions of solids and liquids, using first principles methods. Such approach, the so-called *ab initio* thermodynamics method, has successfully been applied to explain or predict thermodynamic material properties, and in particular surface properties.[([197]–[199])]

The DFT energies obtained from optimized structures covered by organic molecules are calculated without taking into consideration the concentrations, pressure or temperature variables which are crucial in the systems behavior and on surface coverage. Yet, adding the zero-point energy correction to a DFT energy only leads to the 0 K internal energy. This *ab initio* thermodynamics methodology allows to extend the applicability of DFT to realistic environmental conditions in terms of temperature, pressure and composition of the gas and liquid surrounding phase, which is considered as a reservoir of species in equilibrium with the metal NPs.

The procedure has recently been applied to ruthenium surfaces and NPs with a good agreement to experimental findings, those studies were enforced to ruthenium systems in equilibrium with molecular hydrogen only or with syngas (H_2 & CO).[([82],[200]–[202])]

The robustness and predictability of this approach was thus here evaluated for the $Ru_x(CH_3COOH)_{0.4}$ NPs system. For this purpose, different co-adsorption ratios of dissociated H_2 and protonated-deprotonated CH_3COOH were put onto the surface of a 1.0 nm Ru_{55} *hcp* NP model (*see* section 6.2.1). The resulting structures were fully optimized in order to obtain the DFT energy of each system (*see* section 6.2.2). Although it is possible to calculate the adsorption energies of

the different ligands (*see* section 6.2.3), the thermodynamical model relies on the calculation of the free Gibbs adsorption energy:

$$\Delta_a G = \frac{[\Delta G^\circ - n_1\mu(L_1, T, c) - n_2\mu(L_2, T, p)]}{A}$$

Where the adsorption energy usually calculated as

$$E(n_1L_1^*, n_2L_2^*) - E(RuNP) - n_1E(L_1) - n_2E(L_2)$$

Is hidden in ΔG° and in the chemical potentials $\mu(L_1)$ and $\mu(L_2)$, (*see* section 6.2.6).

The studied systems possess a large number of atoms and electrons, the planewave basis set is large (or to be more explicit, the cutoff value is large) and owing to their diameter, the unit cell must be large enough to avoid spurious interactions between images. Therefore, a direct optimization of the built structures is computationally highly demanding. Thus, a progressive optimization of the ligand coverage ratio was performed in order to save computational resources (figure 2.34).

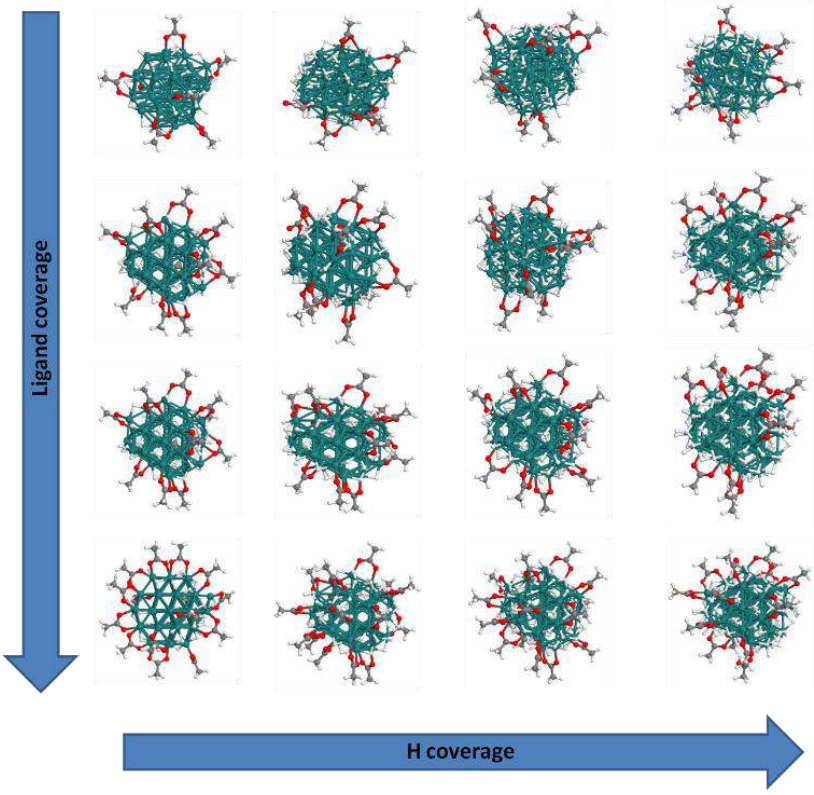

Figure 2.34 Progressive methodology applied to optimize Ru_{55} NP structures with different ligand (H & CH_3COOH) coverages.

Forty-four different coverage possibilities have been considered, the corresponding optimized geometries and energies are reported in sections appendix A.1 and A.4. Previous experimental and theoretical analysis of the vibrational and ^{1}H and ^{13}C-NMR data, as well as the very low CH_3COO-H activation barrier, pointed out the higher stability of adsorbed ethanoates with respect to adsorbed ethanoic acids. This is why, 41 of these 44 structures only exhibit ethanoates on the metal surface. The 44 different coverage ratios of the structures considered in this study are reported in table 2.4.

Table 2.4 Optimized structures used for the DFT surface titration. The total number and coverage ratio of coordinated ligands are also shown with the corresponding DFT energy (eV). (a) Number of hydrides that come from the dissociative adsorption of H_2; (b) total number of hydrides *i.e.* that comes from a and from the CH_3COO-H bond dissociation.

#	ε (eV)	nH (a)	nH/Ru_surf (a)	nH* (b)	nH*/Ru_surf (b)	nCH3COOH	nCOO-*	nCOOH*	Name
1	-424.37	0	*0.0*	0	*0.0*	0	0	0	Ru_{55}
2	-492.69	17	*0.4*	17	*0.4*	0	0	0	H_{17}
3	-564.41	35	*0.8*	35	*0.8*	0	0	0	H_{35}
4	-634.19	53	*1.2*	53	*1.2*	0	0	0	H_{53}
5	-697.69	70	*1.6*	70	*1.6*	0	0	0	H_{70}
6	-612.81	35	*0.8*	36	*0.8*	1	1	0	$(CH_3COO)\,H_{36}$
7	-682.91	53	*1.2*	54	*1.2*	1	1	0	$(CH_3COO)\,H_{54}$
8	-745.93	70	*1.6*	71	*1.6*	1	1	0	$(CH_3COO)\,H_{71}$
9	-660.00	35	*0.8*	37	*0.8*	2	2	0	$(CH_3COO)_2\,H_{37}$
10	-729.60	53	*1.2*	55	*1.3*	2	2	0	$(CH_3COO)_2\,H_{55}$
11	-793.09	70	*1.6*	72	*1.6*	2	2	0	$(CH_3COO)_2\,H_{72}$
12	-708.14	35	*0.8*	38	*0.9*	3	3	0	$(CH_3COO)_3\,H_{38}$
13	-777.89	53	*1.2*	56	*1.3*	3	3	0	$(CH_3COO)_3\,H_{56}$
14	-840.62	70	*1.6*	73	*1.7*	3	3	0	$(CH_3COO)_3\,H_{73}$
15	-618.99	0	*0.0*	4	*0.1*	4	4	0	$(CH_3COO)_4\,H_4$
16	-670.85	13	*0.3*	17	*0.4*	4	4	0	$(CH_3COO)_4\,H_{17}$
17	-756.37	35	*0.8*	39	*0.9*	4	4	0	$(CH_3COO)_4\,H_{39}$
18	-826.00	53	*1.2*	57	*1.3*	4	4	0	$(CH_3COO)_4\,H_{57}$
19	-888.47	70	*1.6*	74	*1.7*	4	4	0	$(CH_3COO)_4\,H_{74}$
20	-814.00	0	*0.0*	8	*0.2*	8	8	0	$(CH_3COO)_8\,H_8$
21	-848.65	9	*0.2*	17	*0.4*	8	8	0	$(CH_3COO)_8\,H_{17}$
22	-863.98	13	*0.3*	21	*0.5*	8	8	0	$(CH_3COO)_8\,H_{21}$
23	-880.14	17	*0.4*	25	*0.6*	8	8	0	$(CH_3COO)_8\,H_{25}$
24	-947.36	35	*0.8*	43	*1.0*	8	8	0	$(CH_3COO)_8\,H_{43}$
25	-1,014.50	53	*1.2*	61	*1.4*	8	8	0	$(CH_3COO)_8\,H_{61}$
26	-1,074.53	70	*1.6*	78	*1.8*	8	8	0	$(CH_3COO)_8\,H_{78}$
27	-912.05	0	*0.0*	10	*0.2*	10	10	0	$(CH_3COO)_{10}\,H_{10}$
28	-976.91	17	*0.4*	27	*0.6*	10	10	0	$(CH_3COO)_{10}\,H_{27}$
29	-1,043.37	35	*0.8*	45	*1.0*	10	10	0	$(CH_3COO)_{10}\,H_{45}$
30	-1,106.51	53	*1.2*	63	*1.4*	10	10	0	$(CH_3COO)_{10}\,H_{63}$
31	-1,168.13	70	*1.6*	79	*1.8*	10	9	1	$(CH_3COO)_9\,(CH_3COOH)\,H_{79}$
32	-1,009.28	0	*0.0*	12	*0.3*	12	12	0	$(CH_3COO)_{12}\,H_{12}$
33	-1,072.83	17	*0.4*	29	*0.7*	12	12	0	$(CH_3COO)_{12}\,H_{29}$
34	-1,137.82	35	*0.8*	47	*1.1*	12	12	0	$(CH_3COO)_{12}\,H_{47}$
35	-1,204.67	53	*1.2*	65	*1.5*	12	12	0	$(CH_3COO)_{12}\,H_{65}$
36	-1,262.42	70	*1.6*	80	*1.8*	12	10	2	$(CH_3COO)_{10}\,(CH_3COOH)_2\,H_{80}$
37	-1,106.85	0	*0.0*	14	*0.3*	14	14	0	$(CH_3COO)_{14}\,H_{14}$
38	-1,168.63	17	*0.4*	31	*0.7*	14	14	0	$(CH_3COO)_{14}\,H_{31}$
39	-1,202.18	0	*0.0*	16	*0.4*	16	16	0	$(CH_3COO)_{16}\,H_{16}$
40	-1,235.95	9	*0.2*	25	*0.6*	16	16	0	$(CH_3COO)_{16}\,H_{25}$
41	-1,264.48	17	*0.4*	33	*0.8*	16	16	0	$(CH_3COO)_{16}\,H_{33}$
42	-1,326.98	35	*0.8*	51	*1.2*	16	16	0	$(CH_3COO)_{16}\,H_{51}$
43	-1,391.54	53	*1.2*	69	*1.6*	16	16	0	$(CH_3COO)_{16}\,H_{69}$
44	-1,449.19	70	*1.6*	84	*1.9*	16	14	2	$(CH_3COO)_{14}\,(CH_3COOH)_2\,H_{84}$

Gibbs free energies, $\Delta_a G°$ (T, p_{H_2}, C_{acid}) were calculated for each one of the 44 structures at three different temperatures (T = 200, 300 and 450 K) by taking into account the DFT energy of the optimized systems and the ligand-metal vibration corrections (*see* section 6.2.7 and appendix D).[([199]–[202])] Even though the acid-metal and ethanoate vibrations have been taken into account, it must be underlined that the Ru-H vibrational contribution to $\Delta_a G°$ is the highest (for a comparison of 1D phase diagrams with and without vibrational contributions.[82]

The thermodynamic model used for the Gibbs free energy calculations and hence the chemical potentials consider H_2 as an ideal gas and the acid as an infinitely dilute solute in the presence of THF. Although the results are less accurate and questionable for very high pressure and concentration, it gives interesting trends. Moreover, the energies are calculated by taking into account the molecular hydrogen pressure and ethanoic acid concentration in equilibrium with the surface (p_{H_2}, [CH_3COOH]).

The structures which have the lowest Gibbs free energy ($\Delta_a G°$) at certain pressure and concentration domains are the most stable, and thus they are the only one plotted in a 2D phase diagram It is good to note that very low pressure and concentration domains are plotted just to show the relative positions of the stability domains with respect to higher pressure and concentration (*see* section 6.2.6). The first phase diagram analysis will now be performed by considering the temperature used for the $Ru_x(CH_3COOH)_{0.4}$ NPs synthesis, *i.e*. 300 K (figure 2.35).

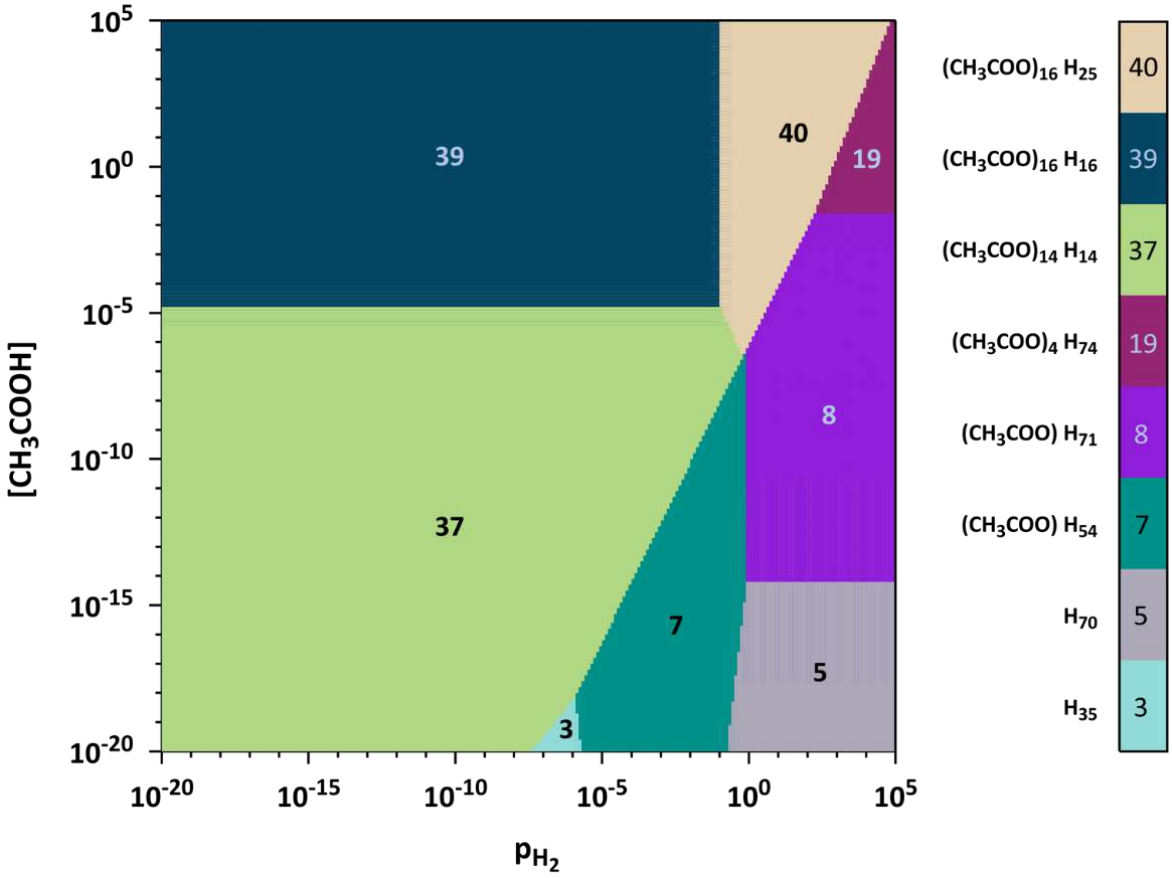

Figure 2.35 $\Delta_a G°$ (p_{H_2}, [CH_3COOH]) phase diagram for H_2 (gas) and CH_3COOH (liquid) adsorption on Ru_{55} NP at 300 K (pressure in bar, concentration in mol.L^{-1}).

From the 44 calculated structures only 8 of them (figure 2.36) appear to be stable in the considered pressure and concentration domains. It can be seen that at high hydrogen pressure and low ethanoic acid concentration, the most stable Ru_{55} NP structures are the one covered with almost only hydrides (domain 3 & 5) or a low quantity of them (domain 7).

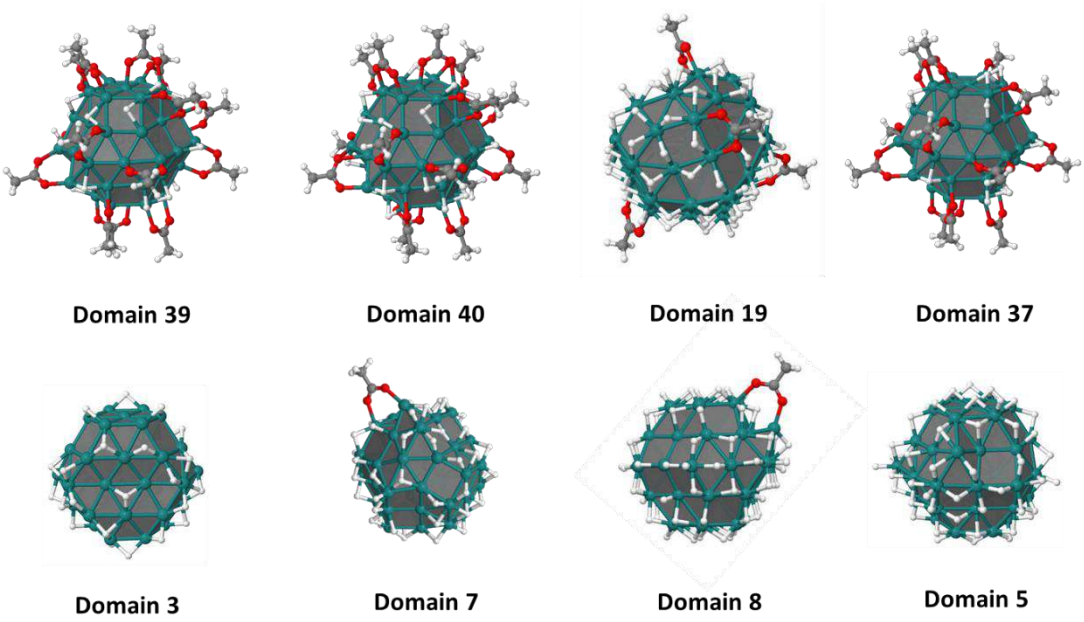

Figure 2.36 Most stable [Ru_{55}] structures in each domain. (Domain 39: $Ru_{55}(CH_3COO)_{16}(H)_{16}$; domain 40: $Ru_{55}(CH_3COO)_{16}(H)_{25}$; domain 19: $Ru_{55}(CH_3COO)_4(H)_{74}$; domain 37: $Ru_{55}(CH_3COO)_{14}(H)_{14}$; domain 3: $Ru_{55}(H)_{35}$; domain 7: $Ru_{55}(CH_3COO)(H)_{54}$; domain 8: $Ru_{55}(CH_3COO)(H)_{71}$; domain 5: $Ru_{55}(H)_{70}$).

In order to make a link with the actual experimental conditions, the ethanoic acid concentration was calculated by taking into account the liquid volume added into the Fisher-Porter reactor for the $Ru_x(CH_3COOH)_{0.4}$ NPs synthesis, this value is *ca.* $10^{-2.7}$ mol.L^{-1}. Also, by measuring the reactor volume, owing to the molecular hydrogen pressure used for this synthesis (3 bar) and to the temperature (r.t.), it was possible to determine a relative H_2 pressure, which ranges at *ca.* [10^{-4} – 10^{-3}] bar.

It comes from Figure 2.35 that two domains (39 and 40) can be considered as consistent with the experimental conditions (roughly, when p_{H_2} and [CH_3COOH] are in the range [10^{-5} - 10^{-2} bar] and [10^{-4} - 10^{-1} mol.L^{-1}], respectively). The corresponding stable structures are shown in figure 2.36 and their coordinates are given in section appendix F.

The first structure exhibits 16 ethanoates and 16 hydrides interacting with the Ru_{55} NP surface, the hydrogen species originate from the ethanoic acid decomposition (figure 2.36; domain 39). Above this threshold when p_{H_2} > 10^{-2} bar, the Ru_{55} NP surface is stabilized by the same amount of ethanoates but can accommodate nine additional hydrides presumably coming from the reductive atmosphere (H_2) used during the RuNPs synthesis. (figure 2.36; domain 40).

The resulting structures have 0.4 CH_3COO per ruthenium surface atom (0.4 CH_3COO/Ru_{surf}) and [0.4 & 0.6 H/Ru_{surf}], respectively. It must be recalled that the hydrides titration (*see* section 2.5.1) showed that the RuNPs surface is covered by 0.3 H_{reac}/Ru_{surf}, meaning that at least around 13 H are adsorbed on the metal surface if this ratio is interpolated to the Ru_{55} NP model. The theoretical findings are slightly overestimated with respect to experiments, but it needs to be considered that the quantification was performed at room temperature and that experiment quantify active hydrides. Thus, as a conclusion this theoretical investigation confirms that *ab initio* thermodynamics accurately account for the number of hydrides coordinated at the nanoparticle surface and it confirms the lower number of adsorbed hydrides in this nanosystem, compared to usually observed and calculated amounts in other RuNPs.[93]

In the other hand regarding ethanoates, DOSY-NMR studies showed the existence of two types of ligands, strongly (*ca.* 45.0 %) and weakly bonded (*ca.* 55.0 %). In order to be compared with the theoretical model, only the ethanoates which have a strong interaction with the metal surface are here studied. Thus, it can be inferred that approximately 28 CH_3COO/Ru_{surf} lie on the RuNP surface. This ratio suggests that around 15 carboxylates are expected to be strongly bonded onto the Ru_{55} NP model, in very reasonable agreement with the surface composition found for domains 39 and 40. Both theoretical studies and experimental findings are thus in a good agreement about the RuNPs surface composition. It further validates the theoretical approach and it provides an accurate mapping of the surface-capping ligands presented in the surface of the $Ru_x(CH_3COOH)_{0.4}$ NPs.

The surface coverage was also evaluated at low temperature (200 K) in order to evaluate what the surface composition would be if a hypothetical synthesis could be performed at this temperature (figure 2.37).

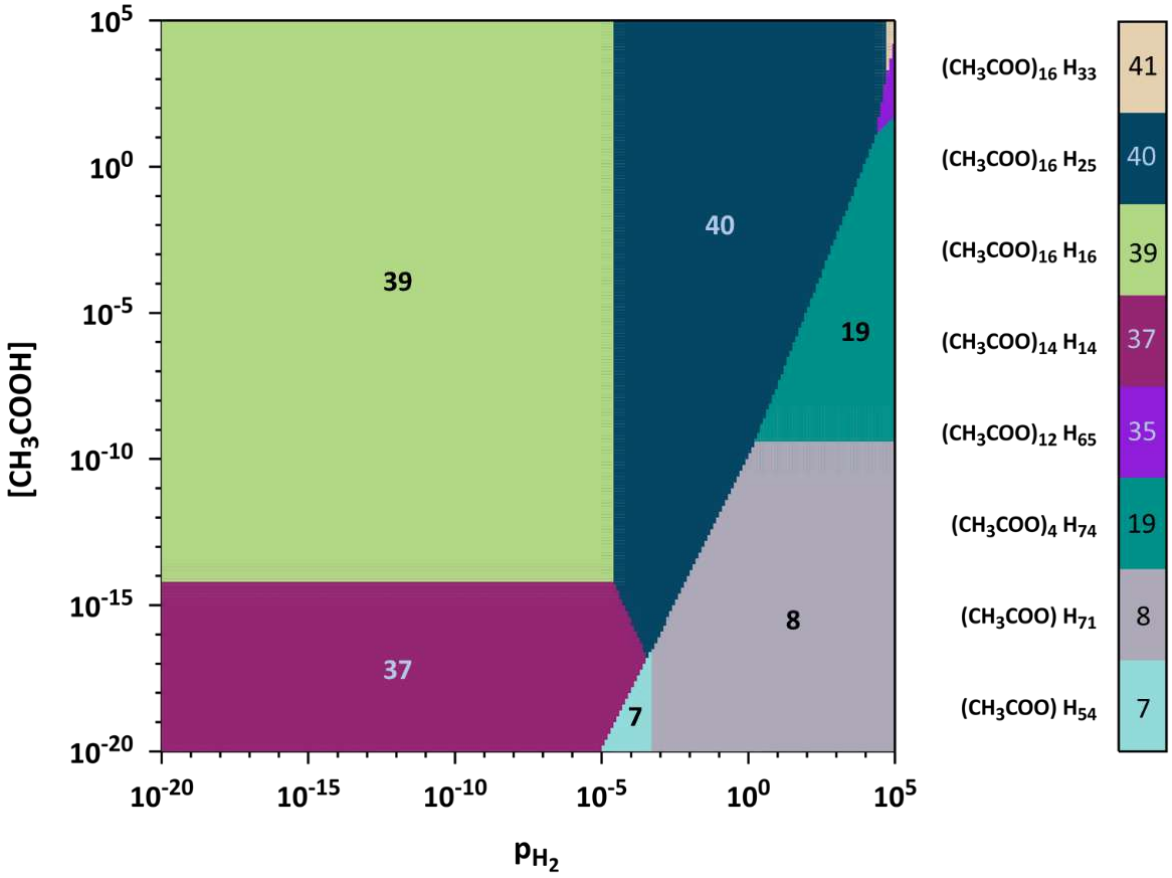

Figure 2.37 $\Delta_o G°$ (p_{H_2}, [CH_3COOH]) phase diagram for H_2 (gas) and CH_3COOH (liquid) adsorption on Ru_{55} NP at 200 K (pressure in bar, concentration in $mol.L^{-1}$).

In this case, 8 Ru_{55} NP among the 44 calculated structures also are found to be the more stable at 200 K (figure 2.37). In comparison with the phase diagram presented at 300 K (figure 2.36) two new optimized structures (figure 2.38) can be observed at low concentration-pressure of both ligands (domain 35; $Ru_{55}(CH_3COO)_{12}(H)_{65}$) and the other one at high concentration-pressure (very small domain 41; $Ru_{55}(CH_3COO)_{16}(H)_{33}$).

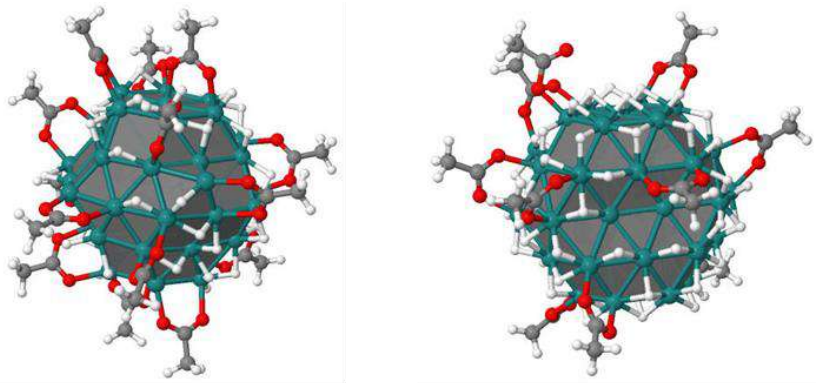

Figure 2.38 Additional stable [Ru_{55}] clusters found at 200 K. (Domain 41: $Ru_{55}(CH_3COO)_{16}(H)_{33}$; domain 35: $Ru_{55}(CH_3COO)_{12}(H)_{65}$).

The decrease in temperature (ΔT = -100 K) involves a lowering of the adsorption Gibbs free energy of the ligands ($\Delta_a G°$) and an increase of the surface energy of the nanoparticles.[203] As a result the surface coverage of the metal nanoparticle is increased that is why optimized structures covered by only hydrogen cannot be found. Also, it explains the appearance of domains with higher quantity of organic molecules *i.e.* domain 41 & 35, their coordinates can be seen in section appendix F. In other words, the lower the temperature the higher the quantity of ligands that can be present at the Ru_{55} NP surface, as expected. In this case the carboxylate form is preferred due to its higher adsorption energy in comparison with that of the hydrides (*see* section appendix A).

The hypothetic experimental conditions are slightly affected by the temperature, thus a similar equilibrium pressure and concentrations as those found at r.t., *i.e*. an hydrogen pressure of [10^{-5} – 10^{-2} bar] and an ethanoic acid concentration in the range [10^{-4} - 10^{-1} mol.L^{-1}] can be considered. In these ranges, the same stable structures were found (domain 39; 16 CH_3COO & 16 H; domain 40; 16 CH_3COO & 25 H). As a conclusion, the surface composition is not affected by a significant decrease of temperature in the experimental range of $(p_{H_2})_{eq}$ and $[CH_3COOH]_{eq}$.

A similar analysis was performed at higher temperature (450 K) in order to see if the opposite behavior can be described and to observe if the same stable structure domains are found (figure 2.39).

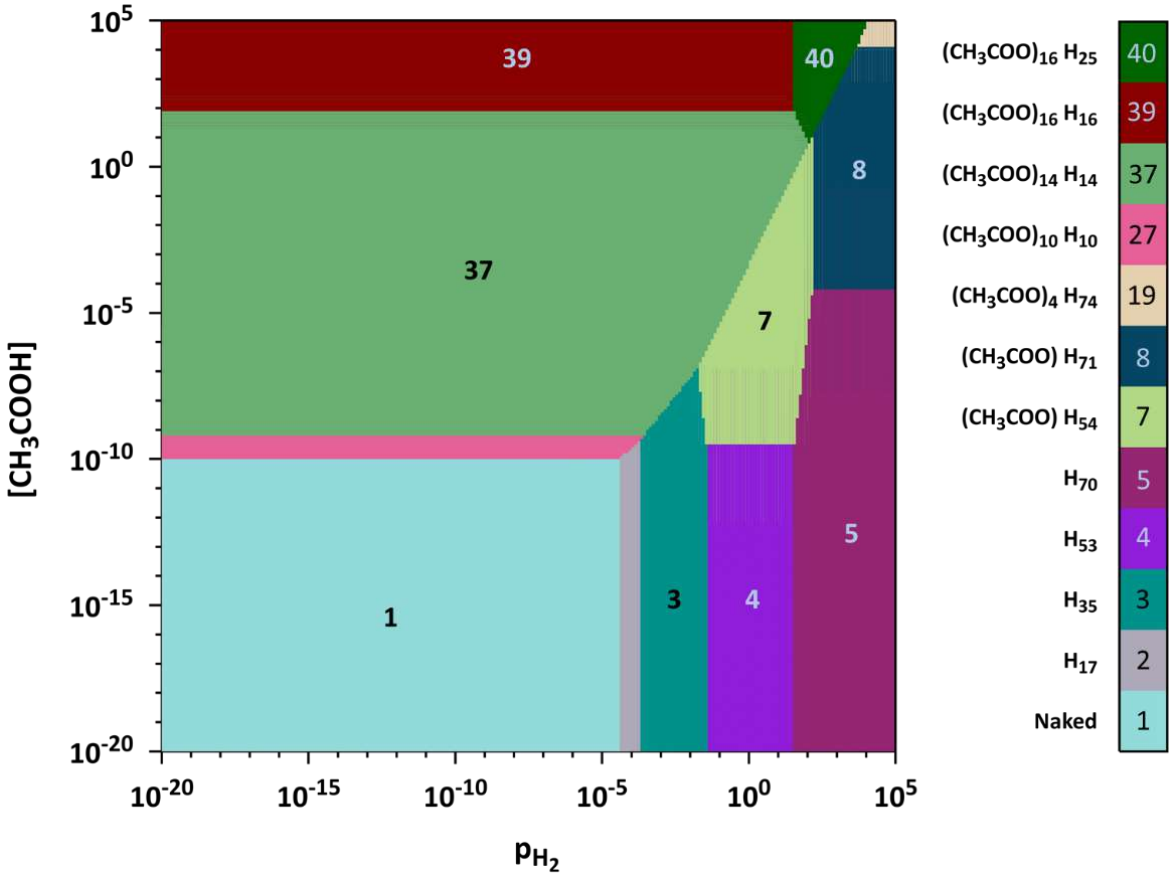

Figure 2.39 $\Delta_o G°$ (p_{H_2}, [CH_3COOH]) phase diagram for H_2 (gas) and CH_3COOH (liquid) adsorption on Ru_{55} NP at 450 K (pressure in bar, concentration in $mol.L^{-1}$).

Previously published studies have demonstrated that the The temperature increase involves to significantly decreasing higher the temperature the lower the catalytic activity in some nanosystems, due to the increase in the system mobility. Also, it has been seen that the adsorption energy of the binding ligand increases letting to a decrease of the surface coverage.[204] As it can be seen in the phase diagram calculated at 450 K (figure 2.39) new stable optimized structures can be found at certain p_{H_2} and [CH_3COOH] ranges. These structures (figure 2.40) are stabilized by less quantity of ligands (domain 27), or even only by hydrides (domains 2 & 3). If the pressure and concentration conditions are too low, the surface of the Ru_{55} NP cannot be stabilized (domain 1). In this case, such NPs would probably not exist, since such 1.0 nm NP would probably coalesce to form larger systems. Again, the coordinates of these structures can be found in section appendix F.

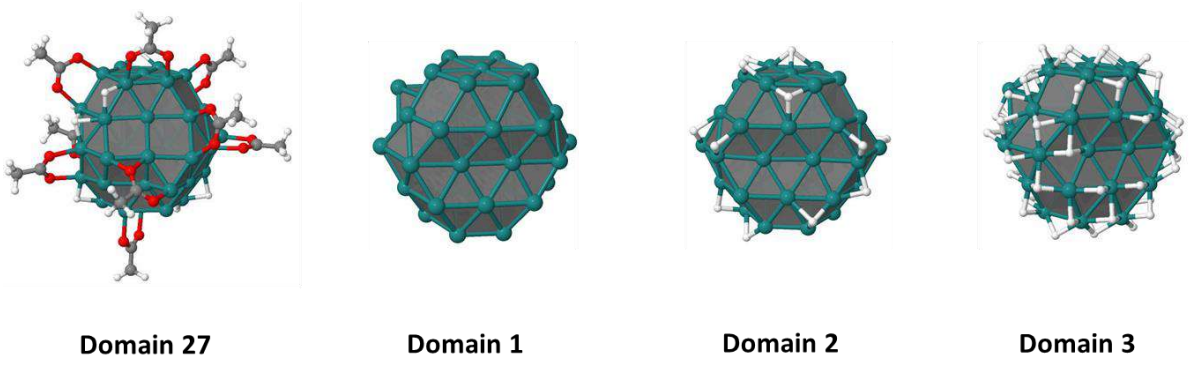

Figure 2.40 Additional stable [Ru_{55}] clusters found at 450 K. (Domain 27: $Ru_{55}(CH_3COO)_{10}(H)_{10}$; domain 1: Ru_{55}; domain 2: $Ru_{55}(H)_{17}$; domain 3: $Ru_{55}(H)_{53}$).

Now, domains 39 and 40, found to be the more stable at 200 and 300K, can be found by significantly increasing p_{H_2} and [CH_3COOH]. If we focus on the same pressure and concentration ramges as done for the other temperatures (p_{H_2}: [10^{-5} - 10^{0} bar]; [CH_3COOH]: [10^{-4}-10^{-1} mol.L^{-1}]), a new domain (37) dominates and less probably a completely different domain (7).

The temperature increase involves to significantly decreasing the amount of carboxylic acid and hydrogen in the surrounding medium, this phenomenon can be observed for the domain 37 where the Ru_{55} NP can accommodate 14 CH_3COO/Ru_{surf} and the same amount of hydrides coming from the carboxylic acid deprotonation 14 H/Ru_{surf}. Although the dissociative adsorption energy of H_2 is low compared to CH_3COOH, when p_{H_2} is high enough, there is a competition between hydrides and ethanoates. This is what is observed in domain 7, with a remarkable reversal of the H/ethanoate stoichiometry (1 CH_3COO/Ru_{surf} and 54 H/Ru_{surf}) for a low acid concentration and a significantly high pressure of hydrogen.

This can be explained in terms of the metal surface energy, which relies upon the adsorption strength of each ligand and on the total number of ligands that are bound on a given metal surface area (*see* section 6.2.6). It turns out that on a crowded metal surface the dissociative adsorption strength of an ethanoic acid is *ca*. -26.7 kcal.mol^{-1} (CH_3COO: 16; H: 51; *see* section appendix A.4) *i.e*. it is not significantly higher than the dissociative adsorption energy of H_2 (*ca.* -24.0 kcal.mol^{-1}; H: 70; *see* section appendix A.1). Yet, owing to steric hindrance considerations, a given surface area cannot accommodate as many ethanoates as hydrides. The balance between

similar adsorption energies, steric hindrance, pressure & concentration and temperature could explain this drastic change in the surface composition on going from domain 37 to domain 7.

2.5.3 On the Possible Presence of THF at the NPs Surface

In this study, the $Ru_x(CH_3COOH)_{0.4}$ NPs were washed with THF prior to spectroscopic studies and used as deuterated solvent for liquid and solid NMR experiments. This opens the possibility for some THF molecules to be adsorbed on RuNPs. Yet, in a previously published work, the presence of THF at the RuNPs surface has been indirectly observed due to its possible polymerization.[190] As well, due to its decomposition *via* a decarbonylation[133].

It is also known that the THF, which is a polar aprotic solvent, has the ability of assist in the MNPs stabilization by coordinating at the NPs surface in some metals (Pt and PdNPs)([205],[206]) but for RuNPs it has been described as simple synthesis assistant or as pollutant mostly after its reaction ar the NP surface.[207] Till now, there is not a clear proof of the RuNPs formation by using just THF as stabilizing agent.[158]

Experimental characterization of $Ru_x(CH_3COOH)_{0.4}$ NPs provided evidences of the THF presence onto these RuNPs. Signals present in FTIR and solid-state NMR experiments have been attributed as coming from THF. In order to evaluate the possible presence of THF, a first evaluation of its ligand viability and stabilizing strength was performed.

A RuNPs synthesis with higher inert conditions and lower presence of oxidants was achieved by using THF both as solvent and stabilizing agent ($Ru_x(THF)_y$). The experimentation was accomplished by decomposing [Ru(COD)(COT)] following the same methodology and conditions as procedure 6.1.2.2 but without any extra ligand. The reaction time was extended overnight (scheme 2.8).

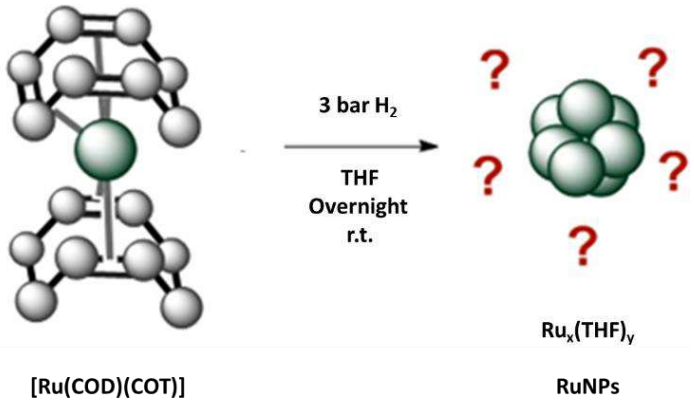

Scheme 2.8 Synthesis of RuNPs stabilized by THF

After evacuation of remaining hydrogen (H_2), a semi-stable suspension was obtained which was concentrated under high-vacuum before preparation of a grid in order to perform TEM analysis. The micrographs show the presence of two different types of particles: Big metal agglomerates of *ca.* 40.0 nm and heterogeneous RuNPs with a mean size of *ca.* 2.9 ± 1.8 nm (figure 2.41), which is a mean size close to that obtained for RuNPs stabilized with alcohols, such as propanol or heptanol.[94]

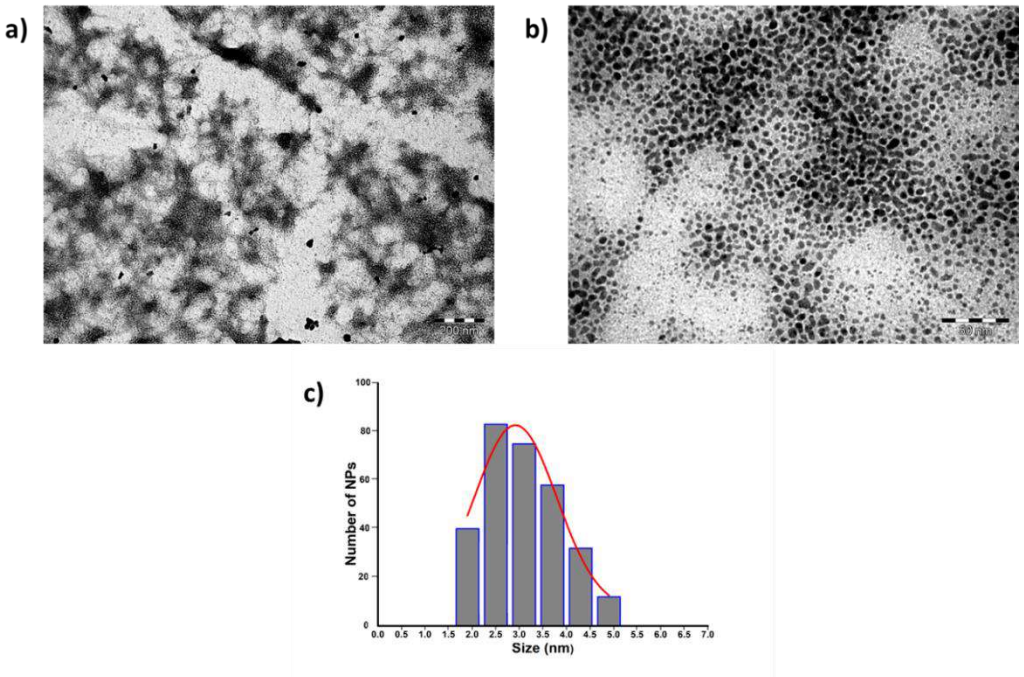

Figure 2.41 TEM micrographs of $Ru_x(THF)_y$ NPs; (a) Ru agglomerates; scale bar: 200 nm; (b) RuNPs; scale bar: 50 nm; (c) size histogram of individual RuNPs.

These finding proves the ability of this solvent to be used as a stabilizer. The formation of agglomerates beside quite large and heterogeneous RuNPs also indicates that it is not the best stabilizing agent, despite the high quantity of THF present in the reaction media. These findings point out that THF can be adsorbed at the RuNPs surface. However, it behaves as a poor electron donor ligand, thus it is unable to reduce the ruthenium nanostructure surface energy, which leads to a poor control of the nanoparticle size and the formation of agglomerates.([93],[208])

Despite these results, the presence of THF on preformed $Ru_x(CH_3COOH)_{0.4}$ NPs cannot be firmly demonstrated by experimental techniques. Thus, a theoretical study was performed in order to provide more information about the THF interaction with the RuNPs surface and on its possible co-adsorption with ethanoates and hydrides

The different ligands (CH_3COOH, CH_3COO & THF) adsorption energies on different hydrogenated Ru_{55} NP ($Ru_{55}(H)_{35\text{-}70}$, *see* section 6.2.1 – 6.2.3) were calculated in order to evaluate the possible competition that could happen between THF and the carboxylic species on the metal surface. The selected hydrogenated model was used with the aim was to decrease the nanoparticle reactivity by partially saturating the NPs surface to offer more relevant results.[209]

The THF adsorption strength is not very sensitive to the hydrogen surface coverage, with adsorption energies that lie between *ca.* [-16.2 - -21.2 kcal.mol^{-1}] (*see* section appendix C.2). Given its low adsorption energy, THF can be considered as moderately chemisorbed. Its adsorption strength is similar to the dissociative adsorption energy of H_2 at the same level of calculation *(ca*. -11 kcal.mol^{-1} x 2; see appendix A.1), which suggests that it can dynamically interact at the surface, as hydrogen does, provided that the adsorption barrier height is low.

When compared the THF adsorption energy with that of the ethanoic acid *ca.* [-17.8 - -25.8 kcal.mol^{-1}], it appears to be slightly weaker but not significantly enough (*see* section appendix C.1) to rule out a possible exchange between these two molecules. At certain point the energies can be similar which led them to a surface area competition or in a ceaseless exchange (scheme 2.9).

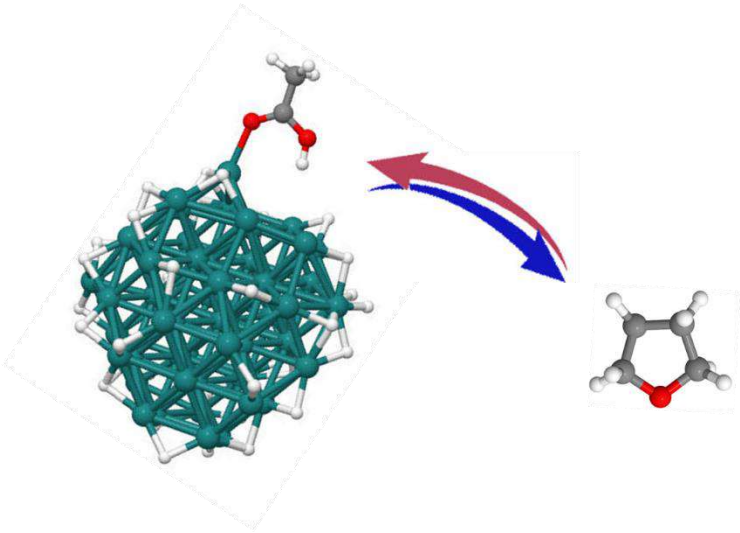

Scheme 2.9 Representation of the possible continuous ligand exchange between ethanoic acid or hydrogen and THF.

Previously it was proven, both experimentally and theoretically, that ethanoic acids are deprotonated. Their dissociative adsorption energies are stronger via values in the range [-40.1 - -51.1 kcal.mol^{-1}] (*see* section appendix A.3.2). Therefore, it is suggested that THF can hardly compete with ethanoates onto the Ru_{55} NP. Also, it explains why controlled and small RuNPs can be synthetized by using ethanoic acid and particles are they are not well-formed when THF is used as stabilizing agent. These results support the relevance of the ligand donor strength in the RuNPs formation.

Since the nanoparticles are covered by ethanoates and not ethanoic acid, at this point becomes difficult to support the hypothesis of having THF coordinated at the RuNPs surface. It is worthy to point that the THF came in contact with the nanoparticles while being already formed (for purification and solution NMR experiments). Thus, in order to have more reliable data it is necessary to evaluate the possible THF presence on ligand-crowded Ru_{55} NP.

To achieve this goal, the THF adsorption energy onto RuNP surface was tested and compared on the model 2 used previously to evaluate the CH_3COO-H bond dissociation (*see* section 2.4.1). This model has a crowded surface and was demonstrated to have a ligand surface coverage ratio ($Ru(CH_3COO)_{15}(H)_{32}$) similar to the optimal compositions found in the phase diagram at 300 K (*see* section 2.5.2).

The grafting of THF on the model 2 metal surface, which involves the σ-donation of one oxygen lone pair to a ruthenium atom, is stable by -28.6 kcal.mol^{-1} (figure 2.42) offering a plausible data of the THF presence when comparing the same adsorption procedure with the ethanoic acid (-14.0 kcal.mol^{-1}) model 2 CH_3COOH* or ethanoate (-29.9 kcal.mol^{-1}) model 2 CH_3COO*, H*.

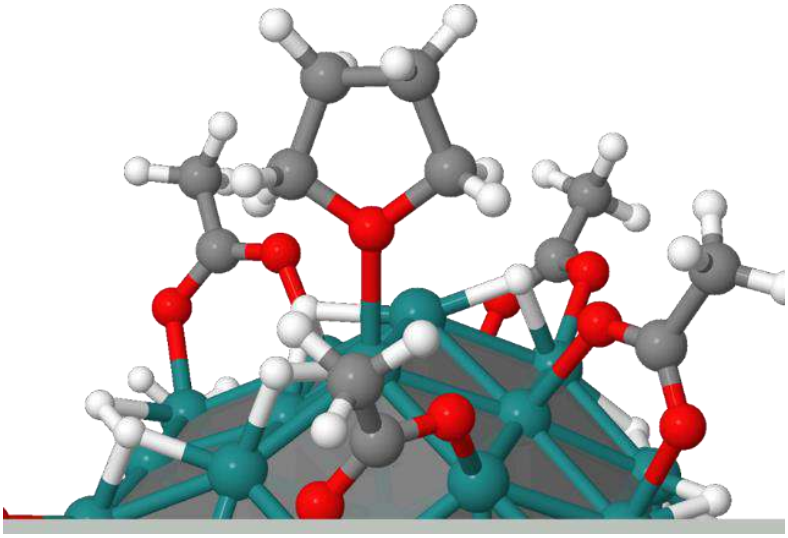

Figure 2.42 Optimized geometry of $Ru_{55}(CH_3COO)_{15}(H)_{32}(THF)$.

It can be inferred from these energies that the equilibrium exchange reaction between the model 2 CH_3COO*, H* and THF is slightly endothermic 4.8 kcal.mol^{-1} in favor of the ethanoate presence, but not significant enough to completely vanish the hypothesis of the THF presence on the $Ru_x(CH_3COOH)_{0.4}$ NPs.

$$Ru_{55}(CH_3COO)_{16}(H)_{33} + THF \rightarrow Ru_{55}(CH_3COO)_{15}(H)_{32}(THF) + CH_3COOH$$

As it has been demonstrated, the adsorption energy of the different adducts changes in function of the total amount of adsorbed species, thus the equilibrium exchange reaction (THF/CH_3COOH) can bring out another outcome if this value is modified. Therefore, another model was explored with less quantity of ethanoates and hydrides.

$$Ru_{55}(CH_3COO)_{14}(H)_{14} + THF \rightarrow Ru_{55}(CH_3COO)_{13}(H)_{13}(THF) + CH_3COOH$$

For this model the reaction becomes even more endothermic (*ca.* 43.0 kcal.mol^{-1}). In conclusion, these results are not in favor of the presence of THF at the surface of RuNPs and any of them support or corroborate the signals attributed to THF in the experimental characterization.

Nevertheless, if a Ru_{55} NP stabilized only by hydrides is considered. As already said on the basis of adsorption energies, hydrides and THF could compete to stabilize the surface

For corroborating this assumption, a phase diagram (p_{H_2}, [THF]) was performed at T = 300K by following the same methodology as in section 2.5.2, but using only the H-Ru vibration correction which is known to have a significant effect on the Gibbs free energy calculation. In this case, 16 different structures with low THF coverage [0.0 – 0.1 THF/Ru_{surf}] and a high quantity of hydrides [0.8 - 1.6 H/Ru_{surf}] were evaluated (table 2.5).

Table 2.5 Optimized structures used for the ($\boldsymbol{p_{H_2}}$, [THF]) phase diagram. Ligand coverage ratios are also shown with the corresponding DFT energy (eV). (a) Number of hydrides that come from the dissociative adsorption of H_2.

#	E (eV)	nH (a)	nH/Ru_surf (a)	nTHF	Name
1	-424.37	0	*0.0*	0	Ru_{55}
3	-564.41	35	*0.8*	0	H_{35}
4	-634.19	53	*1.2*	0	H_{53}
5	-697.69	70	*1.6*	0	H_{70}
45	-637.12	35	*0.8*	1	(THF) H_{35}
46	-707.08	53	*1.2*	1	(THF) H_{53}
47	-770.39	70	*1.6*	1	(THF) H_{70}
48	-709.67	35	*0.8*	2	$(THF)_2$ H_{35}
49	-779.91	53	*1.2*	2	$(THF)_2$ H_{53}
50	-842.86	70	*1.6*	2	$(THF)_2$ H_{70}
51	-782.32	35	*0.8*	3	$(THF)_3$ H_{35}
52	-852.41	53	*1.2*	3	$(THF)_3$ H_{53}
53	-915.20	70	*1.6*	3	$(THF)_3$ H_{70}
54	-854.56	35	*0.8*	4	$(THF)_4$ H_{35}
55	-924.49	53	*1.2*	4	$(THF)_4$ H_{53}
56	-987.23	70	*1.6*	4	$(THF)_4$ H_{70}

As can be seen on the phase diagram plotted in figure 2.43, among the 16 structures, 7 are stable in the considered range of pressure and concentration. Moreover, in the low concentration range (p_{H_2}, [THF]) the most stable structure is the bare nanoparticle (domain 1, Ru_{55}), in line with a weak interaction of these species with the NP surface. This diagram also supports the previous hypothesis concerning the possible ligand exchange between H and THF, because even under a high hydrogen pressure and a low THF concentration, the most stables structures exhibit some THF ligands (domains 46 & 47) instead of having a Ru_{55} NP structure stabilized only by hydrides.

This result suggests the possible presence of a very few number of THF molecules at the nanoparticle surface, not because of a ligand exchange with ethanoates, but rather with hydrides. Nevertheless, this result needs to be taken with caution because none steric hindrance effect from the ethanoates was considered.

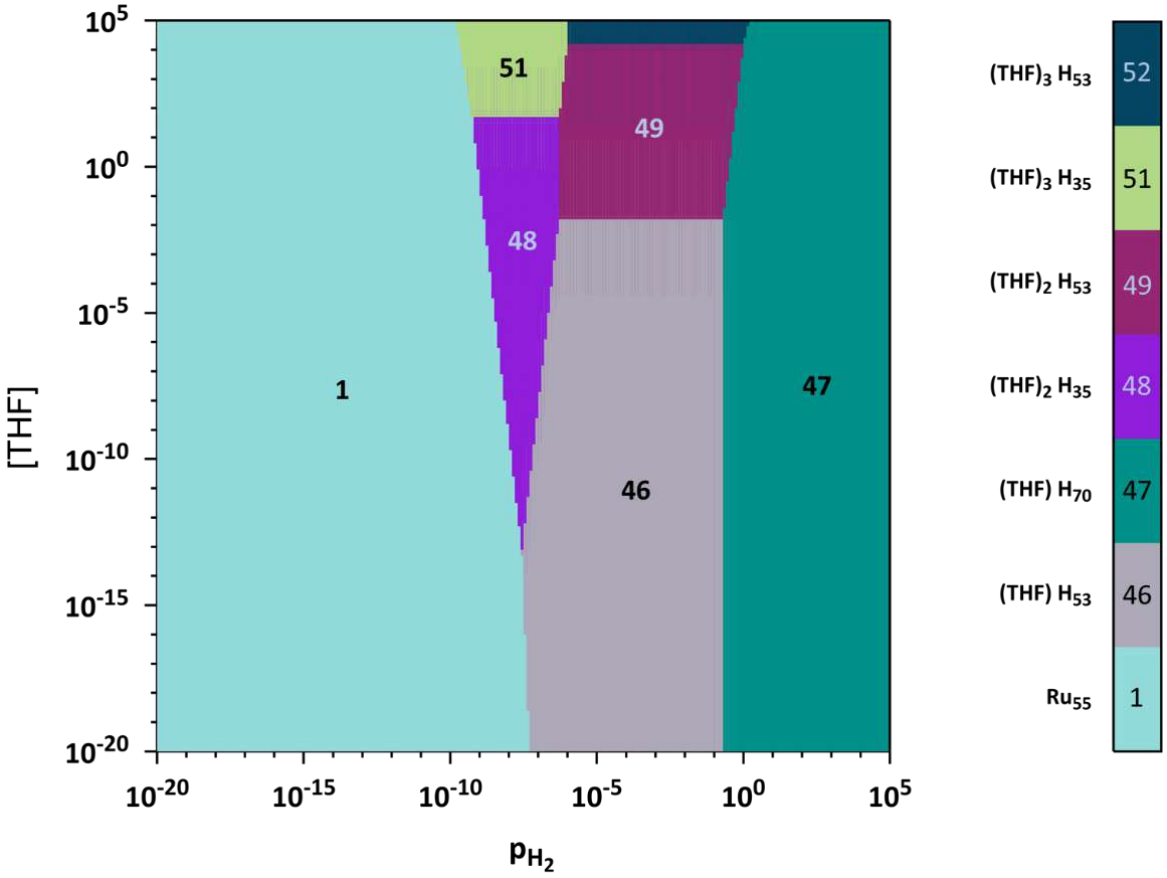

Figure 2.43 $\Delta_a G°$ (p_{H_2}, [THF]) phase diagram for H_2 (gas) and THF (liquid) adsorption on Ru_{55} NP at 300 K (pressure in bar, concentration in $mol.L^{-1}$).

According to the experimental synthetic conditions, three hypothetical stable surface compositions (domains 46, 49 & 52) are found when p_{H_2} and [THF] are in the range [10^{-5} - 10^{-2} bar]. These structures possess the same amount of hydrogen but different quantity of THF according to its concentration under equilibrium (figure 2.44), their coordinates are given in section appendix F.

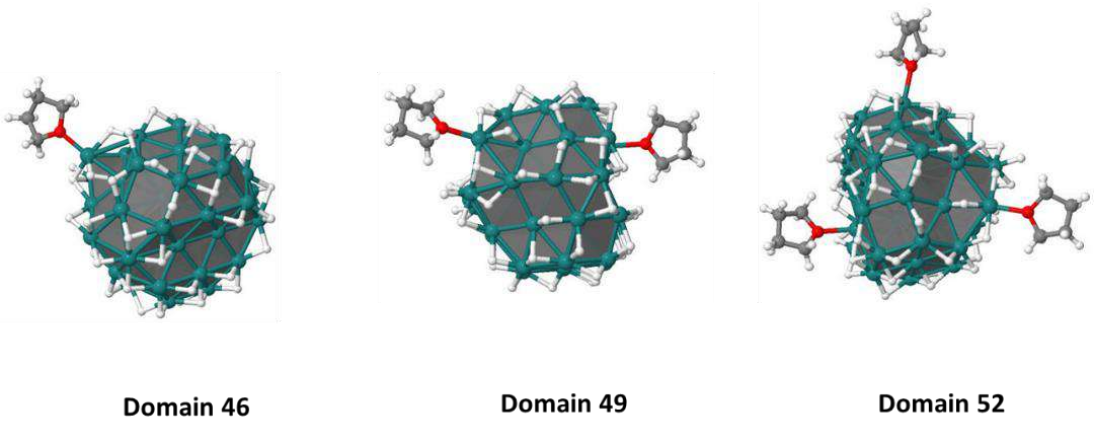

Figure 2.44 More stable [Ru_{55}] clusters found at 300 K. (Domain 46: $Ru_{55}(THF)(H)_{53}$; domain 49: $Ru_{55}(THF)_2(H)_{53}$; domain 52: $Ru_{55}(THF)_3(H)_{53}$).

2.6 Electronic Properties

Knowledge on the electronic structure of the nanoparticles is essential in order to understand their reactivity. In fact, a suitable catalyst for a given reaction has to present an optimal interaction (adsorption/desorption) between the reactants and the chosen catalyst (adsorption energy).[210]

The catalyst-reactant interactions will depend on the electronic properties of the particles and thus can vary following the NP general structure or the ligand coverage ratio. Also, it is possible to establish a relationship between the activation energy in a given reaction and the adsorption energy of the reactant molecules onto the NP surface. This phenomenon can be studied using the Brønsted-Evans-Polanyi relation([211],[212]) or the volcano plots.[213]

Therefore, it is important to know the electronic properties of the $Ru_x(CH_3COOH)_{0.4}$ NPs in order to evaluate its utility as a catalyst. These studies will be described in the following sections.

2.6.1 Electronic States

In order to describe the electronic properties of metal clusters and MNPs, a different approach is required, given the complexity of these systems.[[214],[215]] The density of states (DOS) is a special characteristic of these nanomaterials, which represents the interacting molecular orbitals in MNPs. In other words, this approach allows to determine the occupancy of these states, and thus their electronic properties.[216]

The electronic structure of the Ru_{55} covered NP was evaluated with the Lobster software, where the projector augmented waves (PAW) of the electronic states were projected on a local Slater atomic basis set, hence giving the possibility to derive several properties and indexes, such as projected density of states (*p*DOS), crystal orbital hamilton population (*p*COHP) and bond strength indexes (I*p*COHP) see definitions and methodology in section 6.2.9 & 6.2.10, respectively.

For this study a Ru_{55} NP model which has similar ligand coverage as the optimal one found in the phase diagram at 300 K was used. The density of states determination and orbital-like analysis were realized for the 2 CH_3COO*, H* model by following a published procedure.[[82],[217]]

The interaction between electrons occupying *d*-type orbitals of the metal nanoparticle and those of the adsorbate can be correlated to the adsorbate-substrate adsorption energy.[218] The representation of these NP electrons is so-called *d*-band center.[[219],[172]] Thus, the electronic properties of the model 2 CH_3COO*, H* were compared with those of the bare Ru_{55} NP covered with hydrides, and even capped by carbon monoxide.

The *d*-band center for the 44 surface ruthenium atoms in the model 2 CH_3COO*, H* was found to be at 2.94 eV below the Fermi energy ($\bar{\varepsilon}_d$), meanwhile the 11 core atoms have a $\bar{\varepsilon}_d$ = 3.34 eV. In comparison with the bare Ru_{55}, which displays a *d*-band center that lies at 2.60 eV & 3.60 eV for surface and core atoms, respectively as shown on the projected density of states (*p*DOS) plotted (figure 2.45). It appears that the addition of 16 ethanoates and 33 hydrides stabilizes the nanoparticle surface atoms in *ca.* 7.8 kcal.mol^{-1}.

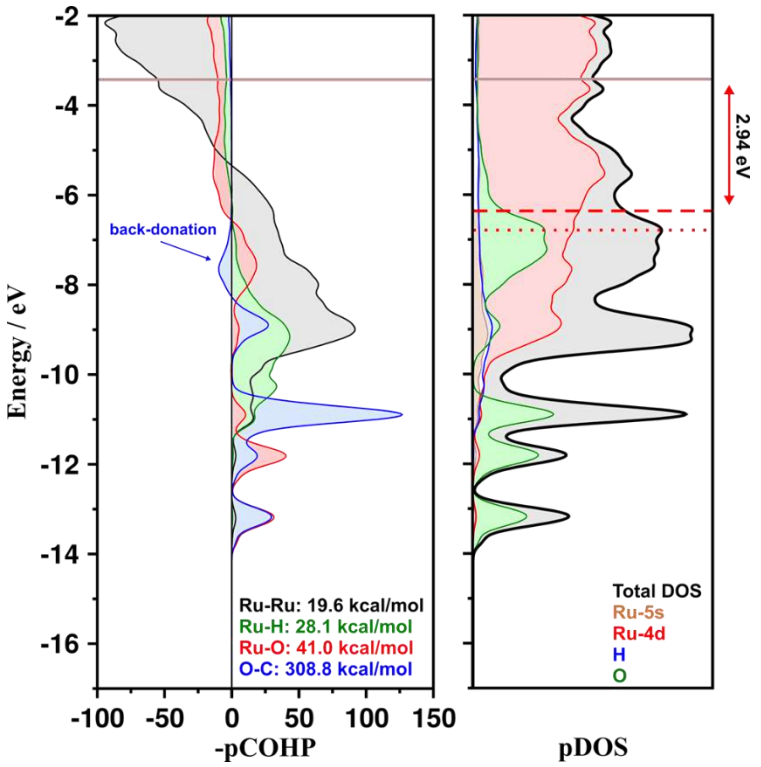

Figure 2.45 Projected COHP & DOS profiles for $Ru_x(CH_3COO)_{16}(H)_{33}$ NP model. Dashed red line and dotted red line on the *p*DOS profile: *d*-band center of surface and core Ru atoms, respectively; brown line: Fermi energy. The backdonation observed is also highlighted.

The *d*-band center is a well-known parameter to determine the reactivity of these types of systems and there is a correlation with the surface coverage and adsorption strength of the adsorbates. For example, the *d*-band center value reported for a Ru_{55} NP covered with a similar amount of hydrides (35) but no ethanoates lies at -2.82 eV,[220] which evidences that a Ru_{55} NP is more reactive in the absence of ethanoates (higher *d*-band center value). This can be related to the adsorption strength of the hydrides *vs* ethanoates at the same level of theory (*ca.* -14.2 *vs* -40.1 kcal.mol^{-1}).

The grafting of ethanoates on the metal surface also involves a weakening of the Ru-Ru bond strength, with the I*p*COHP index per Ru-Ru bond equals to 19.6 kcal.mol^{-1} for 2 CH_3COO*, H* instead of 27.0 kcal.mol^{-1} in the bare Ru_{55} NP. In other words, the coordination of surface ethanoate involves a lowering by *ca.* 30% the cohesive energy of the metal part of the Ru_{55} NP.

It has been reported previously that the highest occupied states are essentially developed upon metal atoms, and that they exhibit an anti-bonding character.[82] In the plotted -*p*COHP

(figure 2.45) this phenomenon can be observed. Also, it is worth mentioning that some electrons populate anti-bonding C-O states (figure 2.45 blue) that lie at the same energy as bonding Ru-C states (figure 2.45 red). This event can be analyzed as a weak back-donation from the metal surface to the π* MOs of the carboxylate groups. The phenomenon can be correlated with the increasing of the average C-O bond length calculated in section 2.4.1.

2.6.2 Atomic Charges in RuNP

Both experimental and theoretical characterization data point out to the presence of ethanoate at the surface of the RuNPs rather than of ethanoic acid. Given that ethanoate is not electrically neutral, but possesses a delocalized negative charge, the knowledge of the evolution of atomic charges in the RuNPs upon its coordination is of high interest.

In order to know evaluate the influence of grafted carboxylates on the possible oxidationof the surface ruthenium atoms oxidation. Bader charges[[221],[222]] as well as the Mulliken population analysis (pMPA charges) obtained by integrating the *p*DOS were calculated (*see* section 6.2.9). These methods have been previously reported for describing the surface state of MNPs,[[223],[224]] but since they are based in different level of theory their reliability needed to be first evaluated for this nanosystem.

The 2 CH_3COO*, H* model was evaluated by these methods due to its closeness to the optimal ligand surface coverage found for Ru_{55} NP at 300 K. The average atomic charge of the hydrides calculated by the two methods (Bader *vs*. pMPA: q_H = -0.19*e*/-0.20*e*) do not show any significance difference. Also, the global charges hold by the ethanoates (Bader *vs*. pMPA: q_{CH_3} = 0.14*e*/0.07*e*; q_{COO} = -0.67*e*/-0.55*e*) as well as the overall charge of the Ru_{55} NP (Bader *vs*. pMPA: q_{Ru} = 0.27*e*/0.26*e*) are found to be similar with both methods.

The main differences lie in the atomic charges of the individual elements that form the ethanoate (Bader *vs*. pMPA: $q_{C_{COO}}$ = 1.52*e*/0.64*e*; q_O = -1.10*e*/-0.59*e*; $q_{H_{CH_3}}$ = 0.07*e*/0.33*e*; $q_{C_{CH_3}}$ = -0.07*e*/-0.91*e*) as well as in the average charge hold by the 11 core metal atoms (Bader *vs*. pMPA: q_{Ru_C} = 0.04*e*/-0.12*e*). Whereas the two methods agree in concluding that surface Ru atoms are significantly oxidized (Bader *vs*. pMPA: q_{Ru_S} = 0.33*e*/0.35*e*), they differ about the charges of the

core atoms. According to the Bader analysis they are almost neutral whereas they are slightly negatively charged according to pMPA. In summary, the most striking difference between Bader and pMPA charges is observed for the core metal atoms and for the individual elements of the ethanoates.

Even when there is not a reinforced experimental data where the chosen methodology can be supported, the pMPA charges are consistent with the *p*COHP obtained data and *d*-band center. Also, a recent published work reported that the pMPA charges are very similar to Natural Population Analysis charges[225] in doped graphene.[226] Therefore the Mulliken population analysis will be preferred to analyze this system.

Three different models were considered to analyze the progress of the oxidation as a function of the ligand surface coverage. Thus, the pMPA charges were calculated for the bare Ru_{55} NP, the moderately hydrogenated Ru_{55} NP ($Ru_{55}(H)_{17}$) and the 2 CH3COO*, H* model ($Ru_{55}(CH_3COO)_{16}(H)_{33}$). The results are graphically compared in figure 2.46.

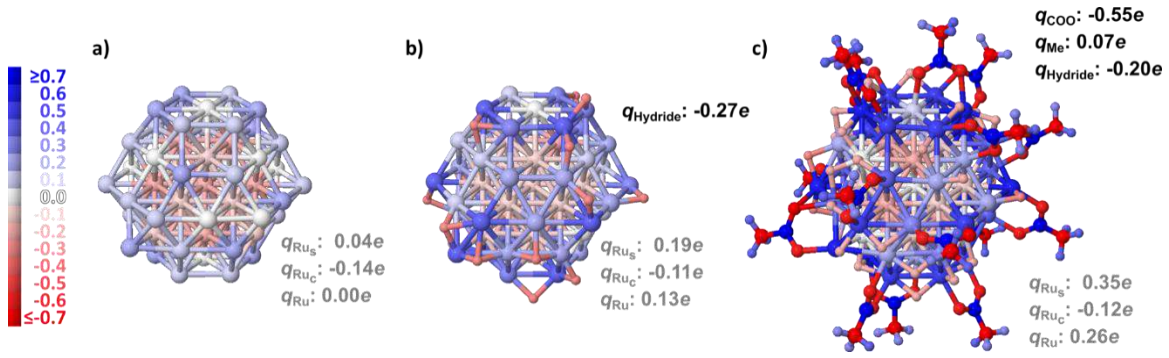

Figure 2.46 Atomic pMPA charges shown as color maps. (a) Ru_{55}; (b) $Ru_{55}(H)_{17}$; (c) $Ru_{55}(CH_3COO)_{16}(H)_{33}$. The charge scale is shown on the left. Charges are also shown: global (q_{Ru}), core (q_{Ru_c}), surface ruthenium atoms (q_{Ru_s}) and ligand ($q_{Hydride}$, q_{COO} & q_{Me}).

The color map of pMPA charges shows that the adsorption of H & CH_3COO ligands which are charged negatively produces a progressive oxidation on the RuNPs. The ruthenium surface atoms are more affected for this phenomenon and even more the metal atoms that are binding to these moieties.

Surface ruthenium atoms in the Ru_{55} NP model are neutral or slightly positive (q_{Ru_s}: 0.04*e*). Whereas in the $Ru_{55}(H)_{17}$, hydrides hold a negative charge ($q_{Hydride}$: -0.27*e*) thus involving a small

oxidation of these atoms (q_{Ru_s}: 0.19*e*). Meanwhile, the dissociative grafting of 16 ethanoic acids $Ru_{55}(CH_3COO)_{16}(H)_{33}$ involves a stronger oxidation of the ruthenium surface atoms (q_{Ru_s}: 0.35*e*). Ru metal atoms on which carboxylates are grafted are even more oxidized, with charges that reach *ca*. 0.5*e*.

It is also worth mentioning that according to the charge calculations, all adsorbed hydrogen atoms in ethanoate-capped ruthenium NPs have an hydridic character, even those that originate from the acids.

Previous published work exhibits that for the same Ru_{55} NP system but grafted by carbon monoxide ($Ru_{55}(CO)_{66}$), the ruthenium surface atoms are less oxidized (q_{Ru_s}: 0.25*e*).[82] The result is not in contradiction with a low π-acceptor character of CO when coordinated to Ru surfaces and it underlines the ability of ethanoate and hydrides to deplete the electronic density of surface Ru atoms. It is also worth mentioning that according to the charge calculations, all adsorbed hydrogen atoms in ethanoate-capped Ru_{55} NPs ($q_{Hydride}$: -0.20*e*) have an hydridic character, even those that originate from the carboxylic acid deprotonation.

2.7 Hydrogen Evolution Reaction: A Possible Application

RuNPs are well-known as interesting materials for hydrogenation catalytic reactions.([59],[93]) and more recently it have been observed their potential catalytic activity towards the hydrogen evolution reaction (HER).[9]

In this work, it has been introduced the use of small alkyl chain length carboxylates as new coating species on RuNPs. For its relevance and previous background, it is worthy to test this nanosystems $Ru_x(CH_3COOH)_{0.4}$ for HER applications in the electrolysis of water. Due to the good correlation between the experimental and the computational chemistry characterization, this issue can be evaluated firstly form a theoretical point of view.

According to the seminal work of Nørskov, there is a correlation between the H_2 dissociative adsorption Gibbs free energy and the exchange current for hydrogen evolution reaction (HER).[10]

$$\Delta G_{H^*} = \frac{1}{n}\left[G(H^*) - G(surf) - \frac{n}{2}G(H_2)\right]$$

A Balandin-Sabatier volcano curve had been found, with platinum electrodes on top of the volcano and ΔG_{H^*} that lies between -2.0 and 0.7 kcal.mol^{-1} as a function of H coverage. The main conclusion of this study is that the requirement for an optimal HER catalyst is that the Gibbs dissociative adsorption energy of H_2 must lie as close as possible to 0 kcal.mol^{-1}.

As it was shown in this published work in addition to several experimental findings, Pt-based catalysts show a high efficiency for reducing protons to H_2 in acidic media (H_3O^+). However, there is a need to find alternative HER catalysts in order to improve their capability and reduce the production costs. Ruthenium, even though is not an abundant metal, can be considered as an interesting candidate to test as catalyst in the HER reaction, due to its closeness to fulfill the H adsorption energy criterion (ΔG* *ca.* [-6.4 to -5.6 kcal.mol^{-1}] for [0.25 – 1.00] hcp monolayer (ML) on Ru (0001))[200] after the empirical addition of 5.5 kcal.mol^{-1}, as representative thermal energy for transitional metals.[10]

$$\Delta G_{H^*} = \Delta E_H + \Delta E_{ZPE} - T\Delta S_H$$

$$\Delta G_{H^*} = \Delta E_H + 0.24\ eV$$

As was previously mentioned in section 2.6.1, there is a high compromise between the adsorbate-substrate adsorption energy and the catalytic performance.[218] Thus, due to the weak adsorption of the hydrogen onto Ru_{55} NP (*ca.* [-12.0 – -14.0 kcal.mol^{-1}]), it could led to a decrease of this catalytic cooperative effect and even more when the co-adsorbed ligands have a strong affinity to the metal surface.

The previous planted phenomenon could be observed in a previous published work, where the RuNPs were exposed to syngas showing that all the grafting free Ru sites were occupied by carbon monoxide and no for hydrides.[82] On the contrary, for this ethanoic acid-capped RuNPs, it was both experimentally and theoretically possible to found hydrides co-adsorbed with ethanoates (Exp: 0.3 H_{reac}/Ru_{surf}; Theo: [0.4 – 0.6 H/Ru_{surf}]) at 300 K (r.t.). The fact that ethanoic acid-capped RuNPs can accommodate both ligands at their surface makes them potentially interesting candidates for HER.

The adsorption energy of hydrogen (ΔE_H) has been calculated (*see* section 6.2.11) on five representatives surfaces sites of the bare Ru_{55} NP, and compared with those of the stable CH_3COO/H covered NP models; $Ru_{55}(CH_3COO)_{16}(H)_{16}$ (domain 39) and of $Ru_{55}(CH_3COO)(H)_{54}$ (domain 7), which involve interactions with the planes (001) and (101) and the surrounding area of B_4 & B_5 surface sites of the Ru_{55} NP model (*see* section 6.2.1). The ΔG_{H^*} values (see section appendix E.1) are presented in the figure 2.47, together with the atomic *d*-band center shown as color map.[217]

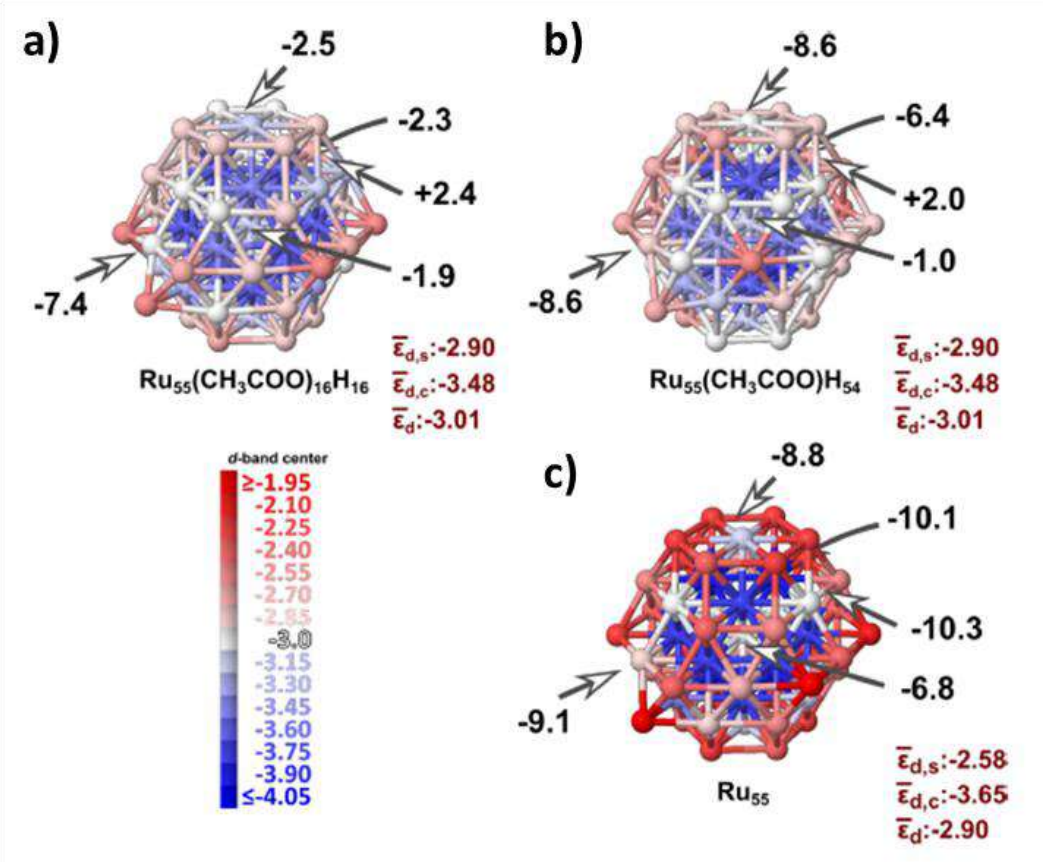

Figure 2.47 atom *d*-band center is shown as color map (scale in eV) for (a) $Ru_{55}(CH_3COO)_{16}(H)_{16}$, (b) $Ru_{55}(CH_3COO)(H)_{54}$ and (c) Ru_{55}. The ΔG_{H^*} are given (kcal.mol^{-1}) and the arrows indicate the adsorption sites. The surface, core and total average *d*-band center values are also presented (eV).

The bare Ru_{55} NP (figure 2.47 c) shows a high energy surface, therefore the single hydrogen adsorption is too strong, whatever the Ru_{55} NP studied site ([-12.3 to -15.8 kcal.mol^{-1}]). This can be interpreted in terms of ΔG_{H^*} by applying the thermal energy previously described. It can be seen that these values oscillate from [-6.8 to -10.3 kcal.mol^{-1}] for the selected Ru_{55} NP

adsorption sites. These values are high enough to make the adduct desorption a difficult and energetic process, and consequently not favorable which indicates that this Ru_{55} NP model is probably a non-suitable catalyst for HER, as expected.

Given these first results, it appears that a more suitable for the HER reaction will require a lower hydrogen adsorption energy than the Ru_{55} NP, but still strong enough for the hydrogen to coordinate to the metal atoms. This phenomenon can be induced by reducing the surface energy of the NP system. Therefore a hydrogen crowded stable structure $Ru_{55}(CH_3COO)(H)_{54}$ found in the phase diagram at 450 K was evaluated (figure 2.47 b).

In this model the presence of hydrides coverage lowered significantly the atomic *d*-band center of the Ru atoms, which can be correlated with a decrease in the ΔG_{H^*} (+2.0 - -8.6 kcal.mol^{-1}) with regards to Ru_{55} naked NP.

As it was seen saturated hydrogen NP seems to be more suitable catalyst for the HER reaction having some sites of high interest (plane (101)), but the Gibbs free energy calculated for the five different sites appears to be highly affected for the NP site and its chemical environment. Even so with this composition it is found a better catalyst but no really promising for be tested for this catalytic reaction.

The last saturated Ru_{55} NP model evaluated possess less quantity of hydrides but higher amount of strongly adsorbed ethanoate ligands, $Ru_{55}(CH_3COO)_{16}(H)_{16}$. This model was shown to be one of the two stable structural domains found in the phase diagram at 300 K, and having a ligand coverage ratio quite similar to that found in the experimental characterization.

The overall calculated H_2 dissociative adsorption Gibbs free energies in the ethanoates saturated model, $Ru_{55}(CH_3COO)_{16}(H)_{16}$, are weaker than those calculated for the hydrogenated model $Ru_{55}(CH_3COO)(H)_{54}$ on the same representative sites (*ca.* -2.3 *vs* -4.5 kcal.mol^{-1}). Also, it shows less influence for the adsorption site, except for the apex region (B_4 and B_5 site) all the other sites hold similar ΔG_{H^*} values.

The difference between the two crowded Ru_{55} NP models, $Ru_{55}(CH_3COO)_{16}(H)_{16}$ and $Ru_{55}(CH_3COO)(H)_{54}$, was previously noted in the overall calculated Gibbs free energies which were plotted in the phase diagram at 300 K. It was observed that the $Ru_{55}(CH_3COO)_{16}(H)_{16}$ model was more stable given a decrease of the Ru_{55} NP surface energy, which was attributed to the presence

of adsorbed ethanoates. This induced a decrease in the hydrogen adsorption energy which explains the difference in the obtained hydrogen adsorption Gibbs free energy (ΔG_{H^*}).

Nevertheless, regarding the *d*-band center mapping, there is not a significant difference between the two crowded models, that show similar values for the surface atoms ($\bar{\varepsilon}_{d,s}$ = -2.90 eV). This result indicates that, the difference observed between the studied models cannot be explained by the *d*-band center model. Hence, the weaker H-adsorption calculated in $Ru_{55}(CH_3COO)_{16}(H)_{16}$ could be attributed to a strong Coulomb repulsion between the adsorbed hydride and the surface ethanoates which can have an effect on the whole surface energy of the Ru_{55} NP.

The low hydrogen adsorption energies found in $Ru_{55}(CH_3COO)_{16}(H)_{16}$, which is the most accurate model with respect to experimental data, locate this catalyst on top of the volcano plot published for HER reaction.[10] All together, these theoretical results show the ethanoic acid-stabilized RuNPs to be a promising nanocatalyst for the HER reaction.

2.8 Conclusion

This chapter provided extended theoretical and experimental characterization studies on RuNPs stabilized by ethanoic acid (CH_3COOH). Hence, this conclusion arises in order to summarize the whole study of the principal analyzed system $Ru_x(CH_3COOH)_{0.4}$.

The synthesis of these particles has been performed in mild conditions following the organometallic approach, by decomposing a pentane solution of the ruthenium precursor, Ru(COD)(COT), under 3 bar H_2 at r.t. The novelty of this work is the use of a carboxylic acids as a stabilizer while there is only one example reported in the literature, with a C60-based carboxylic acid ($C_{66}(COOH)_{12}$). What is also relevant is the fact that ethanoic acid bears a very short alkyl chain, meaning that it cannot be expected to have an influence of the alkyl group on the stabilization of the RuNPs as often observed with stabilizers having alkyl groups with long chain length. Also, it is important to mention the relevance of the solvent used, pentane, which is not known as contribute to the stabilization of metal nanoparticles as THF can do for instance. By this way, the use of ethanoic acid and pentane was a synthesis challenge.

But this strategy appeared to be efficient and an optimized system of RuNPs was obtained with a [ligand]/[Ru] molar ratio of 0.4 equiv. leading to $Ru_x(CH_3COOH)_{0.4}$ sample. As evidenced by TEM and WAXS analysis, the obtained RuNPs display a small size centered at *ca.* 1.5 nm and a poorly crystalline structure with a few plans attributed to the *hcp* crystalline structure of bulk ruthenium. Indeed, the nanosystem was not perfectly controlled in terms of shape and crystalline structure. However, this nanomaterial was a very interesting case study in order to get accurate and relevant data on the surface properties of these RuNPs by two complementary approaches, namely experimental and theoretical chemistry.

Strong efforts have been performed in order to characterize as precisely as possible the surface composition of these nanoparticles and also to evaluate their surface reactivity. For this purpose, both state-of-the-art techniques in nanochemistry including spectroscopic techniques such as IR and solution and solid-state NMR, and theoretical chemistry tools have been used in parallel.

This combination of tools appeared to be very powerful to get qualitative but also quantitative information on the surface state of the particles. All together the obtained results converged towards the coordination of the ligand at the ruthenium surface under ethanoate form, preferably in a bidentate mode. This result is in agreement with a small activation barrier of CH_3COO-H bond dissociation.

Moreover, the results evidenced that the coordination of the ethanoate at the ruthenium surface does not restrain the co-adsorption of a significant amount of hydrogen atoms, making the surface composition of the RuNPs to be a mixture of ethanoates and hydrides.

The DFT titration showed an optimal surface composition of *ca.* [0.4 - 0.6] H/Ru_{surf} and 0.4 CH_3COO/Ru_{surf} at 300 K. These data are in high accordance with the experimental quantification ones, namely *ca.* 0.3 H_{reac}/Ru_{surf} and 0.3 CH_3COO/Ru_{surf} at r.t.

The good agreement obtained between the theoretical and experimental characterization studies, proves that the theoretical chemistry tools applied are very powerful in order to provide a reliable model to describe the structure of the RuNPs system here synthesized. This work shows that it is possible to develop computational chemistry applied to small nanoparticles with the same level of accuracy and relevance as in molecular chemistry

At the optimal surface composition, the RuNPs showed to have a slightly oxidized surface (*ca.* 0.5*e*) according to the pMPA analysis. Better still, with such composition the hydrogen adsorption energy calculated is in the range [-3.1 to -8.0 kcal.mol^{-1}] for the (001) & (101) planes, which is an important pre-requisite to have promising material for the HER application in the electrolysis of water.

CHAPTER III

Carboxylic Acid-Capped RuNPs: Use of Ligands with Longer Alkyl Chain Length

3.A Introduction

Metal nanoparticles (MNPs) have been synthetized by following several methodologies and procedures in order to generate novel materials with different sizes, shapes and morphologies, which possess diverse applications, especially in catalysis. A vast range of them has been obtained by changing the synthesis parameters, *i.e.* metal precursor, reaction media, stabilizing agent, reaction temperature, etc.[([13],[140])]

In the case of ruthenium nanoparticles (RuNPs), they have been produced with different morphologies going from spherical shape to nanorods.[([89],[227])] Also, it has been reported that the synthetic conditions can even change the crystalline structure of RuNPs ranging from face-centered cubic (fcc) to hexagonal close-packed (hcp) structure (figure 3.1)[92] or even amorphous.[228]

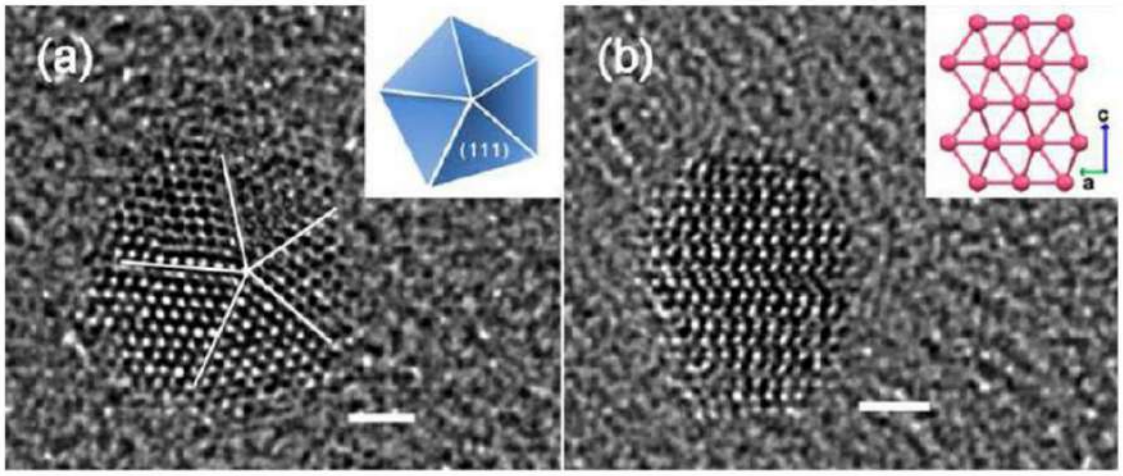

Figure 3.1 HRTEM images of (a) fcc and (b) hcp RuNPs. Insets of decahedral structure and illustration of hcp lattice on the (100) direction, respectively; scales bar 1.0 nm.[92]

The nanoparticles studied and analyzed in this work were synthetized by following the organometallic approach under the same synthesis conditions as shown in chapter II (reaction media, pressure & temperature). The main aim of having the same synthesis procedure was to reduce the variables that can modify the structure and properties of the RuNPs.

The chosen approach consist in a gradual decomposition of a ruthenium metal precursor ([Ru(COD)(COT)]) by reducing its ligands in the presence of molecular hydrogen (H_2), leaving single ruthenium naked atoms, which are quite unstable due to their high surface energy. The ruthenium entities tend to reduce its own instability by suppressing its surface area through a metal agglomeration or by decreasing their surface energy *via* molecule adsorption or electronic stabilization.[157]

In fact, the agglomeration phenomenon of nanoparticles is produced by the presence of attractive van der Waals forces, which can be reduced by the presence of ligands acting as obstacles and restricting the coalescence of nanoparticles (scheme 3.1). Thus, the growth of the nanosystems is stopped by the assistance of the stabilizer, which offers either steric and/or electronic protection.[229]

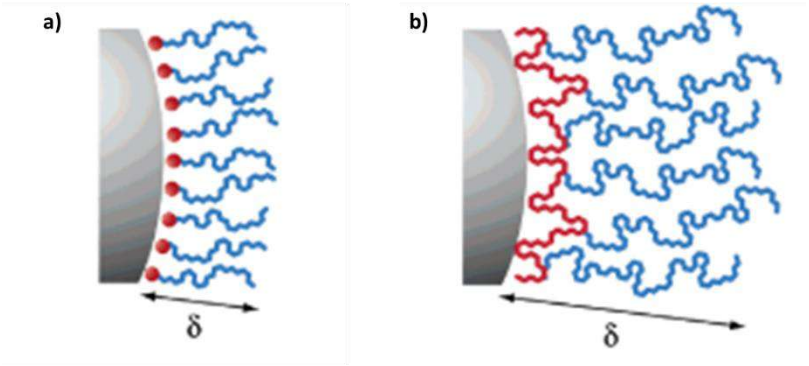

Scheme 3.1. MNPs stabilization layer of (a) coordinated ligand and (b) polymer. δ is the adlayer thickness comparison.[229]

Hence, the MNPs stabilization and their outcoming properties are highly dependent on their synthesis conditions. Since in this work these variables were reduced at maximum as possible, by using only the organometallic approach with fixed conditions. Then, the influence of the stabilizing agent nature can be truly evaluated.

Considering that the nanosystems properties are very sensitive to all the synthesis conditions, it is preferable to apply only small changes in the synthetic procedure. In this way, the influence of the stabilizing agent on the RuNPs formation and, furthermore in their properties, can be analyzed.

In chapter II, it was demonstrated that a carboxylic acid with a short alkyl chain length as ethanoic acid (CH_3COOH) is able to stabilize RuNPs of small size (*ca.* 1.5 nm). However, it is known from the literature data that in a same family of ligands, those which possess a longer alkyl chain can be better stabilizing agents,[230] and also lead to the formation of smaller MNPs.[110] This is principally due to additionally steric effects induced by the long alkyl chain.

Thus, this chapter is dedicated to study the effect of the alkyl chain length of carboxylic acid ligands on the characteristics of the obtained nanoparticles (size, shape, dispersion, crystalline structure, composition, electronic/surface properties). For this purpose, it has been selected firstly pentanoic acid (CH_3-$(CH_2)_3$-COOH) and secondly octanoic acid (CH_3-$(CH_2)_6$-COOH) which corresponds to an increase of the alkyl chain length by addition of three and six carbon atoms respectively, comparatively to the ethanoic acid used at the beginning of this PhD work.

Also, in chapter II, it was shown that a theoretical Ru_{55} NP model covered by ethanoates and hydrides is very appropriate to describe RuNPs stabilized by the ethanoic entities. This was proven by comparing theoretical and experimental data from complementary spectroscopic characterizations for which a good agreement was reached. Therefore, the same theoretical model will be used in order to study the electronic properties of the novel RuNPs (figure 3.2).

Thus, a similar approach as in chapter II will be followed (combination of experimental and theoretical techniques) in order to fully-characterize the composition, surface state and electronic properties of the obtained RuNPs, and also to determine the influence of a carboxylic acid ligand with a longer alkyl chain length on the properties of the RuNPs.

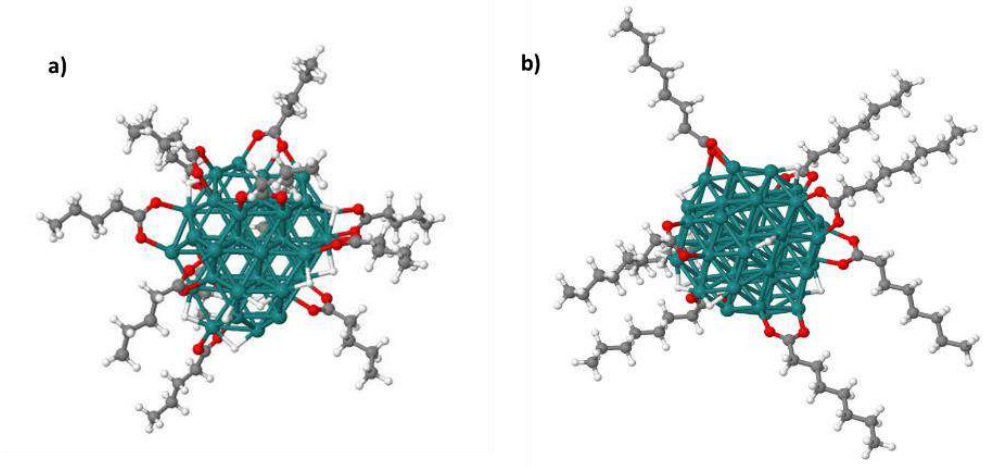

Figure 3.2 Ru_{55} NP model stabilized by (a) pentanoic acid and (b) octanoic acid.

3.1 Pentanoic Acid-Capped RuNPs

Stability of metal nanoparticles (MNPs) depends on the nature of the stabilizing agents used for their synthesis because they have a high influence on the nucleation and the MNPs growth rate. The compromise between these two steps is needed to get stable and well-controlled MNPs.[13],[231] Therefore, ligands which are too strongly or too weakly bonded may not be appropriate for stabilizing MNPs when envisaging their use in applications like catalysis.

Taking this information into account and having demonstrated that the ethanoic acid can be used as ligand to stabilize RuNPs, hereafter will be shown a complete characterization of RuNPs stabilized by pentanoic acid, which is slightly longer than ethanoic acid. Presumably this ligand will offer a better stabilization due to the combination of electronic and steric effects.

A main objective of this section was to determine if the expected positive influence of pentanoic acid longer alkyl chain, in terms of stability, could be verified at both experimental and theoretical levels.

3.1.1 Synthesis of RuNPs Stabilized by Pentanoic Acid

The ruthenium nanoparticles (RuNPs) stabilized by pentanoic acid (C_4H_9COOH) were synthetized by following the organometallic approach from the stablished procedure described in section 6.1.2.2. Given the study with ethanoic acid showed that stable and homogeneous RuNPs were obtained in the presence of 0.4 molar equivalent of ethanoic acid ($Ru_x(CH_3COOH)_{0.4}$), the same [Ligand]/[Ru] ratio has been also applied first. Doing so allowed to directly study the influence of RuNPs stabilized by pentanoic acid compared to ethanoic acid in terms of size, morphology, etc.

For the synthesis of $Ru_x(C_4H_9COOH)_{0.4}$ nanoparticles, the [Ru(COD)(COT] precursor was dissolved under argon in a pentane solution containing 0.4 equiv. of pentanoic acid. The formed

yellowish solution was transferred inside a Fisher -Porter reactor which was then pressurized with hydrogen (3 bar) under vigorous stirring. After *ca.* 4 min, the initial colorful solution turned to brown-black, thus indicating the metal precursor decomposition. In order to ensure the complete decomposition of [Ru(COD)(COT)], the hydrogen pressure was maintained for 30 min (scheme 3.2). After this reaction time, a stable colloidal solution was observed with absence of any precipitates. Then, the reactor was evacuated under vacuum in order to remove the reductive atmosphere and replace it by argon.

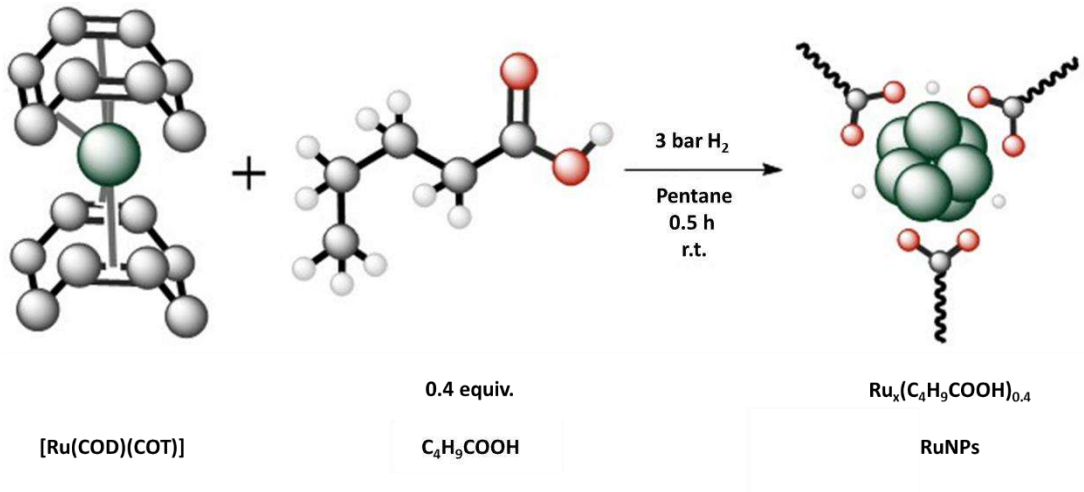

Scheme 3.2 Synthesis of RuNPs stabilized by 0.4 equiv. of pentanoic acid ($Ru_x(C_4H_9COOH)_{0.4}$). The resulting nanoparticle is coverage for pentanoate and hydrides as it is expected from chapter II.

The obtained colloidal suspension of $Ru_x(C_4H_9COOH)_{0.4}$ NPs appeared to be stable for at least one day even without stirring. No precipitate was observed, as a difference from the $Ru_x(CH_3COOH)_{0.4}$ NP system where the particles precipitated when stopping the magnetic stirring. The use of a ligand with a long alkyl chain is known to provide the RuNPs a higher affinity to non-polar solvents. So, one of the properties than can be modulated by changing the stabilizing agent nature is the solubility of the colloidal system.[[232],[233]] The absence of precipitate here observed is thus linked to the influence of the pentanoic acid.

Later on, the colloidal suspension was concentrated to the half volume in order to obtain a drop of the crude concentrated colloidal RuNPs solution to be studied by TEM analysis (*see* section 6.1.3.1). At low magnification (figure 3.3 a), a self-organization of the particles was observed which is attributed to a solvent evaporation effect during the preparation of the grid

(coffee ring phenomenon). TEM micrographs recorded at higher magnification (figure 3.3 b) evidenced the presence of ultra-small nanoparticles which are difficult to distinguish, but its presence was corroborated by calculating the hydrodynamic radii obtained by DOSY NMR studies (*vide infra*). The size distribution built by measuring *ca.* 400 nanoparticles led to a mean size of *ca.* 1.13 ± 0.31 nm (figure 3.3 c).

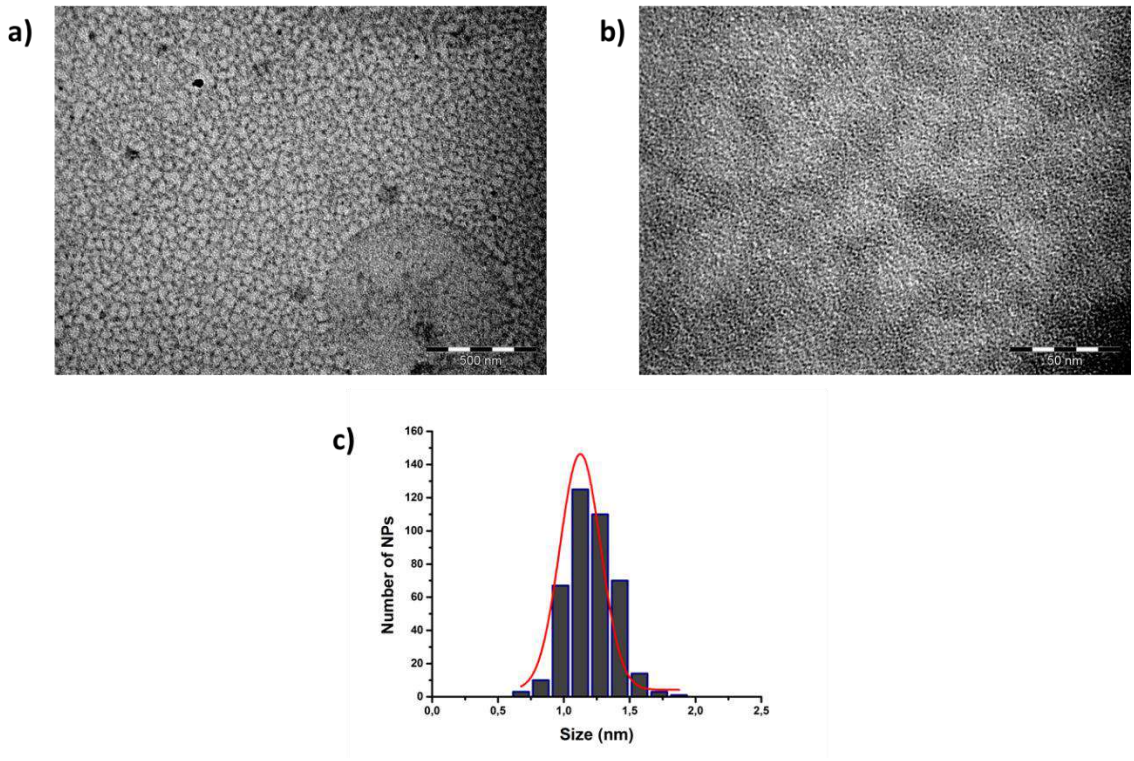

Figure 3.3 TEM micrographs of $Ru_x(C_4H_9COOH)_{0.4}$ NPs; (a) self-organized NPs due to solvent evaporation; scale bar: 500 nm; (b) ultra-small RuNPs; scale bar: 50 nm; (c) size histogram of individual RuNPs.

The mean size of the $Ru_x(C_4H_9COOH)_{0.4}$ NPs is *ca.* 25.2 % smaller than that calculated for the $Ru_x(CH_3COOH)_{0.4}$ NPs system (*ca.* 1.51 nm). Considering that these particles probably have the same crystalline structure (*hcp*) and using as a reference the magic number for ruthenium clusters, the ratio between the ruthenium surface atoms and the total metal atoms was calculated (*see* section 6.1.4.1).

As a result, it was found that the $Ru_x(C_4H_9COOH)_{0.4}$ NPs have more than 75.0 % of atoms at their surface. In comparison with the RuNPs stabilized by ethanoic acid, this means an increase of *ca.* 12.0 % of surface ruthenium atoms. Both RuNPs systems show similar spheroids morphology

but the $Ru_x(C_4H_9COOH)_{0.4}$ NPs form a single homogeneous population with a narrower size distribution.

Unsurprisingly from these first results, the pentanoic acid appeared to be a better stabilizing agent than ethanoic acid, leading to smaller and more soluble RuNPs. Several hypotheses can be formulated for explaining this behavior. Among them two stand out which both concern the effect of the ligand on the NP growth process after the nucleation step. The first hypothesis is that the diffusion of the stabilizing agent to the metal entities is fast which can limit/stop the NPs growth process. The second one suggests that the growth is delimited by the surface reaction due to the ligand adsorption.[([234],[235])] In both cases, changes in the growth process are put forward as the result of the ligand interaction with the surface of growing particles, showing thus a direct influence on the RuNPs synthesis.

3.1.2 Adsorption Energies Analysis in Ru_{55} NP Model Covered by Pentanoic Moieties

To know more about the differences that the stabilizing agent nature can produce on the formation of RuNPs, it is worthy to compare the adsorption energy (E_{ads}) of the coordinated ligand onto the RuNPs. Thus, an analysis was performed using the previously described theoretical Ru_{55} NP model where the same quantity of stabilizing agent was deposed onto the Ru_{55} NP (*see* section 6.2.1).

Considering previous information obtained about the stabilizing mechanism of ethanoic acid in the RuNPs, in particular the easy O-H activation. Twelve ethanoates were settled on the Ru_{55} NP model in the presence of the same amount of hydrides coming from the carboxylic acid deprotonation (figure 3.4; model I). A similar model was built but this time with twelve pentanoates and the same quantity of hydrides (figure 3.4; model II). After structural optimization (*see* section 6.2.2), the corresponding mean adsorption energy of the carboxylic acid entities were calculated (*see* section 6.2.3).

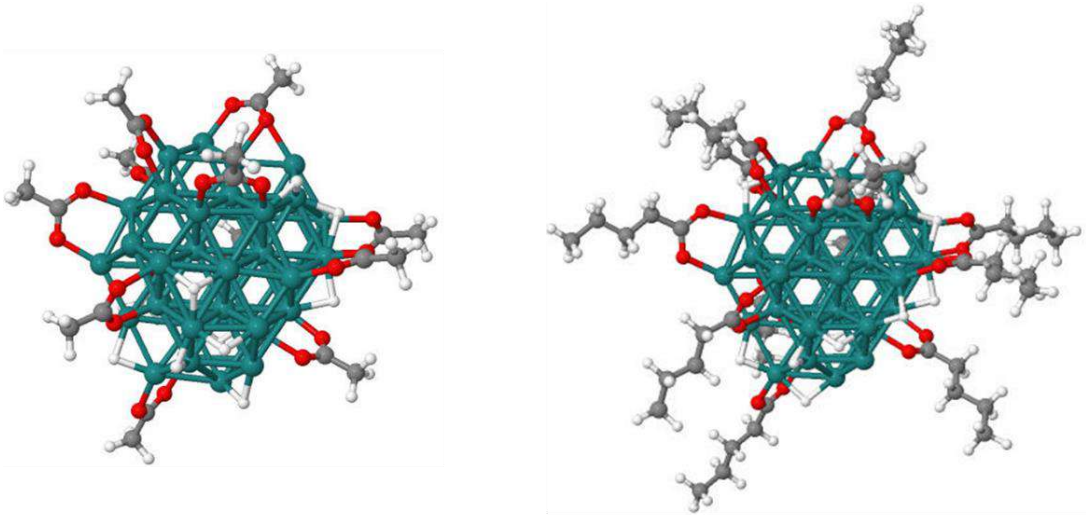

Figure 3.4 Ru_{55} NP models with a high coverage value of carboxylate and hydrides entities; model 1: $Ru_{55}(CH_3COO)_{12}(H)_{12}$; model II $Ru_{55}(C_4H_9COO)_{12}(H)_{12}$.

As a result, it was found that the mean adsorption energy of ethanoic acid in model I is ca. -51.7 kcal.mol^{-1} (*see* section appendix A.4), whilst it was found to be *ca.* -46.2 kcal.mol^{-1} for the pentanoic acid case (*see* section appendix B.1). Since ethanoic moieties have a higher adsorption energy on the ruthenium nanosystems than that of pentanoic entities, and provided that the surface composition is almost the same between the two systems, it seems possible to modulate the electronic properties of the metal core, and hence the catalytic activity of the metal surface, by modifying the carbon chain length.

By taking into account only this data, the model I should be less reactive or more stable than the model II. Given these results are in contrary with the obtained experimentally results (smaller mean size and higher stability observed for pentanoic acid-stabilized RuNPs), other effects have to be taken into consideration, like the electronic barrier produced from the higher steric hindrance generated by the pentanoic acid.

3.1.3 ^{1}H-NMR Study of $Ru_x(C_4H_9COOH)_{0.4}$ NPs

Once the influence of the ligand nature was observed in the RuNPs solubility and in the mean size of the resulting nanosystems, it is reasonably to go deeper in the structural characterization of the novel $Ru_x(C_4H_9COOH)_{0.4}$ NPs. Thanks to the absence of knight shift in these systems[110] and even more by the presence of an oxygen spacer,[106] the RuNPs can be analyzed by NMR with the primarily objective to observe the stabilizing agent interactions with the RuNPs surface as it was shown in chapter II.

The purified and dried NPs were dispersed in THF-d^8 and transferred into an NMR tube in order to record a liquid ^{1}H-NMR spectrum (*see* section 6.1.3.6). The obtained data was compared with that of the free pentanoic acid for which the characteristic signals are as follows: ^{1}H-NMR (THF-d^8): δ 0.90 (t, 3H), 1.35 (sextet, 2H), 1.55 (quintet, 2H), 2.21 (t, 2H), 10.29 (s, 1H) ppm (figure 3.5 red profile).

When comparing with the spectrum of the free pentanoic acid, the ^{1}H-NMR spectrum of $Ru_x(C_4H_9COOH)_{0.4}$ NPs (figure 3.5 blue profile) shows an important broadening between [2.5 & 0.5 ppm]. This phenomenon is well-known to be indicative of a direct interaction between capping ligands and the RuNPs surface (*see* section 2.3.1) and derives from a decreased mobility.

Also, apart from signals attributed to THF and grease, only two signals are well-distinguished at *ca.* 0.92 & 1.33 ppm which can be assigned to the δ and γ protons, of the attached pentanoic moieties, respectively. These assignments can be reasonably inferred from the corresponding peaks of the free pentanoic acid ligand. No other signal can be easily differentiated due to the broadness of the peaks. The small peaks marked with a cross are attributed to impurities that were not possible to eliminate despite the efforts to purify the particles by different cleaning process (*see* section 6.1.2.2.1). Their identification was not possible even with 2D NMR technique.

At this stage, it is important to note that the absence of any sharp signal between [1.4 & 2.2 ppm] where were expected to find the α and β protons of the carboxylic entity as well as at *ca.* 10.3 ppm (acidic proton), points out the absence of free pentanoic acid in solution and consequently the closeness of this ligand to the metal surface.[100]

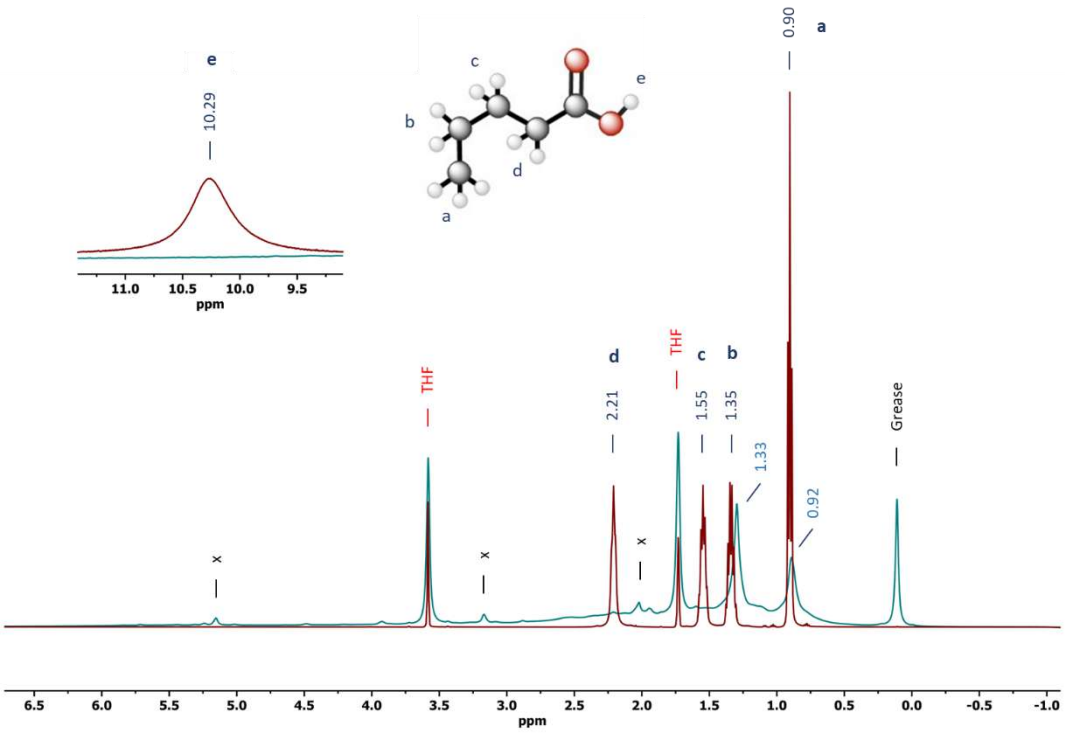

Figure 3.5 ^{1}H-NMR (THF-d^{8}); (blue) $Ru_x(C_4H_9COOH)_{0.4}$ NPs; (red) C_4H_9COOH.

In fact, the gradual broadness of the peaks and the absence of some of them given peaks characteristic of free pentanoic acid allow a mapping of the ligand interaction with the RuNPs.[[164],[236]] Thus, it can be suggested that the pentanoic acid molecules are attached to the RuNPs by their polar head and that the extremity of their alkyl tail clearly has more mobility, meaning that the ligand is not bended on the nanoparticles surface (scheme 3.3).

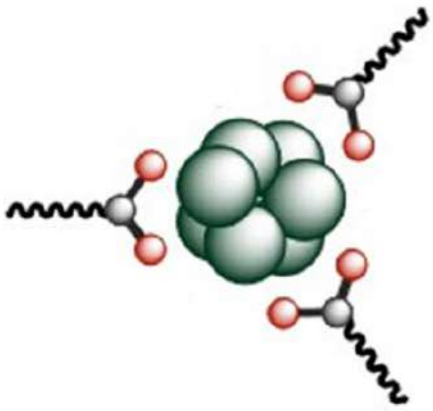

Scheme 3.3 Proposed configuration for $Ru_x(C_4H_9COOH)_{0.4}$ NPs according to solution ^{1}H-NMR spectroscopy.

3.1.4 DOSY ^{1}H-NMR Analysis of $Ru_x(C_4H_9COOH)_{0.4}$ NPs

Diffusion-filtered ^{1}H-NMR spectrum of $Ru_x(C_4H_9COOH)_{0.4}$ NPs (Figure 3.6) revealed the presence of six signals. Among them, the signal at *ca*. 0.1 ppm is assigned to grease coming from the Shlenk techniques used for the RuNPs synthesis. The signal observed at *ca.* 3.3 ppm and marked with an "x" is attributed to an artifact derived from the deuterated solvent (THF-d^8). It is important to note also that the impurities observed in the ^{1}H-NMR spectrum in previous section, are not here visible. Consequently, we can anticipate that these species are not directly interacting with the NPs given that they were filtrated by the applied diffusion-filtered ^{1}H-NMR technique.

The four other signals observed at *ca.* 0.9, 1.3, 1.6 and 2.0 ppm are assigned to the δ, γ, β and α protons, respectively, of the pentanoic moiety attached at the nanoparticle surface. These attributions were performed by referring to the corresponding signals displayed by the free pentanoic acid. The signal of the α protons of the pentanoic acid at *ca.* 2.0 ppm was determined by a Gaussian-Lorentzian fitting on the spectrum (L/G = 1.00) but due to its broadness, it could be shifted to both sides of the spectrum compared to that of the free pentanoic acid.

It is important to point out that the sharpness of the described protons is attributed to the protons mobility. Thus, the protons which are farther of the anchoring point (δ & γ) present sharper signals, but it does not mean that they are free in solution. This data supports the absence of bending ligand onto the RuNPs surface.

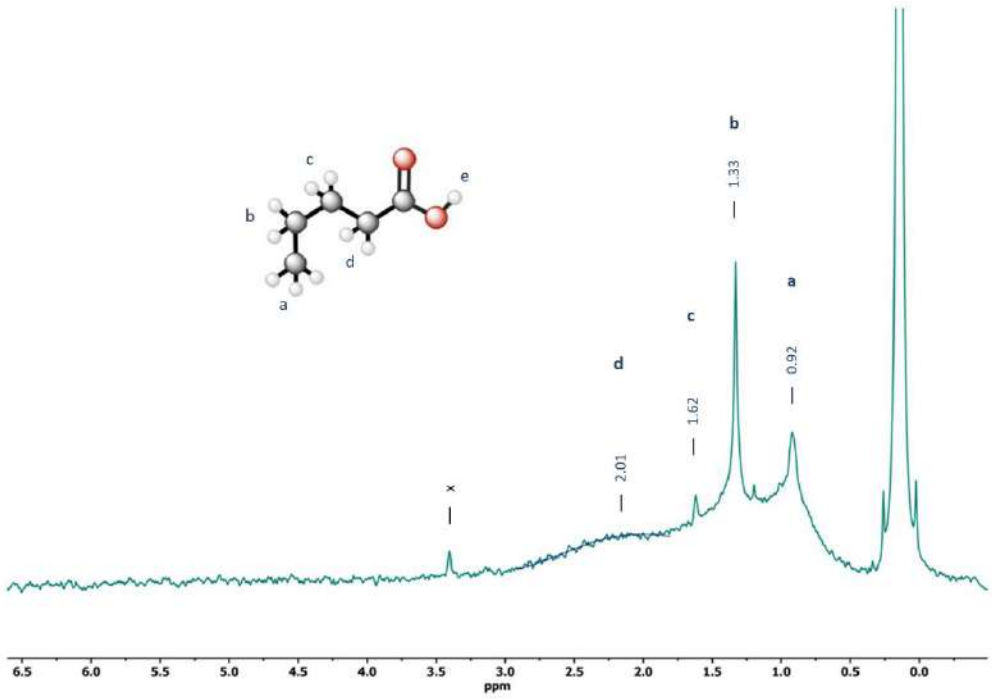

Figure 3.6 Diffusion-filtered DOSY ^{1}H-NMR (THF-d^{8}) spectrum of $Ru_x(C_4H_9COOH)_{0.4}$ NPs.

2D-DOSY NMR allows to see the different species present in solution and to classify them according to their size. It is thus possible to measure the diffusion coefficient of each species which depends on their mobility in the solvent, as a result the hydrodynamic radio (r_H) can be calculated.

DOSY-NMR technique is thus widely used for determining if there is free stabilizing agent in solution, or if it is completely attached at the NP surface or a mixture of both situations. In the presence case, since an impurity was observed in the region between [0.5 and 2.5 ppm] , this procedure cannot be done because it will be compromised. But even so the coefficient diffusion of the bigger objects that lies on this region can be obtained.

The measured diffusion coefficient was D = 4.24 × 10^{-10} $m^2.s^{-1}$. From this value and considering that the experiment was done at 298 K, a hydrodynamic diameter (D_H) of *ca.* 2.2 nm was calculated (*see* section 6.1.3.7.1). In parallel, a sweep of pentanoic acid concentrations in deuterated THF was analyzed by DOSY spectroscopy. As a result, it was found that the D_H of pentanoic acid at low concentration and 298 K was *ca.* 0.6 nm.

By subtracting from the hydrodynamic diameter of the RuNPs the value of the thickness of the ligand layer around the particles (*ca.* 1.2 nm), the hydrodynamic size of the metal core of the $Ru_x(C_4H_9COOH)_{0.4}$ NPs can be estimated to be *ca.* 1.0 nm. Comparing with the TEM data where a mean size of *ca.* 1.1 nm was found for the particles although the difficulty to observe and quantify them, it can be consider there is a good agreement by both techniques. In conclusion, the $Ru_x(C_4H_9COOH)_{0.4}$ NPs are ultra-small with a mean size around 1.0 nm.

3.1.5 Infrared Interpretation of $Ru_x(C_4H_9COOH)_{0.4}$ NPs

Previous FTIR and theoretical studies carried out on ethanoic acid-stabilized RuNPs revealed the presence of the deprotonated carboxylic species at the surface of the nanoparticles and the absence of free ligand. Therefore, after presumably observe the absence of free pentanoic acid in the $Ru_x(C_4H_9COOH)_{0.4}$ NPs (^{1}H-NMR analysis), it is worthy to know if the pentanoic ligands are similarly attached at the surface of $Ru_x(C_4H_9COOH)_{0.4}$ NPs. This information can be obtained by infrared spectroscopy, which will give as a result a better mapping of the RuNPs surface composition.

FTIR data of $Ru_x(C_4H_9COOH)_{0.4}$ NPs was recorded in the ATR mode under inert conditions (*see* section 6.1.3.3). The obtained spectrum was compared with the experimental characteristic peaks of pentanoic acid[237] and THF[190] (figure 3.7).

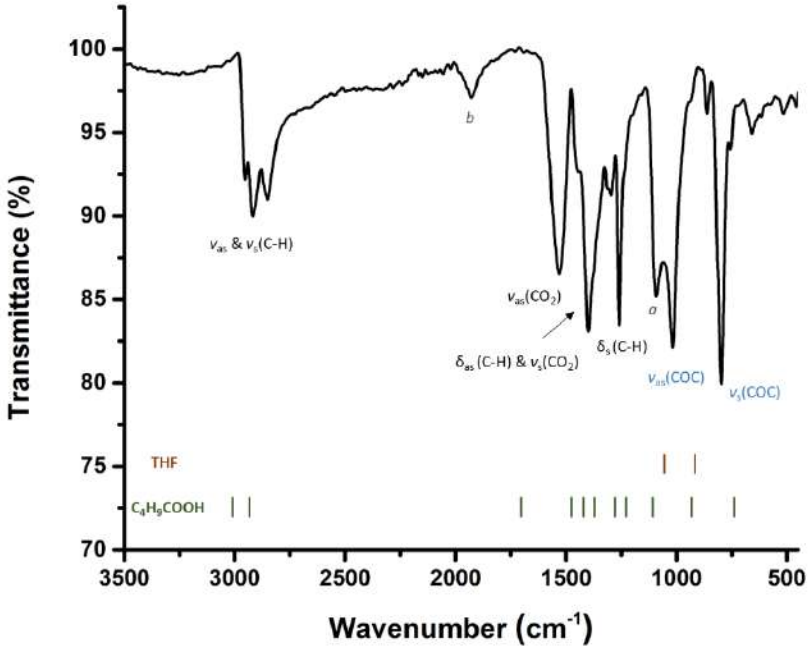

Figure 3.7 Experimental FTIR spectrum of $Ru_x(C_4H_9COOH)_{0.4}$ NPs and main peaks assignments. Experimental characteristic peaks of pentanoic acid (green bars, C_4H_9COOH) and THF (yellow bars) are also indicated. *ν*: stretching; *δ*: bending; s: symmetric; as: asymmetric. Peaks attributed for coordinated THF at the RuNPs surface are likewise shown (blue).

The FTIR spectrum shows at high wavenumber a broad vibration band at *ca*. 3300 cm^{-1} assigned to the stretching vibration modes of water (coming from the RuNPs cleaning process). The three absorption bands observed between *ca.* [2950 - 2850 cm^{-1}] were attributed to the C-H ν_{as} and ν_{ss} vibration modes of the methyl and methylene groups of the alkyl chain of the ligand ($CH_3(CH_2)_3COO(H)$). As already seen for the $Ru_x(CH_3COOH)_{0.4}$ NPs, no signal is visible in the region [1850 - 1600 cm^{-1}], meaning the absence of stretching vibration for pentanoic acid ($C_4H_9C{=}OOH$).

This last observation indicates the absence of the pentanoic acid form (whatever it is free or coordinated) for which signal is expected to be around 1720 cm^{-1}.[237] Rather, the well-defined band present at *ca.* 1530 cm^{-1} can be attributed to the ν_{as} vibration mode of the pentanoate ($C_4H_9C{=}OO$). As it was observed in the RuNPs characterized in the chapter II, the actual interacting moiety onto the RuNPs surface is the deprotonated ligand, pentanoate.

Two other well-separated bands at *ca.* 1400 and 1260 cm^{-1} are observed that can be assigned to the asymmetric stretching mode ν_{as} of the carboxylate group ($C_4H_9C=OO$), and the C-H bending asymmetric δ_{as} and symmetric δ_s vibration mode of the alkyl chain ($CH_3(CH_2)_3COO$).

At lower energy, two strong signals are observed at *ca.* 1010 and 800 cm^{-1}. These bands cannot be assigned to any vibrational mode of the pentanoic acid but are quite similar to those of an ether-type molecule. Since THF was used for the purification of the NPs and that THF was proven to be able to interact with RuNPs surface, it can be inferred that these signals correspond to the asymmetric ν_{as} and symmetric ν_s vibration modes of coordinated THF (blue signals in figure 3.7). It is reliable to point out the absence of free THF due to these shifted signals.[[238],[239]] Bands at *ca.* 1094 & 1930 cm^{-1} (denominated as *a* and *b* on the spectrum) can also be attributed to PTHF[190] and CO[133], respectively, and can be explained by THF degradation as previously reported.

We can thus conclude from this IR study that in $Ru_x(C_4H_9COOH)_{0.4}$ NPs the interacting ligand with the particle surface is deprotonated and attached under the pentanoate form. Consequently, the coordination mode of the ligand is the same as previously observed for RuNPs stabilized with ethanoic acid and prepared at the same [ligand]/[metal] ratio of 0.4 equivalent. However, a significant difference is the clear detection of coordinated THF onto the surface of $Ru_x(C_4H_9COOH)_{0.4}$ NPs compared to $Ru_x(CH_3COOH)_{0.4}$ NPs. In addition, with $Ru_x(C_4H_9COOH)_{0.4}$ NPs a THF degradation is also observed.

This phenomenon can be explained theoretically thanks to the mean absorption energies differences between the ethanoic (-51.7 $kcal.mol^{-1}$) and pentanoic acid (-46.2 $kcal.mol^{-1}$). Since the longer alkyl chain moiety has a weaker adsorption energy, the grafting of THF onto the NPs surface can now become more competitive (*see* section 3.1.2).

Such a difference in adsorption energy can only be related to the influence of the alkyl chain length which is longer by three carbon atoms in the case of pentanoic acid and thus can lead to a more important inductive and steric effects than in ethanoic acid ligand.

FTIR data can also provide interesting information of the electronic charge transmission from the RuNPs to the stabilizing agent (π-backdonation), which is another parameter that can be identified by the vibrational frequencies of the carboxylic moiety.[240] The ν_{as} vibration mode of the ethanoate ($CH_3C=OO$) lies at *ca.* 1545 cm^{-1}, meanwhile that of the pentanoate ($C_4H_9C=OO$) is found at *ca.* 1530 cm^{-1}, meaning that there is a shift of 15 cm^{-1} to lower wavenumbers for the

pentanoate. This shift implies that the retrodonation between the metal and the carboxylate moiety is higher in the pentanoate case. Thus, the stability offered by the pentanoate can be expected to be higher than with ethanoate.

This result agrees with the decreasing of the mean size observed for $Ru_x(C_4H_9COOH)_{0.4}$ NPs (*ca.* 1.1 nm) *vs* $Ru_x(CH_3COOH)_{0.4}$ NPs (*ca.* 1.5 nm), but it differs with the mean adsorption energy calculated for the two ligands onto the Ru_{55} model (*see* section 3.1.2) where the ethanoate showed a higher adsorption energy value. But this last theoretical analysis by itself cannot be consider as a conclusive evidence. Even when it can offer some trends, it is necessary to add thermodynamic parameters (*T, p, [C]*) to make this analysis reliable (*see* section 6.2.6)

3.1.6 Ligand Coverage Optimization

We have observed that for the same amount of introduced ligand (0.40 equiv.), RuNPs stabilized with pentanoic acid display a smaller mean size (*ca.* 1.1 nm) than those stabilized by ethanoic acid (*ca.* 1.5 nm). This result indicates an intrinsic effect of the alkyl chain length on the formation of the nanoparticles and their characteristics, at least their mean size. At this stage of the work, it can be supposed that the longer the alkyl chain the smaller the RuNPs.

However, the differences between the $Ru_x(C_4H_9COOH)_{0.4}$ and $Ru_x(CH_3COOH)_{0.4}$ NPs concern by other features than the mean size, *i.e.* solubility, adsorption energy, retrodonation and THF coordination have been illustrated. These differences in characteristics can arise from two main variables, namely the nature of the capped ligand and the size of the nanoparticles. In order to remove the size variable, a ligand coverage optimization was performed with the aim to obtain with pentanoic acid RuNPs of similar mean size than with ethanoic acid, namely of *ca.* 1.5 nm

3.1.6.1 Synthesis of a Series of $Ru_x(C_4H_9COOH)_y$ NPs

It has been reported that the quantity of stabilizing agent added to the NPs synthesis reaction media can have an intrinsic effect on the sizes and morphologies of MNPs.[([205],[241],[242])]

Therefore, a sweep study of the influence of the pentanoic acid quantity added for the RuNPs synthesis was performed (table 3.1), as size control strategy with the aim to find appropriate conditions to get RuNPs of *ca.* 1.5 nm.

Table 3.1 Sweep of pentanoic acid molar equivalents used for the synthesis of RuNPs. * Previously described.

	System	Pentanoic acid (equiv.)
1	$Ru_x(C_4H_9COOH)_{0.05}$	0.05
2	$Ru_x(C_4H_9COOH)_{0.2}$	0.20
3	$Ru_x(C_4H_9COOH)_{0.3}$	0.30
4*	$Ru_x(C_4H_9COOH)_{0.4}$	0.40
5	$Ru_x(C_4H_9COOH)_{0.5}$	0.50
6	$Ru_x(C_4H_9COOH)_{0.6}$	0.60

Thus, different syntheses of RuNPs were performed by following the organometallic approach with the same procedure described in section 3.1.1, just changing the [ligand]/[metal] ratio from [0.05 to 0.60 equiv.]. In each case, the yellow solution obtained after mixing in pentane the [Ru(COD)(COT)] precursor and pentanoic acid ligand, turned blackish after *ca.* 4 min of pressurizing the Fisher-Porter reactor with 3 bar of hydrogen under inert atmosphere. This change of color is a well-known indicative for the formation of RuNPs.

The presence of a precipitate was observed for the [1 - 3 systems], which can be attributed to the formation of ruthenium bulk and/or, agglomerates or to the difference of solubility of the RuNPs in pentane. Meanwhile, systems [4 – 6] remained stable as colloidal suspensions for at least 24 h. These results indicate that for a quantity of ≥ 0.40 equiv. of pentanoic acid added, the colloidal systems of RuNPs formed are soluble in pentane, increasing their solubility on non-polar solvents.

After the RuNPs synthesis a drop of concentrated crude solutions was deposed onto a grid for TEM analysis (*see* section 6.1.3.1). For systems [1 – 3] that presented a precipitate, the drop was taken while stirring vigorously in order to homogenize the solution. Hereafter, it is presented the obtained TEM micrographs and mean size quantification for each novel system.

TEM micrographs recorder for system 1, $Ru_x(C_4H_9COOH)_{0.05}$, show at first glance the presence of big metal pieces and agglomerates (figure 3.8), which can explain the observed formation of a precipitate.

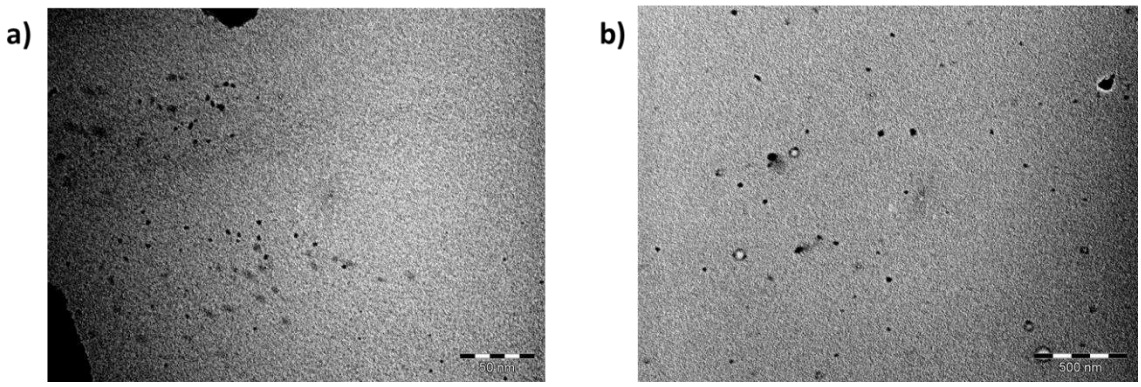

Figure 3.8 TEM micrographs of $Ru_x(C_4H_9COOH)_{0.05}$ NPs; (a) & (b) agglomeration of particles; scale bar: 50 nm & 500 nm, respectively.

Nevertheless, in the background small individual nanoparticles of different mean sizes (*ca.* 0.75 ± 0.34 & 3.36 ± 2.48 nm) can be observed (Figure 3.9). This observation indicates that even at such a low concentration of pentanoic acid (0.05 equiv.) small nanoparticles can be formed even if not stable apparently. A similar trend was observed for the RuNPs prepared with ethanoic acid but using 0.20 equiv. of ligand. The pentanoic acid thus appears to be a much better stabilizing agent than ethanoic acid since it can stabilize RuNPs at a [ligand]/[metal] ratio as low as 0.05 equiv.

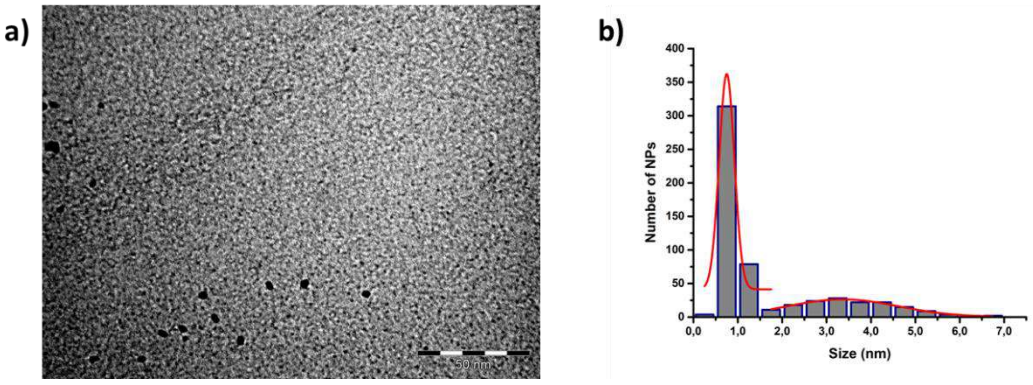

Figure 3.9 (a) TEM micrograph of $Ru_x(C_4H_9COOH)_{0.05}$ NPs; scale bar: 50 nm; (b) corresponding size histogram of individual RuNPs.

The micrographs obtained for the system 2, $Ru_x(C_4H_9COOH)_{0.20}$, show the formation of semi-homogeneous nanoparticles that are well-dispersed on the TEM grid and display a mean size of *ca.* 1.58 ± 0.47 nm (figure 3.10). This mean size is similar to that of $Ru_x(CH_3COOH)_{0.40}$ NPs. However, as it can be seen in the bottom left of the TEM image and in the size histogram, that larger particles are also present which makes this colloidal system to be not a complete homogeneous unidimensional system.

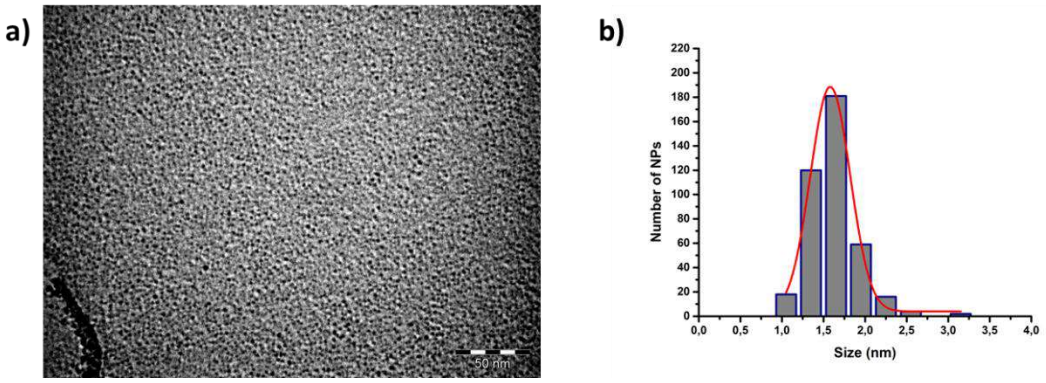

Figure 3.10 (a) TEM micrograph of $Ru_x(C_4H_9COOH)_{0.20}$ NPs; scale bar: 50 nm; (b) corresponding size histogram of individual RuNPs.

For the case of the system 3, $Ru_x(C_4H_9COOH)_{0.30}$, well-dispersed and small RuNPs were formed with a mean size of *ca.* 1.47 ± 0.40 nm (figure 3.11). This nanosystem displays a slightly smaller mean size than system 2 but this decrease is judged to be not significant enough given the standard deviation. However, the obtained RuNPs show a better dispersion on the grid and also higher size homogeneity as shown on the size histogram where bigger particles were not found. This system thus corresponds to a better controlled population of RuNPs that have a quite similar size to those formed with 0.40 equiv. of ethanoic acid (*ca.* 1.51 nm). This makes this system of RuNPs a good candidate for a direct comparison with the $Ru_x(CH_3COOH)_{0.40}$ NPs, as it was looked for.

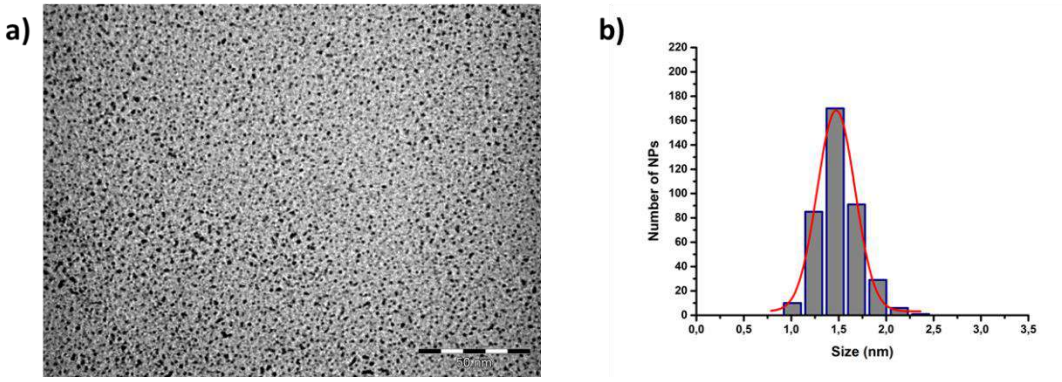

Figure 3.11 (a) TEM micrograph of $Ru_x(C_4H_9COOH)_{0.30}$ NPs; scale bar: 50 nm; (b) corresponding size histogram of individual RuNPs.

As a reminder, the addition of 0.40 equiv. of pentanoic acid ($Ru_x(C_4H_9COOH)_{0.40}$; system 4) led to a NP mean size of *ca.* 1.1 nm (*see* section 3.1.1) without changing their morphology. The important decrease of size (*ca.* 0.4 nm) noticed when comparing the mean size of the RuNPs in systems 3 and 4 (1.5 *vs* 1.1 nm) exhibits a high impact of the ligand in the growth of the particles in this range of concentration ([0.30 - 0.40 equiv.]). As it was described before, the quantity of stabilizing agent added for the NPs synthesis has a high-influence on the morphology and mean size of the nanoparticles.[205]

Also, at this point it can be illustrated that lower quantity of pentanoic acid can stabilize the same mean size of RuNPs than that needed by using ethanoic acid as ligand. In conclusion, these observations are another evidence of the better stabilization properties that possess a longer alkyl chain ligand *vs* a shorter one.

According to the previous observations, it is worth to know more about the impact on RuNPs mean size, while it is exposed to higher quantity of pentanoic acid ≥ 0.40 equiv.

System 5, $Ru_x(C_4H_9COOH)_{0.50}$, presents RuNPs with a mean size of *ca.* 1.18 ± 0.18 nm (figure 3.12). These RuNPs appear to be quite similar to those of system 4, showing the same morphology and no statistical difference in the mean size. Thus, it is probably that smaller NPs than *ca.* 1.1 nm cannot be obtained even if a higher quantity of pentanoic acid is added to the setup used for the RuNPs synthesis, forming a plateau.[167]

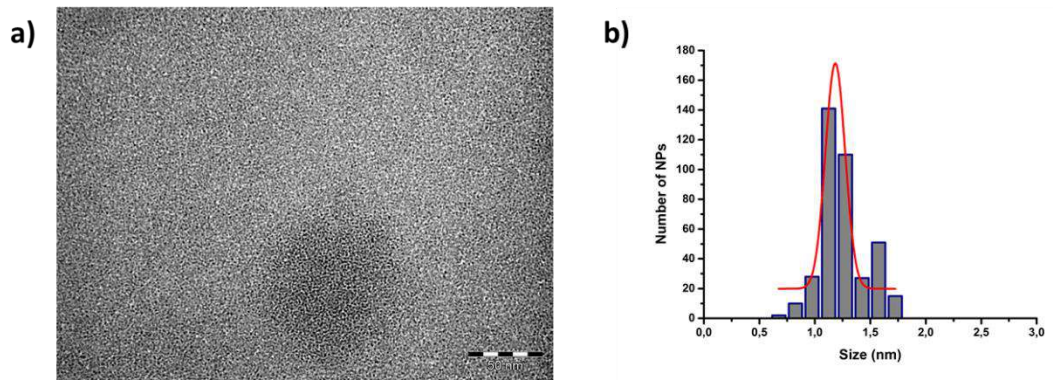

Figure 3.12 (a) TEM micrograph of $Ru_x(C_4H_9COOH)_{0.50}$ NPs; scale bar: 50 nm; (b) corresponding size histogram of individual RuNPs.

The last system (6), $Ru_x(C_4H_9COOH)_{0.60}$, exhibits spherical RuNPs with a mean size of *ca.* 1.02 ± 0.26 nm (figure 3.13), which is very similar to colloidal system 5. This result confirms that the minimum mean size that can be reached by using pentanoic acid as stabilizer agent for the synthesis of RuNPs is *ca.* [1.0 - 1.1 nm].

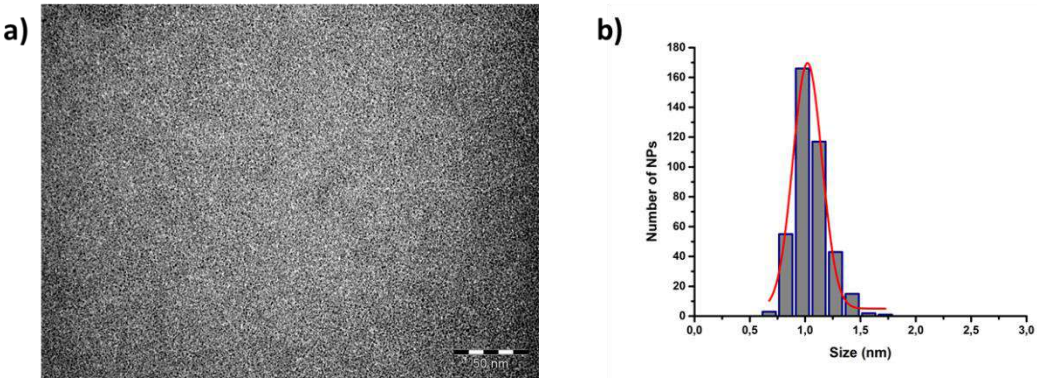

Figure 3. 13 TEM micrograph of $Ru_x(C_4H_9COOH)_{0.60}$ NPs; scale bar: 50 nm; (b) corresponding size histogram of individual RuNPs.

Hereafter, it is presented an extract of the RuNPs mean sizes and size dispersion according to the TEM analyses (table 3.2). Where it can be observed the similarities between some systems, and that the addition of more stabilizing agent for the RuNPs synthesis will render to smaller nanosystems.

Table 3.2 Scope of pentanoic acid quantity used for the RuNPs synthesis with their corresponding mean size and size dispersion obtained by TEM analyses.

	System	Pentanoic acid (equiv.)	Mean size (nm)	Size dispersion (2σ, nm)
1	$Ru_x(C_4H_9COOH)_{0.05}$	0.05	0.75	0.34
			3.36	2.48
2	$Ru_x(C_4H_9COOH)_{0.20}$	0.20	1.58	0.47
3	$Ru_x(C_4H_9COOH)_{0.30}$	0.30	1.47	0.40
4	$Ru_x(C_4H_9COOH)_{0.40}$	0.40	1.13	0.31
5	$Ru_x(C_4H_9COOH)_{0.50}$	0.50	1.18	0.18
6	$Ru_x(C_4H_9COOH)_{0.60}$	0.60	1.02	0.26

In summary, the study performed by a sweep of pentanoic acid concentration, used for the synthesis of RuNPs, evidences three different groups of colloidal systems. First, the formation of a heterogeneous system composed by a mixture of RuNPs, agglomerates and bulk material was observed when adding 0.05 equiv. of the ligand. The second group gathers the nanoparticles synthetized with [0.20 and 0.30 equiv.] that have primarily the same mean size, *ca.* 1.5 nm, although slight differences were observed. Finally, the third type of RuNPs corresponds for the minimum NPs size obtained, *ca.* 1.1 nm, which corresponding to the RuNPs stabilized by [0.40 - 0.60 equiv.] of pentanoic acid (table 3.3).

Table 3.3 Different groups found by sweeping the pentanoic acid concentration for the RuNPs synthesis.

Group	Pentanoic acid (equiv.)	Mean size (nm)
1	0.05	Mixture
2	0.20 – 0.30	1.5
3	0.40 – 0.60	1.1

This study is based on changing the quantity of stabilizing agent in order to have different types of RuNPs, which as was expected can display different mean sizes. But also, whit this analysis, it was seen than it is possible to obtain similar RuNPs with different quantity of added ligand, as it was seen for the group 2 & 3. This phenomenon could indicate that the particles can have a higher ligand surface coverage without changing the morphology or their size.

It is also noteworthy that a lower quantity of pentanoic acid than of ethanoic acid has allowed to get RuNPs of *ca.* 1.5 nm. This highlights the higher capacity of pentanoic acid to stabilize RuNPs compared to the ethanoic counterpart. This result confirms the previous presented hypothesis about the influence of the alkyl chain length of the carboxylic acid ligands in their efficiency to stabilize RuNPs.

From all these results, it can be concluded that the quantity of pentanoic acid introduced for the nanoparticle synthesis has an influence on their formation and that this parameter is a way to have at disposal stable populations of RuNPs of *ca.* [1.5 or 1.1 nm], displaying the same ligand at their surface.

Another important point is that the ligand amount around the particles can also vary for a given mean size (in the ranges [0.20 - 0.30 equiv.] and [0.40 - 0.60 equiv.] for 1.5 and 1.1 nm, respectively). Given that the objective was to have in hands RuNPs of *ca.* 1.5 nm for comparison studies with the most stable ones got with ethanoic acid ($Ru_x(CH_3COOH)_{0.40}$), RuNPs from group 2 are convenient.

According to the literature, the electronic stability of the NPs depends on the ligand coverage, namely, a lower ratio leads to a lesser stability.[243] Therefore the NPs prepared with 0.30 equiv. of pentanoic acid ($Ru_x(C_4H_9COOH)_{0.30}$) that form a more homogeneous population of RuNPs than those prepared with 0.20 equiv. appear to be the best NP system for comparison studies with $Ru_x(CH_3COOH)_{0.40}$ NPs.

3.1.6.2 NMR Analysis of $Ru_x(C_4H_9COOH)_y$ NPs

In this section, is presented a comparative ^1H NMR study performed on the series of pentanoic acid-stabilized RuNPs prepared with different quantities of ligand, as described in previous section 3.1.6.1. The objective of this study was to get information on the interacting ligand at the ruthenium surface (seen as broad signals) and also, to evidence the presence of free ligand (seen as sharp signals).

The proton NMR data (figure 3.14) were recorded as described in section 3.1.3, but from the crude colloidal solutions (the nanoparticles were not purified but just redissolved in

deuterated THF after evaporation of pentane, the same concentration of RuNPs was fixed by using the same volume of deuterated solvent for all systems studied for comparison purpose). The signals attributed to side products are marked with an "*x*".

Peaks assigned to *a* and *b* protons of the pentanoic acid can be seen as broad signals in all the spectra. The intensity of these peaks increases as the result of the increasing quantity of the ligand (see spectra 1 to 6, corresponding to 0.05 to 0.60 equiv. of added ligand). The signal assigned to the *c* protons of pentanoic acid can be observed as a broad peak for the RuNPs systems stabilized by 0.30, 0.50 and 0.60 equiv. of pentanoic acid (spectra 3, 5 and 6), meaning that probably their alkyl chains are more elongated and therefore it can be seen in contrary of what is observed for systems 2 and 4.

Finally, the peak attributed to the *d* protons of pentanoic acids is not observed for the RuNPs stabilized from [0.05 to 0.50 equiv.] of pentanoic acid, but it is for those prepared with 0.60 equiv. (see red circle). The observation of this signal for RuNPs stabilized with 0.60 equiv. indicates the presence of free ligand. Indeed, protons in the proximity of the metal surface are not expected to be visible due to important broadening as previously explained, which is the case for *d* protons that are very close to the carboxylic group interacting with the metal surface (α protons). Thus, the fact they are visible can only be explained by the presence of free ligand in solution.

As a conclusion of this ^{1}H NMR study, it can be inferred that the only RuNPs system that clearly presents free ligand is $Ru_x(C_4H_9COOH)_{0.60}$. For the other pentanoic acid-stabilized RuNPs the whole ligand is suspected to be in complete interaction with the RuNPs, according to the absence of the α protons of the ligand denoted as "*d*" in the spectra.

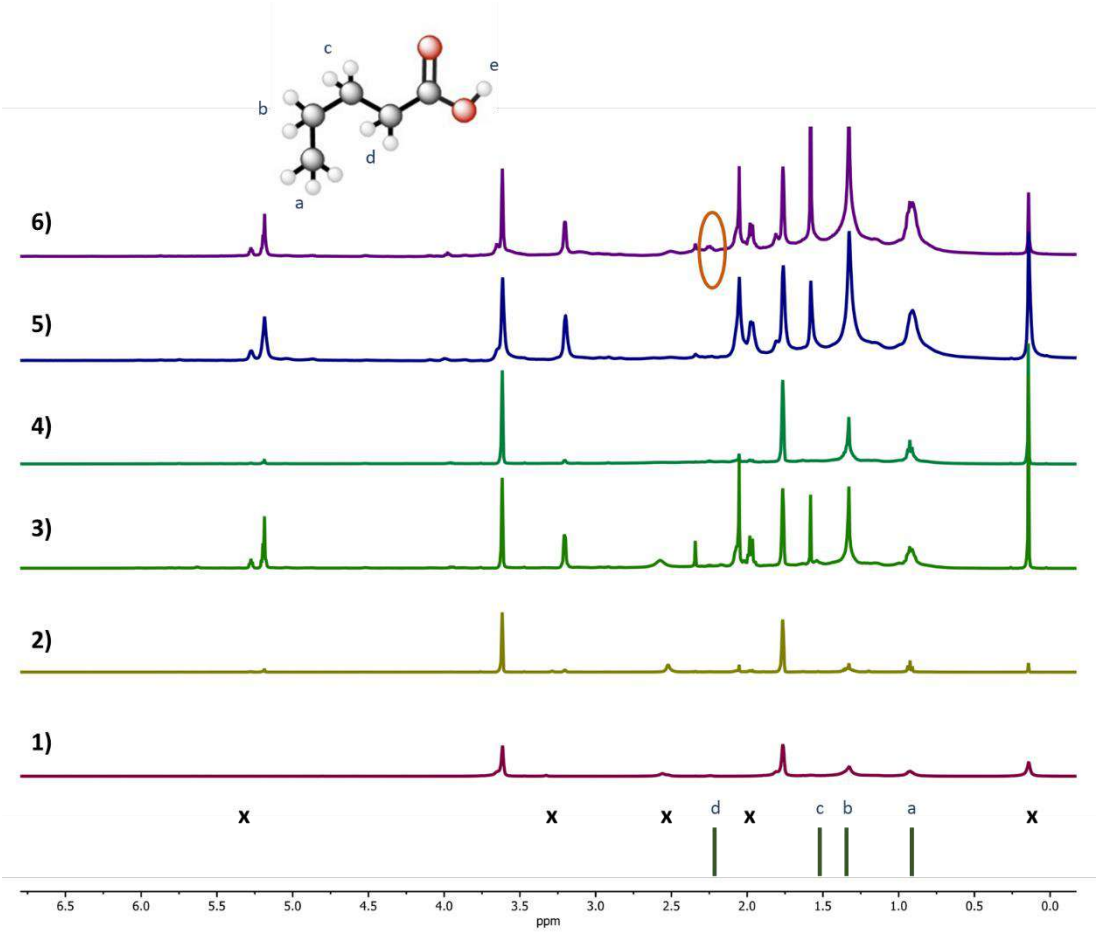

Figure 3.14 ^{1}H-NMR (THF-d^{8}) of RuNPs; (1) $Ru_x(C_4H_9COOH)_{0.05}$; (2) $Ru_x(C_4H_9COOH)_{0.20}$; (3) $Ru_x(C_4H_9COOH)_{0.30}$; (4) $Ru_x(C_4H_9COOH)_{0.40}$; (5) $Ru_x(C_4H_9COOH)_{0.50}$; (6) $Ru_x(C_4H_9COOH)_{0.60}$. Peaks attributed to side products are denoted with an "x" and the signals for pentanoic acid peaks are displayed in bars at the bottom of the figure. The signal surrounded by an orange circle corresponds to free ligand.

Figure 3.15 provides a comparison of the ^{1}H NMR spectra (zoom of [0.6 - 2.4 ppm] region) recorded for RuNPs from the 3 different groups (*see* classification in section 3.1.6.1) that were prepared with 0.05 equiv. (group 1; brown), 0.30 equiv. (group 2; green) and 0.60 equiv. (group 3; purple) of pentanoic acid ligand. As a reminder, these spectra were obtained from the crude colloidal solutions and side products can be observed (marked as "x"). However, the THF deuterated solutions were prepared with a same concentration which allows to make a trustworthy comparison by stablishing the THF as a reference.

From this figure, it can be seen that the broadness of the spectra increases with the quantity of ligand. This can imply that RuNPs from group 3 have higher quantity of ligands interacting with ruthenium surface than those of group 2 and even more group 1.

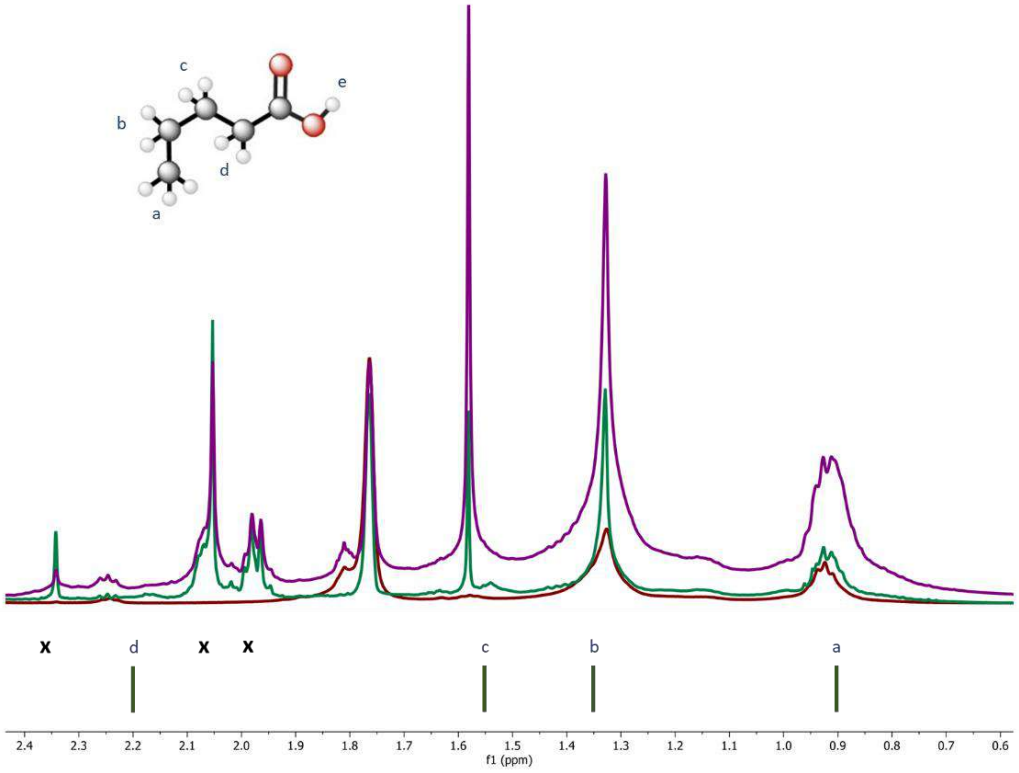

Figure 3.15 ^{1}H-NMR (THF-d^{8}) of RuNPs; (group 1, brown profile), $Ru_x(C_4H_9COOH)_{0.05}$; (group 2, green profile), $Ru_x(C_4H_9COOH)_{0.30}$; (group 3, purple profile), $Ru_x(C_4H_9COOH)_{0.60}$. Peaks attributed to side products are denoted with an "x" and those of pentanoic acid are displayed in bars at the bottom of the figure.

The experiment has shown that the only system that display the presence of free pentanoic acid is the $Ru_x(C_4H_9COOH)_{0.60}$ NPs. Also, it has been demonstrated the difference in the amount of ligand interacting with the nanoparticle surface by looking at the broadness of the different groups found by TEM analysis.

From this observation and by making a parallel between the amount of added ligand and the size of the RuNPs obtained, one hypothesis could be that the higher the quantity of stabilizing agent, the higher the interaction with the metal surface, and the smaller the RuNPs formed.

To corroborate this hypothesis, a similar analysis was performed but looking at the spectra of RuNPs that belong to the same group (2). Hereafter, it is presented the compared spectra

between the RuNPs stabilized by 0.20 equiv. of pentanoic acid *vs* that of 0.30 equiv. (figure 3.16, red and blue respectively).

The same observation can be done as for previous comparison: a broadness increase of the signals is observed with higher quantity of ligand. Meaning that more ligands are interacting with RuNPs surface from 0.30 vs. 0.20 equiv. of pentanoic acid added. But differently from previous comparison, this leads to a more homogeneous population of NPs and not to smaller ones (similar size of *ca.* 1.5 nm for both RuNPs systems).

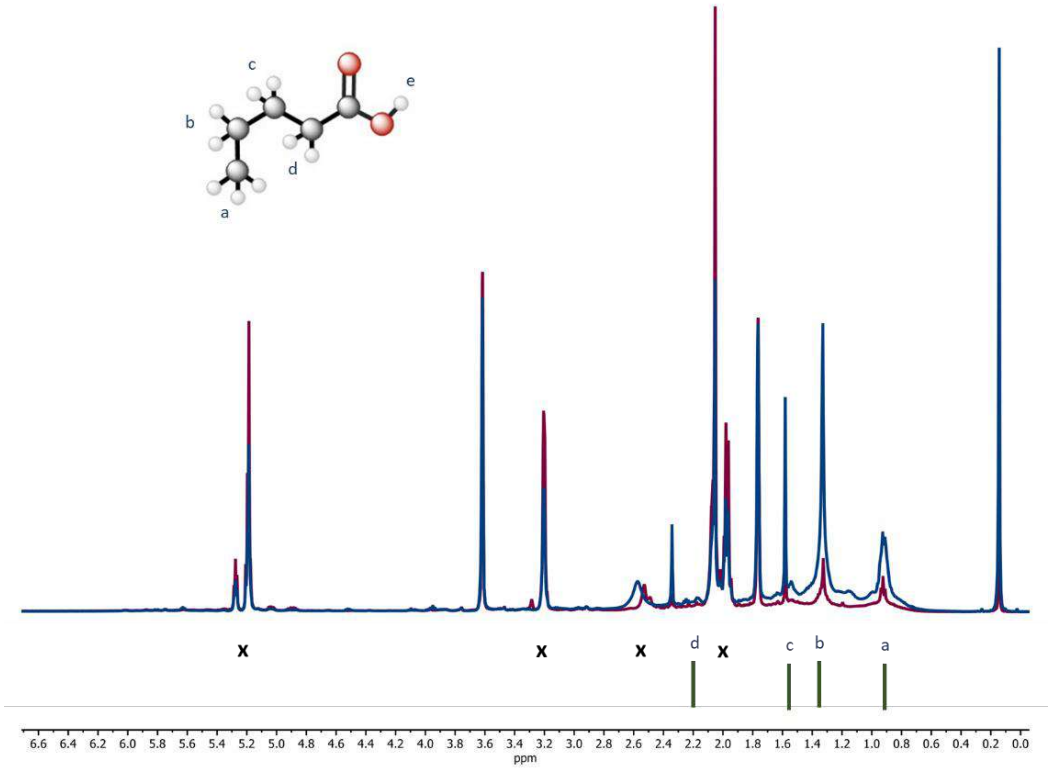

Figure 3.16 ^{1}H-NMR (THF-d^{8}) of RuNPs; (red profile) $Ru_x(C_4H_9COOH)_{0.20}$; (blue profile) $Ru_x(C_4H_9COOH)_{0.30}$. Peaks attributed to side products are denoted with and "x" and the peaks for pentanoic acid are given as bars at the bottom of the figure.

As a reminder, by TEM analysis it was observed that a higher quantity of ligand led to smaller NPs until reaching a plateau at size *ca.* [1.0 - 1.1 nm]. From ^{1}H NMR studies, it was detected that only at 0.60 equiv. of pentanoic acid, free ligand is visible. Also, higher is the quantity of stabilizing ligand added, higher is the amount of ligand interacting with RuNPs. In order

to get more information of the ligand layer around the RuNPs, DOSY NMR studies were performed.

DOSY NMR studies can provide more insights about the possible presence of free ligand into the NPs system, but since as observed in figure 3.14 the broad region assigned to the ligand attached at the NP surface ([0.5 - 2.5 ppm]) is corrupted by the presence of side products ("x"), it is not a trustworthy analysis (figure 3.14). However, the hydrodynamic radio (r_H) for the largest objects (NPs + ligand) can be obtained and compared with size data resulting from TEM studies. These analyses will disperse the possible doubts that could be generated form the TEM analyses due to the NPs small mean sizes.

Hydrodynamic diameters (D_H) given in table 3.4 for each system of NPs analyzed were obtained from the recorded diffusion coefficients of the large species observed, at r.t. in deuterated THF solution (see section 6.1.3.6.1). As it can be seen, except for the first system (no homogeneous NPs formed), the diffusion coefficient increases while the quantity of ligand used for the RuNPs synthesis augments. As a consequence, the calculated size of the objects shows a gradual decrease. Such a phenomenon was not noticed by TEM analysis where the NPs were gathered in size groups. However, these size data need to be taken carefully because the estimated random error in DOSY measurements (signal/noise) could rise to 8.0 % and it can increase even more depending on the experimental treatment and equipment used for the analysis.[244]

Table 3.4 DOSY analyses performed on a scope of RuNPs stabilized by different quantity of pentanoic acid with their corresponding diffusion coefficients, calculated hydrodynamic diameter and estimated size RuNPs species.

	System	Pentanoic acid (equiv.)	Diffusion coefficient ($m^2.s^{-1}$)	D_H (nm)	RuNPs (nm)
1	$Ru_x(C_4H_9COOH)_{0.05}$	0.05	$5.59x10^{-10}$	1.69	0.49
2	$Ru_x(C_4H_9COOH)_{0.20}$	0.20	$3.40x10^{-10}$	2.77	1.57
3	$Ru_x(C_4H_9COOH)_{0.30}$	0.30	$3.14x10^{-10}$	3.00	1.80
4	$Ru_x(C_4H_9COOH)_{0.40}$	0.40	$4.24x10^{-10}$	2.22	1.02
5	$Ru_x(C_4H_9COOH)_{0.50}$	0.50	$4.54x10^{-10}$	2.08	0.88
6	$Ru_x(C_4H_9COOH)_{0.60}$	0.60	$4.75x10^{-10}$	1.99	0.79

Hydrodynamic diameters measured by DOSY analyses exhibit the presence of small and ultra-small nanoparticles, which were difficult to observe by TEM analyses. Therefore, it can be estimated that the count performed by microscopy techniques was accurate enough to display the mean size of the synthetized RuNPs

In addition, by these DOSY NMR analyses nano-objects smaller than *ca.* 1.1 nm are observed ($\geq$ 0.40 equiv. of ligand added). Such small NPs are very difficult to observe by TEM analyses due to their small size and microscopy resolution. Nevertheless, the TEM histograms built for NPs systems prepared with [0.40 to 0.60 equiv.] of ligand report smaller NPs than 1.0 nm.

Also, DOSY analyses indicate an absence of size limit even at high concentration of pentanoic acid (0.60 equiv.) while a plateau at a mean size of *ca.* 1.1 nm was deduced from TEM results for RuNPs prepared with [0.40 - 0.60 equiv.] of ligand. Implicating that the RuNPs mean size is inversely proportional to the amount of stabilizing agent added for the RuNPs synthesis.

Finally, it was noted from TEM studies that between [0.20 - 0.30 equiv.] of pentanoic acid added to the reaction media, statistical similar size of RuNPs were produced. An analogous phenomenon was observed for NPs stabilized by ≥ 0.40 equiv. of pentanoic acid, which makes the assignation of RuNPs groups reliable.

Table 3.5 gives a comparison of the data obtained by TEM and DOSY NMR techniques. It appears that the two techniques provided complementary data, that for some of them are perfectly in agreement while others underestimated. Nevertheless, it can be concluded that the results obtained are reliable enough to provide a good idea of the influence of the quantity of pentanoic acid on the size of the RuNPs formed in a concentration rang of [0.05 to 0.60 equiv.].

Table 3.5 Comparison between the data obtained by TEM studies *vs* DOSY analyses for RuNPs synthetized with different quantities of pentanoic acid.

	System	Pentanoic acid (equiv.)	*Metal D_H* (nm)	TEM size (nm)	Group
1	$Ru_x(C_4H_9COOH)_{0.05}$	0.05	0.49	0.75	1
				3.36	
2	$Ru_x(C_4H_9COOH)_{0.20}$	0.20	1.57	1.58	2
3	$Ru_x(C_4H_9COOH)_{0.30}$	0.30	1.80	1.47	
4	$Ru_x(C_4H_9COOH)_{0.40}$	0.40	1.02	1.13	3
5	$Ru_x(C_4H_9COOH)_{0.50}$	0.50	0.88	1.18	
6	$Ru_x(C_4H_9COOH)_{0.60}$	0.60	0.79	1.02	

3.1.7 Evaluation of $Ru(C_4H_9COOH)_{0.3}$ NPs

As mentioned before, the main objective of section 3.1.6 was to test different quantities of ligand in order to obtain pentanoic-acid stabilized RuNPs of *ca.* 1.5 nm in size as for $Ru_x(CH_3COOH)_{0.4}$ NPs. In order to reduce one of the variables (NPs size and alkyl chain length) presented for comparing the influence of the ligand (ethanoic acid *vs* pentanoic acid) in the RuNPs properties.

From the previous experiments, two [ligand]/[metal] ratio allowed to reach this aim, namely 0.2 and 0.3 equiv. The $Ru_x(C_4H_9COOH)_{0.3}$ NPs was selected because it was observed by TEM analysis that the RuNPs presented a more homogenous population with similar mean size as $Ru_x(CH_3COOH)_{0.4}$ (see section 3.1.6). Despite the efforts made to decrease the variables, another parameter comes out, the probable quantity of capping ligand interacting with the NPs surface (0.3 *vs* 0.4 equiv.).

Nevertheless, the ligand influence comparison can be obtained by studying the ligand coordination type and the amount of coordinated ligand compared to ethanoic acid-stabilized RuNPs. Thus, hereafter an experimental and theoretical characterization of $Ru_x(C_4H_9COOH)_{0.3}$. will be shown to clarify this riddle.

3.1.7.1 Solid-NMR Studies of $Ru_x(C_4H_9COOH)_{0.3}$ NPs

The findings obtained from solution ^{1}H-NMR are not enough to clearly probe the ligand interaction mode at the RuNPs surface (*see* section 2.3.1) due to the proximity of the attached atoms (carboxylate) to the metal surface. Therefore, the use of a solid-NMR with the magic angle spinning (MAS) is a trustworthy methodology to elucidate this unknown parameter (*see* section 2.4.2).

Solid-state ^{13}C CP Hahn-MAS NMR was recorded for the $Ru_x(C_4H_9COOH)_{0.3}$ NPs after their dilution into porous silica in order to avoid electric arching (see section 6.1.3.7). The aim was to obtain the chemical shift of the carboxylic species present in this NPs system (figure 3.17), in comparison with previous findings observed (*see* section 2.4.2) and to elucidate if the ligand is coordinated as carboxylic acid or carboxylate.

The following spectrum presents only broads signals. The biggest ones correspond to THF, a solvent used in the RuNPs silica dilution. Moreover, there is also a signal at *ca.* 12 ppm that can be attributed to the methyl group of the pentanoic acid. This methyl peak was not observed for the $Ru_x(CH_3COOH)_{0.4}$ NPs pointing out a difference in the methyl group proximity to the RuNPs surface for the two systems of NPs. This could be expected because the pentanoic acid has a longer alkyl chain length than ethanoic counterpart which can make the methyl group far from the metal surface if there is no chain folding towards the NP surface. This methyl group being visible means the extremity of the alkyl chains is not interacting or even close to ruthenium surface.

The most important peak is the one found at low field at *ca.* 188 ppm, that can be assigned to carboxylic moiety interacting with the NP surface in comparison to the free pentanoic acid that displays a signal at *ca.* 174 ppm (figure 3.17 bottom bars) for this carbon.

It is important to note that no signal is visible in the [170 – 180 ppm] range, indicating that there is no free pentanoic acid in the sample. The difference in chemical shift between coordinated and free pentanoic acids is more than 10 ppm of deshielding, which is in agreement with previous data obtained for ethanoic acid-stabilized RuNPs (δ 186 *vs*. 172 ppm for coordinated and free ethanoic acid (solution), respectively). This phenomenon was attributed to the coordination of the carboxylic moiety onto the RuNPs as deprotonated specie.

As a result, it can be concluded that for $Ru_x(CH_3COOH)_{0.4}$ NPs, the ligand is also deprotonated and coordinated under the form of pentanoate.

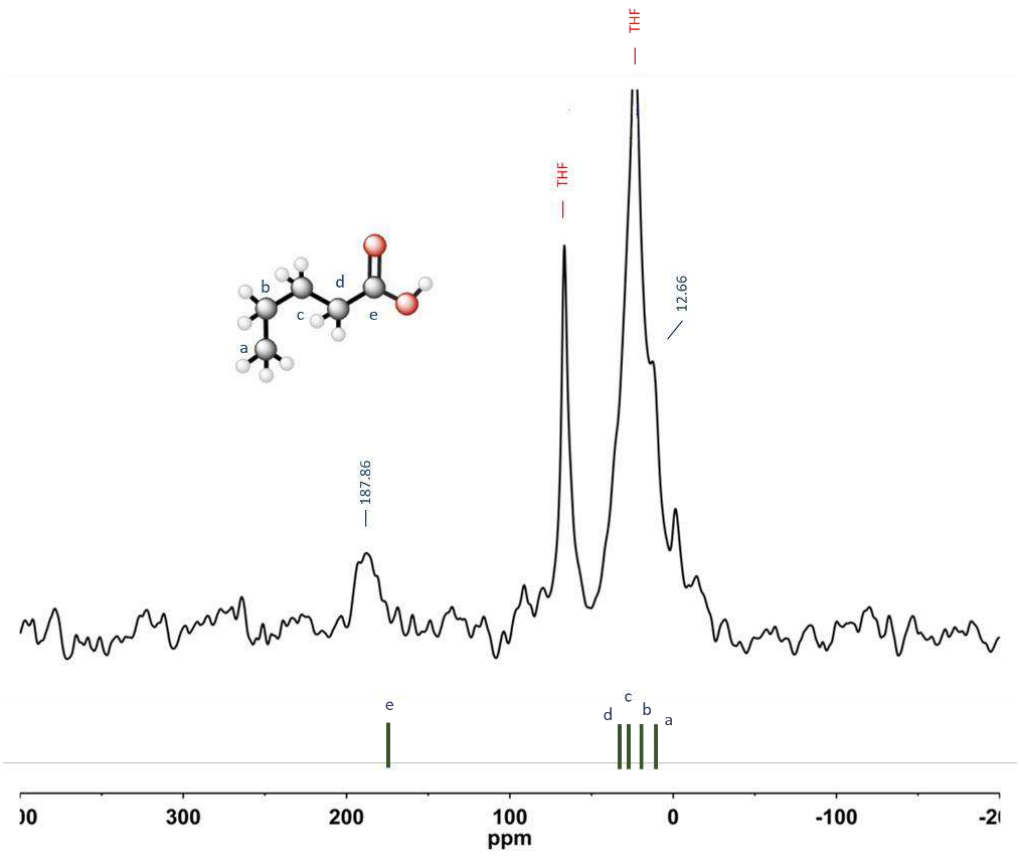

Figure 3.17 ^{13}C CP Hahn-MAS NMR of $Ru_x(C_4H_9COOH)_{0.3}$ NPs diluted in porous silica. Pentanoic acid peaks are given in bars at the bottom of the figure.

3.1.7.2 Elemental Analysis of $Ru_x(C_4H_9COOH)_{0.3}$ NPs

C, H, N analysis was carried out on $Ru_x(C_4H_9COOH)_{0.3}$ NPs after purification (table 3.6) with the principal objective to know if all the pentanoic acid added for the NPs synthesis is attached at the NPs surface or some of it was removed in the cleaning process (THF-pentane cycles; *see* section 6.1.2.2.1). This analysis is also an indirect rough way for the determination of the metal content in the sample. Hereafter is presented the results of mentioned analysis.

Table 3.6 Elemental analysis of $Ru_x(C_4H_9COOH)_{0.3}$ NPs

Element	Sample weight (%)
C	22.4
H	2.0
N	0.1

Considering that all the reported carbon should come from the pentanoic acid, then the quantity of oxygen can be estimated to 11.9 % of sample weight which would lead to 38.0 % of organics in the sample and consequently 62.0 % of ruthenium metal content. When calculating to molar equivalents, it can be observed that around 0.6 equiv. of pentanoic acid are surrounding the RuNPs, which is impossible according to the added ligand (0.3 equiv.).

It is thus clear that another source of carbon (pollution) should be the responsible of increasing the carbon content onto the RuNPs surface. This phenomenon was attribute to the coordination of THF, which was observed by FTIR analysis (*see* section 3.1.5). Thus, THF have a high influence on the elemental analysis determination.

3.1.7.3 Theoretical Titration of $Ru_x(C_4H_9COOH)_{0.3}$ NPs

In chapter II, a combination of theoretical and experimental characterizations proved that hydrides and deprotonated ethanoic acids interact with the $Ru_x(CH_3COOH)_{0.4}$ NPs surface. These capping ligands were experimentally quantified by DOSY NMR (0.3 CH_3COO/Ru_{surf}) and norbornene reduction (0.3 H/Ru_{surf}). Also, a theoretical counterpart was performed by DFT titration, where two stable structures with (0.4 CH_3COO/Ru_{surf}) and ([0.4 - 0.6] H/Ru_{surf}) were found to be stable at r.t., see domains 39 and 40 in figure 2.35 (their respective stability being related to the concentration of acid and pressure of H_2).

On the basis of the ethanoic acid case described in the previous chapter, it can be inferred that (i) theoretical and experimental findings have a high degree of agreement regarding the surface properties of ruthenium NPs; (ii) the theoretical Ru_{55} NP model (*see* section 6.2.1), although slightly smaller than the actual experimental NPs, allows a relevant extrapolation to the

actual case; (iii) DFT-PBE together with the *ab initio* thermodynamics methodology (*see* section 6.2.6) can describe the structural, spectroscopic and electronic properties of RuNPs stabilized by carboxylic acids with high accuracy.

Thus, the same Ru_{55} NP model was used as computational strategy for the DFT titration of the novel $Ru_x(C_4H_9COOH)_{0.3}$ NPs, with the aim to evaluate the quantity of hydrides and pentanoates surrounding the RuNPs. The results can clarify some previous posed inquiries like the low amount of hydrides present in these systems *vs* another RuNPs[93] or the quantity of carboxylate capping ligand that could stabilize RuNPs depending its alkyl length chain.

Hence, the Ru_{55} NP model was covered by different co-adsorbed quantities of hydrogen and pentanoates, assuming an easy O-H activation, as evidenced by FTIR and solid-state NMR experimental analysis. With now large surface ligands, and since the computational cost of DFT calculations is roughly proportional to N^3 (N being the number of atoms) it is necessary to be as efficient as possible.

Therefore, this DFT titration process was performed by using the previous data obtained for the $Ru_x(CH_3COOH)_{0.4}$ NPs system where it was seen a low hydride coverage value and a high amount of ethanoates (figure 3.18). This was possible since FTIR and solid-state NMR spectroscopy results pointed out toward a stabilization of the RuNPs by pentanoates.

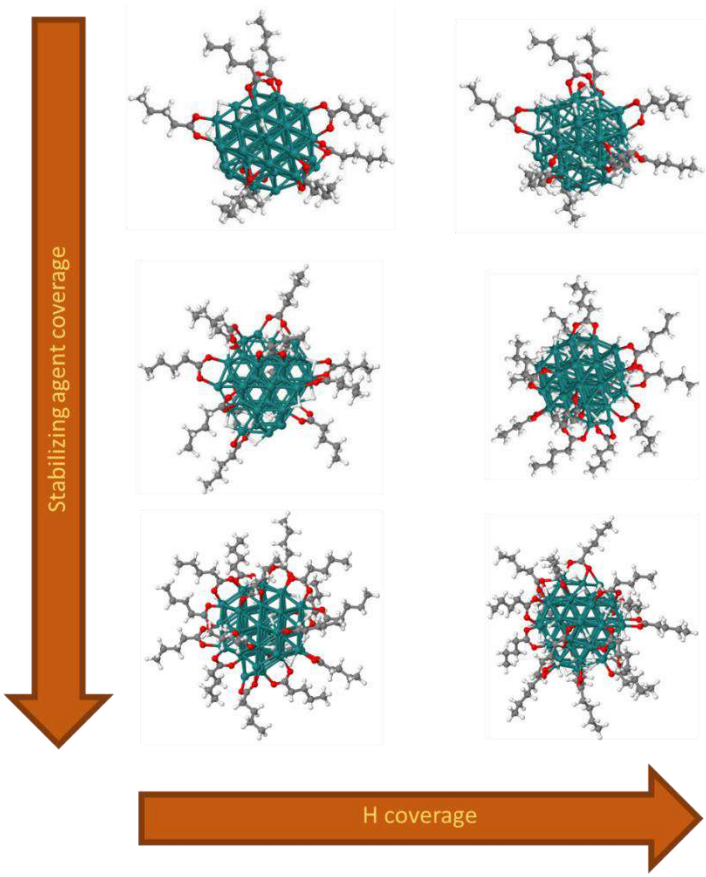

Figure 3.18 Some of the selected Ru_{55} NP optimized structures with different ligand surface coverage (C_4H_9COO & H).

Thus, ten different coverage possibilities have been considered, with a systematic geometry optimization (table 3.7). The surface compositions were set up with a high quantity of pentanoates (between [8 – 16]) and a rather low quantity of hydrides (between [8 - 33]). Details on the DFT energies of the optimized structures are reported in sections appendixes A.1 & B.1. It is important to highlight that during the DFT optimization, no H/ethanoate recombination was found.

Table 3.7 Optimized structures used for the $Ru_x(C_4H_9COOH)_{0.3}$ DFT surface titration. The total number and coverage ratio of coordinated ligands are also given with its corresponding DFT energy (eV). (a) Number of hydrides that come from the dissociative adsorption of H_2; (b) total number of hydrides *i.e.* that comes from a and from the C_4H_9COO-H bond dissociation.

#	E (eV)	nH (a)	nH/Ru_surf (a)	nH* (b)	nH*/Ru_surf (b)	nC4H9COOH	Name
57	-1,210.88	0	*0.0*	8	*0.2*	8	$(C_4H_9COO)_8H_8$
58	-1,276.40	17	*0.4*	25	*0.6*	8	$(C_4H_9COO)_8H_{25}$
59	-1,406.93	0	*0.0*	10	*0.2*	10	$(C_4H_9COO)_{10}H_{10}$
60	-1,471.88	17	*0.4*	27	*0.6*	10	$(C_4H_9COO)_{10}H_{27}$
61	-1,603.41	0	*0.0*	12	*0.3*	12	$(C_4H_9COO)_{12}H_{12}$
62	-1,667.23	17	*0.4*	29	*0.7*	12	$(C_4H_9COO)_{12}H_{29}$
63	-1,799.42	0	*0.0*	14	*0.3*	14	$(C_4H_9COO)_{14}H_{14}$
64	-1,862.33	17	*0.4*	31	*0.7*	14	$(C_4H_9COO)_{14}H_{31}$
65	-1,993.91	0	*0.0*	16	*0.4*	16	$(C_4H_9COO)_{16}H_{16}$
66	-2,056.27	17	*0.4*	33	*0.8*	16	$(C_4H_9COO)_{16}H_{33}$

By using the *ab initio* thermodynamic methodology, the Gibbs free energies ($\Delta_a G°$) were calculated for the ten structures at 300 K, considering the ligand-metal vibration corrections (*see* section 6.2.7 and appendix D) used for the ethanoic acid DFT titrations. This approximation can be done due to the stronger influence on the $\Delta_a G°$ value for the Ru-H vibration modes than that of Ru-carboxylate.

The calculations of $\Delta_a G°$ as a function of p_{H_2} and [C_4H_9COOH] in equilibrium were performed taking in to account the chemical potentials of pentanoic acid in THF (*see* section 6.2.6, calculation done with Gaussian 09). The most stable structures at certain pressure and concentration domains were plotted in a phase diagram (figure 3.19).

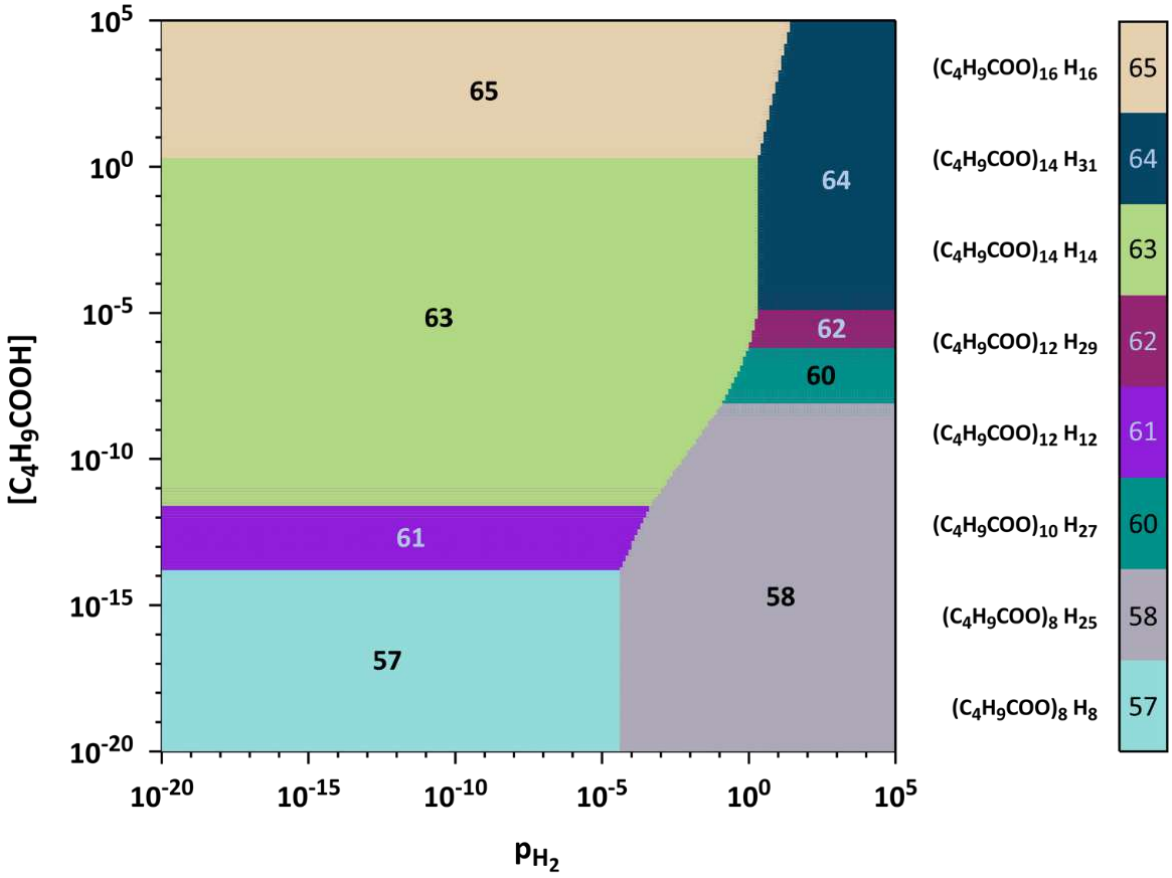

Figure 3.19 $\Delta_o G°$ (p_{H_2}, [C_4H_9COOH]) phase diagram for H_2 (gas) and C_4H_9COOH (liquid) adsorption on Ru_{55} NP at 300 K (pressure in bar, concentration in mol.L^{-1}).

Only two of the ten studied structures (66 & 59) are not stable in any range of the presented phase diagram. The analysis shows that the previous approximations performed to reduce the computational resources used for this study were appropriated (low quantity of hydrides and high amount of carboxylates). Because, the stables structures found in the phase diagram reliable domains ([10^{-10} to 10^{1}] M & bar) presented more pentanoates than the lowest computed system ($\geq$ 8 C_4H_9COO) and the quantity of hydrides was tending to zero ($\leq$ 16 H).

The pentanoic acid concentration domain relevant with respect to experiments can be estimated by calculating the pentanoic acid concentration added for the $Ru_x(C_4H_9COOH)_{0.3}$ NPs synthesis. Since this study is considering the species in equilibrium, it was assumed that all the pentanoic acid remains in the NPs, the obtained concentration was *ca.* $10^{-2.9}$ mol.L^{-1}. The hydrogen reliable range was considered to be similar as calculated from $Ru_x(CH_3COOH)_{0.4}$ NPs, *i.e. ca.* [10^{-4} – 10^{-3}] bar (*see* sections 2.5.1 & 2.5.2). Hence, the only stable domains that can be considered are

number 63 and 64 (figure 3.20) when p_{H_2} and [C_4H_9COOH] are in the range [10^{-5} - 10^{-2} bar] and [10^{-4} - 10^{-2} mol.L^{-1}], respectively. The coordinates of these structures are reported in section appendix F.

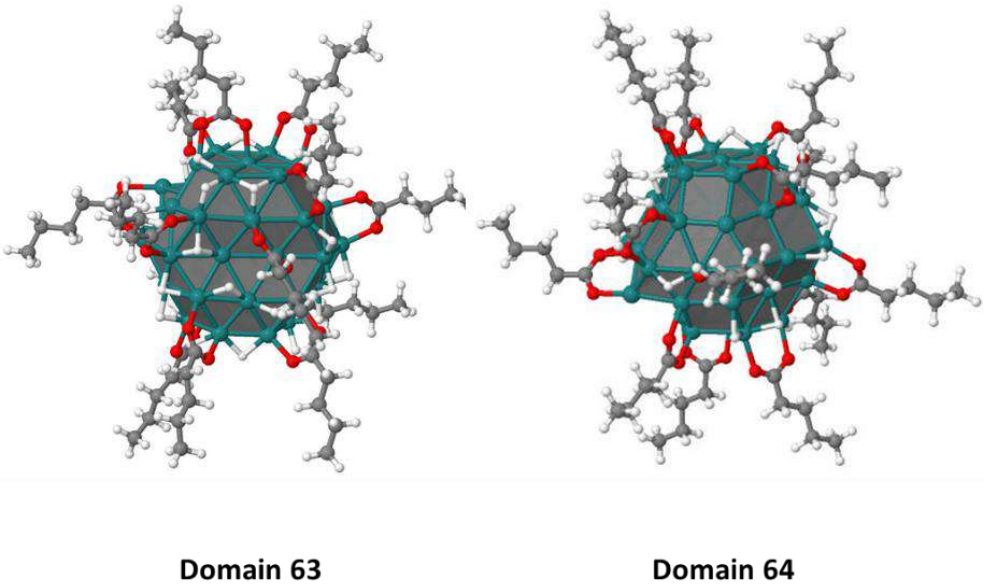

Figure 3.20 More stable [Ru_{55}] structures found at 300 K for $Ru_x(C_4H_9COOH)_{0.3}$ NPs. Domain 63: $Ru_{55}(C_4H_9COO)_{14}(H)_{14}$; domain 64: $Ru_{55}(C_4H_9COO)_{14}(H)_{31}$.

The most stable structure in the described range, presents as capped ligands 14 pentanoates and 14 hydrides raised from the carboxylic acid deprotonation (figure 3.19, domain 63). The other stable structure has additional 17 H coming from the reaction media, but this structure was found in a small domain of the delimited phase diagram (experimental conditions).

The stabilizing agent *vs* metal surface atom ratio was found to be 0.3 C_4H_9COO/Ru_{surf}. This data can be extrapolated to the experimental *hcp* 1.47 nm RuNPs (mean size obtained by TEM), which has an estimated of 79 ruthenium surface atoms that represents the 65.0 % of the total metal atoms of the NP. As a result, the RuNPs can accommodate around 25 pentanoates directly interacting with the $Ru_x(C_4H_9COOH)_{0.3}$ NPs surface. The same ligand *vs* ruthenium surface atoms ratio was found for hydrides (0.3 H/Ru_{surf}).

These results can be compared (table 3.8) with those obtained for $Ru_x(CH_3COOH)_{0.4}$ NPs that displays similar mean size of the metal core. The amount of ethanoates required to stabilize the RuNPs was 0.4 CH_3COO/Ru_{surf} and the quantity of hydrides was [0.4 - 0.6] H/Ru_{surf}. These data

confirm the low quantity of hydrides present at the surface of carboxylic acid capped-particles compared to other ligand-capped RuNPs.[93]

Table 3.8 DFT titration comparison between $Ru_x(CH_3COOH)_{0.4}$ and $Ru_x(C_4H_9COOH)_{0.3}$ NPs.

NP system	Carboxylate ($RCOO/Ru_{surf}$)	Hydrides (H/Ru_{surf})
$Ru_x(CH_3COOH)_{0.4}$	0.4	[0.4 – 0.6]
$Ru_x(C_4H_9COOH)_{0.3}$	0.3	0.3

These theoretical results are in line with experiments, since $Ru_x(C_4H_9COOH)_{0.3}$ NPs were stabilized with 0.1 equiv. less ligand than the $Ru_x(CH_3COOH)_{0.4}$ NPs. Both investigations agree to state that the quantity of carboxylic acids needed to stabilize the same mean size of nanoparticles will depend on its alkyl chain length. For further comparison between these systems, it is thus necessary to take into account that there seems to be a correlation between the alkyl chain length and the quantity of ligands capping the NPs

Finally, this theoretical titration confirms that a low quantity of hydrides is surrounding the nanoparticle, *i.e*. 0.3 to 0.6, to be compared to the usually found 1.3 H/Ru_{surf}. [93] Meaning that RuNPs synthetized by using carboxylic acids as stabilizing agent will have as structural property a low amount of hydrides.

3.1.8 Theoretical Catalytic Assessing: HER Reaction

Electronic stability of the nanosystems depends on the coverage rate by the stabilizing agent and of its adsorption energy. It has been reported that the lower the capping ligand/metal can be correlated ratio, the lesser the NP stability. But this relation also depends on the steric hindrance of the stabilizer which interacts with the MNPs surface due to the ligand barrier that is formed.([205],[243])

It is well-known that metal nanoparticles and specially RuNPs have a good affinity for hydrogen, their catalytic performance in several reduction reactions is also recognized, with easy adsorption and desorption of hydrogen onto the RuNPs surface.([59],[245])

As it was reported in section 2.7, it is possible to evaluate the potential catalytic activity of RuNPs in the hydrogen evolution reaction (HER) by following the seminal work of Nørskov.[10] It is based on the correlation of the H adsorption energy (ΔG_H) that can be correlated with the exchange current in the HER reaction, (after the empirical addition of 5.5 kcal.mol^{-1} to ΔE_H; *see* section 6.2.11). A good catalyst must possess sites for which ΔG_H is close to zero.

Owing to the good agreement previously obtained between experimental and computational chemistry characterization (*see* chapter II), the catalytic performance of $Ru_x(C_4H_9COOH)_{0.3}$ NPs can be assessed for HER reaction by looking at the hydrogen adsorption energy (ΔE_H) on the most stable Ru_{55} NP structure found by DFT titration, namely $Ru_{55}(C_4H_9COO)_{14}(H)_{14}$.

To fulfill this procedure, the hydrogen adsorption energy (ΔE_H) was obtained in five different selected sites on the $Ru_{55}(C_4H_9COO)_{14}(H)_{14}$ NP, *i.e.* planes (001) and (101) and the enclosing B_4 & B_5 zone of the Ru_{55} NP model (*see* section 6.2.1), which involve different type of interactions. The corresponding ΔG_H values (see section appendix E.2) are reported in the figure 3.21.

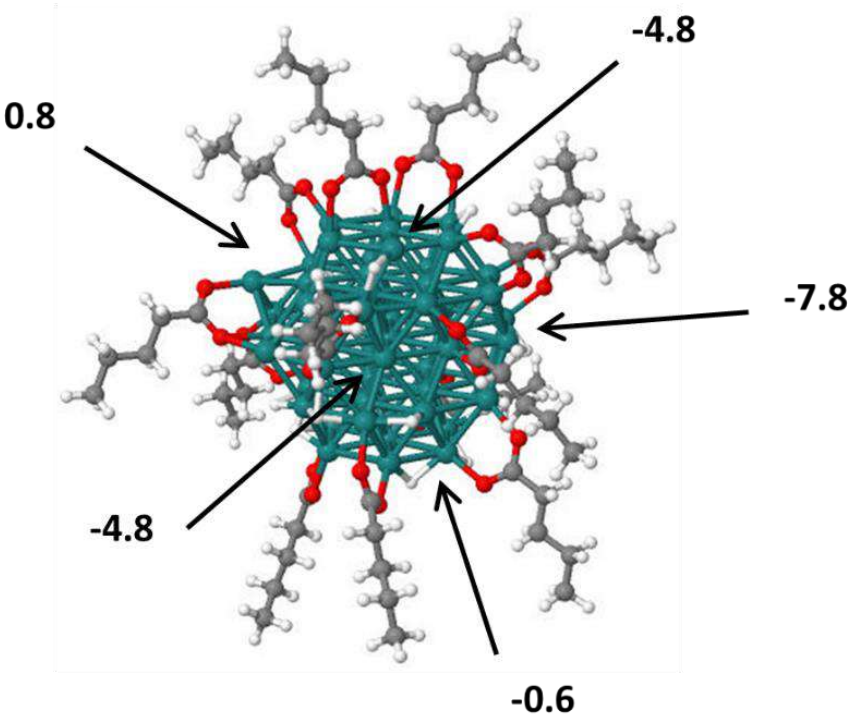

Figure 3.21 ΔG_{H^*} (kcal.mol^{-1}) in different adsorption sites (indicated by arrows) of $Ru_{55}(C_4H_9COO)_{14}(H)_{14}$ NP.

The $Ru_{55}(C_4H_9COO)_{14}(H)_{14}$ NP possess a wide hydrogen adsorption energy which ranges between *ca.* [-13.3 to -4.7 kcal.mol^{-1}], i.e. ΔG_H ranges from [0.8 to -7.8 kcal.mol^{-1}]. This large-scale values make it difficult to analyze, however it is worth noticing that some sites are quite suitable for the hydrogen production due to their low hydrogen adsorption energy, *i.e.* the (001) planes and the surrounding area of B_4 & B_5 sites.

In other words, the hydrogen adsorption energy on this stable NP covered by pentanoates and hydrides is highly influenced on the analyzed site (*see* the difference in ΔG_H for adsorption sites on the same planes *e.g.* (001) & (101)), but lesser than that of the previously studied $Ru_{55}(CH_3COO)_{16}(H)_{16}$ NP (*see* section 2.7).

As can be seen in table 3.9, it is not easy to conclude about the relative performance of ethanoic acid- and pentanoic acid-stablized RuNPs regarding HER. On some sites, the theoretical analyzed Ru_{55} NP covered by pentanoates shows lower affinity to hydrogen than the Ru_{55} NP capped by ethanoates (table 3.9). This study should be completed by considering another arrangement of surface ligands and a slightly different coverage value, but it seems however that

the carboxylic alkyl chain length may have an influence on the HER catalytic reaction. As a result, it is probable that RuNPs covered by pentanoates may be more active for the hydrogen production than its ethanoates-stabilized counterpart

Table 3.9 H_2 dissociative adsorption Gibbs free energy (ΔG_H) comparison in different Ru_{55} NP sites between $Ru_{55}(CH_3COO)_{16}(H)_{16}$ and $Ru_{55}(C_4H_9COO)_{14}(H)_{14}$ models.

Site	$Ru_{55}(CH_3COO)_{16}(H)_{16}$	$Ru_{55}(C_4H_9COO)_{14}(H)_{14}$
(001)	-2.5	-4.8 & -0.6
(101)	-2.3, -1.9 & 2.4	-7.8 & -4.8
B_4 &B_5	-7.9	0.8

3.1.9 Conclusion

In the first part of this chapter, it was explored the possibility to stabilize RuNPs with a carboxylic acid of longer alkyl chain length, by changing from ethanoic to pentanoic acid. In order to make a reliable comparison study the same amount of ligand was first considered for RuNP synthesis, $Ru_x(C_4H_9COOH)_{0.4}$. The obtained nanosystem has shown a better solubility in non-polar solvent than that stabilized by ethanoic acid and also a smaller mean size of *ca.* 1.1 nm vs. 1.5 nm, respectively. These results were a first evidence of the influence of the nature of the carboxylic acid on the properties of the RuNPs.

NMR studies performed on $Ru_x(C_4H_9COOH)_{0.4}$ NPs have shown that the ligand added to the reaction media is fully interacting with the nanoparticle surface due to the absence of visible free ligand. Also, it was noticed that the alkyl chain of the pentanoic species is not folded at the metal surface (protons of methyl groups were clearly observed). It can thus be proposed, that the ligand is attached in an extended way given certain mobility to the tail of the stabilizing agent. DOSY analysis has shown the presence of broad signals in the range of the expected peaks of the ligand and the hydrodynamic diameter calculated from diffusion coefficient measured agrees with the mean size of the NPs determined by TEM analysis.

The FTIR analysis allowed to confirm the pentanoic acid deprotonation in the resulting RuNPs. The signal of a carboxylate moiety was seen but not that expected for a carboxylic acid

moiety (free or coordinated). Also, it was observed by this technique the presence of THF and its probable degradation into CO and PTHF.

Even when the adsorption energy of the pentanoic acid onto the Ru_{55} NP model (-46.2 kcal.mol^{-1}) appeared to be smaller than that of ethanoate (-51.7 kcal.mol^{-1}), the FTIR spectroscopy has exhibited higher retrodonation of the ruthenium metal surface to the pentanoic moiety than for the compared Ru-ethanoate system, as observed by the shift towards lower wavenumber of the carboxylate band.

As a first general conclusion, it can be said that changing the alkyl chain length by three carbons from ethanoic to pentanoic acid provides better solubility in non-polar solvents, smaller NPs and improved homogeneity. Therefore, it can be considered that pentanoic acid is a more suitable stabilizing agent than ethanoic acid.

Then with the aim to reduce the mean size variable and make a more reliable comparison for these RuNPs, a sweep of pentanoic acid quantity introduced for the NP synthesis was performed (from [0.05 to 0.60 equiv.]/[Ru]). This allowed to evidence that NPs of mainly two different sizes can be synthetized (*ca.* 1.1 and 1.5 nm) by changing the amount of the added stabilizing agent (TEM analyses). Moreover, proton NMR studies showed that NPs of similar mean sizes can have different rates of ligand surface coverage.

From the results on the influence of the ligand amount on the size of the particles, the system $Ru_x(C_4H_9COOH)_{0.30}$ system was chosen because of its higher homogeneity and similar mean size than $Ru_x(CH_3COOH)_{0.4}$ NPs (*ca.* 1.5 nm) for a deeper comparison. The fact that a 0.3 equiv. of pentanoic acid allowed to stabilize NPs of same size as 0.4 equiv. of ethanoic acid pointed out the better stabilizing properties of the pentanoic *vs* ethanoic acid.

Solid-state NMR study performed on $Ru_x(C_4H_9COOH)_{0.3}$ NPs confirmed the deprotonation of the pentanoic acid and its interaction with the ruthenium surface as pentanoate. Taking this into account and previous information from chapter II a DFT titration of surface ligands has been performed. As a result, it was found that the most stable structure according to the experimental synthetic variables is $Ru_{55}(C_4H_9COO)_{14}(H)_{14}$, which showed a lower quantity of capping ligand than that determined for the $Ru_x(CH_3COOH)_{0.4}$ system, $Ru_{55}(CH_3COO)_{16}(H)_{16}$. This result also corroborated that the pentanoic acid has better stabilization characteristics than ethanoic acid.

Finally, the evaluation of $Ru_{55}(C_4H_9COO)_{14}(H)_{14}$ system for the HER reaction highlighted that the RuNPs stabilized by pentanoic acid can probably have a better performance in the hydrogen production than those capped by ethanoic acid.

To conclude this first part of chapter III, changing the alkyl chain length by three carbons from ethanoic to pentanoic acid provided RuNPs smaller in size at a lower [ligand]/[Ru] ratio, more homogeneous in size/shape, less crowded and probably more interesting for the catalytic HER reaction. Therefore, to sum up, it can be considered that pentanoic acid is a more suitable stabilizing agent than ethanoic acid.

In order to better understand the influence of the alkyl chain length on the RuNPs properties. The synthesis of RuNPs with octanoic acid will be presented.

3.2 Octanoic Acid-Capped RuNPs

Metal nanoparticles (MNPs) can be modulated by changing several factors *i.e.* synthesis methodology, temperature, ligand nature, quantity of stabilizing agent, reaction time, etc.[([246],[247])] Specially for ruthenium nanoparticles (RuNPs) synthetized by the organometallic approach, they can be tuned by modifying the nature of the stabilizing agent, the reaction media and the reductive gas pressure applied.[([97],[110])]

In the literature, the influence of the stabilizing agent nature in dictating the size, shape and interparticle spacing, is described.[248] In general, the capping ligands modify the internal electronic properties of the systems and moreover the interactions between the nanosystems and its surroundings, in other words the possible interfaces among the media and the MNPs.[249]

Previously, the differences obtained in the RuNPs synthetized by carboxylic acid with different alkyl chain length (solubility, size, dispersion, etc.) were demonstrated (*see* section 3.1). In fact, it was observed that these characteristics can be modulated by modifying the quantity and type of stabilizing agent.

Compared to previous results obtained with ethanoic acid, it appeared that the alkyl chain of this acid has an influence on the stabilization efficiency and also on the characteristics of the particles. Indeed, pentanoic acid-stabilized nanoparticles were more soluble in pentane, more homogeneous in size/shape and with a smaller size at a lower [ligand]/[Ru] ratio, and also potentially of higher interest for HER reaction than those prepared with ethanoic acid.

Since the high impact on increasing the alkyl chain length of the carboxylic acid ligands for obtain RuNPs was demonstrated, now the synthesis of similar RuNPs but stabilized by a longer carboxylic acid is going to be studied. Octanoic acid will be the analyzed molecule which is a saturated moiety that has three carbons more than the previous studied ligand. The obtained results are described in the second part of this chapter.

3.2.1 Assisted-Synthesis of RuNPs Stabilized by Octanoic Acid

Metal nanoparticles (MNPs) can be synthetized by using several ligands and procedures, but there are cases when the nanosystems cannot be formed unless there is a synthesis assistant. For the formation of the MNPs, the use of solution-assisted methodologies *i.e.* sol-gel, hydrothermal, etc., are well-known.[250] In fact, the use of alcohols and polyalcohols has been widely applied for synthetize metal and, even more, ruthenium nanoparticles (RuNPs).[251]

THF is a recurrently used solvent for the synthesis of ruthenium-based nanoparticles. Apart from being an appropriate solvent to solubilize the Ru(COD)(COT) complex used as ruthenium source and the organic ligands used as stabilizers, some works have also shown that THF can assist the stabilization of the NPs formed. In fact, being an ether, THF can coordinate at the surface of RuNPs through the oxygen atom. NMR studies have evidenced that THF can release from the surface of ligands-stabilized Ru NPs.[94] However, THF alone is not able to stabilize homogeneous small RuNPs leading to a mixture of nanosystems and agglomerates (*see* section 2.5.3). That is why THF can be considered as a stabilizing assistant for metal NPs.

Thus, preliminary studies for the synthesis of RuNPs in the presence of octanoic acid were performed by following the organometallic approach (*see* section 6.1.2.2), but with the difference of using THF as solvent in order to improve the morphology homogeneity of the formed RuNPs

(scheme 3.4). Another parameter to take into account was the reaction time, that in these cases was left around 15 h to assure the complete ruthenium metal precursor decomposition.

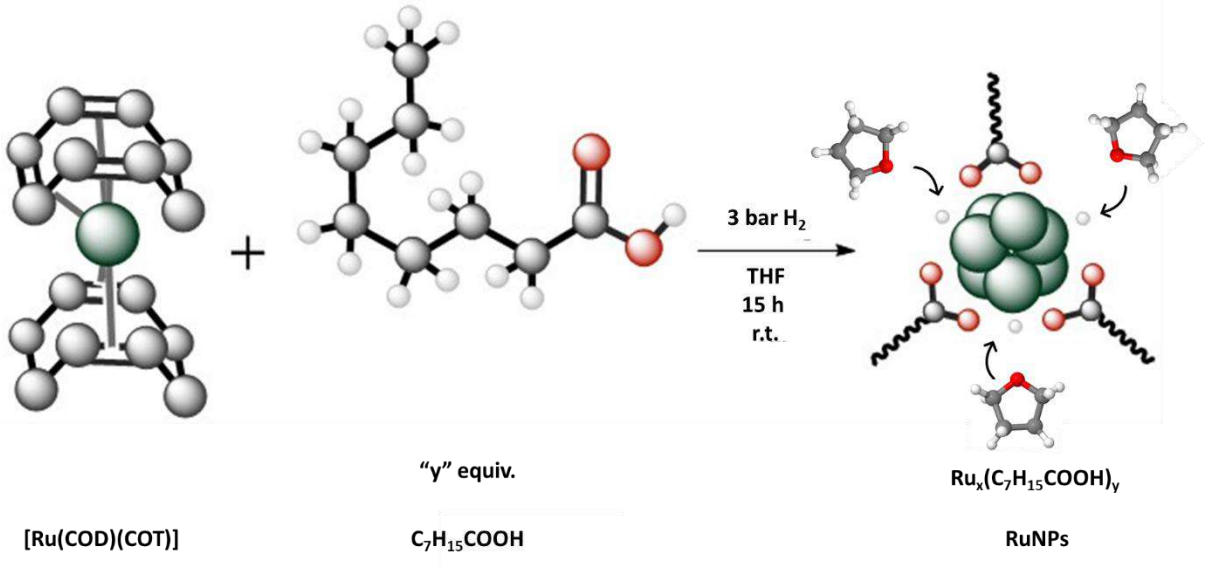

Scheme 3.4 Synthesis of RuNPs stabilized by octanoic acid in THF. The formed nanoparticle is expected to be covered by octanoates, hydrides and THF as were foreseen in chapter II & section 3.1.

Previous obtained information about the synthesis of RuNPs stabilized with carboxylic acids, was considered as the starting point for the synthesis of these nanosystems. Therein, it was observed the formation of semi-homogeneous and homogeneous RuNPs by adding 0.4 equiv. of ethanoic and pentanoic acid, respectively. Therefore, a similar formula ($(Ru_x(C_7H_{15}COOH)_{0.4})_{THF}$) was applied as point of departure for analyzing these systems, aiming to determine the influence of the assisted-solvent.

Aiming to form $Ru_x(C_7H_{15}COOH)_{0.4})_{THF}$ NPs, a ruthenium organometallic precursor ([Ru(COD)(COT]) dissolved in THF (2 mL of THF/3 mg of [Ru]).and in the presence of 0.4 equiv. of octanoic acid (stabilizing agent), was decomposed under reductive atmosphere (3 bar H_2) at r.t. inside a Fisher-Porter reactor under vigorous stirring, as it was described in section 6.1.2.2. When exposed to hydrogen, the yellow solution turned brownish after *ca.* 60 s and then changed to black within another *ca.* 30 s. The reactor was left under dynamic hydrogen pressure for 30 minutes and then under static pressure for 15 h. The reaction was stopped by evacuation of the remaining hydrogen atmosphere under high-vacuum and its replacement by argon. The obtained

colloidal solution of $(Ru_x(C_7H_{15}COOH)_{0.4})_{THF}$ NPs appeared highly stable without any precipitate formed after one week.

The colloidal solution was then concentrated to the half volume for slightly increase the concentration of RuNPs, aiming to obtain a concentrated drop of the crude colloidal synthetized RuNPs to be studied by TEM microscopy (*see* section 6.1.3.1).

The obtained micrographs display the formation of small RuNPs which can be easily identified (figure 3.22 a & b). They show a good dispersion on the grid with a homogeneous spherical morphology, since the RuNPs were highly soluble in THF, no problem in the solvent evaporation process was seen. The mean size of the $(Ru_x(C_7H_{15}COOH)_{0.4})_{THF}$ NPs was observed to be *ca.* 1.34 ± 0.51 nm (figure 3.22 c).

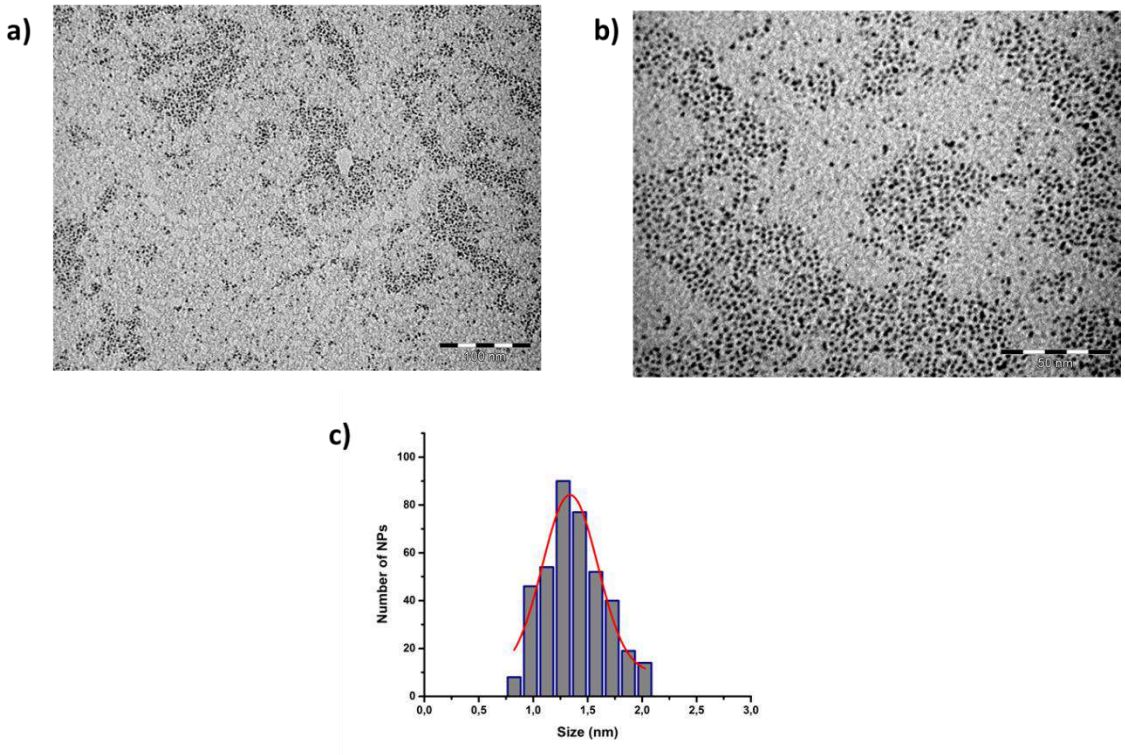

Figure 3.22 TEM micrographies of $(Ru_x(C_7H_{15}COOH)_{0.4})_{THF}$ NPs; (a) general view, scale bar: 100 nm; (b) zoom on the nanosystems, scale bar: 50 nm; (c) corresponding size histogram of individual RuNPs.

As reported in table 3.10, the $(Ru_x(C_7H_{15}COOH)_{0.4})_{THF}$ NPs have a mean size intermediate to that of Ru NPs prepared with ethanoic acid and pentanoic acid at the same [ligand]/[ruthenium] ratio. Thus, despite the increase of the alkyl chain length when passing from pentanoic to

octanoic acid, the NP size did not decrease compared to that of $Ru_x(C_4H_9COOH)_{0.4}$. This effect can be attributed to the use of THF instead of pentane, *vide infra*. However, it appeared that the $(Ru_x(C_7H_{15}COOH)_{0.4})_{THF}$ NPs display a more homogeneous shape than the $Ru_x(C_4H_9COOH)_{0.4}$ NPs. In other words, the THF solvent-assistance produced an increase in the RuNPs morphology but its effect in reducing the NPs mean size seems to be unfavorable.

Table 3.10 Comparison of the mean sizes of RuNPs (obtained by TEM) stabilized with the same amount of ethanoic, pentanoic and octanoic acid. Solvent (a) pentane; (b) THF.

Nanosystem	Mean size (nm)	Distribution (2σ; nm)
$\mathbf{Ru_x(CH_3COOH)_{0.4}}$ [a]	1.51	0.58
$\mathbf{Ru_x(C_4H_9COOH)_{0.4}}$ [a]	1.13	0.31
$\mathbf{Ru_x(C_7H_{15}COOH)_{0.4}}$ [b]	1.34	0.51

As it can be seen in the previous table, the mean size of the RuNPs tend to decrease as a function of the alkyl length chain, but it was observed a higher effect for the RuNPs stabilized with pentanoic acid. Also, the size distribution is higher for the RuNPs formed with octanoic acid, making the THF a poor solvent-assistance at least in this type of RuNPs synthesis.

After the TEM analysis, the crude colloidal solution was purified by several pentane-THF washing cycles. The NPs were thus obtained under the form of a fine black powder.

In order to know more about the THF role in the synthesis of RuNPs or try to explain the observed data in TEM microscopy, a FTIR analysis was performed after dispersion of the purified nanoparticles into dry KBr (using P_2O_5 as desiccant; *see* section 6.1.3.3) and preparation of a pellet. All the procedure was carried out under argon, in a glove-box. The FTIR data obtained for the $(Ru_x(C_7H_{15}COOH)_{0.4})_{THF}$ NPs in KBr are compared to the representative peaks of octanoic acid[252]and THF[190] in the figure 3.23.

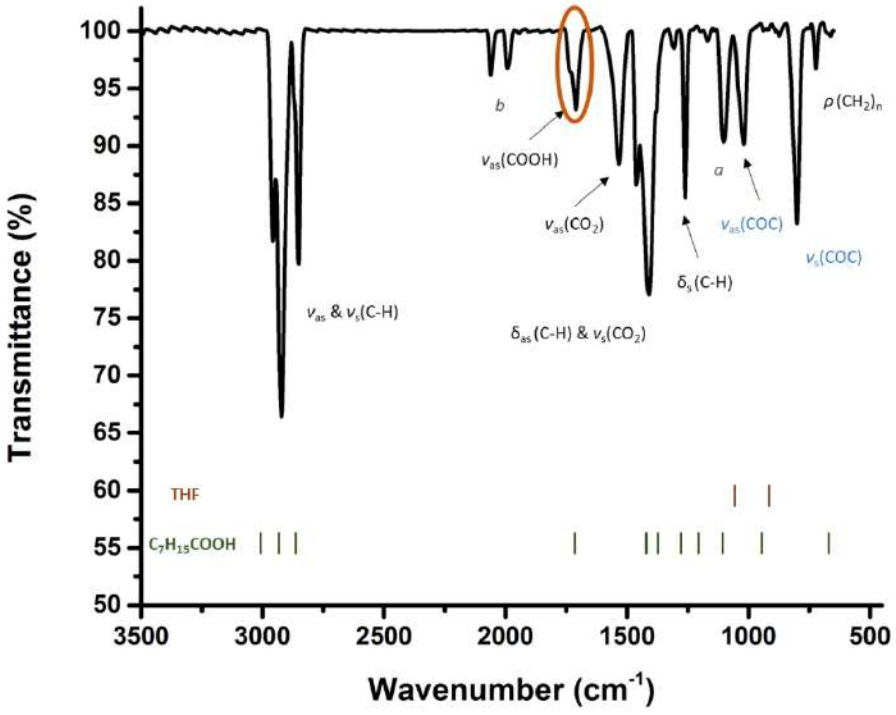

Figure 3.23 Experimental FTIR spectrum of $(Ru_x(C_7H_{15}COOH)_{0.4})_{THF}$ NPs and main peaks assignments. Experimental peaks position for free octanoic acid (green bars, $C_7H_{15}COOH$) and THF (yellow bars) are also indicated. *ν*: stretching; *δ*: bending; *ρ* rocking; s: symmetric; as: asymmetric. Peaks attributed to coordinated THF (blue) are likewise shown. The ν_{as}(COOH) vibrational mode region is highlighted with an orange circle.

The so-obtained infrared spectrum does not show any signals above 3000 cm^{-1}. This indicates the absence of water or any O-H stretching vibration mode, but the absence of free or coordinated octanoic acid cannot be completely discarded. Three well- separated signals can be observed at *ca.* 2980 - 2850 cm^{-1} that were attributed to the C-H ν_{as} and ν_{ss} vibration modes of the alkyl chain ($CH_3(CH_2)_6COOH$).). Between 1850 and 1600 cm^{-1} which is the expected area to observe the specific signals of carboxylic acids, a clear signal is visible at *ca.* 1710 cm^{-1} together with a left shifted shoulder at *ca.* 1730 cm^{-1}. This could be due to the presence of different carboxylic acids and this contrasts with FTIR observations done on previous systems of RuNPs stabilized with carboxylic acids bearing shorter alkyl where only one band for coordinated carboxylate was detected.

Thus, it can be suggested two different hypotheses related to these bands: They could correspond to two different coordination modes of octanoic acid onto the RuNPs surface or the most probable scenario could be that the first signal (shoulder) is attributed to free octanoic acid (reference region[252]) and the second to the coordinated carboxylic acid moiety. Anyway, both hypotheses involve as a conclusion the presence of stabilizing agent excess into the system.

Another sharp and even stronger signal is present at *ca*. 1533 cm^{-1} was assigned to the ν_{as} vibration mode of deprotonated octanoic acid in interaction with the surface of the RuNPs ($C_7H_{15}C{=}OO$). In other words, this band seems to be the signature of the octanoate form of the stabilizing ligand, as already observed for previous systems of carboxylic acid-stabilized RuNPs. Other bands between 1500 and 1250 cm^{-1} could be easily assigned to the asymmetric stretching mode ν_s of the carboxylic group ($C_4H_9C{=}OO(H)$) as well as to the C-H bending asymmetric δ_{as} and symmetric δ_s vibration modes of the alkyl chain ($CH_3(CH_2)_3COO$).

Also, a band commonly observed for organic compound containing more than four linked methylene groups ($\rho(CH_2)_n$) can be found at 720 cm^{-1}. Two narrow bands at *ca.* 1021 and 801 cm^{-1} were attributed to coordinated THF as already observed for previous systems of carboxylic acid-stabilized RuNPs systems purified by THF-washing. It is worth to notice that even when the solvent used for the nanosystems synthesis was THF there is no signals that can be assigned to free THF.([238],[239])

Also, peaks named *a* and *b* on the spectrum can be attributed to THF derivatives: the *a* band at *ca.* 1100 cm^{-1} can be assigned to PTHF[190]originated from its own polymerization and the *b* bands at 2060 and 1995 cm^{-1} to CO coming from the solvent decarbonilation.[133] These observations show the reactivity of THF at the RuNP surface as previously seen with other systems of NPs prepared by the organometallic approach.

To summarize the most important information of this FTIR analysis, it can be mentioned that it evidenced three different signals corresponding to asymmetric carboxylic vibration modes which indicate the presence of at least three different types of molecules interacting with the ruthenium surface. On the basis of previous results obtained in chapter II and section 3.1, it can be proposed that the ν_{as} (COOH) vibration band at *ca*. 1533 cm^{-1} corresponds to the octanoate form of the stabilizing ligand. The other two bands may result from a ligand excess that would interact with the metal surface as carboxylic acid or its free state.

Figure 3.24 allows to compare the FTIR data of $(Ru_x(C_7H_{15}COOH)_{0.4})_{THF}$ NPs directly prepared in THF (figure 3.24 c) with those of RuNPs synthetized with 0.4 equiv. of ethanoic (figure 3.24 a) and of pentanoic (figure 3.24 b) acids in pentane and then purified by THF washings. The comparative analysis will concern three main zones of the spectra highlighted in blue, orange and green.

In the blue zone, the presence of a CO band resulting from THF degradation can be observed in all cases. It can be seen well-defined bands for $(Ru_x(C_7H_{15}COOH)_{0.4})_{THF}$ NPs while the two other systems show ill-defined and large bands, nevertheless this characteristic band is more observable for the $Ru_x(C_4H_9COOH)_{0.4}$ NPs. This difference can derive from the use of THF as solvent when preparing $(Ru_x(C_7H_{15}COOH)_{0.4})_{THF}$ NPs. It can be assumed that the reactivity of THF at the surface of the particles is different depending on whether it is present during the NP synthesis or added on RuNPs already formed.

The second region shows at *ca.* 1530 cm^{-1} a carboxylate vibration band assigned to the deprotonated stabilizing agent (carboxylate form of the stabilizing ligand) for each case of carboxylic acid-stabilized RuNPs. However, the spectrum of the RuNPs synthesized with octanoic acid displays two other carboxylic vibration bands attributed to the protonated ligand in contrast to the two other cases. This may be explained by a ligand excess due to the longer alkyl chain length of the ligand or the presence of THF as solvent.

Finally, the last highlighted zone (green) that correspond to the R-O-R vibration area evidenced the presence of coordinated THF with differences observed in terms of intensities.

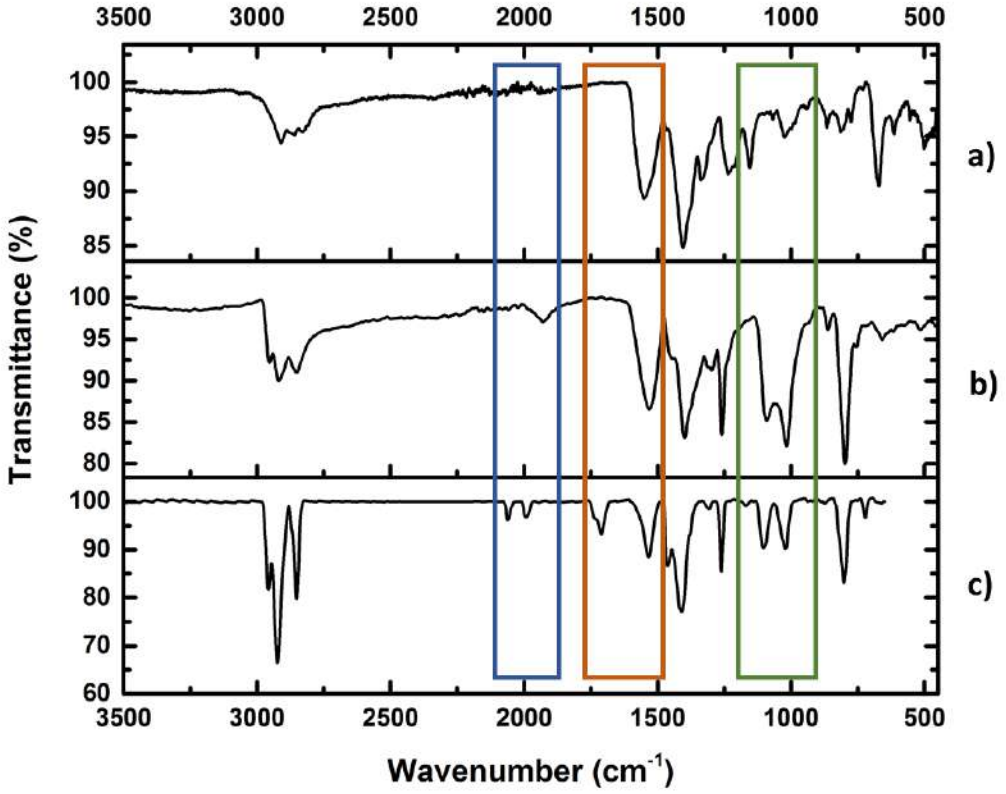

Figure 3.24 Comparison of experimental FTIR data: (a) $Ru_x(CH_3COOH)_{0.4}$; (b) $Ru_x(C_4H_9COOH)_{0.4}$; (c) $(Ru_x(C_7H_{15}COOH)_{0.4})_{THF}$ NPs. Highlighted regions: (blue) *v* (CO); (orange) *v* (COO(H)); (green) *v* (THF).

Previously, the retrodonation observed between the ruthenium atoms and the coordinated ligand was used as a stabilization parameter. For instance, previous studies have evidenced that the RuNPs stabilized by pentanoic acid have presented a lower vibrational energy in the deprotonated carboxylic vibration compared to RuNPs synthetized with ethanoic acid (1530 *vs* 1545 cm^{-1}), meaning a better stabilization. However, for the case of RuNPs prepared with octanoic acid, the carboxylate band is seen at a similar wavenumber than for the pentanoate case (1533 *vs* 1530 cm^{-1}). This result indicates that the interaction of the dimetallacycle formed at the RuNP surface by octanoates is quite similar to that of dimetallacycle from pentanoate (figure 3.25 a). In the area of the characteristic ether vibration bands, the presence of two twin shifted signals attributed to coordinated THF can be detected for the RuNPs synthetized by pentanoic and octanoic acid (figure 3.25 b).

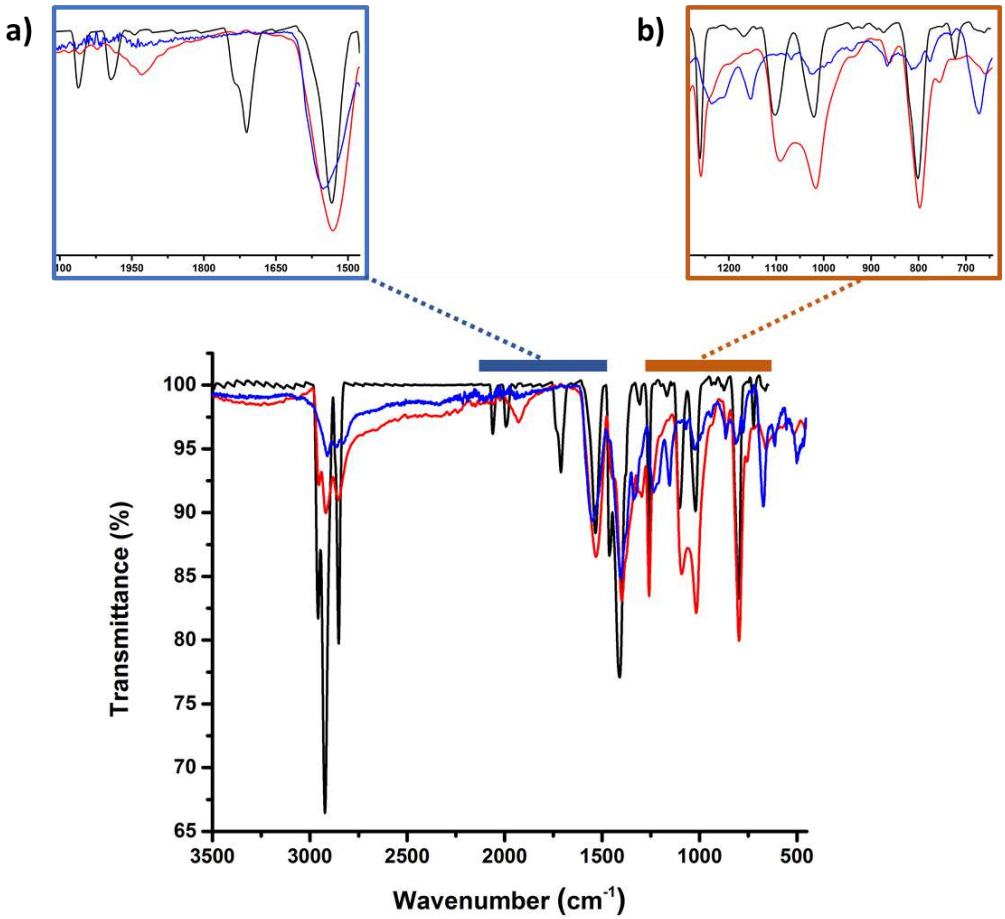

Figure 3.25 Comparison of experimental FTIR data: (blue) $Ru_x(CH_3COOH)_{0.4}$; (red) $Ru_x(C_4H_9COOH)_{0.4}$; (black) $(Ru_x(C_7H_{15}COOH)_{0.4})_{THF}$ NPs. Zoom in two different regions: (a) *v* (CO & COO(H)); (b) *v* (THF).

The characterization of $(Ru_x(C_7H_{15}COOH)_{0.4})_{THF}$ NPs cannot be completed without comparing the ^{1}H-NMR spectrum of the obtained nanoparticles *vs* free octanoic acid (figure 3.26). Differently from RuNPs systems stabilized with 0.4 equiv. of ethanoic and pentanoic acid, apart from the narrow signals of THF, the spectrum clearly presents sharped signals in the area [0.8 - 1.7 ppm] where signals of methyl and methylene groups are expected as well as another methylene signal at ca. [2.0 - 2.5 pmm] characteristic of a methylene group having vicinal electronegatives atoms (figure 3.26 red profile).

In comparison with the data of free octanoic acid ligand (figure 3.26 blue profile), the sharp signals clearly correspond to those of free octanoic acid [2.24, 1.60, 1.35 and 0.94 ppm].In addition, a broad signal is visible at low field (*ca.* 10.60 ppm) that can be assigned to the acidic

proton of the free octanoic acid. These results corroborate the previous information obtained by FTIR from which the hypothesis of the presence of free octanoic acid with the RuNPs was proposed. Besides the sharp signals attributed to free octanoic acid, the broad signals observed in close positions can be assigned to coordinated ligands (octanoate or/and octanoic acid).

It is worth to notice that in the area corresponded for the methyl group [0.8 - 1.0 ppm] there is a decrease of the bottom broadness and the peaks attributed for this signal are sharper than others. Thus, it can be said that the coordinated ligand is not bended onto the NPs surface and its tail posses higher dynamism.

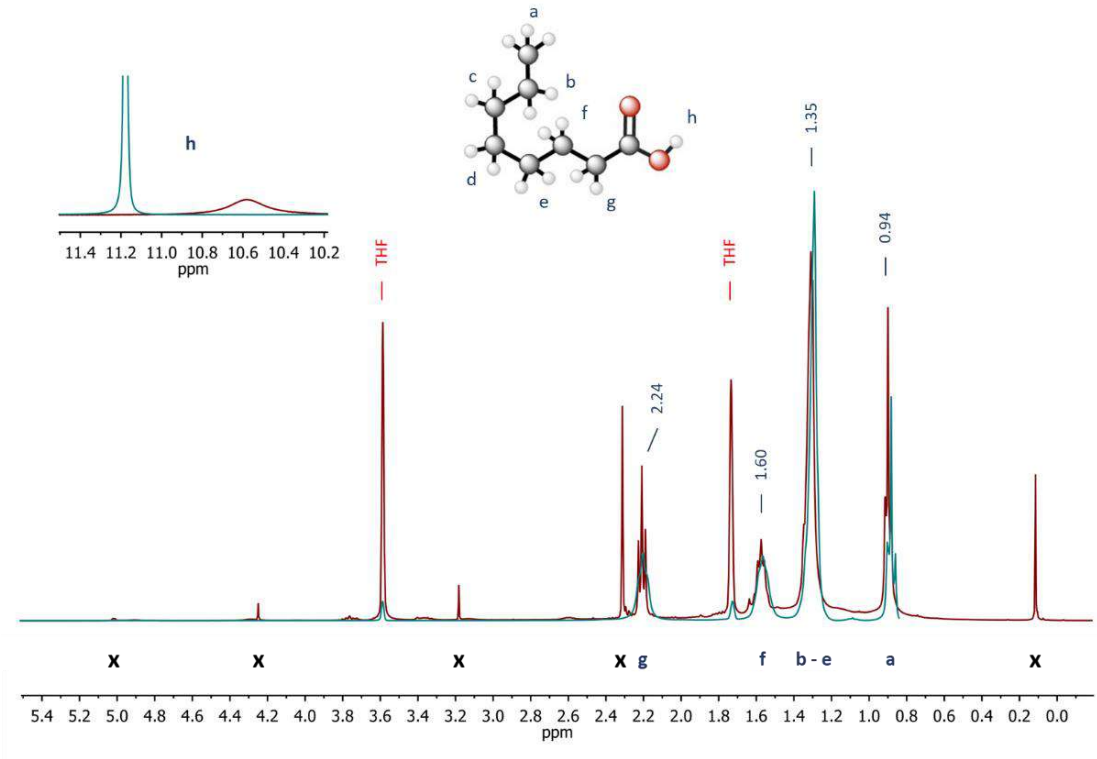

Figure 3.26 ^{1}H-NMR (THF-d^{8}) of $(Ru_x(C_7H_{15}COOH)_{0.4})_{THF}$ (red profile) vs free $C_7H_{15}COOH$ (blue profile). Side products are denoted as "x" and the proton assignation is displayed at the bottom.

The conbination of these spectroscopic techniques can offer information on the RuNPs surface state, where it can be clearly observed for the fist time in this work the presence of free and coordinated ligand. In other words, the presence of THF as a solvent and the longer alkyl chain legnth of the octanoic acid has as a consequence a better nanosystem stabilizitation and therefore

an excess of ligand can be observed by adding the same quantity of stabilizng agent into the RuNPs synthesis ([ligand]/[metal] ratio 0.4 equiv.).

3.2.2 Theoretical Determination of Adsorption Energies of Carboxylic Acids onto Ru_{55} Model

In previous section 3.2.1, it was described the synthesis of RuNPs in the presence of 0.4 equiv. of octanoic acid and THF as a stabilizer and a solvent, respectively. It was observed a decrease of the RuNPs mean size when a longer alkyl chain length ligand was used for the RuNPs synthesis, but a direct trend was not found.

FTIR and ^{1}H- NMR data revealed the presence of octanoate and/or octanoic acid coordinated at the ruthenium surface together with the presence of free octanoic acid. The later point indicated the presence of a ligand excess. FTIR data also indicated the presence of coordinated THF at the RuNPs surface, as well as its reactivity as seen by the detection of CO bands. Moreover, when comparing the FTIR characteristics of the RuNPs prepared with ethanoic acid and pentanoic acid, it was observed an increase of π-backdonation with pentanoic acid system *vs* ethanoic acid system. Such an increase was not detected between the octanoic and pentanoic acid stabilized nanosystems. This could result from similar behavior and adsorption energy (E_{ads}) of these ligands onto the surface of RuNPs.

Thus, the highlighted question is which is the real role of the THF in the synthesis of RuNPs? This section will be dedicated to theoretical studies aiming at understanding the behavior of THF at the NP surface. Adsorption energies will be calculated (*see* section 6.2.3) by attaching the three carboxylic acids studied (ethanoic, pentanoic and octanoic acid) onto the Ru_{55} NP model (*see* section 6.2.1). Different carboxylic coverage values will be studied in order to exclude the THF variable.

The carboxylic moieties were settled on the Ru_{55} NP under the form of carboxylates, owing to the information obtained from previous experimental and theoretical studies. For each RuNPs system of RuNPs, ten, twelve and fourteen carboxylate molecules were thus deposed on the Ru_{55}

NP in the presence of the same quantity of hydrides that result deprotonation of the carboxylic acids, as seen previously (figure 3.27). After structural optimization (*see* section 6.2.2), the mean adsorption energy of the carboxylate entities was obtained.

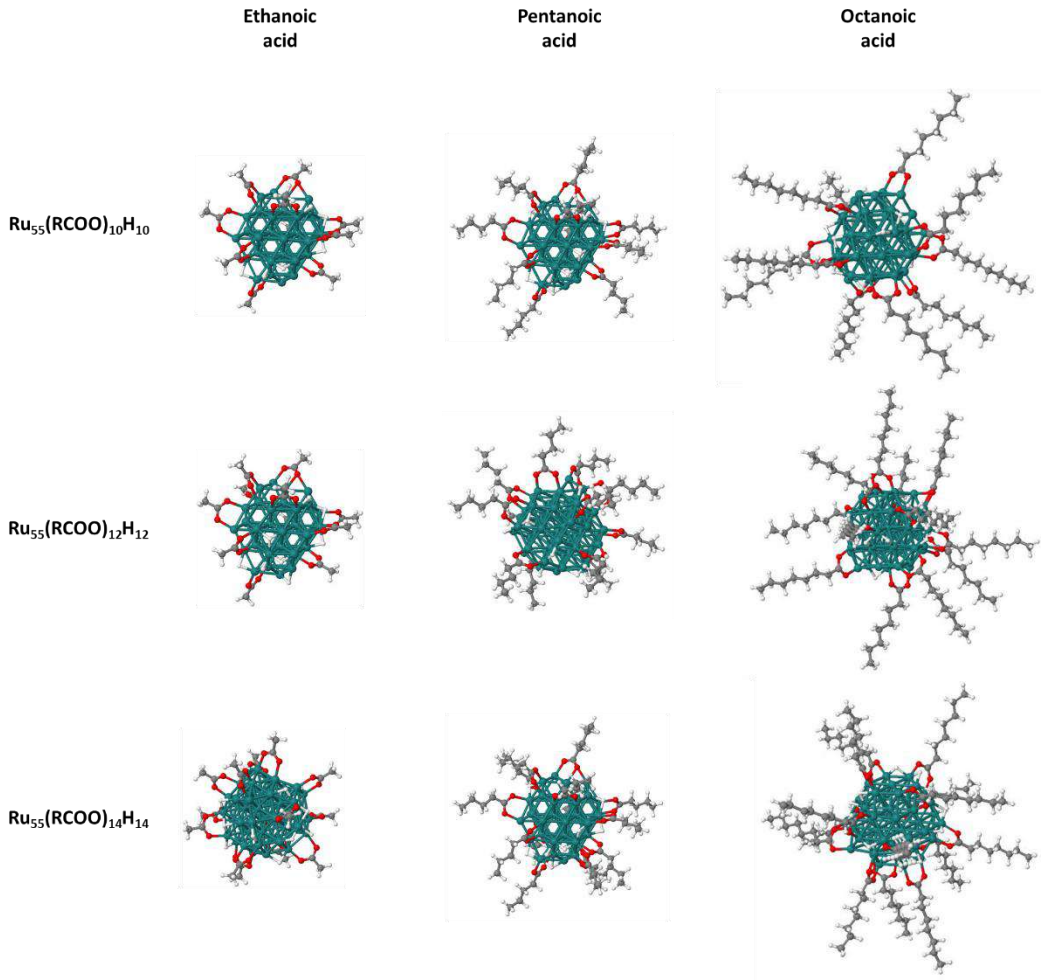

Figure 3.27 Ru_{55} NP optimized models with different coverage values of carboxylic acid entities.

The mean adsorption energy obtained with the ethanoic acid at the three coverage values was *ca.* -51.5 kcal.mol^{-1} (*see* section appendix A.4), meanwhile it decreased to *ca.* -45.8 kcal.mol^{-1} for the pentanoic acid models and to -44.7 kcal.mol^{-1} for the octanoic acid systems (*see* section appendix B). The values of adsorption energies for pentanoic and octanoic acids are clearly reduced in comparison with that of ethanoic acid. Comparing the adsorption energies between pentanoic and octanoic acid, a slightly decrease is observed for octanoic acid *vs* pentanoic acid. This may indicate a similar interaction strength for these two ligands.

Table 3.11, reports the E_{ads} calculated for each studied system. There is no significant difference (< 2 kcal.mol^{-1}) when the coverage value changed, at least between [10 – 14] carboxylate moieties. Also, it can be observed that the longer the alkyl chain length, the lower is the adsorption energy of the carboxylic moiety onto Ru_{55} NP. Interestingly, the adsorption energies of the pentanoic and octanoic acids are quite similar which can explain why no significant difference was observed by FTIR possibly as the result of a similar retrodonation phenomenon.

Table 3.11 Mean adsorption energies calculated for different carboxylic moieties deposed onto Ru_{55} NP models at different coverage values.

Nanosystem	Ethanoic acid (E_{ads}; kcal.mol^{-1})	Pentanoic acid (E_{ads}; kcal.mol^{-1})	Octanoic acid (E_{ads}; kcal.mol^{-1})
$Ru_{55}(RCOO)_{10}H_{10}$	-52.3	-46.3	-45.8
$Ru_{55}(RCOO)_{12}H_{12}$	-51.7	-46.2	-43.8
$Ru_{55}(RCOO)_{14}H_{14}$	-51.9	-45.4	-44.7

The coordination of THF molecules at the surface of RuNPs synthesized with pentanoic acid and octanoic acid as stabilizers, as observed by FTIR analysis, may be due to the lower adsorption energies of these carboxylate moieties compared to that of ethanoic acid. The decrease in adsorption energy can cause instability of the NP surface. This may be the reason for THF to coordinate at the NP surface which compensates the stability of the metal surface.

The difference in adsorption energy observed with the length of the alkyl chain bearded by the carboxylic acids allows to explain the coordination of THF at the NP surface. But this result does not allow to explain why the π-backdonation is lower in the case of ethanoic acid compared to the two other ligands and also why a higher quantity of ethanoic acid is required to get stable RuNPs. One hypothesis is that the steric hindrance of the carboxylic ligands related to the alkyl chain also affects the formation of the nanoparticles and their stability.

To corroborate this assumption DFT calculations with dispersion effects were performed in the most crowded, $Ru_{55}(RCOO)_{14}H_{14}$ NP. The methodology was used in order to describe correctly the van der Waals interaction resulting form the ligand-ligand interactions, which can change the adsorption energy of the substrates onto the Ru_{55} NP and explain the obtained data.

The new computed DFT energies with the dispersion effects term were obtained by the empirical methodology developed by Grimme *et al.*,[253] and corrected by the Becke-Jonson damping,[254] the so-called the DFT-D3 method. The adsorption energies of the carboxylic moieties obtained by adding the dispersion effects is compared with its corresponding DFT-PBE adsorption energy (table 3.12).

Table 3.12 Comparison of the Mean adsorption energy of carboxylic moieties in a Ru55(RCOO)14H144 NP obtained by DFT vs DFT-D3 methods.

Ru_{55} NP system	**DFT-D3 energy (eV)**	**E_{ads} – DFT-D3 (kcal.mol^{-1})**	**E_{ads} – DFT (kcal.mol^{-1})**
$Ru_{55}(CH_3COO)_{14}H_{14}$	-1128.71	-59.2	-51.9
$Ru_{55}(C_4H_9COO)_{14}H_{14}$	-1825.27	-53.9	-45.4
$Ru_{55}(C_7H_{15}COO)_{14}H_{14}$	-2522.70	-52.9	-44.7

The average adsorption energies (DFT-D3) are slightly stronger than in calculations done without this correction (DFT), but it is shifted by an almost identical value, *i.e.* [7.3 to 8.5 kcal.mol^{-1}]. Also, it does not change the relative adsorption energies, *i.e.* a lowering on going from ethanoic to octanoic moieties is still observed. Therefore, even considering the dispersion effects, it cannot be explained why the ligands with longer alkyl chain length have lower adsorption energies than the shorter ones, meanwhile they appear to be better stabilizing agents.

Also, owing to the similar adsorption energy obtained for the pentanoic and octanoic acids onto the Ru_{55} NP model, the presence of free ligand in the $(Ru_x(C_7H_{15}COOH)_{0.4})_{THF}$ NPs cannot be explained without taking into account the influence of THF even with the dispersion effects. Therefore, more studies need to be performed in order to understand the role of THF.

3.2.3 THF Strength as Solvent-Controlled RuNPs

In the section 3.2.1, it was described the synthesis of RuNPs stabilized by 0.4 equiv. of octanoic acid in THF. The analysis provides a general panorama of the THF role and importance in the synthesis of this type of RuNPs. It is well-known that the organic solvent used for the synthesis

of NPs plays a special role in the formation of nanosystems and even is utilized as control agent for the particle growth. Reports elucidate that the organic solvents can act as capping agents which bind onto the nanoparticles surface and limite its growth avoiding the metal agglomeration.[255]

The ratio of ligand/solvent is crucial for controlling the size of the NPs and the relevance of this parameter depends on the solvent nature.[205] Previously it has been reported that the use of this type of solvents led to smaller nanoparticles, *e.g.* THF has been described for being used as controlled-growth agent for the synthesis of several MNPs, including RuNPs.[256]

In the previous section it was described the synthesis of RuNPs in THF using 0.4 equiv. of octanoic acid as capping ligand. Characterization data evidenced the presence of free octanoic acid in the obtained powder of RuNPs even after their purification. Therefore, the objective is now to study the influence of a lower quantity of octanoic acid on the RuNPs formation while keeping the other parameters of the synthesis unfluctuating (3 bar H_2; r.t.; 15 h). Two [ligand]/[metal] ratios will be studied, namely 0.30 and 0.15 equiv.

After the chosen reaction time, the reaction was stopped by evacuation of the remaining hydrogen and the colloidal solution concentrated under high-vacuum before preparing grids for TEM analysis of the crude samples. This procedure is with the aim to see if the nanoparticles mean size can be reduced or if lower quantity of stabilizing agent can produce similar RuNPs.

The micrographs obtained for the RuNPs synthetized with 0.15 and 0.30 equiv. of octanoic acid in THF are presented in figures 3.28 a and 3.28 c, respectively. In both cases, RuNPs of similar morphology that are well-dispersed on the TEM grid can be observed. Both systems display a mean size around 1.5 nm.

The size histogram built for $(Ru_x(C_7H_{15}COOH)_{0.15})_{THF}$ NPs gives a mean size of *ca.* 1.51 ± 0.80 nm (figure 3.28 b) and that of the $(Ru_x(C_7H_{15}COOH)_{0.30})_{THF}$ NPs a mean size of *ca.* 1.49 ± 0.71 nm (figure 3.29 d). For both systems it can be observed small NPs that seems to be semi-homogeneous due to its large size dispersion that is slightly beyond of 50.0 % (standard deviation of 0.3 - 0.4 nm).

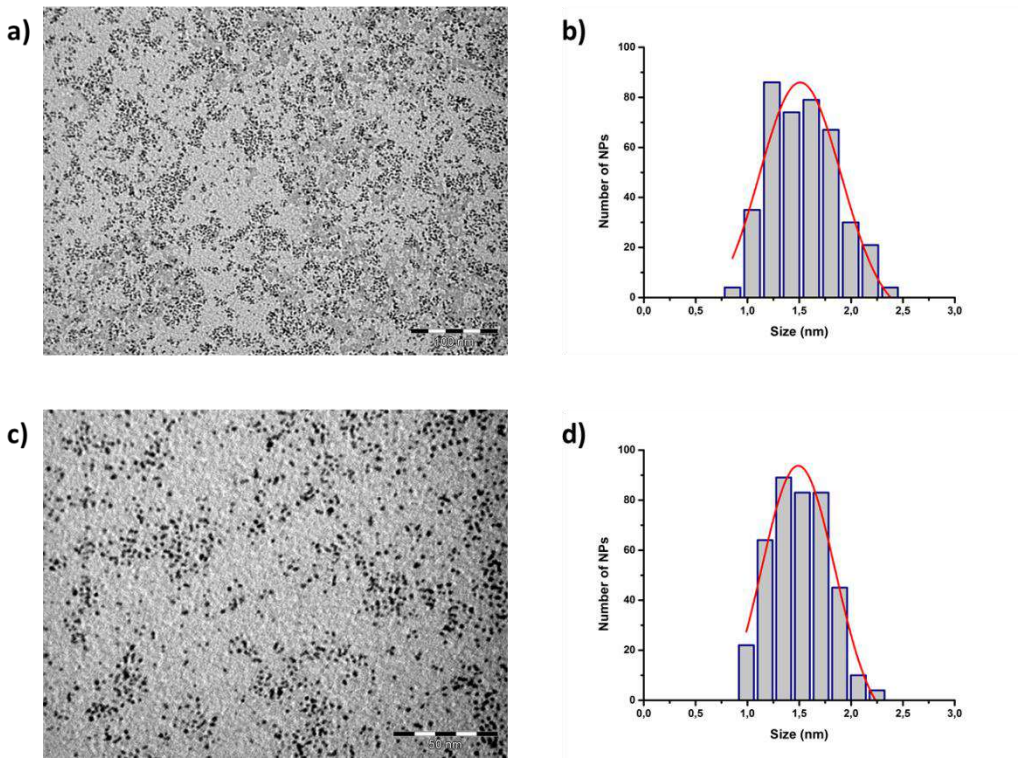

Figure 3.28 TEM micrograph of (a) $(Ru_x(C_7H_{15}COOH)_{0.15})_{THF}$ NPs; scale bar: 100 nm; (b) corresponding size histogram of individual -a- RuNPs. TEM micrograph of (c) $(Ru_x(C_7H_{15}COOH)_{0.30})_{THF}$ NPs; scale bar: 50 nm; (d) corresponding size histogram of individual -c-RuNPs.

Compared to previous observations when using 0.4 equiv. of octanoic acid, these new results show that the dispersion and morphology of the particles did not change when decreasing the [ligand]/[metal] ratio to 0.3 and 0.15 equiv. As a conclusion, it can be said that even with a low quantity of ligand the metal particles can be formed (0.15 equiv.) and that there is not a direct influence on the RuNPs size by adding the double amount of octanoic acid (0.30 equiv.). Probably, the only effect will be in the quantity of capping ligand surrounding the nanosystems as it was seen in section 3.1.6.

However, when a higher quantity of stabilizing agent (0.40 equiv.) is used for the synthesis of these RuNPs, a decrease in the NPs mean size was observed (*ca.* 0.15 nm), while the morphology was maintained. Since the standard deviation found for these systems is quite, a statistical treatment can be performed in order to show if the NPs mean size is really affected by the presence of higher amount of octanoic acid.

The statistical treatment used was based on the Fisher test[257] and the bilateral Student's t-test,[258] the combination of these spectroscopic techniques allowed to have a clear information of the ligand effect on the mean size of the RuNPs.

$$F = \frac{(s_1)^2}{(s_2)^2} \qquad F_{(500,500)\alpha=0.01} = 1.23$$

$$H0: S_1 = S_2 \qquad H1: S_1 \neq S_2$$

$$F = \frac{(0.35)^2}{(0.25)^2} = 1.93 \qquad \therefore H0 \; is \; rejected$$

$$t = \frac{\overline{X_1} - \overline{X_2}}{\sqrt{\frac{s_1^2}{n_1} + \frac{s_2^2}{n_2}}} \qquad t_{(\infty)\alpha=0.01} = 2.57$$

$$H0: \overline{X_1} = \overline{X_2} \qquad H1: \overline{X_1} \neq \overline{X_2}$$

$$t = \frac{1.49 - 1.34}{\sqrt{\frac{(0.35)^2}{400} + \frac{(0.25)^2}{400}}} = 6.86 \qquad \therefore H0 \; is \; rejected$$

According to the statistical tests performed on the populations of $(Ru_x(C_7H_{15}COOH)_{0.30})_{THF}$ and $(Ru_x(C_7H_{15}COOH)_{0.40})_{THF}$ NPs, it can be concluded that there is a significant difference with 99.0% of level of reliability between these two systems of RuNPs. It appeared that a ligand quantity over to 0.30 equiv. has a direct influence on the mean size of the RuNPs, but no when lesser quantity is added (0.30 vs 0.15 equiv.).

Since the RuNPs stabilized with 0.40 equiv. of octanoic acid showed the presence of ligand excess, the nanosystems stabilized with 0.30 and 0.15 of ligand equiv. will be analyzed by infrared in similar conditions (see section 6.1.3.3) from purified NPs. The FTIR data are provided on figure 3.29. together with those of $(Ru_x(C_7H_{15}COOH)_{0.4})_{THF}$ NPs for comparison purpose.

In the region of the CO stretching vibration [2100 – 1800 cm^{-1}] all the three nanosystems show vibration bands corresponding to terminal CO resulting from THF degradation (zone highlighted in blue), but the bands are more intense for the systems stabilized by 0.30 and 0.40 equiv. of octanoic acid (figure 3.29 b and c respectively), showing different types of CO coordination modes or sites. Thus, evidencing a lower coordination/reactivity of THF at the NP surface prepared in the presence of 0.15 equiv. ligand.

In the [1750 – 1600 cm^{-1}] area (green zone) where are expected the vibration bands of octanoic acid in its protonated form (either free or coordinated), the system $(Ru_x(C_7H_{15}COOH)_{0.15})_{THF}$ NPs does not show any vibrational bands meaning the absence of free and of protonated coordinated ligand (figure 3.30 a), which suggest that all the introduced ligand is coordinated under the form of octanoate. For the two other systems some signals are visible. While $(Ru_x(C_7H_{15}COOH)_{0.40})_{THF}$ NPs present two signals attributed to free and coordinated octanoic ligand, the $(Ru_x(C_7H_{15}COOH)_{0.30})_{THF}$ NPs show only one band, that is attributed to coordinated octanoic acid.

Finally, in the [1580 – 1500 cm^{-1}] region (orange zone) the signal of the carboxylates is observed in the three nanosystems. As a conclusion, it was seen that the increase of the ligand in the synthesis of these RuNPs produced different type of moieties surrounding the nanosystem (free and coordinated (HA/A^-)). Also, the lower the quantity of ligand, the cleaner the surface or more selective the ligand coordination will take place, going through the RuNPs stabilized by octanoates.

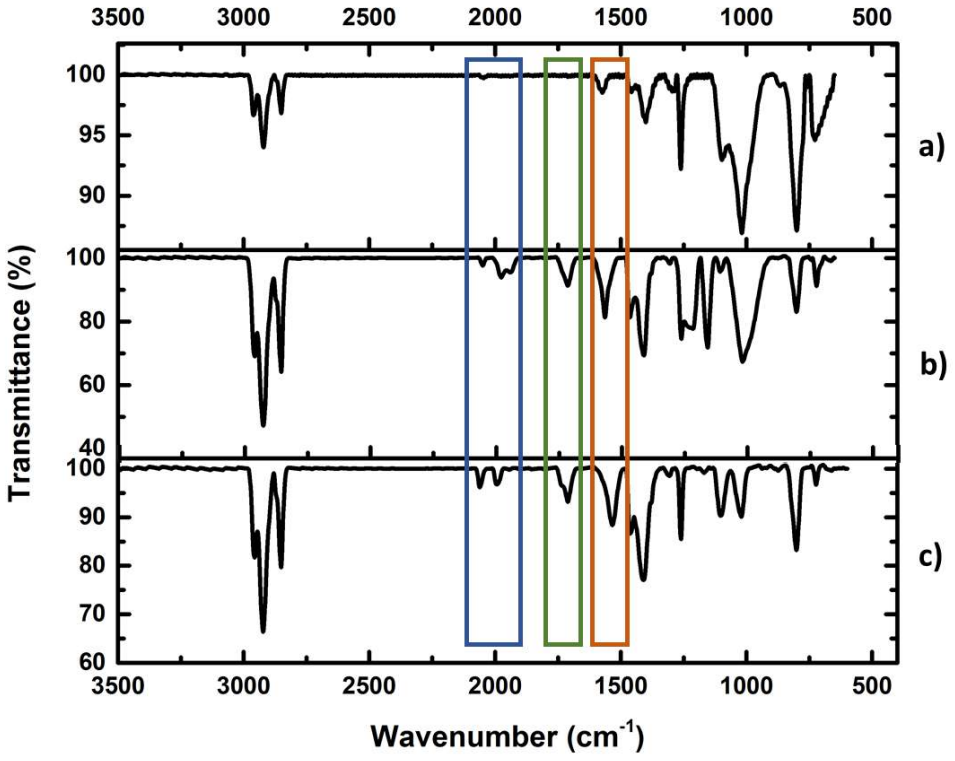

Figure 3.29 Experimental FTIR spectra: (a) $(Ru_x(C_7H_{15}COOH)_{0.15})_{THF}$; (b) $(Ru_x(C_7H_{15}COOH)_{0.30})_{THF}$;(c) $(Ru_x(C_7H_{15}COOH)_{0.40})_{THF}$ NPs. Three specific vibration regions are highlighted: (blue) *ν*(CO); (green) *ν*(COOH); (orange) *ν*(COO).

Scheme 3.5. provides a schematic view of the ligand molecules (free octanoic acid, coordinated octanoic acid or coordinated octanoate) surrounding the RuNPs proposed on the basis of the FTIR data. For purpose of better differentiation, only the $(Ru_x(C_7H_{15}COOH)_{0.40})_{THF}$ and $(Ru_x(C_7H_{15}COOH)_{0.15})_{THF}$ NPs systems were described.

For the first system (scheme 3.5 a) three molecules can be noticed (free ligand and octanoic acid coordinated in its protonated and deprotonated mode), meanwhile in the other system (scheme 3.5 b) only one moiety coming from the stabilizing agent was found (octanoate).

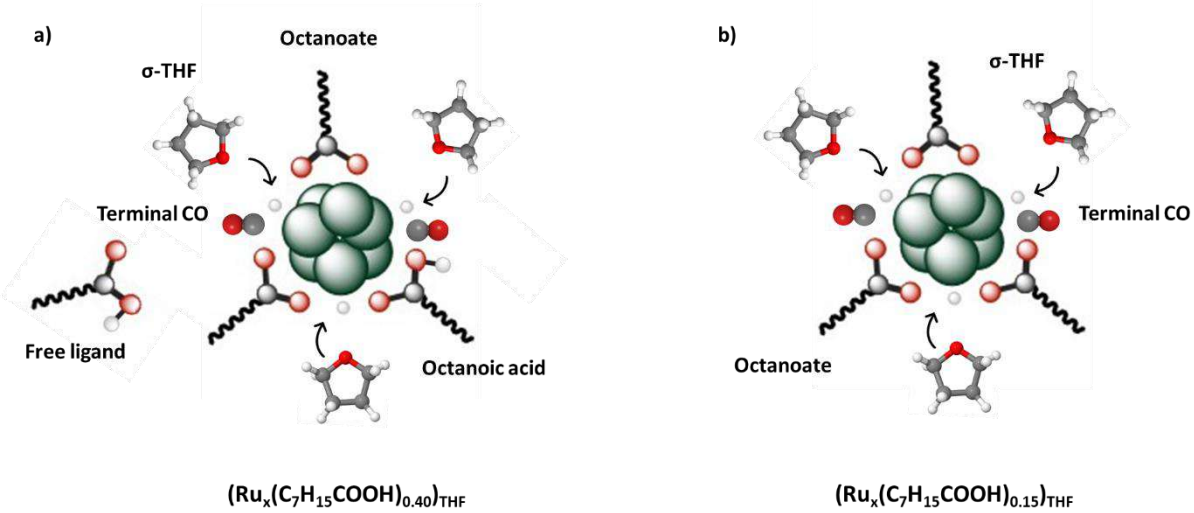

Scheme 3.5 Ligands interacting with the RuNPs surface for (a) $(Ru_x(C_7H_{15}COOH)_{0.40})_{THF}$ *vs* (b) $(Ru_x(C_7H_{15}COOH)_{0.15})_{THF}$.

This study provides a nice understanding of the coordination of the octanoic acid at the surface of RuNPs prepared in THF (solvent-assisted) depending on the amount of ligand introduced. It was observed that a [ligand]/[metal] ratio, as low as 0.15 equiv., is enough to have an efficient stabilization of small NPs of *ca.* 1.5 nm, even if the size distribution is quite large. This is attributed to the presence of THF, which was not observed in previous RuNPs stabilized with ethanoic or pentanoic acid. The THF presence was clearly observed onto the RuNPs surface as σ-THF or CO, which comes from its own degradation.

Increasing the ratio to 0.3 equiv. did not change significantly the mean size of the particles neither the broadness of the size histogram. But FTIR data provided a clear view of the difference between these two systems, namely the presence of only octanoates at the NP surface for 0.15 equiv. and the co-presence of octanoate and protonated acid both coordinated at the NP surface

for 0.3 equiv. The nanosystem prepared with 0.4 equiv. led to smaller RuNPs (*ca.* 1.3 nm) with a surface interacting with both octanoates and protonated acids, and free ligand was also observed.

Therefore, the best system to take into account is $(Ru_x(C_7H_{15}COOH)_{0.15})_{THF}$ because it provides a cleaner surface with one type of interacting molecule (octanoate). Anyway, since the THF can be also considered as pollutant, the stabilization of RuNPs with octanoic acid will be performed as in previous cases with a non-coordinated solvent (pentane).

3.2.4 RuNPs Stabilized with Octanoic Acid in Pentane

MNPs have been widely synthetized by several methodologies, within which the organometallic approach was selected due to the well-defined homogeneous nanoparticles that can be obtained, leading as well to MNPs with a cleaner surface.[77] Several ligands have been used as stabilizing agents that led to different NPs size and morphologies, this offers the possibility to have a big range of metal NPs with various properties.[97] The formation of this type of hybrid material (RuNPs and organic ligand)[89] led to different applications due to its change in their characteristics and reactivity.[110]

In this study, it was shown that RuNPs can be synthetized by using linear alkyl carboxylic acids as stabilizing agents. Also, the formation of NPs even with small alkyl chain ligands (ethanoic acid) has been demonstrated, which is not often seen in the synthesis of MNPs.[94] Previously, it was also determined that the amount of stabilizing agent that will be needed to stabilize RuNPs depends on the alkyl chain length (*see* chapter II & section 3.1), effect that is magnified if a coordinated solvent it is used into the NPs synthesis (*see* and section 3.2.3).

In the section 3.2.3 was described that RuNPs can be synthetized by using 0.15 equiv. of octanoic acid in the presence of THF. Therefore, similar nanosystems will be attempted to form, but without coordinated solvents which will lead to cleaner NPs surface, as observed in previous systems synthetized with ethanoic and pentanoic acid.

In a first attempt, RuNPs were synthetized by following the organometallic approach in the presence of 0.10 equiv. of octanoic acid in a pentane solution ($Ru_x(C_7H_{15}COOH)_{0.10}$). This quantity

was chosen to see the real advantage to use octanoic acid as stabilizing agent by removing the coordinated solvent variable (THF). The synthetic procedure was performed as described in section 6.1.2.2. The reactants ([Ru(COD)(COT)] & octanoic acid) were dissolved in *n*-pentane inside a Fisher-Porter reactor. Then the reaction mixture was exposed to 3 bar of H_2 under vigorous stirring. The initial yellowish solution turned black in *ca.* 15 s and metal pieces have fallen down at the bottom of the reactor in less than 30 s.

It was evident that the RuNPs was not well-formed and probably only big metal pieces were produced or a mixture of different type of particles. Therefore, before any purification process and after elimination of the remaining hydrogen pressure, a drop of the concentrated crude solution was deposed on a c-flat holey carbon grid in order to perform a TEM analysis (*see* section 6.1.3.1).

Heterogeneous population of nanobjects including large nanoparticles of different sizes in the range [25 – 100 nm] and disparate morphologies (figure 3.30 b) together with big agglomerates and metal pieces of ruthenium at the micrometer scale (figure 3.30 a).

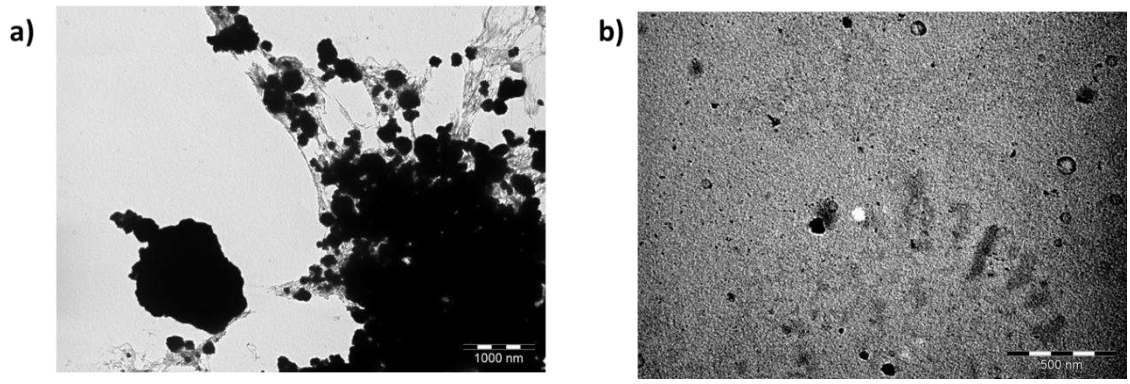

Figure 3.30 TEM micrographs of $Ru_x(C_7H_{15}COOH)_{0.10}$ sample; (a) general view, scale bar: 1000 nm; (b) focus on the nanosystem, scale bar: 500 nm.

Thus, no well-defined ruthenium nanoparticles were synthetized by using only 0.10 equiv. of octanoic acid in pentane (without THF). Displaying the real properties of solvent-assisted ligands like that the THF possess. Meaning that higher quantity of ligand needs to be added into the RuNPs synthesis if pentane is used as reaction media instead of THF.

Consequently, in order to get well-defined particles, an optimization of the quantity of octanoic acid was necessary to perform. This study is described in the following part.

3.2.5 Optimized Synthesis of RuNPs Stabilized with Octanoic Acid

To optimize the synthesis of the RuNPs, it was decided to add a double quantity of octanoic acid ligand, namely 0.20 equiv. ($Ru_x(C_7H_{15}COOH)_{0.20}$ NPs). Thus, the [Ru(COD)(COT)] was decomposed with hydrogen (3 bar) in the presence of 0.20 equiv. of octanoic acid dissolved in a non-coordinated solvent (pentane) at r.t. (scheme 3.6).

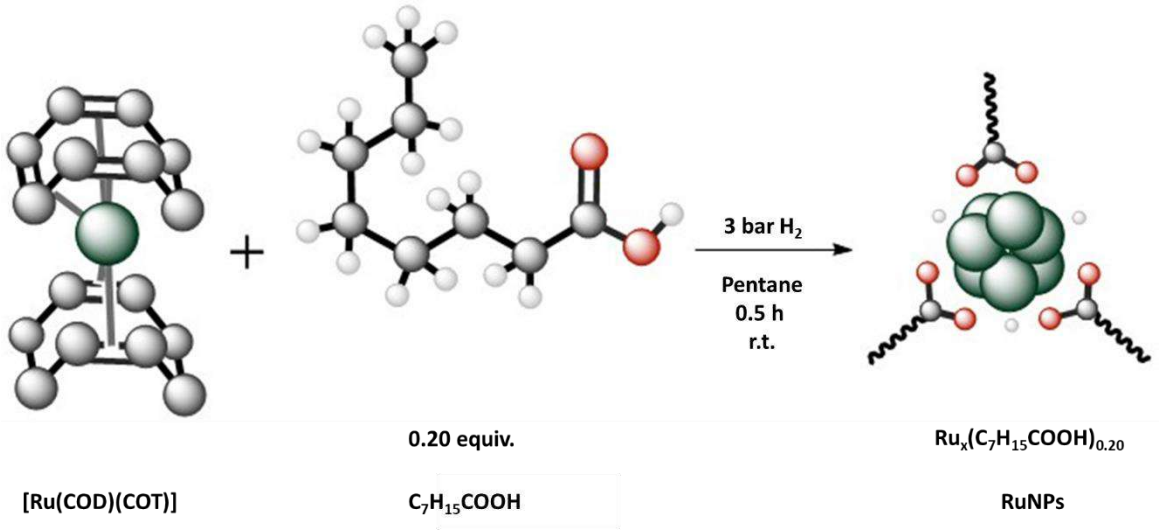

Scheme 3.6 Synthesis of RuNPs in pentane using 0.20 equiv. of octanoic acid. The formed $Ru_x(C_7H_{15}COOH)_{0.20}$ NPs are expected to be covered by octanoates and hydrides.

In these synthesis conditions, the initial pentane yellow solution changed to black very quickly (*ca.* 30 s) indicating the formation of RuNPs. The so-obtained colloidal solution appeared to be stable with no precipitate observed for more than two months. After 30 min under hydrogen pressure (splitted in 10 and 20 min of dynamic and static pressure, respectively), the reaction has been stopped by removing the gas phase under high-vacuum and the colloidal solution was concentrated for further electron microscopy analysis.

Since the obtained colloidal solution has shown to be stable for a long period of time, it can be assumed (due to previous empiric knowledge) that a high-stable RuNPs were synthetized, but to corroborate this assumption different studies needs to be done. For that purpose, a TEM grid was prepared by depositing a drop of the pentane crude and concentrated colloidal solution

onto a holey carbon-covered copper grid (*see* section 6.1.3.1). The obtained dry grid was used for TEM and furthermore for HRTEM analyses (*vide infra*).

TEM micrographs (figure 3.31 a & b) show a population of RuNPs that are well-dispersed on the grid. They have a homogeneous morphology similar to round particles with small elongation in one of its axes (spheroidal NPs). The frequency count analysis revealed the presence of RuNPs with a mean size of *ca.* 1.65 ± 0.65 nm (figure 3.31 c).

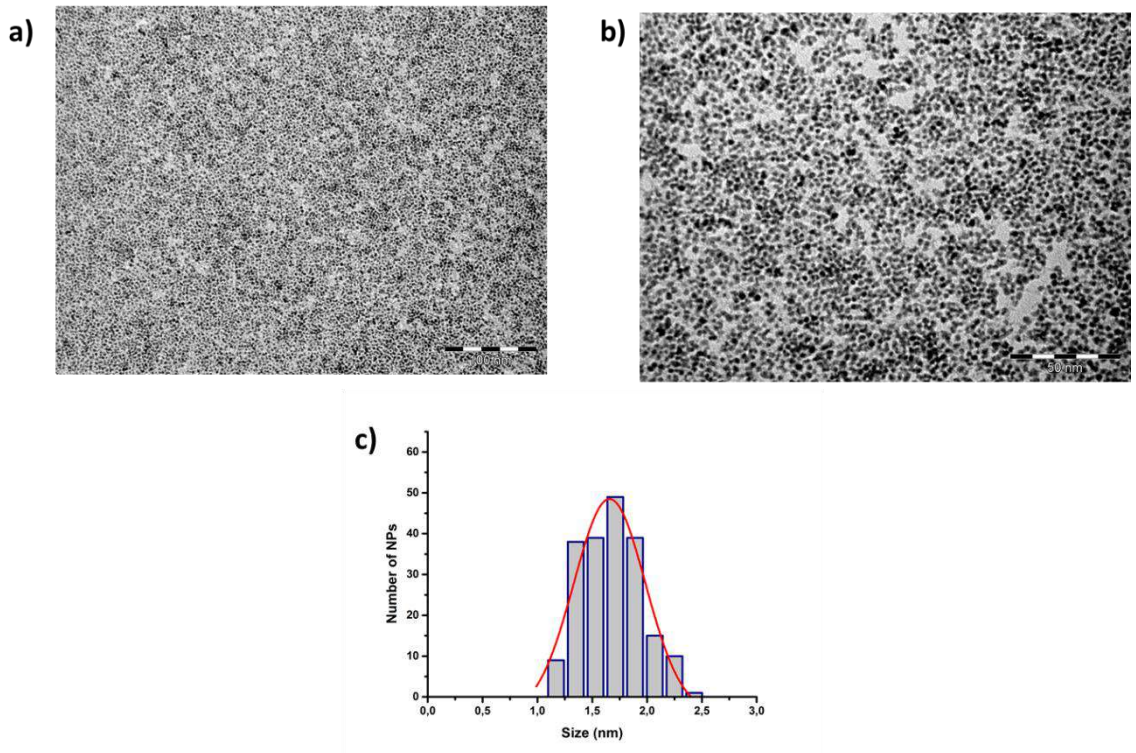

Figure 3.31 TEM micrographs of $Ru_x(C_7H_{15}COOH)_{0.20}$ NPs; (a) general view, scale bar: 100 nm; (b) focus on the nanosystems, scale bar: 50 nm; (c) corresponding size histogram of individual RuNPs.

The formed $Ru_x(C_7H_{15}COOH)_{0.20}$ NPs present a higher mean size (*ca.* 1.65 nm) than previous RuNPs synthetized with the same ligand but in THF (*ca.* 1.5 nm), again the influence of THF as solvent-assisted is noticed. Nevertheless, it is worth to point out the formation of the RuNPs with a low quantity of ligand (0.20 equiv.).

Since this system shows good stability and can be synthetized with a low quantity of ligand (avoiding solvent pollution), it can be taken as starting point to study the surface state of RuNPs

stabilized with carboxylic acids that have longer alkyl chain length ($Ru_x(C_7H_{15}COOH)_{0.20}$) vs shorter ones ($Ru_x(C_4H_9COOH)_{0.30}$ & $Ru_x(CH_3COOH)_{0.40}$).

In order to compare more precisely the three systems of RuNPs, the required ligand quantities for obtaining similar RuNP sizes in the same synthetic conditions are reported in table 3.13. Even if there is a slight deviation of the size measured comparing to a mean size of 1.5 nm, that is more pronounced in the case of octanoic acid, it appears that a lower quantity of carboxylic acid is required to get this mean size when the ligand has a longer alkyl chain length. In other words, using a carboxylic acid with a longer alkyl chain makes lower the required amount of ligand to stabilize the RuNPs.

Table 3.13 Comparative data in terms of required quantity of carboxylic ligand to stabilize RuNPs with similar mean size.

Nanosystem	Quantity of ligand (equiv.)	Mean size (nm)	Size dispersion (nm)
$Ru_x(CH_3COOH)_{0.40}$	0.40	1.51	0.60
$Ru_x(C_4H_9COOH)_{0.30}$	0.30	1.47	0.40
$Ru_x(C_7H_{15}COOH)_{0.20}$	0.20	1.65	0.65

In the following sections, the structural analysis and composition analysis of the $Ru_x(C_7H_{15}COOH)_{0.20}$ NPs will be described

3.2.5.1 Structural Analysis of $Ru_x(C_7H_{15}COOH)_{0.20}$ NPs

Structural analysis of $Ru_x(C_7H_{15}COOH)_{0.20}$ NPs was firstly performed by HRTEM using, the same grid as for TEM analysis. The HRTEM images revealed well-crystalline RuNPs displaying numerous atomic plans that lead to determine easily their crystalline structure (figure 3.32 a). FFT of the HRTEM images allowed to measure interplanar distances of 0.214, 0.207, 0.134 and 0.112 that could be attributed to crystalline (002), (101), (110) and (201) plans of the bulk ruthenium hexagonal close pack structure (figure 3.33 b)

Compared to those RuNPs prepared with 0.4 equiv. of ethanoic acid ($Ru_x(CH_3COOH)_{0.40}$ NPs) which were poorly crystallized, $Ru_x(C_7H_{15}COOH)_{0.20}$ NPs present a high crystalline character and there is no doubt about the atomic packing.

Therefore, it can be implied that the use of longer alkyl chain in the synthesis of RuNPs induces the formation of NPs with higher crystallinity and higher homogeneity than found for RuNPs stabilized with carboxylic acids which have shorter alkyl chain length.

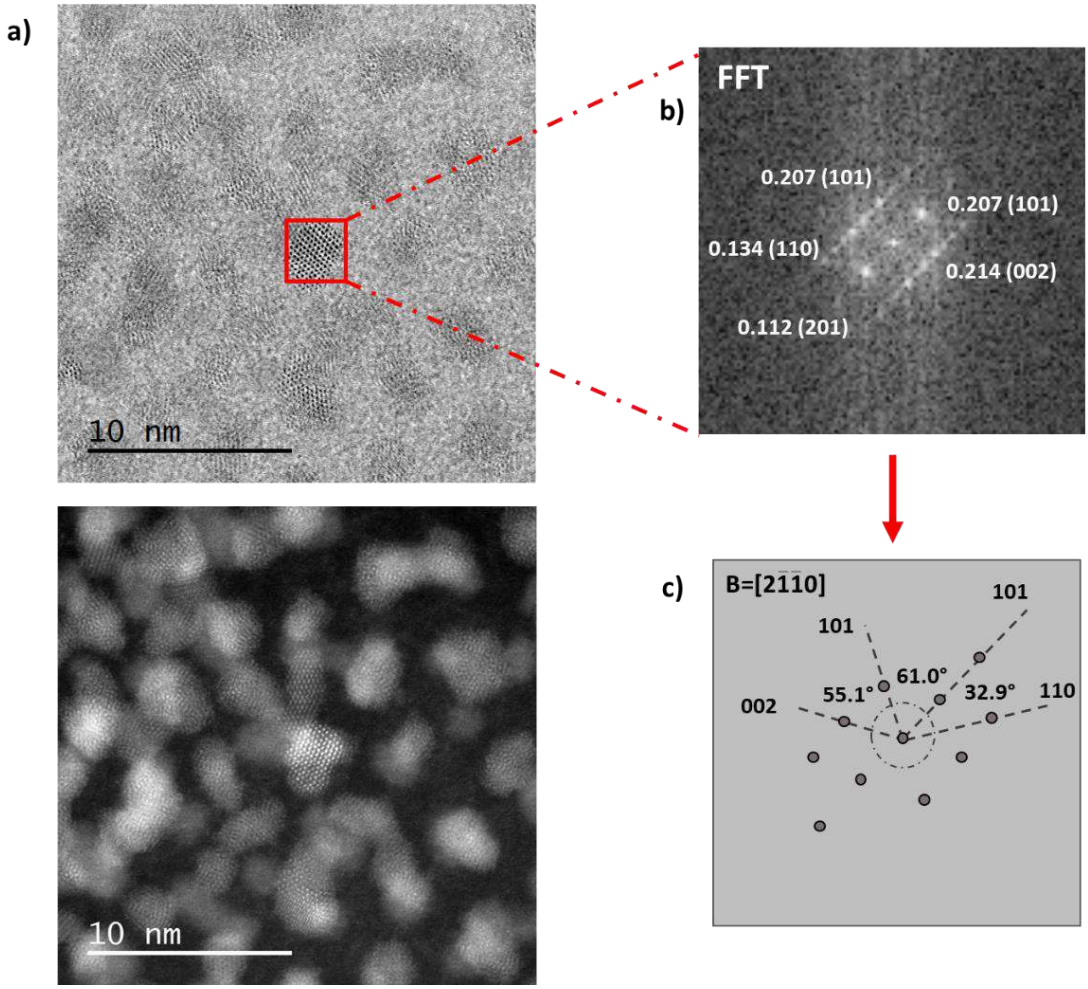

Figure 3.32 HRTEM analysis of $Ru_x(C_7H_{15}COOH)_{0.20}$ NPs; (a) micrographs; (b) FFT (c) Miller pattern.

In order to corroborate the data observed by HRTEM, a WAXS analysis was performed on $Ru_x(C_7H_{15}COOH)_{0.20}$ NPs in the solid-state (see section 6.1.3.5), after the RuNPs purification by several THF-pentane washing cycles.

The analysis shows in the real space (figure 3.33 a) a well-defined function which is consistent with pure crystalline metallic Ru^0 NP. Fourier treatment led to an RDF that corresponds to highly crystalline and non-oxidized RuNPs with a narrow size dispersion and in agreement with the *hcp* structure (figure 3.33 b). As a result of this study, it was found that the $Ru_x(C_7H_{15}COOH)_{0.20}$ NPs have a coherence length estimated to *ca.* 2.2 nm.

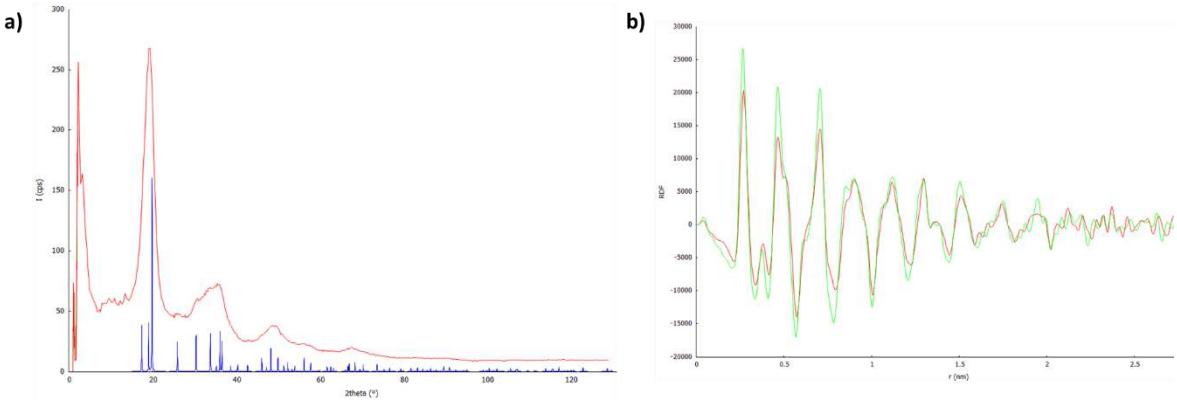

Figure 3.33 (a) WAXS spectrum of $Ru_x(C_7H_{15}COOH)_{0.20}$ NPs (red profile) compared with Ru *hcp* pattern (blue profile); (b) RDFs comparison in real space of two different batches of $Ru_x(C_7H_{15}COOH)_{0.20}$ NPs.

The WAXS analysis is consistent with the well-crystalline Ru *hcp* NPs determined by HRTEM, the estimated coherence length of *ca.* 2.2 nm is slightly overestimated from the mean size measured by TEM analysis. Such a difference has been previously observed by other authors in ruthenium[97] and palladium[205] NPs.

Moreover, this last data is not in contradiction with TEM results since WAXS is a statistical technique which is highly sensitive to different size of synthetized objects. Therefore, these complementary studies provide a good notion on the mean size and crystalline structure of the $Ru_x(C_7H_{15}COOH)_{0.20}$ NPs.

3.2.5.2 Organic Molecules Surrounding the $Ru_x(C_7H_{15}COOH)_{0.20}$ NPs Surface

After their structural analysis by HRTEM and WAXS, the composition of the particles was determined by FTIR and NMR experiments.

FTIR study was performed with the aim to see which products can be found surrounding the formed nanoparticles, especially to discover if the octanoic acid act as protonated or deprotonated entity when is used as RuNPs stabilizer. The vibrational spectroscopy analysis of $Ru_x(C_7H_{15}COOH)_{0.20}$ NPs was performed in the solid-state under inert atmosphere in a glove-box after dispersing the material into dried KBr. (see section 6.1.3.3).

As it can be seen from the vibrational spectrum (figure 3.34), there is no evidence of carboxylic acid asymmetric stretching vibration mode (R-COOH) in the [1800 - 1600 cm^{-1}] range. Only one absorption band at *ca.* 1530 cm^{-1} is visible, same signal as observed for the $(Ru_x(C_7H_{15}COOH)_{0.20})_{THF}$ NPs. Thus, it can be said that this system behaves in a similar way than previous RuNPs systems stabilized with shorter alkyl chain carboxylic acids. In other words, the only signal that is observed in the [1800 - 1500 cm^{-1}] range (ν_{as} R-COO zone) corresponds to the deprotonated carboxylic acid (octanoate) which is found at *ca.* 1530 cm^{-1}. Thus, the octanoic acid ligand followed the same deprotonation reaction when approaching to the metal surface, as for ethanoic and pentanoic acids.

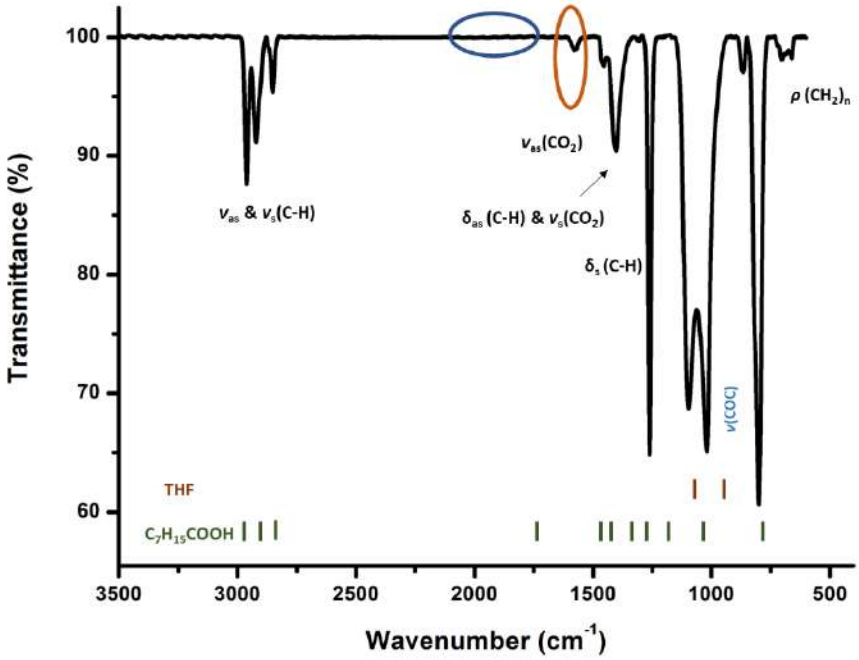

Figure 3.34 Experimental FTIR spectrum of $Ru_x(C_7H_{15}COOH)_{0.20}$ NPs and main peaks assignments. Characteristic peaks of octanoic acid (green bars, $C_7H_{15}COOH$) and THF (yellow bars) are also indicated. *ν*: stretching; *δ*: bending; *ρ* rocking; s: symmetric; as: asymmetric. Regions corresponding to *ν*(CO) & ν_{as}(COO) are highlighted in blue and orange respectively.

In the right part of the infrared spectrum, it can be identified three well-separated signals in the area [3000 - 2850 cm^{-1}] that can be attributed to the asymmetric (ν_{as}) and symmetric stretching (ν_s) vibration modes of the methyl and methylene groups of the carboxylic acid alkyl chain ($CH_3(CH_2)_6COOH$). It is important to note that no water is detected, as it was found in other systems stabilized with pentanoic or ethanoic acid. This can be explained from the decreasing of the ligand polarity and its affinity for water.

The vibration band observed at *ca*. 1530 cm^{-1} was assigned to the ν_{as} vibration mode of the deprotonated octanoic acid interacting with the RuNPs ($C_7H_{15}C{=}OO$). The absence of any other signal in this region indicates the absence of free ligand or protonated ligand coordinated to the NPs (orange highlighted region; figure 3.34). At this point it can be said that there is no free carboxylic acid and that all the stabilizing agent present is surrounding the RuNPs as octanoate.

Other bands within [1500 and 1250 cm^{-1}] could be identified for the asymmetric stretching mode (ν_s) of the carboxylic group ($C_7H_{15}C{=}OO$), and the C-H bending asymmetric (δ_{as}) and symmetric (δ_s) vibration modes of the alkyl chain ($CH_3(CH_2)_6COO$). In addition, a band attributed to the alkyl chain rocking mode ($\rho(CH_2)_n$) is visible at 720 cm^{-1}, meaning that there was no degradation of the ligand during the RuNPs synthetic procedure.

In the left part of the spectrum, two intense bands are present at *ca.* 1020 and 800 cm^{-1} that are assigned to coordinated THF.[[238],[239]] As previously mentioned for other carboxylic acid-stabilized RuNPs, the presence of THF can be explained by the washing process applied to purify the $Ru_x(C_7H_{15}COOH)_{0.20}$ NPs. It is important to notice that no CO band is observed in the spectrum (blue highlighted region; figure 3.34), meaning that the THF degradation previously observed in other systems was not accomplished here.

In summary, FTIR spectroscopy provided good insights about the type of molecules surrounding the nanoparticles and contributed with general idea of the interaction occurred in the interface of this hybrid material. However, this technique is not sensitive enough to fully describe the type of molecules found at the RuNPs periphery. Therefore, to complete the $Ru_x(C_7H_{15}COOH)_{0.20}$ NPs characterization, NMR techniques (^1H and ^{13}C) were utilized.

Contrary to other type of MNPs, which present some paramagnetic effects,[[259],[260]] the RuNPs present only a small residual effect till no longer is considered as a NMR signal modifier and, even more, when there is an atom spacer between the recorded atoms affected for this

phenomenon and the metal surface.[106] Therefore, it is possible to go deeper in the $Ru_x(C_7H_{15}COOH)_{0.20}$ NPs surface characterization.

Previously, it was observed for $(Ru_x(C_7H_{15}COOH)_{0.40})_{THF}$ NPs, the presence of ligand excess and, in some point, the appearance of different type of molecules coordinated at the nanoparticle surface (protonated and deprotonated octanoic acid, THF, CO and sometimes PTHF). However, for other experiments performed with purified NPs (Pentane-THF cycles), less signals were observed. Thus, it can be suggested that certain part of information could be lost once the particles are cleaned, due to the probable removal of weak bound organic molecules. As a consequence, the data could be biased. Therefore, in order to avoid this issue, the resonances experiments were performed form the fresh RuNPs colloidal solution.

^{1}H-NMR data were recorded from non-purified NPs. The crude colloidal suspension was just evaporated under high-vacuum and the residual powder dried under high-vacuum for 36 h. Then the black powder containing the particles was re-dispersed into deuterated benzene (C_6D_6), under inert atmosphere, just before performing ^{1}H-NMR experiments (see section 6.1.3.6).

Figure 3.35 presents the ^{1}H-NMR spectrum recorded for the $Ru_x(C_7H_{15}COOH)_{0.20}$ NPs (red profile) together with that of free octanoic acid (blue profile). In the spectra, the deuterated solvent signal can be found at *ca*. 7.16 ppm. Apart from this signal only one extra sharp peak attributed to grease at *ca.* 0.29 ppm can be observed in the red spectrum ($Ru_x(C_7H_{15}COOH)_{0.20}$ NPs), no other well-defined signal was found.

The spectrum of free octanoic acid shows five narrow signals at *ca.* 2.13, 1.50, 1.21, 1.13 & 0.87 ppm that were attributed to protons in positions α, β, γ, δ, ε, ζ of the alkyl chain as shown on the drawn molecule. None of these sharp signals of the free octanoic acid are visible in the $Ru_x(C_7H_{15}COOH)_{0.20}$ NPs spectrum. The absence of these characteristic signals suggests that there is no free stabilizing agent in the solution, meaning that all the stabilizing ligand acid is interacting with the RuNPs surface.

This is reinforced by the fact that the $Ru_x(C_7H_{15}COOH)_{0.20}$ NPs spectrum presents a very broad signal located between [2.70 and 0.50 ppm] where a few ill-defined peaks can be distinguished. To remember, molecules with higher mobility produce sharper signals in the NMR spectrum (free ligands) that low dynamic compounds (ligands attached at the NPs surface). Thus,

the presence of this type of peaks is usually used as a good proof of the ligand coordination at the NPs surface.[([163],[164])]

Thus, this broad peak can be assigned to carboxylic moieties interacting with the surface of the RuNPs. This assignation will be corroborated later on by complementary NMR techniques (*vide infra*).

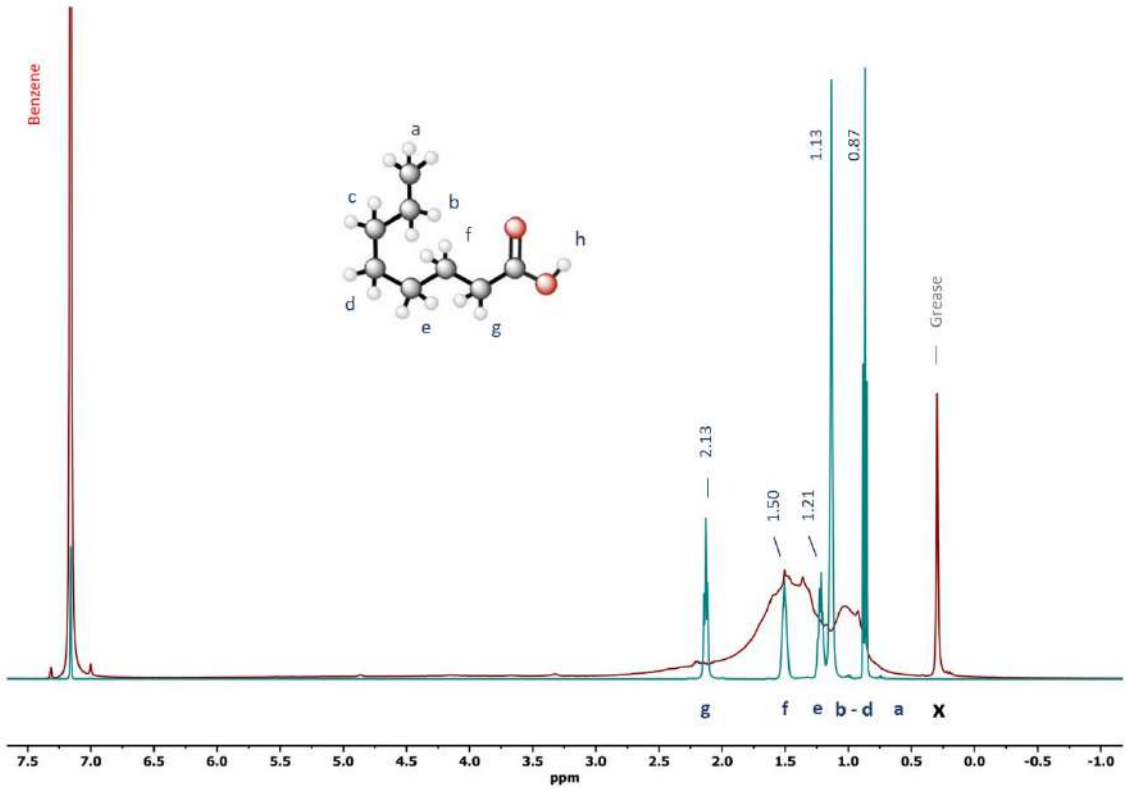

Figure 3.35 ^{1}H-NMR (benzene-d^{6}); (red) $Ru_x(C_7H_{15}COOH)_{0.20}$ NPs; (blue) $C_7H_{15}COOH$.

Till know it was observed that the use of 0.20 equiv. of octanoic acid to stabilize RuNPs in pentane, was enough to produce small homogeneous nanoparticles with a mean size of *ca.* 1.65 nm, this quantity of ligand was established as the minimum amount of ligand needed for the formation of the nanosystem without adding any coordinated solvent (THF).

Due to the combination of these spectroscopic techniques, it was possible to elucidate which molecules are surrounding and interacting with the $Ru_x(C_7H_{15}COOH)_{0.20}$ NPs. The FTIR indicates that the RuNPs are stabilized by octanoates. Also, the vibrational study proved the

presence of coordinated THF and no other molecules was observed (CO, PTHF, free or coordinated protonated ligand). These data were corroborated by the ^{1}H-NMR spectrum where it was observed the absence of free ligand and THF, this last molecule was possible to be observed in the FTIR, because it was coming from the washing procedure. As a general conclusion, it can be said that the $Ru_x(C_7H_{15}COOH)_{0.20}$ NPs are stabilized by octanoates and that all the ligand added is interacting with the metal surface (no excess).

The absence of free ligand was corroborated by both spectroscopies techniques, but the nonexistence of the protonated carboxylic entity coordinated onto the RuNPs was only proved by FTIR. Therefore, it is necessary to find another characterization technique that can validate this assumption. In previous experiment, it was reported the utility of use solid-NMR to verify the absence of free ligand and also the type of coordinating molecule onto the RuNPs surface.

This technique provides new information that was previously lost in the liquid state-NMR due to poor resolution of the spectrum induced by the low mobility of the ligands. The loss of motion generate an increase on the T_2 relaxation time and leads to broader signals that are difficult to interpret.[([179],[180])]

This phenomenon is magnified for atoms that are closer to the NP surface and even more those which are directly attached.[261] Due to this phenomenon, it was not possible to identify any signals of the α-protons and carboxylic species from liquid state ^{1}H and ^{13}C-NMR data, respectively.

Solid-state NMR at the magic angle spinning (MAS) in high-speed condition is a powerful technique to circumvent problems of rigidity at NP surface and thus characterize deeper the interacting ligands. Hence, the obtained NMR spectrum show signals that were not possible to observe by solution NMR. In other words, it is possible to run ^{13}C solid-state NMR to observe precise data on the carbon atoms which are closer to the NPs surface.[262]

The solid-state ^{13}C CP Hahn-MAS NMR was recorded from purified $Ru_x(C_7H_{15}COOH)_{0.20}$ NPs. To avoid electric arching that appeared when using a powder of RuNPs as the result of the high metal content, it was necessary to dilute the particles into an inorganic support. For this purpose, the purified RuNPs were redispersed in THF solution, in concentrated condition. Then, the solution was deposed onto porous silica and dried by slow evaporation under inert conditions (see section 6.1.3.7).

The ^{13}C CP Hahn-MAS NMR spectrum recorded for $Ru_x(C_7H_{15}COOH)_{0.20}$ NPs diluted in silica is given on figure 3.36. It shows an intense peak close to 0 ppm corresponding to grease. Also, it presents two intense peaks at *ca*. 24.2 and 66.8 ppm that are assigned to the carbon atoms from THF as this solvent has been used for NPs deposition onto silica and can be present in the solid. The first signal attributed to THF (ca. 24.2 ppm) is quite broad in comparison with the second one. This can result from the presence of other signals in this region as it is expected for those of the methylene and methyl groups of the carboxylic molecules. In fact, on the right part of this signal, at lower ppm a small shoulder is observed that can be assigned to the methyl group of the carboxylic moieties (tail).

The signals marked with an "x" are assigned to molecules coming from the THF degradation. There is also a broad signal at *ca.* 192.1 ppm which can be attributed to the carboxylic carbon atom of the ligand when comparing with the same carbon of the free octanoic acid (*ca.* 180.4 ppm in $CDCl_3$[263]). Previously, for the RuNPs stabilized with ethanoic and pentanoic acid, the peaks in solid ^{13}C-NMR were observed to appear at lower field than those of the free ligand.

In particular, carboxylate molecules interacting with the RuNP surface presented left shifted signals. Here also, the peak observed at *ca.* 192.1 ppm and assigned to carboxylic carbon of the ligand interacting with the metal surface resonates at a lower field compared to that of free ligand (*ca.* 180.4 ppm in $CDCl_3$[263]). The difference in chemical shift observed between the two peaks (≥ 10 ppm) associated to FTIR data presented before are in favor of the presence of octanoates at the RuNP surface and allows to exclude the existence of free octanoic acid and also of coordinated octanoic acids (protonated).

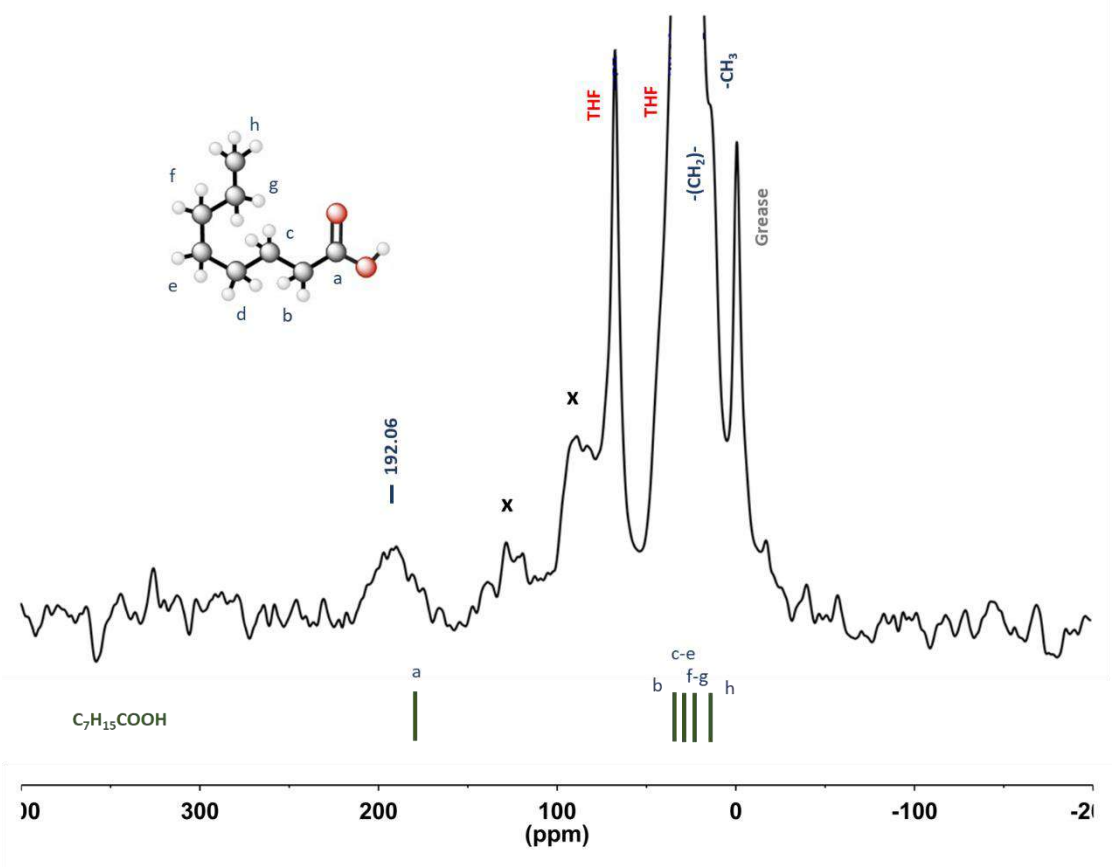

Figure 3.36 ^{13}C CP Hahn-MAS NMR spectrum of $Ru_x(C_7H_{15}COOH)_{0.20}$ NPs dispersed in porous silica. $C_7H_{15}COOH$ peaks ($CDCl_3$) are displayed in bars at the bottom of the figure.

NMR studies lead to think that the three carboxylic acids used as ligands to stabilize RuNPs have a same fate at the NP surface. Once coordinated onto the ruthenium surface a deprotonation process takes place which makes them to interact with the ruthenium surface in carboxylate form. Given the carboxylate form of the ligands, the carboxylic carbons suffer an electronic deprotection and their NMR signal is shifted to higher chemical shift (lower field).

The next comparison is performed in order to know the level of deprotection experienced by the carboxylates ligands when they are interacting with the RuNPs (table 3.14).

Table 3.14 Comparison of the chemical shift of free carboxylic acids and coordinated carboxylate depending on the alkyl chain length of the ligand used for stabilize RuNPs. (a) THF-d^8; (b) Solid state; (c) $CDCl_3$.

Nanosystem	Stabilizing agent	Chemical shift observed for coordinated carboxylates (ppm)	Chemical shift of the free ligands (ppm)
$\mathbf{Ru_x(CH_3COOH)_{0.40}}$	Ethanoic acid	186.0	171.7[a]
$\mathbf{Ru_x(C_4H_9COOH)_{0.30}}$	Pentanoic acid	187.9	174.0[b]
$\mathbf{Ru_x(C_7H_{15}COOH)_{0.20}}$	Octanoic acid	192.1	180.4[c]

As it can be seen in the previous table, the value of the chemical shift of the carboxylate carbon increases with the length of the alkyl chain of the ligand. This type of correlation has been already observed and could be related to different variables as *d*-band center, ligand adsorption energies, NPs mean size, etc.[264]

In this work, it was stablished that the signals found in the range of [186.0 - 193.0 ppm] of the solid-state ^{13}C CP Hahn-MAS NMR spectrum correspond to the carbon of the carboxylate molecule attached at the surface of the RuNPs. However, in previous works, it has been reported that for different types of MNPs, the carboxylic acids underwent a decarbonylation or decarboxylation reaction once they approach to the metal surface.([265],[266]) As a consequence, it appeared necessary to corroborate if the signals observed in the region [186.0 - 193.0 ppm] could correspond to CO or CO_2 molecules attached at the RuNPs surface as the result of a carboxylic acid degradation process.

For this purpose, a 2D solid-state NMR experiment has been performed. The ^{13}C Heteronuclear Correlation (HETCOR) MAS NMR program was chosen in order to define the atom correlation between the carbon and proton atoms of the ligands which lie on the RuNPs surface. Thus, an HETCOR NMR spectrum has been recorded for $Ru_x(C_7H_{15}COOH)_{0.20}$ NPs using the same probe as for ^{13}C solid-state NMR, namely RuNPs dispersed into silica support (figure 3.37).

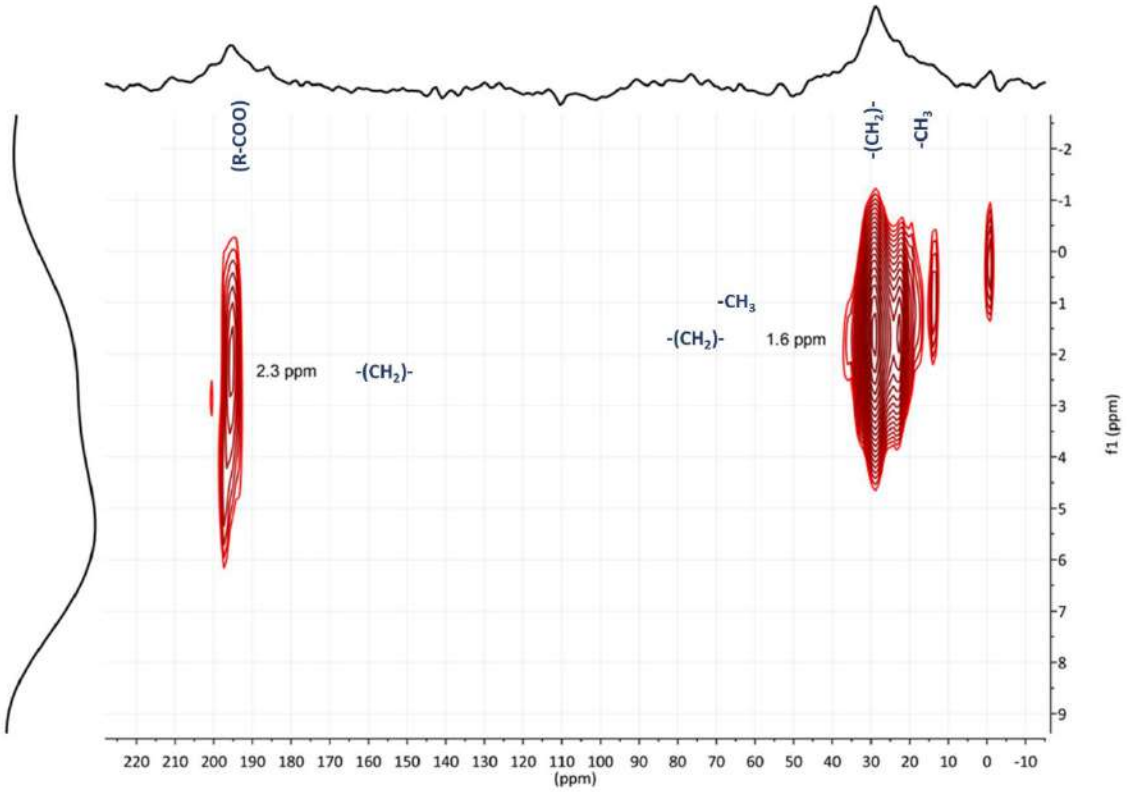

Figure 3.37 ^{13}C HETCOR MAS NMR of $Ru_x(C_7H_{15}COOH)_{0.20}$ NPs diluted in porous silica.

The 2D HETCOR MAS NMR spectrum recorded shows a correlation between the CO signal at *ca.* 192.1 ppm and that of hydrogen atoms at *ca.* 2.3 ppm whose chemical shift is similar to that of the carboxylic moiety α-methylene (R-CH_2-COO) *ca.* 2.1 ppm ($CDCl_3$). Therefore, it can be concluded that the CO group resonating at *ca.* 192.1 ppm is close to the alkyl chain of the carboxylic acid molecules. Consequently, it can be affirmed that the stabilizing agent did not suffer any decarboxylation or decarbonylation during the RuNPs formation and also through the time.

The other signals observed in the spectrum evidence the correlation between the proton and carbon atoms of the alkyl chain. From these results, it can be concluded that the octanoic acid ligand remains as octanoate at the surface of the RuNPs. Therefore, the suggested hypothesis is that the two other carboxylic acids tested for the synthesis of RuNPs (ethanoic and pentanoic acid) have the same behavior, because it is expected a similar surface reactivity for ligands from the same family.

3.2.5.3 Quantification of Organic Molecules Attached onto the Surface of $Ru_x(C_7H_{15}COOH)_{0.20}$ NPs

The elucidation of the NPs surface state is widely known in this field, there are several techniques that help to characterize MNPs. Some of them were used in this work, such as WAXS and HRTEM.[207] Normally, the mean size and morphology of the nanoparticles are obtained by microscopy techniques[127] and NMR experiments, such as DOSY, can contribute to corroborate the size of the MNPs by obtaining its hydrodynamic radii.[267]

While different techniques (FTIR, UV-vis, RAMAN, NMR, thermogravimetric methodologies, etc.)[268] can be used to identify the nature of organic molecules present at the NP surface (like stabilizers, solvents, hydrides or pollutants) the quantification of these surrounding species is not so common in the literature.

Therefore, in the following section, it will be shown a well-defined surface mapping of the $Ru_x(C_7H_{15}COOH)_{0.20}$ NPs. Experimental and theoretical techniques will be combined in order to estimate the quantities of stabilizing ligands and hydrides interacting with the nanoparticle surface. As previously done, NMR and theoretical tools will be mainly applied for this purpose.

3.2.5.3.1 Quantification of Stabilizing Agent Interacting with the $Ru_x(C_7H_{15}COOH)_{0.20}$ NPs by 2D-NMR

Diffusion-Ordered NMR spectroscopy (DOSY-NMR) allows to determine the dynamic behavior of chemical compounds dispersed into a deuterated solvent. It is also a powerful tool to study the mobility of ligands attached or interacting with the surface of nanoparticles and to distinguish from free ligands in solution if any.[267] This technique has already been used to characterize the surface composition of ethanoic- and pentanoic-stabilized RuNPs.

Firstly, a diffusion-filtered ^{1}H-NMR experiment was performed in order to see if the broad signal observed in the liquid ^{1}H-NMR spectrum ([0.5 – 2.7 ppm]) corresponds to the ligand attached at the surface of the RuNPs (*see* section 3.2.5.3). This procedure allows to eliminate the

contribution of dynamic molecules with fast diffusion like solvents or impurities, remaining only visible the signals corresponding to the molecules attached at the RuNPs surface.

The DOSY ^{1}H-NMR experiment was conducted on non-purified $Ru_x(C_7H_{15}COOH)_{0.20}$ NPs that were just dried under vacuum and then re-dispersed in deuterated benzene (see section 6.1.4.1). It was necessary to carry out like this in order to have comparable conditions with previous liquid NMR experiments. The obtained data are presented on figure 3.38.

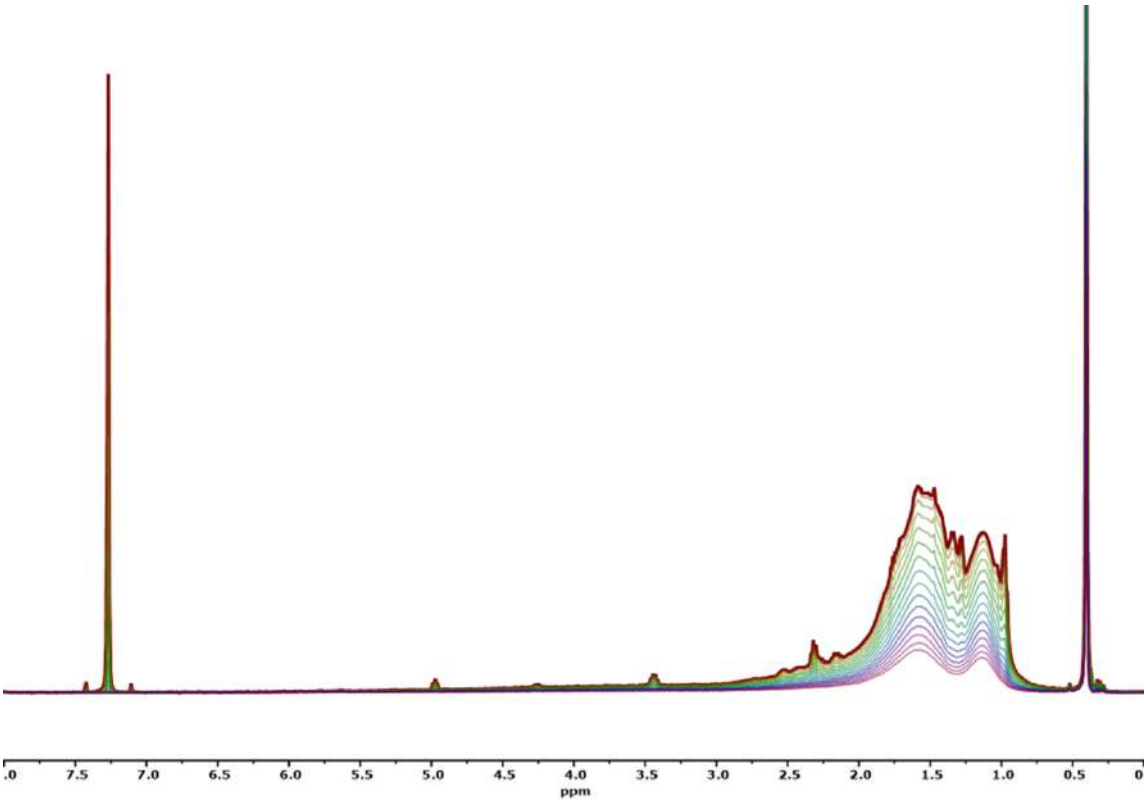

Figure 3.38 DOSY ^{1}H-NMR (C_6D_6) recorded for non-purified $Ru_x(C_7H_{15}COOH)_{0.20}$ NPs. The different observed curves presented are obtained as a result of the different gradient strength applied.

The diffusion-filtered ^{1}H-NMR spectrum shows that the broad peaks previously observed in the ^{1}H-NMR spectrum between [0.5 – 2.7 ppm] corresponds to rigid molecules with low motion. In fact, it can be seen how this broad signal remains as two broad peaks even when a high diffusion-filtration is applied.

The remaining peaks were attributed to the β -CH_2 (ca. 1.6 ppm) and [δ – ζ]-CH_2 (ca. 1.1 ppm) of coordinated ligands when comparing with the signals of free octanoic acid. These

assignations were made on the basis of the chemical shifts obtained for the maximum height of the signals. However, it can be assumed that all the protons of the octanoic ligands resonate in this region due to the broadness of the signals observed. Given previous FTIR and NMR data, we can assume that the stabilizing ligand is under the form of octanoate. A better look of this diffusion-filtration can be observed in the figure 3.39.

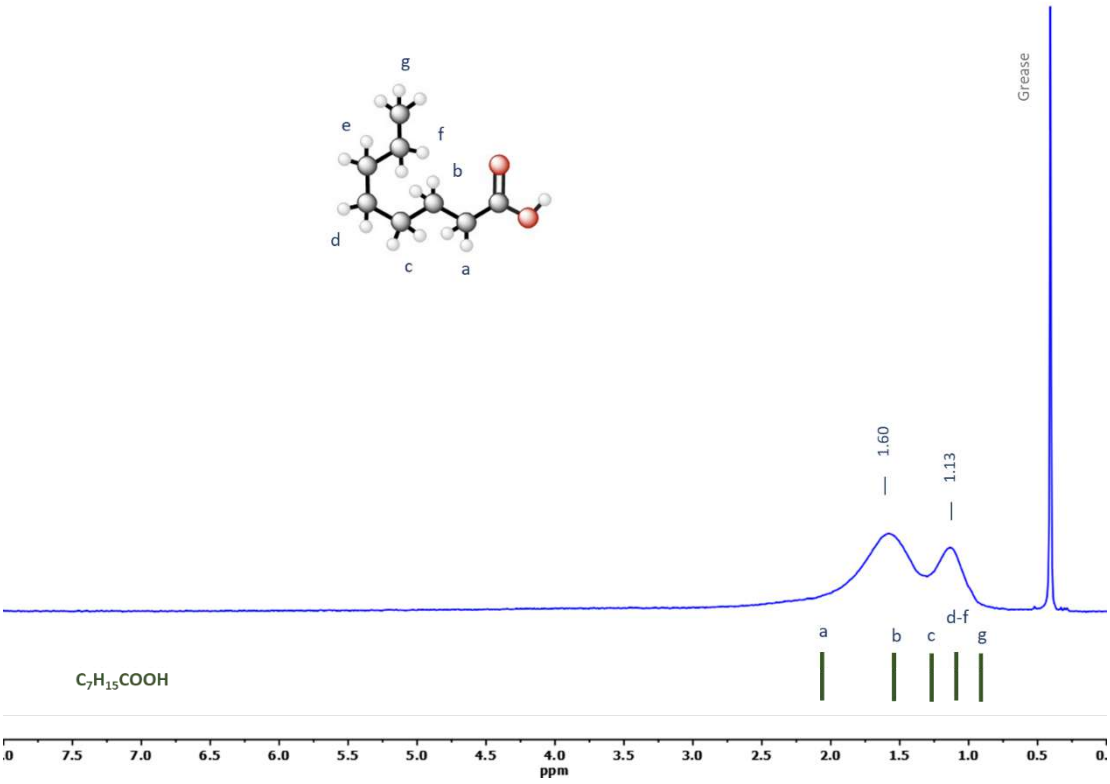

Figure 3.39 Diffusion-filtered ^{1}H-NMR spectrum (C_6D_6) recorded for $Ru_x(C_7H_{15}COOH)_{0.20}$ NPs. $C_7H_{15}COOH$ protons chemical shifts are represented in green bars at the bottom of the figure.

It is important to notice than in this region there were some peaks or signal that were removed for the diffusion-filtration process. Since from other techniques, it was observed the absence of free ligand, a second type of interacting ligand can be proposed (weakly coordinated).

A possibility to try to corroborate this assumption is to consider the ^{1}H DOSY NMR data and analyze the evolution of the integration of the peaks in the [2.05 – 0.85 ppm] area (that correspond to the methyl and methylene groups of the octanoates in interaction with the RuNPs surface), with the gradient strength. Thus, the diffusional attenuation was fitted to a Stejskal-

Tanner equation. This showed that it was not adequate to perform a mono-exponential analysis and indicated the probable presence of different types of interactions for the octanoates at the ruthenium surface.[269] Thus, the previous planted hypothesis of the presence of different type of coordinated ligands can be corroborated.

Then, the diffusional attenuation was fitted by a bi-exponential analysis which validated the presence of two different types of molecules interacting with the RuNPs surface. As a result, two different diffusion coefficients (*D*) were extracted. The first one with a value of D_1 = 1.7 x 10^{-10} $m^2.s^{-1}$ which represents the 67.6 % of the signal weight and the second one, with a value D_2 = 6.4 x 10^{-10} $m^2.s^{-1}$, that possess 32.4 % of the measured signal weight. These two values are quite smaller than that extracted for free octanoic acid (monomer), namely D_{OcAc} = 1.3 x 10^{-9} $m^2.s^{-1}$.

These results corroborate the absence of free ligand in solution as previously deduced from ^{1}H-NMR data. Concerning the two diffusion coefficients measured (D_1 and D_2) they reflect the behaviour of molecules with a different interaction strength at the RuNPs surface. The lowest diffusion coefficient (D_1) can be assigned to ligand molecules in strong interaction with the metal surface and the highest one (D_2) to ligand molecules with higher mobility that can be in fast exchange with free ligand in solution. Thus, it can be proposed that the ligand molecules are organized in different layers around the metal surface according to their interaction strength as represented in scheme 3.7.

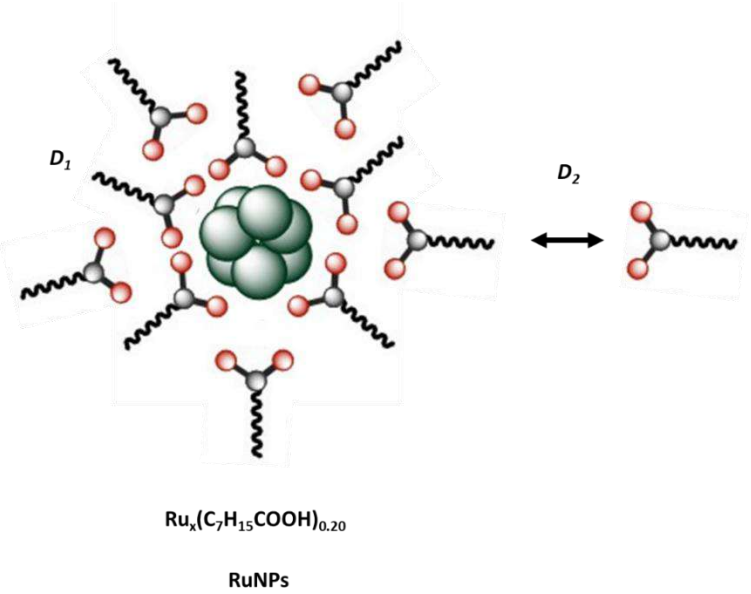

Scheme 3.7 Graphical representation of two types of interacting molecules for $Ru_x(C_7H_{15}COOH)_{0.20}$ NPs as suggested by DOSY NMR. (D_1) Strongly coordinated ligand and (D_2) ligand weakly coordinated in fast exchange.

By applying the Stokes-Einstein equation to the data extracted from the DOSY analysis, allowed to determine the hydrodynamic radii of the two types of species present in solution (*see* section 6.1.3.6.1). According to this mathematical relation, the system with the lowest diffusion coefficient (D_1) have a hydrodynamic diameter of 3.8 nm and those with the highest diffusion coefficient (D_2) presents a hydrodynamic diameter of 1.0 nm.

It is important to remind that the detected species in solution can be either organic molecules or metal nanoparticles surrounded by ligands. Thus, the 3.8 nm hydrodynamic diameter can be compared to the mean size of the particles determined by TEM analysis (*ca.* 1.65 nm), that corresponds only to the metal core of the particles by removing the stabilizing ligand contribution. Withdrawing two times the hydrodynamic diameter of the free ethanoic acid (also determined from its coefficient diffusion; 0.5 nm) from 3.8 nm leads to *ca.* 2.8 nm, a value which is quite higher than 1.65 nm obtained by TEM. This effect could be explained from a relaxation of the ligand attached at the RuNPs in the organic solvent[270] and the temperature of the experiment.[271]

Concerning the second type of interacting ligand, 1.0 nm hydrodynamic diameter, this value is not high enough to be assigned to another type of coordinated ligand and surprisingly it corresponds to the double of the hydrodynamic diameter of free octanoic acid monomer (0.5 nm). Therefore, the previous assumption for being exchanging ligand can be validated.

Finally, the DOSY analysis results (diffusion coefficients, *D*, and repartition in % of the corresponding species) can be taken as a huge advantage to define a mapping of the surface coverage of the NPs (see section 6.1.3.6.2).[267] It is important to notice that this procedure is not easy to perform and that it requires to have a clean nanosystem, meaning that RuNPs with only the stabilizing agent attached at their surface are desired. The obtained results will provide the relative amount of strongly (D_1), weakly and exchanging ligand (D_2) interacting with the RuNPs surface.

Another important point is that the DOSY NMR experiments were carried out on non-purified nanoparticles. As a consequence, it is assumed that all the ligand introduced for the synthesis of the particles (0.20 equiv.) is still present in analyzed sample. The ligand species interacting with the RuNPs are of three types and noted as I_s, I_w and I_f (see table 3.15). They correspond to strongly coordinated (I_s), weakly coordinated (I_w) and exchanging (I_f) ligands, respectively. The results show a high quantity of strongly coordinated ligand (67.6 %), a low quantity of weakly bonded ligand (18.7 %) and the lowest quantity of exchanging "free" ligand (13.7 %).

Then, given the RuNPs were not purified, these percentages have been converted into ligand quantities expressed in equiv. on the basis of the ligand amount introduced for the synthesis of the NPs (0.2 equiv.).

It is important to remark that the free ligand is the one which has no interaction at all with the metal surface. Meanwhile the exchanging "free" ligand is in continuous fast exchange with the weakly bonded ligand.

Table 3.15 Quantification of the different type of interacting ligands surrounding the $Ru_x(C_7H_{15}COOH)_{0.20}$ NPs.

Type of interaction	Diffusion coefficient ($m^2.s^{-1}$)	Signal weight (%)	Quantity of ligand (equiv.)
I_s	1.7×10^{-10}	67.6	0.14
I_w	6.4×10^{-10}	18.7	0.04
I_f	1.3×10^{-9}	13.7	0.02

By applying the principle of the magic number for Ru *hcp* metal cluster, the quantities of ligand previously obtained and the mean size of the particles (*ca.* 1.65 nm) determined by TEM

allowed to estimate the number of ligands per RuNP and also the ratio of surface Ru atoms per ligand (table 3.16), providing thus an approximative mapping of the surface of the $Ru_x(C_7H_{15}COOH)_{0.20}$ NPs.

Table 3.16 Determination of the number of ligands per RuNP and of the ratio of Ru surface atoms per ligand for each type of octanoic ligands surrounding the $Ru_x(C_7H_{15}COOH)_{0.20}$ NPs

	Type of interaction	**Ligand/Ru_{NP}**	**Ru_{surf}/ligand**	**Ligand/Ru_{surf}**
I_s	Strong	23.5	4.4	0.22
I_w	Weak	6.5	16.1	0.06
I_f	Exchanging	4.8	21.8	0.04

According to the results, there is around 35 octanoic ligands ($I_s + I_w + I_f$) interacting for each 1.65 nm RuNP. Also, it was obtained an estimated number of *ca.* [23 – 24] octanoate ligands strongly interacting with the RuNP surface (I_s). This value led to *ca.* 4.4 surface Ru atoms per ligand showing that not all the surface atoms are occupied (in other words that the ruthenium surface is not totally covered by the stabilizing ligand) which leaves some place for other molecules like hydrides for instance. It is believed that these ligands are directly coordinated to the metal surface thus forming an inner shell of ligands around the NPs.

The other two type of interacting ligands have lower presence and can be considered to be present in an outer shell.[272] Their estimated numbers were *ca.* 6.5 and 4.8 per RuNP for (I_w) (weakly coordinated) and I_f, ("free" in exchange), respectively. The hypothesis is that the weakly coordinated ligands (I_w) are less grafted to the metal surface and thus they can be suitable for exchanging with the third type of ligands I_f. It is worth to point out that these ligands which forms the outer shell are in constant fast exchange, namely in equilibrium. A better view of the findings can be observed in the scheme 3.8.

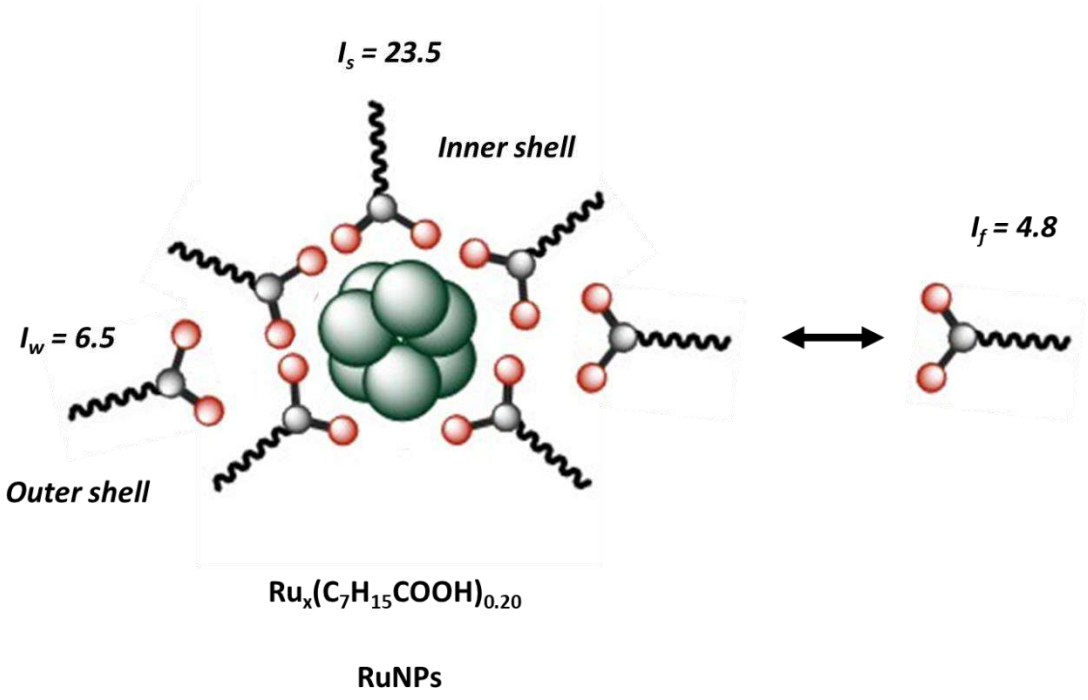

Scheme 3.8 Representation of the surface mapping of $Ru_x(C_7H_{15}COOH)_{0.20}$ NPs completed by the estimated numbers of each type of ligand per RuNP. (I_s) Strongly coordinated, (I_w) weakly coordinated and (I_f) "free"in exchange.

The presence of a weakly bonded ligand which is in constant exchange with labile stabilizing agent, it is sometime difficult to understand because it can be confused with the real free ligand (no interaction with the metal surface). Thus, in order to complete these results and try to better understand the difference between I_w/I_f ligands and totally free ligands in solution, a Nuclear Overhauser Effect (NOESY) NMR experiment was performed from the same deuterated benzene solution as for previous DOSY NMR experiment (*see* section 6.1.3.6.3).

The signals of the NOESY spectrum (figure 3.40) can be correlated with the molecular weight of the corresponding solubilized species.[273] It is admitted that a positive NOE signal corresponds to small molecules which are not interacting with the NP surface (free in solution).[274] The NOESY spectrum recorded for the $Ru_x(C_7H_{15}COOH)_{0.20}$ NPs shows only positive NOE (blue shapes) for the signal in the region [3.5 - 5.0 ppm] that belong to an impurity which is free and no interacting with the metal surface.

However, there is no positive NOE in the region [0.5 - 2.7 ppm], that corresponds to the area where the peaks of free octanoic acid are expected to appear (figure 3.40 blue signals).

Therefore, this result corroborates that there is no free ligand in the colloidal solution and that the weakly bonded ligands (I_w) are actually in fast exchange with so-called "free" exchanging carboxylates.

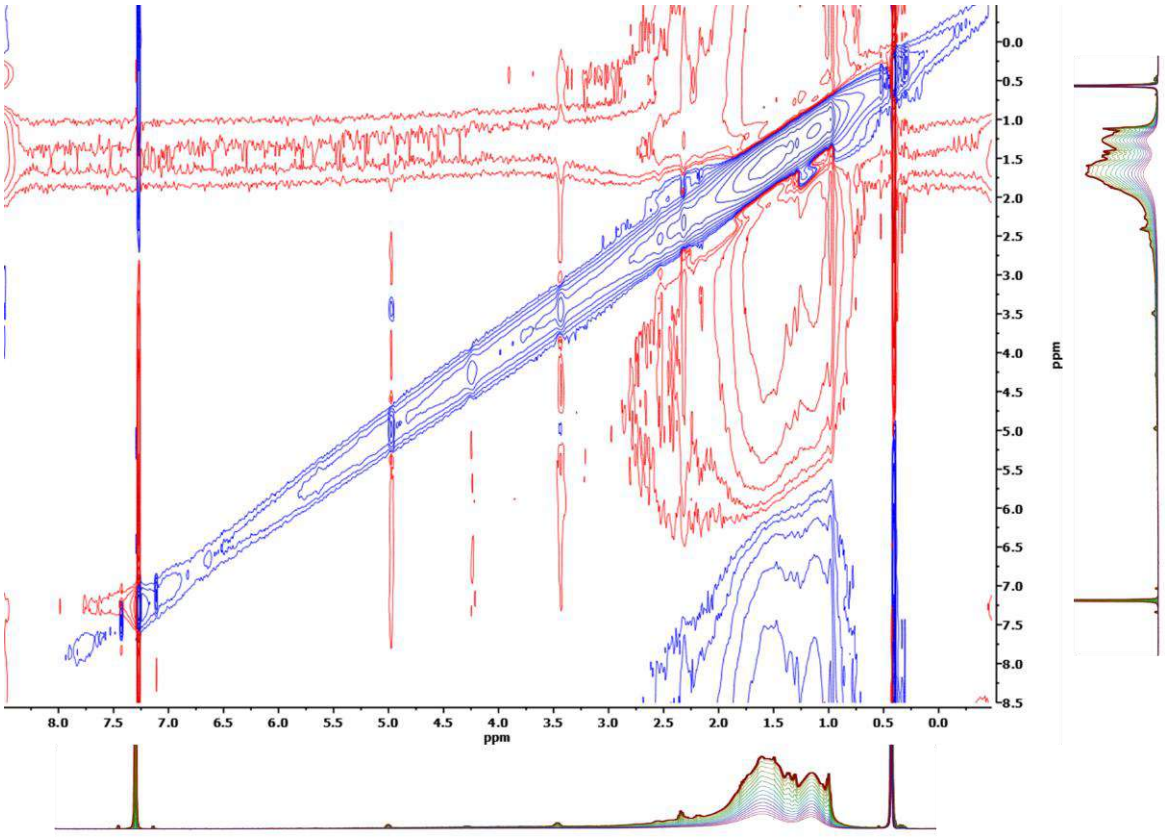

Figure 3.40 NOESY NMR spectrum (C_6D_6) of $Ru_x(C_7H_{15}COOH)_{0.20}$ NPs.

3.2.5.3.2 Microanalyses applied to $Ru_x(C_7H_{15}COOH)_{0.20}$ NPs

The surface mapping, obtained from the combined characterization techniques, offers a good approximation to the real state of the RuNP surface, the type of coordinated ligands, the variety of interactions in the hybrid material interface and the quantification of the different type of carboxylates bonded onto the $Ru_x(C_7H_{15}COOH)_{0.20}$ NPs. However, to complete the characterization study is necessary to perform microanalyses.

Elemental analysis (EA) and Inductively Coupled Plasma Atomic Emission Spectroscopy (ICP-AES) were performed to determine the carbon, hydrogen, nitrogen and ruthenium contents

in $Ru_x(C_7H_{15}COOH)_{0.20}$ NPs (see section 6.1.3.2). These analyses were performed for a batch of purified NPs.

Elemental analysis was performed aiming to corroborate if the added ligand (0.20 equiv.) remains in the sample or part of it was removed in the cleaning process (THF-pentane cycles). The results from this EA are shown in the table 3.17.

Table 3.17 C, H, N analysis of $Ru_x(C_7H_{15}COOH)_{0.20}$ NPs.

Element	Content (wt %)
C	20.7
H	2.9
N	0.0

The oxygen cannot be quantified by this analysis but considering that the whole carbon source is the octanoic acid added for the RuNPs synthesis, is possible to calculate the weight percentage of oxygen (6.8 %), meaning than 69.6 % of the sample weight is metal and 30.4 % comes from an organic source. This data can be converted to molar equivalents leading to a result of 0.31 molar equivalents of octanoic acid into the sample.

This result is slightly higher than the expected for the organic phase (0.2 equiv.), which means that the octanoic acid is not the only carbon source. This is not surprising because the elemental analysis was performed after washing the RuNPs by several cycles of pentane-THF and previously the presence of coordinated THF (FTIR) was observed. Therefore, it can be implied that the THF is present into the purified sample and affect the elemental analysis measurements.

The $Ru_x(C_7H_{15}COOH)_{0.20}$ NPs metal content can be obtained by (ICP-AES).[275] The analysis was performed for the purified RuNPs in the same way that the elemental analysis (*see* section 6.1.3.2) was done. The results are presented in the table 3.18.

Table 3.18 ICP-AES analysis of $Ru_x(C_7H_{15}COOH)_{0.20}$ NPs.

Element	Content (wt %)
Ru	62.2

The ICP results indicate that the particles contain 62.2 wt% of ruthenium, which leads to 37.8 wt% of organics. The result can also be transformed to molar equivalents, which indicates that if all the organic source comes from octanoic acid, it should be around 0.43 equiv. of it, being this the double of the added ligand into the NPs synthesis. However, the presence of another organic molecules attached at the NPs surface, once the purification process is performed (THF), is known. Still, the obtained result indicates a notable yield of RuNPs into the analyzed sample. [262]

3.2.5.3.3 Quantification of Reactive Hydrogen at the Surface of $Ru_x(C_7H_{15}COOH)_{0.20}$ NPs

The number of octanoates ligands that surround the RuNPs has been estimated through NMR analyses. But given the synthesis conditions applied to produce the particles, hydrogen atoms are expected to be coordinated at the RuNPs surface.

From previous published work, it has been seen than these hydrides are highly reactive.[59] Therefore, it is possible to titrate the reactive hydrogen that lies on the RuNPs surface by exposing the $Ru_x(C_7H_{15}COOH)_{0.20}$ NPs to 2-norbornene, as previously described for the RuNPs stabilized by ethanoic acid. For this methodology, the RuNPs were used as a reductive catalyst for the olefin, the procedure was performed at r.t. with no extra hydrogen added (*see* section 6.1.4.1). The alkene conversion was low but sufficient to be detected by GC analysis (*see* section 6.1.3.4).

The reaction performance is an indirect way to quantify the number of reactive hydrogens at r.t., because the olefin can only be reduced by the hydrogen present at the RuNPs surface (scheme 3.9). Thus, the GC obtained data allowed to calculate the hydrogen surface coverage on the $Ru_x(C_7H_{15}COOH)_{0.20}$ NPs by taking into account the RuNPs size obtained by TEM (*ca.* 1.65 nm), their crystalline structure (hcp) and the magic number for metal clusters.

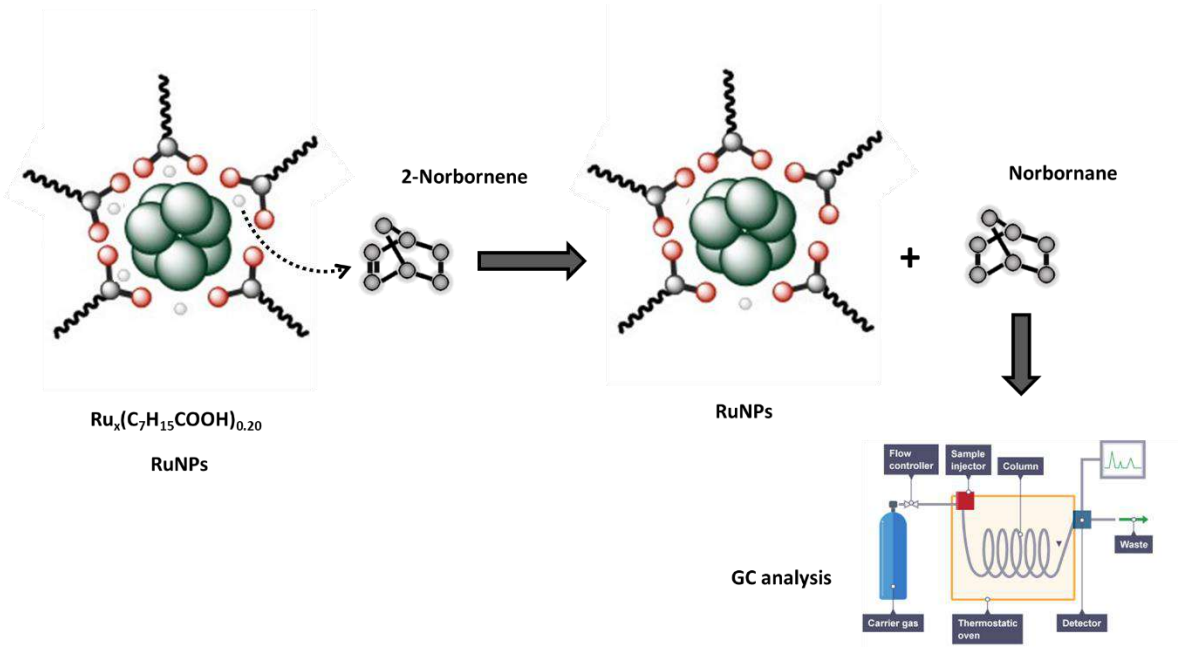

Scheme 3.9 Hydrides titration at the surface of $Ru_x(C_7H_{15}COOH)_{0.20}$ NPs by the norbornene test.

The obtained value was *ca*. 0.2 reactive hydrogens per ruthenium surface atom (0.2 H_{reac}/Ru_{surf}) at r.t. Considering that there are *ca.* [100 – 110 ruthenium surface atoms], this result leads to at least *ca.* 21 hydrogens per RuNP (21 H/Ru_{NP}). It is worthy to note that the number of hydrides per Ru_{surf} is similar to that of octanoates (see table 3.15).

Given the previous estimation of strongly coordinated ligands by NMR (*ca.* 23 - 24 octanoates) and the hydride quantification (*ca.* 21), an approximated composition of the $Ru_x(C_7H_{15}COOH)_{0.20}$ NPs can be proposed, as shown on scheme 3.10.

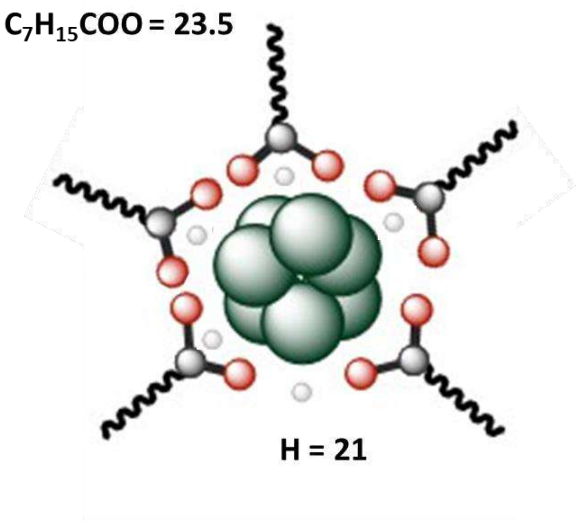

Scheme 3.10 Approximated composition of $Ru_x(C_7H_{15}COOH)_{0.20}$ NPs

In the next section, theoretical tools will be used in order to apprehend the surface composition of the $Ru_x(C_7H_{15}COOH)_{0.20}$ NPs.

3.2.5.3.4 Titration of $Ru_x(C_7H_{15}COOH)_{0.20}$ NPs by DFT calculations

A combination of theoretical and experimental characterization has been proven to be an efficient approach for get a relevant map of the surface of RuNPs stabilized with carboxylic acids (*see* chapters II and section 3.1). For example, both agreed to evaluate the surface composition of $Ru_x(CH_3COOH)_{0.40}$ NPs, to be around 0.4 ethanoates and [0.4 – 0.6] hydrides per ruthenium surface atom. The minimum value in this last range was obtained from experimental techniques, assumed to underestimate the actual number of surface hydrides, and the second one by DFT calculations. It was concluded that the theoretical titration can be used to map the NPs surface or to corroborate the experimental findings. Therefore, it is possible to obtain reliable theoretical data by using the Ru_{55} NP model (*see* section 6.2.1), DFT-PBE energies, and the *ab initio* thermodynamics procedure (*see* section 6.2.6).

Similar procedure, but based mainly in the theoretical titration, was performed for the $Ru_x(C_4H_9COOH)_{0.30}$ NPs. A surface coverage value of 0.3 pentanoates and the same amount of hydrides per ruthenium surface atom has been found

The surface mapping obtained for the $Ru_x(C_7H_{15}COOH)_{0.20}$ NPs by NMR studies for coordinated ligands and norbornene test for hydrides quantification revealed numbers equal to *ca.* 0.2 octanoates and *ca.* 0.2 hydrides per ruthenium surface atom.

Thus, on the surface of the Ru_{55} NP model different co-adsorbed quantities of octanoates and hydrogen were set up, as previously performed with other NPs systems . The structures were then optimized and the DFT energies were obtained (*see* section 6.2.2). We shall again recall that DFT energies are calculated for a 0 K, 0 Pa system in vacuum, and that the aim of the *ab initio* thermodynamics method is to introduce thermodynamic variables (*T*, *p*) for the same system in equilibrium with a reservoir of stabilizing species. This strengthens with the comparison with experimental findings and it is expected to shed light on the actual surface state of the metal NP.

The *ab initio* thermodynamics program has a database of standard enthalpies and entropies of ligands, in gas phase or in a solvent, gives the possibility to obtain Gibbs free energies in a suitable format for surface plotting softwares. This graphical representation highlights which is the most stable optimized structure when the adsorbed ligands are in equilibrium at certain thermodynamic conditions (*T*, *p*).

Owing to previous theoretical analysis here reported and the experimental findings for this nanosytem, it can be infered than the $Ru_x(C_7H_{15}COOH)_{0.20}$ NPs will have a relatively high amount of octanoate and a low amount of hydrides, i.e. significantly lower than 1.3 H/Ru_{surf}.[93] Therefore, it is not necessary to study structures with possess a lot of hydrides and a low quantity of stabilizing agent, because they will not be stable at least in the synthetic thermodynamic conditions.

The selected structures that have been considered are presented in figure 3.41. The information obtained from these built nanostructures will be taken as a basis for corroborating the information found experimentally during the ligand coverage titration.

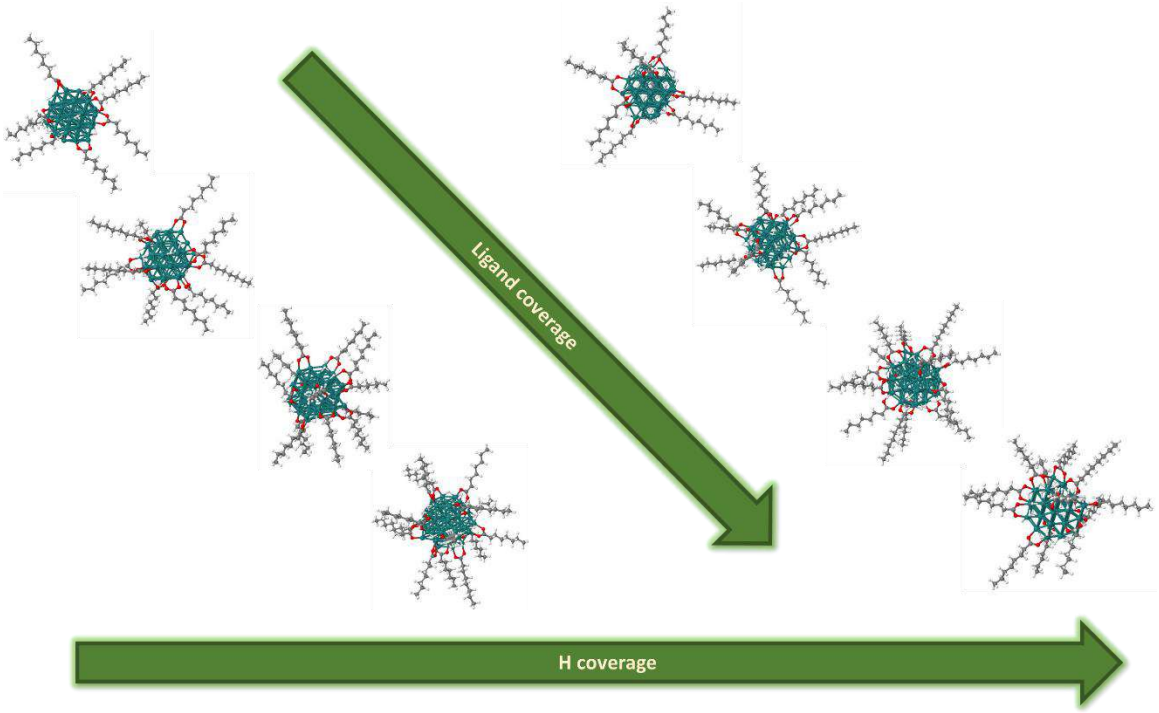

Figure 3.41 Selection of Ru_{55} NP optimized structures with different ligand surface coverage ($C_7H_{15}COO$ & H).

As done for the theoretical titration performed form the $Ru_x(C_4H_9COOH)_{0.30}$ NPs, the Ru_{55} NP model was built with a low quantity of hydrides [8 – 31] whereas the quantity of carboxylates put on the Ru_{55} NP model was decreased [8 - 14] due to what has been observed with the RuNPs stabilized by pentanoic acid (longer the alkyl chain, lower the carboxyl surface coverage).

An easy O-H dissociation has also been assumed, based on the experimental techniques where it was pointed out that the RuNPs are stabilized by the deprotonated octanoic acid. The considered geometries were built with only octanoates, meaning that the acid proton was directly coordinated onto the Ru_{55} NP surface. No internal recombination was observed during after geometry optimizations.

Eight different structures whit different coverage values of the co-adsorbed ligands were set up (table 3.19). These structures were optimized, and their adsorption energies of the different ligands deposed on each Ru_{55} NP structure are described in section appendixes A.1 and B.2.

Table 3.19 Optimized structures used for the $Ru_x(C_7H_{15}COOH)_{0.20}$ DFT surface titration. The total number and coverage ratio of coordinated ligands and its corresponding DFT energy (eV) are also provided. (a) Number of hydrides coming from the dissociative adsorption of H_2; (b) total number of hydrides coming from a and from the $C_7H_{15}COO$-H bond dissociation.

#	E (eV)	nH (a)	nH/Ru_surf (a)	nH* (b)	nH*/Ru_surf (b)	nC7H15COOH	Name
67	-1,210.88	0	*0.0*	8	*0.2*	8	$(C_7H_{15}COO)_8H_8$
68	-1,276.40	17	*0.4*	25	*0.6*	8	$(C_7H_{15}COO)_8H_{25}$
69	-1,406.93	0	*0.0*	10	*0.2*	10	$(C_7H_{15}COO)_{10}H_{10}$
70	-1,471.88	17	*0.4*	27	*0.6*	10	$(C_7H_{15}COO)_{10}H_{27}$
71	-1,603.41	0	*0.0*	12	*0.3*	12	$(C_7H_{15}COO)_{12}H_{12}$
72	-1,667.23	17	*0.4*	29	*0.7*	12	$(C_7H_{15}COO)_{12}H_{29}$
73	-1,799.42	0	*0.0*	14	*0.3*	14	$(C_7H_{15}COO)_{14}H_{14}$
74	-1,862.33	17	*0.4*	31	*0.7*	14	$(C_7H_{15}COO)_{14}H_{31}$

The Gibbs free energies ($\Delta_a G°$) were obtained for these eight optimized structures by setting the temperature at 300 K. This was possible by using the *ab initio* thermodynamics methodology where the ligand-metal vibration corrections were accounted for (*see* section 6.2.7 and appendix D). As already done in the pentanoic acid case, the metal-COO corrections were transferred from the ethanoic acid case. This approximation can safely be used because the most important vibrational corrections are originated from H-metal vibrations and not from the carboxylic moiety.

The Gibbs free energies calculations were obtaining by using the chemical potentials of octanoic acids solvated in THF (*see* section 6.2.6). Again, a phase diagram has been calculated by considering the octanoic acid concentration and hydrogen pressure in equilibrium with the Ru_{55} NP metal surface (p_{H_2}, [$C_7H_{15}COOH$]) (figure 3.42).

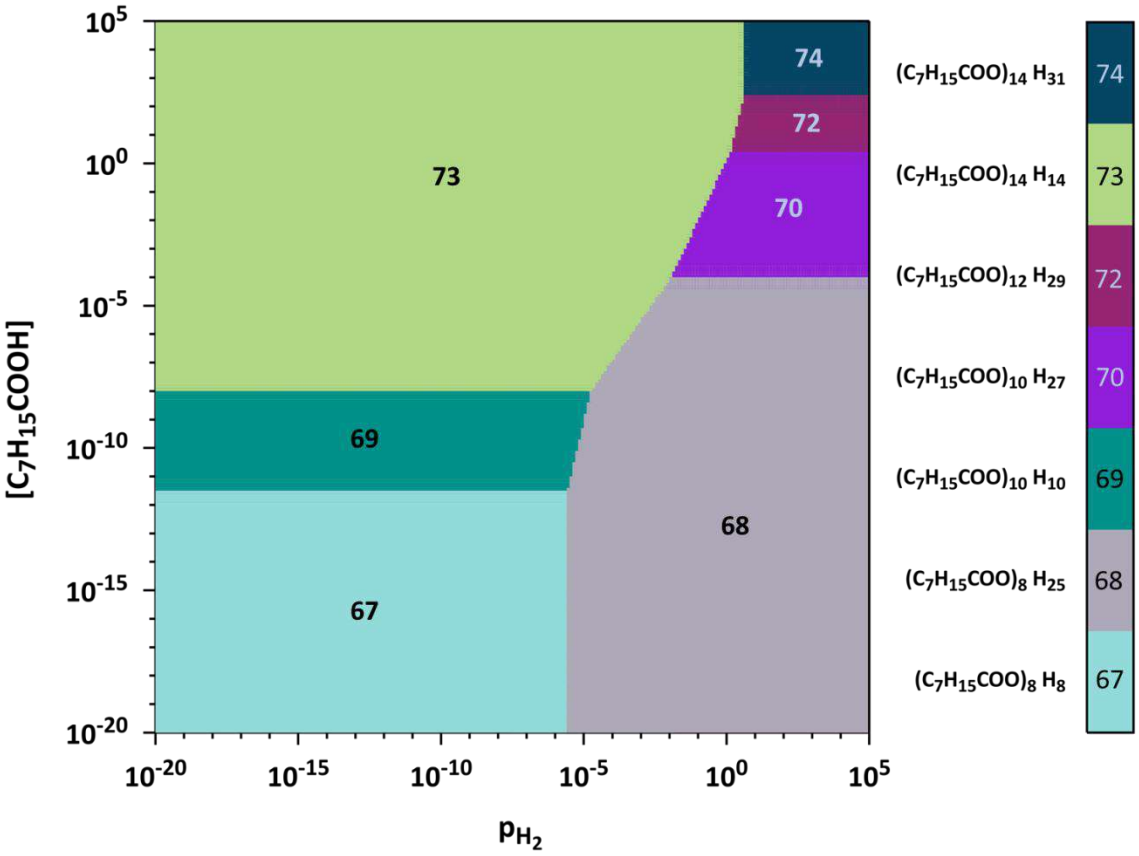

Figure 3.42 $\Delta_a G°$ (p_{H_2}, [$C_7H_{15}COOH$]) phase diagram for H_2 (gas) and $C_7H_{15}COOH$ (liquid) adsorption on Ru_{55} NP at 300 K (pressure in bar, concentration in mol.L^{-1}).

The phase diagram shows that only one of the optimized structures (71) is not stable in any range of the displayed graphic. In the diagram, it can be seen that the most stables structures have low quantity of hydrides together with a high quantity of octanoates.

The low and high concentration and pressure domains considered in the phase diagram are displayed only to give reference data, although they do not correspond to the actual experimental synthesis conditions. Regarding the experimental octanoic acid concentration, we considered the amount of ligand introduced for the NPs synthesis. It can be considered as quite accurate due to the data obtained by DOSY analysis, that reveal an absence of free octanoic acid and that all the added ligand interacts with the NPs surface. Meanwhile, similar calculations were performed for the hydrogen pressure taken into account the remaining reductive entities after the RuNPs synthesis (hydrogen titration).

The obtained results indicate that at the equilibrium there is a concentration of octanoic acid of *ca.* $10^{-3.0}$ mol.L^{-1}, while for the hydrogen pressure is *ca.* [10^{-4} – 10^{-3} bar]. For this reason, the area to consider in the phase diagram for p_{H_2} and [$C_7H_{15}COOH$] is in the range [10^{-5} - 10^{-2} bar] and [10^{-4} - 10^{-2} mol.L^{-1}], respectively. The stability domains that lie correspond to isomers 73 & 70 and possibly to structure 68, whose corresponding structures are given in figure 3.43. The coordinates of these structures are reported in section appendix F

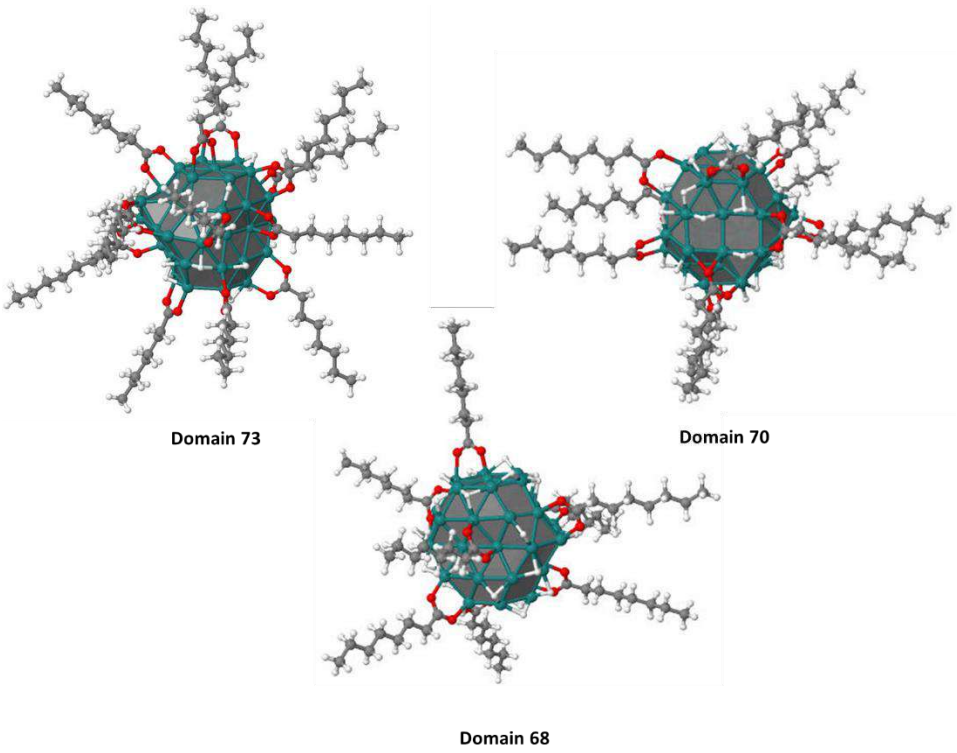

Figure 3.43 More stable [Ru_{55}] NP found at 300 K for $Ru_x(C_7H_{15}COOH)_{0.20}$ NPs. (Domain 73: $Ru_{55}(C_7H_{15}COO)_{14}(H)_{14}$; domain 70: $Ru_{55}(C_7H_{15}COO)_{10}(H)_{27}$; domain 68: $Ru_{55}(C_7H_{15}COO)_8(H)_{25}$.

According to the phase diagram displayed before there are two stables structures for the $Ru_x(C_7H_{15}COOH)_{0.20}$ NPs. One is stable in a wide range of pressure and concentrations, it has the same number of each capping ligand, namely 14 octanoates and 14 hydrides which come from the octanoic acid deprotonation (figure 3.43, domain 73). This composition was also found for the $Ru_x(C_4H_9COOH)_{0.30}$ NPs (14 pentanoates and 14 hydrides). The other stable structure which is relevant owing to the synthesis conditions, exhibits 10 octanoates and 27 hydrides which can be considered as originating from the ligand deprotonation and from the reaction media (figure 3.45, domain 70). In this case, the results indicate a similar trend as previously observed in the cases of

ethanoic and pentanoic acids: the longer the alkyl chain, the lower is the quantity of carboxylates needed to stabilize the metal nanoparticles.

After conversion of the absolute number of surface species to coverage ratio found in the domain 70 & 73, the theoretical titration gives a [0.2 - 0.3] $C_7H_{15}COO/Ru_{surf}$ and [0.3 – 0.6] H/Ru_{surf} surface composition. These data can be extrapolated to the 1.65 nm Ru *hcp* NPs stabilized with octanoic acid which has *ca.* [100 – 110 ruthenium atoms] in its surface (*ca.* 60.0 %). As a result, the theoretical titration indicates that the quantity of octanoates surrounding the $Ru_x(C_7H_{15}COOH)_{0.20}$ NPs should be around [21 – 31 molecules], meanwile for hydrides should be in the range of [31 - 63 molecules].

The DFT titration results can be compared with the experimental ones obtained by DOSY NMR analysis and hydrides titration, where it was observed similar behavior (low quantity of hydrides and high amount of octanoates). As can be seen in table 3.20, both techniques are in very good agreement providing close values. This combined approach gives as an outcome a nice accurate and precise surface mapping of this $Ru_x(C_7H_{15}COOH)_{0.20}$ NPs. In other words, the combination of the experimental and theoretical characterization gives the possibility to have an overall picture of this hybrid material that is not easy to characterize due to its size and to several more issues, such as the titration of such low-concentration surface species by DOSY-NMR.

Table 3.20 Comparison between the experimental and theoretical surface coverage characterization of $Ru_x(C_7H_{15}COOH)_{0.20}$ NPs.

Approach	**Octanoate ($C_7H_{15}COO/Ru_{surf}$)**	**Hydrides (H/Ru_{surf})**
Experimental	0.2	0.2
Theoretical	[0.2 – 0.3]	[0.3 – 0.6]

Owing the results obtained by the theoretical titration and its reliability, some trends can be evaluated. For example, it was observed that RuNPs can be synthesized by using diverse carboxylic acids which have different alkyl chain length. But curiously, it was detected that the shorter the alkyl chain length of the ligand the higher was the quantity of stabilizers needed to form similar size of RuNPs. In order to corroborate this trend, a parallel can be performed with the results obtained by the DFT titration (table 3.21).

Table 3.21 Comparison between experimental and theoretical titrations of RuNPs stabilized by the studied carboxylic acid.

RuNPs System	Quantity of ligand (equiv.)	Mean size (nm)	Experimental titration		Theoretical titration	
			Carboxylate ($RCOO/Ru_{surf}$)	Hydrides (H/Ru_{surf})	Carboxylate ($RCOO/Ru_{surf}$)	Hydrides (H/Ru_{surf})
$Ru_x(CH_3COOH)_{0.40}$	0.40	1.51	0.3	0.3	0.4	[0.4 – 0.6]
$Ru_x(C_4H_9COOH)_{0.30}$	0.30	1.47	- - -	- - -	0.3	0.3
$Ru_x(C_7H_{15}COOH)_{0.20}$	0.20	1.65	0.2	0.2	[0.2 -0.3]	[0.3 – 0.6]

This comparison highlights the high agreement achieved by applying in parallel experimental and theoretical titrations of the RuNPs stabilized by carboxylic acids bearing different alkyl chain lengths. From these data it can be proposed that the longer the alkyl chain length of the ligand, the lesser the quantity of stabilizing agent needed to stabilize the nanosystem. This can be explained by a steric hindrance effect of the alkyl chain of the ligand that is expected to increase with its length increase, that can reinforce the stabilization effect of the ligand.

3.2.5.3.5 Surface Saturation of $Ru_x(C_7H_{15}COOH)_{0.20}$ NPs

In section 3.2.5.3.1, DOSY NMR analysis allowed to determine the ratio between coordinated octanoate ligands and surface ruthenium atoms leading to a value of 4,4 Ru_{surf}/octanoate ligand. Given this low quantity of coordinated octanoates at the RuNP surface the question of the saturation of this NP surface arises. It can be assumed that the metal surface is not completely crowded and even if the formed $Ru_x(C_7H_{15}COOH)_{0.20}$ NPs are well-stabilized, it could host a higher quantity of carboxylates species. With the aim to try answering this question, a complementary solution NMR study combining 1D and 2D NMR experiments (^1H, DOSY, NOESY) was performed on $Ru_x(C_7H_{15}COOH)_{0.20}$ NPs by adding an increasing quantity of ligand in the colloidal solution and recording new NMR data (*see* section 6.1.3.6). Since the experiments were done in the same setup, the grease presented in the NMR spectrum was taken as internal reference.

First, 0.05 equiv. of octanoic acid was added and the reaction mixture was sonicated during 30 min before recording the NMR data. This methodology was then pursued by adding step by step 0.05 eq more of ligand in order to get up to 0.10, 0.15 and 0.20 equiv. of added ligand (leading to a series of experiments in the presence of 0.25, 0.30, 0.35, and 0.40 ligand in total) in the NMR tube. Evolution of the NMR signals depending on the quantity of free ligand added was thus studied using as reference points the ^{1}H, DOSY, NOESY NMR data described in section 3.2.5.3.1 for the starting $Ru_x(C_7H_{15}COOH)_{0.20}$ NPs.

^{1}H NMR data recorded for each ligand addition are presented in figure 3.44. A signal appeared in the region [10.5 - 12.5 ppm] where the acidic proton is expected. This signal is very difficult to distinguish for a total quantity of ligand of 0.25 equiv., but it displays a better definition when increasing the ligand content. In the region [0.5 - 2.7 ppm] where the signals of the alkyl chain of octanoic acid are expected, the very broad signal visible for the starting RuNPs decreased while increasing the ligand amount. In parallel sharp signals appeared whose positions correspond to the peaks of free octanoic acid.

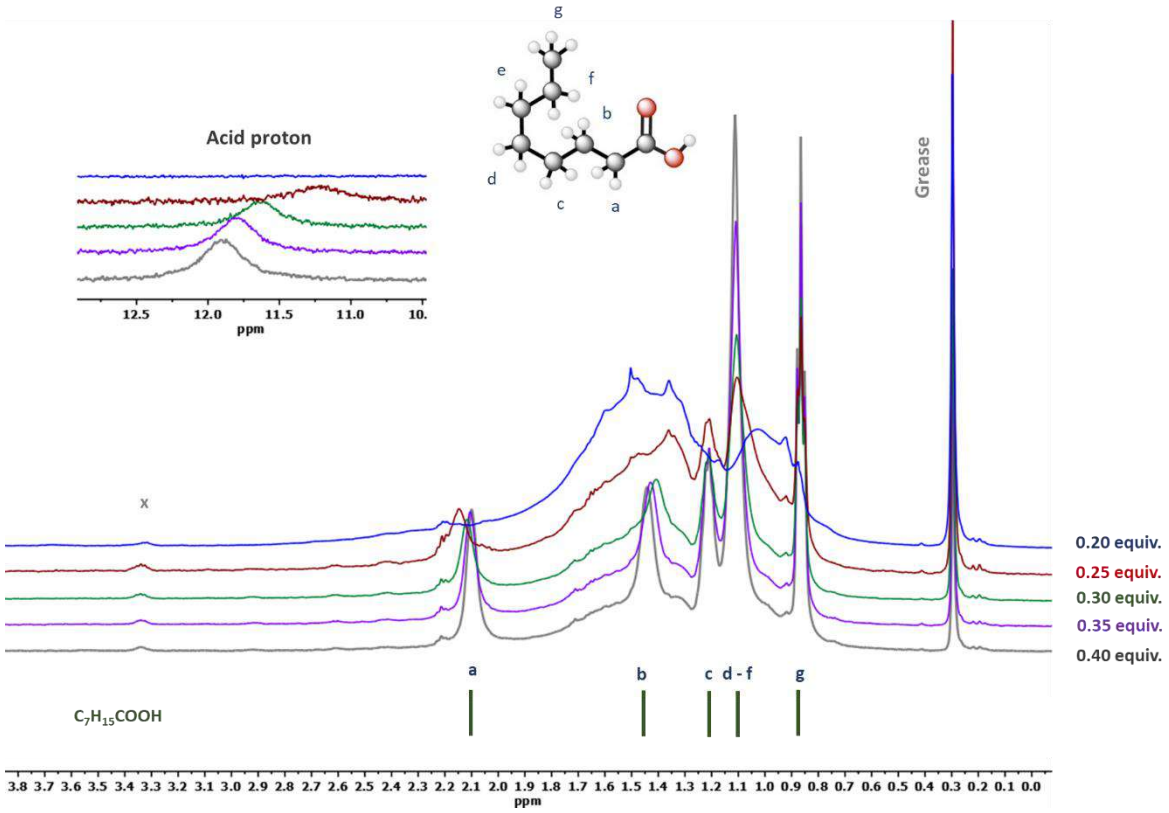

Figure 3.44 ^{1}H-NMR (C_6D_6) spectra of $Ru_x(C_7H_{15}COOH)_{0.20}$ NPs with different ligand addition. (blue) reference, 0.20 equiv.; (red) + 25 %, 0.25 equiv.; (green) + 50 %, 0.30 equiv.; (purple) + 75 %, 0.35 equiv.; (gray) + 100 %, 0.40 equiv. $C_7H_{15}COOH$ protons chemical shifts are represented in green bars at the bottom of the figure.

These NMR experiments clearly evidence the presence of free octanoic acid or/and exchanging ligand in the solution from 0.30 equiv. of total ligand (figure 3.44 green profile) and this in increasing quantity when adding more ligand in the NMR tube. However even at a high quantity of added ligand (100 %; 0.40 equiv. in total; figure 3.44 gray profile) broad peaks remain visible which are the signature of remaining coordinated ligands at the RuNPs surface. These signals appear less intense than for the starting $Ru_x(C_7H_{15}COOH)_{0.20}$ RuNPs because of the intensity of the other signals.

The increase of the sharper signals is a direct proof of the escalation of the organic molecules mobility in the solution. However, at this stage of the study these molecules can be either free in solution, or weakly interacting (I_w) with the RuNP surface or in fast exchange (I_f). The only possible conclusion is that there is more ligand that can be exchanged or that can be free in

the solution. 2D DOSY NMR experiments were then carried out for each step of the addition of free octanoic acid in order to estimate the quantities of ligands depending on their nature (I_s, I_w, I_f).

From the ^{1}H DOSY NMR results (table 3.22) it can be observed that the quantity of strongly coordinated ligands (I_s) did not vary so much and remained in the range [20.7 – 25.0 L/Ru_{NP}] despite the increasing addition of free octanoic acid in the NMR tube (*see* section 6.1.3.6.2). This observation leads to the conclusion that no other octanoate got coordinated at the surface of the $Ru_x(C_7H_{15}COOH)_{0.20}$ NPs probably because their surface was already saturated or due to their steric hindrance. It can also be inferred that no coordinated ligands were released from the surface of the particles and that the strongly coordinated ligands form a strongly protective ligand shell.[276]

This assumption is not in contradiction of the possible coordination of other small moieties like THF due to its size in comparison with the carboxylates (coordination in bridging mode forming a five ring metallacycle).

The DOSY calculations need to be taken carefully due to the error presented in DOSY NMR measurements which is at minimum 8.0 % and can increase depending on the experimental variable and the type of equipment used for the study.[244]

Table 3.22 Estimated quantities of the different type of interacting ligands in the $Ru_x(C_7H_{15}COOH)_{0.20}$ NPs determined by DOSY NMR data.

Ligand added (equiv.)	**Total ligand (equiv.)**	I_s **($C_7H_{15}COOH/Ru_{NP}$)**	I_w **($C_7H_{15}COOH/Ru_{NP}$)**	I_f **($C_7H_{15}COOH/Ru_{NP}$)**
0.00	0.20	23.5	6.5	4.8
0.05	0.25	25.0	7.1	11.5
0.10	0.30	23.2	8.6	20.4
0.15	0.35	21.8	8.8	30.2
0.20	0.40	20.7	7.7	41.1

When looking at the weakly coordinated ligands (I_w), it can be seen that it is possible to allocate one or two extra molecules which are in an outer shell of the RuNPs. This assumption can be observed by the increasing trend of this type of ligand, till is stabilized around eight carboxylates per RuNP. In other words, this shell was not completely full. According to this result,

the saturation of the RuNP (strongly and weakly coordinated ligand, inner and outer shell respectively) was obtained when it was added among [0.05 or 0.10 extra equiv.] to preformed $Ru_x(C_7H_{15}COOH)_{0.20}$ NPs (scheme 3.11). In terms of synthesis, the RuNPs saturation will be obtained when between [0.25 and 0.30 equiv.] of octanoic acid is added into the setup for the RuNPs formation.

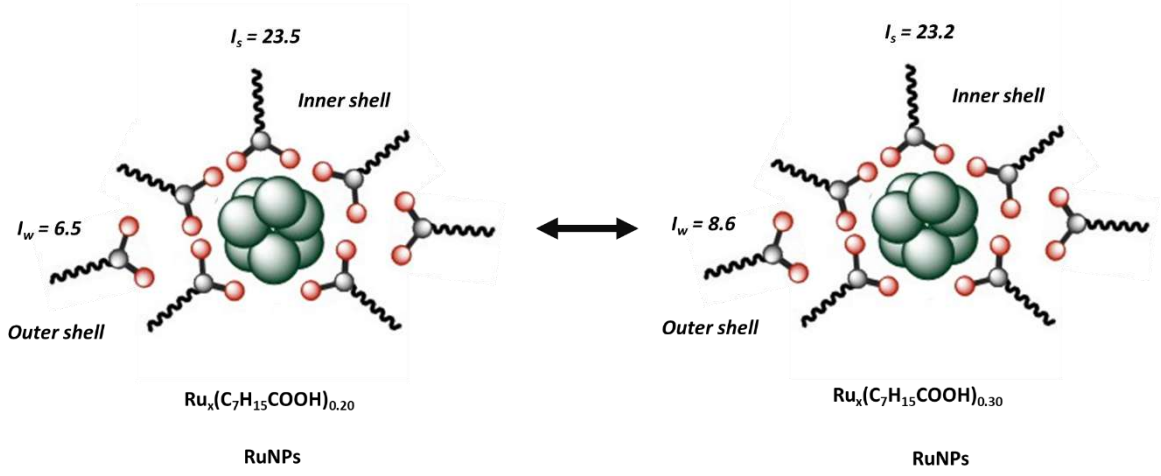

Scheme 3.11 Representation of the evolution of the quantity of I_s and I_w ligands depending on the quantity of ligand added. The scheme is focus on the RuNPs saturation that was obtained for the $Ru_x(C_7H_{15}COOH)_{0.30}$ NPs.

Studies have demonstrated that with 0.20 equiv. of octanoic acid it was possible to almost fully covered the inner and outer shell of a 1.65 nm RuNPs. The addition between [0.05 – 0.10] equiv. has been considered as the surface saturation point of these $Ru_x(C_7H_{15}COOH)_{0.20}$ NPs. Also, it was observed that the addition of extra ligand does not affect the inner shell (I_s) of this system (no release or incorporation of ligand). In addition, the quantity of weakly coordinated ligand (I_w) is maintained after 0.10 equiv. of ligand is added meanwhile the amount of free exchanging ligand increases (I_f).

NMR results indicate that there was no significant variation of the number of octanoate ligands in the inner (I_s) and outer (I_w) ligand shells, one can wonder on a hydrodynamic size compression or expansion depending on the quantity of extra ligand added.[[277],[278]] With the objective to find an answer to this question, it is reported in table 3.23 the hydrodynamic diameters of the different I_s and I_w ligands for each amount of octanoic acid added in the NMR tube.

The calculation of the hydrodynamic diameter of the strongly coordinated ligands will determine if the main entity of the hybrid material (inner shell) stand or it is modified. Also, it is plausible to observe the ligand addition influence in the outer shell, which should be decreased with each addition approaching to the hydrodynamic size of the free octanoic acid monomer (0.5 nm).

It can be seen that the hydrodynamic diameter of the strongly coordinated ligands (I_s) remains almost the same (size range 3.8-4.1 nm) even at high quantity of octanoic acid added. On the other hand, the values calculated for weakly bonded and exchanging ligands (I_w) show a decrease of the hydrodynamic size from *ca.* [1.0 to 0.7 nm]. This can be due to an increase of the "free" fast exchanging ligand in comparison with the octanoic moieties weakly coordinated. To remember that the I_w ligands is the average of weakly bonded octanoates and the "free" exchanging ligands.

Table 3.23 Hydrodynamic diameters *vs* the extra-ligand added for preformed $Ru_x(C_7H_{15}COOH)_{0.20}$ NPs.

Ligand added (equiv.)	**Total ligand (equiv.)**	**Hydrodynamic diameter**	
		I_s (nm)	I_w (nm)
0.00	0.20	3.8	1.04
0.05	0.25	4.0	0.79
0.10	0.30	4.3	0.74
0.15	0.35	4.0	0.70
0.20	0.40	4.1	0.69

The evidence reported from the DOSY analyses are not enough to determine if there is a compression or extension of the inner shell of the nanoparticles, due to the error presented in the measurements. Therefore, to know more about the metal component behavior, a TEM analysis was performed for the $Ru_x(C_7H_{15}COOH)_{0.20}$ NPs once + 100 % of ligand was added. Meaning that the analysis was performed after the last NMR experiment which has 0.40 equiv. of octanoic acid into the dissolved RuNPs.

The microscopy analysis was obtained from the deposition of a single drop of the deuterated solution onto a holey carbon-covered copper grid (*see* section 6.1.3.1). The TEM

micrographs shows that the RuNPs have similar morphology as the observed for $Ru_x(C_7H_{15}COOH)_{0.20}$ NPs (figure 3.45 b *vs* c). The mean size of the $Ru_x(C_7H_{15}COOH)_{0.20\ +0.20}$ NPs (calculated by fast counting) was *ca.* 1.68 ± 0.41 nm, which is quite similar as the achieved from preformed $Ru_x(C_7H_{15}COOH)_{0.20}$ NPs (*ca.* 1.65 nm). As a conclusion, it can be said that the metal component of the RuNPs was not affected by adding extra quantity of ligand.

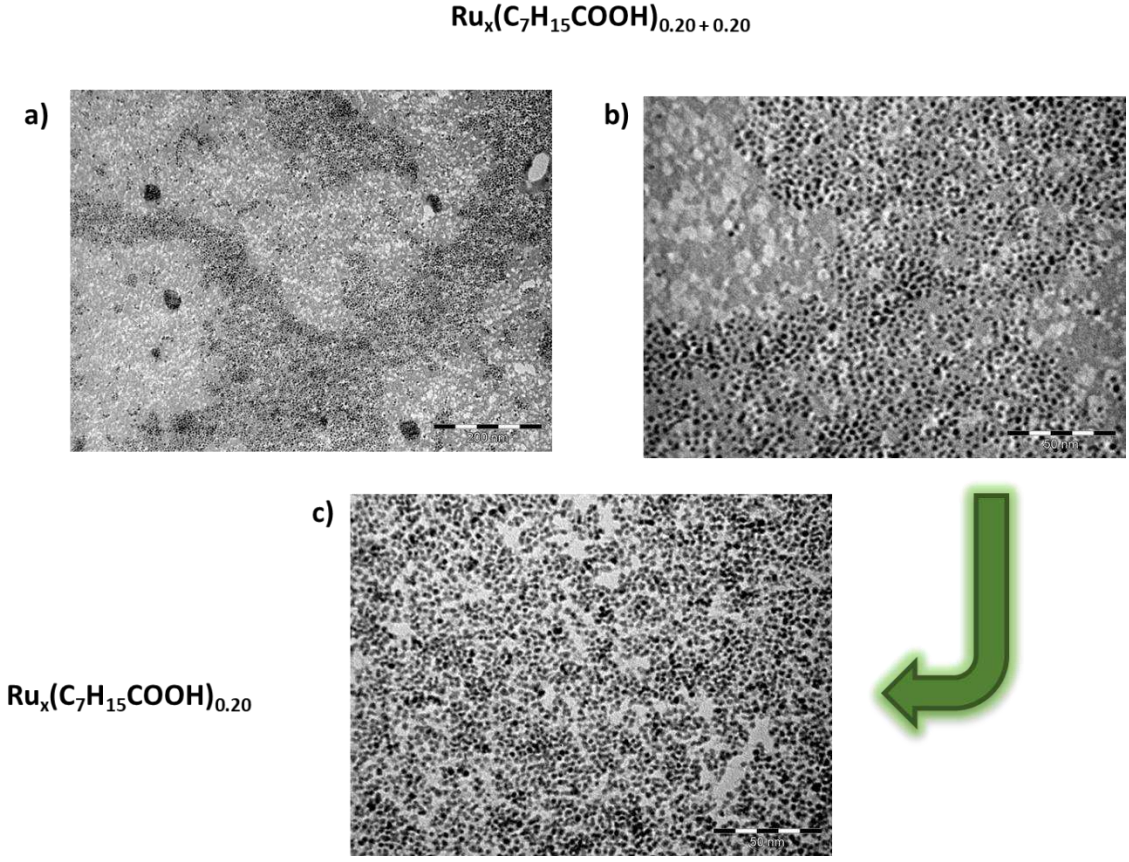

Figure 3.45 TEM micrographs of $Ru_x(C_7H_{15}COOH)_{0.20\ +0.20}$ NPs; (a) general view, scale bar: 200 nm; (b) focus on the nanosystems, scale bar: 50 nm; (c) micrograph of initial $Ru_x(C_7H_{15}COOH)_{0.20}$ NPs; scale bar: 50 nm.

Even with all these studies, it is difficult to identify the difference between free octanoic acid and "free" fast exchanging ligand (I_f). Therefore, NOESY NMR data were also recorded for each ligand addition right after the DOSY analysis. It is important to remind that a positive NOE indicates an organic moiety that is completely free which has no interaction with the RuNP surface (*see* section 6.1.3.6.3).

No positive NOE signals were observed for a low addition of extra ligand, even when the ^{1}H NMR indicates the presence of sharp peaks. This can be explained by the fact that the biggest species have a higher weight on the NOE spectra.

However, for the last addition of octanoic acid, $Ru_x(C_7H_{15}COOH)_{0.20\,+0.20}$ NPs, at least three different signals that present a positive NOE were found at *ca.* 2.2, 1.5 and 1.3 ppm. These chemical shifts are similar to those of the α, β and γ protons of the free octanoic acid (figure 3.46 blue signals). From these results, it can be concluded that after addition of 0.2 equiv. of octanoic acid a part of it is clearly free and does not exchange with ligands interacting at the metal surface. These extra octanoic acid molecules seem to be totally free in the solution.

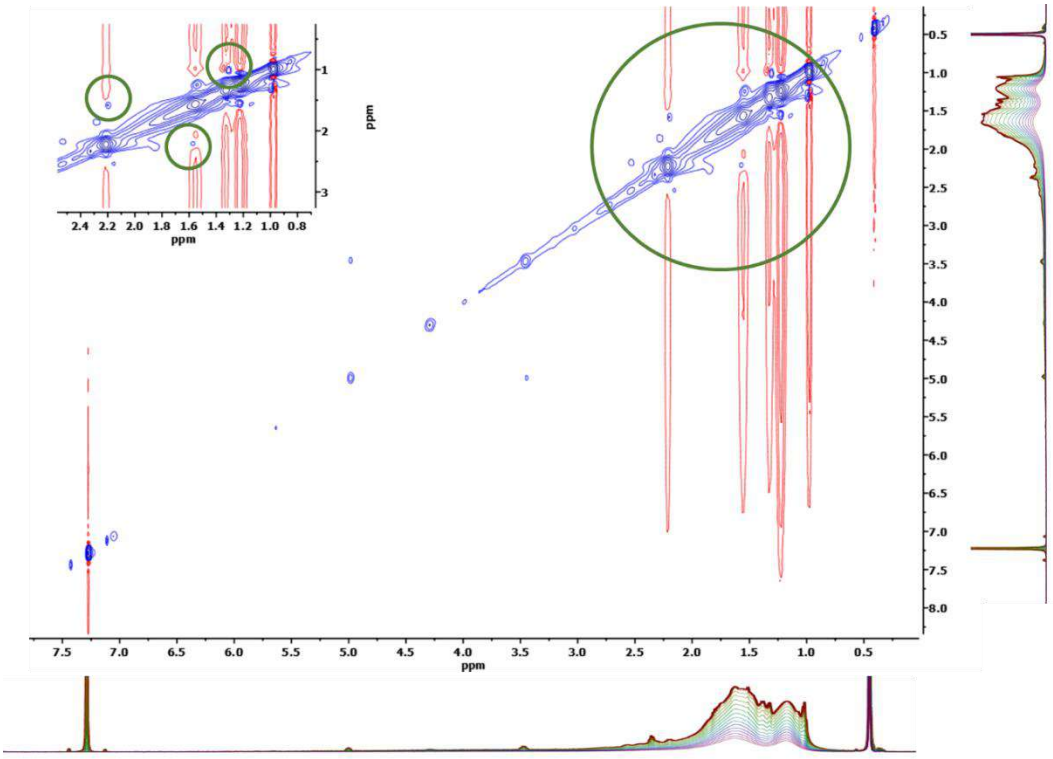

Figure 3.46 NOESY-NMR spectrum (C_6D_6) obtained for $Ru_x(C_7H_{15}COOH)_{0.20\,+0.20}$ NPs. Positive NOE is highlighted in green circles.

3.2.5.3.6 Exposure of $Ru_x(C_7H_{15}COOH)_{0.20}$ NPs under ^{13}CO Atmosphere

It is well-known in the field of MNPs that establishing the location of the capping ligands is highly helpful to understand better the catalytic reactivity at the MNPs surface.[279] Thus, in order to complete the surface mapping of the $Ru_x(C_7H_{15}COOH)_{0.20}$ NPs, it is worthy to know which sites of the metal surface are available to host extra molecules (like ligands, hydrides or CO) or perform catalysis.[280]

Solid state-NMR spectroscopy is a powerful tool to get information not only concerning the ligand atoms that are close to the MNPs surface, as it was described before, but also to evaluate the presence of potential active sites at the MNP surface. For that purpose, CO can be used as a probe molecule by reacting it with preformed RuNPs. By this way, trustworthy information can be reached about the available sites for catalysis in different nanosystems.

Previous published works dictates that the coordination of CO at RuNPs surface can take place in terminal, bridging or multicarbonyl modes. The knowledge on the existing coordination modes can be correlated to the nature of active sites present at the NP surface. In general, terminal CO are found to coordinate onto apexes or edges of the NPs, meanwhile bridging CO is coordinates onto the NP faces (figure 3.47).[93]

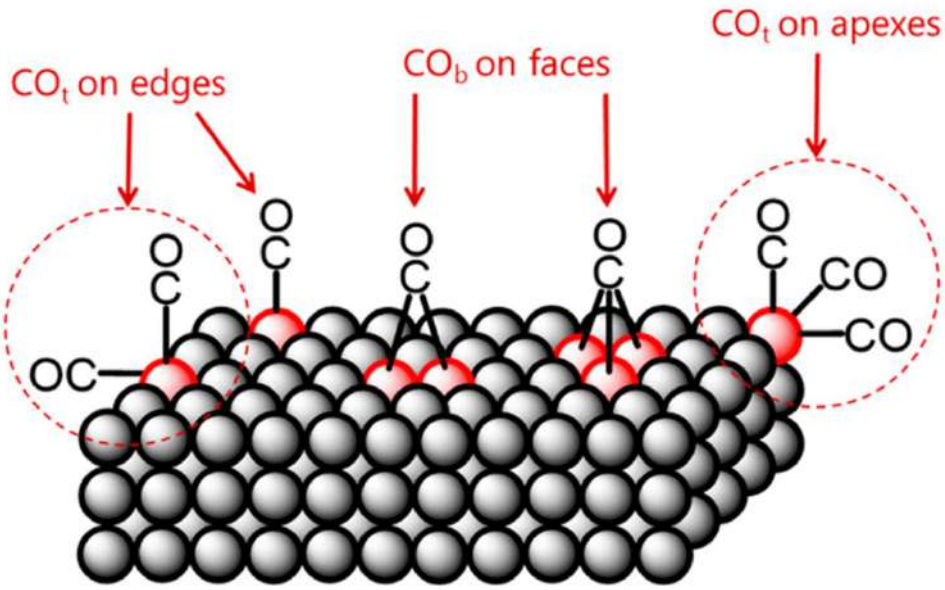

Figure 3.47 Coordination modes of CO at the NPs surface in relation with the free surface sites.[93]

Apart from the information on the coordination sites of CO at metal surface, information on its mobility onto the NP surface can also be obtained. For example, RuNPs stabilized with polyvinylpyrrolidone (PVP) have been reported to present only bridging COs at low concentration of CO but also terminal COs at higher concentration. Meanwhile RuNPs stabilized by bis(diphenylphosphino)butane (dppb) showed an intense signal for terminal COs together with a broad signal of bridging CO. This derives from a lower quantity of free surface sites for the

dppb-stabilized RuNPs due a high surface coverage by the bulky diphosphine ligands. As a consequence, some RuNPs can be more appropriate compared to others for a given selective catalysis depending on the quantity and nature of their free surface which may depend strongly on the stabilizing agent used.[105]

Carbon monoxide was reacted with a sample of $Ru_x(C_7H_{15}COOH)_{0.20}$ NPs dispersed into porous silica inside a Fisher-Porter (1 bar of ^{13}CO; *see* section 6.1.3.7). After 24 h under vigorous stirring followed by evacuation of the rest of CO gas under high-vacuum, the preparation of the NMR rotor was performed under inert atmosphere in a glove-box (*see* section 6.1.4.2).

As a blank test, porous silica was impregnated with a THF solution of octanoic acid, then dried by slow evaporation and finally exposed to 1 bar of ^{13}CO for 24 h. NMR data recorded on this sample did not show any signal of CO (figure 3.48). This result indicated that the porous silica itself does not adsorb CO, and the probable deposition of CO onto the diluted $Ru_x(C_7H_{15}COOH)_{0.20}$ NPs can be only performed onto the RuNPs.

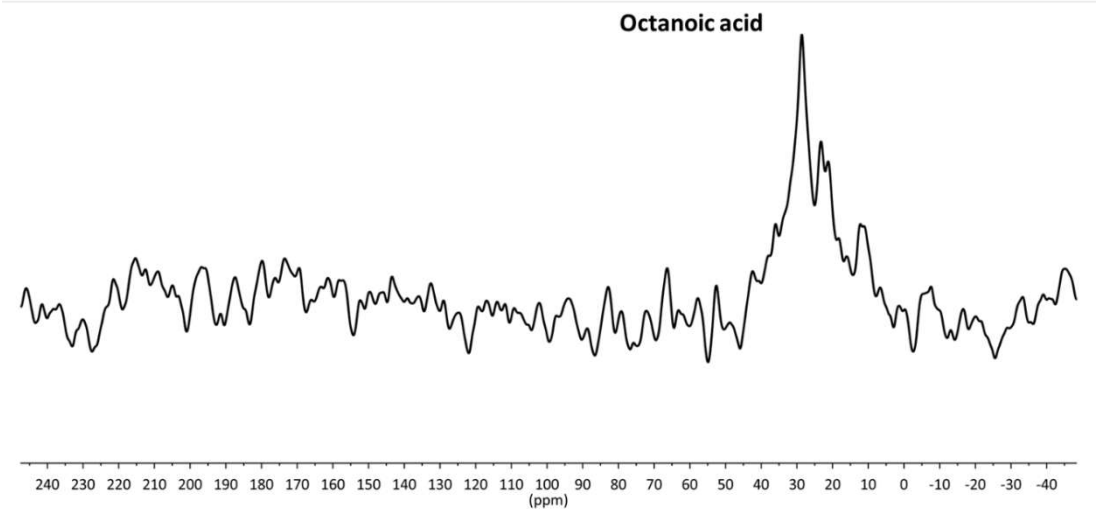

Figure 3.48 ^{13}C MAS NMR spectrum of a sample of porous silica impregnated with octanoic acid after exposure under 1 bar of ^{13}CO.

Besides signals for the octanoic acid and grease, the ^{13}C MAS NMR spectrum of the $Ru_x(C_7H_{15}COOH)_{0.20}$ NPs dispersed in porous silica and reacted with 1 bar ^{13}CO for 24 h (figure 3.49) shows only one peak for coordinated CO at *ca.* 200 ppm that can be attributed to terminal CO. This result indicates that there are free ruthenium surface sites to coordinate CO in the edges and

apexes of its surface. This is not surprising since previous NMR data evidenced that the metal surface was not fully covered showing an octanoate ligand coordinated for each 4.4 Ru_{surf} and 0.2 hydrides per Ru_{surf}.

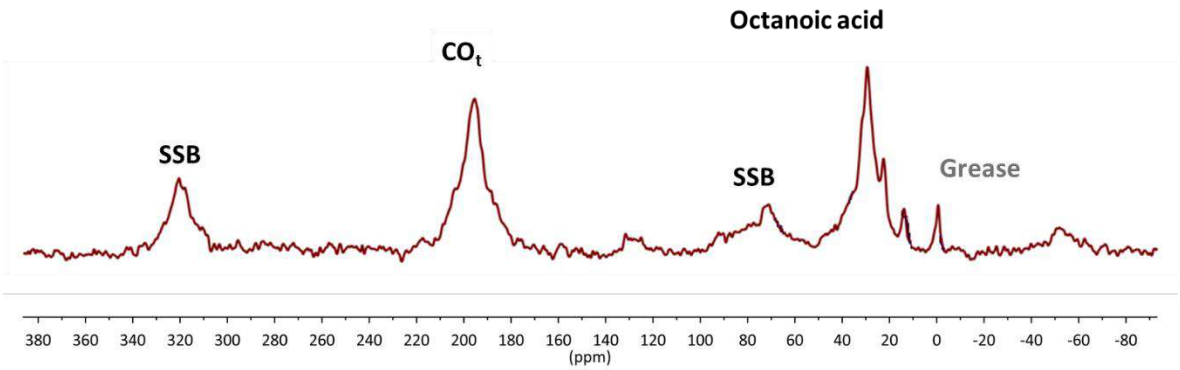

Figure 3.49 ^{13}C MAS NMR spectrum of $Ru_x(C_7H_{15}COOH)_{0.20}$ NPs dispersed in porous SiO_2. After exposure under 1 bar of ^{13}CO for 24 h. Spinning side bands are identified as SSB.

The shape and intensity of the terminal CO peak and the observation of associated spinning side bands indicates a lack of mobility of the CO molecules. It thus appears that the CO molecules cannot move onto the NP surface. The CO mobility is probably impeded by the coordinated octanoates that block at least two neighboring surface ruthenium atoms due to its coordination mode (five center metallacycle), and probably more when considering the probable electronic and steric influence of the O-C(R)-O fragment, letting the surface less accessible for the deposition of small molecules, as CO, at least in the RuNPs faces.

Thus, due to the octanoate coordination mode, it should be unlikely to be coordinated onto apexes and edges and consequently should happen only onto faces. This seems to be supported by the observation of COs deposition only on the edges and apex or the RuNPs surface. In other words, it can be assessed that the $Ru_x(C_7H_{15}COOH)_{0.20}$ NPs have less quantity of free ruthenium surface sites in comparison with PVP- and dppb-stabilized RuNPs and that CO molecules can only interact with the metal surface on edges or apexes.

All together the experimental and theoretical findings provide a precise surface mapping of the $Ru_x(C_7H_{15}COOH)_{0.20}$ NPs. It was estimated certain quantities of coordinated octanoates and

hydrides which are similar (ca. 0.2 of octanoate and hydride per Ru_{surf}). It was described that there are strongly coordinated ligands and others which are weakly coordinated or in exchange. Also, it was shown that the stabilizing effect offered by the octanoates is very high and that the formed RuNPs do not evolve even in the presence of extra ligand (up to 0.2 equiv. of added octanoic acid). Finally, CO can coordinate only onto apexes and edges. The next step is to apprehend the catalytic reactivity of these RuNPs. This will be presented in the next section on the basis of DFT-calculations regarding the HER reaction.

3.2.5.4 Evaluation of $Ru_x(C_7H_{15}COOH)_{0.20}$ NPs for the HER by DFT Calculations

In this work, a deep view of the relationship between the metal ruthenium NP core and the carboxylic acid ligands for stable hybrid materials (RuNPs) has been reported. Given the quantity of ligand needed to stabilize similar mean size of RuNPs, we can assume that the longer the alkyl chain length of the studied ligands, the better the stabilization of the system.

According to this, it could be assumed that the adsorption energy for the longer alkyl chain ligands should be superior than shorter stabilizing agents, but the DFT results shows the opposite (*see* section 3.2.2). It means that that other variables or principles have a bigger role in the metal nanoparticles stabilization.

From a general point of view, it is known that the stabilization of these nanosystems relies on the ligand coverage, on adsorption energies and on steric hindrance.[281] It has also been suggested by some authors that a higher amount of ligands produce more stable nanoparticles.[272] In this work, this property was observed by changing the synthesis L/[Ru] ratio. Taking into account the obtained data about the RuNPs stabilization with linear carboxylic acids, it can be inferred that the steric hindrance of the organic moieties which interacts with the RuNPs surface produce a protective barrier that makes them more stable, making highly important this variable.([205],[282])

Metal nanoparticles possess a high affinity for hydrogen, and RuNPs is well-known to be remarkable in this area. As well, these nanosystems are well-known for their catalytic performance

in various reduction reactions.([59],[245]) In such reactions, the relationship between the adsorption and desorption of hydrogen (or any moiety) onto the RuNPs surface becomes crucial and will determine the nanosystems catalytic performance.[283]

Thus, the previous reported studies about the surface mapping of the RuNPs and especially the recognition of the metal surface free sites becomes a variable of high interest. Knowing these data could offer the advantage of performing selective chemistry based on metal nanoparticles surface studies.[105]

The theoretical evaluation of $Ru_x(CH_3COOH)_{0.40}$ and $Ru_x(C_4H_9COOH)_{0.30}$ NPs in the hydrogen evolution reaction (HER) has been described in previous sections, by following the Nørskov fundamental work.[10]

In Nørskov published methodology, the H adsorption Gibbs free energy (ΔG_H) is related to the exchange current in the HER reaction, the best catalysts such as platinum electrodes being characterized by ΔG_H close to be zero. Therefore, the assessment of this reaction can be performed by calculating the hydrogen adsorption Gibbs free energy (ΔG_H) on the most stable Ru_{55} NP structure found by DFT titration, $Ru_{55}(C_7H_{15}COO)_{14}(H)_{14}$, focusing specially in the free sites observed by CO deposition (edges and apexes). In order to save computational time, it was followed the usual strategy which consists in evaluating ΔG_H by an empirical addition of 5.5 $kcal.mol^{-1}$ to ΔE_H (*see* section 6.2.11).

However, in order to have a complete view of the surface properties of this system and to compare them with the previous calculations done on the ethanoate- and pentanoate-stabilized RuNPs, the hydrogen adsorption energy (ΔE_H) was calculated in five different sites at the surface of the $Ru_{55}(C_7H_{15}COO)_{14}(H)_{14}$ NP. Again, the chosen sites were the (001) and (101) planes, as well as the periphery of the added apex (B_4 & B_5 zone) which involve different type of interactions (*see* section 6.2.1). The ΔG_H values are reported in figure 3.50 and in section appendix E.3

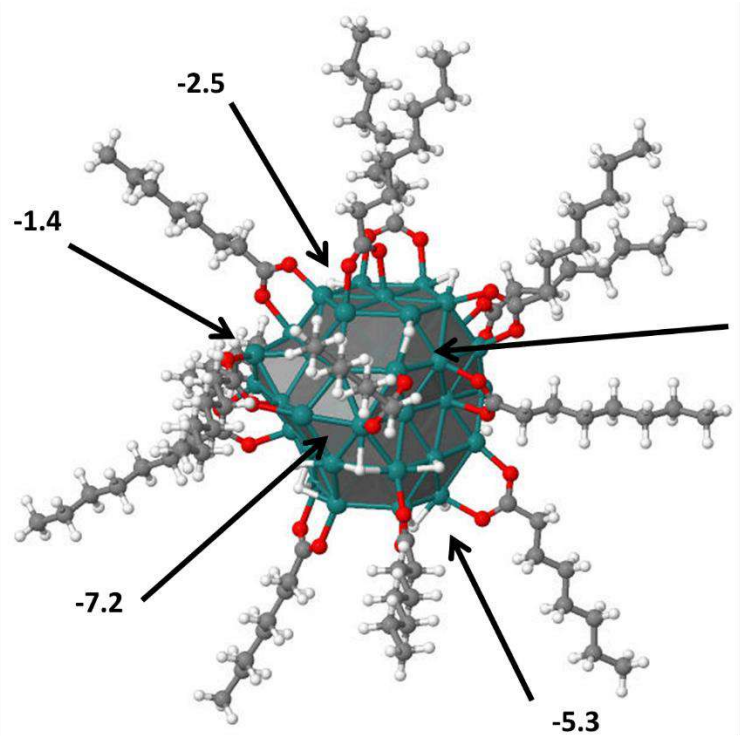

Figure 3.50 ΔG_H (kcal.mol^{-1}), arrows indicate the adsorption sites of $Ru_{55}(C_7H_{15}COO)_{14}(H)_{14}$ NP.

The results show that the adsorption energies of hydrogen (ΔE_H) onto the $Ru_{55}(C_7H_{15}COO)_{14}(H)_{14}$ NP are in the range *ca.* [-6.9 to -16.7 kcal.mol^{-1}]. They can be analyzed in terms of ΔG_H as displayed in the figure 3.50, by the empirical addition of 5.5 kcal.mol^{-1}. The results range from [-1.4 to -11.2 kcal.mol^{-1}]. According to small ΔG_H values, the most suitable sites for the HER reaction are close to the tip as well as on edges (B_4 & B_5 and plane (100)).

It is interesting to notice that the favorable sites which have a good relationship between the adsorption and desorption of hydrogen are also the free sites found by CO RuNPs deposition (apexes and edges), previously described.

From these results, it can be concluded that the $Ru_x(C_7H_{15}COOH)_{0.20}$ NPs are promising catalysts for the HER reaction because they show a few ΔG_H values close to zero. However, as previously observed on ethanoate- and pentanoate-stablized systems, hydrogen adsorption energies in this system are highly depending on the studied DFT adsorption site.

It is possible to compare these energies of the HER evaluation with previous data obtained for the $Ru_x(CH_3COOH)_{0.40}$ and $Ru_x(C_4H_9COOH)_{0.30}$ NPs, for which the same procedure was performed on the basis of the most stable DFT structure found for each nanosystem.

All the data obtained for the H_2 dissociative adsorption Gibbs free energy (ΔG_H) in the three different models are summarized in table 3.24. It can be observed that there is not a global direct trend because the found values depends on the nature of the analyzed sites. Therefore, it is necessary to analyze them by the type of adsorption sites.

ΔG_H in the (101) plane is lower for $Ru_x(CH_3COOH)_{0.40}$ that represents the faces of the RuNPs, whereas in the case of edges and apexes (plane (001) & B_4 - B_5 sites), ΔG_H is lower for $Ru_x(C_4H_9COOH)_{0.30}$ NPs.

Table 3.24 H_2 dissociative adsorption Gibbs free energy (ΔG_H). Comparison by different Ru_{55} NP sites of $Ru_{55}(CH_3COO)_{16}(H)_{16}$, $Ru_{55}(C_4H_9COO)_{14}(H)_{14}$ and $Ru_{55}(C_7H_{15}COO)_{14}(H)_{14}$ models.

Site	$Ru_{55}(CH_3COO)_{16}(H)_{16}$	$Ru_{55}(C_4H_9COO)_{14}(H)_{14}$	$Ru_{55}(C_7H_{15}COO)_{14}(H)_{14}$
(001)	-2.5	-4.8 & -0.6	-2.5 & -5.3
(101)	-2.3, -1.9 & 2.4	-7.8 & -4.8	-11.2 & -7.2
B_4 & B_5	-7.9	0.8	-1.4

In summary, according to the ΔG_H descriptor, none of these RuNPs appears clearly to be the best nanocatalysts for HER, although $Ru_x(C_4H_9COOH)_{0.30}$ NPs seem to be slightly more promising due to its ΔG_H value in the B_4 - B_5 site. Another interesting trend is that the turn-over could be increased in $Ru_x(C_4H_9COOH)_{0.30}$ NPs, owing to the higher number of active sites. $Ru_x(C_7H_{15}COOH)_{0.20}$ NPs could also be interesting catalysts owing to the good compromise between the number of available active sites (edges and corners) and the ΔG_H criterion. It is noteworthy to observe that the carboxylic acid alkyl chain length has an influence, both on the stability of RuNPs (the most stable system is $Ru_x(C_7H_{15}COOH)_{0.20}$, in terms of added ligand quantity), and on the catalytic property regarding HER (the best system seems to be $Ru_x(C_4H_9COOH)_{0.30}$). Therefore, it can be said that for this catalytic reaction it is necessary to find one system that exhibits the best compromise in terms of stabilization, of available active sites and on ΔG_H adsorption energies, such as the pentanoate-stabilized RuNPs

3.2.6 Conclusion

In previous sections, RuNPs were synthetized in pentane by using carboxylic acids with different alkyl chain length (ethanoic and pentanoic acid), both were characterized by experimental and theoretical approaches. Consequently, some trends about the ligand stabilization and the surface composition (better stabilization and lower surface coverage for NPs stabilized with pentanoic acid) were observed. The role of THF as cleaning agent was observed by its deposition and degradation onto the RuNPs surface.

Thus, in order to study the influence of an even longer alkyl chain compared to the system prepared with ethanoic and pentanoic acid previously described, RuNPs were synthetized by using octanoic acid. The study, characterization and its corresponding comparison with RuNPs previous synthetized was described in the second part of this chapter.

Firstly, RuNPs were synthetized by adding the same amount of octanoic acid (0.40 equiv.), as previously performed for other nanosystems but in THF, solvent-assisted. As a result, highly-stable RuNPs, presenting an excess of ligand and different type of coordinated molecules (protonates and deprotonated octanoic acid), were found. Due to its high stabilization, DFT studies about their adsorption energy onto the Ru_{55} NP model were completed. The results were not favorable because they show lower adsorption strength even when dispersion effects were added. However, a trend was observed: longer the alkyl chain length of the adsorbed molecule (linear carboxylate), the lower its adsorption energy on the Ru_{55} NP surface. Meaning that probably another factors are involved in the RuNPs stabilization, like the solvent or the ligand barrier.

Considering the previous result and to determine the real role of THF, different RuNPs were synthetized by decreasing the amount of stabilizing agent (0.30 & 0.15 equiv.), observing that even when a low quantity of ligand (0.15 equiv.) is used to the synthesize the nanosystems, it was possible to stabilize RuNPs with a nice morphology and a small mean size. Also, an absence of extra ligand and coordinated octanoic acid was observed. The only molecule that interact was the octanoate, but still it can be observed some THF pollution at the surface of the RuNPs.

In order to eliminate this intermediate and see the real effect of the alkyl chain length, the RuNPs were synthetized with a fewer amount of octanoic acid (0.1 equiv.), without the presence

of THF, in pentane. The results were not promising, since it leads to a mixture of different nano and microstructures. Thus, the role of THF and its importance was completely described. Next, the RuNPs were synthetized with a higher quantity of ligand (0.2 equiv.) and as a result, the formation of very nice NPs, which seems to be homogeneous, well-dispersed and with a mean size of *ca.* 1.65 nm, being quite like previous optimized RuNPs stabilized by ethanoic and pentanoic acid (*ca.* 1.5 nm), was observed. The quantity of stabilizing agent used for the synthesis of this RuNPs was lower than the one needed for other systems (0.40 and 0.30 for ethanoic and pentanoic acid, respectively), which shows a direct trend about the influence of the alkyl chain length. It was observed that longer the alkyl chain length of the ligand, lower will be the quantity of ligand needed to form similar mean size of RuNPs ([1.5 - 1.7 nm]). This information, in addition to the previous one obtained for the ligand adsorption energy, indicates that the steric hindrance of the stabilizing agent has a big effect on the RuNPs formation.

Thus, the addition of 0.20 equiv. of octanoic acid for the RuNPs synthesis in pentane was taken as the optimal L/[Ru] ratio for the formation of a homogeneous well-dispersed nanosystem, that can be comparable with other systems, without THF pollution. Therefore, the $Ru_x(C_7H_{15}COOH)_{0.20}$ NPs were fully characterized.

The $Ru_x(C_7H_{15}COOH)_{0.20}$ NPs, analyzed by HRTEM and WAXS, showed to be a highly crystalline sample with a *hcp* crystalline structure. Previous experiments performed on the $Ru_x(CH_3COOH)_{0.40}$ NPs, showed a poorly crystalline sample. Thus, it was observed that RuNPs display better homogeneity and crystallinity, if they are synthetized with carboxylic moieties with longer alky chain length.

Also, by NMR and FTIR studies, it was noticed that the RuNPs were stabilized by the deprotonated carboxylic moiety (octanoates) without the presence of any excess, meaning that no free ligand was found. Similar behavior was observed for RuNPs stabilized by ethanoic and pentanoic acid, were it was found that they lie onto the RuNP surface as carboxylates due to the low energy activation of the O-H bond.

Following with the characterization, it was possible to quantify the number of octanoates and hydrides surrounding the $Ru_x(C_7H_{15}COOH)_{0.20}$ NPs by using deep NMR studies (^{1}H, DOSY & NOSESY NMR) and catalytic analysis (norbornene reduction). As a result, it was observed that there are 0.2 octanoates per Ru_{surf} and 0.2 hydrides per Ru_{surf}. A parallel study was performed by a

DFT titration over the Ru_{55} NP model, where a similar trend was found: hydrides [0.3 - 0.6]/Ru_{surf} and octanoates [0.2 – 0.3]/Ru_{surf}. These results highly agree with the experimental titration, showing once more the potentiality of these model to describe small RuNPs

In comparison with other DFT titrated RuNPs, pentanoic – 0.3 H/Ru_{surf} & 0.3 C_4H_9COO/Ru_{Surf} and ethanoic – [0.4 – 0.6] H/Ru_{surf} & 0.4 CH_3COO/Ru_{Surf}, it can be observed a direct trend. Longer the carboxylic alkyl chain length, the lesser quantity of ligand will be needed to stabilize similar size of RuNPs. Similar behavior was observed experimentally.

From DOSY analyses, it was observed that probably the surface of the RuNPs was not completely crowded in both, the inner and outer shell, because it was found that each 4.4 Ru_{surf} one octanoate is present. Therefore, a study on the $Ru_x(C_7H_{15}COOH)_{0.20}$ NPs saturation was performed. It was observed that the addition between [0.05 & 0.10 equiv.] of extra ligand is the optimal quantity of octanoic acid needed to cover the outer shell of the RuNPs. However, it was also noticed that the $Ru_x(C_7H_{15}COOH)_{0.20}$ NPs has a completed inner shell and it suffers no modifications, even when 100 % more of stabilizing agent was added. The presence of ligand that do not take part of a fast exchange with weakly bonded ligand at the NPs surface was observed in the last part of the experiment, when 0.20 equiv. more of ligand ($Ru_x(C_7H_{15}COOH)_{0.20+0.20}$ NPs) was introduced. In this case, the presence of free ligand was finally observed.

In order to complete the surface mapping of this system, ^{13}CO was deposed onto the nanosystem. Then, it was observed that the surface of the nanoparticle was crowded, and the deposition of this marked gas only can be performed in the apexes and edges of the $Ru_x(C_7H_{15}COOH)_{0.20}$ NPs. Meaning that the available sites for catalysis in this nanosystem are in the apexes and edges.

Finally, in order to evaluate its possible catalytic activity, an evaluation of the hydrogen adsorption and desorption on the optimal RuNPs found by DFT calculations ($Ru_{55}(C_7H_{15}COO)_{14}(H)_{14}$) was performed. It was observed that this parameter was too high in the planes and quite good at the apexes and edges, which was a quite good result owing the data obtained by ^{13}CO deposition.

Also, this last data was compared with previously obtained results for the HER reaction on other optimal RuNPs stabilized by ethanoic ($Ru_{55}(CH_3COO)_{16}(H)_{16}$) and pentanoic acid ($Ru_{55}(C_4H_9COO)_{14}(H)_{14}$). As a result, it was observed that the best conditions for the HER reaction

are obtained with RuNPs stabilized by pentanoic acid ($Ru_x(C_4H_9COOH)_{0.30}$). Thus, it can be said that even when the use of octanoic acid produce a more stable system with lower surface coverage, it is not necessarily the best catalyst. In other words, a suitable catalyst for HER reaction will be the RuNPs which possesses middle surface coverage and middle alkyl chain length, namely RuNPs stabilized by pentanoic acid, $Ru_x(C_4H_9COOH)_{0.30}$.

Due to the hydrogenation catalytic properties of the RuNPs, it is possible that the synthesis of RuNPs with aryl carboxylic ligands will produce a reduction of the ligand. Therefore, in order to circumvent this issue a ligand exchange was proposed as strategy aiming to introduce aryl ligands onto the RuNPs surface. This study will be presented in the next chapter.

CHAPTER IV

Ligand Exchange at the Surface of Octanoic Acid Stabilized RuNPs

4.1 Introduction

MNPs have demonstrated to be a promising material for catalysis because they combine the advantages present in both, homogeneous and heterogenous catalysis. Their driving force relies on their properties, which lies between bulk materials and molecular compounds. For example, MNPs present catalyst recycling, product separation, catalytic mild reaction conditions, etc.[284] In fact, the interest in these materials is increasing in both academia and industry domains, mainly due to their higher active surface area that can be tuned to improve their stability, viability and selectivity.[36]

The reactivity of MNPs was reported to be strongly linked to their synthesis methodology, *i.e.*, variety of the supports, reaction solvent, nature of the metal source, etc., since all these parameters will lead to different sizes, morphologies and structures.[285] Also, it has been determined that the viability and functionality of MNPs, in a specific catalytic reaction, can be modified by exchanging the surrounding molecules that interact with the metal surface as a ligand barrier.[116]

Moreover, these nanomaterials can act as catalysts for several reduction reactions, especially for the arenes hydrogenation,([286],[287]) which cannot be obtained in normal conditions (figure 4.1).[126] Several published reports have shown the potentiality of RuNPs to perform partial[288] or total hydrogenation of arenes.([289],[290]) Therefore, these nanosystems are suitable for being intensively investigated in order to increase their selectivity in several hydrogenation reactions, such as aromatic compounds reductions and their derivatives.[291]

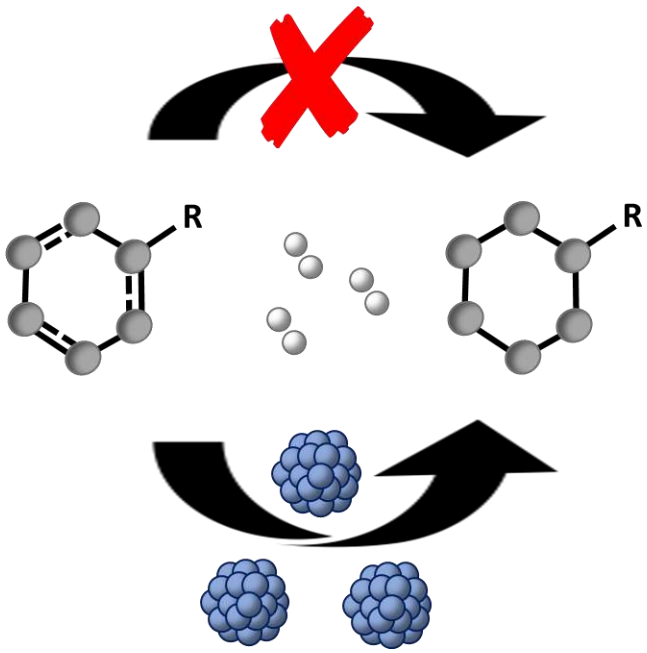

Figure 4.1 Representation of the arene reduction pathways: Influence of the MNPs as catalyst in mild conditions.

The RuNPs presented in this dissertation were synthetized by following the organometallic approach using hydrogen as reactive gas to decompose the metal precursor and reduce the olefinic ligands into alkanes (*see* section 1.2.3). It has been shown that the formed RuNPs bear hydrides at their surface coming from the synthesis conditions and also from the deprotonation of the carboxylic acid ligands.

Owing to the well-known catalytic properties of RuNPs towards the hydrogenation of insaturated molecules and most particularly of aromatic systems, partial or total reduction of aryl groups can be expected when they are present in the skeleton of the stabilizing agents used for the synthesis of the RuNPs (figure 4.2).

This side-reaction has been already observed in RuNPs stabilized by arylphosphines for instance[99] but not for RuNPs synthesized in the presence of 4-(3-phenylpropyl)pyridine.([104],[132]) This difference may result from the coordination of the two aromatic parts of 4-(3-phenylpropyl)pyridine ligand onto the metal surface, as shown by NMR studies, while in the case of the arylphosphines the phenyl groups are not interacting since the ligand coordination takes place through the phosphorous atom.

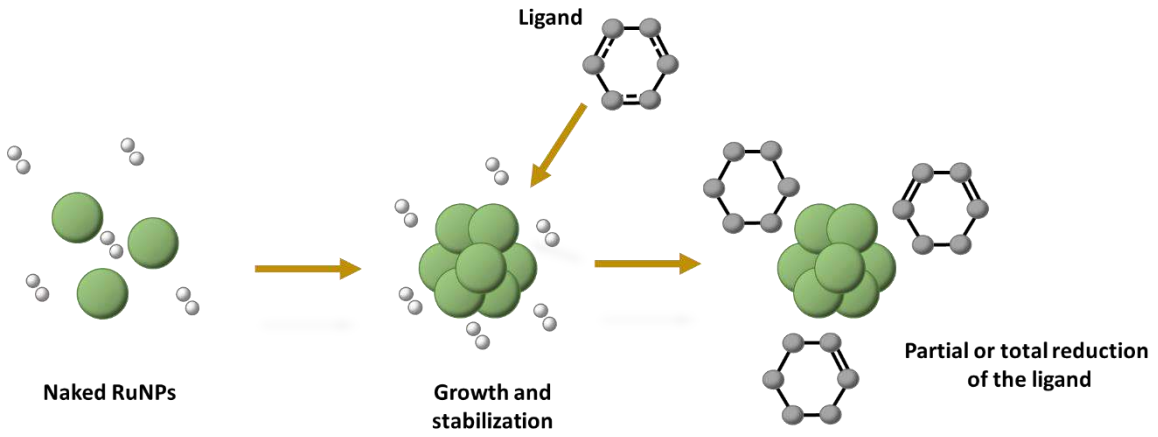

Figure 4.2 Expected partial or total reduction of aryl groups in stabilizing ligands of RuNPs.

Thus, the direct synthesis of RuNPs by using as stabilizer a photosensitive ruthenium complex containing aromatic groups like the ruthenium trisbipyridine complex ($[Ru(bpy_3)]^{2+}$) envisaged to get hybrid nanomaterials can be problematic, due to the pyridine moieties possible reduction that would change the optical properties of the ruthenium complex and consequently of the hybrid material.

In order to avoid such difficulties, an alternative strategy has been envisaged to perform the anchoring of bipyridine containing ruthenium complexes with pending carboxylic acid groups at the surface of RuNPs, namely a ligand exchange reaction.

In this chapter, studies on ligand exchange between preformed RuNPs stabilized by octanoic acid and added benzoic acid or trifluoracetic acid will be presented. Benzoic acid was selected because it contains an aryl group, thus mimicking the PS complex, and also due to its different acidic properties compared to alkyl carboxylic acids. Trifluoroacetic acid was chosen in order to study the ligand exchange reaction using an even more acidic ligand. The obtained results will be presented in the next parts of this chapter.

.

4.2 Ligand Exchange at RuNPs Surface: Octanoic Acid *vs* Benzoic Acid

As previously described, the ligand exchange between performed RuNPs and aryl ligands was the chosen methodology to introduce ligands which possess aromatic behavior onto hydrogen catalytic reactive NPs. In this case, the selected moiety to be studied was the simplest aromatic carboxylic acid, the benzoic acid. This molecule will be used as prove of content to further ligand exchange with the actual photosensitizer that has carboxylic acid as anchoring groups.

In the precedent chapters, theoretical calculations have shown that among the different samples of carboxylic acid-stabilized RuNPs prepared, apparently the most reactive ones for HER should be those prepared with 0.3 equiv. of pentanoic acid ($Ru_x(C_4H_9COOH)_{0.30}$) which possess an intermediate crowded surface in comparison to RuNPs synthetized with ethanoic and octanoic acid. But also, it was observed that the longer the alkyl chain length, the lower will be the amount of carboxylates surrounding the ruthenium metal surface and also the higher will be the stability of the particles.

Moreover, according to theoretical DFT calculation the octanoic acid has the lowest adsorption energy onto the Ru_{55} NP model, in comparison with pentanoic and ethanoic acid. In addition, to have favorable conditions for a ligand exchange reaction it is necessary that the exchanged ligand should have lower interaction strength with the RuNP than the incorporated moiety. For all these reasons, the chosen NPs system for studying the ligand exchange *versus* benzoic acid was the RuNPs prepared by 0.2 equiv. of octanoic acid in pentane, namely $Ru_x(C_7H_{15}COOH)_{0.20}$.

It is worth to note that the behavior of carboxylic acids is highly dependent on the solvent and that this can influence their acidic properties. In this case, in fact the benzoic acid has a slightly higher acidity (*pKa* = 4.2) than the octanoic acid (*pKa* = 4.9).[292] Nevertheless, it is expected these two acids have a sufficient difference in terms of interaction with the metal surface to observe a ligand exchange. Thus, this variable can be partially avoided due to the difference in *pKa* (< 1), and the real effect of the ligand exchange strength can be observed.

1D and 2D NMR spectroscopy (^{1}H & DOSY) was used to follow ligand exchange reactions at RuNP surface between octanoic acid and benzoic acid, with the objective to estimate the quantity of ligands exchanged. For comparison purpose, a one-step synthesis of RuNPs using benzoic acid as a stabilizer was first performed in order to get the ^{1}H NMR signature of RuNPs stabilized by benzoic acid.

4.2.1 One-Step Synthesis of RuNPs Stabilized by Benzoic Acid

Owing to the reductive catalytic properties of RuNPs, it was suggested that the direct synthesis of RuNPs in the presence of photosensitizer could decompose the ligand (bpy based) and thus lose their photonic properties. On the other hand, it was observed that in some cases RuNPs can be stabilized with pyridine ligands, even when they are formed by following the organometallic approach using 3 bar of hydrogen. Therefore, a study of the RuNPs formation using benzoic acid as stabilizing agent was performed and followed by continuous ^{1}H-NMR experiments.

The synthesis of benzoic acid-stabilized RuNPs was carried out in a valved NMR tube dedicated to high pressure experiments with the aim to follow the decomposition of the [Ru(COD)(COT)] and in parallel the formation of the RuNPs. The experiment consisted in the reduction of the organometallic precursor in the presence of 0.2 equiv. of benzoic acid (L/[Ru]) under 3 bar of H_2 using deuterated THF as a solvent. The reaction was performed at low temperature (-15 °C), in order to decrease the reaction kinetics, for 24 h (scheme 4.1).

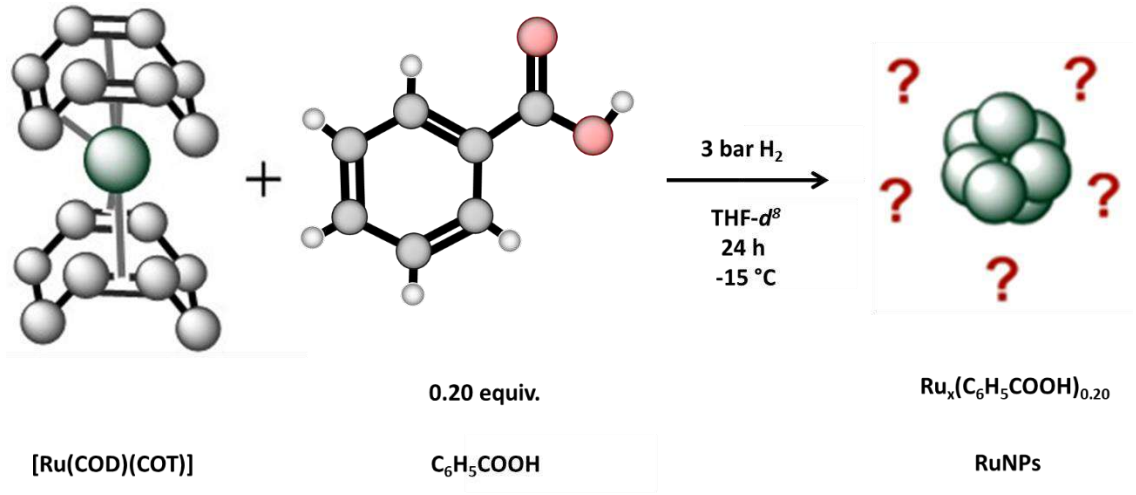

Scheme 4.1 Synthesis of RuNPs stabilized by benzoic acid in THF-d^8.

In order to assure a total decomposition of the metal precursor in the absence of stirring, the NMR tube was repressurized with 3 bar of H_2, each 4 h (three times). The formation of the RuNPs was visually detected with time via a gradient of color from the top to the bottom of the NMR tube.

By ^{1}H NMR, it was observed the appearance of a signal at *ca.* 1.5 ppm corresponding to the cyclooctane released from the decomposition of the [Ru(COD)(COT)] while the reaction time advanced. In parallel, the signals of the benzoic acid (aromatic and alkyl proton range) became broader with time. The broadening of this aromatic proton signal was attributed to the proximity of the ligand with the metal surface. However, other signals at *ca.* [1.2 - 1.4 ppm], also appeared that correspond to alkyl protons. Finally, in the last spectrum it was possible to assign this signals to cyclohexyl methanol[293] (figure 4.3). The presence of it can be explained by the hydrogenation of the benzoic acid.

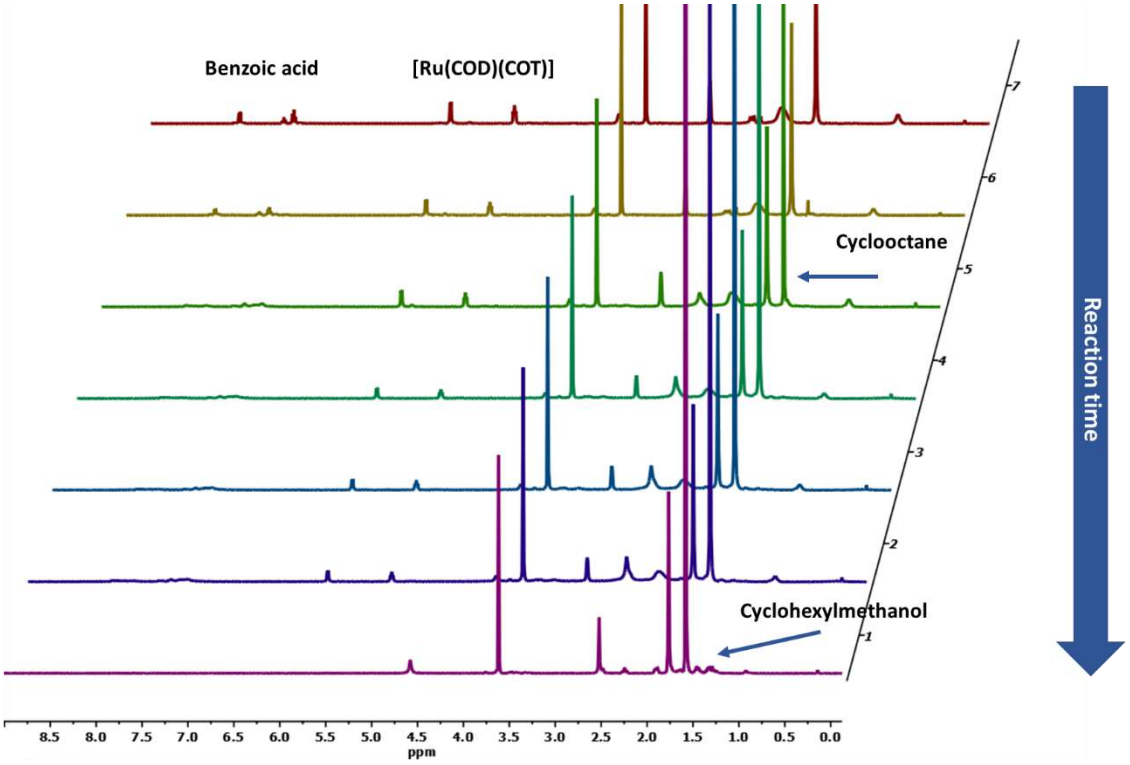

Figure 4.3 ^{1}H-NMR (THF-d^{8}) analyses of the decomposition of [Ru(COD)(COT)] under 3 bar H_2 in the presence of 0.2 equiv. of benzoic acid and of the possible formation of RuNPs.

On figure 4.4. which is a zoom of the aromatic region of the ^{1}H-NMR spectrum, the broadness of the benzoic acid signals is more visible as well as the appearance of new peaks that can be attributed to a partial reduction of the aromatic ring, which later on appeared to be completely reduced into cyclohexylmethanol. At the end of the experiment (violet spectrum, 24 h of reaction time) no signals are visible in the spectrum meaning no free ligand is present in solution.

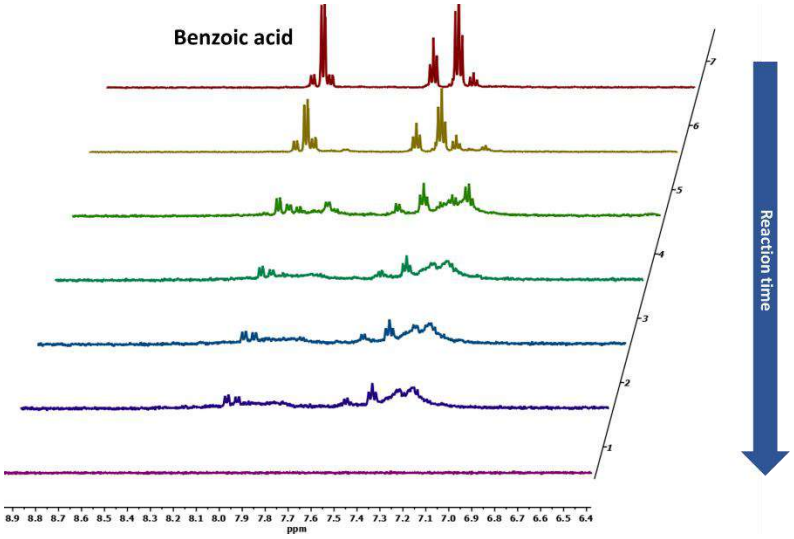

Figure 4.4 Zoom of the aromatic region of the ^{1}H-NMR (THF-d^{8}) spectra provided in figure 4.3.

From these ^{1}H NMR results, it can be concluded that the formation of RuNPs happened and that the benzoic acid ligand was reduced. But these data do not provide information on the quantity of benzoic acid reduced. It can be totally or partially decomposed.

As a consequence, the ligand exchange strategy becomes a reliable methodology for the incorporation of aryl ligands onto the RuNPs surface.

4.2.2 Titration of Octanoic vs Benzoic Acid Ligand Exchange at RuNPs Surface

As announced before, the RuNPs chosen for the ligand exchange studies are those stabilized by 0.2 equiv. of octanoic acid (OcAc). The experimental titration done by NMR on this system of $Ru_x(C_7H_{15}COOH)_{0.20}$ NP indicated that *ca.* 23.5 octanoates lie on the NP surface being strongly coordinated while approximately 6.5 octanoates are in an outer shell, interacting with the metal surface in a weaker manner.

For the titration experiment, the $Ru_x(C_7H_{15}COOH)_{0.20}$ NPs were dispersed in deuterated benzene inside an NMR tube. Then, an increasing quantity of benzoic acid (BAc) was added in the

NMR tube (0.05, 0.10, 0.20 & 0.30 equiv.). After, the tube was plunged in an ultrasound bath for 30 min (scheme 4.2).

^{1}H-NMR and DOSY analyses were performed after each addition with the aim to follow the ligand exchange between these carboxylic molecules and quantify it. The grease present in the sample was used as internal standard (*see* section 6.1.3.7.4).

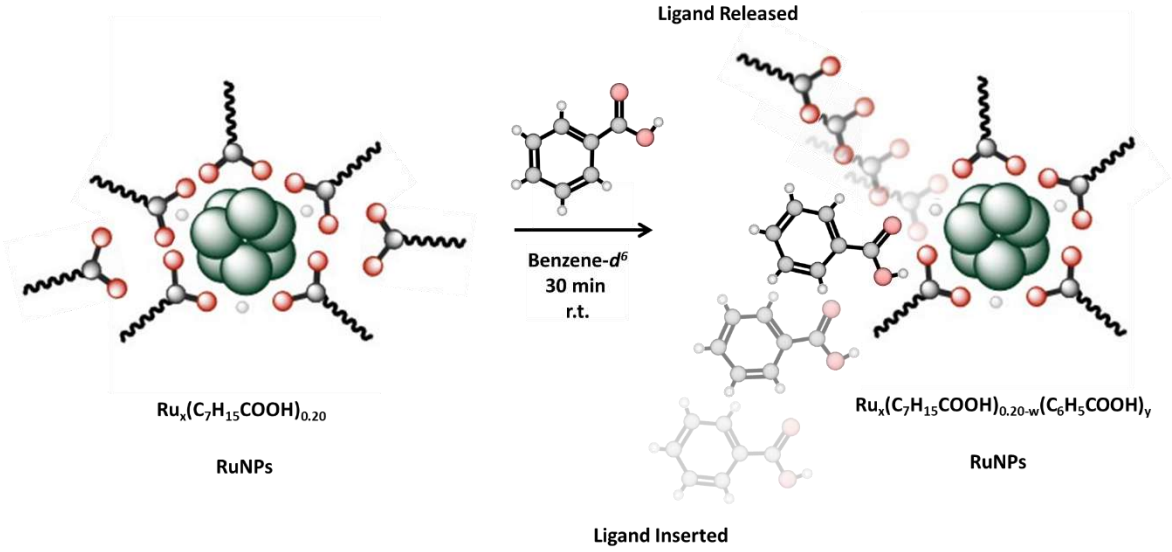

Scheme 4.2 Representation of the ligand exchange studied between $C_7H_{15}COOH$ and C_6H_5COOH onto preformed $Ru_x(C_7H_{15}COOH)_{0.20}$ NPs.

Given the differences in the located proton signals (aromatic an alkyl proton range) for octanoates and benzoic acid, one of the best techniques to analyze the possible ligand exchange is the ^{1}H-NMR. Thus, each time that the benzoic acid is added into the reactor, new sharp signals should appear at low field without changing the observed peaks of the octanoates moieties if a ligand exchange or addition is not presented. However, a positive indication of a ligand addition will be found if some broad peaks are observed at low field, without changing the signals at high filed. Meanwhile, a ligand exchange will be found if both regions are modified.

From the first addition of BAc, namely 0.05 equiv., an evolution of the spectrum of the RuNPs was observed. Indeed, the signals of the coordinated octanoic acid protons (high field broad signal) started to change showing a decrease of their broadness. In parallel narrow peaks appeared at position corresponding to those expected for octanoic acid thus indicating that

octanoic acid has less interaction with the metal surface. This phenomenon amplified while increasing the quantity of benzoic acid added as clearly observed until addition of 0.20 equiv. of benzoic acid, which indicates the release of certain amount of octanoic acid to the solution. However, it is important to point out that not all the octanoic acid ligand was released since broad signals are still visible even after addition of 0.30 equiv. of benzoic acid into the setup (figure 4.5 high field).

Looking at the low field part of the spectra, apart from the sharp signal of benzene at *ca.* 7.16 ppm, it was observed the appearance of signals in the range of [6.5 – 8.5 ppm] that grew while adding more benzoic acid in the NMR tube. These signals correspond to benzoic acid and their ill-definition and broadness are indicative of an interaction with the RuNPs (figure 4.5 low field). It is worth to say that the presence of this deprotected proton signals indicates the absence of the benzoic acid reduction.

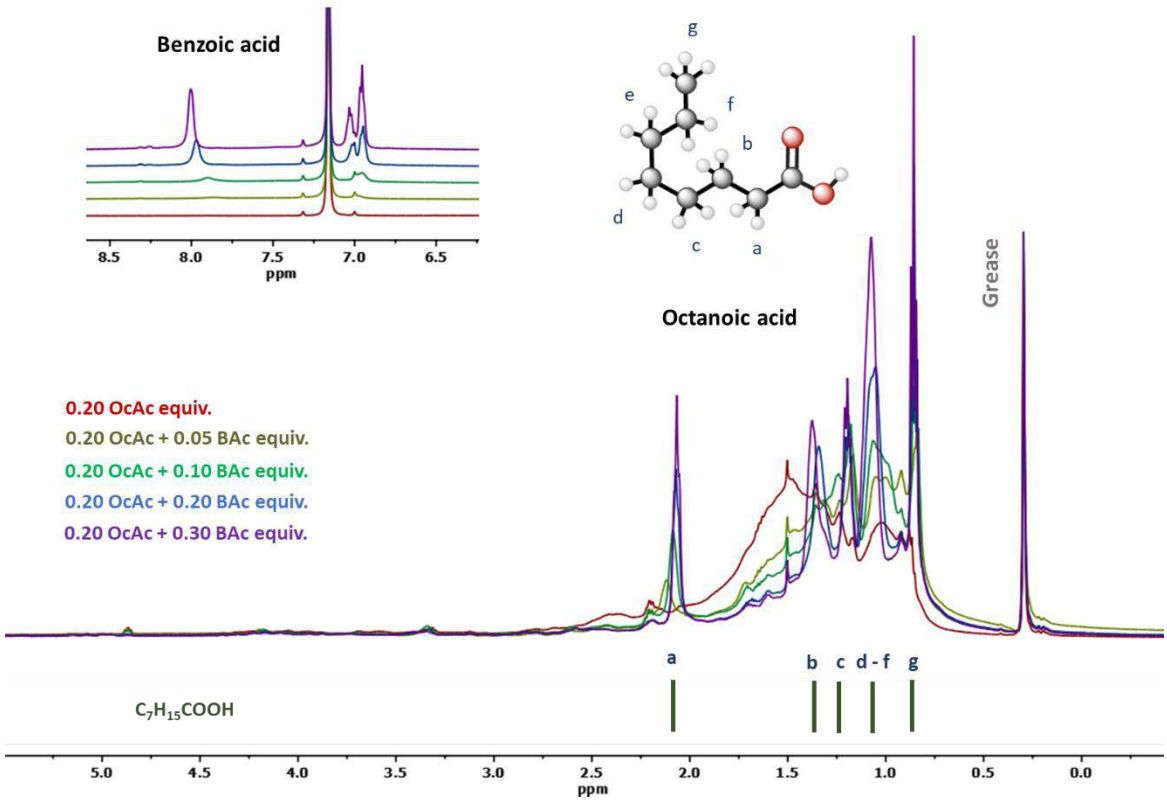

Figure 4.5 ^{1}H-NMR (C_6D_6) spectra of $Ru_x(C_7H_{15}COOH)_{0.20}$ NPs, represented as 0.20 OcAc, after addition of an increasing quantity of benzoic acid. (red) initial RuNPs stabilized with 0.20 equiv. of OcAc; (dark green) 0.20 OcAc + 0.05 equiv. of BAc; (green) 0.20 OcAc + 0.10 equiv. of BAc; (blue) 0.20 OcAc + 0.20 equiv. of BAc; (purple) 0.20 OcAc + 0.30 equiv. of BAc. Chemical shifts of the octanoic acid protons ($C_7H_{15}COOH$) are presented in green bars at the bottom.

From these NMR data, it can be concluded that the addition of benzoic acid into the solution of $Ru_x(C_7H_{15}COOH)_{0.20}$ NPs provoked the release of octanoic acid to the reaction medium and most probably the coordination of benzoic acid onto the RuNPs surface. Meaning that the ligand exchange was presumably done.

^{1}H NMR allowed to evidence the dynamism of carboxylic acid ligands at the NPs surface when adding benzoic acid in a NMR tube containing octanoic acid-stabilized RuNPs. A ligand exchange was observed but the obtained data did not allow us to conclude about the real interaction of benzoic acid with the metal surface neither and about the quantity of ligand exchanged and released. In order to solve these questions, another type of NMR study needs to be performed.

DOSY-NMR was thus selected in order to get more information about the dynamic behavior of the ligands involved in the exchanging process. As described in section 3.2.5.3, this technique was expected to provide information on the interaction strength of the ligands with the RuNPs. In this way, it can be corroborated the inclusion of ligands at the metal surface or their release.

The diffusion-filtered ^{1}H-NMR spectra recorded at different quantity of added benzoic acid are given on figure 4.6. Broad signals are seen in alkyl and aromatic protons regions as previously observed in the ^{1}H-NMR spectra. Due to their broadness, the signals between [0.7 – 2.5 ppm] can be assigned to alkyl protons that have low motion, thus to rigid octanoates molecules. In the aromatic region, the broad signal observed in the range of [6.5 – 8.3 ppm] can be assigned to benzoic acid that is in interaction with the metal surface. Thus, a certain amount of octanoic and benzoic acids are strongly interacting with the RuNPs.

But when looking at the spectra evolution with the increasing quantity of benzoic acid added it can be observed at high field a continuous diminish of the signals for coordinated octanoic acid ligands up to the addition of 0.2 equiv. of BAc but no more evolution after the last addition (0.3 equiv.). This indicates that up to the addition of 0.2 equiv. of BAc, octanoates were released but some still remained, and the BAc cannot displace them. Meanwhile, at low field, an increase of the signal of benzoic acid is noted for each step of the experiential process, meaning a continuous coordination of the benzoic acid onto the RuNPs surface.

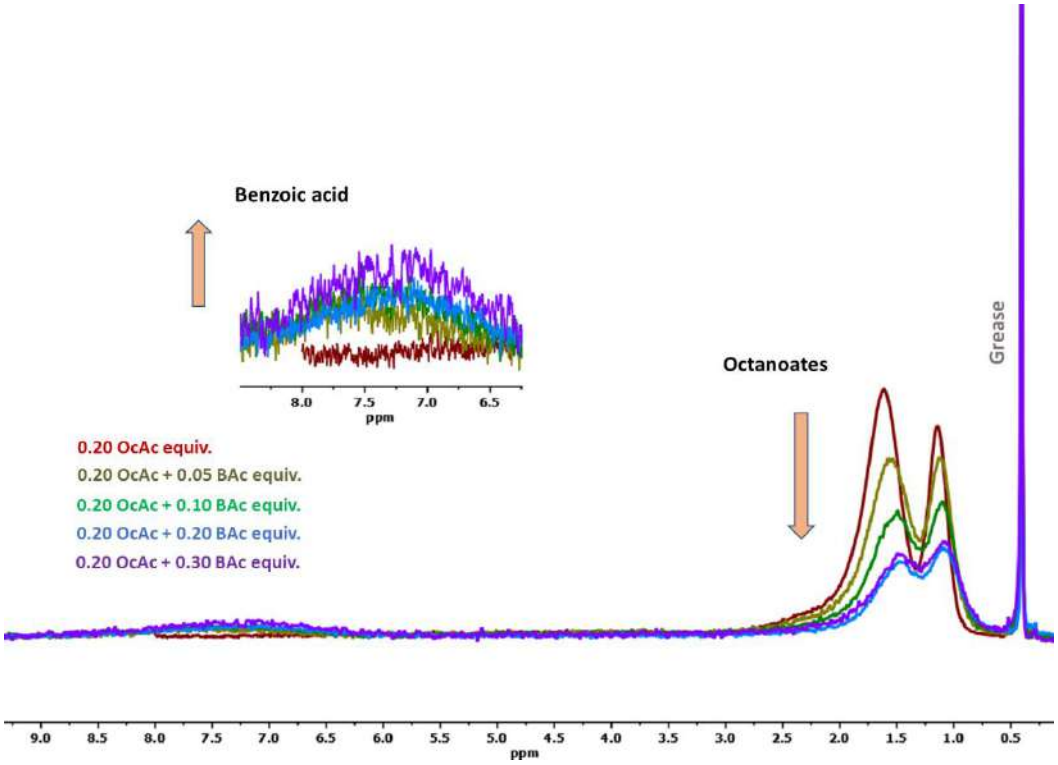

Figure 4.6 Diffusion-filtered ^{1}H-NMR spectra (C_6D_6) obtained for $Ru_x(C_7H_{15}COOH)_{0.20}$ NPs, represented as 0.20 OcAc, during addition of benzoic acid. (red) initial RuNPs stabilized with 0.20 equiv. of OcAc; (dark green) 0.20 OcAc + 0.05 equiv. of BAc; (green) 0.20 OcAc + 0.10 equiv. of BAc; (blue) 0.20 OcAc + 0.20 equiv. of BAc; (purple) 0.20 OcAc + 0.30 equiv. of BAc.

These NMR data highlighted that the addition of benzoic acid to a suspension of octanoic acid-stabilized RuNPs induced the release of octanoic acid in solution but not of all coordinated ligands. Benzoic acid is thus able to displace octanoates but not totally, even when forcing its concentration by adding it in more than the initial quantity of octanoic acid used for the preparation of the particles (see data for 0.3 equiv. of added BAc). Benzoic acid is thus not able to replace all the octanoates, probably for sterical hindrance reasons.

However, these results are of interest because they show that the addition of an aromatic carboxylic moiety can be done at the surface of RuNPs previously stabilized with an alkyl carboxylic acid. The combination of these two NMR experiments reinforce the selected approach to incorporate photosensitizers at the surface of RuNPs, due to the observed ligand exchange between the studied moieties.

In order to know the ligand exchange efficiency, the next logical step will consist in a quantitative estimation of the exchanged ligands.

With the aim to get a titration of the surface ligands, namely of carboxylic and benzoic acid molecules strongly and weakly interacting with the nanoparticles, 2D-NMR DOSY analyses were carried out as previously described in section 3.2.5.3.1. Due to technical issues, the surface mapping could be done only for the addition of 0.10, 0.20 and 0.30 equiv. of benzoic acid to the colloidal suspension of $Ru_x(C_7H_{15}COOH)_{0.20}$ NPs. The studies were performed by integrating the evolution of the octanoates signals (*ca.* [2.5 – 0.75 ppm]) and the benzoic acid peaks (*ca.* [6.5 – 8.3 ppm]).

The diffusional attenuation could be fitted with a Stejskal-Tanner equation by using a bi-exponential analysis for both the alkyl and aromatic proton regions. This indicated the presence of two different types of molecules interacting with the RuNPs surface for each proton region, namely with strong (D_s) and weak interaction (D_w). As a consequence, two different diffusion coefficients (D) were extracted for each proton type and related with their corresponding signal contribution (weight; table 4.1).

Table 4.1 Diffusion coefficients of octanoic acid and benzoic acid moieties and corresponding signal weight for each addition of benzoic acid to colloidal suspension of $Ru_x(C_7H_{15}COOH)_{0.20}$ NPs.

Benzoic acid added (equiv.)	**Octanoic acid region**				**Benzoic acid region**			
	D_s ($m^2.s^{-1}$)	Weight (%)	D_w ($m^2.s^{-1}$)	Weight (%)	D_s ($m^2.s^{-1}$)	Weight (%)	D_w ($m^2.s^{-1}$)	Weight (%)
0.00	$1.5x10^{-10}$	66.2	$6.1x10^{-10}$	33.8	---	---	---	---
0.10	$1.8x10^{-10}$	42.9	$9.1x10^{-10}$	57.1	$1.9x10^{-10}$	41.0	$1.0x10^{-9}$	59.0
0.20	$1.7x10^{-10}$	37.8	$9.4x10^{-10}$	62.2	$1.8x10^{-10}$	22.8	$1.1x10^{-9}$	77.2
0.30	$2.1x10^{-10}$	31.8	$1.0x10^{-9}$	68.2	$2.1x10^{-10}$	12.5	$1.1x10^{-9}$	87.5

D_{OcAc} = 1.3 x 10^{-9} $m^2.s^{-1}$; D_{BAc} = 1.4 x 10^{-9} $m^2.s^{-1}$; s = strongly and w = weakly interacting ligand

The enlisted data in the previous table describe several phenomena. First, the value of the diffusion coefficient of the strongly bonded ligand (D_s), in the alkyl region and thus corresponding to the octanoic acid, remained quite similar ([1.5 to 2.1 x10^{-10} $m^2.s^{-1}$]). While, the same variable but for the benzoic acid, displays similar value ([1.8 to 2.1 x10^{-10} $m^2.s^{-1}$]). This indicates that the RuNPs

was not affected by the ligand exchange and its metal structure remains the same during the whole process. This assumption will be later corroborated by TEM analyses.

Also, It is noteworthy that the signal contribution of the strongly bonded octanoic acid decreases with each new addition of benzoic acid. Meanwhile, the diffusion coefficient of the weak interacting octanoic acid (D_w) going toward the value of free ligand (D_{OcAc} = 1.3 x 10^{-9} $m^2.s^{-1}$), which means that there is more quantity of "free" exchanged ligand. These phenomena can be interpreted by a continuous decrease of the quantity of strongly coordinated octanoates.

Finally, the diffusion coefficient values for both strongly and weakly interacting benzoic acids did not significantly evolve during the study. But if the contribution of the signal for the benzoic acid strongly bonded appeared high at the beginning of the study, it decreased significantly when adding 0.2 and 0.3 equiv. of benzoic acid. This may indicate that only a certain quantity of ligands can be exchanged at the surface of the RuNPs, probably up to the surface saturation, and then, the added ligand in excess, either remains free in solution or exchanges with coordinated ones.

By taking into account the mean size of the $Ru_x(C_7H_{15}COOH)_{0.20}$ NPs (ca. 1.65 nm), the crystallinity (*hcp*), the magic number for metal clusters rule and the extracted data from DOSY analyses (diffusion coefficients and corresponding contributions), the quantity of ligands laying at RuNPs surface can be estimated in order to get a surface mapping for each addition step (*see* section 6.1.3.7.2). The obtained data are reported in table 4.2

Table 4.2 Mapping of the RuNPs surface after ligand exchange experiments between octanoic and benzoic acid.

Benzoic acid added (equiv.)	**Octanoic acid molecules**			**Benzoic acid molecules**		
	I_s	I_w	I_f	I_s	I_w	I_f
0.00	23.5	6.5	4.8	---	---	---
0.10	14.9	6.5	13.2	7.1	3.1	7.1
0.20	13.1	6.2	15.2	7.9	6.1	20.8
0.30	11.1	4.8	18.6	6.5	10.5	35.0

s= strongly interacting ligand; w= weakly interacting ligand; f = "free" exchanging ligand.

The addition of benzoic acid to the preformed nanosystems cause the release of octanoic acid from the metal surface and the incorporation of benzoic acid on it. This criterion can be clearly be observed by a decrease of the calculated quantity of strongly bonded octanoic acid (I_s) after the addition of 0.1 equiv. of benzoic acid. This value remains quite stable after. The number of strongly bonded benzoic acid does not evolve so much also. This can be seen that after a certain point, it becomes impossible to add more ligand at the NP surface, thus the exchange is low.

The addition of higher quantity of benzoic acid seems to The same variable shows provoke a saturation of the outer shell of ligands and the release of more adsorbed species. As it can be seen for the continuous increase of the quantity of benzoic acid weakly bonded (I_w; 3.1 -10.5 molecules) and the stabilization of the same variable but for octanoic acid (6.5 molecules) till 0.30 equiv. of benzoic acid is added into the setup (4.8 molecules).

The release of the octanoic moieties can be corroborated by the information of the "free" fast exchanging ligand (I_f), which increase for each addition step. The same variable shows the same trend for the benzoic acid, indicating that till certain point no more ligand can be exchanged or added onto the RuNPs surface and remains as "free" exchanging ligand.

These data provide interesting information on the ligand exchange ratio, meaning on the quantity of octanoic acid released *vs* that of benzoic acid incorporated (OcAc I_s released / BAc I_s incorporated). For the same quantity of the two ligands present in the reaction medium, that is after addition of 0.20 equiv. of benzoic acid added vs $Ru_x(C_7H_{15}COOH)_{0.20}$, the obtained ratio is 1.3. Because 10.4 OcAc molecules are released and 7.9 BAc are incorporated. This ratio indicates that the quantity of octanoic acid released is superior to the quantity of benzoic acid incorporated. Thus, the RuNPs surface is probably less crowded. This can be explained by the fact that benzoic acid has more steric hindrance and needs more place to be coordinated. But benzoic acid may be also a stronger stabilizing agent for which less molecules are needed to cap the RuNPs.

As a conclusion, it can be seen that the addition of the aryl ligand can remove certain quantity of octanoic acid from the RuNPs but at the end only around 37.6 % ([⅓ - ⅔]) of the capping ligand are composed of benzoic acids and the rest as octanoic acids (13.1 OcAc *vs* 7.9 BAc).

Figure 4.7 provides a view of the surface coverage of the particles after addition of 0.1 equiv. of benzoic acid in comparison with the initial surface coverage for $Ru_x(C_7H_{15}COOH)_{0.20}$ NPs

together with estimated numbers of the different types of ligands, namely ligand strongly attached (I_s), weakly interacting (I_w) and "free"in exchange (I_f). This view has been built from the estimated numbers of ligands given in table 4.2.

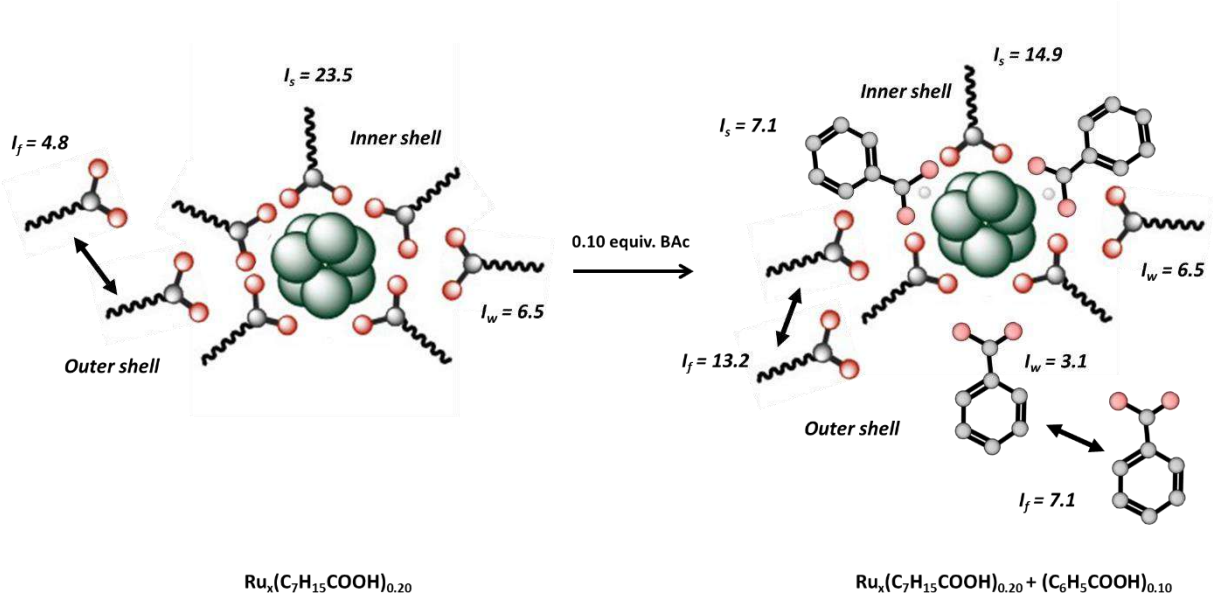

Figure 4.7 Left: Estimated initial surface mapping of $Ru_x(C_7H_{15}COOH)_{0.20}$ NPs; right: estimated new surface coverage obtained after the ligand exchange with 0.10 equiv. of benzoic acid.

In order to corroborate that the octanoic acid was released into the reaction medium, a NOESY analysis has been performed for each step of the experiment (*see* section 6.1.3.6.3). Figure 4.8 presents the spectrum corresponding to the addition of 0.05 equiv. of benzoic acid to the colloidal suspension of $Ru_x(C_7H_{15}COOH)_{0.20}$ NPs.

It can be observed that even at this low amount of benzoic acid added, octanoic acid has been released and that it does not present any interaction with the RuNPs (figure 4.8 positive NOE in blue), supporting the ligand exchange previously described by other NMR techniques.

To remember, the positive NOE can only be observed when small molecules are free in the solution, meaning that they are not part of the inner or outer shell of the RuNPs.

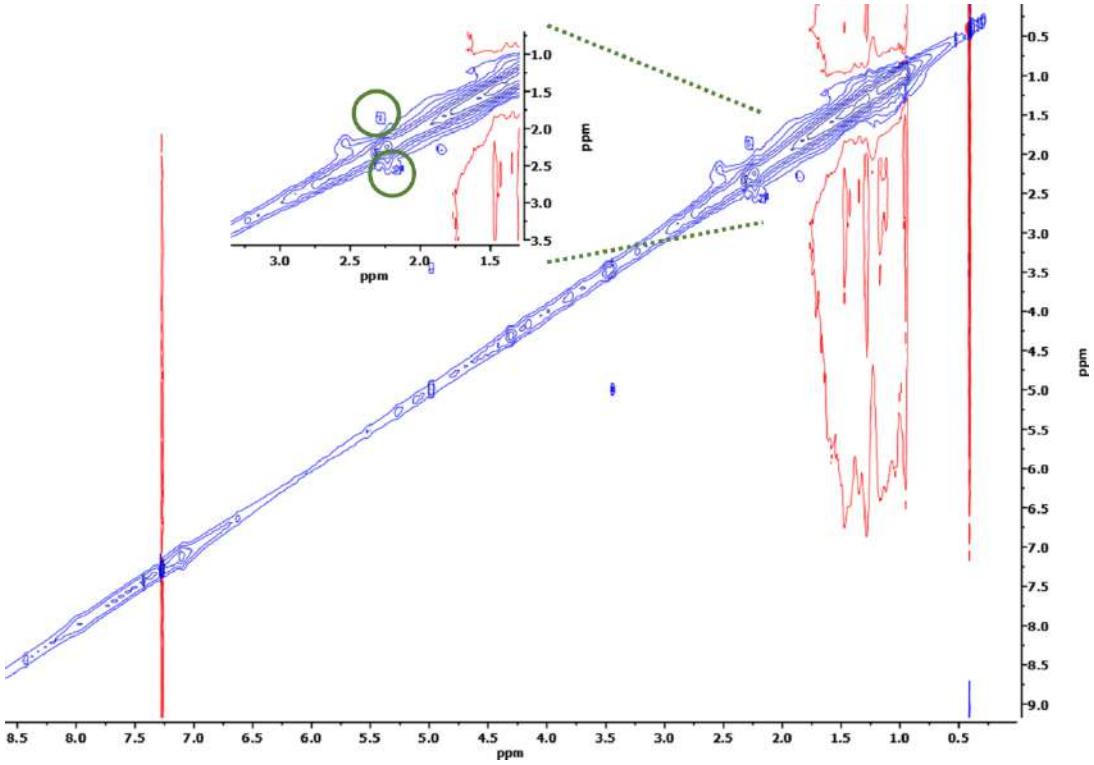

Figure 4.8 NOESY NMR spectrum (C_6D_6) recorded gathered after addition of 0.05 equiv. of benzoic acid to colloidal suspension of $Ru_x(C_7H_{15}COOH)_{0.20}$ NPs. The positive NOE is highlighted in green circles.

DOSY analyses shown that the diffusion coefficient of the strongly bonded ligand (D_s) remains quite similar during the whole ligand exchange experiment. Thus, it is expected that the RuNPs did not suffer any size or morphology modifications. However, it is important to corroborate the surface state of the nanosystem by TEM analysis.

After these NMR studies that showed the ligand exchange taking place at the NP surface, one question arises about the evolution of the particles in terms of size or/and shape. DOSY analyses shown that the diffusion coefficient of the strongly bonded ligand (D_s) remains quite similar during the whole ligand exchange experiment. Thus, it is expected that the RuNPs did not suffer any size or morphology modifications. However, it is important to corroborate the surface state of the nanosystem by TEM analysis in order have a better answer to this question.

The TEM analysis has been performed after the last step of the ligand exchange study (addition of 0.30 equiv. of benzoic acid) and the results were compared to the TEM data of the initial $Ru_x(C_7H_{15}COOH)_{0.20}$ NPs as illustrated in figure 4.9. Similar morphology and size (ca. 1.55 ±

0.21 nm for initial $Ru_x(C_7H_{15}COOH)_{0.20}$ NPs against ca. 1.57 ± 0.28 nm after addition of 0.30 equiv. BAc) have been observed in both cases indicating that the particles did not evolve significantly during the ligand exchange study.

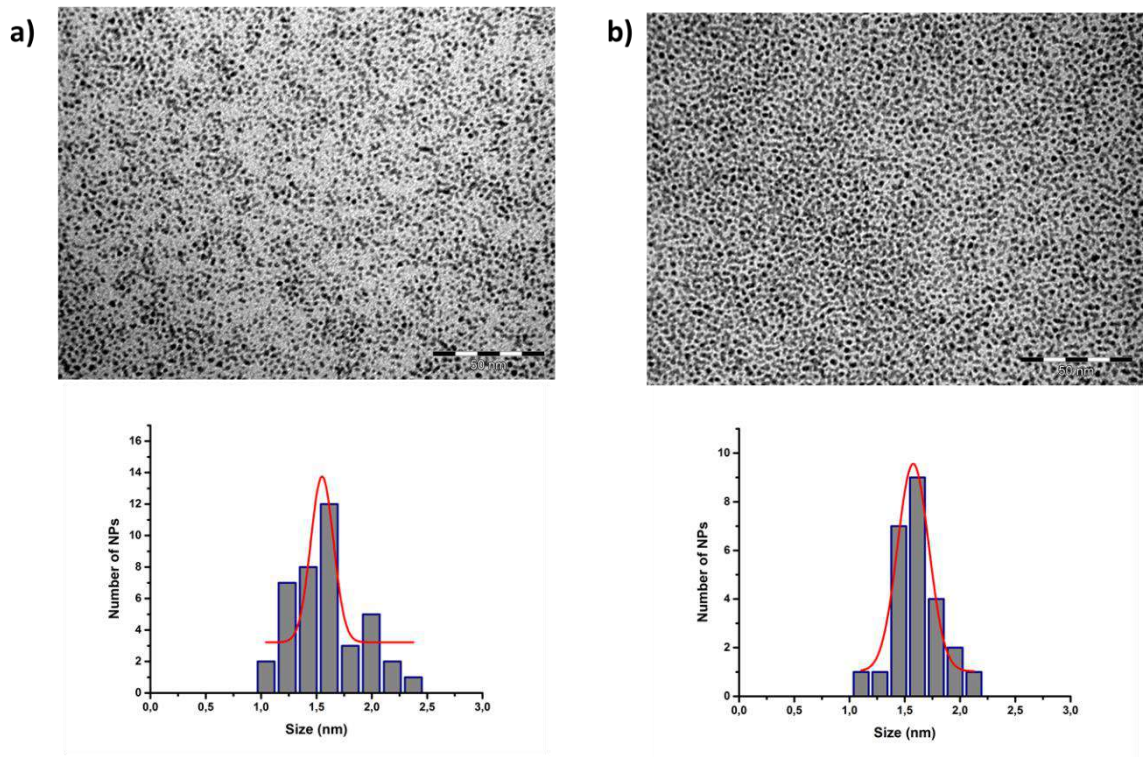

Figure 4.9 TEM micrographs of (a) $Ru_x(C_7H_{15}COOH)_{0.20}$ NPs, scale bar: 50 nm; and (b) $Ru_x(C_7H_{15}COOH)_{0.20}$ NPs + 0.30 equiv. of BAc, scale bar: 50 nm. Fast NPs frequency count is presented for each sample.

The experimental tools used to follow the ligand exchange experiments evidenced that benzoic acid could be incorporated at the surface of octanoic acid pre-stabilized RuNPs through the release of octanoic acid molecules from the metal surface, up to a certain quantity, without observing any reduction of the aryl ligand. In the reaction conditions applied, the exchange was not complete, but it could be estimated that at least *ca.* ([⅓ - ⅔]) of the RuNPs surface was covered by benzoic acid. TEM analysis showed no evolution of the NP morphology thus indicating a good stability of the particles. These results point out it is possible to introduce a second carboxylic acid like benzoic acid at the surface of octanoic acid-stabilized RuNPs without modification in morphology and size of the particles.

There are two main parameters to consider in order to explain the ligand exchange observed, namely steric hindrance and acidity (figure 4.10). Benzoic acid having higher steric hindrance than octanoic acid it is expected to occupy a higher bulk volume at the NP surface. This means, it can be difficult for benzoic acid to coordinate onto a crowded NP surface as it was the case for the initial $Ru_x(C_7H_{15}COOH)_{0.20}$ NPs (figure 4.10 a).

Thus, the driving force for the ligand displacement observed may arise from the difference in acidity between the two types of carboxylic acids. Indeed, benzoic acid displays an acidity five times higher than that of octanoic acid. This suggests that the benzoate form is easier to get than the octanoate one. Thus, when benzoic acid was added into the colloidal suspension of $Ru_x(C_7H_{15}COOH)_{0.20}$ NPs, an acid-base exchange may have happened, thus weakening the adsorption energy of the octanoate and provoking its release which probably allowed the benzoate to coordinate at the metal surface (figure 4.10 b).

These processes are interdependent and the fact that not all octanoates were replaced indicates that the affinity of the benzoic acid onto the RuNPs is quite similar to that of octanoic acid or even slightly lower due to the exchanging ratio. It is thus more reasonable to propose an equilibrium between the two carboxylate species that can be governed by steric reasons. This is illustrated on figure 4.10 a.

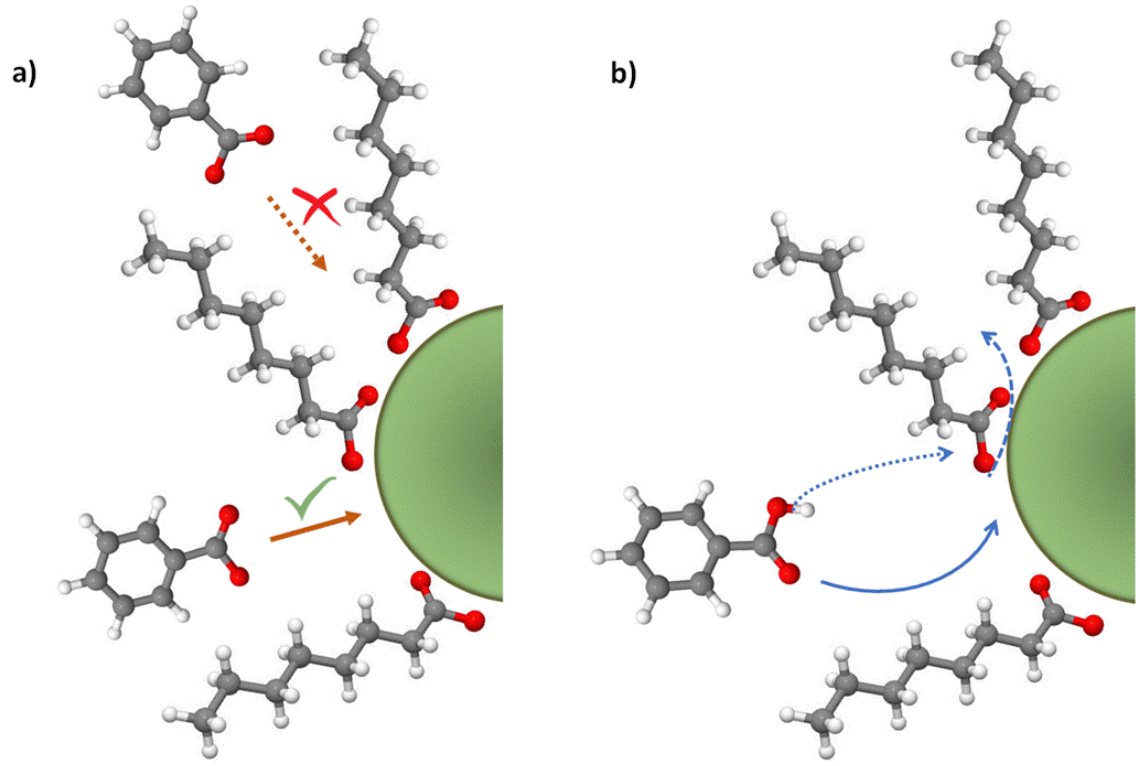

Figure 4.10 Representation of the octanoic *vs* benzoic acid ligand exchange at the RuNPs surface. Possible driving forces: (a) steric hindrance; (b) acidity.

The results of this ligand exchange study indicate that such a strategy may be followed in order to achieve the anchoring of a photosensitizer bearing pending carboxylic acid groups at the surface of pre-formed RuNPs stabilized by octanoic acid and probably also in the case of pentanoic acid-stabilized RuNPs. Doing so, it can be expected to have at least a certain amount of the PS grafted onto the metal surface and thus to get a hybrid nanomaterial for the target water-splitting reaction.

The next section will provide theoretical calculation results that were performed in order to understand better the ligand exchange reaction.

4.2.3 DFT Modelling of the Involved Species in the Ligand Exchange

The ligand exchange between interacting molecules with a metal surface is expected to be possible only if the exchanged ligand has a lower affinity with the metal surface than the incorporated moiety. In other words, it is expected from the new capped ligand to better stabilize the NPs or the ligand exchange phenomenon will not be able to be achieved.[117]

The stability granted by a capping ligand to the metal surface can be related to its adsorption energy.[294] In order to study the affinity of both octanoic and benzoic acids with the ruthenium surface, the protonated and deprotonated carboxylic species involved in the ligand exchange experimentally studied were deposited onto the (001) plane of the Ru_{55} NP model (*see* section 6.2.1). Then a periodic DFT optimization was performed for each studied system (*see* section 6.2.2) and the ligand adsorption energy obtained for each capping ligand (*see* section 6.2.3). The obtained values are presented in section appendix B.3 and corresponding coordinates in section appendix F.

The carboxylic acid isomers considered in the structures reported in Figure 4.11 are not the most stable one. In the ethanoic acid case, the presented structures for the adsorption of carboxylic acids are more stable (7.7 kcal.mol^{-1}) when the acid proton rotated 180° in order to have higher interaction with the metal surface ($E_{ads\text{-}bi\text{-}H}$ = -16.2 kcal.mol^{-1} $E_{ads\text{-}bi\text{-}H\ 180°}$ = -23.9 kcal.mol^{-1}).

As it was observed from previous carboxylic acid ligands analyses, the most stable configuration is the carboxylate form (figure 4.11) due to the low activation energy of the O-H bond (*see* section 2.4.1).

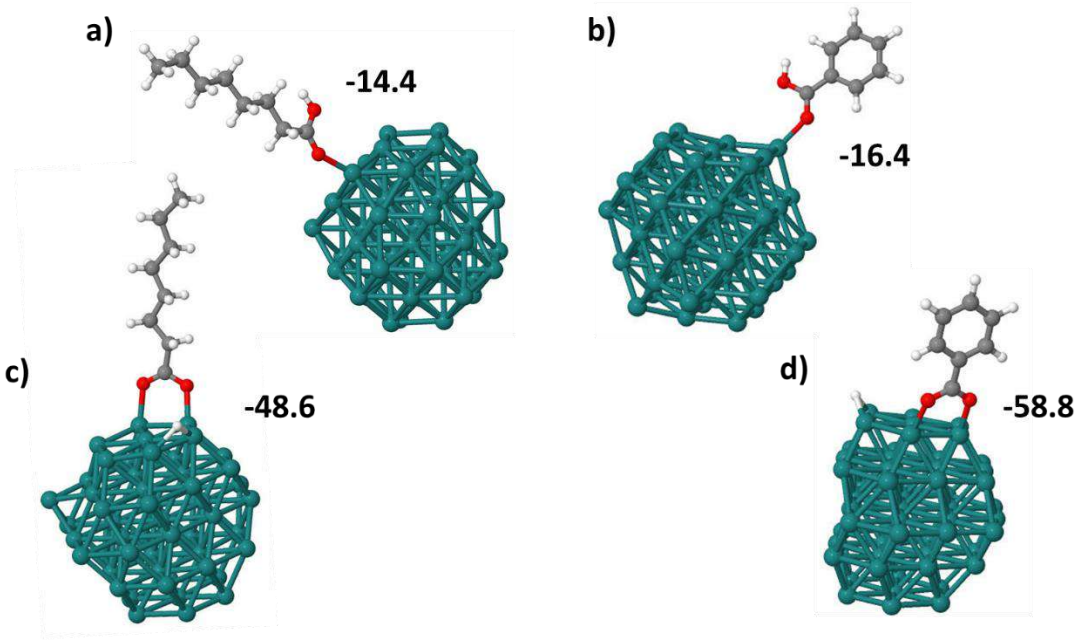

Figure 4.11 Theoretical models representing the interaction of carboxylic moieties with the Ru_{55} NP over the (001) plane. (a) octanoic acid; (b) benzoic acid; (c) octanoate; (d) benzoate. The E_{ads} (kcal.mol^{-1}) are also presented.

Comparing the adsorption energies of the deprotonated moieties, it was observed that the benzoate stabilizes the Ru_{55} NP 10.2 kcal.mol^{-1} more than the octanoate adsorbed in the same Ru_{55} NP (001) plane. This preliminary result, although obtained on a bare surface, is in favor of positive octanoate *vs* benzoate ligand exchange owing to higher stability that the benzoate is expected to provide to the metal system.

Previously, it was proposed two parameters susceptible to influence the ligand exchange onto preformed RuNPs, namely acidity and steric hindrance. The acidity can be discussed on the basis of DFT adsorption energy values calculated for protonated and deprotonated carboxylic entities. These data completed by the inductive effect provided by the aryl group in benzoic molecule, lead to a stronger electron donor property for the benzoate in comparison with the octanoate (electronic effects). Thus, this could explain the values observed for the adsorption energies of the carboxylate moieties. Therefore, at this stage, the benzoate appears as a better stabilizer and the exchange of octanoate by benzoate should be favored.

However, the steric effects between ligands plays an important role to determine the surface composition of the Ru_{55} NP and thus, corroborate the viability of a ligand exchange.[295] Indeed the blockage of binding sites by coordinated ligands can prevent the adsorption of new

species, and even more when the incoming ligands have a higher steric hindrance than those already adsorbed. [296] Moreover, surface ligands have an effect on the electronic properties of the metal surface and, in the case of RuNPs, tend to weaken adsorption strengths. Therefore, a theoretical study was also performed on surface crowded nanoparticles. In order to describe a more trustworthy ligand exchange reaction (figure 4.12).

The DFT analyses were carried out by taking into account the DFT capped ligand titration previously described for $Ru_x(C_7H_{15}COOH)_{0.20}$ NPs (*see* section 3.2.5.3.4). In this study, the $Ru_{55}(C_7H_{15}COO)_{14}(H)_{14}$ NP was found to be a stable composition at the experimental conditions range *p*, [$C_7H_{15}COOH$]. But, due to technical issues two slightly less crowded Ru_{55} NP ($Ru_{55}(C_7H_{15}COO)_{10}(H)_{10}$ and $Ru_{55}(C_7H_{15}COO)_{12}(H)_{12}$) were used in order to study the viability of the ligand exchange.

Owing to the aim of the studies, two Ru_{55} NP models with a combination of octanoates and benzoates as capping ligands were built and optimized ($Ru_{55}(C_7H_{15}COO)_3(C_7H_{15}COO)_8(H)_{11}$ & $Ru_{55}(C_7H_{15}COO)_5(C_7H_{15}COO)_8(H)_{13}$). The coordinates of the obtained structures are reported in section appendix F. The ligand exchange proposed reactions are presented on figure 4.12.

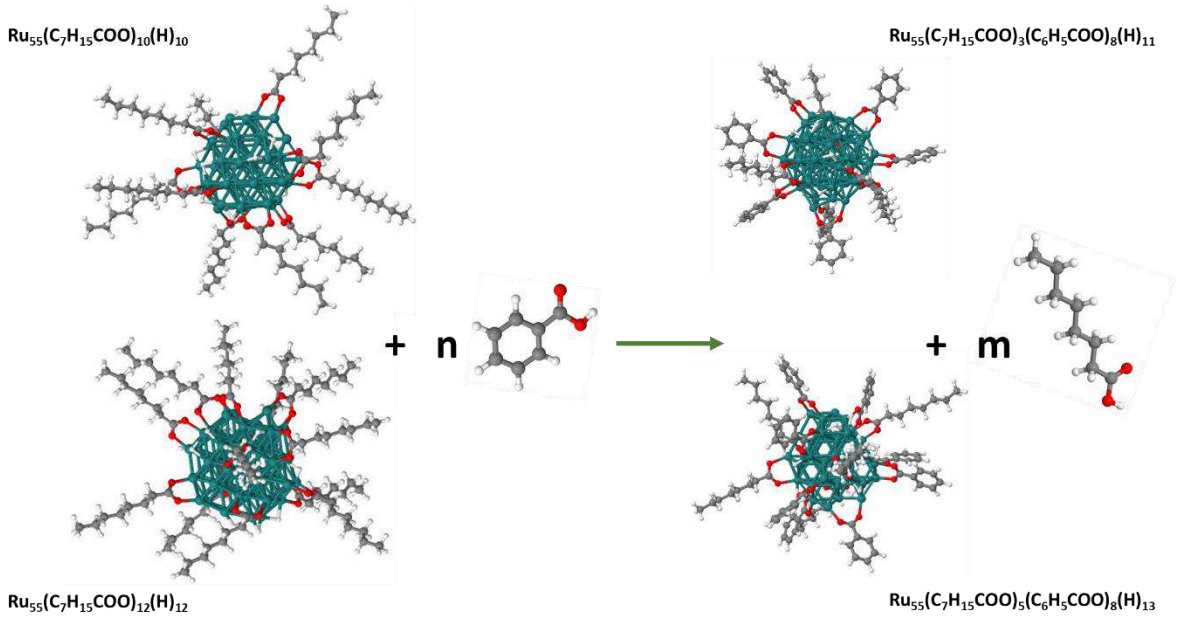

Figure 4.12 Ligand exchange reactions between octanoic and benzoic acids onto Ru_{55} NP studied by DFT.

The DFT energies obtained for the optimized structures of figure 4.12 (*see* section appendix B.4), are summarized in table 4.3. These data can be used to determine the thermodynamically direction of a reaction in order to predict the viability of a ligand exchange.

Table 4.3 DFT energies obtained for ligand exchange reactions between octanoic and benzoic acid onto Ru_{55} NP.

DFT optimized structure energies (eV)				**DFT reaction energy (kcal.mol^{-1})**
$Ru_{55}(C_7H_{15}COO)_{10}(H)_{10}$ + 8 C_6H_5COOH → $Ru_{55}(C_7H_{15}COO)_{10-m}(C_6H_5COO)_8(H)_{18-m}$ + m $C_7H_{15}COOH$				
-1902.94	8*(-98.87)	-1970.43	5*(-145.87)	-135.65
		-1676.49	7*(-145.87)	-85.02
$Ru_{55}(C_7H_{15}COO)_{12}(H)_{12}$ + 8 C_6H_5COOH → $Ru_{55}(C_7H_{15}COO)_{12-m}(C_6H_5COO)_8(H)_{20-m}$ + m $C_7H_{15}COOH$				
-2197.64	8*(-98.87)	-1970.43	7*(-145.87)	-67.46
		-1676.49	9*(-145.87)	-16.84

This DFT study does not represent the ligand exchange reaction as experimentally studied in section 4.2.2. Consequently, the optimized structures do not correspond exactly to the surface mapping found in the experimental study, and this study will be completed in the nearest future by considering the best surface coverage value according to the present DFT calculations. However, a clear trend in the octanoic acid releasing *vs* the incorporation of benzoic acid can be seen. According to the DFT reaction energy results, the ligand exchange is thermodynamically favorable and viable in all described reactions (figure 4.13).

However, the subsequently addition of ligands to the Ru_{55} NP stabilize the *d*-band center of the NP,[297] making it more stable.[298] Thus, it is not possible to evaluate the real meaning of the DFT reaction energy for the first proposed reaction, where three more carboxylates were incorporated. However, the second reaction involves the addition of only one benzoate obtaining an energy stabilization of -85.02 kcal.mol^{-1}. This value is higher than for the adsorption of a single benzoate into Ru_{55} bare NP, which is -58.8 kcal.mol^{-1}, considered as probable maximum adsorption value. Thus, it can be concluded that there is an electronic effect that makes the adsorption of benzoates more favorable than octanoates.

This phenomenon could be attributed to the higher sigma donation of the benzoic species and thus, higher retrodonation to the π* orbital, making it more stable in terms of electronic

effects. In order to corroborate this assumption, it will be necessary to perform a COHP analysis and compare with Ru_{55} NP fully covered by octanoates and/or benzoates.

The third reaction also involves the adsorption of one extra carboxylate but onto a more crowded Ru_{55} NP. For this situation the obtained energy is -67.46 kcal.mol^{-1} which is closer to the adsorption of a single benzoate (-58.8 kcal.mol^{-1}) but still greater. This means that the exchange is still favorable but it also indicates that the higher the coverage value, the lower the exothermicity of the exchange reaction.

This could be correlated to the steric hindrance effects previously proposed. Anyway, this conclusion was corroborated with the last reaction where even with the decrease of one carboxylate, less crowded surface, the reaction is still thermodynamically favorable.

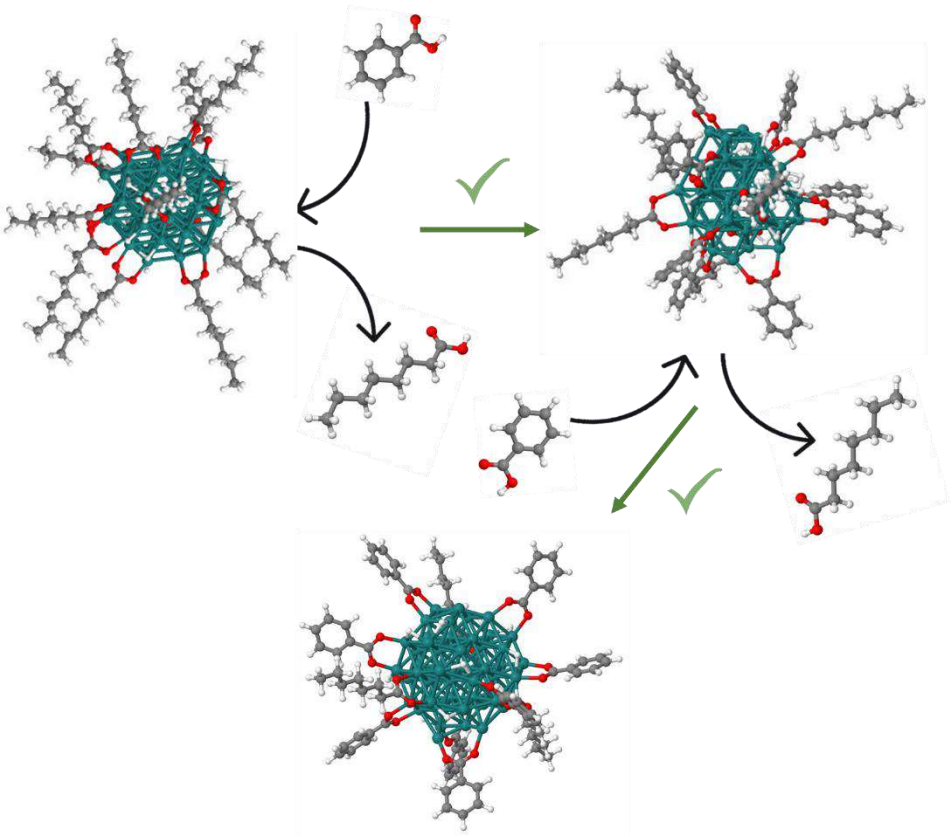

Figure 4.13 Representation of ligand exchange between octanoic and benzoic acids according to the obtained DFT energies for the studied reactions.

The obtained data can be analyzed as the average adsorption energy for all capped ligands. The data for the Ru_{55} NP covered by octanoates were interpolated for the adsorption

energies reported in section appendix B.2, meanwhile for the ligand exchange studied systems, the mean adsorption energy of the carboxylates is described in the section appendix B.4.

As a result, it was observed that, considering the ligand mean adsorption energy for the two systems, the stabilization is higher for the particle covered by a ligand mixture than when it is only covered by octanoates (table 4.4). For example, for the eleven adsorbed carboxylates, the Ru_{55} NP covered by a ligand mixture is stabilized by *ca.* 4.5 kcal.mol^{-1} for each capped moiety. Hence, the result shows that the benzoate has a higher affinity to the metal center and thus, the ligand exchange is possible. As a consequence, a more stable system was obtained but less reactive, as expected.

Table 4.4 Average adsorption energy in Ru_{55} NP covered by octanoates and a mixture of capped ligands.

Carboxylates species	**Ru_{55} NP covered by**	
	Octanoates (kcal.mol^{-1})	Octanoates & Benzoates (kcal.mol^{-1})
11	-44.8	-49.3
13	-44.1	-45.7

In conclusion, the DFT results indicate that a certain amount of octanoic acid ligands can be replaced for benzoic acid ligands which induces the octanaote release to the reaction medium, which agrees with the experimental findings. Moreover, the theoretical approach evidenced that the benzoic acid has a better affinity for the Ru_{55} NP due to electronic effects. However, as also estimated in the experimental titration, it was observed that [⅗ - ⅔] of octanoates remain at the RuNPs surface. This indicates that the initial steric hindrance of the inner and outer shells presented in the experimental conditions (crowded $Ru_x(C_7H_{15}COOH)_{0.20}$ NPs) plays an important role in the ligand exchange. In order to corroborate this steric effect more DFT calculations need to be performed.

4.3 Ligand Exchange at RuNPs Surface: Octanoic Acid *vs* TFA

The ligand exchange experiments described before were carried out in order to study the possibility of introducing benzoic acid (aryl ligand) at the surface of RuNPs pre-stabilized by octanoates. Even so, the octanoate *vs* benzoate ligand exchange was not complete, the obtained results have shown that this strategy could be followed, thus opening the way to integrate a molecule of interest (bpy-based photosensitizer) at the surface of the particles *via* the same anchoring mode (carboxylic acid) for a target application (water splitting process).

It has been reported in the literature that the ligand exchange in nanomaterials can be affected for the acidity of the incorporated species.[299] This phenomenon has been observed in the frame of a ligand exchange involving a proton exchange, as it was the case in the previous study. It has been also observed that highly negative charged molecules often provide more stability to the NP surface thus making the facility to liberate the protons a key-point.[300] As well, some stabilizing agents were observed to have different affinity properties with the metal surface depending on the acidity of the reaction medium. Hence, the ligand exchange ratio can be tuned via the acidity properties of the ligands or of the reaction medium.[301]

In section 4.2, the ligand exchange between pre-stabilized RuNPs by octanoic acid and benzoic acid was shown possible but with a process efficiency lower than *ca.* 40.0 % ($I_{s\text{-}BAc}/I_{s\text{-}total}$). According to the obtained experimental and theoretical data, this low efficiency can result from the steric hindrance of the benzoic acid ligand, because its affinity and acidity appeared higher than those of the octanoic counterpart. Therefore, in order to force the coordination of a carboxylic acid ligand onto the RuNPs surface, it was decided to repeat the ligand exchange study by using of a smaller ligand that has a higher acidity. For this purpose, trifluoracetic acid (TFA) has been chosen.

4.3.1 Titration of Octanoic vs TFA Exchange on the RuNPs Surface

In order to analyze the influence of the acidity in the ligand exchange process at the surface of RuNPs stabilized by octanoic acid, an experiment as described in section 4.2.2 was performed. The RuNPs system chosen for this experiment was a sample of $Ru_x(C_7H_{15}COOH)_{0.20}$ NPs synthetized in pentane after the addition of extra 0.20 equiv. of octanoic acid (OcAc). This system was selected in order to have a completely crowded RuNP surface and thus, observe the real potential of the acid through its acidic character and reduce the steric hindrance effect.

The TFA has a *pKa* of 0.2, a value of four orders of magnitude stronger than that of the initial attached ligand (OcAc; *pKa* = 4.9) . This difference results from the presence of three fluorine atoms in the ligand which renders the proton of the carboxylic acid highly acidic and its liberation easy. However, the presence of these halogens also reduces the electronic donor strength of the whole molecule.[302] Therefore, this system is suitable for observing the influence of the incoming ligand acidity (due to the probable acid-base exchanges onto the RuNPs surface) and removing the "affinity effect" in the ligand exchange process.

Previous titration experiment (*see* section 3.2.5.3.5; table 3.19) indicated that the initial $Ru_x(C_7H_{15}COOH)_{0.20}$ NPs are stabilized by *ca.* 23.5 octanoates strongly attached at their surface (I_s) and *ca.* 6.5 carboxylates that are weakly interacting and present in an outer shell (I_w). After the addition of 0.2 equiv. of extra octanoic acid, a similar quantity of ligands was found in the outer and inner shells (*ca.* I_s = 20.7; I_w = 7.7). However, a high quantity (*ca.* 41 molecules) of free or exchanging ligand was observed. Therefore, this system is suitable for observe the influence of the acidity in the ligand exchange.

The sample of pre-formed RuNPs was redispersed in deuterated benzene inside an NMR tube under argon atmosphere. After, 0.10 equiv. of trifluoroacetic acid (TFA) was added and the NMR tube was plunged in an ultrasonic bath for 30 min at r.t. Scheme 4.3 provides a schematic representation of the ligand exchange reaction at the surface of the particles. ^{1}H, ^{19}F-NMR and DOSY analyses were then performed (*see* section 6.1.3.7.4). In these analyses, the grease present in the solution was used as internal standard.

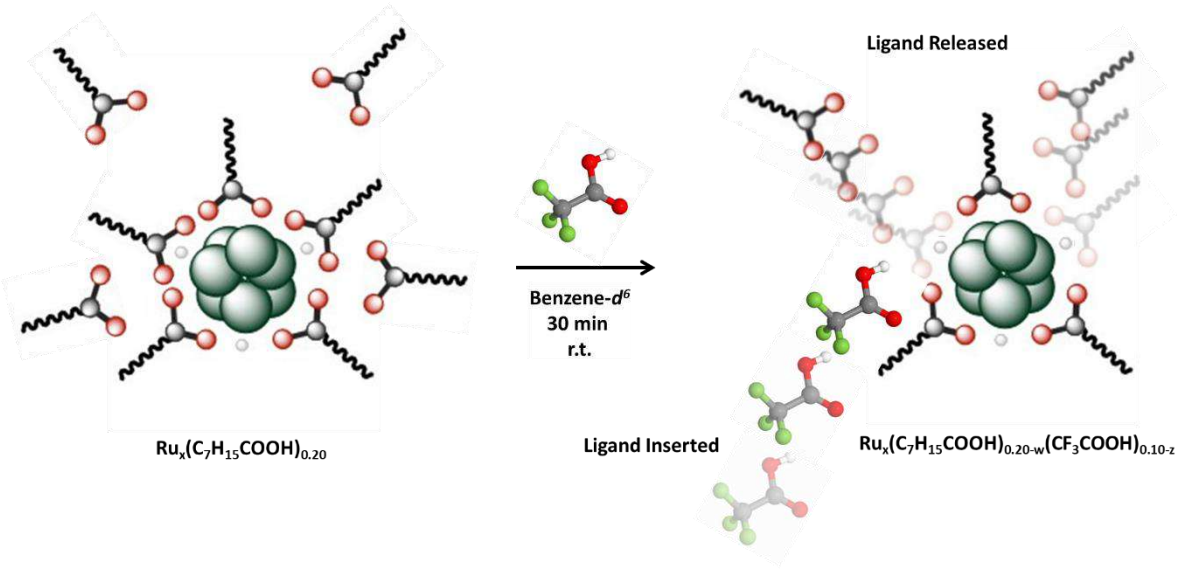

Scheme 4.3 Representation of the ligand exchange reaction between $C_7H_{15}COOH$ and CF_3COOH at starting from RuNPs sample $Ru_x(C_7H_{15}COOH)_{0.20}$ NPs + 0.2 equiv. OcAc.

^{1}H-NMR allowed to follow only the fate of the octanoic acid ligand due to the absence of measurable protons in TFA. ^{19}F-NMR was thus used to follow the coordination of added TFA ligand. These NMR experiments allowed to observe variations of the signals, namely their broadness or sharpness, a parameter which is indicative of the interaction strength of the studied ligands with the RuNPs.

On the ^{1}H-NMR spectrum (figure 4.14) it can be observed that the addition of TFA leads to a decrease of the signal broadness in the alkyl region of pre-formed $Ru_x(C_7H_{15}COOH)_{0.20+0.20}$ NPs. The observation of narrower signals can be explained by the presence of higher quantity of octanoic acid in solution as the result of a release of octanoic acid from the metal surface. This is particularly highlighted when comparing the spectrum of the initial $Ru_x(C_7H_{15}COOH)_{0.20}$ NPs with that recorded after addition of TFA. Moreover, there is still broadness in the region corresponding to octanoic acid which indicates that coordinated octanoic acid remains and the exchange was not complete.

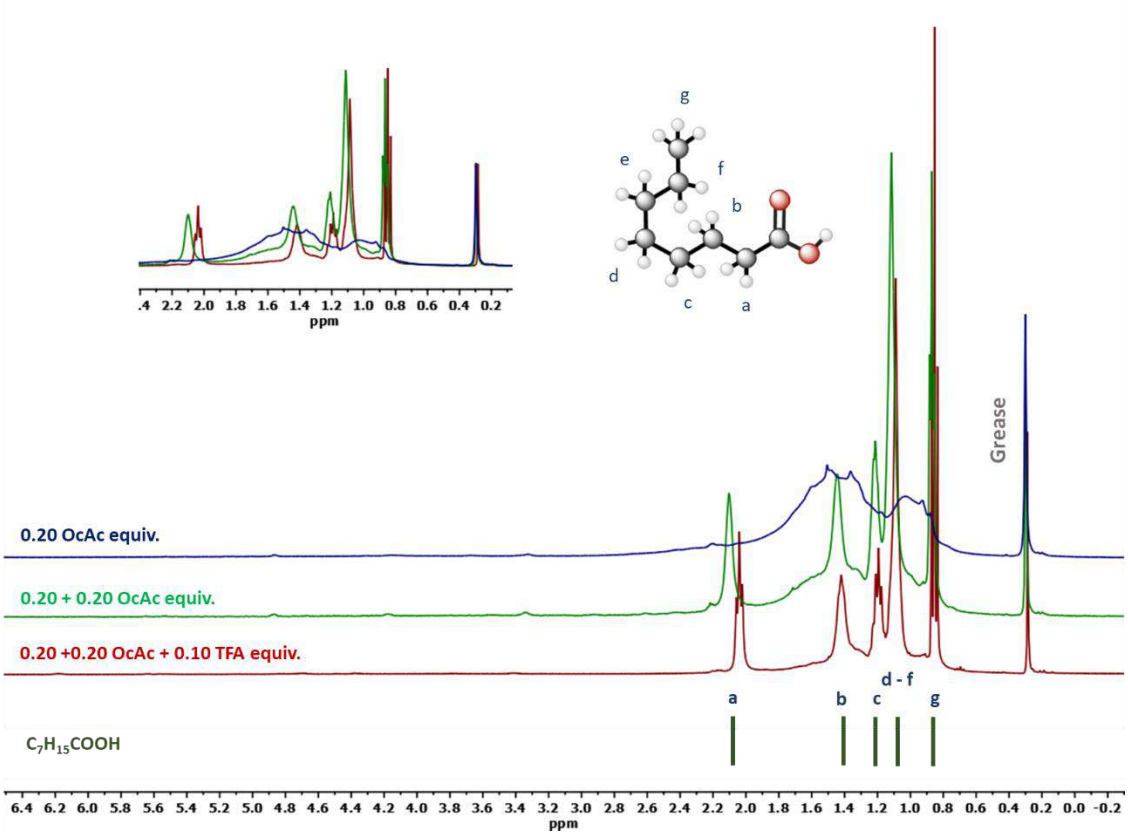

Figure 4.14 ^{1}H-NMR (C_6D_6) spectra of initial $Ru_x(C_7H_{15}COOH)_{0.20}$ NPs, represented as 0.20 equiv. OcAc, and after addition of octanoic and TFA. (blue) initial NPs stabilized with 0.20 equiv. of OcAc; (green) $Ru_x(C_7H_{15}COOH)_{0.20}$ NPs + 0.20 equiv. of OcAc; (red) $Ru_x(C_7H_{15}COOH)_{0.20}$ NPs + 0.20 equiv. of OcAc + 0.10 equiv. of TFA. Chemical shifts of the protons of free octanoic acid ($C_7H_{15}COOH$) are given as green bars at the bottom

The proton-NMR shows that the addition of TFA to pre-formed $Ru_x(C_7H_{15}COOH)_{0.20 + 0.20}$ NPs provokes a release of octanoic acid, but not totally. This means that the acidity properties of TFA allowed displacing some octanoates from the metal surface. Since, the chosen system was crowded, inner (*ca.* 20.7 molecules) and outer shell (*ca.*7.7 molecules) and full of octanoates in the reaction media (*ca.* 41 molecules), the effect of the steric hindrance is reduced and define that the acidity of these ligands is crucial in the ligand exchange process. The next logical question is how the TFA is interacting at the metal surface? In order to answer this question, a ^{19}F-NMR spectrum was recorded.

The ^{19}F-NMR spectrum (figure 4.15) shows a broad signal (*ca.* 74.0 ppm) attributed to TFA in a strongly interacting mode with the RuNPs. A sharp peak at the same chemical shift as free TFA (*ca.* 75.6) is also visible. Therefore, it can be assumed that a certain quantity of the 0.10 equiv. of

added TFA is coordinated and also that there are TFA molecules which do not interact with the ruthenium surface being present as free or in dynamic exchange. The deconvolution of the ^{19}F-NMR spectrum indicates a contribution of 74.9 % of the signal for coordinated TFA the rest of the signal (25.1 %) corresponding to free ligand in solution or in dynamic exchange.

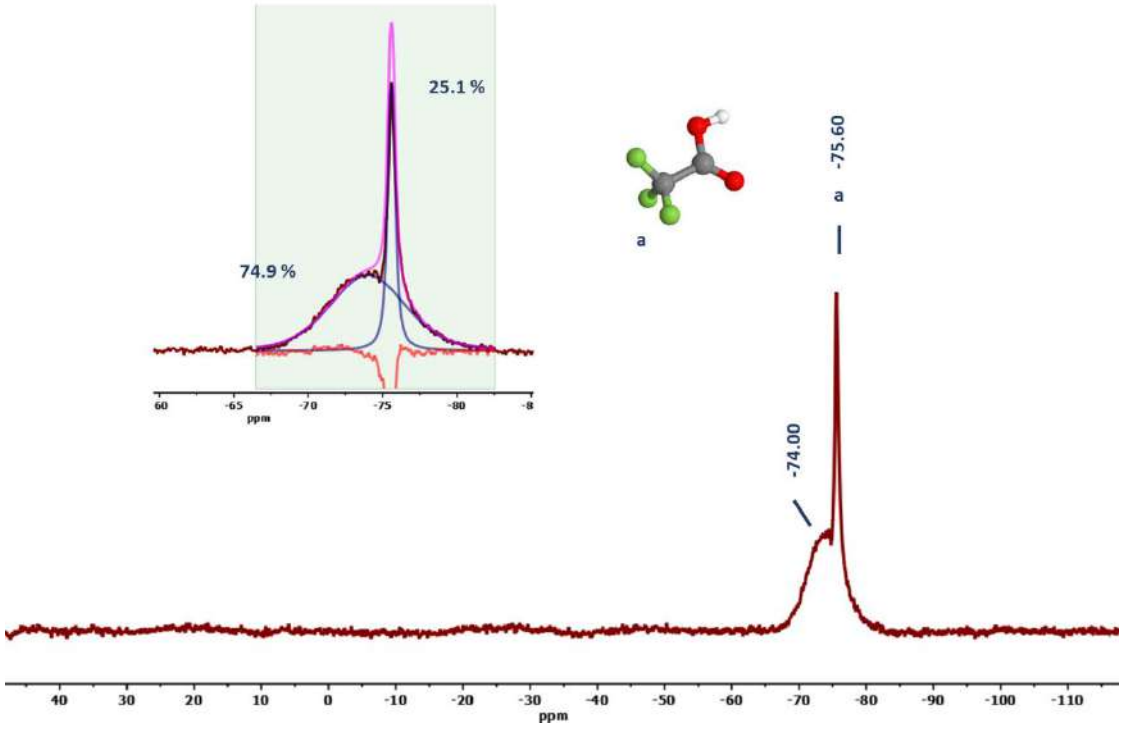

Figure 4.15 ^{19}F-NMR (C_6D_6) spectra of $Ru_x(C_7H_{15}COOH)_{0.20+0.20}$ NPs after the addition of 0.10 equiv. of TFA. The deconvolution of the spectrum and contribution percentage (%) of the signal are also presented.

The quantity of coordinated TFA ligands was determined by taking into account the size of the NPs (*ca.* 1.65 nm), their crystallinity (*hcp*), the magic number for metal clusters rules and the signal contributions obtained by deconvolution treatment of the ^{19}F NMR spectrum. This allowed to propose a mapping of the surface of the RuNPs. The calculations gave an estimated value of *ca.* 13 TFA molecules per RuNP that interact strongly with the metal surface (*see* table 4.6). Since, owing to technical issues, it was not possible to perform DOSY NMR for the fluorine isotopes. Thus, it was assumed that the rest of TFA is weakly interacting with the ruthenium surface, being either free in solution or in dynamic exchange. The estimated quantity of weakling interacting TFA is *ca.* 4.3 per RuNP.

With the aim to get a complete titration of the surface ligands, namely of octanoic acid molecules strongly and weakly interacting with the nanoparticles, 2D-NMR DOSY analyses were carried out as previously described in section 3.2.5.3.1 & 4.2.2. Proton DOSY NMR experiments were performed on the $Ru_x(C_7H_{15}COOH)_{0.20+0.20}(CF_3COOH)_{0.10}$ NPs. As it will be seen, these analyses allowed to complete the surface mapping of the RuNPs surface after addition of 0.10 equiv. of TFA and to determine the ratio of the octanoic vs TFA ligand exchange.

The studies were obtained by integrating the evolution of the octanoates signals (*ca.* [1.8 – 0.8] ppm) in DOSY analysis and their contributions were determined. As in previous DOSY NMR experiments, the diffusional attenuation could be fitted with a Stejskal-Tanner equation by using a bi-exponential analysis. This indicated the presence of two types of molecules interacting with the RuNPs surface, namely ligands with strong (D_s) and weak interaction (D_w).

The diffusion coefficients found for two these two types of ligands are D_s = 3.4x10^{-10} m^2.s^{-1} and D_w = 1.4x10^{-9} m^2.s^{-1}, respectively. It is worth to note that the second coefficient value (D_w) is very similar to that obtained for free octanoic acid (1.3x10^{-9} m^2.s^{-1}). This result indicates that there is a high quantity of free octanoic acid in the reaction medium, as expected for the release of octanoic acid into the reaction medium (table 4.5).

Table 4.5 Diffusion coefficients of octanoic acid moieties and corresponding signal weight for the addition of TFA to a colloidal suspension of $Ru_x(C_7H_{15}COOH)_{0.20+0.20}$ NPs.

OcAc added (equiv.)	**TFA added (equiv.)**	***Octanoic acid region***			
		D_s ($m^2.s^{-1}$)	Weight (%)	D_w ($m^2.s^{-1}$)	Weight (%)
0.00		1.5x10^{-10}	66.2	6.1x10^{-10}	33.8
0.20		1.6x10^{-10}	29.8	9.6x10^{-10}	70.2
0.20	0.10	3.4x10^{-10}	15.9	1.4x10^{-9}	84.1

D_{OcAc} = 1.3 x 10^{-9} m^2.s^{-1}; s = strongly and w = weakly interacting ligand

In the previous table, it can be observed the decrease of the strongly coordinated ligand contribution (D_s), meanwhile the quantity of weakly bonded species increases (D_w). The decrease

of almost *ca.* 50.0 % of strongly attached ligand evidences the release of the moiety to the outer shell or to the reaction medium.

The table 4.5 evidences the increase of the hybrid system mobility, represented for the increase in the diffusion coefficient of the strongly bonded ligand (D_s; $1.6x10^{-10}$ to $3.4x10^{-10}$ $m^2.s^{-1}$). This result is represented as a diminish of the hydrodynamic diameter of the RuNPs system. Which is expected, since smaller particles (TFA) are included in the inner shell of the system and bigger particles are released (OcAc). However, it is possible that the metal core is digested for the acid or modified. Thus, a TEM microscopy needs to be performed in order to solve this question (*vide infra*).

From the extracted data of DOSY analysis (diffusion coefficients of the observed species and corresponding contribution) it could be determined the quantity of octanoic acid ligands surrounding the RuNPs (*see* section 6.1.3.7.2). This allowed to define a reliable surface mapping of the RuNPs obtained after the addition of TFA (table 4.6).

Table 4.6 DOSY NMR data extraction of the quantity of different type of interacting ligands in the $Ru_x(C_7H_{15}COOH)_{0.20+0.20}$ NPs.

OcAc added (equiv.)	**TFA added (equiv.)**	**Is (OcAc/Ru_{NP})**	**Iw (OcAc/Ru_{NP})**	**If (OcAc/Ru_{NP})**	**Is (TFA/Ru_{NP})**	**Iw (TFA/Ru_{NP})**
0.00	---	23.5	6.5	4.8	---	---
0.20	---	20.7	7.7	41.1	---	---
0.20	0.10	12.3	1.8	50.0	13.0	4.3

A representation of this surface mapping is given in figure 4.16 that illustrates the ligand exchange between octanoic acid and TFA.

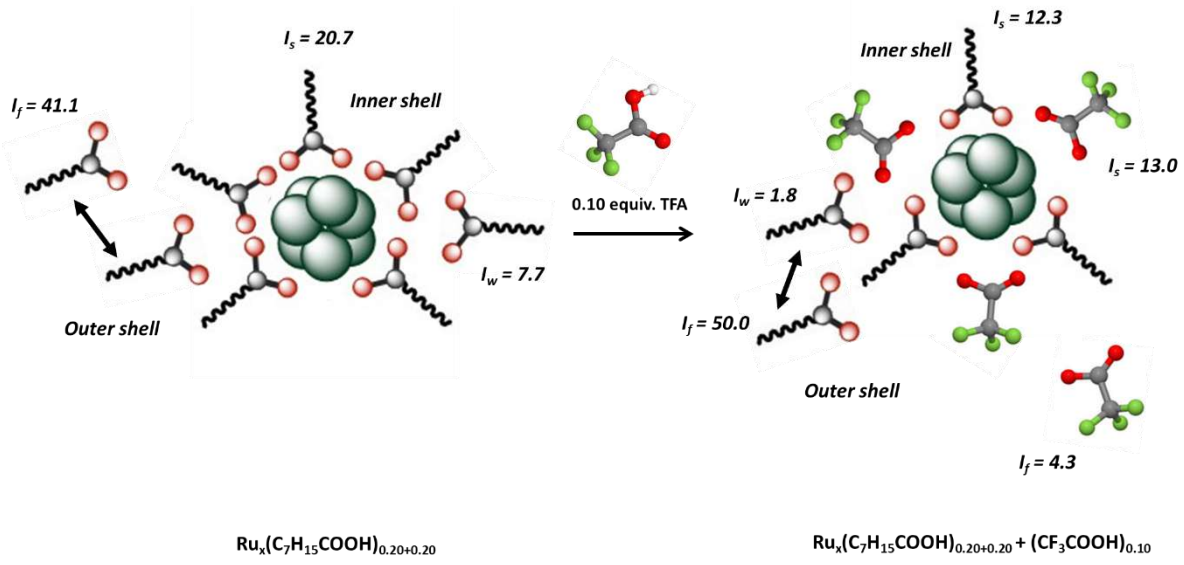

Figure 4.16 Representation of the octanoic acid vs trifluoroacetic acid ligand exchange with estimated numbers of each type of ligand surrounding the particles in initial $Ru_x(C_7H_{15}COOH)_{0.20+0.20}$ NPs and those obtained after addition of 0.10 equiv. of TFA. Ligand strongly attached (I_s), weakly interacting (I_w) and in exchange or free (I_f).

The data in table 4.6 show that the final RuNPs have a higher quantity of carboxylates (ca. five carboxylic molecules) that surround the inner shell. It appears that *ca.* 8.4 octanoates have been removed from the NP surface while 13 trifluoroacetates were incorporated. This result evidences that a higher number of trifluoroacetates (*ca.* 13/8.3 = 1.56) were coordinated compared to the number of octanoates released. This result can be attributed to the lower steric hindrance of TFA compared to that of octanoic acid.

It also highlights an increase of the surface coverage in the presence of TFA ligands. It is worth to mention that these results were obtained using only a small amount of ligand (0.10 equiv.) compared to the total quantity of octanoic acid present in the reaction medium (0.4 equiv.). This thus evidences the higher affinity of TFA for the ruthenium surface compared to octanoic acid, probably for a combined effect of acidity and steric hindrance.

In order to compare the ligand exchange reaction depending on adding either benzoic acid or trifluoroacetic acid onto RuNPs pre-stabilized with octanoic acid, data obtained for the addition of 0.10 equiv. of each incoming ligand have been reported in table 4.7. These data clearly reflect the different behavior observed for the two carboxylic acids added.

Table 4.7 Comparison of the ligand exchange reaction depending on the nature of the incoming ligand, namely benzoic acid or trifluoroacetic acid. The data correspond to the addition of 0.10 equiv. of each incoming ligand.

Ligand added	pKa	OcAc released (# molecules)	# Ligand incorporated (# molecules)	Ligand exchange ratio ($OcAc_r/A_i$)	Added ligand surface coverage (%)
BAc	4.2	10.4	7.1	1.46	40.57
TFA	0.2	8.4	13.0	0.64	51.38

From these data, it can be seen that the experiment performed by adding TFA led to the coordination of more trifluoroacetates than the number of benzoates incorporated (*ca.* 13.0 *vs* 7.1). This was accompanied to the release of less octanoates in the reaction medium. Given the lower *pKa* of trifluoroacetic acid compared to benzoic acid it can be expected that this carboxylic acid will have more ability to be introduced and exchange onto the RuNPs surface. But also, the higher number of TFA incorporated at the metal surface indicates the positive influence of the lower steric hindrance of this carboxylic acid compared to octanoic acid.

All together these observations, it can be proposed that both acidity and steric hindrance of the incoming ligand play a role in the exchange reaction. In the present comparative studies, for a same quantity of added ligand (0.10 equiv.) these two factors favored the coordination of more trifluoroacetates than octanoates at the surface of pre-stabilized RuNPs by octanoic acid. Complementary experiments would be to start from octanoic acid-stabilized RuNPs reacted with benzoic acid and then add TFA.

It has seen that the whole effects of TFA have led to a surface coverage of the final NPs with a higher quantity of added ligand. Even when TFA is thus a better exchanging ligand than benzoic acid, for the two systems, in the experimental conditions applied, it was not possible to remove all the octanoic acid. Therefore, more studies of the ligand exchange with TFA need to be done in order to try to release all the octanoates and get RuNPs with only TFA at their surface.

The RuNPs were exposed to a strong acid ligand in the ligand exchange process. Thus, it is possible that the system suffers a metal ripening[303] due to the change strength of the binding molecules.[304] This hypothesis can be reinforced due to the decrease of the hydrodynamic diameter observed by DOSY analysis (D_s; $1.6x10^{-10}$ to $3.4x10^{-10}$ $m^2.s^{-1}$).

Thus, one question arises about the fate of the particles in terms of size or/and shape. To answer this question, TEM analysis was performed from the reaction mixture obtained after addition of 0.10 equiv. of TFA.

The TEM images obtained were compared to those of $Ru_x(C_7H_{15}COOH)_{0.20}$ NPs and of $Ru_x(C_7H_{15}COOH)_{0.20+\ 0.20}$ NPs (Figure 4.17). Similar sizes were observed for the tree samples of RuNPs (*ca.* 1.69 nm for $Ru_x(C_7H_{15}COOH)_{0.20+\ 0.20}$ NPs vs 1.65 nm for $Ru_x(C_7H_{15}COOH)_{0.20}$ NPs).

However, a slightly different morphology was noticed. Indeed, the final particles seem to be more ill-defined, looking more elongated than spherical. But these results allowed to conclude that the morphology of RuNPs did not change importantly during the ligand exchange study.

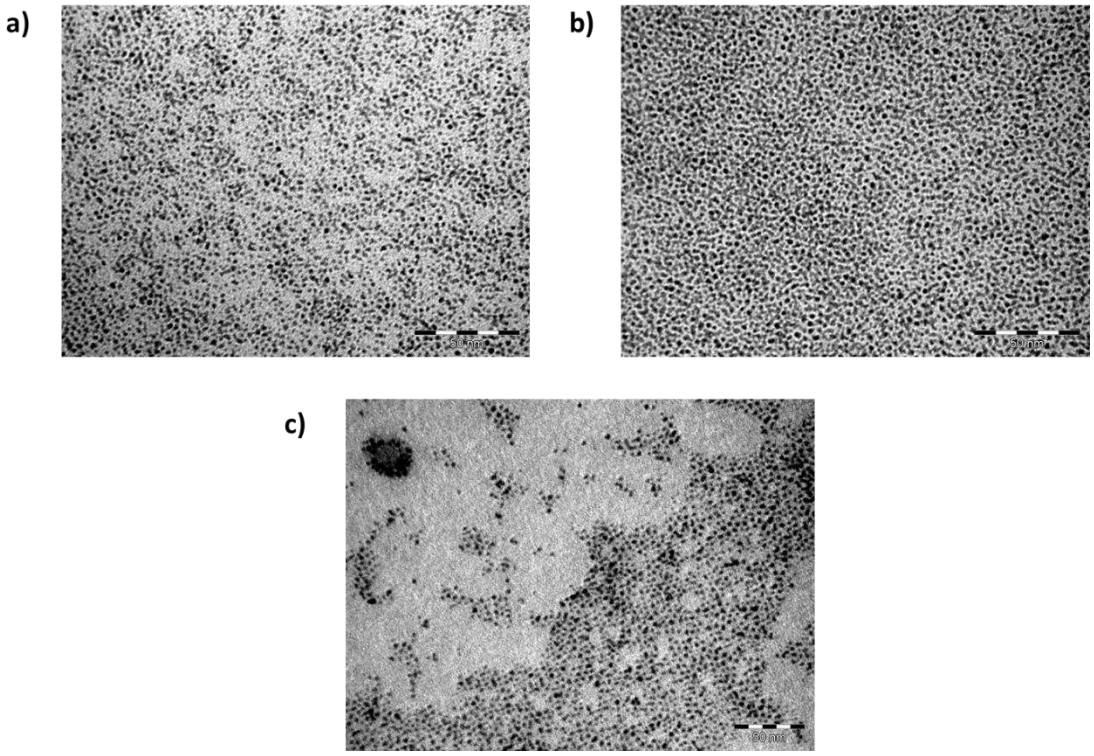

Figure 4.17 TEM micrographs of (a) $Ru_x(C_7H_{15}COOH)_{0.20}$ NPs, scale bar: 50 nm; (b) $Ru_x(C_7H_{15}COOH)_{0.20+0.20}$ NPs, scale bar: 50 nm; (c) $Ru_x(C_7H_{15}COOH)_{0.20+0.20}$ NPs + 0.10 equiv. of TFA, scale bar: 50 nm.

In conclusion of this part, a ligand exchange was achieved between octanoic acid and TFA that led to the release of octanoic acid and the coordination of TFA at the RuNP surface. No significant modifications of the RuNPs is terms of morphology and mean size have been observed. The exchange process was possible without adding a high quantity of incoming ligand. And even

more important the efficiency of exchange was observed to be higher than in the case of the exchange with benzoic acid. More trifluoroacetates were incorporated at the surface of the RuNPs compared to benzoic acid case. However, the exchange was not total and some octanoates remained at the surface of the RuNPs as already seen with benzoic acid.

All together the results obtained indicate that both the acidity and steric hindrance of the incoming ligand play a role in the ligand exchange process. But it cannot be assured that these variables are the only ones involved in the increase of the ligand exchange efficiency observed with TFA. Indeed, it can be expected that the inductive effect of TFA due to the fluorine atoms (ligand affinity strength) affects also the process. However, with the data in hand it is clear that the TFA is a better ligand for exchanging with octanoates than the benzoic acid.

In the next section, the observed ligand exchange and the role of the acidity and steric hindrance will be briefly discussed in terms of DFT calculations.

4.3.2 DFT Modelling of the Involved Species in the Ligand Exchange

As described in previous sections, the incorporation of a new capping ligand at the surface of preformed RuNPs involves that the incoming ligand possesses a higher affinity towards the metal surface, than the initial one. Meaning that the new ligands are better stabilizing agents.[117]

The experimental studies have shown that the addition of TFA gave rise to better ligand exchange ratio than the benzoic acid did. This effect was attributed to both the acidity and its steric hindrance of the TFA. However, one can also expect electronic effects in a ligand to influence the affinity of the molecule towards the surface of the RuNPs. This inductive effect of benzoic acid was discussed in section 4.2.3 and found to be quite important for the ligand exchange process and the stabilization of the particles.

The presence of three fluorine atoms in the TFA molecule induce a high acidity. Thus, a high rate for its deprotonation can be expected and so its fast coordination at the NP surface as carboxylate. However, TFA has a low sigma donor strength due to the inductive electronic effects provided by the fluorine atoms (attractive effects).[302] Therefore, the absorption energy of this

molecule onto the Ru_{55} NP model should be very useful in order to clarify its affinity towards the surface of RuNPs.

A similar procedure as previously described for benzoic acid was performed in order to estimate ligand affinity with the ruthenium surface (*see* section 4.2.3). The deprotonated species involved in the ligand exchange (octanoate and trifluoroacetate) were deposited onto the same crystalline plane (001) of the Ru_{55} NP model (*see* section 6.2.1) as schematized in figure 4.18. The obtained values are provided in the section appendix B.3 and structural coordinates in the section appendix F.

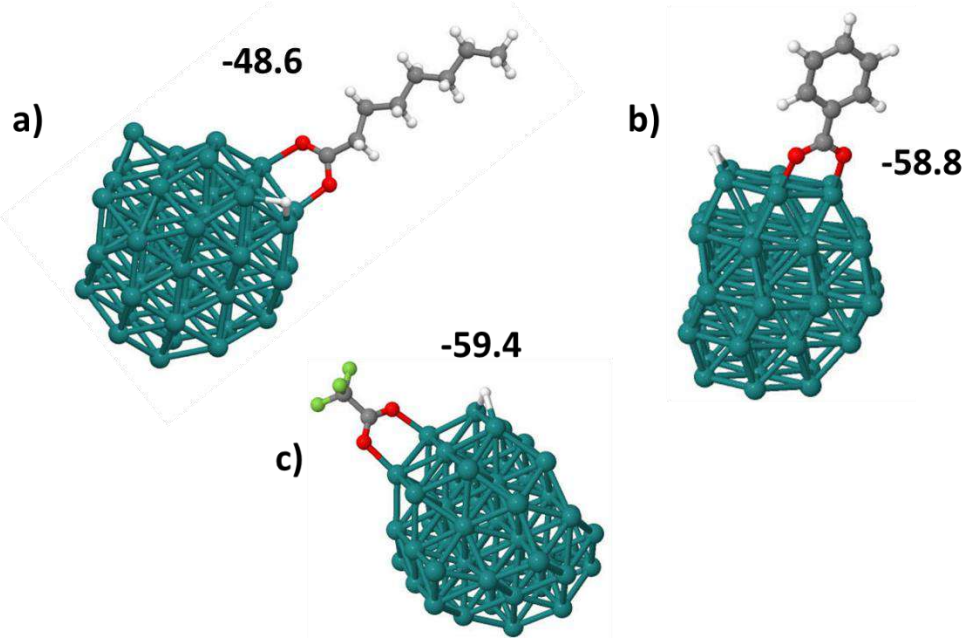

Figure 4.18 Theoretical models used to study the interaction of the three carboxylates with the Ru_{55} NP over the (001) plane. (a) octanoate; (b) benzoate; (c) trifluoroacetate. The E_{ads} (kcal.mol^{-1}) are given for each case.

The values of adsorption energy obtained show that, for the considered adsorption plane, the trifluoroacetate has a higher affinity than octanoate given the observed difference of *ca.* 11.0 kcal.mol^{-1}. This preliminary result clearly confirms that a ligand exchange is possible between these two ligands and that it is slightly in favor of the coordination of trifluoroacetate.

Looking at the adsorption energy calculated for benzoate and trifluoroacetate, one can see that they are not significantly different (> 1 kcal.mol^{-1}). Therefore, from these data, it is not possible to discuss about any difference in the electronic effects of benzoate and trifluoroacetate.

Thus, if was observed that TFA led to a more efficient ligand exchange *vs* octanoic acid than benzoic acid did (see section 4.3.1), this behavior cannot be explained by their different adsorption energy strength (electronic effects). Therefore, the acidity and steric hindrance are crucial to explain the ligand exchange phenomenon experimentally observed.

All the results evidence that several parameters are implicated in the efficiency of the ligand exchange like acidity, steric hindrance and electronic effects. With the aim to be able to conclude more precisely on the importance of each parameter, more DFT calculations are required.

4.4 Conclusion

After the full characterization of RuNPs stabilized with different carboxylic acids bearing an alkyl chain (ethanoic, pentanoic and octanoic acid), the mapping of their surface (capping ligand titration) and the specification of their electronic properties, it was described in this chapter the reaction of a higher acidic carboxylic acid with pre-formed RuNPs synthesized with octanoic acid.

The main objective of this study was to determine if a second carboxylic acid can be anchored at the surface of pre-stabilized RuNPs. This reaction was chosen as a model reaction with the aim to define if it can be an interesting strategy to graft a photosensitizer having pending carboxylic acid groups at the surface of pre-formed RuNPs in order to get an hybrid nanomaterial for testing in the water-splitting process.

The chosen photosensitizer is based in bipyridines ligands, that can be suitable to be reduced in the presence of RuNPs catalyst and hydrogen. Therefore, a direct synthesis of RuNPs in the presence of the photosensitizer as stabilizing agent under hydrogen pressure (organometallic approach) was not performed, due to the ligand bipyridine reduction risk.

This assumption was corroborated by the direct synthesis of RuNPs in the presence of benzoic acid as stabilizing agent. In this experiment, it was observed the partial and total reduction of the aryl ligand. Therefore, another strategy needs to be selected for including the photosensitizer onto the RuNPs surface. The chosen strategy was the ligand exchange.

For this purpose, in the first part of this chapter, preformed RuNPs stabilized with 0.20 equiv. of octanoic acid were first exposed to an increasing certain quantity of benzoic acid. The obtained nanosystems were characterized by NMR techniques and DFT tools. The combination of these approaches provided fruitful informations of the efficiency of the chosen strategy.

As a result, it was found possible to remove a certain quantity of the octanoate ligand and to incorporate benzoic moieties at the RuNPs surface without modifying the size and the morphology of the preformed RuNPs. According to the obtained results this exchange process was found to be favorable owing to a combination of effects, namely electronic, steric hindrance and probably acidity effects of the incoming ligand

Even when the process was achieved, it was not total. Indeed, only *ca.* [⅓ - ⅖] of the octanoates initially coordinated at NP surface were replaced by benzoates, and the addition of higher quantity of benzoic acid did not increase the ligand exchange ratio. DFT calculations supported the viability of the ligand exchange as the result of electronic effects (higher adsorption energy in bare and crowded Ru_{55} NP and thermodynamically spontaneity of the ligand exchange reactions). However, it was thought probable that the efficiency of the exchange process is affected by the steric hindrance of the ligands.

It is worth to point out, that the two approaches (experimental and theoretical) have a high degree of agreement in the characterization of this strategy. But in order to explain all the experimental finding and the difference in the electronic effects between the exchanged molecules, more DFT calculations need to be performed.

Hence, it can be said that the ligand exchange is a good methodology to be followed in order to include the photosensitizer onto preformed RuNPs, without reducing the inserted molecule and thus, conserving its photonic properties.

The second part of this chapter focused on a second ligand exchange study, keeping the octanoic acid pre-stabilized RuNPs and using this time trifluoroacetic acid as incoming ligand. The choice of trifluoroacetic acid (TFA) was based on its higher acidity and lower steric hindrance compared to those of benzoic acid.

It was found that TFA has a better efficiency in the ligand exchange process than the benzoic acid. The experimental titration results indicated that the surface of preformed

$Ru_x(C_7H_{15}COOH)_{0.20+0.20}$ NPs can be modified by substituting a slightly more than the half of the initial capping ligands by trifluoroacetates by adding only 0.10 equiv. of TFA. Also, the surface of the modified RuNPs was observed to display a higher quantity of carboxylic ligands, thus highlighting a clear effect of the low steric hindrance of TFA

On the basis of a significant difference of adsorption energy values (*ca.* 11.0 kcal.mol^{-1}) between octanoate *and* trifluoroacetate, DFT calculations provided insights of the favorable situation with TFA, a ligand exchange. Nevertheless, the theoretical results pointed out that there is no significant variation between the adsorption energy of the benzoate and the trifluoroacetate. As a consequence, the difference in the ligand exchange ratio observed between the benzoic acid and TFA *vs* octanoic acid cannot be easily explained. More DFT calculations need to be done to elucidate the driving force of this different behavior.

All together the obtained results underline that for the ligand exchange process, not only the electronic effects play and important role, but also the steric hindrance and the acidity of the incorporated ligand. It is worth to point out, that once more the two approaches (experimental and theoretical) have shown a high degree of agreement in the evaluation of the ligand exchange strategy. But in order to explain all the phenomenon, more DFT calculations are required

To conclude, the carboxylic acid exchange studies performed allowed to evidence that the grafting of a photosensitizer with free carboxylic acid groups at the surface of preformed RuNPs may be realized by following a ligand exchange strategy. But several parameters (like acidity, steric hindrance or electronic effects) have to be taken into account for the exchange to be favorable. However, even if one can expect the process to not be highly effective, at least a few molecules of photosensitizer should be incorporated at the RuNP surface which should allow to build the desired hybrid catalytic material for evaluation in water-splitting.

In the next and last chapter of results in this PhD manuscript, theoretical data about the grafting of a ruthenium polypyridyl complex, namely a photosensitizer (PS) onto preformed RuNPs will be presented.

CHAPTER V

Toward Hybrid $[Ru(bpy)_3]^{2+}$-NPs nanomaterials: Preliminary Study by DFT

5.1 Introduction

Photosensitizers (PS) are often described as light activated compounds which produce a photochemical change in an adjacent moiety. PS are initiators of a chemical reaction by facilitating energy transfer (solar to chemical) that allows the reaction to happen. When activated by light, photosensitizers are able to transfer electrons to another molecule by following a type I mechanism.[305] The effectivity of such a process depends on several parameters such as the chemistry of the photosensitizer, absorption wavelength, light intensity, etc.

The photosensitizers have been widely employed in photodynamic therapy (PDT) for cancer treatment and drug delivery systems. Scientific community has focused its efforts in improving the efficiency of the procedure. Several publications have reported the use of a hybrid material (photosensitizer + nanoparticles) in order to increase the capability and selectivity of the material in the PDT.[306]

The functionality of MNPs in this hybrid material (PS + MNPs) can be divided into passive carriers or active participants in the PS excitation. Passive nanoparticles (like AuNPs) have been used as pure carrier of PS or applied as encapsulating material for drug delivery (such as iron oxide nanomaterials). Meanwhile, active nanoparticles are used to transfer energy to produce reactive oxygen species (CdSe) or to transduce low energy light to higher energetic emissions ([Y]:Yb).[307]

The combination of photosensitizers and nanoparticles produce new hybrid materials that combine their properties to increase the functionality, selectivity and effectivity in PDT and several other applications ranging from medicine[308] to energy storage.[309] In fact, some types of nanoparticles, can be used as photosensitizer by itself, like quantum dots.[310]

Porphyrins, naphtalocyanines, chlorins, pthalocyanines are some of the photosensitizers widely used in the industry and academia.[305] Also, pyridine-based (bpy) photosensitizers in combination with several metal centers, is another family of well-studied compounds specially used for the production of hydrogen from water.[311]

Pyridine-based ruthenium organometallic compounds (figure 5.1) were developed as an inexpensive dye sensitized for solar cells, which exhibits a light to electrical conversion efficiency

of 10 %.[312] Also, they have large extinction coefficients that allow the detection of donor-acceptor reactions a low sensitizer concentration.[313]

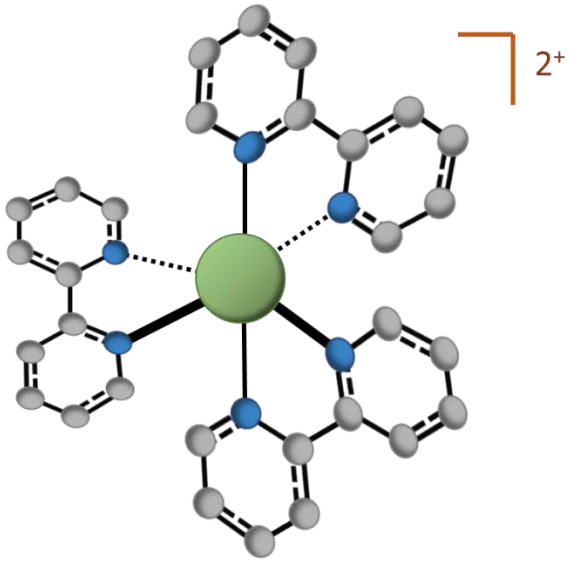

Figure 5.1 Example of bipyridine-based ruthenium (II) photosensitizer. $[Ru(bpy)_3]^{2+}$.

In these ruthenium polypyridyl complexes, a metal-to-ligand charge transfer of the triplet excited state can happen. In principle, this phenomenon can happen even if there is just one bipyridine in the organometallic compund, but it can be magnified and assured if more bipyridine units are present.[314] However, these compounds are not highly-effective at high wavelength and the incorporation of a fluorescent ligand in the structure of Ru-bpy based photosensitizer can provide a wider range of applications.[315]

Ruthenium bipyridine-based photosensitizers have been extensively used for the generation of hydrogen by the water splitting process. More recently, their association with metal NPs into hybrid [PS]-NP nanomaterials showed to be an interesting strategy to produce hydrogen from water.[316] Such hybrid nanomaterials are expected to present high catalytic activity owing to the high surface to volume ratio of the catalyst part (nanoparticle) that will be able activated due to the light harvesting PS part. A key point may be the connection between the two parts of the hybrid nanomaterial, the PS and the NP. It is thus required to have at disposal an effective methodology to anchor the photosensitizer at the surface of metal-based nanoparticles. This can be achieved by using carboxylic acids as grafting groups.[317]

Owing to the results obtained in previous chapter regarding the exchange of carboxylic acids at the surface of pre-formed RuNPs. It was envisaged to apply this strategy in order to anchor a ruthenium complex at the RuNPs surface. In this chapter, it will thus describe the DFT analysis performed in order to probe the coordination of a polypyridyl ruthenium complex containing a bipyridine functionalized with carboxylic acid groups[318] at the surface of ethanoate-stabilized RuNPs. For this purpose, it was used the same theoretical tools as previously described in other chapter of this PhD manuscript (*see* chapter IV).

The main objective of this study was to determine if the coordination of the ruthenium complex is feasible or not by this route. A schematic representation of the study performed is given in figure 5.2.

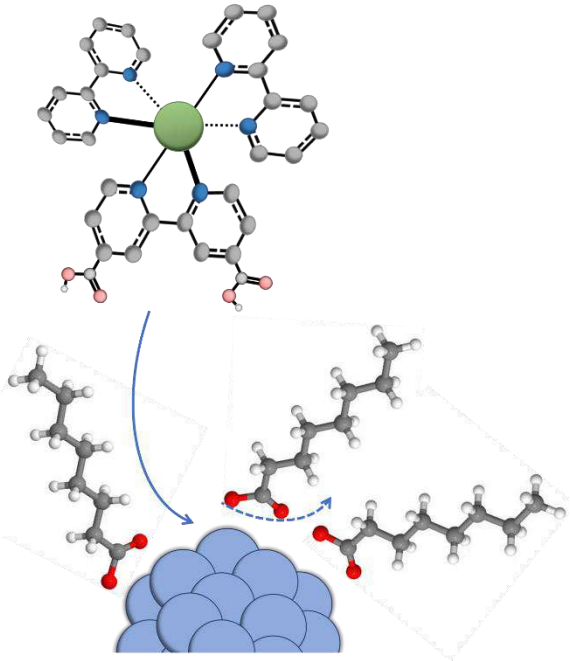

Figure 5.2 Representative diagram of the PS incorporation on preformed RuNPs.

Due to different issues, the possible incorporation of ruthenium polypyridyl compounds (PS) onto the preformed RuNPs, will be only studied by a theoretical approach.

5.2 Study of the Coordination of a Bipyridine-based Ruthenium Complex onto RuNPs by DFT Calculations

Modelling of MNPs and its relationship with different covered ligands is the principal tool in this PhD thesis to elucidate the electronic properties of the RuNPs stabilized with ethanoic acids (*see* chapter II). Thus, it was possible to build a reliable Ru_{55} NP model that provides trustful insights due to their high agreement with the experimental findings. By using this model, it was plausible to describe general properties of the RuNPs. Also, it was possible to titrate the number of capping ligands surrounding the nanosystems, its molecular composition (deprotonated), its reliability for the HER reaction, etc.

Once the model was corroborated to be a reliable source of information, it was feasible to extrapolate the gathered information to a Ru_{55} NP model capped with more flexible and longer alkyl chain ligands (pentanoic and octanoic acid, *see* chapter III). Moreover, it was possible to propose several ligand exchange reactions and determine their viability (*see* chapter IV).

The coordination of a bipyridine-based ruthenium complex (photosensitizer, PS) at the surface of preformed RuNPs was studied by DFT calculations using the same Ru_{55} NP model as previously described (*see* section 6.2.1).

Four different $[Ru(bpy)_3]^{2+}$ type complexes with bipyridine ligands functionalized by carboxylic acid groups (carboxylates to assure the electroneutrality of the system) were considered (figure 5.3).

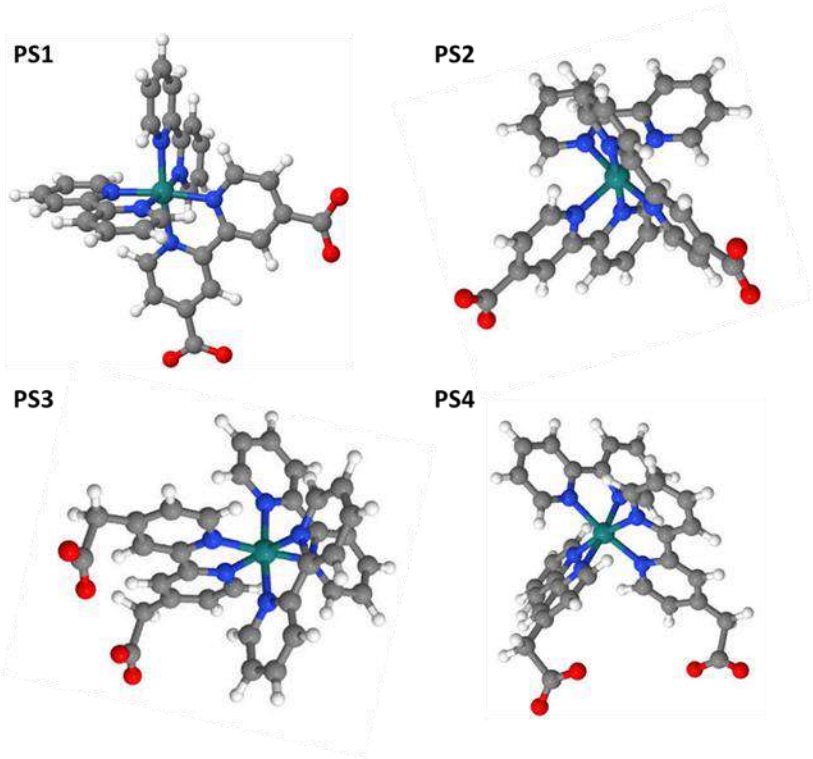

Figure 5.3 Bipyridine-based ruthenium complexes photosensitizers used for DFT calculations.

The chosen photosensitizers were based in three bipyridine ligands connected to a ruthenium metal center $[Ru(bpy)_3]^{2+}$. PS1 presents two carboxylates (pending group) mode of functionalization already described.[318] This PS1 shows a high-degree of rigidity, thus in the contrary, in PS2 complex carboxylate substituents are located in two different bipyridine entities, making it to be a more flexible and as a pincer type ligand. This was designed in order to facilitate the interaction of the carboxylic groups with the Ru_{55} NP.

With the aim to improve the anchoring point mobility of the ligand, two other complexes were built by adding a methylene group as spacers between the bipyridine and the carboxylate function (anchoring point). Thus, PS3 has two acetates in the same bipyridine unit and PS4 has them into two different bipyridines.

In the next sections, the interaction of these photosensitizers with the model Ru_{55} NP will be analyzed in order to determine the probable incorporation of these dyes onto preformed RuNPs, aiming to predict the formation of the hybrid nanocatalyst.

5.2.1 Interaction of PS with Ru_{55} NP with at Low Surface Coverage

Previous ligand exchange studies were analyzed by a combination of experimental and theoretical tools using as starting point octanoate-stabilized RuNPs. The replacements were examined by using preformed ruthenium nanoparticles stabilized with octanoates as a base. However, due to technical issues, the analyses with the PS were performed with a Ru_{55} NP model covered by ethanoates. The obtained coordinates for the optimized structures are presented in the section appendix F.

It is worth to mention that in the previous computational experiments, the most stable coordination mode of carboxylate entities onto the RuNPs was a carboxylate coordinated in a bridging mode (*see* chapter II & III). Therefore, it was expected that the photosensitizer will have the same behavior. Thus, preliminary DFT calculations were performed by considering a deprotonated photosensitizer with low crowded ruthenium surface (with two ethanoates), following the methodology described in section 6.2.2 and 6.2.3. The results obtained are presented in figure 5.4 for PS1 and PS2 and in figure 5.5 for PS3 and PS4.

The carboxylates of PS1 interact with the Ru_{55} NP by only one oxygen atom for each anchoring group. This coordination mode can derive from the rigidity of the photosensitizer. The total adsorption energy obtained was *ca.* -77.8 kcal.mol^{-1}, meaning that each carboxylate provides a stability of ca. 38.9 kcal.mol^{-1} (*see* section appendix B.5). When comparing these results with the adsorption energy of ethanoates in similar conditions (*ca.* -50.6 kcal.mol^{-1}) one can assume that, in these conditions, a ligand exchange between preformed RuNPs and PS1 will not be favorable.

With a value of *ca.* -175.5 kcal.mol^{-1}, the PS2 displays a higher stabilization energy. However, in this case, the bipyridine ligands also interact with the surface of the NPs which can explain the better stabilization (figure 5.4). But it is probable that this interaction mode cannot be achieved in a more crowded RuNPs, which is the case in the synthetized nanosystems.

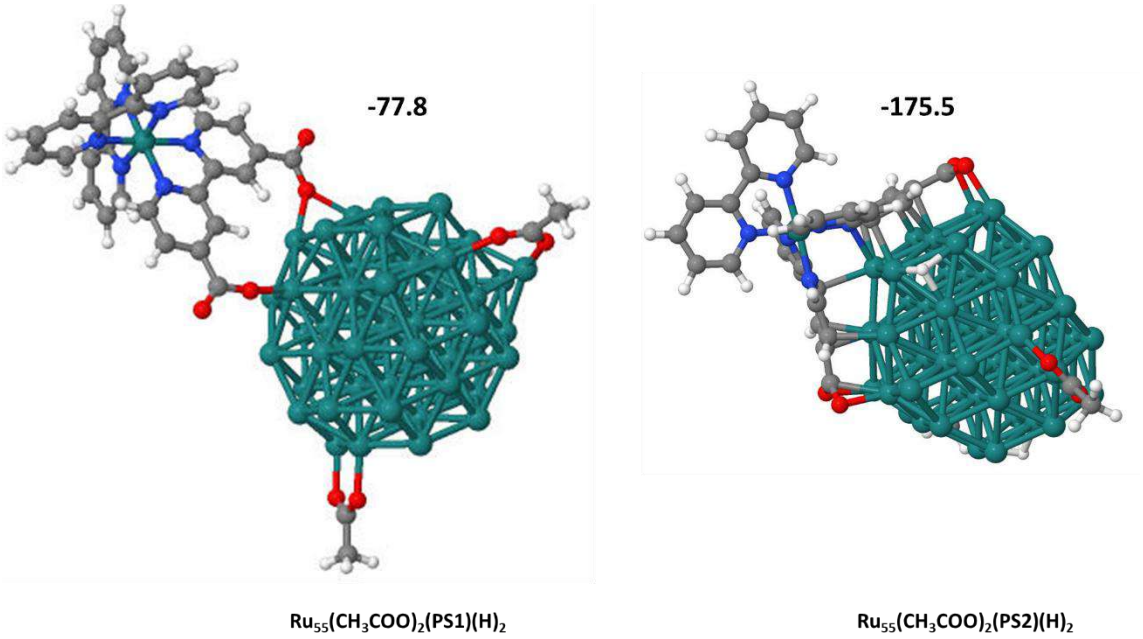

Figure 5.4 Optimized theoretical models for the interaction of PS1 (left) & PS2 (right) molecules with the $Ru_{55}(CH_3COO)_2(H)_2$. The E_{ads} (kcal.mol^{-1}) are also presented.

The influence of a spacer (CH_2) was observed by deposing the PS3 and PS4 onto the same low covered Ru_{55} NP, where it was noticed the importance of the photosensitizers pending group mobility.

In the case of PS3, the coordination involves the interaction of one of the two carboxylates in a bridging mode and the second one by an oxygen atom only. These data illustrate the influence of the carboxylate coordination mode, monodentate vs interaction in bridging mode. The obtained adsorption energy is ca. -89.3 kcal.mol^{-1}, which is *ca.* 10 kcal.mol^{-1} more than that for PS1 (see section appendix B.5). From this value, one can assume that each carboxylate unit of the PS3 stabilizes the Ru_{55} NP with ca. -44.6 kcal.mol^{-1}, which is still weaker than the adsorption energy of ethanoic acids in the same NP model (*ca.* -50.6 kcal.mol^{-1}).

However, the difference observed in adsorption energies are getting smaller (from PS1 to PS3) and adsorption energies should be even closer to each other with RuNPs stabilized by carboxylic acids bearing longer alkyl chains (less adsorption energy ethanoic *vs* octanoic acid|). Mind that since it was compared, adsorption energies of carboxylates with dissociative adsorption energies on carboxylic acids, it is not easy to conclude whether an equilibrium between

exchanging ligands (carboxylate vs PS3) could be achieved. It could however be favored if the preformed particles are stabilized by carboxylates with longer alkyl chain

The last complex, PS4, interacts differently than PS2, showing interaction with the NP surface only *via* the carboxylates. The corresponding adsorption energy is of *ca.* 106.4 kcal.mol^{-1} (figure 5.5), which is quite higher (> 15 kcal.mol^{-1}) than the value obtained for PS3 and even more than that of PS1. Thus, with PS4, each pending group provides -53.1 kcal.mol^{-1} of stability to the Ru_{55} NP. This value is *ca.* 2.5 kcal.mol^{-1} higher than the adsorption energy of an ethanoic acids in the same Ru_{55} NP. However, a deeper investigation of the possible exchange mechanisms should be done in order to safely conclude about an effective ligand exchange between PS4 and carboxylates in preformed RuNPs. It is in particular necessary to assess whether the leaving ethanoates will recombine or not with protons.

Nevertheless, it can be proposed an effective ligand exchange between PS4 and carboxylates in preformed RuNPs, at least when there is a low coverage value.

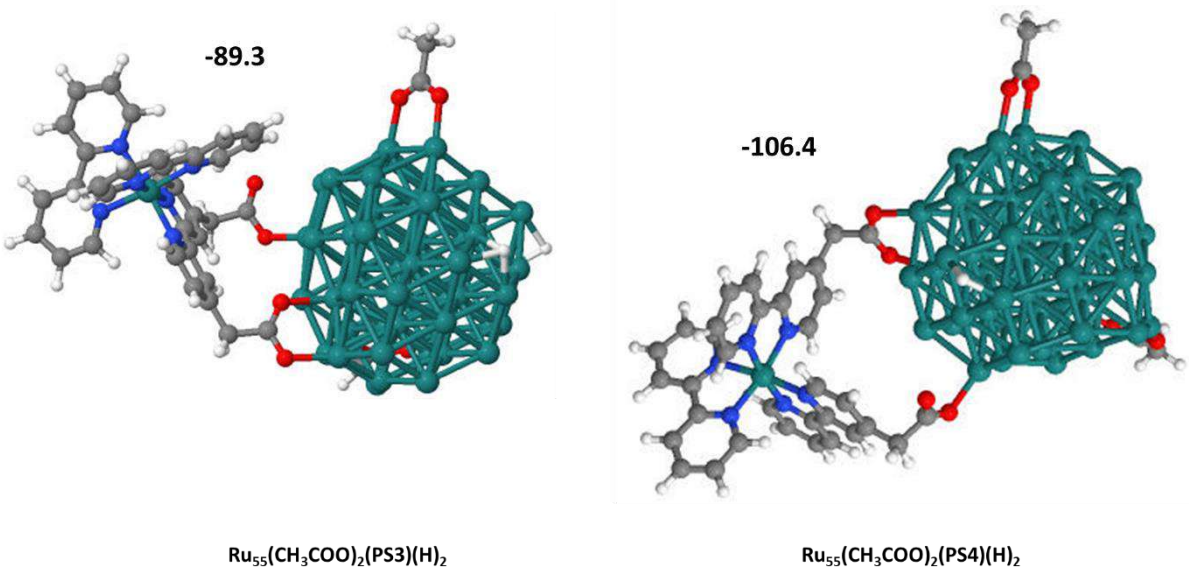

Figure 5.5 Optimized theoretical models for the interaction of PS3 (left) & PS4 (right) molecules with $Ru_{55}(CH_3COO)_2(H)_2$ NP. The E_{ads} (kcal.mol^{-1}) are also presented.

As a conclusion, the obtained results evidence that the adsorption of the studied PS on the Ru_{55} NP at low ligand coverage is stronger when the PS has CH_2 spacers between the bipyridine motives and the carboxylate function. This can be explained by higher flexibility of such anchoring

groups. In addition, the ligand exchange reaction could be more favorable when the PS used has anchoring groups in different bipyridine entities (PS4). This can be attributed to the larger angle between the carboxylates thus making the carboxylate pincer more adapted for a connection with the ruthenium surface.

5.2.2 Interaction of PS with Ru_{55} NP at Intermediate Surface Coverage

According to the data presented in chapter II, a more trustful model compared to real in synthesized RuNPs in order to evaluate ligand exchange at the surface of NPs could be obtained by using a more crowded Ru_{55} NP. To perform so, the adsorption energies of the PS were calculated onto a Ru_{55} NP bearing 10 ethanoates.

Three of the four PS were considered for this study. First, PS1 and PS2 due to their similitudes with the experimental available compounds despite their adsorption energies at the Ru_{55} NP at low surface coverage were not as high as expected for a positive ligand exchange. Second, the PS4 was also assessed because the higher adsorption energy value obtained with it in previous section showed it was the best PS for a ligand exchange.

The adsorption energy of two ethanoic moieties can be compared with that of the different PS in order to offer trustworthy trends to predict a possible, one to one, ligand exchange. Again, it must be underlined that it was compared here, the adsorption energies of carboxylates with dissociative adsorption energies of ethanoic acids, *i.e*. it was implied to consider that the leaving groups will be ethanoic acids. This is one scenario, that should be completed with other exchange mechanisms.

Using a low covered Ru_{55} NP, it was observed that the adsorption energy of two ethanoic moieties was higher than that of ethanoates in almost all the cases, except for the PS2 which was shown to interact with the Ru_{55} NP *via* the aryl part of the bipyridine ligand and the PS4 which presented higher adsorption energy value while only interacting *via* its carboxylic groups. From the

obtained results, it appeared that the best conditions for an efficient ligand exchange were with PS4 which bears anchoring points in different bipyridine ligands with CH_2 spacers.

Table 5.1 provides a comparison of the adsorption energies calculated for the interaction of PS1, PS2 & PS4 with Ru_{55} NP of low and intermediate surface coverage as described in figure 5.6 (*see* section appendix B.6 and its coordinates in appendix F). It can be observed that for all cases, the adsorption energy values are lower at higher Ru_{55} NP surface coverage (10 ethanoates *vs* 2 ethanoates). This is not surprising given that an increase of capping ligands tend to reduce the whole surface energy. It is important to point out that this coverage degree for the NPs is more alike the experimental conditions.

Moreover, all PS show higher adsorption energies than that of two ethanoic species in the same conditions. These results indicate that it is highly probable that for RuNPs with intermediate surface coverage, a ligand exchange between ethanoates and PS will be achieved, if the exchange is one to one carboxylate. Again, the ligand exchange reaction appears to be more favorable with PS4

Table 5.1 Comparison of adsorption energies for different PS onto Ru_{55} NP with low and intermediate surface coverage with that of two ethanoates in the same conditions.

Preformed RuNPs	**Adsorption energy (kcal.mol^{-1})**			
	2 (CH_3COOH)	PS1	PS2	PS4
$Ru_{55}(CH_3COO)_2(H)_2$	-101.16	-77.84	-175.50	-106.35
$Ru_{55}(CH_3COO)_{10}(H)_{27}$	-67.40	-73.63	-88.15	-90.95

The adsorption energy of the more rigid photosensitizer (PS1; figure 5.6 a) is *ca.* 4.2 kcal.mol^{-1} lower for an intermediate surface coverage ($Ru_{55}(CH_3COO)_{10}(H)_{27}$) than for a less crowded Ru_{55} NP ($Ru_{55}(CH_3COO)_2(H)_2$). This indicates that the difference in Ru_{55} NP surface coverage does not have a big impact on the adsorption energy of PS1. This can be attributed to the coordination angle of the pincer ligand. This is probably because this PS interacts with the metal surface *via* only one oxygen atom of each anchoring group. Moreover, on $Ru_{55}(CH_3COO)_{10}(H)_{27}$, the adsorption energy of PS1 is *ca.* 6.2 kcal.mol^{-1} more stable than the adsorption strength of two ethanoates moieties

For $Ru_{55}(CH_3COO)_{10}(H)_{27}$ model, PS2 shows also a better stabilization than the ethanoates and even higher than PS1. But as already observed PS2 interacts with the Ru_{55} NP surface *via* the whole bipyridine ligand and not only *via* the anchoring groups (figure 5.6 b). If such π coordination can occur at the surface of actual RuNPs, it could favor ligand exchange.

Finally, PS4 displays the highest stability. But the adsorption energy is affected by the surface coverage as seen by the reduced value of *ca.* 16 kcal.mol^{-1} between $Ru_{55}(CH_3COO)_2(H)_2$ to ($Ru_{55}(CH_3COO)_{10}(H)_{27}$) models. PS4 has an adsorption energy similar to that observed with PS2, but only due to the σ coordination of carboxylate moieties. This means that the presence of CH_2 spacers does influence the adsorption energy by facilitating the coordination of carboxylates. These observations suggest that the presence of carboxylates in two different bipyridine ligands is a driving force for increasing the PS affinity with the RuNPs. (figure 5.6 c).

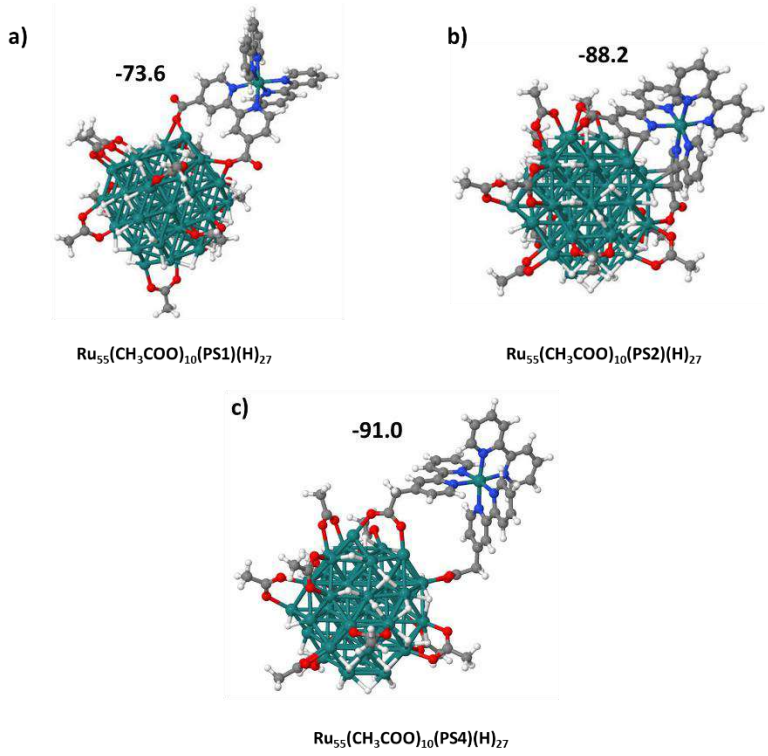

Figure 5.6 Optimized theoretical models for the interaction of (a) PS1, (b) PS2 and (c) PS4 molecules with $Ru_{55}(CH_3COO)_{10}(H)_{27}$ NP and corresponding E_{ads} (kcal.mol^{-1}).

The results indicate that the PS adsorption energy is highly affected by the position of their anchoring points on the bipyridine moieties, meaning that the coordination angle is crucial for the

ligand exchange. It is important to highlight that the PS molecules studied present a high steric hindrance which can influence their coordination. However, given the space generated between the PS and the Ru_{55} NP (pincer elongate ligand) this effect is reduced at least with the models used that are preformed nanoparticles stabilized by ethanoates.

As previously mentioned, the adsorption energies of PS1 and PS4 were found higher than that observed for two ethanoic acids in the same conditions of surface coverage. These results led to the conclusion of a possible ligand exchange between ethanoates and PS1 or PS4. However, it is essential to study a ligand exchange by introducing the DFT energies in a reliable reaction profile in order to stablish the thermodynamic variable. Thus, in order to probe the thermodynamic viability of the ligand exchange between ethanoates and PS1 or PS4, two reaction profiles were studied, namely the insertion of PS1, and then of PS4, onto $Ru_{55}(CH_3COO)_{10}(H)_{27}$ together with the liberation of two ethanoic acids (figure 5.7). The obtained results are described in table 5.2

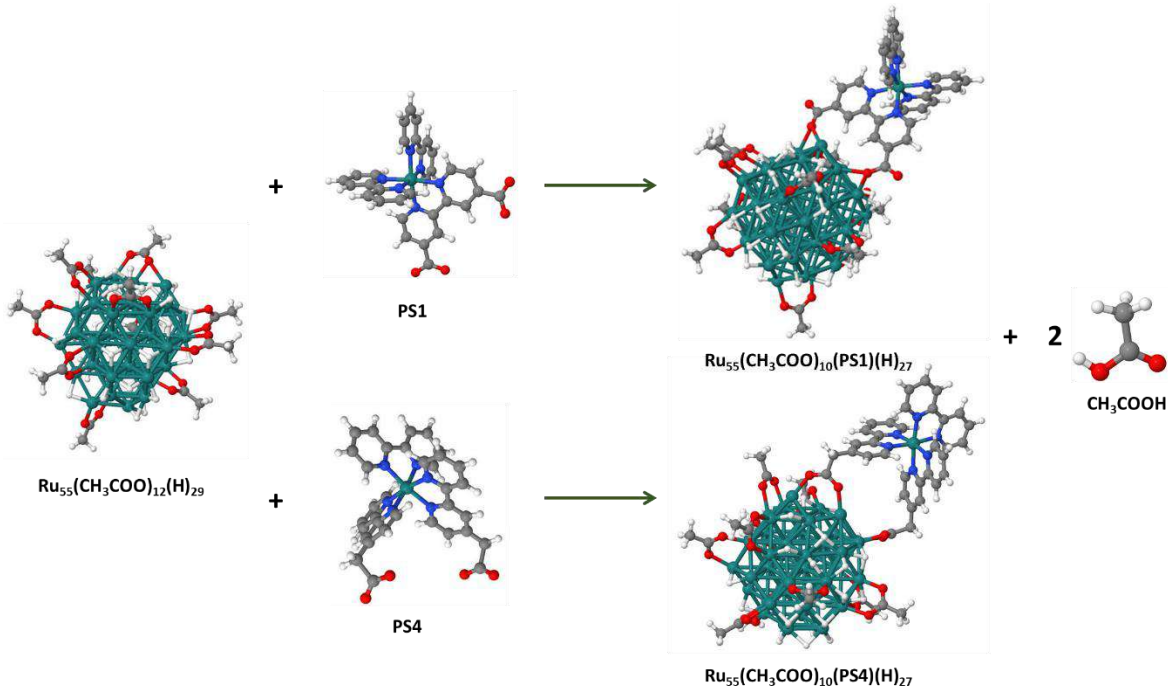

Figure 5.7 Optimized theoretical calculations for the reaction of PS1 and of PS4 with $Ru_{55}(CH_3COO)_{12}(H)_{29}$ NP.

Table 5.2 DFT reaction energies for the ligand exchange reaction between $Ru_{55}(CH_3COO)_{12}(H)_{29}$ NP and PS1 & PS4.

DFT optimized structure energies (eV)				DFT reaction energy ($kcal.mol^{-1}$)
$Ru_{55}(CH_3COO)_{12}(H)_{29}$ + PS1 → $Ru_{55}(CH_3COO)_{10}(PS1)(H)_{27}$ + 2 CH_3COOH				
-1072.83	-453.44	-1433.54	2*(-46.50)	-6.23
$Ru_{55}(CH_3COO)_{12}(H)_{29}$ + PS4 → $Ru_{55}(CH_3COO)_{10}(PS4)(H)_{27}$ + 2 CH_3COOH				
-1072.83	-486.57	-1467.42	2*(-46.50)	-23.55

The examined ligand exchange reactions are only another way to interpret the adsorption energies obtained for the PS coordination onto Ru_{55} NP at intermediate surface coverage ratio. It can be clearly observed that the incorporation of a PS onto $Ru_{55}(CH_3COO)_{12}(H)_{29}$ is possible by removing two ethanoic moieties. These results can be compared with those previously obtained when studying the DFT reaction energy for the ligand exchange between octanoic and benzoic acids (see section 4.2.3). In those cases, the obtained DFT reaction energy was also directed towards a spontaneous reaction but much more efficient.

As a preliminary conclusion, the results obtained evidence that a ligand exchange between ethanoates and $[Ru(bpy)_3]^{2+}$ type complexes containing carboxylic acids groups can be performed onto RuNPs at an intermediate surface coverage ratio, provided that ethanoate moieties recombine with protons. At this point of our studies, the strategy (ligand exchange) envisaged in order to incorporate a PS onto RuNPs to get hybrid nanocatalysts looks to be appropriate and achievable, at least if the stabilization of the preformed NPs is performed with ethanoic acid.

When considering the other models of carboxylic acid stabilized RuNPs studied (using pentanoic and octanoic acids) they present a higher steric hindrance. Consequently, with such RuNPs a change in the ligand exchange reaction spontaneity may be observed. DFT calculations and experimental data would be required in order to corroborate the reactions viability in these pre-stabilization conditions.,

In the next section, the coordination of the more rigid photosensitizer (PS1) will be analyzed into a ligand exchange reaction using a Ru_{55} NP model whose surface composition was previously determined by DFT titration (*see* section 2.5.2). This model corresponds to a high ratio of surface coverage and is closer to real synthesized RuNPs.

5.2.3 Interaction of PS1 with Ru_{55} NP at High Surface Coverage

The ligand exchange strategy can be used to incorporate aryl ligand, like benzoic acid, onto the surface of preformed RuNPs without modifying the metal and the ligand structures, as observed using experimental and theoretical tools. Also, the formation of the desired hybrid catalyst can be performed by following this strategy, as demonstrated by the DFT calculations Specially, when the RuNPs have an intermediate crowded coverage. Moreover, it was observed that the most efficient ligand exchange process can be achieved with a PS4 type of photosensitizer.

Besides, DFT calculations previously showed that the rigid studied photosensitizer PS1 could be adsorbed onto the metal surface, but the process spontaneity was not clear. Therefore, in order to elucidate this last point, a DFT analysis of the reaction of PS1 with a more crowded Ru_{55} NP having a similar surface composition as the optimal surface coverage found previously by DFT titration (*see* section 2.5.2), was performed.

The methodology followed was the same as that described in section 5.2.2. The only difference is that, in this case, PS1 was reacted with a $Ru_{55}(CH_3COO)_{14}(H)_{31}$ NP, which is a more crowded entity. The adsorption energy obtained for PS1 in these conditions was *ca.* -58.7 kcal.mol^{-1}. At first view this value seemed quite high (*see* section appendix B.7 and coordinates in section appendix F). However, it is lower than the *ca.* -65.8 kcal.mol^{-1} value observed for the interaction of two ethanoic acid molecules on the same Ru_{55} NP model, (table 5.3).

Table 5.3 Comparison of adsorption energies for PS1 onto different Ru_{55} NP models (at low, intermediate and high surface coverage ratio) with that of two ethanoates in the same conditions.

Preformed system	**Moieties adsorption energy (kcal.mol^{-1})**	
	2 (CH_3COOH)	PS1
$Ru_{55}(CH_3COO)_2(H)_2$	-101.16	-77.84
$Ru_{55}(CH_3COO)_{10}(H)_{27}$	-67.40	-73.63
$Ru_{55}(CH_3COO)_{14}(H)_{31}$	-65.83	-58.72

It can be observed that the PS1 adsorption energy dropped of *ca*. 15 kcal.mol^{-1} between intermediate ($Ru_{55}(CH_3COO)_{10}(H)_{27}$) and high ($Ru_{55}(CH_3COO)_{14}(H)_{31}$) surface coverage ratio. Even more important, the value observed for PS1 at high surface coverage ratio is higher than that of two ethanoic acids, thus indicating that the ligand exchange is less likely to occur in these conditions. Nevertheless, these results look inadequate because the coordination mode of PS1 in both $Ru_{55}(CH_3COO)_{10}(H)_{27}$ and $Ru_{55}(CH_3COO)_{14}(H)_{31}$ NP models seems to be similar (figure 5.8). Thus, the difference in adsorption energy cannot be easily explained.

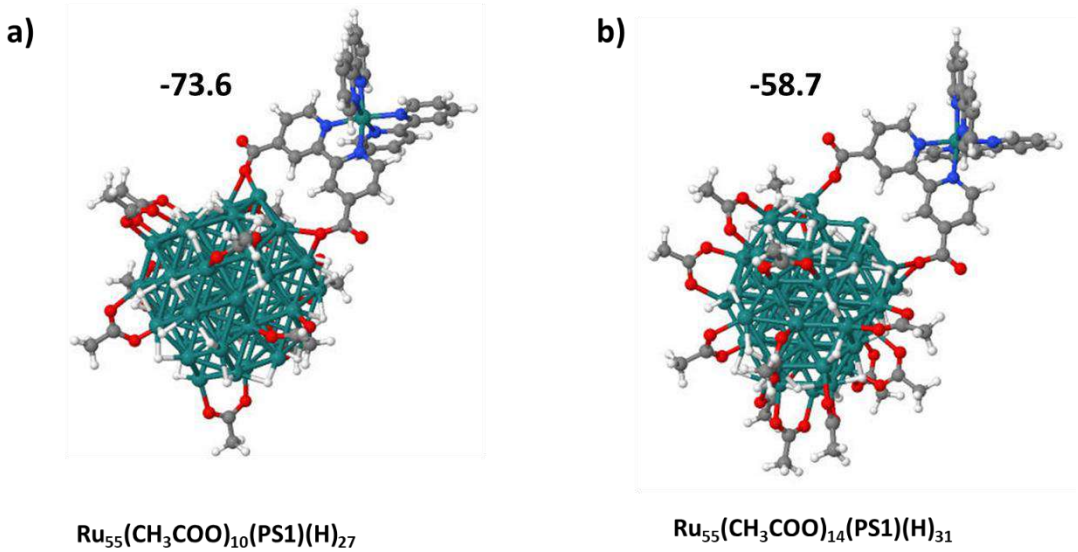

Figure 5.8 Optimized theoretical calculations for the interaction of PS1 with the (a) $Ru_{55}(CH_3COO)_{10}(H)_{27}$ NP and (b) $Ru_{55}(CH_3COO)_{14}(H)_{31}$ NP. The E_{ads} (kcal.mol^{-1}) are also presented.

The observed difference in the adsorption energy may be attributed to the different coordination sites onto the Ru_{55} NP model. The spontaneity of the ligand exchange reaction was estimated by considering as reaction profile, the adsorption of PS1 onto $Ru_{55}(CH_3COO)_{16}(H)_{33}$ together with the liberation of two ethanoic acids (table 5.4).

Table 5.4 DFT reaction energy for the ligand exchange reaction between $Ru_{55}(CH_3COO)_{16}(H)_{33}$ NP and PS1

DFT optimized structure energies (eV)				**DFT reaction energy (kcal.mol^{-1})**
$Ru_{55}(CH_3COO)_{16}(H)_{33}$ + PS1 → $Ru_{55}(CH_3COO)_{14}(PS1)(H)_{31}$ + 2 CH_3COOH				
-1264.48	-453.44	-1624.61	2*(-46.50)	7.11

As in previous sections, the ligand exchange reaction profile was analyzed by considering a one to one carboxylate exchange meaning that the introduction of PS1 induces the release of two ethanoic acid molecules. In these conditions, it was observed a positive DFT reaction energy. This result indicates that the adsorption of PS1 ligand at the surface of crowded RuNPs stabilized by ethanoates is not feasible by a ligand exchange strategy, again provided that ethanoates recombine with adsorbed hydrides.

However, this data only points out the importance to select the right photosensitizer to favor the ligand exchange. Indeed, PS1 is the most rigid ligand among the series of PS studied in this work. Thus, its adsorption could be expected to not be an easy task, as supported by the DFT calculations. Owing to the better effectiveness observed in the ligand exchange process when studying the adsorption of PS4. It can be assumed that this PS should be the target molecule to build an hybrid nanocatalyst. This reaction is described in scheme 5.1 and will be the object of future work.

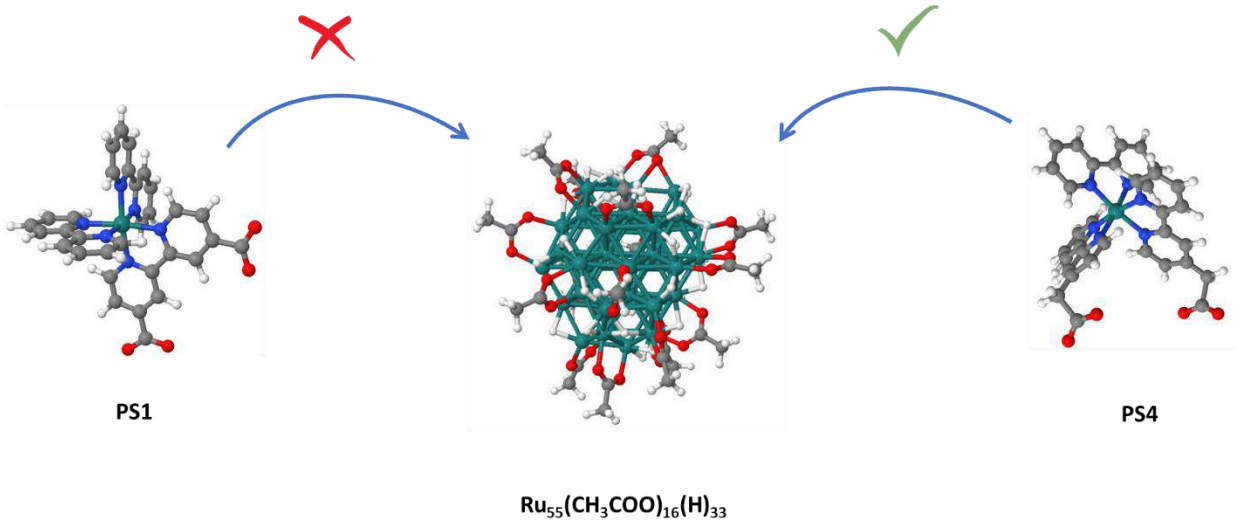

Scheme 5.1 Representation of an incorporation of a PS adsorption onto crowded Ru_{55} NP. (left) PS1 and (right) PS4 ligand

According to the DFT calculations, the coordination of $[Ru(bpy)_3]^{2+}$ type complexes that contain bipyridine ligands functionalized by carboxylic acids groups onto RuNPs depends on the surface coverage of the metal nanoparticles and of the structure of the photosensitizer. Therefore,

it is necessary to study each case in order to anticipate the best strategy to favor the building of the hybrid [PS]-RuNP nanomaterial.

Anyway, it is worth to point out that the best catalyst to assay, will be the PS4 in an intermediate surface covered RuNPs. Like the one obtained by the system $Ru_x(C_4H_9COOH)_{0.30}$ NPs.

5.3 Conclusion

The main target of this PhD work was to generate a base of scientific knowledge in the formation of hybrid nanocatalyst, composed of RuNPs and photosensitizers. A crucial point of this study was to find a proper methodology that allows the grafting of these materials without modifying its own properties. Moreover, the principal aim was to combine their properties to obtain a reliable hybrid nanocatalyst that can be used for the water splitting process.

The combination of experimental and theoretical tools allowed to create a solid base where the structure/properties of the ruthenium nanomaterials could be understood. In the firsts chapters, it was described the formation of RuNPs with different stabilizing agent (ethanoic, pentanoic and octanoic acid) and their characterization. Once the nanosystems properties were described, it was stablished a trustworthy strategy (ligand exchange) to include aryl ligands onto stable, homogeneous and well-dispersed RuNPs without observing a significant modification in its structure. Therefore, this strategy was chosen to build the hybrid nanocatalyst.

In this chapter, four different $[Ru(byp)_3]^{2+}$ type complexes containing bipyridine ligands modified with carboxylic acid as anchoring groups were designed in order to study their adsorption at the surface of models of RuNPs. These complexes were selected owing to their interest as photosensitizers to harvest light energy and facilitate the electron transfer towards a catalyst for the production of hydrogen by photolysis of water molecules. The main objective of this theoretical study was thus to determine the ability of these complexes to anchor at metal surface in order to determine which of them is the best PS to favor the formation of hybrid nanomaterial with $[Ru(byp)_3]^{2+}$-RuNP structure. The chosen strategy for studying the PS adsorption was a ligand exchange reaction. This choice was based on results of previous chapters where it was demonstrated that aryl arboxylic acids can exchange at the surface of RuNPs but only if their

adsorption energies are appropriate to allow this exchange. This meant that the exchanging ligands had to have an enough difference in terms of adsorption energy to favor the adsorption and release reactions in parallel.

Firstly, the study focused on the determination of PS adsorption onto non-crowded Ru_{55} NP surface. It was observed that the bipyridine ligands with a CH_2 spacer between the bipyridine pattern and the anchoring point (carboxylic acid group), are more apt to adsorb at the metal surface. A better adsorption was also observed when the anchoring groups were beard by two different bipyridine ligands. This was attributed to the higher ligand flexibility obtained in these conditions and its ability to act as a pincer ligand given a more appropriate angle for coordination at the RuNPs surface. All observations led to PS4 to be the more appropriate photosensitizer.

Then, the adsorption of the photosensitizers was studied by considering model Ru_{55} NPs with an intermediate surface coverage ratio. A spontaneous ligand exchange was observed, mainly with PS1 and PS4 photosensitizers. Moreover, PS4 proved to have best effectivity in the ligand exchange process. From these results we could conclude that the structure of the photosensitizer and the surface coverage ratio of the RuNPs, that is the quantity of capping ligands, are two key-points that influence strongly the viability of the PS adsorption onto RuNPs *via* a ligand exchange strategy.

From the theoretical studies performed, one can conclude that the anchoring of a photosensitizer onto preformed RuNPs is feasible and, depending upon the experimental conditions, can be thermodynamically spontaneous. However, these are preliminary results that need to be taken with caution due to several other variable that can affect the ligand exchange effectivity, like the nature of the photosensitizers, their steric hindrance, acidity, the NP surface coverage ratio, the exchanged ligand, the possible recombination with protons, etc. Therefore, in order to finish this study and make it more reliable, more calculations are required.

Nevertheless, the presented data indicate that the strategy chosen in order to anchor photosensitizers onto preformed RuNPs is efficient and that the formation of the hybrid [PS]-RuNP nanomaterials is achievable by this way. Lastly, the gathered information points out that the synthesis of the desired hybrid nanocatalysts to be used in the water splitting process, may be easier obtained by using a photosensitizer like PS4 and an intermediate crowded nanoparticle system. Given these conclusions, the RuNPs stabilized by 0.3 equiv. of pentanoic acid may be

those to experiment first in an exchange reaction with PS4 in order to get a hybrid nanocatalyst and evaluate its catalytic properties in the photolysis of water for the production of hydrogen.

CHAPTER VI

Experimental and Theoretical DFT Specifications

6.1 Experimental Part

6.1.1 Generals and Chemical Products

All the operations for the synthesis of ruthenium nanoparticles were carried out using standard Schlenk tubes, Fisher-Porter bottle (Avitec) techniques or in a globe-box (MBRAUN) under argon atmosphere (Air Liquide, Alphagaz Smartop). The solvents (tetrahydrofuran, toluene and *n*-pentane) were purchased from Carlo-Erba, dehydrated through filtration on adequate columns in a purification apparatus (MBRAUN) and degassed according to freeze-pump-thaw process just before use. The ruthenium precursor, [Ru(COD)(COT)] (ruthenium-1,5-cyclooctadiene -1,3,5-cyclooctatriene), was synthesized from $RuCl_3 \cdot xH_2O$ (Janssen) by following an established procedure.[155]

Glacial ethanoic acid was gathered from Acros Organics and degassed before used by bubbling argon for 30 min. The other liquid carboxylic acids (pentanoic and octanoic acid) were purchased from Sigma-Aldrich, purified by fractional distillation under reduced pressure, degassed under vacuum at the liquid nitrogen temperature by 3 vacuum/argon cycles, dried under molecular sieves and preserved in the globe-box. Benzoic acid (Alfa Aesar) was purified by recrystallization in benzene,[319] dried under vacuum overnight and stored in the globe-box. Hydrogen gas was bought from Air liquid (Alphagaz). Chloroform-d^1 benzene-d^6, toluene-d^8 and THF-d^8 for NMR studies were obtained from Euriso-top and stored on activated molecular sieves (4 Å beads, Alfa Aesar) into the globe-box. TFA-d^1 for ligand exchange experiments was acquired from Euriso-top and used right after opening below a continuous argon flow. Silica gel (pore size 60 Å) was purchased from Fluka Analytical, dried by thermal treatment (*ca.* 590 °C) under vacuum and then stored in the globe-box. Methanol (VWR Chemicals) was purified, dried and degassed by distillation under inert atmosphere, using magnesium as a drying agent previously activated with iodine and stored under argon. Potassium bromide (Sigma-Aldrich) was dried over P_2O_5 (Sigma-Aldrich) before usage and conserved in the globe-box for FTIR analysis. The other chemicals were employed as received unless otherwise specified.

The chemical reagents used are enlisted hereafter with indication of the supplier and their purity degree.

- Alumina (Merck)
- Argon (Alphagaz Smartop, < 3 ppm H_2O, < 2 ppm O_2)
- Benzene (Sigma-Aldrich, 99.8 %)
- Benzene-d^6 (Euriso-top, 99.5 %)
- Celite (Merck)
- Chloroform-d^1 (Euriso-top, 99.8 %)
- ^{13}CO (Euriso-top, 99.1 %)
- 1,5-cyclooctadiene (Sigma-Aldrich, 99.0 %)
- Glacial ethanoic acid (Acros Organics, 99.8 %)
- Hydrogen gas (Alphagaz Smartop, < 3 ppm H_2O, < 2 ppm O_2)
- Iodine (Sigma-Aldrich, 99.8 %)
- Magnesium turnings (Sigma-Aldrich, 99.9 %)
- Methanol (VWR Chemicals, 99.9 %)
- Molecular sieve 4 Å bends (Alfa Aesar)
- 2-Norbornene (Sigma-Aldrich, 99.0 %)
- Octanoic acid (Sigma-Aldrich, 99.0 %)
- *n*-Pentane (Carlo-Erba, 99.0 %)
- Pentanoic acid (Sigma-Aldrich, > 99.0 %)
- Phosphorous pentoxide (Sigma-Aldrich, > 98.0 %)
- Potassium bromide (Sigma-Aldrich, > 99.0 %)
- [Ru(COD)(COT)] (Nanomeps, > 97.0 %)
- $RuCl_3 \cdot xH_2O$ (Janssen); ICP: x = 17.3
- Silica gel (40-63 μm, Fluka Analytical)
- Silica gel (60 Å, Fluka Analytical)
- THF (Carlo-Ebra, 99.9 %)
- THF-d^8 (Euriso-top, 99.5 %)
- Toluene (Calrlo-Erba, 99.8 %)
- Toluene-d^8 (Euriso-top, 99.6 %)
- TFA-d^1 (Euriso-top, 99.5 %)
- Granular zinc (Merck, 95.0 %)

6.1.2 Synthesis Procedures

6.1.2.1 Synthesis of [Ru(COD)(COT)]

Before starting the [Ru(COD)(COT)] (figure 6.1) synthetic procedure, the 1,5-cyclooctadiene was degassed by bubbling argon for *ca.* 60 min. Then, 1,5-cyclooctadiene was filtrated using a 5 cm column of previously dried alumina under inert atmosphere. The purified 1,5-cyclooctadiene was stored under argon and kept protected from the light to avoid the formation of reactive peroxides.

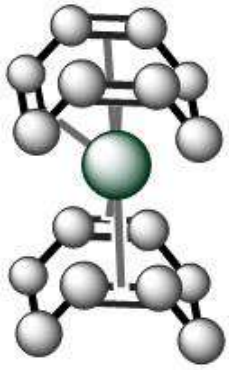

Figure 6.1 3D ball representation of [Ru(COD)(COT)] complex.

Ruthenium-1,5-cyclooctadiene-1,3,5-cyclooctatriene ([Ru(COD)(COT)]) was prepared conforming to a published methodology[155] from $RuCl_3 \cdot xH_2O$. Inside a 250 mL Schlenk flask, 3 g (5.8 mmol) of $RuCl_3 \cdot xH_2O$ were dissolved in 30 mL of dried and degassed methanol under vigorous stirring. After, 80 mL (1.53 mol) of purified 1,5-cyclooctadiene were added to the flask under stirring till a homogeneous solution was achieved. Then, 5 g of granular zinc were added (catalyst) to the reaction mixture which was heated till reflux (90 °C) for 3 h under continuous flux of argon. After that, the reaction mixture was cooled down before filtration through a 3 cm column of dried alumina and washings (≤ three times) with 20 mL of degassed toluene. Then, the solution was evaporated to dryness leading to a solid that was extracted with pentane. The obtained solution was filtered on a 5 cm column of dried alumina with successive additions of degassed pentane. Then, the collected yellow solution was concentrated to 10 mL under high-vacuum before stored overnight in a freezer (*ca.* -20 °C). The yellow crystals formed were then purified by recrystallization in dried pentane. Finally, the resulting air-sensitive yellow crystals were preserved under argon at -30 °C inside the globe-box. The purity of the sample was confirmed by ^{1}H-NMR spectroscopy (figure 6.2) in comparison to a reported spectrum. ^{1}H-NMR (C_7D_8): δ 0.8 (m, 2 H), 1.7 (m, 2 H), 2.2 (m, 8 H), 2.9 (m, 4 H), 3.8 (m, 2 H), 4.7 (m, 2 H) & 5.2 ($\delta\delta$, 2 H) ppm. Yield: 65.0 %.

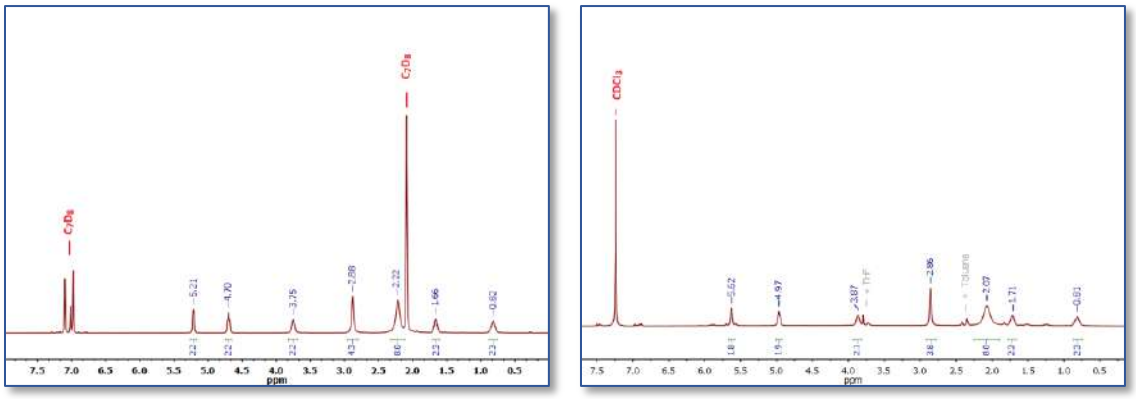

Figure 6.2 ^{1}H-NMR of [Ru(COD)(COT)]: (right) C_7D_8; (left) $CDCl_3$.

6.1.2.2 General Synthesis of Ruthenium Nanoparticles

As a general procedure (scheme 6.1), 30 mg of ruthenium organometallic precursor (0.095 mmol), [Ru(COD)(COT)], were dissolved in 20 mL of a given solvent (pentane or THF) into a Fisher-Porter reactor under vigorous stirring till a yellow homogeneous solution was obtained. The procedure was performed inside the globe-box. After, a solution of a given dried carboxylic acid in the same solvent was added *via* syringe under argon atmosphere using vacuum line techniques (volatile carboxylic acids) or inside the globe-box (other ligands). After addition of the stabilizing agent, the argon atmosphere was evacuated under high-vacuum and the reactor was pressurized with 3 bar of molecular hydrogen at r.t. In all cases, the initial yellow solution turned black in a few minutes. The gas pressure and the vigorous stirring were maintained for 30 min or overnight. In the first case, the time was split into 10 min of dynamic hydrogen pressure and 20 min of static gas pressure. After this reaction time, a blackish brown suspension was obtained. Finally, the remained hydrogen was evacuated under high-vacuum and the reaction mixture was concentrated for electron microscopy analyses.

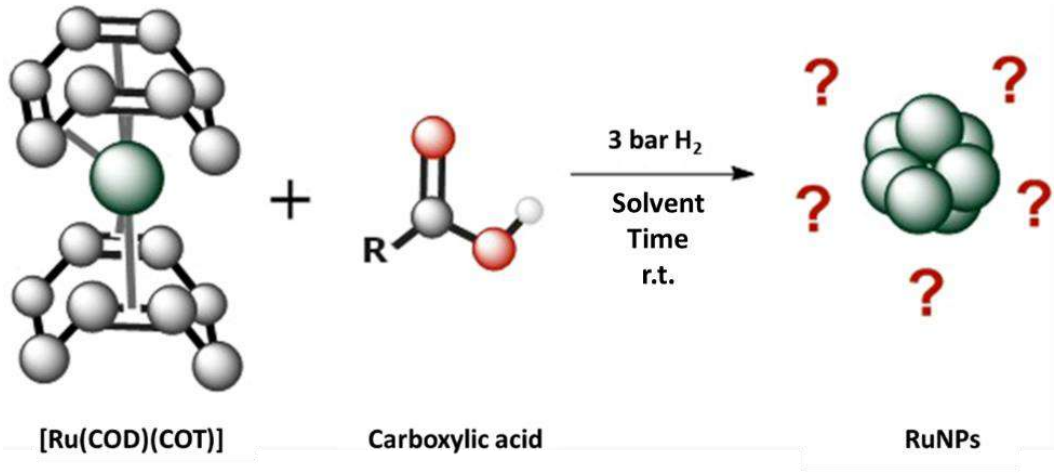

Scheme 6.1 General synthesis of RuNPs.

The purification treatment to isolate the samples consisted in the gradual evaporation of the organics (solvent, cyclooctane released from the ruthenium precursor [Ru(COD)(COT)] decomposition and possible free ligand) under high-vacuum for at least 15 h until getting a fine dark powder. Additionally, the RuNPs powder was obtained by precipitation from the colloidal suspension with pentane and THF and then filtration. By this way, a dark grey powder was obtained which was further used for characterizations in the solid state or re-dispersed in deuterated solvent for liquid NMR studies.

Carboxylic acids with different alkyl chain lengths were used as ligands for the synthesis of RuNPs, namely ethanoic (CH_3COOH), pentanoic (C_4H_9COOH) and octanoic acid ($C_7H_{15}COOH$), in order to evaluate the surface state and the catalytic performance of the obtained nanoparticles. The RCOOH/[Ru] ratios (molar equivalents per ruthenium precursor) used are described below (table 6.1).

Table 6.1. Different quantities of ligand used for RuNPs synthesis.

Ligand	**Molar equivalents of ligand per ruthenium precursor RCOOH/[Ru] (equiv.)**
CH_3COOH	0.20, 0.40
C_4H_9COOH	0.05, 0.20, 0.30, 0.40, 0.50, 0.60
$C_7H_{15}COOH$	0.10, 0.15, 0.20, 0.30, 0.40

6.1.3 Characterization Techniques

Synthetized ruthenium nanoparticles (RuNPs) were characterized by a combination of different techniques. Size, morphology and crystalline structure of the particles were determined by transmission electron microscopy (TEM), high-resolution transmission electron microscopy (HRTEM) and wide-angle X-ray scattering (WAXS). Elemental analysis (EA) and Inductively Coupled Plasma Atomic Emission Spectroscopy (ICP-AES) and Energy-dispersion X-ray (EDX) allowed to get the ratio between metal and organics (ligands) at the RuNPs surface, nuclear magnetic resonance (NMR) and infrared (IR) spectroscopies were used to analyze the surface composition of the nanoparticles. Gas chromatography (GC) was used in order to titrate the quantity of hydrogen atoms (hydrides) present at the surface of the nanoparticles by a home-made titration method (*vide infra*).

6.1.3.1 Transmission Electron Microscopy (TEM), High-Resolution TEM (HRTEM) and Energy-Dispersive X-Ray Spectroscopy (EDX)

Transmission electron microscopy analyses were performed at the "Centre de Microcaractérisation Raymond Castaing" in Toulouse, France (UMS-CNRS 3623). Samples were prepared by slow evaporation of a drop of crude concentrated colloidal RuNPs suspension deposited under oxidizing atmosphere (air) onto a holey carbon-covered copper grid. TEM analyses were performed using JEOL JEM 1011 or JEOL JEM 1400 microscope, operating at 100 and 120 kV, respectively with a point of resolution of 0.45 nm. TEM was used as standard tool to determine the shape, morphology and mean size of the ruthenium nanoparticles. Size distributions were built by measuring *ca.* [400 – 300] nanoparticles through a manual counting of several enlarged TEM micrographs. The mean diameters were determined by fitting a Gaussian curve to each statistical size distribution.

HRTEM analyses were carried out by Vincent Collière with a JEOL JEM-ARM 200F microscope working at 200 kV with a point of resolution of < 0.19 nm. Fast-Fourier Transform (FFT) treatments of HRTEM micrographies were carried out with the Digital Micrograph software

version 1.80.70 in order to determine the crystalline planes, structure and lattice parameter of the synthetized nanoparticles.

EDX spectroscopy were performed by Vincent Collière and obtained with a JEOL JEM-ARM 200F (URP) ED microscope, equipped as well as for HRTEM, working at 200 kV. The spectra were evaluated using JED-2300 Analysis Station software taking into account the sensitive factors for the different elements (*k*-factor corrections). The beam spot sizes depended on the nanoparticle system but in general they ranged between [1 – 10] nm. The analyses were obtained for different sections of the characterized grids.

6.1.3.2 Microanalysis

Elemental analyses (EA) were performed by Isabelle Borget in the "Service d´Analyses Chimiques" at the LCC-CNRS for carbon and hydrogen concentration determinations.

The metal content in the nanoparticles was obtained by Alain Moreau in the same facilities by using a ICAP 76001ICP-AES Analyser of ThemoScientific equipment.

6.1.3.3 Vibrational Spectroscopy

Ruthenium nanoparticles vibrational properties were obtained by attenuated total reflectance infrared (ATR-FTIR) and simple Fourier-transform infrared (FTIR). The spectra were recorded under inert atmosphere in a Perkin-Elmer GX2000 spectrometer installed inside a globe-box at the range of [400 - 4000 cm^{-1}]. FTIR spectra were obtained in the same conditions as ATR-FTIR but with potassium bromide (KBr) as support and diluent.

6.1.3.4 Gas Chromatography

The quantity of reactive hydrogen atoms present at the RuNPs surface was obtained by gas chromatography (GC). The analyses were performed with a Hewlett Packard HP-5890 Series II instrument equipped with a flame ionization detector and a 30 m non-polar 100.0 % capillary column (0.32 mm diameter, 0.25 mm film thickness) of dimethyl polysiloxane (SGE PB1), using helium (2 $mL.min^{-1}$) as carried gas.

Methodology for surface reactive hydrogen atoms: The temperature of the injector and detector was set at 250 °C and that of the column at 60 °C. The initial stabilization time was 3 min and then, a temperature ramp was set from 60 to 170 °C (15 $°C.min^{-1}$), three extra minutes were left as final program time.

6.1.3.5 Wide-Angle X-Ray Scattering

Wide-angle X-ray scattering (WAXS) measurements were performed at CEMES-CNRS by Pierre Lecante. Small amounts of purified RuNPs were put in 1.0 or 0.5 mm diameter Lindermann glass capillaries under inert atmosphere and then sealed. The samples were irradiated with graphite-monochromatized molybdenum kα (0.071069 nm) radiation and the X-ray scattering intensity measurements were performed using a dedicated two-axis diffractometer. Time for the data collection was typically 20 h for a set of 457 measurements collected at r.t. in the range of 0° < θ < 65° for equidistant s values ($s = 4\pi\left(\sin\frac{\theta}{\lambda}\right)$). The reduced data were extracted in order to see the structure-related component of WAXS normalized to a number of atoms corresponding to the nanoparticles size. Radial distribution functions (RDF) were obtained after Fourier transformation of the corrected and reduced intensity functions.

6.1.3.6 Liquid Nuclear Magnetic Resonance

Solution nuclear magnetic resonance (NMR) at high-resolution were accomplished by Christian Bijani in the "Service de Resonance Magnétique Nucléaire" at the LCC-CNRS, Toulouse, France. Liquid proton (^{1}H-NMR) and fluorine nuclear magnetic resonance (^{19}F-NMR), diffusion-ordered spectroscopy (DOSY) and nuclear Overhauser effect spectroscopy (NOESY) experiments were performed on four different Bruker spectrometers (Avance 400, Avancelll 400, Avance 500 and Avance NEO 600) at 298 K. Preparation of the NMR tubes was carried out under argon atmosphere using deuterated solvents (chlorophorm-d^1, benzene-d^6, toluene-d^8 and THF-d^8) to re-disperse the dried nanoparticles powder.

DOSY measurements were performed with a diffusion delay (Δ) between [150 – 200 ms], and a gradient pulse length (δ) among [2.0 - 3.0 m]. The peak integration decay curves of the DOSY spectra were fitted according to the Stejskal-Tanner function.[320]

$$S(G) = S_0 e^{[-D\gamma^2 G^2 \delta^2 \Delta']}$$

Where S and S_0 are the signal amplitude in presence and absence of diffusion, D is the diffusion coefficient of the moiety, γ is a linear combination of the gyromagnetic ratios, δ is the time where the pulse was switched on, G is the gradient amplitude and Δ' is the diffusion delay time corrected of the diffusions effects during the gradient pulse.

NOESY measurements were performed with delay time of 2.0 s and the mixing time was set to 100.0 ms. These studies were done with the aim to find the exchange-transferred nuclear Overhauser effect (et-NOE) sign. This variable depends mainly on the correlation time (τ_c) which relies on the molecular weight of the solubilized moieties.[273] Typically, small molecules (MW < 600) displays positive et-NOES, medium size moieties (600 < MW < 1200) exhibit et-NOE close to zero, if this case is presented a rotating-frame Overhauser spectroscopy (ROESY) NMR experiment should be performed. Finally, big species as the MNPs present a negative et-NOE (Figure 6.3).

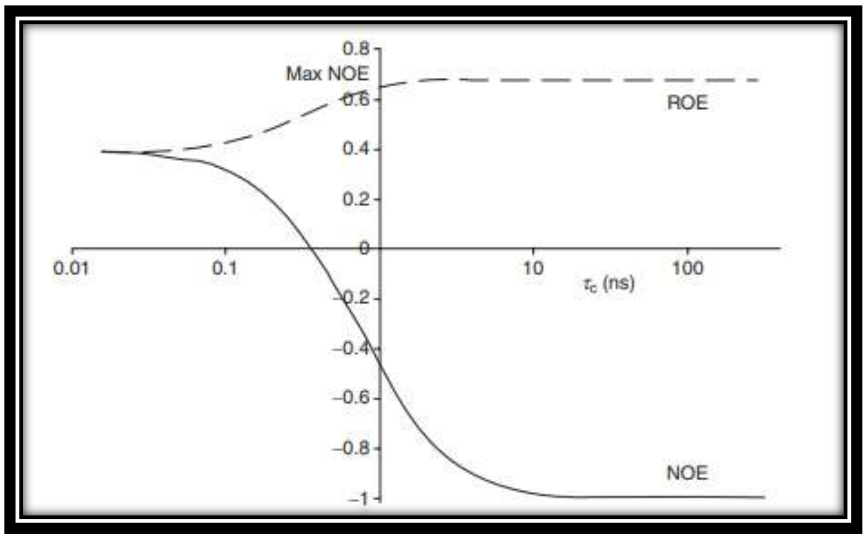

Figure 6.3 Maximum NOE obtained in NOESY (solid line) and ROESY experiment (dash line) as a function of τ_c.[274]

6.1.3.6.1 Calculation of Hydrodynamic Radius

Hydrodynamic radii (r_H) were estimated from the diffusion coefficients measured in 2D DOSY experiments [192] performed in benzene-d^6 or THF-d^8 by following the Stokes-Einstein law for spherical particles diffusion in solution.([303],[304])

$$D = \frac{k_B T}{6\pi\eta r_H}$$

Temperature (T) and viscosity (η) are the principal variables to consider for the hydrodynamic radius calculation, which are intrinsically related. Benzene-d^6 viscosity value has a higher dependence with the temperature than THF-d^8 (table 6.2), DOSY experiments were performed at r.t. ([20 - 25 °C]).

Table 6.2 Benzene and THF viscosity in relation with their temperature.

Benzene[305],[306]	***T*** **(K)**	***η*** **(mPa.s)**	**THF**[325]	***T*** **(K)**	***η*** **(mPa.s)**
	293	0.649		298	0.463
	298	0.604		308	0.428
	323	0.436		318	0.390

The hydrodynamic radii were related with the RuNPs mean sizes obtained by TEM studies according to the next mathematical relation gathered from the literature.[326]

$$r_H = \frac{D_{RuNP}}{2} + D_{H(Ligand)}$$

6.1.3.6.2 Quantification of Ligand Surface Coverage

The quantifications of ligand surface coverage were performed from DOSY ^{1}H-NMR spectra, according to a published methodology.[267] From the integration ($I_{[0]}$) of the resonances of a specific region (ligand chemical shift) in the 1D DOSY ^{1}H-NMR spectra, the relative amounts (X) of ligands either strongly attached (X_{Is}) and weakly bonded or in exchange (X_{Iw} + X_{If}) were obtained. Then, considering the observed diffusion coefficients as the weighted average of the surface-linked (D_{Is}), exchanging ligand (D_{Iw}) and free ligand (D_{If}) measured, the quantification of different types of ligand surrounding the RuNPs were calculated by following the next equations.

$$I_{[0]} = X_{I_s} + X_{I_w}$$

$$D_{I_w} = \left(X_{I_w}\right)\left(D_{I_s}\right) + \left(X_{I_f}\right)\left(D_{I_f}\right)$$

$$X_{I_w} = 1 - X_{I_s} - X_{I_f}$$

$$X_{I_f} = \frac{\left(D_{I_w}\right) + \left(D_{I_s}\right)\left(X_{I_s} - 1\right)}{\left(D_{I_f}\right) - \left(D_{I_s}\right)}$$

The surface coverage value per ruthenium surface atoms ($I_{s,w,f}/Ru_{surf}$) and the quantity of ligand interacting per ruthenium nanoparticles ($I_{s,w,f}/Ru_{NP}$) were obtained by using the RuNPs mean size obtained by TEM, the crystalline close pack (WAXS and HRTEM) and the magic number for metal clusters according to the next equations.

$$I_{s,w,f}/Ru_{surf} = \frac{[RCOOH]_{(equiv.)}\left(X_{I_{s,w,f}}\right)}{[Ru]_{(equiv.)}\left(\frac{N_{Ru_{surf}}}{N_{Ru}}\right)}$$

$$I_{s,w,f}/Ru_{NP} = \left(I_{s,w,f}/Ru_{surf}\right)\left(N_{Ru_{surf}}\right)$$

6.1.3.6.3 RuNPs Surface Saturation

NOESY ^{1}H-NMR allowed to get information on the surface saturation of the RuNPs. 2D NOESY experiments permit to observe the presence of negative NOE cross-peaks in the chemical shifts assigned for the ligands. These negative NOE signals are observed when a fast exchange between the weakly interacting (I_w) and exchanging ligand (I_f) is predominating, meaning the confirmation of free ligand present in the deuterated solvent.

6.1.3.6.4 Ligand Exchange Quantification

Quantifications of the ligand exchange between different carboxylic acids at RuNPs surface were performed by carrying out a serial of ^{1}H and DOSY NMR experiments with spectra deconvolution. The quantity of a given ligand present at the RuNPs surface in each step of the ligand exchange was calculated according to the equations described in the section 6.1.3.6.2. NOESY NMR studies as described in section 6.1.3.6.3, allowed to determine the interaction of the entering ligand as well as to detect the ligand released after the exchange.

6.1.3.7 Solid-State Nuclear Magnetic Resonance

Solid-state NMR analyses were performed by Yannick Coppel on a Bruker Avance 400WB spectrometer in the “Service de Resonance Magnétique Nucléaire” at the LCC-CNRS, Toulouse, France. Preparation of the samples was carried out under argon inside a globe-box. The powder of RuNPs was dispersed on porous silica gel (60 Å) by impregnation from a THF NPs colloidal suspension, followed by slow solvent evacuation before filling a 3.2 mm probe ZrO_2 rotor. Experiments were conducted at a spinning speed of *ca.* 12 kHz using a ^{13}C spin -Echo and CPMG pulse sequence.

Heteronuclear correlation spectroscopy (HETCOR) NMR experiments were performed in order to describe the proton-carbon (^{1}H-^{13}C) correlation at the surface of the RuNPs. Specially, the vicinity of the ^{13}CO deposited on preformed RuNPs stabilized by carboxylic acids.

6.1.4 Surface Reactivity Studies and Catalysis

6.1.4.1 Quantification of Surface Reactive Hydrogen Atoms

The quantification of hydrogen attached onto the ruthenium nanoparticles surface was carried out by GC analyses. The RuNPs were dissolved in THF inside a Schlenk reactor to form a homogeneous stable colloidal solution under inert conditions. Then, 10.0 equiv. of olefin (2-norbornene) were added to the reaction mixture and maintained under vigorous stirring at r.t. during 72 h, the procedure was done according to a previously published methodology.[99] The solution was filtrated with silica/celite plugs and the resulting samples were taken for estimation of the norbornene conversion into norbornane by GC analyses. The measurements of the amount of alkane formed allowed to determine the necessary quantity of hydrogen atoms for reducing the alkene, and further to calculate the reactive hydrogen per ruthenium surface atom (H_{reac}/Ru_{surf}) considering the nanoparticle mean size obtained by TEM, the crystalline structure (HRTEM and WAXS) and the magic number theory for metal clusters.

The calculation of surface reactive hydrogen atoms per ruthenium surface atom at r.t. was obtained by applying the next equations.

$$N = \left(\frac{NP_d}{2b(Ru_r)}\right)^3$$

$$N = \frac{1}{3}(10n^3 - 15n^2 + 1n - 3)$$

$$N_{surf} = 10n^2 - 20n + 12$$

$$n_H = 2(n_{oleofin})(\%_{Conv})$$

$$H_{reac}/Ru_{surf} = \left(\frac{n_H}{n_{Ru}}\right)\left(\frac{N_{surf}}{N}\right)$$

In the first equation, *N* is the total number of ruthenium atoms per nanoparticle and *b* is the crystalline closed pack parameter.[141] For the second mathematical statement, *n* is the number of shells according to the magic number for metal clusters. In the third equation, N_{surf} is the number of ruthenium surface atoms per nanoparticle.[327] The quantity of reactive hydrogen was obtained with the fourth equation, where $\%_{Conv}$ is the 2-norbornene hydrogenation percentage. Finally, the number of hydrides per ruthenium surface atom was obtained with the last relation.

6.1.4.2 Surface Mapping with ^{13}CO

The reaction of ^{13}CO with ruthenium-based nanoparticles was performed in the solid-state, following a previously described procedure.[114] A powder of RuNPs was introduced into a small Fisher-Porter reactor (*ca.* 5 mL) under inert conditions. After, the reactor was evacuated and then pressurized with 1 bar of ^{13}CO under vigorous stirring. The reaction time was fixed to 15 h. Then, the remaining ^{13}CO was evacuated by high-vacuum and then the RuNPs sample was analyzed by solid-state NMR.

6.2 DFT Calculations

6.2.1 Ru_{55} Nanoparticle Model

An ultra-small *ca.* 1.0 nm 55-atom hcp metal ruthenium nanoparticle (Ru_{55}), which is smaller *ca.* [35.0 – 40.0 %] than the approximate mean size of the RuNPs synthetized ([1.5 – 1.7 nm]), was utilized as a basis model to perform DFT calculations. The chosen Ru_{55} model, designed in a previous published work, has been shown to properly describe the surface properties of ultra-small RuNPs (figure 6.4).[82]

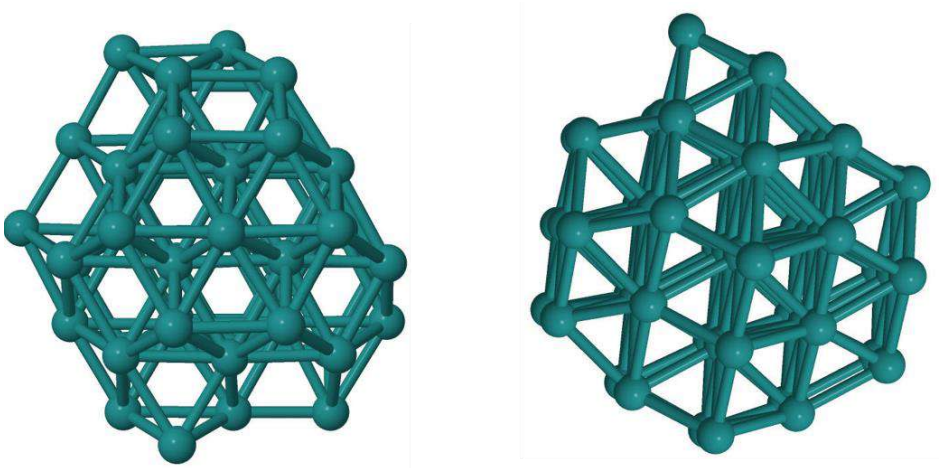

Figure 6.4 Ultra-small Ru_{55} model.

This Ru_{55} NP model has a cubo-octahedral full-shell organization[[13],[328]] which possesses an overall spherical morphology. The originally designed RuNP has a hcp structure with twelve (101) and two (001) planes, that was shaped in order to establish structural modifications close to the experimental surface heterogeneity. Therefore, the resulting Ru_{55} hcp model is not a perfect crystalline structure.

Firstly, an adatom was introduced with the purpose to generate a B_4 and a B_5 sites. A slightly corrugated facet was also obtained by removing an atom line between two (101) planes (figure 6.5). The surface area of the chosen DFT-PBE optimized Ru_{55} nanoparticle, which possess 11 ruthenium atoms in the core and 44 at the surface, is 258 $Å^2$, this value is *ca.* 25 $Å^2$ less than a perfect spherical 1.0 nm particle.[329]

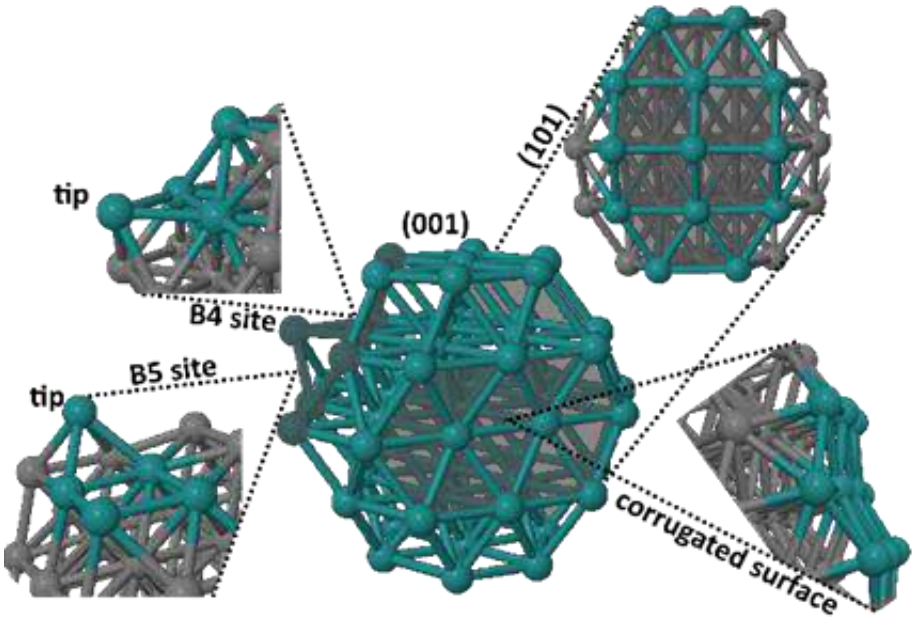

Figure 6.5 Ru_{55} hcp-based NP; different surface sites are highlighted.[82]

6.2.2 Periodic DFT Calculations of Ru_{55} Nanoparticles

Spin polarized density functional theory (DFT) calculations were performed using the Vienna *ab initio* simulation package (VASP) software,[[313],[314]] that is a periodic-first principles software that uses the projector augmented wave (PAW) method to describe the electron-core interaction in atoms and a plane wave basis set.[[315],[316]] The software has been widely used to describe liquids, metals, nanostructures, semiconductors and insulators, and general surfaces.[332] The resolution of the Schrödinger equation for metal systems is quite efficient by using this methodology, specially due to the usually HOMO-LUMO degeneracy which is a common phenomenon found for the iterative resolution of the Schrödinger equation in these systems.

Calculations were performed with the PBE functional developed by Perdew, Burke, and Ernzerhof (PBE),[73] which is a conventional functional among the generalized gradient approximation (GGA) functionals that is widely used in surface science.[75] Projector augmented waves (PAW) potentials were utilized with kinetic energy cutoff of 500 eV. PAW data sets for metal atom treating *ns*, (*n*-1)*p* and (*n*-1)*d* states (14 e^- for ruthenium). Γ-centered[333] calculations were

performed with a Gaussian smearing width (σ) of 0.02 eV. Geometry optimizations were done till the criteria of the residual forces on any direction were less than 0.02 eV.Å^{-1}. The used supercell size was set to ensure a *ca.* 16 Å vacuum space between periodic images of the ruthenium cluster (figure 6.6). For example, a 27.0 x 27.0 x 27.5 Å large supercell was set up for a $Ru_{55}(CH_3COO)_{16}H_{16}$ NP whereas a 35.0 x 35.0 x 36.0 Å large supercell was set up for a $Ru_{55}(C_7H_{15}COO)_{14}H_{14}$ NP.

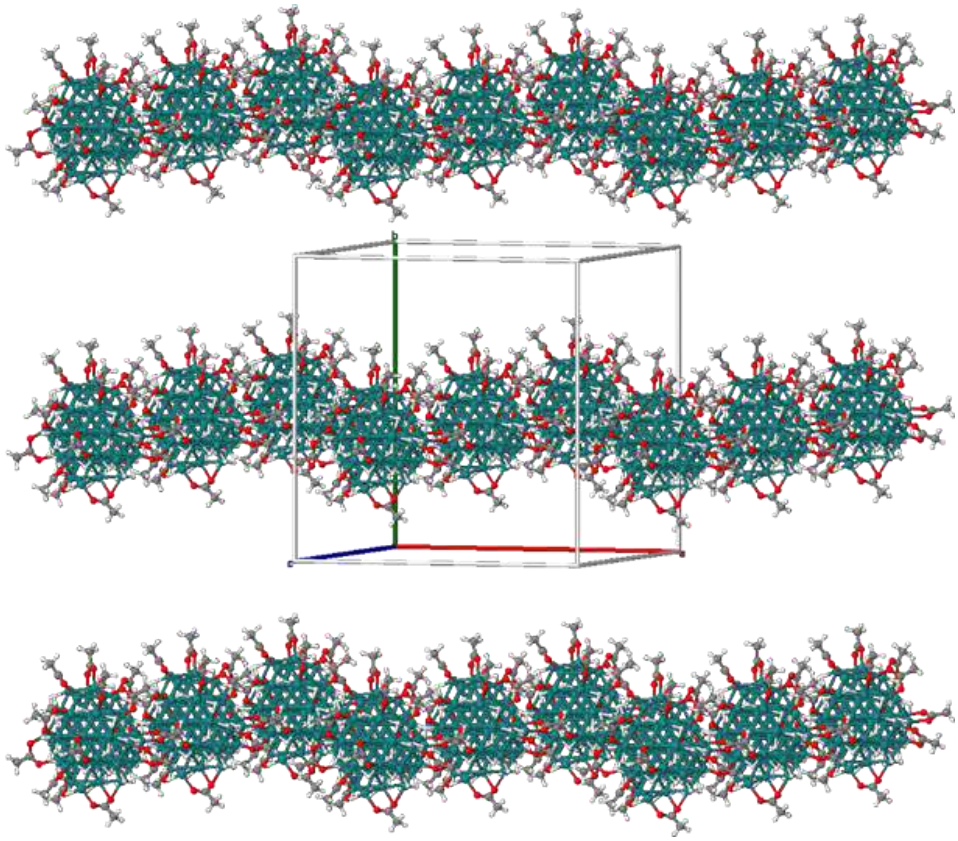

Figure 6.6 Translational symmetry of the supercell method within periodic-DFT calculations: Orthorombic unitcell (*a* = 27.0 Å, *b* = 27.0 Å, *c* = 27.5 Å) that contains $Ru_{55}(CH_3COO)_{16}H_{16}$ periodically replicated 3 x 3 x 3.

Frequency calculations were performed at the same level of theory. Finite differences are used to calculate the Hessian matrix. In other words, each ion is displaced in every direction by a small positive and negative displacement. The selective dynamics method available in VASP allows the calculation of vibrational normal modes of a subset of atoms by computing frequencies within atoms far away from an adsorption or a catalytic site (reducing the use of computational resources).

6.2.3 Ligand Adsorption Energies Calculations

The adsorption energies of a given ligand ($\Delta E_{ads_{L_i}}$) were obtained through first principles DFT studies by consider the adsorption of *n* ligands (L_i) at the surface of the Ru_{55} NP. The calculation of the average adsorption energy requires to fully optimize the free ligand, the reference NP and its counterpart stabilized with the *n* ligands (*L*). Thus, the adsorption energy was calculated as follows.

$$\Delta E_{ads_{L_i}} = \frac{1}{n}\left(E_{Ru_{55}(L_i)_n} - E_{Ru_{55}} - nE_{L_i}\right)$$

Where the obtained energy (*E)* are represented by the DFT-PBE energies of the molecules at 0 K, without taking into account zero-point energy and thermal corrections.

Regarding the coordination modes, there is some arbitrariness in the recognition of a chemical bond. But criteria are needed in order to define the possible bridging (μ_n) character and hapticity (η_m) between surface ligands and the Ru_{55} NP. Thus, it was considered that a bond exists between a metal atom (Ru) and a ligand atom when the distance between them was less than 2.1 Å for H, 2.5 Å for C, 2.5 Å for N, 2.5 Å for O and 3.5 Å for F.

6.2.4 Reaction Barriers

The reaction barriers of single step reactions were calculated by exploring with a nudged elastic band method the minimum energy pathway (MEP) between two stable states of the reactants and the products. The method consists in the optimization of a set of interpolated structures between R and P. Each optimized point on the path is an energy minimum in all directions perpendicular to the path and there is a highest energy lying structure which is the transition state.

The climbing image nudge elastic band method (CINEB)[[319],[320]] has been used with a spring force between images of 5 eV and a tolerance force of 0.02 eV/Å. The harmonic vibrational

frequencies were systematically calculated in order to distinguish minima and saddle points by using the dynamical matrix code implement in VASP, as well as the VASPTST tool.[336]

6.2.5 NMR Calculations of Organic Moieties on Small Ruthenium Clusters

The calculation of half-integer spin NMR properties with the gauge including projected augmented wave (GIPAW) method is available with VASP.[337] However, the methodology for metal-type electronic structures is not currently available.[338] Thus, all NMR calculations were done on small [Ru_6] clusters by using the Gaussian09 software (taking advantage that NMR chemical shieldings are local properties).[339]

Pseudopotentials and basis sets for [Ru_6] clusters were obtained from a previous published procedure (basis set I).[166] It was used the Stuttgart-Dresden relativistic effective core potential (SDD-ECP) and its basis set developed for ruthenium-augmented core with an *f*-polarization function (ζ_f = 1.235).[340] The SDD-ECP and is basis were also used for carbon, oxygen and fluorine augmented with a set of *d*-polarization functions (C: ξ_d = 0.587, O: ξ_d = 0.961, F: ξ_d = 1.577).[341] Hydrogen atoms were treated with the polarized double-zeta quality 6-31G(*d*,*p*) basis set.([327],[328])

The correlation-consistent polarized valence triple zeta (cc-pvtz) basis set was considered for ethanoic acid and ethanoate (basis set II). ^{1}H and ^{13}C chemical shifts of ethanoic acid were similar with both basis set (I and II), but there was a higher dependence for the ethanoate.

The chemical shieldings were calculated on fully optimized structures without any geometry constraints at the DFT-PBE0 level of theory, where PBE0 is a hybrid functional,[344] and gauge Including Atomic Orbital method (GIAO).([345]–[349]) The reliability of this computational strategy has already been proven in several applications.([166],[114])

Theoretical chemical shifts can be obtained by computing isotropic chemical shieldings (σ) for both the investigated compounds and the reference (TMS) at the same level of theory, as it is described hereafter.

$$\delta_i = (\sigma_{Ref} - \sigma_i)(10^6)$$

Where σ is calculated in ppm.

Two different TMS chemicals shielding (σ_{ref}) were used to calculate the chemical shift (δ) from the isotropic shielding constants (σ_i).[350] The cc-pvdz basis set: $\sigma_{H\text{-}TMS}$ = 31.66 and $\sigma_{C\text{-}TMS}$ = 196.81 ppm and the cc-pvtz basis set: $\sigma_{H\text{-}TMS}$ = 31.57 and $\sigma_{C\text{-}TMS}$ = 189.16 ppm.([336],[337])

6.2.6 Ab initio Thermodynamics

The energies obtained by *ab initio* calculations were implicitly obtained in vacuum (p = 0 Pa) and without any thermal nor zero-point energies (ZPE, T = 0 K). Nevertheless, it is possible to describe, analyze or even predict thermodynamic properties such as Gibbs free energies ($\Delta_a G°$) by combining first principles calculations and a thermodynamic based methodology,([338],[339]) which is the base of the *ab initio* thermodynamics method.

Phase diagrams were obtained by using this methodology, as shown in section 2.5.2, where the standard Gibbs free energies of adsorption of the most stable structures, at certain fixed temperature, as a function of concentration and pressure were plotted. Layouts were conceived when the interacting moieties (ligands) - carboxylic acid (R-COOH) solution (THF) and hydrogen pressure (H_2) - were found in the equilibrium. As well, phase diagrams were obtained by looking at the relationship of the ligands with THF at the equilibrium.

As an example, the co-adsorption of two species at the surface of Ru_{55} NP (liquid and gas phases): L_1 (R-COOH) & L_2 (H_2). Such process is the starting point of the Langmuir-Hinshelwood mechanism in heterogeneous catalysis.([340],[341]) The general ligand adsorption reaction onto the Ru_{55} NP and the Gibbs free energy ($\Delta_a G°(T,[L_1],p_{L_2})$) calculations are briefly presented hereafter.

$$RuNP + n_1 L_1 + n_2 L_2 = n_1 L_1^* + n_2 L_2^*$$

The adsorption energy can be calculated as:

$$\Delta_a E = E(n_1 L_1^*, n_2 L_2^*) - E(RuNP) - n_1 E(L_1) - n_2 E(L_2)$$

For $\Delta_a G°$ calculations, the two co-adsorbed species (L_1 & L_2) are considered in thermodynamic equilibrium with the metal NP, as follows:

$$\Delta_a G = \frac{[\Delta G^\circ - n_1\mu(L_1,T,c) - n_2\mu(L_2,T,p)]}{A}$$

Where *A* is the surface area of the optimized Ru_{55} NP (258 $Å^2$). Thus, the standard Gibbs free energies (*ΔG°*) can be obtained from the next equation.

$$\Delta G^\circ = E(n_1L_1^*, n_2L_2^*) - E(RuNP) + F^{vib}(n_1L_1^*) + F^{vib}(n_2L_2^*)$$

F^{vib} stand for the vibrational contributions to the standard Gibbs free energy of the metal lattice. These do not appear in this last equation, because it has been considered identical between the reference Ru_{55} NP and the ligand-stabilized Ru_{55} NP. This approximation avoids the expensive calculation of metal-metal normal modes of vibrations.

As the surrounding medium acts as a reservoir of ligands (L_i), the chemical potentials (μ) were calculated from the standard chemical potential and the activity of the ligand, as follows:

$$\mu(L_i,T,p) = \mu^\circ\left(L_i,T,p^\circ\right) + kT\ln a\,(L_i)$$

The standard chemical potentials ($\mu^\circ(L_i, T, p)$) were obtained from a previous mathematical statement report, where the standard enthalpy ($H_T^\circ(L_i)$) and entropy ($S_T^\circ(L_i)$) were calculated from the *L* partition function, as it is described hereafter.[357]

$$\mu^\circ\left(L_i,T,p^\circ\right) = E^{DFT}(L_i) + H_T^\circ(L_i) - TS_T^\circ(L_i)$$

Surface adsorption Gibbs free energies ($\Delta_a G$) can be plotted as a function of two chemical potentials $\mu(L_1)$ and $\mu(L_2)$ for several surface compositions (n_1 & n_2). As a consequence, reasonable thermodynamically stable geometries are highlighted on surface phase diagrams in the [$\mu(L_1)$, $\mu(L_2)$] ranges.

Standard enthalpy (H_T°(R-COOH, g)) and entropy (S_T°(R-COOH, g)) were obtained with the Gaussian09 software, THF was taken into account as a solvent thanks to the solvation model density (SMD)[358] variation of the integral equation formalism of the polarizable continuum model (IEFPCM).[359] While, standard enthalpy ($H_T^\circ(H_2, g)$) and entropy ($S_T^\circ(H_2, g)$) were taken from the JANAF tables.[360] The chemical potential for H was obtained as ½ $\mu(H_2, T, p)$, since the dissociative adsorption is the one that is considered. Free energy thermodynamic diagrams were produced with the home-made *aithermo* program.[202]

The *ab initio* thermodynamics analyses were performed in the range of [10^5 - 10^{-20} M] for R-COOH in THF and the scope of [10^5 - 10^{-20} bar] for H_2. The mapping of the RuNPs surface in

different conditions range were previously reported.[82] For this case, the study was performed at three different temperatures: 200, 300 and 450 K.

6.2.7 Normal Modes of Vibration

The normal modes of vibration were calculated with the VASP transitional state theory tools by using the dynamical matrix methodology which allows to find vibrational modes of pre-optimized structures.[361]

6.2.8 Calculation of Atomic d-Band Centers

The coordination and averaged *d*-band centers([172],[64]) were calculated with the home-made *tools4vasp* suite of utilities,[202] which uses the density of states (DOS) projected on a local basis set by the Lobster package.[362] The atomic *d*-band center of an atom α, $\bar{\varepsilon}_d(\alpha)$ was calculated as follows.

$$\bar{\varepsilon}_d(\alpha) = \frac{\left(\sum_m \int_{E_{min}}^{E_F} \epsilon n_{d_m}(\alpha,\epsilon) d\epsilon\right)}{\left(\sum_m \int_{E_{min}}^{E_F} n_{d_m}(\alpha,\epsilon) d\epsilon\right)}$$

In the equation, *m* runs over the five *d* atomic orbitals (AOs) and n_{d_m} (α, ϵ) is the DOS projected on the d_m AO of atom α. The bar sign above ε_d means that it is averaged over all *d* AOs. Besides, E_{min} is readily set to the bottom of the occupied *d*-band. Finally, the DOS integrated up to the Fermi level (E_F).[217]

6.2.9 pDOS, pCOHP and Atomic Charges Calculations

The projected density of states (*p*DOS) and the projected crystal orbital hamilton population (*p*COHP) profiles as well as bond energy analysis were achieved with the Lobster software, using the pbeVASPfit basis set.([362]–[364]) Calculations in VASP were at least 12*n* + *m* +8*k*

for a given Ru_{55} NP optimized structure with certain ligand coverage: Ru {4*p*, 4*d*, 5*s*, 5*p*}; C, N, O and F {*ns*, *np*}; H {1*s*}.

The charge spilling, a criterion that assesses the quality of the projection, was systematically lower than 0.7 %. Atomic charges were provided both by integrating the *p*DOS up to the Fermi energy and by carrying out the atoms-in-molecules (AIM) analysis of the charge density.[365] This methodology is the Mulliken population analysis (MPA) performed with an orthonormal basis set. Since it first starts with a projection of the wavefunction from a planewave basis set to a local basis set, such charges are called *p*MPA atomic charges. It has recently been shown that, in the case of non-covalent graphene doping, *p*MPA charges and natural populations (NPA)[225] are rather similar.[226]

6.2.10 Qualitative Average Bond Strength

The qualitative average bond strengths were obtained for a given *A*-*B* bond by integrating up to the Fermi energy the *p*COHP values calculated between all valence μ and ν AOs that belong to *A* and *B* atoms, the values were obtained as follows:

$$IpCOHP(A-B) = \sum_{\mu \in A} \sum_{\nu \in B} \int_{E_{min}}^{E_F} pCOHP_{\mu\nu}(\varepsilon) d\varepsilon$$

Such one-electron derived index must not be considered as a bond dissociation energy (BDE), but it gives a valuable bond strength index which variation follows BDE variations or any property related to bond strength, such as *A*-*B* stretching frequencies.[82]

6.2.11 Gibbs Free Energy for HER Reaction

The Gibbs free energy of the adsorbed hydrogen state (ΔG_{H*}) in the most stables optimized Ru_{55} NP structures was obtained by adding the zero-point energy (ΔE_{ZPE}) and subtracting the enthalpic term ($T\Delta S_H$) from the hydrogen adsorption energy on a given optimized structure. It was considered that this value was 5.5 kcal.mol^{-1}, as reported in a previous published work.[10] The

Gibbs free energy for an hydrogen adsorption (ΔG_{H^*}) was obtained with the next mathematical statement.

$$\Delta G_{H^*} = E(H^*) - E(surf) - \frac{1}{2}E(H_2) + \Delta E_{ZPE} - T\Delta S_H$$

GENERAL CONCLUSION

Nowadays, the water splitting process is not a viable methodology for the production of energy due to several issues, like the cost and efficiency. Thus, in order to increase the effectiveness of the process, an efficient photocatalyst needs to be designed. Several new materials have been synthetized to be used in the water splitting process. However, their functionality is not well described. Moreover, a good catalyst that can overcome with the presented water splitting issues has not be found. Therefore, a well-understanding of the photophysical and catalytic properties of these materials is crucial to design a suitable catalyst, that can be used for the photoproduction of hydrogen from water.

The aim of this PhD work was contributing to the improvement of hydrogen (H_2) production using solar power. Hence, our efforts were focused in the separation of water using light in order to obtain the desired energy source. This work provides a solid scientific base that gives some insights about the proper design of a reliable catalyst for the water splitting process.

This doctorate thesis was an upstream study in the large context of hydrogen production by photolysis of water molecules. The main objective was to determine the appropriateness of a family of ruthenium-based nanomaterials as catalysts for the hydrogen evolution reaction (HER), which is the second reaction involved in the water splitting process, where ruthenium has known a renewed attention these last years.

For that purpose, the PhD work was centered on the synthesis of model ruthenium nanoparticles (RuNPs) using carboxylic acids as stabilizing agents and their full characterization by

means of different tools including theoretical studies. A second objective was to evaluate the potential of the obtained nanoparticles in the HER reaction. The final aim was the design of hybrid nanomaterials based on the association of RuNPs and a photosensitizer derived from the $[Ru(bipy)^3]^{2+}$ complex for their evaluation in photocatalytic conditions.

In the first chapter of this PhD manuscript is based on an experimental and a theoretical background based on the synthesis, stability, and catalytic activity of RuNPs. In the second chapter, it was described the synthesis of RuNPs by following the organometallic approach and using ethanoic acid as a stabilizer. A synthesis optimization and a full characterization of the obtained nanoparticles were performed. By this way, it was obtained a homogenous population of small and well-dispersed ethanoic acid stabilized RuNPs of *ca.* 1.5 nm, the composition of which was precisely determined in particular by deep NMR analyses.

Then, the characterization data were taken as a starting point to build a trustworthy theoretical model able to explain the surface and electronic properties of these RuNPs. First, it was determined that the ethanoic acid interacts with the metal surface as a carboxylate. Then, it was possible to define a precise mapping of the RuNPs surface, both in terms of nature of surface species (stabilizer and hydrides) and of their quantity, thanks to a good agreement between experimental and theoretical data. It is worth to note that the quantity of hydrides was low compared to previous systems of RuNPs.

The findings allowed to corroborate the reliability of the theoretical model used and to evidence its interest in order to get trustful trends for a better understanding of the ligand influence on the RuNPs properties. The theoretical model also allowed achieving reliable trends in order to predict the catalytic viability of the RuNPs regarding the hydrogen evolution reaction (HER), thus evidencing the need to find a good compromise between stability and reactivity

Chapter III was focused on the use of carboxylic acids with longer alkyl chains to stabilize RuNPs, namely pentanoic and octanoic acids. This choice was made aiming to study the influence of the alkyl chain length of carboxylic acids on the surface properties of the particles. More homogeneous and well-defined particles were formed with these carboxylic acids. Moreover, optimization of the synthesis conditions allowed to get particles of similar size as with ethanoic acid. Thus, a comparison of the RuNPs surface composition and properties was performed in order to rationalize the influence of the stabilizer.

As previously observed with ethanoic acid, experimental and theoretical results were in good accordance towards the coordination of the pentanoic and octanoic acid to be under the carboxylate form and the quantity of co-adsorbed hydrides to be low. Comparative studies highlighted the direct influence of the alkyl part of the stabilizing ligand. In fact, longer the alkyl chain, lower is the necessary quantity of ligand to stabilize RuNPs of similar mean sizes.

Theoretical evaluation of the systems of RuNPs for the HER reaction led to the conclusion that among the carboxylic acid stabilized RuNPs analyzed, the particles with a moderate surface coverage by a carboxylate ligand not too long is probably the best compromise in terms of catalytic activity, presenting an hydrogen adsorption energy close to that of platinum which is presently the best catalyst for the HER reaction. From these results it appeared that the most appropriate nanomaterial is the RuNPs stabilized by 0.3 equiv. of pentanoic. Preliminary catalytic tests tend to indicate that this nanomaterial is able to catalyze the HER reaction but more experiments are needed before being able to judge on its real potential.

Once the properties of the RuNPs stabilized by carboxylic acids were determined, the next logical step was to build the hybrid material. However, it was noticed that the reduction of aryl ligands could occur in the presence of RuNPs. Therefore, a one-step synthesis to form the hybrid material was not possible due to the risk of changing the photonic properties of the bipyridine based photosensitizers. Thus, chapter IV is dedicated to ligand exchange reactions at the surface of carboxylic acid stabilized RuNPs, which was the strategy chosen to avoid this issue.

Thus, these studies were performed in order to determine the appropriate conditions to perform an exchange of ligands at the ruthenium surface, the final aim being to exchange a photosensitizer bearing carboxylic groups with preformed RuNPs and thus get a hybrid [PS]-RuNP nanomaterial for photocatalysis studies.

Even if the efficiency of the exchange process was not so high, the results demonstrated that it is possible to exchange a carboxylic acid by another one (benzoic or TFA) at RuNP surface. However, it is necessary to take into account parameters like the acidity and steric hindrance. In particular, it was shown that octanoic acid can be exchanged by benzoic acid. These results are encouraging enough to follow the same way to graft a photosensitizing molecule at the surface of preformed RuNPs through the use of carboxylic acid as anchoring groups.

In the last chapter of this manuscript, a theoretical study was performed in order to anticipate the grafting of a photosensitizer at the surface of preformed RuNPs stabilized by ethanoates. For this purpose, well-known complexes in HER catalysis was chosen as starting point, namely $[Ru(bipy)^3]^{2+}$ based compounds. Four different $[Ru(bipy)^3]^{2+}$ complexes with carboxylic groups on bipyridine ligands at different locations were modelized in order to evaluate their coordination at the metal surface. The results showed that anchoring a carboxylic acid modified $[Ru(bipy)^3]^{2+}$ complex at the surface of preformed RuNPs is plausible by substituting initial ligands (ethanoates). One important parameter for such a grafting appeared to be the presence of carboxylic acid functions onto two different bipyridine ligands of the complex, the angle obtained in these conditions seeming favorable for the coordination. However, these results are preliminary and need to be completed. The next step will be to test experimentally the anchoring and when the hybrid nanomaterial will be obtained to evaluate its catalytic properties in the HER.

Beside the novelty of the ligands used for the synthesis of ruthenium nanoparticles, the major contribution of this PhD work is the development in parallel of experimental and theoretical approaches in order to bring a better understanding of the structure/properties relationships at the nanoscale of RuNPs stabilized by carboxylic acids. The results obtained reinforce the interest of doing so to characterize better or anticipate the behavior of metal nanoparticles.

The catalytic reaction envisaged for the application of the studied nanomaterials was the water splitting process that allows hydrogen production. Unfortunately, only preliminary theoretical results on synthetizing the catalyst were obtained and the results obtained, even if they are encouraging, need to be confirmed before fully describing them and later on, teste them.

As a final statement, the results obtained during this PhD will be very useful in the future to continue the development of this research. The tools developed can be applied in order to improve other nanocatalysts for the same target reaction or for other catalytic transformations.

RESUME DE LA THESE

La mise au point de modes de production d'énergies renouvelables figure parmi les grands défis actuels de notre société en raison de l'augmentation continue des gaz polluants provenant de l'utilisation de combustibles fossiles et de la demande croissante en énergie.

Si l'énergie solaire peut être considérée comme une source d'énergie quasi inépuisable et renouvelable, son exploitation nécessite de la convertir en combustibles stockables, tels que l'hydrogène (H_2).[[1],[2]] Ce travail de doctorat constitue une étude amont dans le contexte général de la production d'hydrogène solaire par craquage photocatalytique de la molécule d'eau (photosynthèse artificielle ; illustration 1).

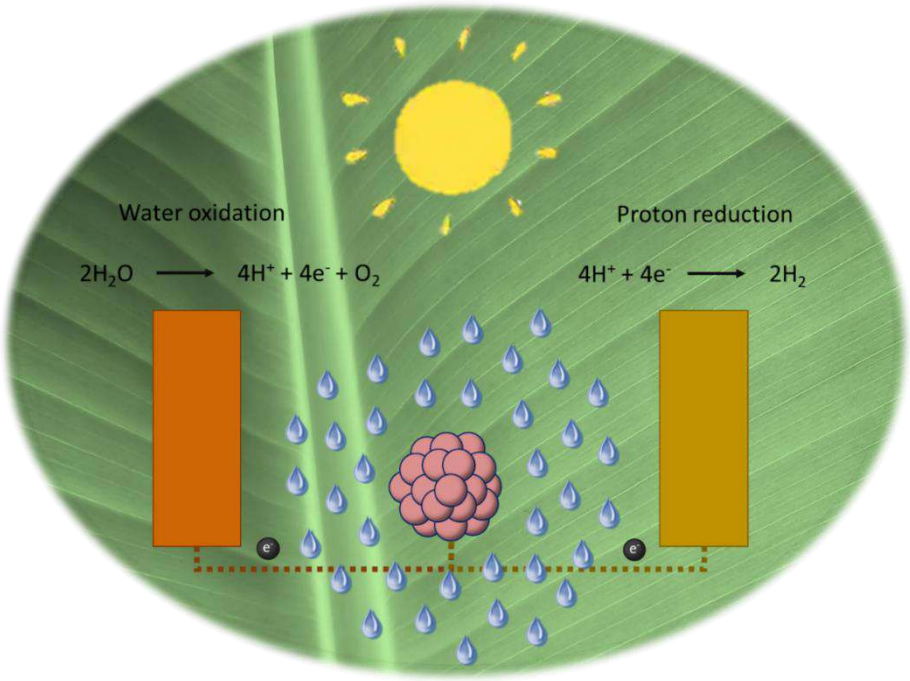

Illustration 1. Représentation schématique du processus du craquage de l'eau.

Deux réactions catalytiques combinées sont impliquées dans la photoproduction de l'hydrogène à partir de l'eau : la réaction d'oxydation de l'eau (WOR) et la réaction de dégagement d'hydrogène (HER). Ces réactions catalytiques intimement liées présentent des cinétiques différentes ce qui rend la mise en œuvre du processus complet compliqué et peu efficace. Le développement de catalyseurs appropriés pour une meilleure efficacité est donc requis et suscite l'attention de la communauté scientifique mondiale.

Qu'ils s'agissent de catalyseurs moléculaires ou sous forme de nanomatériaux, la conception rationnelle des catalyseurs,[[3],[4]] ainsi que la compréhension de leurs propriétés photophysiques et catalytiques, sont de véritables défis à surmonter. Des nanoparticules métalliques (MNPs) se sont avérées des catalyseurs efficaces pour les réactions HE et WO,[[5]–[7]] montrant des activités électrocatalytiques élevées, et une faible surtension. Contrairement aux métaux massifs, les nanoparticules sont dans un état de la matière finement divisé ce qui induit une surface spécifique élevée et une plus grande proportion de sites actifs. On peut en attendre une plus grande efficacité sous réserve de pouvoir en contrôler les caractéristiques.

Pour ce qui est de la HER, le platine demeure le métal de référence. Cependant, différents nanomatériaux à base de ruthénium présentant des compositions, morphologies, structures cristallines et tailles diverses ont été rapportés dans la littérature comme catalyseurs pour le processus du craquage de l'eau. Ainsi, des nanomatériaux de ruthénium ont été reportés comme des alternatives intéressantes aux catalyseurs à base de platine et de palladium pour la réaction de HE.[8] L'amélioration des performances électrocatalytiques de nanoparticules de ruthénium (RuNPs) comparativement à une poudre de ruthénium massif a été établie et attribuée à la plus grande surface active que les RuNPs possèdent. Très récemment, le potentiel de RuNPs poreuses stabilisées par un mélange MeOH/THF et de RuNPs bien définies stabilisées par la 4-phénylpyridine (illustration 2), pour la réaction de HE a été démontré.[[5],[9]]

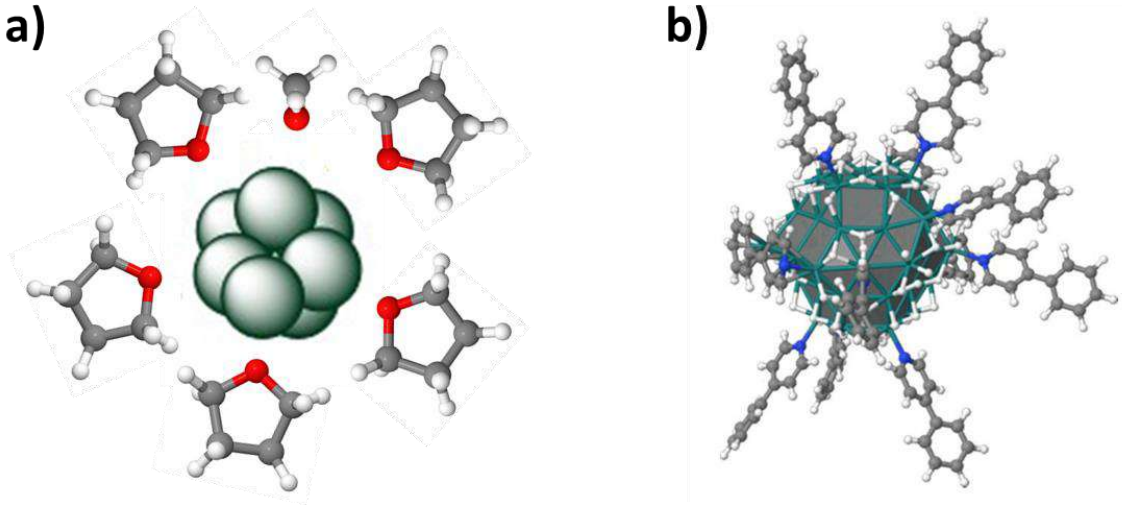

Illustration 2. Schémas de RuNPs stabilisées par (a) mélange de MeOH/THF et (b) 4-phénylpyridine.[9]

Malgré la diversité des RuNPs reportées dans la littérature, il demeure nécessaire de modifier leur état de surface afin d'améliorer leurs propriétés catalytiques. Les propriétés physiques et chimiques des RuNPs dépendent de leurs caractéristiques structurales telles que leur taille moyenne, leur forme, leur structure cristalline, mais aussi la nature et la quantité des ligands présents à leur surface. Les ligands assurent la stabilité des nanoparticules mais peuvent également influer sur leurs propriétés de surface. Bien que les acides carboxyliques soient largement utilisés comme tensioactifs en synthèse colloïdale, l'adsorption directe d'acides carboxyliques sur les surfaces métalliques de nanoparticules de ruthénium est très peu reportée.

Ce manuscrit de doctorat constitue une étude fondamentale amont dans le but de concevoir une nouvelle classe de nanocatalyseurs pour la réaction HE activée par la lumière. Afin de disposer de catalyseurs activables par la lumière du soleil, il est nécessaire d'élaborer des matériaux hybrides combinant des NPs métalliques (ici de Ru) avec des molécules photosensibles (PS) greffées à leur surface, dénotés RuNPs-PS. Par exemple, des complexes polypyridyl du ruthénium présentant des groupements acides carboxyliques comme fonctions d'ancrage peuvent être greffés sur des NPs. Cette stratégie a été précédemment démontrée comme étant un moyen efficace pour atteindre les matériaux hybrides souhaités.

Dans cet objectif, nous avons étudié les propriétés de surface de RuNPs stabilisées par des acides carboxyliques comme systèmes modèles. Des ligands acides carboxyliques portant des

chaînes alkyles de différentes longueurs ont été utilisés comme stabilisants pour la synthèse de RuNPs. Ces RuNPs ont été synthétisées dans des conditions douces selon l'approche organométallique développée au laboratoire (illustration 3) en utilisant les acides éthanoïque, pentanoïque et octanoïque. Cette méthode de synthèse est connue pour conduire, de façon reproductible, à la formation de RuNPs de petites tailles et homogènes ce qui permet de mener des études de caractérisation de leur propriétés de surface très fines.

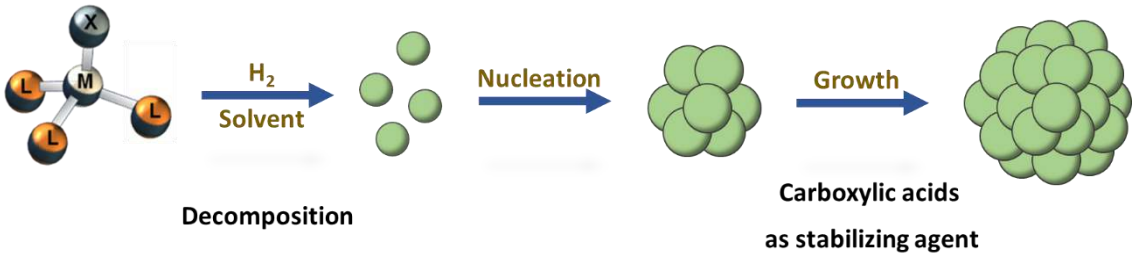

Illustration 3. Schéma général de synthèse des MNPs par approche organométallique.

L'originalité de ce travail tient dans l'utilisation d'un acide carboxylique comme stabilisant. A notre connaissance, un seul exemple est rapporté dans la littérature, qui repose sur l'utilisation d'un C60 à fonctions acide carboxylique, $C_{66}(COOH)_{12}$).[109]

En parallèle, des calculs basés sur la théorie de la fonctionnelle de la densité (DFT) ont été effectués à partir d'un modèle de Ru_{55} NP de structure de base *hcp*, (illustration 4) selon un modèle thermodynamique alimenté par des énergies de DFT. Une analyse systématique des propriétés des liaisons et de la structure électronique (densité des États, population de Crystal orbital Hamilton, charges atomiques) a été réalisée pour les différentes RuNPs stabilisées par les acides carboxyliques cités auparavant.

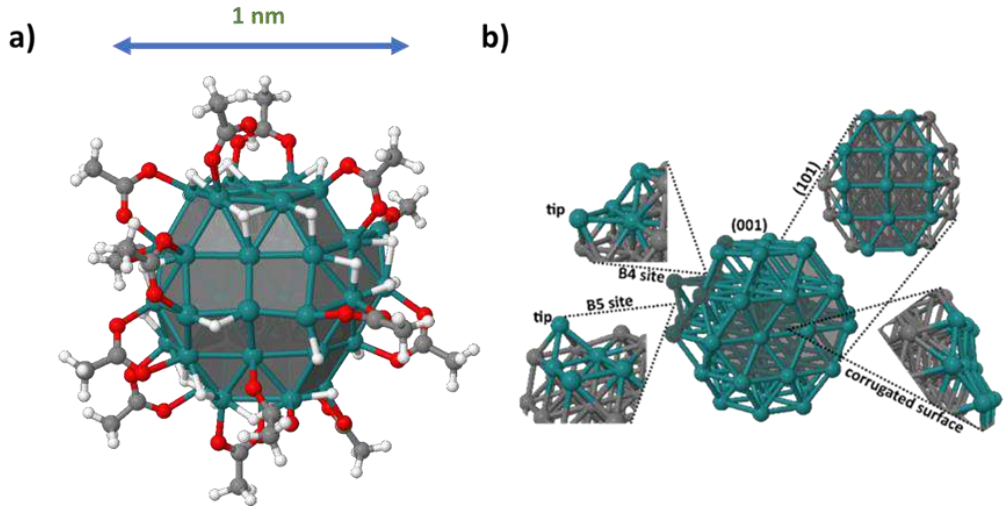

Illustration 4. Modèle de NP Ru_{55} basé sur une structure *hcp* . a) Modèle Ru_{55} optimisé stabilisé par la coadsorption des éthanoates et des atomes d'hydrogène ; b) les différents sites de surface construits dans le modèle Ru_{55}.

Ce manuscrit de thèse comporte cinq chapitres. Après une introduction générale (chapitre 1) qui se termine par la présentation des objectifs fixés, le chapitre 2 rassemble les résultats de l'étude approfondie menée pour la caractérisation théorique et expérimentale de RuNPs stabilisées par 0,4 équivalents molaires (equiv. ; RCOOH/[Ru]) d'acide éthanoïque.

La synthèse de ces nanoparticules (illustration 5) a été réalisée en décomposant une solution dans le pentane du précurseur de ruthénium, [Ru(COD)(COT)], sous 3 bar de H_2 à r.t., pendant 30 min.

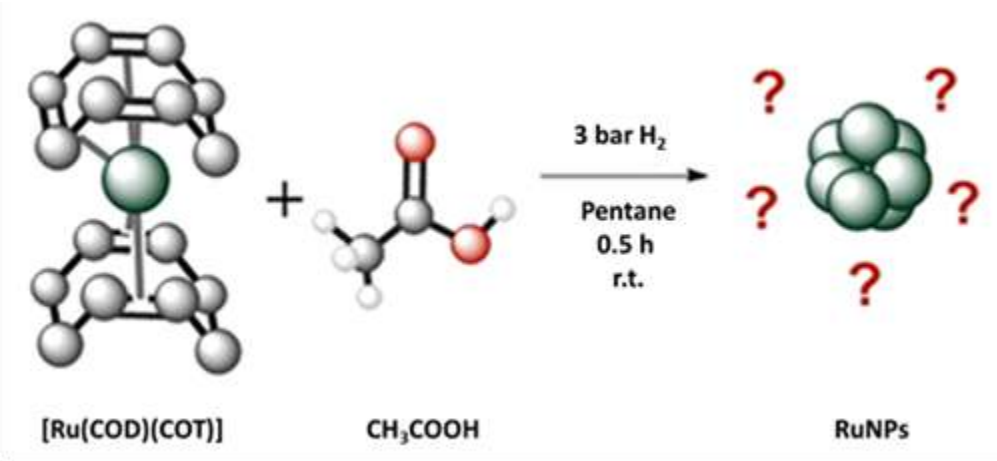

Illustration 5. Schéma de synthèse des RuNPs stabilisées par l'acide éthanoïque.

Le fait que l'acide éthanoïque porte une chaîne alkyle très courte rend l'utilisation de ce ligand très pertinente puisqu'ainsi il n'y a pas ou très peu d'influence du groupement alkyle sur la stabilisation des RuNPs, comme on peut l'observer avec des stabilisants portant des chaînes alkyles plus longues. Il est aussi important de souligner la nature du solvant utilisé pour la synthèse des RuNPs (pentane) qui n'est pas connu pour contribuer à la stabilisation des nanoparticules métalliques contrairement au THF par exemple. Ainsi, l'utilisation de l'acide éthanoïque et du pentane constituait déjà un défi de synthèse.

Après optimisation des conditions de synthèse, une population homogène de RuNPs ($Ru_x(CH_3COOH)_{0.4}$) a été obtenue avec un ratio [ligand]/[Ru] de 0,4 equiv. Les analyses TEM et WAXS ont mis en évidence des RuNPs de taille moyenne centrée à *ca.* 1,5 nm et peu cristallines, avec certaines particules présentant des plans attribuables à la structure cristalline *hcp* du ruthénium massif (illustration 6).

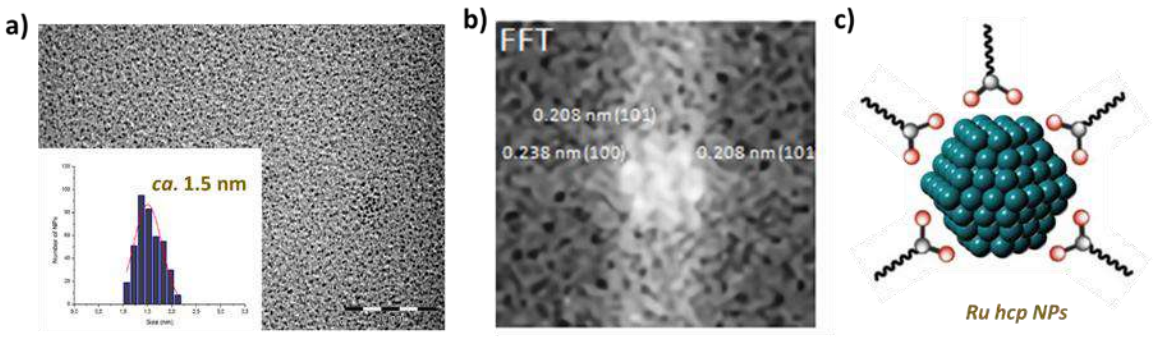

Illustration 6. Analyses de microcopie pour le $Ru_x(CH_3COOH)_{0,4}$ NPs. (a) Micrographe de TEM ; échelle graphique 50 nm ; son histogramme de taille est aussi présenté ; b) analyse FFT de HRTEM ; c) structure cristalline des RuNPs.

Les propriétés de surface et la réactivité de ces nanoparticules ont été étudiées par deux approches complémentaires, la chimie expérimentale et la chimie théorique. À cette fin, les techniques spectroscopiques, IRFT et RMN (en solution et à l'état solide) ont été utilisées en parallèle de calculs théoriques DFT. Cette combinaison d'outils est apparue très puissante pour obtenir des informations qualitatives mais aussi quantitatives sur l'état de surface des nanoparticules. Tous les résultats obtenus ont convergé vers la coordination du ligand à la surface du ruthénium sous la forme carboxylate (éthanoate), et de préférence en mode bidente formant ainsi un dimétallacycle stable. Ce résultat est en accord avec une faible barrière d'activation pour la dissociation de liaison CH_3COO-H, ceci quelle que soit la composition de surface des RuNPs. Par ailleurs, les résultats ont montré la co-adsorption d'atomes d'hydrogène à la surface des particules, en quantité plus faible comparativement à d'autres résultats antérieurs sur des RuNPs stabilisées par d'autres ligands (amines phosphines, etc.). Au total, les résultats obtenus convergeaient.

Plus précisément, la titration par DFT a montré une composition de surface optimale de *ca.* [0,4 - 0,6] H/Ru_{Surf} et 0,4 CH_3COO/Ru_{Surf} à 300 K (illustration 7). Ces données sont en bon accord avec les données obtenues par quantification expérimentale (analyse RMN DOSY et titration par hydrogénation d'une oléfine simple), à savoir 0,3 H/Ru_{Surf} et 0,3 CH_3COO/Ru_{Surf} à r.t.

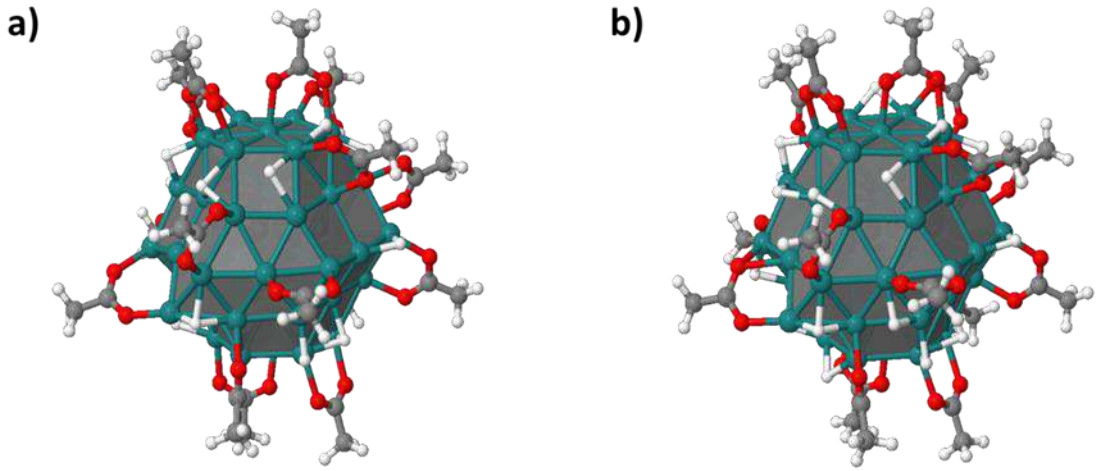

Illustration 7. Structures [Ru_{55}] les plus stables trouvées par calculs DFT pour la modélisation des RuNPs par l'acide éthanoique à 300 K. (a) $Ru_{55}(CH_3COO)_{16}(H)_{16}$; (b) $Ru_{55}(CH_3COO)_{16}(H)_{33}$.

La très bonne concordance des résultats obtenue entre les études de caractérisation théoriques et expérimentales a permis de conclure quant à l'efficacité des outils de chimie théoriques appliqués pour construire un modèle théorique fiable afin de décrire les RuNPs étudiées. Ce travail a donc montré que la chimie computationnelle peut être appliquée à la compréhension de petites nanoparticules, entre [1,0 à 2,0 nm], avec un niveau de précision et de pertinence similaire à celui connu en chimie moléculaire.

L'analyse du *p*MPA a mis en évidence une surface légèrement oxydée (*ca.* 0,35e) pour la composition de surface optimale De plus, pour cette composition, l'énergie d'adsorption de l'hydrogène calculée se situe dans la fourchette [-3,1 à -8,0 kcal.mol^{-1}] pour les plans (001) et (101). Ce résultat est très intéressant car il montre l'intérêt potentiel de ces RuNPs en tant que catalyseur pour la réaction de HE dans l'électrolyse de l'eau (Illustration 8).[10]

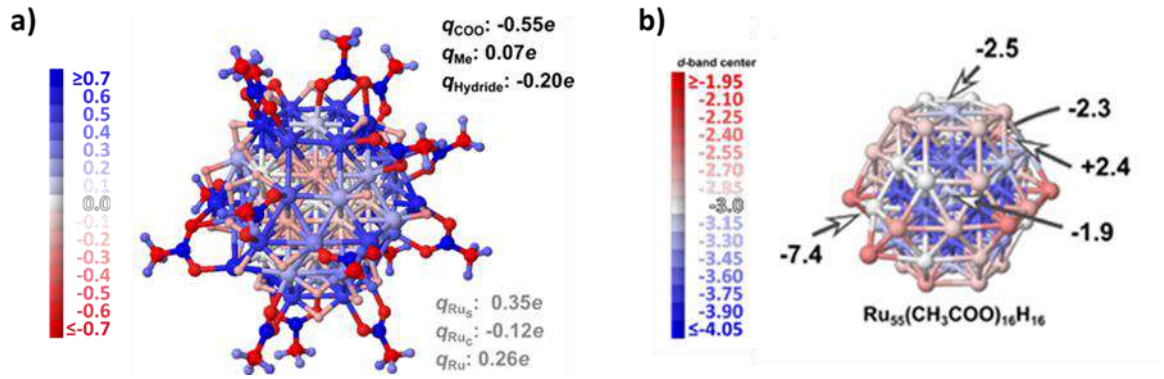

Illustration 8. Études structurales sur la structure [Ru_{55}] la plus stable trouvée par DFT. (a) les charges atomiques *p*MPA atomiques sont indiqués par niveau de couleur ; les charges sont indiquées selon : global (q_{Ru}), noyau (q_{Ru_c}), atomes de surface (q_{Ru_s}) et ligand ($q_{Hydride}$, q_{COO} & q_{Me}). (b) le centre de la bande d est indiqué par un code couleur (eV) ; les ΔG_{H^*} sont donnés en kcal.mol^{-1}) et les flèches indiquent les sites d'adsorption.

Disposant d'un modèle fiable pour la caractérisation théorique des RuNPs stabilisées par l'acide éthanoïque, l'étude a été étendue à des acides carboxyliques portant des chaines alkyles plus longues, à savoir les acides pentanoïque et octanoïque. Ces résultats sont présentés au chapitre 3.

A des fins de comparaison, la synthèse de RuNPs en présence d'acide pentatonique a été menée dans le pentane avec la même quantité de ligand que précédemment (0.4 equiv. molaire). Ceci a conduit à des RuNPs, $Ru_x(C_4H_9COOH)_{0,4}$, plus solubles dans le pentane et de plus faible taille (ca. 1.1 nm contre 1.5 nm avec l'acide éthanoïque), montrant ainsi l'efficacité de l'acide pentatonique à stabiliser les particules et aussi l'influence de la nature du ligand acide carboxylique sur leurs caractéristiques.

Des études RMN en solution ont mis en évidence l'absence de signaux correspondant au ligand libre, indiquant donc que le tout le ligand est en interaction avec la surface des nanoparticules. De plus, le signal correspondant aux protons du groupement méthyle s'est avéré bien visible, indiquant ainsi que la chaîne alkyle du ligand n'est pas repliée vers la surface métallique mais étendue. Par RMN DOSY des signaux larges dans la plage des signaux attendus pour le ligand ont été observés, comme attendu pour la coordination du ligand à la surface des particules. Le diamètre hydrodynamique calculé à partir du coefficient de diffusion mesuré par DOSY s'est avéré en bon accord avec la taille moyenne des RuNPs déterminées par l'analyse TEM.

L'analyse FTIR (illustration 9) a permis de confirmer la déprotonation de l'acide pentatonique à la surface des nanoparticules : le signal d'une fraction carboxylate a été observé, mais pas celui correspondant à l'acide éthanoïque (libre ou coordonné). L'IRFT a également mis en évidence la présence de THF (utilisé lors de la purification des particules) et produits de dégradation (CO et polyTHF).

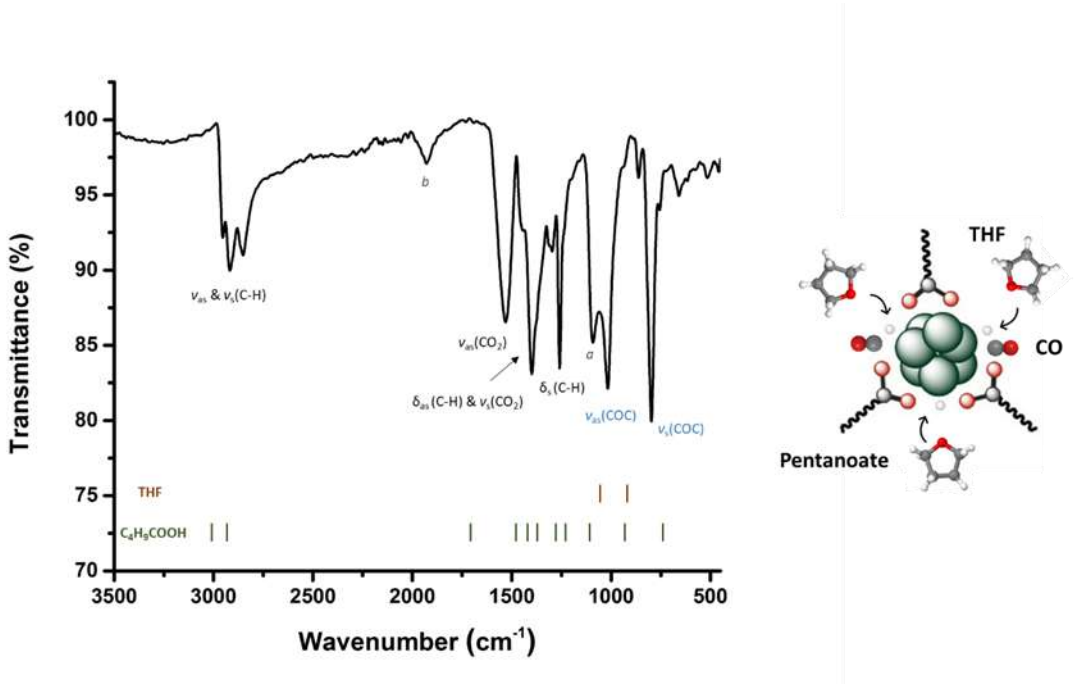

Illustration 9. Spectre IRFT de $Ru_x(C_4H_9COOH)_{0,4}$ NPs et indication des principaux pics. Les pics caractéristiques de l'acide pentanoïque (barres vertes, C_4H_9COOH) et du THF (barres jaunes) sont également indiqués. N : étirement ; δ : flexion ; s : symétrique ; as : asymétrique. Les pics attribués au THF coordonné à la surface des RuNPs sont également indiqués (bleu). Le signal noté -a- est assigné au PolyTHF et celui noté -b- au CO. Un schéma de la composition de surface des RuNPs est également montré.

L'énergie d'adsorption calculée pour l'acide pentanoïque sur le modèle de NP Ru_{55} (-46,2 kcal.mol^{-1}) s'est avérée plus faible d'environ 5 kcal.mol^{-1} que celle pour l'acide éthanoïque (-51,7 kcal.mol^{-1}). Avec une bande d'absorption déplacée vers les bas nombres d'onde pour la forme carboxylate, la spectroscopie IRFT a mis en évidence une rétrocoordination plus élevée de la surface métallique de ruthénium vers la fraction pentanoïque que dans le cas des RuNPs stabilisées par l'éthanoate.

La synthèse de particules a ensuite été réalisée en introduisant différentes quantités de ligand acide pentanoïque (de [0,05 à 0,60 equiv.]/[Ru]), afin de trouver des conditions de synthèse

permettant l'obtention de NPs de taille moyenne proche de celles des RuNPs stabilisées par l'acide éthanoique (ca. 1.5 nm) et au-delà, pouvoir faire une comparaison plus fine de leur état de surface. Ceci a été possible en utilisant un ratio [ligand]/[Ru] de 0.3 équivalent molaire, démontrant la possibilité d'accéder à différentes tailles de NPs en variant la quantité de ligand introduit. La population de particules formées avec ce ratio, $Ru_x(C_4H_9COOH)_{0,30}$, s'est avérée très homogène et avec une distribution en tailles étroite centrée à 1.5 nm. Comparativement à l'acide éthanoïque, une quantité plus faible d'acide pentanoïque a permis de stabiliser des RuNPs de même taille (0.3 / 0.4 équiv. molaire), ce qui peut s'expliquer par la longueur de la chaine alkyle de l'acide pentanoïque qui permet une meilleure stabilisation. Les NPs $Ru_x(C_4H_9COOH)_{0,30}$ ont été entièrement caractérisées par IRFT et RMN. Les spectres RMN ^1H en solution (illustration 10) ont mis en évidence que des RuNPs de tailles similaires peuvent présenter des taux de couverture de leur surface par le ligand différents.

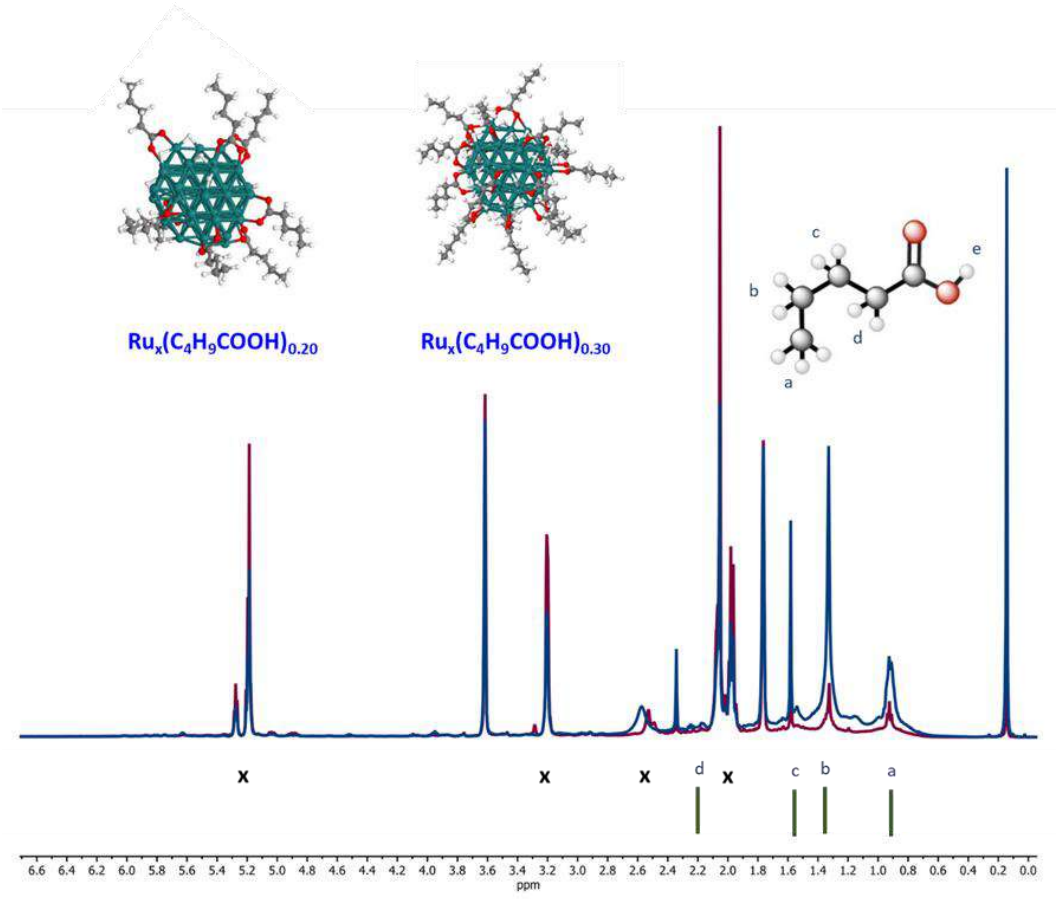

Illustration 10. Spectre ^{1}H-NMR (THF-d^8) des RuNPs ; (profil rouge) Ru$_x$(C$_4$H$_9$COOH)$_{0,20}$ NPs ; (profil bleu) Ru$_x$(C$_4$H$_9$COOH)$_{0,30}$ NPs. Les pics attribués à des sous-produits sont signalés par «x» et les pics de l'acide pentanoïque sont indiqués sous forme de barres. La différence de largeur de bandes entre les 2 systèmes de particules démontre la quantité différente de ligand en interaction. Une composition schématique des RuNPs est également présentée.

Les données RMN à l'état solide enregistrées pour les particules Ru$_x$(C$_4$H$_9$COOH)$_{0,3}$ ont confirmé la déprotonation de l'acide pentanoïque et son interaction avec la surface de ruthénium sous forme pentanoate. Sur la base de ce résultat et des informations obtenues antérieurement par un titrage DFT, la quantification des ligands de surface a été réalisée en extrapolant le modèle de NP Ru$_{55}$. Il a été constaté que la structure la plus stable en accord avec les données expérimentales est Ru$_{55}$(C$_4$H$_9$COO)$_{14}$(H)$_{14}$. Cette structure possède des quantités de ligands carboxylates et d'hydrures inférieures à celles déterminées pour les particules Ru$_x$(CH$_3$COOH)$_{0,4}$ à savoir Ru$_{55}$(CH$_3$COO)$_{16}$(H)$_{16}$ (illustration 11). Ce résultat a confirmé le meilleur effet stabilisant de l'acide pentanoïque comparativement à l'acide éthanoïque.

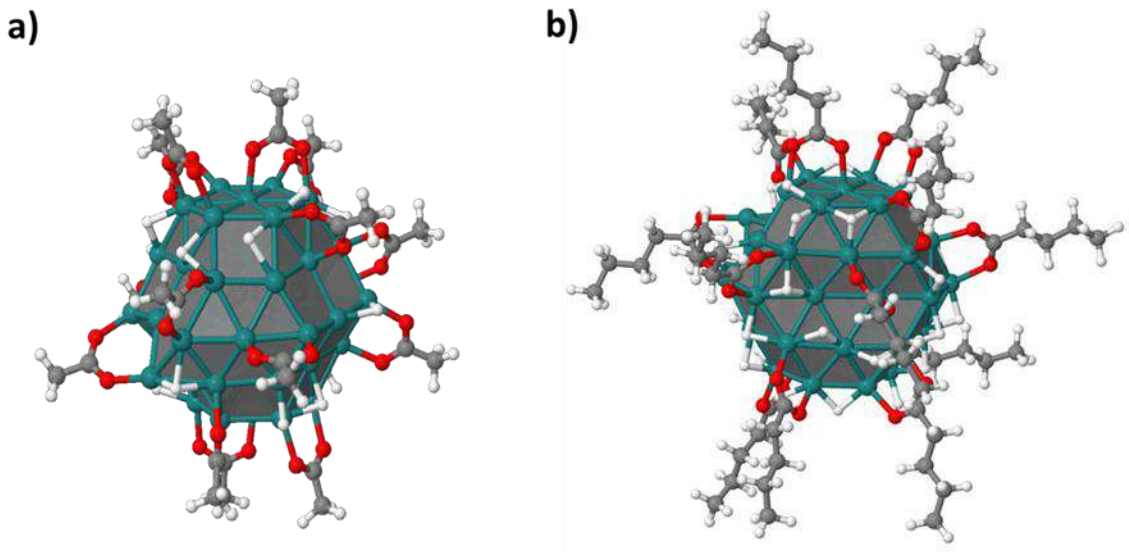

Illustration 11. Structures [Ru_{55}] les plus stables obtenues par titration DFT à 300 K. (a) RuNPs stabilisées par l'acide éthanoïque ; $Ru_{55}(CH_3COO)_{16}(H)_{16}$; b) et l'acide pentanoïque ; $Ru_{55}(C_4H_9COO)_{14}(H)_{14}$.

L'évaluation théorique de l'intérêt du système de RuNPs le plus stable ($Ru_{55}(C_4H_9COO)_{14}(H)_{14}$) pour la réaction HE été réalisée. Les résultats obtenus ont indiqué que les RuNPs stabilisés par l'acide pentanoïque s'avèrent plus performantes pour la production d'hydrogène que celles stabilisées par l'acide éthanoïque.

En première conclusion, l'augmentation de la longueur de la chaîne alkyle par trois atomes de carbone (acide éthanoïque à pentanoïque) a permis de produire des RuNPs de taille plus faible à un ratio [ligand]/[Ru] plus bas. Les RuNPs formées se sont avérées plus homogènes en taille et forme, leur surface moins encombrée et *a priori* plus intéressantes pour la réaction catalytique de l'HE. Dans le but de mieux comprendre l'influence de la longueur de la chaîne alkyle sur les propriétés des RuNPs, la synthèse de RuNPs avec un acide carboxylique portant une chaîne alkyle encore plus longue, l'acide octanoïque, a été réalisée. Ces résultats sont présentés dans la seconde partie du chapitre 3. Des synthèses ont été réalisées en utilisant le THF ou le pentane comme solvant.

La synthèse de RuNPs en présence de 0.4 equiv. molaires d'acide octanoïque dans le THF a conduit à des RuNPs très stables pour lesquelles des analyses RMN et IRFT ont mis en évidence la présence de ligand libre et de différentes molécules coordonnées (acide octanoïque protoné et déprotoné). Les études DFT sur La détermination des énergies d'adsorption par calculs DFT à partir

du modèle Ru_{55} NP ont montré une plus faible force d'adsorption de l'acide octanoïque y compris lorsque des effets de dispersion ont été considérés. Cependant, une tendance a été observée : plus la longueur de la chaîne alkyle de la molécule adsorbée (carboxylate linéaire), plus son énergie d'adsorption sur la surface du Ru_{55} NP est faible (illustration 12). Cela signifie que d'autres facteurs sont probablement impliqués dans la stabilisation des RuNPs, comme le solvant ou la barrière de ligand.

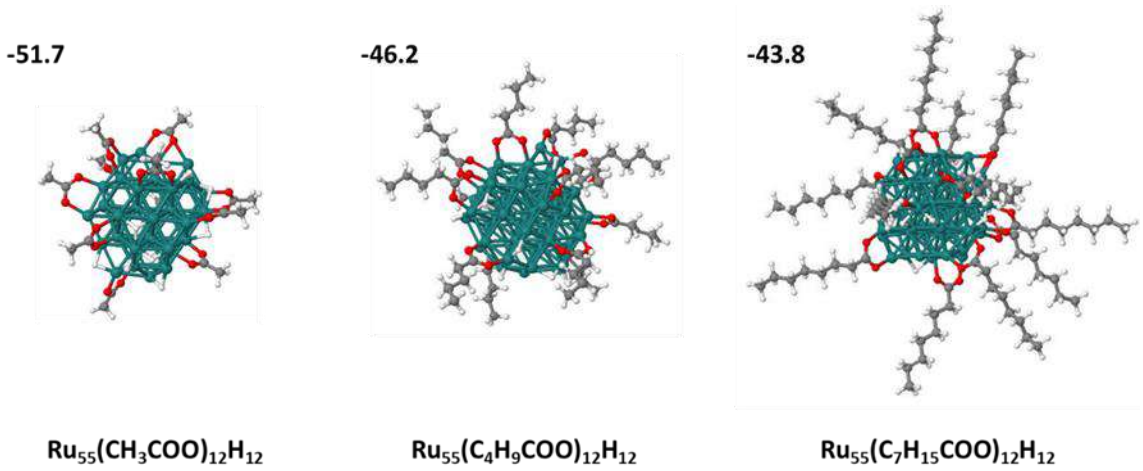

Illustration 12. Structures Ru_{55} NP optimisées recouvertes de 12 carboxylates (éthanoate, pentanoate ou octanoate) et 12 atomes d'hydrogène. Les énergies moyennes d'adsorption des acides sont indiquées ($kcal.mol^{-1}$).

Les synthèses réalisées en diminuant la quantité d'acide octanoïque (0,30 et 0,15 equiv. molaire) ont montré que même une faible quantité de ligand (0,15 equiv.) permet de stabiliser des RuNPs de petite taille et de forme régulière. Par IRFT, aucun signal attribuable à de l'acide octanoïque libre n'a été détecté mais la présence d'octanoate a été observée (illustration 13), ainsi que potentiellement du THF. Une étude a ensuite été menée en utilisant le pentane comme solvant de synthèse.

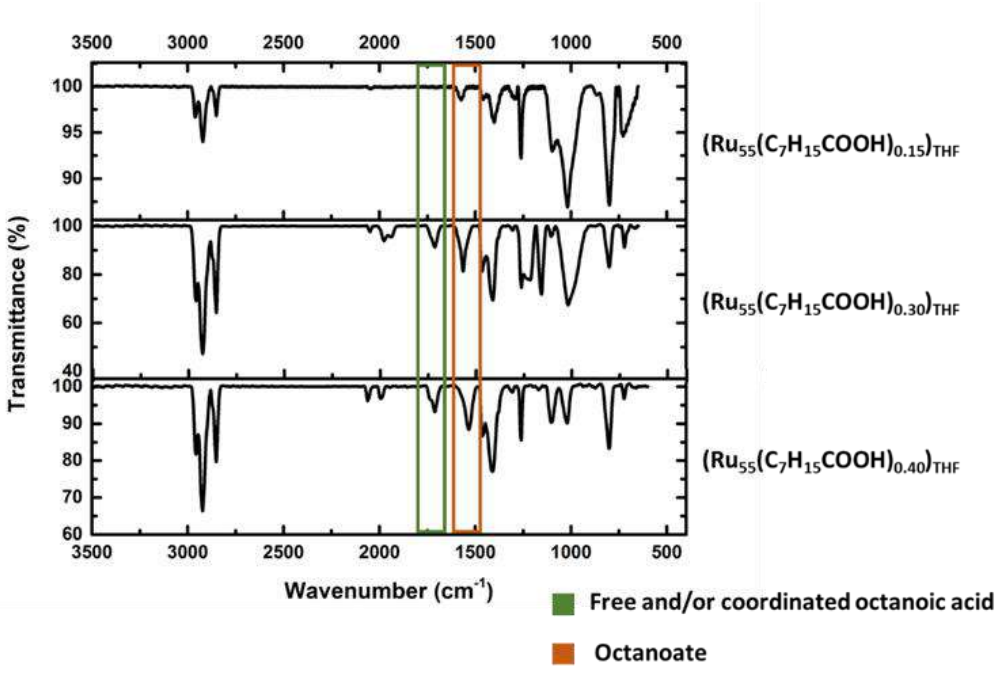

Illustration 13. Spectres IRFT expérimentaux. Deux régions vibratoires sont surlignées : (vert) ν(COOH) ; (orange) ν(COO).

Après optimisation, l'introduction de 0.2 equiv. molaire d'acide octanoïque a conduit à la formation d'une population de nanoparticules bien dispersées, homogènes en forme et présentant une taille moyenne de 1.6 nm ($Ru_x(C_7H_{15}COOH)_{0,2}$ NPs), soit une taille proche de celle des particules étudiées précédemment avec les acides ethanoïque et pentanoïque. Ce résultat a confirmé l'observation faite précédemment avec l'acide pentanoïque comparativement à l'acide éthanoïque, à savoir que l'utilisation d'un acide carboxylique portant une chaine alkyle plus longue permet de diminuer la quantité de ligand à introduire pour obtenir une taille de NPs similaire dans la gamme 1.5-1.7 nm (illustration 14). Ce résultat a donc confirmé l'influence de la nature du ligand et de son encombrement stérique sur le contrôle de la taille des RuNPs.

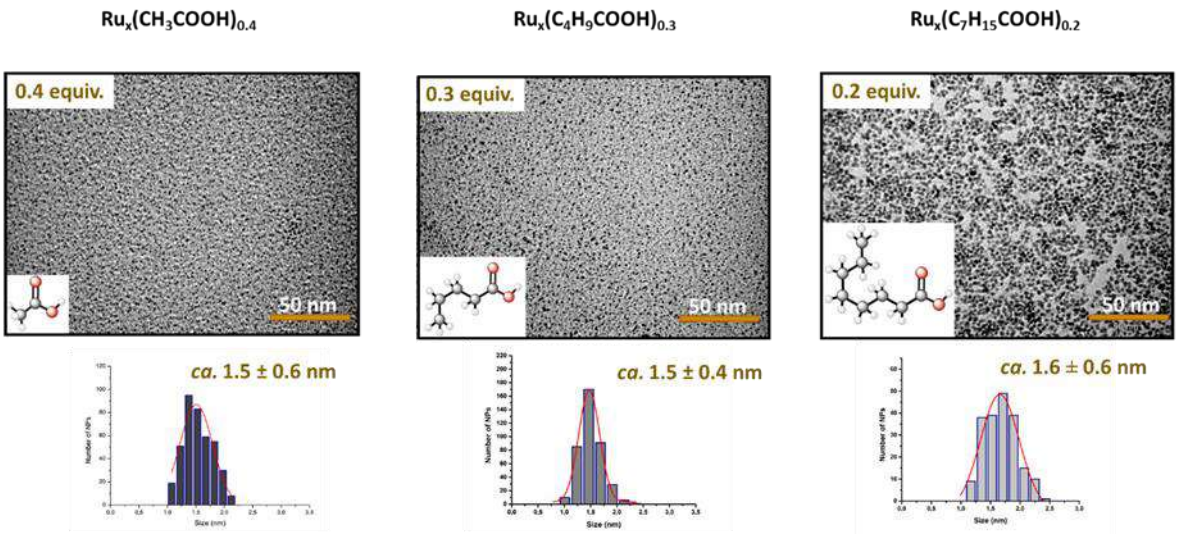

Illustration 14. Images TEM des RuNPs stabilisées par différentes quantités d'acides carboxyliques (acide éthanoïque, pentanoïque or octanoïque). Comparaison du ratio RCOOH/[Ru] utilisé pour l'obtention de RuNPs de taille similaire .

Ce système de RuNPs ($Ru_x(C_7H_{15}COOH)_{0,2}$ NPs) a ensuite été finement caractérisé par différentes techniques expérimentales et théoriques. Les analyses par HRTEM et WAXS ont montré des particules assez bien cristallisées et de structure *hcp*. Les études RMN et IRFT, ont mis en évidence l'absence d'acide octanoïque libre et la présence d'octanoate. La quantification des octanoates et d'hydrures coordonnés à la surface des $Ru_x(C_7H_{15}COOH)_{0,2}$ NPs, réalisée par des études de RMN approfondie (^{1}H, DOSY & NOESY) et une analyse catalytique (réduction du norbornène) a conduit à 0,2 octanoates par Ru_{Surf} (21 H/RuNP) et 0,2 hydrures par Ru_{Surf} (23,5 $C_7H_{15}COO$/RuNP). Un titrage DFT à partir du modèle Ru_{55} NP a indiqué une tendance similaire: hydrures [0,3 - 0,6]/Ru_{Surf} et octanoates [0,2 – 0,3]/Ru_{Surf} (illustration 15), montrant de nouveau un bon accord entre les données expérimentales et théoriques. La comparaison de ses valeurs avec celles obtenues précédemment pour les deux autres acides (acide pentanoïque : 0,3 H/Ru_{Surf} et 0,3 C_4H_9COO/Ru_{Surf}; acide éthanoïque : [0,4 – 0,6] H/Ru_{Surf} et 0,4 CH_3COO/Ru_{Surf}) souligne que plus la longueur de la chaîne alkyle de l'acide carboxylique est importante, plus la quantité de ligand nécessaire pour stabiliser des RuNPs de taille similaire est moindre.

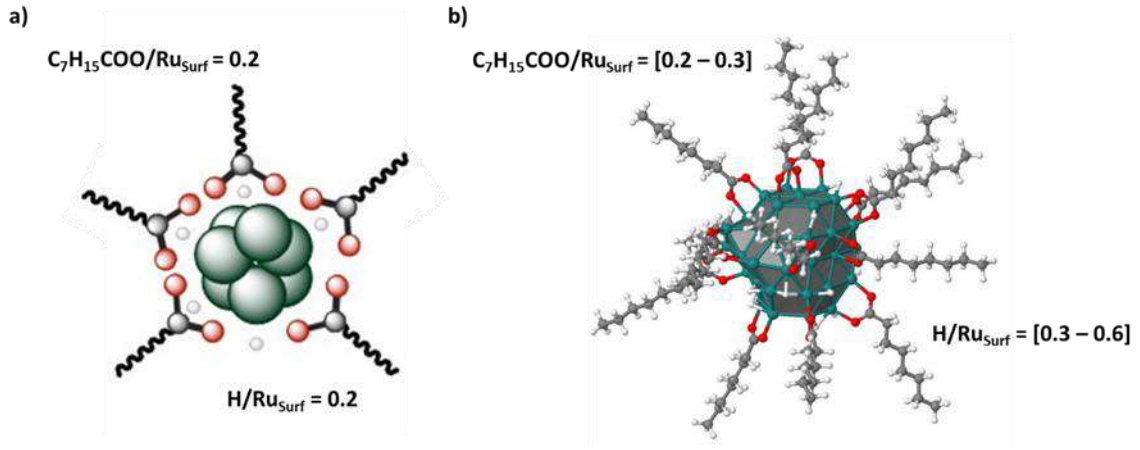

Illustration 15. Résultats des titrages des RuNPs $Ru_x(C_7H_{15}COOH)_{0,2}$. (a) expérimental et (b) quantification théorique des ligands adsorbés.

Afin de compléter la cartographie de la surface des RuNPs $Ru_x(C_7H_{15}COOH)_{0,2}$, elles ont été exposées à une atmosphère de ^{13}CO afin de saturer les atomes libres de Ru. Les analyses RMN (illustration 16) menées après cette exposition ont montré que la coordination du CO a lieu principalement sur les sites de surface correspondant aux arrêtes et sommets, ce qui a permis de déduire que la coordination de l'acide octanoïque est sur les faces. Quant à l'évaluation théorique de l'intérêt de ces RuNPs dans leur structure la plus stable ($Ru_{55}(C_7H_{15}COO)_{14}(H)_{14}$) pour la réaction HE, les résultats obtenus ont indiqué que l'énergie d'adsorption de l'hydrogène était très élevée sur les plans mais tout à fait appropriée pour les sommets et arêtes (ΔG_{H^*} près de 0 $kcal.mol^{-1}$), confirmant la nature des sites d'adsorption libres déterminées par l'adsorption de CO.

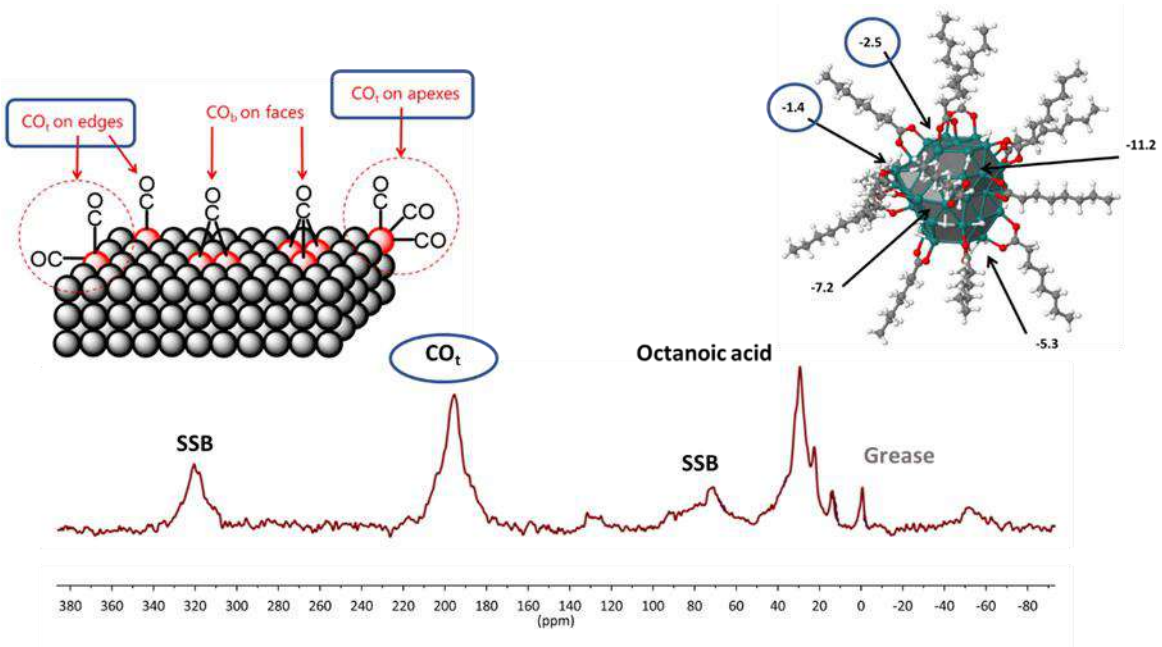

Illustration 16. Spectre RMN du ^{13}C-MAS de $Ru_x(C_7H_{15}COOH)_{0,2}$ NPs dispersés dans une matrice de SiO_2 poreuse après exposition sous 1 bar de ^{13}CO. SSB correspond à des bandes de rotation. Les modes de coordination du CO à la surface des NPs en relation avec les sites de surface libres sont indiqués.[93] ΔG_{H^*} (kcal.mol^{-1}) pour différents sites d'adsorption de $Ru_{55}(C_7H_{15}COO)_{14}(H)_{14}$ NP est également indiquée.

La comparaison de ces données avec celles obtenues antérieurement pour les RuNPs stabilisées par l'acide éthanoïque ($Ru_{55}(CH_3COO)_{16}(H)_{16}$) et l'acide pentanoïque ($Ru_{55}(C_4H_9COO)_{14}(H)_{14}$) a permis de conclure que les particules stabilisées par l'acide pentanoïque présentent le meilleur potentiel en tant que catalyseur pour la HER. Ainsi, des RuNPs présentant un taux de couverture de leur surface plus faible, telles que celles obtenues avec l'acide pentanoïque, ne conduisent pas nécessairement au meilleur catalyseur.

Les résultats de ce chapitre, ont conduit à la conclusion qu'un catalyseur approprié pour la HER sera plutôt des RuNPs possédant un taux de couverture de leur surface moyen par un ligand ayant une longueur de chaîne alkyle moyenne.

En vue de synthétiser des systèmes hybrides RuNPs-PS, le chapitre suivant (n°4) est consacré à des réactions d'échange d'acides carboxyliques à la surface de RuNPs préformées. Cette étude a été menée afin de trouver une alternative à la synthèse directe de RuNPs en présence du PS. En effet, les RuNPs étant connues pour être des catalyseurs actifs pour la réduction des arènes,[289] l'utilisation directe d'un complexe de polypyridyle comme stabilisant

pendant la synthèse des RuNPs sous atmosphère d'hydrogène peut potentiellement conduire à la réduction des ligands bipyridine.

Des RuNPs préformées en utilisant 0,2 equiv. d'acide octanoïque ont été exposées à une quantité croissante d'acide benzoïque (Illustration 17). Les nanosystèmes obtenus ont été caractérisés par des techniques de RMN et des outils de DFT. La combinaison de ces approches a fourni des informations fructueuses sur l'efficacité de la stratégie choisie.

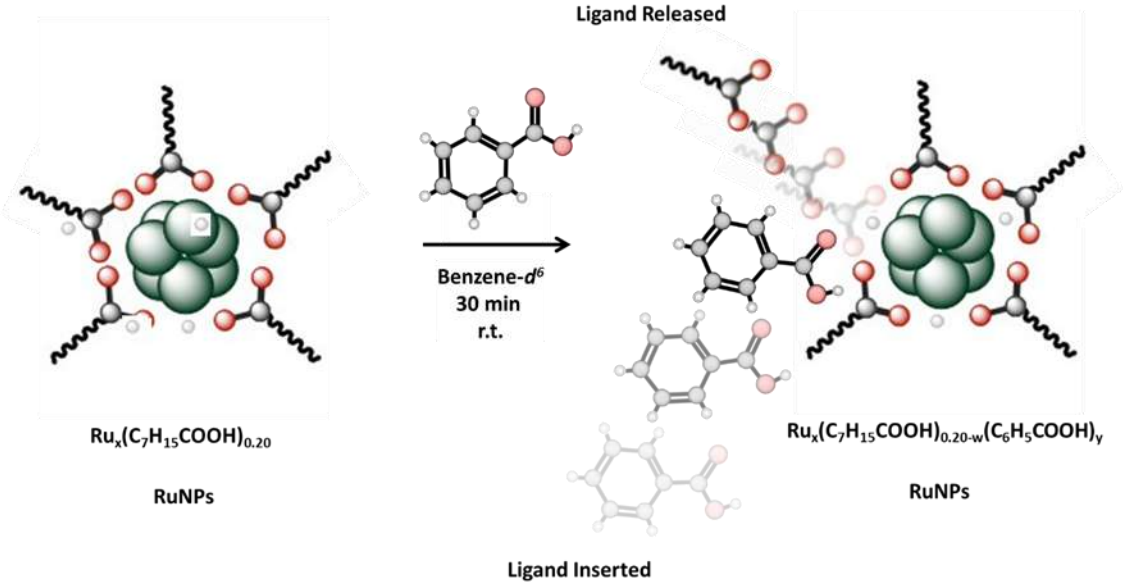

Illustration 17. Réaction d'échange de ligand entre $C_7H_{15}COOH$ et C_6H_5COOH sur des RuNPs préformées $Ru_x(C_7H_{15}COOH)_{0,2}$ NPs.

Les résultats d'analyse ont montré qu'il est possible d'enlever une certaine quantité d'octanoates et d'incorporer des molécules d'acide benzoïque à la surface des RuNPs sans modifier leur taille ni morphologie. Ce processus d'échange s'est révélé favorable en raison d'une combinaison d'effets, à savoir électroniques, stériques et probablement l'acidité du ligand entrant. Par contre ce processus d'échange s'est avéré non total. En effet, seulement environ [⅓ - ⅔] des octanoates initialement coordonnés à la surface des RuNPs ont été remplacés par des de l'acide benzoïque (Illustration 18). De plus, l'addition d'une quantité plus élevée d'acide benzoïque n'a pas augmenté le ratio d'échange des ligands. Des calculs DFT ont étayé la viabilité de cet échange de ligands en raison d'effets électroniques (augmentation de l'énergie d'adsorption dans la NP nue et saturée en surface Ru_{55} et spontanéité thermodynamique des réactions

d'échange de ligands). Cependant, l'efficacité du processus d'échange est probablement affectée par l'encombrement stérique des ligands.

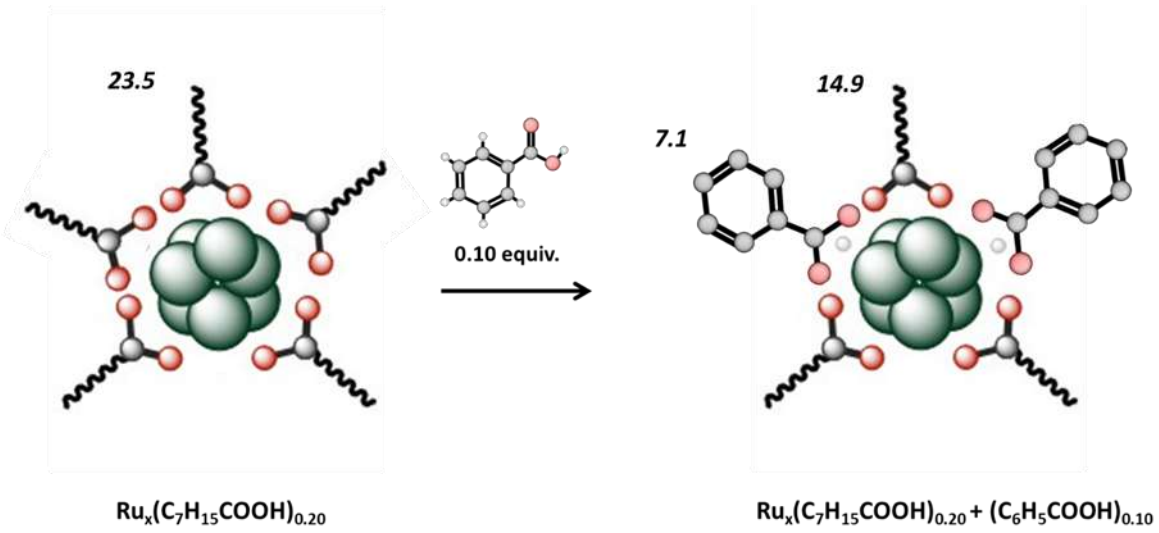

Illustration 18. Estimation de la surface initiale estimée de $Ru_x(C_7H_{15}COOH)_{0,20}$ NPs et la nouvelle couverture de surface obtenue après l'échange de ligands avec 0,10 equiv. d'acide benzoïque.

Une autre étude d'échange de ligands a été menée à partir des mêmes RuNPs pré-stabilisées avec l'acide octanoïque mais en utilisant l'acide trifluoroacétique comme ligand entrant. Le choix de l'acide trifluoroacétique (TFA) a été basé sur l'acidité plus élevée et le plus faible encombrement stérique qu'il présente par rapport à ceux de l'acide benzoïque. Les résultats obtenus ont montré une meilleure efficacité du processus d'échange de ligand que celui observé avec l'acide benzoïque. Les résultats du titrage par RMN ont indiqué que la surface des particules $Ru_x(C_7H_{15}COOH)_{0,20\,+\,0,20}$ NPs préformée a été modifiée par substitution d'un peu plus de la moitié des ligands octanoates initiaux par des trifluoroacétates en ajoutant seulement 0,10 equiv. de TFA. En outre, la surface des RuNPs modifiées présentait une quantité plus élevée de ligands carboxylates, mettant ainsi clairement en évidence l' effet de l'encombrement stérique faible du TFA (illustration 19).

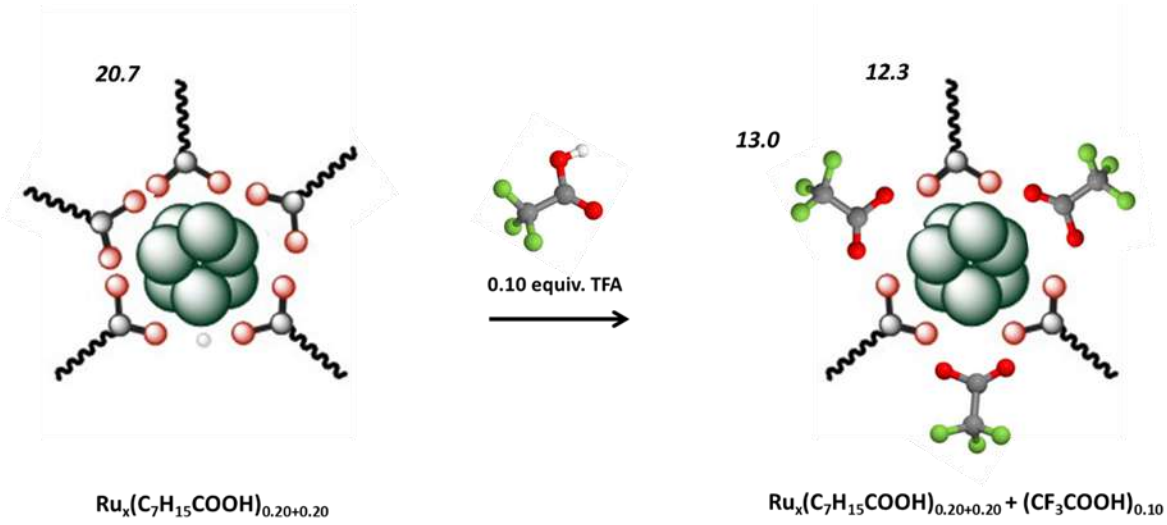

Illustration 19. Estimation de l'état de surface initial des RuNPs $Ru_x(C_7H_{15}COOH)_{0,20+0,20}$ NPs et après l'échange de ligand avec 0,10 equiv. de TFA.

Sur la base d'une différence significative des valeurs d'énergie d'adsorption (*ca.* 11,0 kcal.mol^{-1}) entre l'acide octanoïque et le trifluoroacétique à la surfcae de NPs Ru_{55}, des calculs de DFT ont indiqué un échange de ligand plus favorable avec le TFA. Par contre, les résultats théoriques ont montré qu'il n'y a pas de variation significative entre l'énergie d'adsorption d'un acide benzoïque et d'un trifluoroacétique (< 1,0 kcal.mol^{-1}). Par conséquent, la différence du ratio d'échange de ligand observée entre l'acide benzoïque et le TFA *vs* l'acide octanoïque ne peut pas être facilement expliquée. Plus de calculs DFT sont nécessaires pour compléter ces travaux.

En conclusion, cette étude a permis de démontrer qu'un échange de ligands carboxylates est possible à la surface des RuNPs, et qu'il dépend à la fois d'effets électroniques, de l'encombrement stérique et de l'acidité du ligand incorporé. Il est à noter qu'une fois de plus les deux approches expérimentale et théorique ont présenté une très bonne concordance. Il en découle que le greffage d'un photosensibilisateur à la surface des RuNPs peut être envisagé par un processus d'échange de ligands à condition de tenir compte des paramètres susceptibles de l'influencer. Pour un processus peu efficace, on peut tout de même s'attendre à l'ancrage de quelques molécules de photosensibilisateur à la surface des RuNPs, ce qui peut s'avérer suffisant pour accéder à un matériau catalytique hybride pour le craquage de l'eau.

Le chapitre suivant (n°5) est dédié à des calculs DFT ayant pour objectif de tester la fiabilité de la stratégie d'échange de ligands par un photosensibilisateur (PS) réel (illustration 20). A cette fin, ont été choisis des complexes $[Ru(bpy)_x(bpy(RCOOH)_x)_{3-x}]^{2+}$. Ainsi, quatre complexes du type $[Ru(bpy)_3]^{2+}$ contenant des ligands bipyridine modifiés par des fonctions acide carboxylique comme groupes d'ancrage ont été conçus et leur adsorption à la surface des modèles RuNPs étudiée. Ces complexes ont été sélectionnés en raison de leur intérêt comme PS pour récolter l'énergie lumineuse et faciliter le transfert d'électrons vers un catalyseur pour produire de l'hydrogène par photolyse des molécules d'eau.

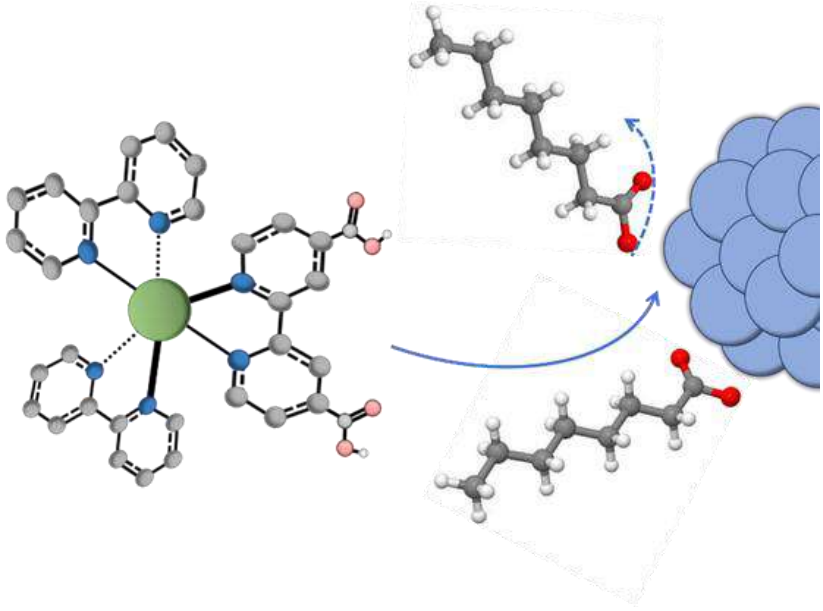

Illustration 20. Schéma représentatif du greffage d'un PS à la surface ds RuNPs préformées par échange de ligands.

Cette étude a d'abord été axée sur la détermination de l'énergie d'adsorption du PS sur une surface de $Ru_{55}(CH_3COO)_2(H)_2$ NP non saturée. Il a été observé que les ligands bipyridine avec un groupement méthylène entre les entre le motif bipyridine et le point d'ancrage acide carboxylique (PS3 et PS4) sont plus aptes à être adsorbé à la surface métallique que les PS avec des acides carboxyliques directement liés aux bipyridines (PS1 et PS2). Une plus grande énergie d'adsorption a également été observée lorsque les groupes d'ancrage étaient portés par deux ligands bipyridine différents (PS4). Ce résultat a été attribué à une flexibilité plus élevée du ligand dans ces conditions et à sa capacité à agir comme un ligand pince en raison d'un angle plus

approprié pour la coordination à la surface des RuNPs. L'ensemble des résultats de DFT a conduit à la conclusion que le complexe PS4 est le plus approprié pour la réaction visée (illustration 21).

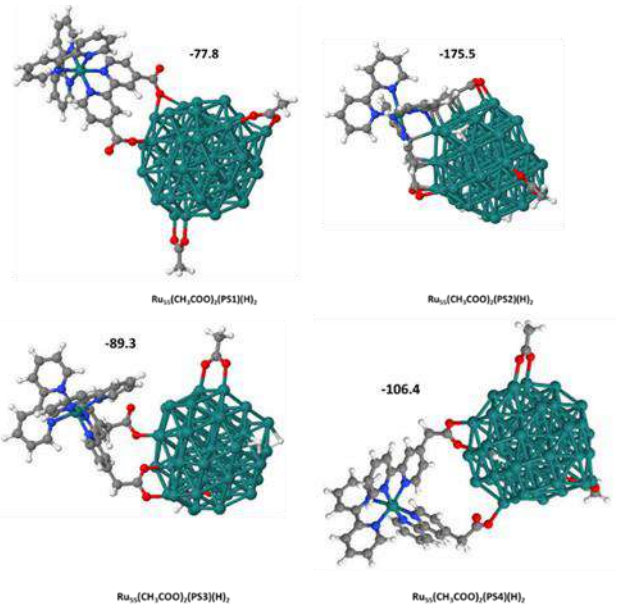

Illustration 21. Modèles théoriques optimisés pour l'interaction des complexes PS1, PS2, PS3 et PS4 avec les NPs $Ru_{55}(CH_3COO)_2(H)_2$. Les E_{ads} (kcal.mol^{-1}) sont également indiquées.

Ensuite, a été étudiée l'adsorption des PS sur un modèle de RuNP présentant un degré de couverture de surface moyen ($Ru_{55}(CH_3COO)_{10}(H)_{27}$ NP). Un échange spontané de ligands a été observé, principalement avec les photosensibilisants PS1 et PS4, en remplaçant deux entités carboxyliques par un PS. En outre, une meilleure efficacité processus d'échange de ligand a été observée avec le complexe PS4 (illustration 22). Des résultats obtenus il a pu être conclus que la structure du photosensibilisateur et le degré de couverture de la surface des RuNPs, sont deux points clés qui influencent fortement l'adsorption du PS sur des RuNPs une réaction d'échange de ligands.

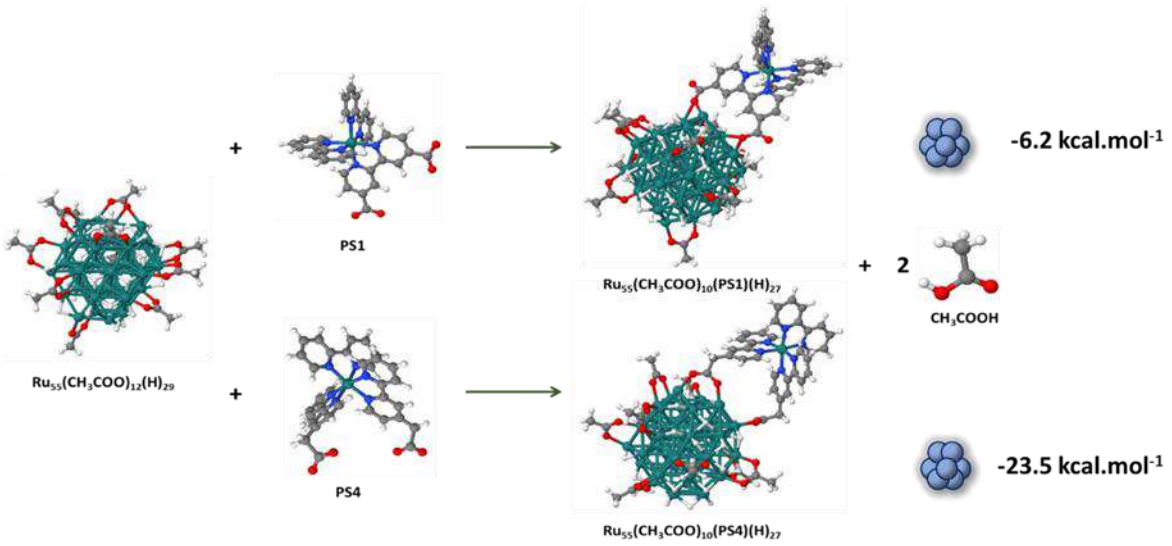

Illustration 22. Calculs théoriques optimisés pour la réaction de PS1 et de PS4 avec $Ru_{55}(CH_3COO)_{12}(H)_{29}$ NP. L'équilibre énergétique de DFT (kcal.mol^{-1}) de la réaction est également indiqué.

Les études théoriques menées, ont permis de conclure que l'ancrage d'un photosensibilisateur sur des RuNPs préformées est faisable. Cependant, ces résultats préliminaires doivent être considérés avec prudence en raison de plusieurs variables pouvant affecter l'efficacité de l'échange de ligands, comme la nature des photosensibilisateurs, leur encombrement stérique, l'acidité, le taux de couverture de la surface des NPs, la nature du ligand échangé, la recombinaison possible avec des protons, etc. Davantage de calculs DFT s'avèrent nécessaires pour compléter cette étude. Cependant, les données obtenues indiquent que la stratégie choisie pour ancrer un photosensibilisateur sur des RuNPs préformées peut permettre la formation de nanomatériaux hybrides PS-RuNP. Plus précisément, les informations recueillies font ressortir que la synthèse des nanocatalyseurs hybrides pour le craquage de l'eau peut être facilitée par l'utilisation d'un photosensibilisateur du type PS4 et d'un système de nanoparticules dont la surface est moyennement saturée. Compte tenu de ces conclusions, les RuNPs stabilisées par 0,3 equiv. d'acide pentanoïque apparaissent comme étant celles à tester en premier dans une réaction d'échange avec le PS4.

En conclusion générale, ce travail de doctorat a permis de constituer une base de connaissances expérimentales et théoriques solides et complémentaires sur des nanoparticules de ruthénium modèles en vue de l'élaboration de nanomatériaux hybrides RuNPs-PS. La combinaison d'outils expérimentaux et théoriques a généré des informations en très bon accord et permis de

déterminer les relations structure/propriétés de nanoparticules de ruthénium stabilisées par différents acides carboxyliques (acides éthanoïque, pentanoïque et octanoïque). Une stratégie d'échange de ligands à la surface de RuNPs préformées a également été éprouvée, ce qui permet d'envisager l'accès à des hybride RuNPs-PS sans modification significative des caractéristiques initiales de RuNPs préformées. Une perspective de ce travail est de synthétiser expérimentalement des catalyseurs nanomatériaux hybrides RuNPs-Ps et de les tester comme photocatalyseurs dans le processus de craquage de l'eau.

APPENDIX A

A.1 Adsorption of Hydrogen (H) onto Ru_{55} NP

Table A.1 Hydrogen coverage ratio, hydrogen coordination modes, DFT energy of the optimized structures and hydrogen mean adsorption energy.

Coverage H/Ru_{surf}	H coordination mode	E_{DFT} (eV)	E_{ads} (kcal.mol^{-1})
0.2	7 μ 2 μ^3	-460.48	-14.44
0.4	9 μ 8 μ^3	-492.69	-14.61
0.8	18 μ 17 μ^3	-564.41	-14.20
1.2	2 η 31 μ 19 μ^3 19 μ^4	-634.19	-13.23
1.6	8 η 43 μ 19 μ^3	-697.69	-11.98

A.2 Adsorption of a Single Ethanoic Moiety (CH_3COOH/ CH_3COO) onto Ru_{55} NP

A.2.1 Adsorption of Ethanoic Acid on different Ru_{55} NP Sites

Table A.2 Ru_{55} NP adsorption site of ethanoic acid, CH_3COOH coordination mode, DFT energy of the optimized structure and ethanoic acid adsorption energy.

NP site	CH_3COOH coordination mode	E_{DFT} (eV)	E_{ads} (kcal.mol^{-1})
B_4	μ	-471.66	-18.22
(001)	π	-471.91	-23.80
(101)	η-(O)	-471.72	-19.57
Corrugated surface	η-(O)	-471.38	-11.77
(101)	η-(OH)	-471.06	-4.26
(101)	μ	-471.57	-16.15
Corrugated surface	η-(O)	-471.49	-14.13
Apex	η-(OH)	-471.38	-11.65

A.2.2 Adsorption of Ethanoate on a Ru_{55} NP Single Site

Table A.3 Ru_{55} NP adsorption site of ethanoate, (CH_3COO) coordination mode, DFT energy of the optimized structure and ethanoate adsorption energy.

NP site	(CH_3COO) coordination mode	E_{DFT} (eV)	E_{ads} (kcal.mol^{-1})
B_4	μ	-473.26	-54.95
(001)	μ	-473.61	-63.01
(101)	μ	-473.38	-57.90
Corrugated surface	η-(O)	-472.51	-37.81

A.3 Adsorption of Ethanoic Acid and THF onto Hydrogenated Ru_{55} NP

A.3.1 Adsorption of Ethanoic Acid onto Hydrogenated Ru_{55} NP

Table A.4 Hydrogen coverage ratio, Ru_{55} NP adsorption site of ethanoic acid and coordination mode, DFT energy of the optimized structure and ethanoic acid adsorption energy.

Coverage H/Ru_{surf}	CH_3COOH coordination mode	E_{DFT} (eV)	E_{ads} (kcal.mol^{-1})
0.8	Apex η-(OH)	-611.68	-17.80
1.2		-681.52	-19.10
1.6		-745.31	-25.84

A.3.2 Adsorption of THF onto Hydrogenated Ru_{55} NP

Table A.5 Hydrogen and THF coverage ratio, THF adsorption site in η mode, DFT energy of the optimized structure and THF mean adsorption energy.

Coverage H/Ru_{surf}	Coverage THF/Ru_{NP}	THF coordination site or plane	E_{DFT} (eV)	E_{ads} (kcal.mol^{-1})
0.8	1	Apex	-637.128	-17.04
	2	Apex, (101)	-709.67	-15.21
	3	Apex, (101), (001)	-782.32	-15.36
	4	Apex, (101), (001), corrugated surface	-854.56	-13.08
1.2	1	Apex	-707.08	-21.23
	2	Apex, (101)	-779.91	-20.53
	3	Apex, (101), (001)	-852.41	-17.73
	4	Apex, (101), (001), corrugated surface	-924.49	-13.90
1.6	1	Apex	-770.39	-16.88
	2	Apex, (101)	-842.86	-14.18

	3	Apex, (101), (001)	-915.20	-12.25
	4	Apex, (101), (001), corrugated surface	No converged, led to spontaneous decoordination of one THF	

A.4 Adsorption of Ethanoate onto Hydrogenated and Bare Ru_{55} NP

Table A.6 Ethanoate & hydrogen coverage ratios, (CH_3COO) & H coordination modes, DFT energy of the optimized structure and carboxylic moiety mean adsorption energy.

Coverage (CH3COO)/Ru_{NP}	**Coverage H/Ru_{Surf}**	**(CH_3COO) & H coordination mode**		**E_{DFT} (eV)**	**E_{ads} (kcal.mol^{-1})**
1	0.8	1 μ	20 μ 16 μ^3	-612.81	-43.84
	1.2	1 μ	2 η 33 μ 18 μ^3 1 μ^4	-682.91	-51.11
	1.6	1 μ	8 η 46 μ 17 μ^3	-745.93	-40.12
2	0.8	1 μ 1 μ^3	1 η 20 μ 16 μ^3	-660.00	-29.89
	1.3	2 μ	1 η 36 μ 17 μ^3 1 μ^4	-729.60	-27.78
	1.6	2 μ	6 η 49 μ 17 μ^3	-793.09	-27.74
3	0.9	2 μ 1 μ^3	1 η 23 μ 14 μ^3	-708.14	-32.57
	1.3	3 μ	2 η 35 μ 18 μ^3	-777.89	-32.33

			1 μ^4		
	1.7	3 μ	6 η 50 μ 17 μ^3	-840.62	-26.36
4	0.1	4 μ	2 μ 2 μ^3	-618.99	-49.68
	0.4	4 μ	12 μ 5 μ^3	-670.85	---------
	0.9	2 μ 2 μ^3	2 η 22 μ 15 μ^3	-756.37	-34.37
	1.3	4 μ	1 η 35 μ 20 μ^3 1 μ^4	-826.00	-33.53
	1.7	4 μ	8 η 48 μ 18 μ^3	-888.47	-27.59
8	0.2	7 μ 1 μ^3	6 μ 2 μ^3	-814.00	-50.81
	0.4	7 μ 1 μ^3	13 μ 4 μ^3	-848.65	---------
	0.5	7 μ 1 μ^3	12 μ 9 μ^3	-863.98	---------
	0.6	7 μ 1 μ^3	1 η 14 μ 10 μ^3	-880.14	-44.55
	1.0	6 μ 2 μ^3	1 η 30 μ 12 μ^3	-947.36	-31.60
	1.4	1 η 7 μ	7 η 36 μ 17 μ^3 1 μ^4	-1014.50	-23.98
	1.8	8 μ	11 η 44 μ 22 μ^3	-1074.53	-13.96
10	0.2	9 μ 1 μ^3	9 μ 1 μ^3	-912.05	-52.31

	0.6	9 μ 1 μ^3	18 μ 9 μ^3	-976.91	-44.34
	1.0	7 μ 3 μ^3	1 η 29 μ 15 μ^3	-1043.37	-32.20
	1.4	1 η 9 μ	4 η 41 μ 18 μ^3	-1106.51	-16.89
	1.8	1 η 8 μ	11 η 47 μ 20 μ^3 1 μ^5	-1168.13	-12.56
12	0.3	11 μ 1 μ^3	9 μ 3 μ^3	-1009.28	-51.72
	0.7	10 μ 2 μ^3	20 μ 8 μ^3 1 μ^4	-1072.83	-42.57
	1.1	10 μ 2 μ^3	3 η 28 μ 15 μ^3 1 μ^5	-1137.82	-29.62
	1.5	1 η 11 μ	3 η 43 μ 17 μ^3 2 μ^4	-1204.67	-24.00
	1.8	2 η 8 μ	9 η 53 μ 18 μ^3	-1262.42	-12.94
14	0.3	13 μ 1 μ^3	10 μ 4 μ^3	-1106.85	-51.85
	0.7	12 μ 2 μ^3	1 η 18 μ 11μ^3 1 μ^4	-1168.63	-41.09
16	0.4	16 μ	10 μ 4 μ^3 2 μ^4	-1202.18	-48.74
	0.6	15 μ 1 μ^3	16 μ 7 μ^3	-1235.95	-45.37

		2 μ^4		
0.8	15 μ 1 μ^3	1 η 25 μ 7 μ^3	-1264.48	-40.07
1.2	14 μ 2 μ^3	5 η 33 μ 11 μ^3 2 μ^5	-1326.98	-26.78
1.6	1 η 12 μ 1 μ^3	7 η 36 μ 23 μ^3 2 μ^4 1 μ^5	-1391.54	-19.25
1.9	2 η 12 μ^3	14 η 50 μ 19 μ^3 1 μ^4	-1449.19	-10.82

Three structures highlighted in blue (table A.6) present coverage modifications due to species recombination. In the $Ru_{55}H_{80}(CH_3COO)_{10}$ structure one of the carboxylates combines with a surface hydride and coordinates onto the Ru_{55} NP as carboxylic acid in η-(O) coordination mode. Meanwhile for $Ru_{55}H_{82}(CH_3COO)_{12}$, two carboxylates recombine with surface hydrides and interact as ethanoic acids with the same coordination mode as in the previous structure. Finally, in the structure $Ru_{55}H_{86}(CH_3COO)_{16}$ two carboxylates are also grafted as carboxylic acid in the same coordination mode.

These three structures are described hereafter with their correct composition: $Ru_{55}H_{79}(CH_3COO)_9(CH_3COOH)$, $Ru_{55}H_{80}(CH_3COO)_{10}(CH_3COOH)_2$ & $Ru_{55}H_{84}(CH_3COO)_{14}(CH_3COOH)_2$.

APPENDIX B

B.1 Adsorption of Pentanoate onto Hydrogenated and Bare Ru_{55} NP

Table B.1 Pentanoate & hydrogen coverage ratios, (C_4H_9COO) & H coordination modes, DFT energy of the optimized structure and pentanoate mean adsorption energy.

Coverage (C_4H_9COO)/Ru_{NP}	Coverage H/Ru_{Surf}	(C_4H_9COO) & H coordination mode		E_{DFT} (eV)	E_{ads} (kcal.mol^{-1})
8	0.2	6 μ 2 μ^3	8 μ	-1210.88	-47.62
	0.6	8 μ	18 μ 6 μ^3 1 μ^4	-1276.34	-39.40
10	0.2	9 μ 1 μ^3	6 μ 4 μ^3	-1406.93	-46.29
	0.6	10 μ	1 η 17 μ 8 μ^3 1 μ^4	-1471.88	-38.54
12	0.3	11 μ 1 μ^3	9 μ 3 μ^3	-1603.41	-46.24
	0.7	10 μ 2 μ^3	1 η 18 μ 9 μ^3 1 μ^4	-1667.23	-37.60

14	0.3	13 μ 1 μ^3	9 μ 5 μ^3	-1799.42	-45.41
	0.7	13 μ 1 μ^3	2 η 18 μ 9 μ^3 2 μ^4	-1862.33	-36.51
16	0.4	15 μ 1 μ^3	2 η 8 μ 6 μ^3	-1993.91	-42.62
	0.8	14 μ 2 μ^3	1 η 22 μ 10 μ^3	-2056.27	-34.03

B.2 Adsorption of Octanoate onto Hydrogenated and Bare Ru_{55} NP

Table B.2 Octanoate & hydrogen coverage ratios, ($C_7H_{15}COO$) & H coordination modes, DFT energy of the optimized structure and octanoate mean adsorption energy.

Coverage ($C_7H_{15}COO$)/Ru_{NP}	**Coverage H/Ru_{Surf}**	**($C_7H_{15}COO$) & H coordination mode**		**E_{DFT} (eV)**	**E_{ads} (kcal.mol^{-1})**
8	0.2	7 μ 1 μ^3	5 μ 3 μ^3	-1607.28	-45.92
	0.6	7 μ 1 μ^3	14 μ 11 μ^3	-1673.39	-39.58
10	0.2	9 μ 1 μ^3	7 μ 3 μ^3	-1902.94	-45.76
	0.6	9 μ 1 μ^3	18 μ 9 μ^3	-1968.13	-38.58
12	0.3	11 μ 1 μ^3	9 μ 3 μ^3	-2197.64	-43.84
	0.7	10 μ 2 μ^3	20 μ 8 μ^3 1 μ^4	-2262.33	-36.86
14	0.3	13 μ 1 μ^3	9 μ 5 μ^3	-2493.46	-44.27

	0.7	12 μ 2 μ^3	1 η 17 μ 11 μ^3 2 μ^4	-2556.30	-35.26

B.3 Adsorption of a Single Octanoic, Benzoic and Trifluoroacetic Carboxylic Moiety onto Bare Ru_{55} NP

Table B.3 Studied carboxylic moieties deposed onto the same adsorption site over the plane [100], DFT energy of the optimized structure and carboxylic moiety adsorption energy.

Moiety	E_{DFT} (eV)	E_{ads} (kcal.mol^{-1})
Octanoate	-572.35	-48.64
Octanoic acid	-570.87	-14.43
Benzoate	-525.79	-58.77
Benzoic acid	-523.96	-16.43
Trifluoroacetate	-474.54	-59.43
Trifluoroacetic acid	-472.57	-13.94

B.4 Adsorption of Combined Octanoates and Benzoates Moieties onto Bare Ru_{55} NP

Table B.4 Octanoate, benzoate & H coverage ratios, DFT energy of the optimized structure and carboxylic mean adsorption energy.

Coverage ($C_7H_{15}COO$)/Ru_{NP}	Coverage (C_6H_5COO)/Ru_{NP}	Coverage H/Ru_{Surf}	E_{DFT} (eV)	E_{ads} (kcal.mol^{-1})
5	8	0.3	-1970.43	-45.65
3	8		-1676.49	-49.34

B.5 Adsorption of PS onto Low Crowded Ru_{55} NP

Table B.5 DFT energy of the optimized $Ru_{55}(CH_3COO)_2(H)_2$ structures interacting with different photosensitizer and its adsorption energy.

PS	PS formula	Ru NP composition	E_{DFT} (eV)	E_{ads} (kcal.mol^{-1})	E_{ads} /COO (kcal.mol^{-1})
1	$[Ru(bpy)_2(bpy(COO)_2)]$	$Ru_{55}(CH_3COO)_2(PS1)(H)_2$	-978.41	-77.84	-38.92
2	$[Ru(bpy)(bpy(COO))_2]$	$Ru_{55}(CH_3COO)_2(PS2)(H)_2$	-982.86	-175.50	-87.75
3	$[Ru(bpy)_2(bpy(CH_2COO)_2)]$	$Ru_{55}(CH_3COO)_2(PS3)(H)_2$	-1011.99	-89.25	-44.62
4	$[Ru(bpy)(bpy(CH_2COO))_2]$	$Ru_{55}(CH_3COO)_2(PS4)(H)_2$	-1012.78	-106.35	-53.18

B.6 Adsorption of PS onto Intermediate Crowded Ru_{55} NP

Table B.6 DFT energy of the optimized $Ru_{55}(CH_3COO)_{10}(H)_{27}$ structures interacting with different photosensitizer and its adsorption energy.

PS	PS formula	Ru NP composition	E_{DFT} (eV)	E_{ads} (kcal.mol^{-1})	E_{ads} /COO (kcal.mol^{-1})
1	$[Ru(bpy)_2(bpy(COO)_2)]$	$Ru_{55}(CH_3COO)_{10}(PS1)(H)_{27}$	-1433.54	-73.63	-36.82
2	$[Ru(bpy)(bpy(COO))_2]$	$Ru_{55}(CH_3COO)_{10}(PS2)(H)_{27}$	-1434.38	-88.15	-44.07
4	$[Ru(bpy)(bpy(CH_2COO))_2]$	$Ru_{55}(CH_3COO)_{10}(PS4)(H)_{27}$	-1467.42	-90.95	-45.48

B.7 Adsorption of PS1 onto High Crowded Ru_{55} NP

Table B.7 DFT energy of the optimized $Ru_{55}(CH_3COO)_{14}(H)_{31}$ structures interacting with PS1 and its adsorption energy.

PS	PS formula	Ru NP composition	E_{DFT} (eV)	E_{ads} (kcal.mol^{-1})	E_{ads} /COO (kcal.mol^{-1})
1	$[Ru(bpy)_2(bpy(COO)_2)]$	$Ru_{55}(CH_3COO)_{14}(PS1)(H)_{31}$	-1624.61	-58.72	-29.36

APPENDIX C

C.1 Adsorption of Ethanoic Acid on Crowded Ru_{55} NP

Table C.1 Ethanoate & hydrogen coverage ratios, DFT energy of the optimized structure and ethanoic acid adsorption energy.

Coverage $(CH_3COO)/Ru_{NP}$	Coverage H/Ru_{Surf}	E_{DFT} (eV)	E_{ads} (kcal.mol^{-1})
14	0.3	-1105.03	-48.86
	0.7	-1167.49	-39.21

C.2 Adsorption of THF on Crowded Ru_{55} NP

Table C.2 Ethanoate & hydrogen coverage ratios, DFT energy of the optimized structure and THF mean adsorption energy.

Coverage $(CH_3COO)/Ru_{NP}$	Coverage H/Ru_{Surf}	Coverage THF/Ru_{NP}	E_{DFT} (eV)	E_{ads} (kcal.mol^{-1})
14	0.3	1	-1130.46	-48.79
	0.7	1	-1193.92	-40.80
		2	-1218.37	-39.11

C.3 Adsorption of THF on Crowded Ru_{55} NP

Table C.3 Ethanoate & hydrogen coverage ratios, DFT energy of the optimized structure and THF mean adsorption energy.

Coverage $(CH_3COO)/Ru_{NP}$	**Coverage H/Ru_{Surf}**	**Coverage THF/Ru_{NP}**	**E_{DFT} (eV)**	**E_{ads} (kcal.mol^{-1})**
14	0.3	1	-1130.46	-48.79
	0.7	1	-1193.92	-40.80
		2	-1218.37	-39.11

APPENDIX D

D.1 Vibration Corrections for Ru-H onto Ru_{55} NP

Table D.1 Hydrogen coordination modes and their corresponding vibrational frequencies (Ru-H) onto Ru_{55} NP.

Coordination mode	Vibrational frequencies (cm^{-1})
η	1860 & 400
μ	1400, 940 & 630
μ^3	1300, 900, 550 & 500
μ^4	1040, 840 & 580
μ^5	1010, 670 & 540

D.2 Vibration Corrections for Ru-CH_3COOH onto Ru_{55} NP

Table D.2 Ethanoic acid coordination mode and its corresponding vibrational frequencies (Ru-COOH) onto Ru_{55} NP.

Coordination mode	Vibrational frequencies (cm^{-1})
η-(O)	125, 140, 215, 445 & 670

D.3 Vibration Corrections for Ru-CH_3COO onto Ru_{55} NP

Table D.3 Ethanoate coordination modes and their corresponding vibrational frequencies (Ru-COO) onto Ru_{55} NP.

Coordination mode	**Vibrational frequencies (cm^{-1})**
η	65, 120, 140, 220 & 555
μ	150, 205, 210, 230, 450 & 530
μ^3	170, 175, 190, 195, 215, 225, 370 & 490

APPENDIX E

E.1 Adsorption of Hydrogen on $Ru_{55}(CH_3COO)_x(H)_y$ NP Model.

Table E.1 Ethanoate & hydrogen coverage ratios, H coordination site in μ mode, hydrogen adsorption energy and hydrogen Gibbs free energy.

Coverage $(CH_3COO)/Ru_{NP}$	Coverage H/Ru_{Surf}	H coordination site or plane	E_{H*} (kcal.mol^{-1})	ΔG_{H*} (kcal.mol^{-1})
0	0	B_{4-5}	-14.6	-9.1
		(001)	-14.3	-8.8
		(101)	-15.6	-10.1
			-15.8	-10.3
			-12.3	-6.8
1	1.2	B_{4-5}	-14.1	-8.6
		(001)	-14.1	-8.6
		(101)	-11.9	-6.4
			-3.5	2.0
			-6.5	-1.0
16	0.2	B_{4-5}	-12.9	-7.4
		(001)	-8.0	-2.5
		(101)	-7.8	-2.3
			-3.1	2.4
			-7.4	-1.9

E.2 Adsorption of Hydrogen on $Ru_{55}(C_4H_9COOH)_{14}(H)_{14}$ NP Model.

Table E.2 Pentanoate & hydrogen coverage ratios, H coordination site in μ mode, hydrogen adsorption energy and hydrogen Gibbs free energy.

Coverage (C_4H_9COO)/Ru_{NP}	**Coverage H/Ru_{Surf}**	**H coordination site or plane**	**E_{ads} (kcal.mol^{-1})**	**ΔG_{H*} (kcal.mol^{-1})**
14	0.3	B_{4-5}	-4.7	0.8
		(001)	-6.1	-0.6
			-10.3	-4.8
		(101)	-13.3	-7.8
			-10.3	-4.8

E.3 Adsorption of Hydrogen on $Ru_{55}(C_7H_{15}COOH)_{14}(H)_{14}$ NP Model.

Table E.3 Octanoate & hydrogen coverage ratios, H coordination site in μ mode, hydrogen adsorption energy and hydrogen Gibbs free energy.

Coverage ($C_7H_{15}COO$) /Ru_{NP}	**Coverage H/Ru_{Surf}**	**H coordination site or plane**	**E_{ads} (kcal.mol^{-1})**	**ΔG_{H*} (kcal.mol^{-1})**
14	0.3	B_{4-5}	-6.9	-1.4
		(001)	-8.0	-2.5
			-10.8	-5.3
		(101)	-12.7	-7.2
			-16.7	-11.2

APPENDIX F

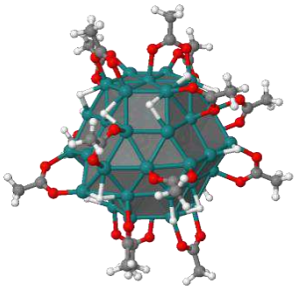

Domain 39 – $Ru_{55}(CH_3COO)_{16}(H)_{16}$

1	Ru	15.0173	12.7465	15.8444	36	Ru	14.6395	15.7453	17.9023
2	Ru	15.2427	12.6815	11.479	37	Ru	14.8343	17.2985	11.473
3	Ru	15.2188	11.1852	13.6687	38	Ru	14.507	17.3073	15.6874
4	Ru	13.5793	14.9275	15.7529	39	Ru	14.0838	8.8908	13.5489
5	Ru	13.7098	14.9248	11.4439	40	Ru	13.04	7.9088	15.4822
6	Ru	12.355	12.4865	15.6907	41	Ru	15.2413	11.0713	9.4523
7	Ru	13.806	13.4053	13.5866	42	Ru	13.943	10.3045	11.4488
8	Ru	12.503	12.541	11.3875	43	Ru	13.8085	10.2593	15.7253
9	Ru	12.4648	10.9403	13.5567	44	Ru	14.926	11.1658	17.8446
10	Ru	12.311	15.6525	13.5429	45	Ru	16.4413	13.5423	9.4058
11	Ru	11.1515	13.2263	13.4641	46	Ru	16.483	13.4845	13.7272
12	Ru	8.5093	13.0702	13.3949	47	Ru	16.09	13.682	17.9153
13	Ru	9.639	15.299	13.5257	48	Ru	16.3755	14.973	11.524
14	Ru	9.807	10.73	13.5083	49	Ru	16.2095	15.0613	15.9255
15	Ru	10.671	17.6115	13.4664	50	Ru	16.5178	8.921	13.9563
16	Ru	11.126	13.0912	9.2869	51	Ru	16.575	10.4088	11.7039
17	Ru	9.8845	12.3163	11.4876	52	Ru	17.8725	11.2163	13.7873
18	Ru	9.7368	12.3535	15.4744	53	Ru	16.4658	10.5477	15.8145
19	Ru	10.8253	13.1545	17.6387	54	Ru	17.7705	12.82	11.6228
20	Ru	12.5203	15.7248	9.359	55	Ru	17.6333	12.7507	15.9726
21	Ru	11.003	14.7175	11.3485	56	C	5.4263	10.019	13.5476
22	Ru	10.903	14.6848	15.5841	57	C	6.755	10.7282	13.5047
23	Ru	12.021	15.5583	17.8217	58	C	14.1905	12.0058	22.0748
24	Ru	12.187	17.1855	11.5016	59	C	14.241	12.1393	20.5741
25	Ru	13.493	18.089	13.6282	60	C	20.4808	12.6983	8.1052
26	Ru	12.028	17.0958	15.6333	61	C	19.259	12.7823	8.9812
27	Ru	11.4165	8.5947	13.5798	62	C	7.3835	15.313	8.7994
28	Ru	12.7105	11.0372	9.3267	63	C	8.6818	14.773	9.3431
29	Ru	11.297	10.1538	11.4265	64	C	9.6782	20.6885	16.4143
30	Ru	11.2168	10.0693	15.6504	65	C	10.2235	19.45	15.756
31	Ru	12.4268	10.9503	17.7515	66	C	19.1765	17.6663	14.1528
32	Ru	13.8523	13.4278	9.3155	67	C	17.8872	16.9463	14.45
33	Ru	13.524	13.3988	17.8755	68	C	16.3037	4.9278	15.7867
34	Ru	15.2138	15.605	9.4159	69	C	15.708	6.2452	15.36
35	Ru	14.9925	15.8173	13.6102	70	C	14.1753	9.506	5.5094

71	C	14.078	10.0737	6.8999
72	C	21.8883	11.8908	15.3928
73	C	20.399	11.9365	15.1822
74	C	9.0112	6.4407	10.6626
75	C	9.8503	7.5118	11.3082
76	C	9.0783	8.7008	19.3175
77	C	10.0303	9.3653	18.3586
78	C	10.0255	14.735	21.6369
79	C	10.5178	14.5887	20.2202
80	C	17.403	19.2575	8.5072
81	C	16.5248	18.228	9.1692
82	C	16.884	19.4395	18.6857
83	C	16.087	18.3608	18.0001
84	C	12.1135	21.6475	11.5099
85	C	12.3578	20.2132	11.9051
86	C	13.3845	14.8815	5.1589
87	C	13.4025	14.7865	6.6625
88	O	6.7223	12.0165	13.4802
89	O	7.8163	10.0167	13.4893
90	O	13.5355	13.0478	20.0273
91	O	14.9888	11.301	19.9412
92	O	18.1485	13.0903	8.3944
93	O	19.373	12.5638	10.2258
94	O	9.1623	15.3275	10.3862
95	O	9.2112	13.7708	8.7402
96	O	10.9705	18.6813	16.4614
97	O	9.9273	19.237	14.5306
98	O	16.9288	17.0477	13.6245
99	O	17.8413	16.2363	15.5238
100	O	14.5327	6.529	15.7812
101	O	16.4353	6.9798	14.6011
102	O	15.1723	10.2977	7.5306
103	O	12.9153	10.2643	7.4017
104	O	19.7055	12.636	16.002
105	O	19.902	11.261	14.2163
106	O	10.3398	7.2518	12.4727
107	O	10.0217	8.6088	10.6943
108	O	9.8018	9.3038	17.1135
109	O	11.0585	9.9543	18.8773
110	O	10.2253	13.505	19.6053
111	O	11.1695	15.5708	19.7148
112	O	16.183	18.4503	10.3836
113	O	16.1893	17.1943	8.4898
114	O	15.8485	17.294	18.654
115	O	15.683	18.5865	16.7986
116	O	11.9763	19.3045	11.0945
117	O	12.9245	19.998	13.0356
118	O	13.067	15.841	7.3151
119	O	13.7338	13.6715	7.1913
120	H	5.564	8.9363	13.6217
121	H	4.8558	10.2605	12.6396
122	H	4.8425	10.384	14.4032
123	H	15.1493	11.6375	22.4575
124	H	13.4173	11.2665	22.3343
125	H	13.9255	12.9615	22.5389
126	H	21.3105	12.2298	8.6437
127	H	20.774	13.7145	7.8029
128	H	20.25	12.1378	7.1908
129	H	7.191	14.9245	7.7943
130	H	7.4133	16.4095	8.7909
131	H	6.563	15.0098	9.4663
132	H	8.7673	21.0253	15.9091
133	H	10.4332	21.4858	16.3413
134	H	9.4888	20.5023	17.4777
135	H	19.7615	17.8155	15.067
136	H	18.97	18.6233	13.6594
137	H	19.7643	17.0463	13.4581
138	H	16.727	4.4148	14.9136
139	H	15.5523	4.2983	16.2726
140	H	17.13	5.1145	16.4874
141	H	13.2255	9.621	4.9769
142	H	14.4115	8.4335	5.5817
143	H	14.9918	9.9878	4.959
144	H	18.1323	14.5848	11.6366
145	H	16.2268	9.6607	10.1301
146	H	13.7073	17.013	9.8506
147	H	10.3115	14.9483	17.3183
148	H	11.2968	16.9395	9.9949
149	H	13.2535	16.6043	18.6207
150	H	9.324	12.2795	17.2461
151	H	18.3125	10.9317	12.0203
152	H	22.3918	11.4845	14.5098
153	H	22.1068	11.2478	16.2583
154	H	22.265	12.8943	15.6255
155	H	17.8265	13.2203	17.7052
156	H	8.9282	6.6153	9.5846
157	H	8.0038	6.4655	11.1041
158	H	9.4383	5.4513	10.8638
159	H	9.0168	17.0045	13.2839
160	H	8.8948	9.3505	20.182
161	H	9.5372	7.7728	19.6901
162	H	8.1385	8.4545	18.8136
163	H	11.3097	14.7423	8.5938
164	H	10.5482	15.551	22.146
165	H	10.1613	13.7908	22.1783
166	H	8.9478	14.9565	21.6206
167	H	14.9965	18.5127	12.7106
168	H	17.535	19.0315	7.4443
169	H	18.384	19.26	9.0051
170	H	16.9705	20.2585	8.6356
171	H	11.3163	8.1443	15.4463
172	H	17.0808	20.2745	18.0066
173	H	17.829	19.0193	19.0549
174	H	16.3238	19.799	19.5601
175	H	10.5348	11.468	9.7646
176	H	12.5683	22.3338	12.2304
177	H	11.0308	21.8283	11.4605
178	H	12.5203	21.8265	10.5063
179	H	16.2258	9.8423	17.4034
180	H	13.9258	14.0423	4.7107
181	H	13.818	15.8365	4.8389
182	H	12.3395	14.8605	4.816
183	H	12.6072	9.362	10.4572

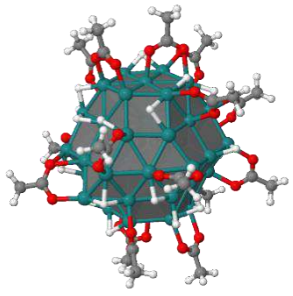

Domain 40 – $Ru_{55}(CH_3COO)_{16}(H)_{25}$

1	Ru	15.1519	12.6385	15.6818	73	C	20.3876	11.1676	14.9540
2	Ru	15.1375	12.5719	11.4131	74	C	8.5548	6.6214	10.9165
3	Ru	15.1478	11.0585	13.6018	75	C	9.5122	7.6289	11.4929
4	Ru	13.7584	14.9056	15.7912	76	C	10.2406	14.8533	21.7065
5	Ru	13.6393	14.8752	11.4318	77	C	10.7281	14.6903	20.2911
6	Ru	12.4469	12.4701	15.7123	78	C	9.1068	9.1133	19.6285
7	Ru	13.8169	13.3551	13.5782	79	C	10.1173	9.5754	18.6102
8	Ru	12.4079	12.5107	11.4471	80	C	15.6835	19.7007	7.8588
9	Ru	12.4097	10.8611	13.5995	81	C	15.4706	18.5267	8.7813
10	Ru	12.4028	15.6600	13.6054	82	C	15.9805	19.7133	19.0982
11	Ru	11.1449	13.1985	13.5853	83	C	15.5772	18.5304	18.2532
12	Ru	8.5265	13.2080	13.5898	84	C	12.6087	21.5480	11.2224
13	Ru	9.7137	15.3657	13.6531	85	C	12.6827	20.1127	11.6719
14	Ru	9.7487	10.8006	13.6772	86	C	12.9972	14.7404	5.1435
15	Ru	10.8423	17.6519	13.5878	87	C	13.0747	14.6535	6.6457
16	Ru	10.9131	13.0872	9.4133	88	O	6.6999	12.2333	13.4274
17	Ru	9.7875	12.3406	11.6301	89	O	7.7284	10.2073	13.2187
18	Ru	9.7676	12.4586	15.6655	90	O	14.0569	13.1839	19.9917
19	Ru	11.0237	13.2185	17.7235	91	O	16.1618	12.3961	19.6577
20	Ru	12.3521	15.6223	9.3754	92	O	17.9685	12.7862	8.1988
21	Ru	10.9784	14.7136	11.4610	93	O	19.3183	12.5435	9.9983
22	Ru	11.0704	14.7336	15.6690	94	O	9.0594	15.3245	10.6477
23	Ru	12.3162	15.5195	17.9125	95	O	8.9698	13.7976	8.9750
24	Ru	12.1624	17.1720	11.4868	96	O	11.0669	18.4453	16.6990
25	Ru	13.5752	18.0111	13.6011	97	O	10.1182	19.1824	14.7792
26	Ru	12.3305	17.0908	15.7153	98	O	16.8739	18.0242	15.1641
27	Ru	11.2447	8.6013	13.7084	99	O	18.0656	16.1022	15.1914
28	Ru	12.4433	11.0186	9.3552	100	O	14.1723	6.3551	15.6989
29	Ru	11.1569	10.1431	11.5054	101	O	15.2953	6.9317	13.8302
30	Ru	11.1926	10.1238	15.7787	102	O	14.7721	10.3756	7.3673
31	Ru	12.5931	10.9937	17.8466	103	O	12.5108	10.4155	7.3745
32	Ru	13.7009	13.3520	9.2876	104	O	19.8164	11.9233	15.8173
33	Ru	13.7522	13.3286	17.8416	105	O	19.8152	10.6743	13.9215
34	Ru	15.0415	15.5903	9.1995	106	O	10.0171	7.3616	12.6493
35	Ru	15.0066	15.6637	13.5139	107	O	9.7678	8.6837	10.8355
36	Ru	15.0849	15.6131	17.8419	108	O	11.4243	15.6408	19.7906
37	Ru	14.9549	17.1170	11.3932	109	O	10.4275	13.6051	19.6806
38	Ru	14.9668	17.1648	15.6260	110	O	9.8809	9.3819	17.3808
39	Ru	13.9402	8.7706	13.6148	111	O	11.1663	10.1718	19.0654
40	Ru	12.7754	7.8852	15.5823	112	O	15.3406	18.7439	10.0241
41	Ru	15.0089	11.0202	9.3098	113	O	15.4232	17.3640	8.2188
42	Ru	13.8003	10.1962	11.3638	114	O	15.7273	17.3663	18.7738
43	Ru	13.8046	10.2084	15.7338	115	O	15.1290	18.7477	17.0833
44	Ru	15.1130	11.0530	17.7438	116	O	12.0978	19.2310	10.9603
45	Ru	16.3142	13.3933	9.2542	117	O	13.3070	19.8710	12.7655
46	Ru	16.4782	13.3608	13.5178	118	O	12.7741	15.7162	7.3051
47	Ru	16.3366	13.3728	17.7576	119	O	13.4179	13.5416	7.1690
48	Ru	16.2920	14.9216	11.2369	120	H	9.1603	17.0559	13.3454
49	Ru	16.3822	14.9590	15.6454	121	H	11.0641	14.7065	8.6603
50	Ru	16.3928	8.8363	13.5487	122	H	9.1584	10.7394	15.3474
51	Ru	16.4525	10.2715	11.3856	123	H	15.2456	18.1077	12.7759
52	Ru	17.8111	11.0137	13.4720	124	H	13.1294	18.6416	15.1514
53	Ru	16.5608	10.4085	15.6488	125	H	12.4909	9.1653	10.6846
54	Ru	17.7067	12.7533	11.3669	126	H	13.9270	10.2764	18.8648
55	Ru	17.8241	12.5347	15.7453	127	H	16.6591	16.7406	11.5287
56	C	5.3468	10.3022	13.0812	128	H	16.6057	10.0688	9.6585
57	C	6.6958	10.9518	13.2617	129	H	16.8319	15.2371	17.4272
58	C	15.2466	12.3318	21.8736	130	H	18.2314	12.8321	13.9985
59	C	15.1362	12.6747	20.4132	131	H	17.2474	8.7958	15.0903
60	C	20.2950	12.4322	7.8148	132	H	5.4227	9.2142	13.1725
61	C	19.1213	12.5887	8.7446	133	H	4.9582	10.5547	12.0836
62	C	7.1827	15.3773	9.1818	134	H	4.6391	10.7007	13.8189
63	C	8.4986	14.7954	9.6298	135	H	16.2686	12.0420	22.1359
64	C	9.7647	20.4460	16.7766	136	H	14.5622	11.4977	22.0872
65	C	10.3501	19.2737	16.0360	137	H	14.9222	13.1877	22.4790
66	C	19.1806	18.1083	14.5455	138	H	21.1253	11.9351	8.3268
67	C	17.9538	17.3661	15.0080	139	H	20.6263	13.4298	7.4893
68	C	16.2062	5.1891	15.2048	140	H	19.9984	11.8713	6.9207
69	C	15.1578	6.2174	14.8995	141	H	6.8064	14.8567	8.2957
70	C	13.6270	9.9127	5.3191	142	H	7.3153	16.4455	8.9642
71	C	13.6362	10.2718	6.7790	143	H	6.4532	15.2995	10.0001
72	C	21.8322	10.8161	15.1929	144	H	8.8589	20.8073	16.2781

145	H	10.5068	21.2588	16.7815	169	H	18.0697	12.8356	17.4468
146	H	9.5559	20.1739	17.8173	170	H	9.2797	14.3439	21.8414
147	H	20.0880	17.6389	14.9418	171	H	10.1583	15.9151	21.9625
148	H	19.1251	19.1631	14.8351	172	H	10.9710	14.3891	22.3859
149	H	19.2194	18.0531	13.4470	173	H	9.5869	8.9300	20.5958
150	H	16.4997	4.6606	14.2896	174	H	8.5874	8.2166	19.2732
151	H	15.8542	4.4859	15.9660	175	H	8.3603	9.9115	19.7602
152	H	17.0985	5.7104	15.5859	176	H	16.1492	14.7380	8.0933
153	H	12.7926	10.4108	4.8120	177	H	16.4001	19.4418	7.0704
154	H	13.4799	8.8265	5.2205	178	H	16.0263	20.5745	8.4223
155	H	14.5813	10.1772	4.8517	179	H	14.7264	19.9424	7.3728
156	H	18.0163	14.4909	11.5810	180	H	11.0660	8.2460	15.5683
157	H	13.5908	16.8453	9.9987	181	H	15.4914	20.6233	18.7355
158	H	10.6160	15.2176	17.3808	182	H	17.0693	19.8483	19.0186
159	H	11.2666	16.9695	9.9745	183	H	15.7384	19.5341	20.1523
160	H	13.6908	16.0865	18.8449	184	H	10.3611	11.4246	9.9541
161	H	9.4414	12.4609	17.4409	185	H	13.3908	22.1437	11.7043
162	H	18.1629	10.9115	11.6070	186	H	11.6270	21.9585	11.5012
163	H	22.3120	10.5058	14.2589	187	H	12.6967	21.6023	10.1309
164	H	21.8789	9.9800	15.9069	188	H	16.3403	9.7011	17.2204
165	H	22.3598	11.6670	15.6394	189	H	13.5568	13.9227	4.6780
166	H	8.3480	6.8430	9.8648	190	H	13.3778	15.7112	4.8045
167	H	7.6150	6.6590	11.4867	191	H	11.9420	14.6718	4.8393
168	H	8.9631	5.6082	11.0230	192	H	15.2271	9.0320	11.1949

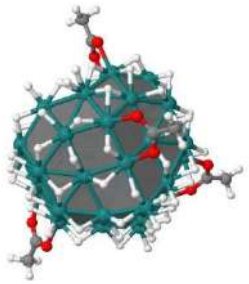

Domain 19 – $Ru_{55}(CH_3COO)_4(H)_{74}$

1	Ru	15.3816	12.8156	15.2482	28	Ru	12.0539	11.7244	8.9415
2	Ru	15.0911	13.0185	10.9542	29	Ru	10.9334	10.7973	11.2101
3	Ru	15.1038	11.3416	13.0558	30	Ru	11.2163	10.5713	15.365
4	Ru	14.0368	15.1687	15.5358	31	Ru	12.6268	11.1122	17.5314
5	Ru	13.6758	15.4231	11.1776	32	Ru	13.4935	13.942	9.0003
6	Ru	12.5574	12.8414	15.496	33	Ru	14.0972	13.3645	17.5882
7	Ru	13.868	13.7448	13.2628	34	Ru	14.8427	16.17	9.0247
8	Ru	12.2459	13.0889	11.1838	35	Ru	15.1556	16.0584	13.2908
9	Ru	12.4184	11.4604	13.2266	36	Ru	15.4551	15.642	17.6056
10	Ru	12.4808	16.1026	13.5234	37	Ru	15.1384	17.7249	11.1905
11	Ru	11.083	13.8157	13.47	38	Ru	15.464	17.4499	15.6414
12	Ru	8.2563	13.7225	13.7127	39	Ru	13.6669	9.0244	13.1242
13	Ru	9.7988	16.1917	13.7634	40	Ru	12.5747	8.4208	15.4899
14	Ru	9.6468	11.3814	13.44	41	Ru	14.7841	11.6751	8.7142
15	Ru	11.2536	18.3087	13.8466	42	Ru	13.5853	10.7478	10.9645
16	Ru	10.8553	13.9843	9.2526	43	Ru	13.878	10.5105	15.2121
17	Ru	9.6503	13.1513	11.4411	44	Ru	15.3195	11.0377	17.3883
18	Ru	9.9212	12.9192	15.6064	45	Ru	16.1341	13.8658	8.7984
19	Ru	11.4664	13.4431	17.6994	46	Ru	16.5521	13.6843	13.0782
20	Ru	12.2448	16.2245	9.2128	47	Ru	16.7098	13.3565	17.3351
21	Ru	10.9909	15.4701	11.4307	48	Ru	16.419	15.3805	11.0146
22	Ru	11.306	15.1957	15.694	49	Ru	16.76	15.1374	15.3642
23	Ru	12.838	15.6877	17.7397	50	Ru	16.2605	9.0893	12.9139
24	Ru	12.3852	17.7578	11.478	51	Ru	16.2289	10.6158	10.8097
25	Ru	13.9042	18.4863	13.5562	52	Ru	17.9196	11.2527	12.8626
26	Ru	12.8188	17.4787	15.7937	53	Ru	16.5669	10.4382	15.073
27	Ru	10.9982	9.078	13.2219	54	Ru	17.6118	13.0004	10.8091

55	Ru	17.9129	12.7177	15.1318	107	H	14.9909	7.8939	12.7022
56	C	12.7443	7.197	19.6787	108	H	16.3496	10.9104	9.0432
57	C	12.7097	8.1851	18.5444	109	H	16.6533	8.8806	11.2028
58	C	19.7351	18.4379	15.7909	110	H	18.0322	9.5805	13.2874
59	C	18.4243	17.7009	15.6663	111	H	16.5202	9.9118	16.8218
60	C	13.1668	8.4497	6.2224	112	H	16.2335	8.7629	14.7342
61	C	13.2392	9.6069	7.1823	113	H	17.7293	13.2149	8.9897
62	C	7.9804	18.8931	16.6939	114	H	17.9874	11.1136	11.0093
63	C	8.9151	18.2853	15.6864	115	H	19.4106	10.7839	12.5264
64	O	9.9236	18.9772	15.3051	116	H	18.4267	13.1324	16.7549
65	O	8.6765	17.0945	15.2818	117	H	18.0166	14.2684	14.1907
66	O	14.408	10.0271	7.5023	118	H	19.0528	11.6454	14.061
67	O	12.1424	10.0919	7.6236	119	H	18.0139	11.1584	15.8903
68	O	18.481	16.4409	15.463	120	H	9.177	11.2888	11.7004
69	O	17.3534	18.3928	15.7903	121	H	9.4338	11.1433	15.2639
70	O	12.5631	9.4127	18.8143	122	H	9.8018	12.8939	17.397
71	O	12.8404	7.6885	17.353	123	H	10.4428	15.7867	9.6813
72	H	6.6571	13.6796	13.6475	124	H	12.0577	14.8209	8.0548
73	H	13.7106	20.0291	12.8458	125	H	12.8423	14.0902	18.781
74	H	10.3289	7.6175	13.1166	126	H	13.7581	18.7743	10.8643
75	H	15.9368	19.0773	10.869	127	H	10.7557	12.6107	8.0864
76	H	8.07	15.3599	13.382	128	H	12.1703	9.8648	10.3239
77	H	7.9388	12.0181	13.4305	129	H	10.8678	8.6083	14.959
78	H	9.7511	17.8643	13.0858	130	H	14.7982	14.7769	7.842
79	H	8.0004	13.7712	11.9731	131	H	15.1745	18.9426	14.6798
80	H	9.2162	13.5253	9.7331	132	H	15.5372	14.1001	18.6088
81	H	8.0463	13.1783	15.3146	133	H	16.8064	17.1878	11.1944
82	H	9.4241	15.7941	12.0924	134	H	12.2264	8.0647	12.5378
83	H	11.0287	15.3211	17.5437	135	H	14.4061	9.6935	16.9333
84	H	12.3876	17.4006	17.5115	136	H	13.3061	7.59	14.1926
85	H	10.7663	17.2915	11.2062	137	H	14.1434	11.7128	18.571
86	H	12.1673	17.9586	9.725	138	H	17.2238	15.1091	17.1867
87	H	11.5217	19.1194	12.3113	139	H	18.0938	14.7087	10.9511
88	H	12.7113	19.1029	14.7493	140	H	16.8898	15.5172	12.7288
89	H	9.3147	9.581	13.4674	141	H	18.6513	12.7501	12.2475
90	H	10.4304	8.9859	11.6236	142	H	12.0072	6.4028	19.5014
91	H	10.5503	11.0259	9.4388	143	H	12.5472	7.6956	20.6318
92	H	11.4515	11.9394	18.6264	144	H	13.7357	6.7224	19.7058
93	H	11.0813	10.4228	17.1486	145	H	16.4039	16.8801	14.2461
94	H	13.5038	17.0319	8.2172	146	H	19.5915	19.5107	15.6274
95	H	14.2511	16.3886	18.6656	147	H	20.4647	18.0298	15.0816
96	H	15.2574	17.8962	9.4833	148	H	20.1304	18.2834	16.8056
97	H	14.1888	20.174	13.6139	149	H	7.4388	14.6988	14.672
98	H	15.7731	17.3481	17.3978	150	H	12.136	8.2825	5.8962
99	H	13.3696	12.4317	7.8288	151	H	13.5429	7.5466	6.7236
100	H	13.6104	9.056	11.3439	152	H	13.8178	8.6413	5.3595
101	H	14.8597	9.7611	10.1363	153	H	14.1788	18.32	16.546
102	H	15.4734	10.0141	18.6066	154	H	6.9798	18.458	16.5987
103	H	16.6749	15.6866	9.2658	155	H	7.9472	19.9818	16.5757
104	H	16.0102	12.5565	7.6446	156	H	8.3589	18.6709	17.703
105	H	16.7416	11.7378	18.179	157	H	9.6252	14.6311	15.8642
106	H	15.4659	18.6115	12.6423					

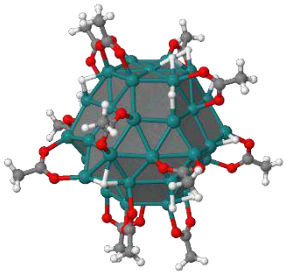

Domain 37 – $Ru_{55}(CH_3COO)_{14}(H)_{14}$

1	Ru	14.9345	13.0475	15.4721
2	Ru	15.1973	13.0265	11.1553
3	Ru	15.1605	11.4898	13.3827
4	Ru	13.4935	15.2238	15.4276
5	Ru	13.6088	15.283	11.0695
6	Ru	12.2615	12.7755	15.3806
7	Ru	13.7193	13.7148	13.248
8	Ru	12.4098	12.907	11.0627
9	Ru	12.3728	11.2698	13.2114
10	Ru	12.2238	15.923	13.2517
11	Ru	11.062	13.5338	13.1526
12	Ru	8.404	13.3348	13.0528
13	Ru	9.4645	15.5403	13.2699
14	Ru	9.7513	10.9955	13.1786
15	Ru	10.5578	17.868	13.0884
16	Ru	11.1088	13.5403	8.9523
17	Ru	9.806	12.625	11.1332
18	Ru	9.6505	12.6278	15.1325
19	Ru	10.7648	13.4463	17.3181
20	Ru	12.367	15.9813	9.0293
21	Ru	10.8808	15.0673	11.0885
22	Ru	10.8043	14.955	15.2552
23	Ru	11.975	15.9035	17.4814
24	Ru	12.1438	17.425	11.1894
25	Ru	13.3988	18.2838	13.4186
26	Ru	11.8643	17.3833	15.3286
27	Ru	11.373	8.9165	13.1651
28	Ru	12.6063	11.3703	9.0067
29	Ru	11.2095	10.5363	11.0391
30	Ru	11.1648	10.3303	15.2849
31	Ru	12.3815	11.2328	17.4164
32	Ru	13.7715	13.7335	9.0262
33	Ru	13.4603	13.664	17.5167
34	Ru	14.946	16.102	9.0587
35	Ru	14.82	16.1663	13.2925
36	Ru	14.5965	16.0453	17.5794
37	Ru	14.5693	17.7533	11.1974
38	Ru	14.432	17.6183	15.4651
39	Ru	14.0253	9.2123	13.136
40	Ru	12.99	8.2065	15.0834
41	Ru	15.1553	11.4288	9.1463
42	Ru	13.8533	10.7112	11.1264
43	Ru	13.7323	10.5433	15.3626
44	Ru	14.8803	11.4753	17.4866
45	Ru	16.2818	14.1153	9.1471
46	Ru	16.4525	13.7578	13.3718
47	Ru	16.029	14.0003	17.5097
48	Ru	16.3478	15.3663	11.2975
49	Ru	16.161	15.3685	15.4799
50	Ru	16.4525	9.2263	13.6513
51	Ru	16.4545	10.7165	11.363
52	Ru	17.7762	11.4938	13.3908
53	Ru	16.3825	10.8503	15.4976
54	Ru	17.7155	13.173	11.2141
55	Ru	17.5668	13.0465	15.5938
56	C	5.361	10.2542	13.2012
57	C	6.6843	10.9743	13.1628
58	C	14.2638	12.3218	21.7155
59	C	14.2733	12.4685	20.2155
60	C	20.1485	13.0382	7.5096
61	C	19.008	13.1715	8.4835
62	C	7.6403	16.1118	8.249
63	C	8.868	15.4875	8.8595
64	C	9.6395	21.1063	15.8681
65	C	10.1813	19.8373	15.2677
66	C	19.1333	17.7848	13.3455
67	C	17.851	17.0758	13.6729
68	C	16.2443	5.2333	15.4955
69	C	15.66	6.5487	15.0467
70	C	14.0843	9.696	5.2666
71	C	14.0008	10.3013	6.6407
72	C	21.7993	12.1255	15.0316
73	C	20.3125	12.1978	14.8096
74	C	9.3283	6.7	10.0248
75	C	10.114	7.765	10.7401
76	C	9.0045	9.003	18.9498
77	C	9.978	9.6415	17.9954
78	C	9.9985	15.0855	21.3151
79	C	10.5063	14.9003	19.9082
80	C	17.2898	19.7545	8.4029
81	C	16.3695	18.7218	8.9983
82	C	16.88	19.6932	18.4205
83	C	16.0825	18.614	17.7388
84	O	6.6398	12.264	13.1659
85	O	7.751	10.2755	13.1206
86	O	13.5525	13.375	19.6916
87	O	15.0113	11.6335	19.5572
88	O	17.891	13.6188	8.0067
89	O	19.1878	12.8515	9.6977
90	O	9.1467	15.7925	10.0682
91	O	9.5558	14.683	8.1377
92	O	10.895	19.08	16.0176
93	O	9.9218	19.5935	14.0387
94	O	16.9605	16.9773	12.7436
95	O	17.6865	16.6148	14.8489
96	O	14.4695	6.8283	15.4266
97	O	16.4115	7.2858	14.3159
98	O	15.0933	10.5938	7.2384
99	O	12.838	10.468	7.1625
100	O	19.6318	12.946	15.6016
101	O	19.8018	11.501	13.8692
102	O	10.478	7.5233	11.9486
103	O	10.359	8.8558	10.1265
104	O	9.7543	9.5823	16.7487
105	O	11.0135	10.2123	18.5193
106	O	10.2195	13.8078	19.3151
107	O	11.1688	15.8723	19.3911
108	O	15.8825	18.97	10.159
109	O	16.1363	17.66	8.3322
110	O	15.86	17.534	18.3747
111	O	15.6533	18.8483	16.5461
112	H	5.5083	9.1725	13.2683
113	H	4.7898	10.4955	12.2936
114	H	4.7732	10.6102	14.0582
115	H	15.2363	11.9643	22.0722
116	H	13.5078	11.5693	21.9869
117	H	13.9962	13.27	22.1941
118	H	20.988	12.5093	7.9716
119	H	20.4753	14.04	7.1955
120	H	19.8115	12.5078	6.6097
121	H	7.611	15.9333	7.1692
122	H	7.6245	17.188	8.462
123	H	6.7468	15.6703	8.7131
124	H	8.7425	21.4338	15.3322
125	H	10.404	21.8933	15.7786
126	H	9.4275	20.9628	16.9335
127	H	19.7447	17.9203	14.2433
128	H	18.9105	18.7545	12.8814
129	H	19.6893	17.1863	12.6084
130	H	16.6418	4.6918	14.6268
131	H	15.493	4.626	16.0098
132	H	17.0893	5.4248	16.1723
133	H	13.1288	9.7962	4.7414
134	H	14.3218	8.626	5.3635
135	H	14.8933	10.1653	4.694
136	H	18.0558	14.906	10.9452
137	H	16.159	9.992	9.7609
138	H	13.577	16.7533	8.0005
139	H	10.2535	15.2045	17.0269
140	H	11.5325	17.5258	9.5295
141	H	13.234	16.8925	18.3232
142	H	9.2825	12.547	16.9216
143	H	18.2225	11.368	11.6173
144	H	22.2983	11.68	14.1653
145	H	21.9987	11.5058	15.9185
146	H	22.1983	13.127	15.235
147	H	17.7563	13.545	17.3329
148	H	9.3618	6.8563	8.9419
149	H	8.2805	6.7593	10.3568
150	H	9.7043	5.7045	10.2885
151	H	8.9005	17.289	12.9665
152	H	8.77	9.6983	19.766

153	H	9.4697	8.1123	19.3973
154	H	8.0913	8.7073	18.4246
155	H	12.427	14.4158	7.905
156	H	10.549	15.8818	21.8262
157	H	10.0768	14.1422	21.8689
158	H	8.934	15.3605	21.2745
159	H	14.2958	19.2338	12.2132
160	H	17.4987	19.5283	7.3528
161	H	18.2338	19.7583	8.9671
162	H	16.846	20.7533	8.5012
163	H	11.2555	8.4035	14.9991
164	H	17.144	20.488	17.7156
165	H	17.7845	19.2608	18.8672
166	H	16.281	20.1188	19.2382
167	H	9.8268	12.3788	9.3311

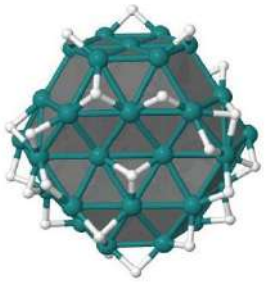

Domain 3 – $Ru_{55}(H)_{35}$

1	Ru	17.5082	8.6051	10.9313
2	Ru	17.6177	8.5722	6.6214
3	Ru	17.5507	7.0962	8.7546
4	Ru	16.0901	10.9369	10.9886
5	Ru	16.1601	10.9894	6.6099
6	Ru	14.8500	8.5636	10.8940
7	Ru	16.2496	9.4378	8.7521
8	Ru	14.8584	8.5829	6.6027
9	Ru	14.8613	7.0074	8.7478
10	Ru	14.9037	11.7145	8.7762
11	Ru	13.4647	9.2969	8.7589
12	Ru	10.9211	9.4800	8.5794
13	Ru	12.2012	11.6624	8.7685
14	Ru	12.0712	7.0034	8.6022
15	Ru	13.3589	13.7202	8.8338
16	Ru	13.5668	9.3035	4.5435
17	Ru	12.2282	8.5407	6.5920
18	Ru	12.1007	8.6077	10.7625
19	Ru	13.4046	9.1473	12.8676
20	Ru	14.9009	11.5859	4.5411
21	Ru	13.5201	10.9241	6.7176
22	Ru	13.4467	10.8751	10.8183
23	Ru	14.6933	11.5206	12.9682
24	Ru	14.8349	13.1943	6.6878
25	Ru	16.1388	14.1057	8.8219
26	Ru	14.7171	13.1891	10.9477
27	Ru	13.6291	4.8044	8.7983
28	Ru	14.9832	7.1464	4.5359
29	Ru	13.6031	6.3327	6.6056
30	Ru	13.3180	6.4171	10.7155
31	Ru	14.7761	6.9685	12.8876
32	Ru	16.2288	9.4092	4.5623
33	Ru	16.0694	9.2918	13.0921
34	Ru	17.4677	11.6251	4.5577
35	Ru	17.5209	11.8236	8.8460
36	Ru	17.3666	11.5828	13.1651
37	Ru	17.4929	13.1849	6.7152
38	Ru	17.3729	13.1717	10.9725
39	Ru	16.3275	4.7576	8.9945
40	Ru	14.7788	4.5779	11.3203
41	Ru	17.4881	7.1924	4.5574
42	Ru	16.2559	6.2327	6.6774
43	Ru	16.3212	6.3032	10.8955
44	Ru	17.5305	7.0854	12.9700
45	Ru	18.7623	9.4098	4.5541
46	Ru	18.9550	9.4242	8.8473
47	Ru	18.6982	9.4050	13.0934
48	Ru	18.8425	10.9325	6.7182
49	Ru	18.6958	10.9471	11.0099
50	Ru	18.7293	4.8506	8.8260
51	Ru	18.9012	6.3300	6.7703
52	Ru	20.4161	7.1466	8.8873
53	Ru	18.8715	6.3865	10.8821
54	Ru	20.1545	8.6723	6.7552
55	Ru	20.0771	8.6456	11.0456
56	H	10.4736	11.1977	8.8682
57	H	13.3844	14.3709	10.4684
58	H	14.4082	13.2590	12.7478
59	H	13.3038	7.6089	13.7620
60	H	10.7039	7.8635	7.6772
61	H	10.4205	8.7101	10.1144
62	H	11.8725	8.8187	4.8421
63	H	13.1051	11.1202	4.8652
64	H	12.9278	10.9891	12.6588
65	H	14.5801	14.7026	7.7667
66	H	17.0172	14.7807	7.4522
67	H	15.8172	14.5958	10.5174
68	H	12.3902	5.2446	7.5783
69	H	13.8018	7.9466	3.4039
70	H	14.7102	5.4214	5.5564
71	H	12.3303	4.9808	9.9062
72	H	16.1850	12.4255	3.5616
73	H	15.9962	10.8270	14.2175
74	H	16.0466	7.6929	14.0830
75	H	17.6255	14.4647	9.6382
76	H	18.6368	10.8267	14.2093
77	H	18.8484	12.5148	5.6535
78	H	18.6864	12.5830	12.0885
79	H	14.5716	5.1156	13.0267
80	H	14.8683	3.6393	9.7112
81	H	18.8664	7.8923	3.5607
82	H	17.7137	5.4612	5.7129
83	H	18.8717	5.9780	12.6593
84	H	19.3772	11.2216	9.3659
85	H	20.3601	10.1760	5.8180
86	H	20.4756	9.1166	12.7042
87	H	21.2816	8.5087	8.1912
88	H	20.2509	5.5278	9.8017

89	H	20.6446	6.7784	7.0896	90	H	21.4213	7.6725	10.2425

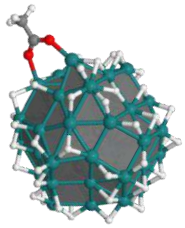

Domain 7 – $Ru_{55}(CH_3COO)(H)_{54}$

1	Ru	15.2555	13.2301	15.2999	53	Ru	16.6563	11.0489	15.0575
2	Ru	15.2729	13.4717	10.9019	54	Ru	17.7996	13.7629	10.9973
3	Ru	15.3276	11.8386	13.0253	55	Ru	17.7755	13.3978	15.1688
4	Ru	13.7432	15.5274	15.4535	56	C	12.3887	7.4475	19.3396
5	Ru	13.7082	15.8514	11.0265	57	C	12.4486	8.4245	18.1957
6	Ru	12.4808	13.1544	15.3014	58	O	12.3625	7.9145	17.0099
7	Ru	13.9177	14.1491	13.1428	59	O	12.5810	9.6580	18.4529
8	Ru	12.5007	13.4572	10.9044	60	H	6.8862	13.9433	13.1067
9	Ru	12.6620	11.8028	12.9668	61	H	10.5115	8.0106	13.4634
10	Ru	12.4181	16.4222	13.3098	62	H	8.0086	15.5872	13.4961
11	Ru	11.2446	14.0344	13.1317	63	H	9.5970	17.7051	14.3580
12	Ru	8.4929	13.9587	13.0340	64	H	8.3081	12.4553	12.0700
13	Ru	9.7098	16.1812	13.3189	65	H	9.4855	13.2475	16.7969
14	Ru	9.7572	11.5249	12.9931	66	H	10.5714	15.9807	9.3518
15	Ru	10.9190	18.4563	13.4106	67	H	9.6504	17.7316	12.3489
16	Ru	11.1075	14.2194	8.9469	68	H	9.4616	13.6701	9.4208
17	Ru	9.9279	13.1754	11.0682	69	H	10.5974	15.4230	17.1674
18	Ru	9.8999	13.0055	15.0525	70	H	11.7902	18.2241	9.5046
19	Ru	11.1262	13.6488	17.3412	71	H	12.0243	19.5081	12.3749
20	Ru	12.3231	16.6074	9.0538	72	H	11.7441	17.6708	17.2343
21	Ru	11.0532	15.6590	11.1695	73	H	11.1897	12.7454	7.9278
22	Ru	11.0925	15.3761	15.3477	74	H	10.5127	9.4813	11.2626
23	Ru	12.3746	16.0402	17.5251	75	H	11.4933	10.5850	9.2367
24	Ru	12.3097	18.0309	11.2352	76	H	9.6507	9.6848	13.2633
25	Ru	13.5239	18.8701	13.4586	77	H	11.0071	10.7020	16.7099
26	Ru	12.3594	17.7410	15.5411	78	H	12.3657	15.0986	7.8394
27	Ru	11.3017	9.3038	12.8866	79	H	12.4095	14.3771	18.5329
28	Ru	12.5693	12.0121	8.8170	80	H	13.6230	17.4871	8.1295
29	Ru	11.2713	11.0721	10.9255	81	H	13.6773	16.8624	18.5160
30	Ru	11.3167	10.8329	14.9008	82	H	14.8275	19.5019	12.4388
31	Ru	12.4967	11.3871	17.2289	83	H	15.2510	18.3952	9.5334
32	Ru	13.7504	14.3452	8.8222	84	H	16.6544	17.6478	11.6154
33	Ru	13.7917	13.7362	17.4817	85	H	14.7670	19.4031	14.6121
34	Ru	14.9544	16.7477	9.0278	86	H	13.9493	10.7784	8.9673
35	Ru	15.0756	16.5684	13.3038	87	H	12.8173	9.6352	11.7028
36	Ru	14.9807	16.1600	17.5743	88	H	14.1637	9.1299	15.4814
37	Ru	14.8514	18.1099	11.2916	89	H	13.8802	12.0992	18.3464
38	Ru	14.8684	17.8364	15.5137	90	H	15.1122	15.2789	7.8122
39	Ru	14.0480	9.4513	12.9950	91	H	16.5973	12.3592	18.2007
40	Ru	12.5530	8.7073	15.1698	92	H	18.0964	15.5324	11.3580
41	Ru	15.1620	12.1892	8.7560	93	H	15.3909	17.8532	17.2354
42	Ru	14.0164	11.0953	10.8664	94	H	15.4416	8.3171	13.1613
43	Ru	13.9316	10.8974	15.0789	95	H	16.6160	11.1228	8.9832
44	Ru	15.2825	11.5844	17.1914	96	H	15.4776	9.9459	10.8896
45	Ru	16.3852	14.5193	8.8823	97	H	18.2372	10.2264	12.4299
46	Ru	16.5579	14.3505	13.1684	98	H	16.4697	10.3483	16.6935
47	Ru	16.4577	13.9355	17.3930	99	H	17.2750	9.3664	14.3329
48	Ru	16.3881	15.9657	11.1688	100	H	18.0794	14.1150	9.2614
49	Ru	16.3720	15.6681	15.3430	101	H	18.3943	12.0168	11.0949
50	Ru	16.5452	9.6438	12.8267	102	H	18.4605	13.5885	13.3629
51	Ru	16.6533	11.3206	10.7539	103	H	18.4694	11.6115	14.6250
52	Ru	18.0127	11.9118	12.9315	104	H	8.1063	12.9886	14.3618

105	H	11.9401	19.3428	14.6219
106	H	11.1260	12.1452	18.2335
107	H	15.1322	14.5614	18.5604
108	H	12.7269	8.1792	13.4222
109	H	16.4191	13.1204	7.8131
110	H	16.7703	16.3316	9.3959
111	H	16.8120	15.7835	17.1534
112	H	18.1466	13.6914	16.9029
113	H	12.5713	7.9528	20.2925
114	H	13.1278	6.6508	19.1812
115	H	11.3973	6.9721	19.3562
116	H	16.6172	17.3855	14.9735

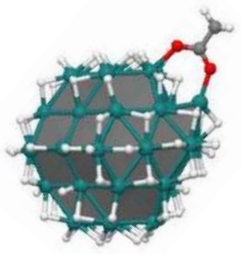

Domain 8 – $Ru_{55}(CH_3COO)(H)_{71}$

1	Ru	15.2024	13.2106	15.2851
2	Ru	15.1739	13.3197	10.9700
3	Ru	15.1293	11.6714	13.1346
4	Ru	13.7584	15.5301	15.4503
5	Ru	13.6826	15.6656	11.0139
6	Ru	12.4252	13.1421	15.3901
7	Ru	13.8348	14.0445	13.1569
8	Ru	12.3638	13.2476	11.0147
9	Ru	12.4762	11.6854	13.1286
10	Ru	12.4189	16.3614	13.2622
11	Ru	11.1192	13.9436	13.2004
12	Ru	8.3776	14.0824	13.2334
13	Ru	9.6948	16.2274	13.3846
14	Ru	9.6231	11.5844	13.1543
15	Ru	10.9056	18.4091	13.3961
16	Ru	11.0323	14.0795	9.0175
17	Ru	9.7105	13.2782	11.1175
18	Ru	9.7815	13.1793	15.3000
19	Ru	11.1230	13.8194	17.4386
20	Ru	12.3079	16.3995	9.0337
21	Ru	11.0038	15.6025	11.2389
22	Ru	11.1266	15.4448	15.3143
23	Ru	12.4300	16.1353	17.5028
24	Ru	12.3305	17.9420	11.2190
25	Ru	13.6541	18.8705	13.3539
26	Ru	12.3766	17.7929	15.4862
27	Ru	11.0651	9.3004	13.1584
28	Ru	12.3840	11.8341	8.8941
29	Ru	11.0844	10.9261	11.0538
30	Ru	11.1044	10.9016	15.2016
31	Ru	12.3574	11.4938	17.4381
32	Ru	13.6757	14.1470	8.8715
33	Ru	13.7686	13.8146	17.5382
34	Ru	14.9290	16.4211	8.9129
35	Ru	15.0600	16.3915	13.2114
36	Ru	15.0376	16.1969	17.5105
37	Ru	15.0172	18.0527	11.1271
38	Ru	15.0310	17.7686	15.3708
39	Ru	13.7391	9.2930	13.1879
40	Ru	12.5210	8.7728	15.5188
41	Ru	15.0238	11.8586	8.8738
42	Ru	13.7850	10.8895	10.9930
43	Ru	13.8059	10.8482	15.2232
44	Ru	15.0859	11.5498	17.4552
45	Ru	16.3177	14.1621	8.8303
46	Ru	16.4669	14.1017	13.1352
47	Ru	16.4012	13.9349	17.4218
48	Ru	16.4352	15.7083	11.0342
49	Ru	16.4506	15.5619	15.3319
50	Ru	16.4312	9.5106	13.1082
51	Ru	16.4730	10.9672	10.9944
52	Ru	17.9533	11.7631	13.1223
53	Ru	16.4991	10.8669	15.2139
54	Ru	17.6938	13.3607	10.9532
55	Ru	17.7404	13.2576	15.2819
56	C	12.6647	7.6855	19.7468
57	C	12.5504	8.6201	18.5740
58	O	12.3290	9.8465	18.7900
59	O	12.7061	8.0826	17.4017
60	H	6.7791	14.1896	13.2917
61	H	14.0093	20.4295	13.3637
62	H	10.3921	7.8431	13.0753
63	H	15.8001	19.3726	10.6703
64	H	7.9282	15.7270	13.3973
65	H	8.0138	12.2874	13.1572
66	H	9.2303	17.9921	13.5139
67	H	8.0323	13.9542	11.5255
68	H	9.3568	13.6409	9.3949
69	H	8.0347	13.7469	14.9027
70	H	9.6196	16.3993	10.9719
71	H	10.6442	15.6184	17.1545
72	H	11.8966	17.7934	17.2063
73	H	10.8170	18.8124	11.6469
74	H	11.8417	18.0434	9.4722
75	H	12.2354	19.7871	13.2803
76	H	10.9637	18.8897	15.0940
77	H	9.3636	9.7680	13.2851
78	H	10.5467	9.1531	11.5437
79	H	10.9641	10.8831	9.2340
80	H	11.1546	12.3525	18.4487
81	H	10.8645	10.7608	17.0029
82	H	13.5621	17.1982	8.0471
83	H	13.7522	16.9119	18.4927
84	H	15.0083	18.1760	9.3825

85	H	13.5744	19.2266	15.0614
86	H	15.4176	17.8653	17.1489
87	H	13.7105	12.5347	7.7707
88	H	14.1058	9.2374	11.4133
89	H	13.8582	10.4965	9.1588
90	H	15.2623	10.5790	18.7167
91	H	16.7423	15.9644	9.2237
92	H	16.3153	12.6406	7.9036
93	H	16.4247	12.3320	18.2971
94	H	15.9001	18.8667	12.1828
95	H	15.2269	8.2517	13.1475
96	H	16.3211	10.6884	9.2258
97	H	16.7803	9.2719	11.2992
98	H	18.1836	10.0531	13.2563
99	H	16.4267	10.5349	17.0289
100	H	16.5378	9.1338	14.9000
101	H	17.9472	13.6215	9.1850
102	H	17.9736	11.6721	10.4033
103	H	19.4043	11.3175	12.6287
104	H	18.1239	13.6642	16.9661
105	H	18.0350	14.9226	14.6569
106	H	19.0653	12.2784	14.3115
107	H	17.8091	11.6555	16.0663
108	H	9.3059	11.4044	11.3583
109	H	9.2537	11.3616	14.8821
110	H	9.4284	13.4573	17.0226
111	H	10.5615	15.8700	9.4307
112	H	12.2952	14.9387	7.8736
113	H	12.4475	14.5571	18.5910
114	H	13.7929	19.3104	11.5781
115	H	11.1058	12.6171	7.9525
116	H	12.4086	9.8682	10.5625
117	H	10.8414	8.8691	14.8698
118	H	14.9850	14.9975	7.7682
119	H	15.2783	18.9689	14.0084
120	H	15.1284	14.6498	18.5753
121	H	16.6892	17.5095	10.9772
122	H	12.3280	8.2912	12.5566
123	H	14.3434	10.1127	17.0009
124	H	13.3118	7.8944	14.2741
125	H	13.8087	12.1679	18.5471
126	H	16.8798	15.7114	17.1184
127	H	18.1133	15.1175	11.0810
128	H	16.9307	15.9597	12.6824
129	H	18.7679	13.1071	12.3942
130	H	12.0058	6.8197	19.6021
131	H	12.4223	8.2026	20.6792
132	H	13.6963	7.3066	19.7924
133	H	16.7637	17.3317	15.1366

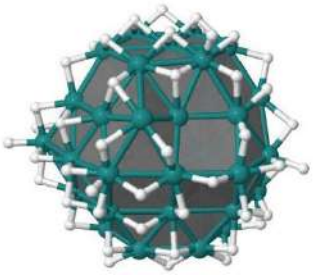

Domain 5 – $Ru_{55}(H)_{70}$

1	Ru	17.6621	8.6171	10.8969
2	Ru	17.6788	8.5871	6.6038
3	Ru	17.6113	7.0102	8.7904
4	Ru	16.2315	10.8846	11.0004
5	Ru	16.2067	10.9508	6.5707
6	Ru	14.8762	8.5483	10.9692
7	Ru	16.3064	9.3765	8.7484
8	Ru	14.8526	8.5242	6.6346
9	Ru	14.9256	7.0294	8.8207
10	Ru	14.9373	11.7314	8.7869
11	Ru	13.6024	9.3229	8.7736
12	Ru	10.8257	9.5253	8.7346
13	Ru	12.2126	11.6274	8.9133
14	Ru	12.0210	7.0142	8.7601
15	Ru	13.4580	13.8128	8.8515
16	Ru	13.5586	9.3405	4.5954
17	Ru	12.1907	8.6354	6.6928
18	Ru	12.1648	8.7148	10.8512
19	Ru	13.5366	9.2691	12.9929
20	Ru	14.8654	11.6465	4.5571
21	Ru	13.5207	10.9314	6.7766
22	Ru	13.5987	10.8895	10.8411
23	Ru	14.8816	11.5871	13.0181
24	Ru	14.8707	13.2413	6.7001
25	Ru	16.1921	14.2547	8.8077
26	Ru	14.9362	13.2120	10.9688
27	Ru	13.4534	4.7107	9.0035
28	Ru	14.8707	7.0751	4.5422
29	Ru	13.5288	6.2648	6.7211
30	Ru	13.3075	6.4235	10.9057
31	Ru	14.8513	6.9249	12.9763
32	Ru	16.1992	9.3653	4.4757
33	Ru	16.1887	9.2643	13.1338
34	Ru	17.4805	11.6341	4.4601
35	Ru	17.5805	11.7433	8.7896
36	Ru	17.5017	11.6251	13.0528
37	Ru	17.5656	13.3160	6.6393
38	Ru	17.4802	13.1372	10.9054
39	Ru	16.1525	4.6373	8.9443
40	Ru	14.8314	4.5437	11.3836
41	Ru	17.5255	7.0665	4.5489
42	Ru	16.2332	6.2005	6.6794
43	Ru	16.4049	6.2468	10.8973
44	Ru	17.5421	6.9668	13.1479
45	Ru	18.8373	9.3561	4.4587
46	Ru	18.9700	9.4077	8.7449
47	Ru	18.8258	9.3322	13.0440
48	Ru	18.9451	10.9707	6.6220
49	Ru	18.9201	10.8960	10.8984
50	Ru	18.8584	4.8109	8.8298
51	Ru	18.9335	6.1939	6.6887
52	Ru	20.4173	7.0459	8.7863
53	Ru	18.9454	6.2291	10.9239
54	Ru	20.1937	8.5993	6.5908

55	Ru	20.1957	8.5774	10.9301
56	H	9.2308	9.6575	8.6777
57	H	16.5701	15.8064	8.7676
58	H	12.7527	3.2835	8.8072
59	H	18.3649	14.6233	6.1719
60	H	10.4330	11.1993	8.8653
61	H	10.4227	7.7226	8.6757
62	H	11.7746	13.3932	8.8590
63	H	10.5418	9.3756	7.0128
64	H	11.8685	8.9662	4.9635
65	H	10.4652	9.2438	10.4447
66	H	12.1958	11.8019	6.4599
67	H	13.1054	11.0725	12.6901
68	H	14.4450	13.2698	12.6859
69	H	13.3628	14.1726	7.1075
70	H	14.4437	13.3093	4.9227
71	H	14.7820	15.1787	8.6766
72	H	13.5006	14.2531	10.5709
73	H	11.7690	5.1898	9.0032
74	H	13.0375	4.5559	7.3483
75	H	13.4648	6.0837	4.9312
76	H	13.4992	7.7234	13.8659
77	H	13.7335	5.5135	12.6285
78	H	16.1354	12.4031	3.5569
79	H	16.2193	12.3916	13.9802
80	H	17.5885	13.3889	4.8861
81	H	15.9606	14.7737	10.4083
82	H	18.0465	13.2408	12.6263
83	H	16.2124	7.7288	3.4224
84	H	16.5501	4.5463	7.2331
85	H	16.3158	5.7283	4.8804
86	H	17.7601	6.0434	14.4369
87	H	19.2833	11.1652	4.8070
88	H	18.8164	7.8187	3.5539
89	H	18.9085	7.7277	13.9326
90	H	18.3724	14.1639	7.7392
91	H	17.6301	3.5818	8.9842
92	H	18.8253	5.9171	4.9107
93	H	19.1672	4.4870	7.0412
94	H	20.6243	5.3408	8.9470
95	H	18.8036	5.8488	12.7305
96	H	19.0171	4.5072	10.6370
97	H	20.4736	8.8331	4.8253
98	H	20.4282	6.8887	6.0864
99	H	21.8632	6.5125	8.3664
100	H	20.5679	9.0633	12.5744
101	H	20.4647	10.1697	10.1560
102	H	21.5061	7.5599	10.0023
103	H	20.2704	7.0276	11.7941
104	H	11.7550	6.7674	6.9545
105	H	11.5614	6.8561	10.5018
106	H	11.8233	8.9542	12.5737
107	H	13.1078	11.1455	4.9628
108	H	14.8415	10.1362	3.4429
109	H	14.8358	10.0109	14.1458
110	H	16.3195	14.5903	6.9952
111	H	13.5878	7.8460	3.5859
112	H	14.8470	5.1668	6.3091
113	H	13.1969	3.9587	10.4990
114	H	17.5208	10.1775	3.3613
115	H	17.7493	14.4102	9.5688
116	H	17.5366	10.0807	14.1694
117	H	19.2291	12.7777	6.5214
118	H	14.7271	3.6443	8.4533
119	H	16.2689	5.6574	12.8804
120	H	15.7827	3.4991	10.3296
121	H	16.1976	7.6715	14.1676
122	H	19.3221	11.1252	12.6825
123	H	20.6229	10.3396	6.7132
124	H	19.4073	11.2791	8.2864
125	H	21.3262	8.2791	7.9973

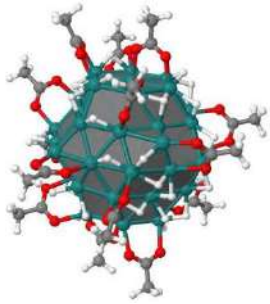

Domain 41 – $Ru_{55}(CH_3COO)_{16}(H)_{33}$

1	Ru	15.1588	12.7918	15.7157
2	Ru	15.0758	12.679	11.3357
3	Ru	15.1448	11.1643	13.5127
4	Ru	13.802	15.0995	15.7323
5	Ru	13.6115	15.015	11.4085
6	Ru	12.4563	12.6223	15.7381
7	Ru	13.7843	13.472	13.5756
8	Ru	12.3438	12.6443	11.4709
9	Ru	12.432	11.0278	13.6009
10	Ru	12.3658	15.7815	13.5551
11	Ru	11.1208	13.364	13.6045
12	Ru	8.5033	13.4368	13.8341
13	Ru	9.73	15.5813	13.6022
14	Ru	9.657	10.9805	13.7561
15	Ru	10.8773	17.8425	13.6614
16	Ru	10.8733	13.2288	9.4206
17	Ru	9.7038	12.5038	11.7315
18	Ru	9.8158	12.677	15.7495
19	Ru	11.1338	13.4998	17.8591
20	Ru	12.395	15.783	9.3306
21	Ru	10.9408	14.8633	11.4455
22	Ru	11.1115	14.9535	15.6289
23	Ru	12.493	15.7698	17.9153
24	Ru	12.1265	17.3008	11.4221
25	Ru	13.5078	18.1478	13.5556
26	Ru	12.3935	17.2848	15.6616
27	Ru	11.1685	8.7485	13.7493
28	Ru	12.3573	11.193	9.3012
29	Ru	11.046	10.3443	11.5869
30	Ru	11.1515	10.3097	15.8301

31	Ru	12.4888	11.172	17.8651
32	Ru	13.6323	13.4375	9.2791
33	Ru	13.7913	13.5393	17.8212
34	Ru	15.07	15.6178	9.1931
35	Ru	14.9853	15.7948	13.4729
36	Ru	15.1845	15.7843	17.7572
37	Ru	14.9085	17.222	11.3305
38	Ru	15.0273	17.3745	15.5579
39	Ru	13.9858	8.793	13.5348
40	Ru	12.847	8.1677	15.6016
41	Ru	15.0435	11.109	9.1926
42	Ru	13.727	10.3152	11.3261
43	Ru	13.8598	10.3295	15.7524
44	Ru	15.1877	11.301	17.8459
45	Ru	16.3188	13.4165	9.2032
46	Ru	16.3993	13.501	13.487
47	Ru	16.4723	13.5843	17.7104
48	Ru	16.2862	15.0397	11.2343
49	Ru	16.4435	15.116	15.5399
50	Ru	16.4165	8.9545	13.5551
51	Ru	16.4275	10.3975	11.3589
52	Ru	17.8453	11.158	13.4121
53	Ru	16.5358	10.5858	15.6502
54	Ru	17.6685	12.8297	11.4192
55	Ru	17.8368	12.703	15.6216
56	C	5.2472	10.6102	13.4017
57	C	6.6165	11.2238	13.5351
58	C	14.0865	12.1698	22.0324
59	C	14.232	12.2703	20.5351
60	C	20.6135	13.6003	8.2597
61	C	19.316	13.3288	8.977
62	C	7.338	15.7728	9.0171
63	C	8.624	15.1543	9.4994
64	C	9.9653	20.6655	16.8784
65	C	10.5025	19.4998	16.0956
66	C	19.245	18.21	14.3231
67	C	18.0125	17.4995	14.8216
68	C	16.2465	5.4383	15.5529
69	C	15.1795	6.4023	15.1224
70	C	13.3608	9.3088	5.5214
71	C	13.4833	9.95	6.8778
72	C	21.805	10.8738	15.2456
73	C	20.3825	11.2798	14.9666
74	C	8.5078	6.8285	10.8163
75	C	9.457	7.8015	11.4717
76	C	10.045	15.6878	21.5322
77	C	10.664	15.3193	20.2085
78	C	10.2278	7.7608	19.4056
79	C	10.8342	8.8005	18.4967
80	C	15.8223	19.655	7.7446
81	C	15.5415	18.5165	8.6915
82	C	16.502	19.7473	19.0094
83	C	15.908	18.629	18.1906
84	C	12.2493	21.6985	11.311
85	C	12.4317	20.268	11.7445
86	C	13.0145	14.856	5.1095
87	C	13.0635	14.774	6.6136
88	O	6.679	12.5093	13.5626
89	O	7.6208	10.4373	13.5975
90	O	13.8557	13.35	19.9696
91	O	14.6993	11.2475	19.9173
92	O	18.2285	13.573	8.3478
93	O	19.3723	12.8898	10.1735
94	O	9.1783	15.672	10.5282
95	O	9.0658	14.1328	8.8657
96	O	11.2925	18.6878	16.7029
97	O	10.1697	19.383	14.8668
98	O	16.9538	18.1783	15.0046
99	O	18.1103	16.2328	15.0098
100	O	14.163	6.561	15.879
101	O	15.3388	7.0298	14.0028
102	O	14.6475	10.1408	7.352
103	O	12.3867	10.2413	7.4911
104	O	19.85	12.148	15.7409
105	O	19.7818	10.712	13.987
106	O	9.929	7.478	12.6126
107	O	9.728	8.8853	10.8508
108	O	11.462	16.1705	19.6771
109	O	10.377	14.178	19.7142
110	O	10.433	8.8385	17.2861
111	O	11.7138	9.589	18.9917
112	O	15.4305	18.7692	9.9281
113	O	15.4125	17.3428	8.1624
114	O	15.9848	17.445	18.6872
115	O	15.3893	18.899	17.0664
116	O	11.8845	19.3595	11.0315
117	O	13.1035	20.0505	12.8115
118	O	12.8073	15.8563	7.2618
119	O	13.34	13.65	7.1477
120	H	9.1373	17.2535	13.4537
121	H	11.1995	14.7785	8.5909
122	H	8.308	13.2075	11.2752
123	H	9.703	11.1198	16.5334
124	H	15.0793	18.376	12.622
125	H	14.5003	18.9125	14.7516
126	H	12.3462	9.373	10.7645
127	H	11.178	11.9925	18.7387
128	H	13.917	9.9612	17.5471
129	H	16.5983	16.8403	11.6085
130	H	12.541	7.8615	13.0268
131	H	16.0595	12.0518	8.0826
132	H	16.5395	10.2472	9.5035
133	H	16.6473	12.0288	18.5611
134	H	16.9523	15.3483	17.3394
135	H	18.2318	12.9305	13.8772
136	H	17.2195	8.969	15.1541
137	H	5.2795	9.5375	13.6144
138	H	4.8888	10.7635	12.3731
139	H	4.5425	11.1153	14.0738
140	H	14.7968	11.445	22.444
141	H	13.0665	11.8248	22.2604
142	H	14.223	13.1545	22.4936
143	H	21.3795	12.8838	8.5774
144	H	20.959	14.609	8.5327
145	H	20.4712	13.5645	7.1744
146	H	7.1393	15.4925	7.9773
147	H	7.38	16.8628	9.1265
148	H	6.5155	15.4023	9.6473
149	H	9.0608	21.0643	16.4081
150	H	10.7308	21.456	16.899
151	H	9.7673	20.367	17.9148
152	H	20.132	17.8597	14.865
153	H	19.1323	19.2943	14.4199
154	H	19.383	17.9578	13.2613
155	H	16.7675	5.0175	14.6861
156	H	15.816	4.6478	16.1767
157	H	16.9803	5.9915	16.1593
158	H	12.5058	9.7305	4.9806
159	H	13.178	8.2318	5.6516
160	H	14.2863	9.4393	4.9512
161	H	17.9425	14.5955	11.707
162	H	17.018	8.7538	11.8888
163	H	13.401	17.1695	9.9913
164	H	10.7448	15.2883	17.3748
165	H	11.279	17.0535	9.782
166	H	13.8435	16.2835	18.8653
167	H	9.3575	13.2543	17.3272
168	H	18.1785	10.9735	11.5944
169	H	22.275	10.4695	14.3429
170	H	21.8028	10.091	16.0194
171	H	22.3725	11.7273	15.6338
172	H	9.7527	9.2748	14.6242
173	H	8.2703	7.1465	9.7965
174	H	7.5835	6.7738	11.4088
175	H	8.952	5.8248	10.8077
176	H	18.1635	13.2123	17.2965
177	H	9.108	15.1418	21.6853
178	H	9.8803	16.7698	21.5881
179	H	10.7445	15.411	22.335
180	H	14.428	9.5765	9.9224
181	H	10.7923	7.6865	20.3406
182	H	10.1963	6.7895	18.8968

183	H	9.1905	8.048	19.6313
184	H	15.9658	14.5853	7.9745
185	H	16.211	19.2843	6.7907
186	H	16.5255	20.3598	8.2033
187	H	14.8817	20.1935	7.5551
188	H	11.1415	7.5638	14.9677
189	H	16.133	20.716	18.6576
190	H	17.5955	19.7238	18.8906
191	H	16.2788	19.6068	20.0736
192	H	9.949	11.8403	9.957
193	H	12.8607	22.369	11.9223
194	H	11.1895	21.9733	11.4114
195	H	12.516	21.7998	10.2513
196	H	16.2897	9.8253	17.1389
197	H	13.5673	14.0248	4.66
198	H	13.4178	15.818	4.7718
199	H	11.9638	14.8015	4.7869
200	H	14.115	8.6443	11.7775

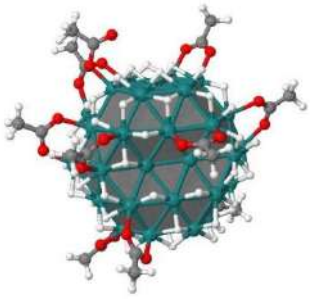

Domain 35 – $Ru_{55}(CH_3COO)_{12}(H)_{65}$

1	Ru	15.3368	13.343	15.2235
2	Ru	15.402	13.3393	10.8927
3	Ru	15.3955	11.8123	13.0946
4	Ru	13.932	15.6608	15.3192
5	Ru	13.9	15.6448	10.9127
6	Ru	12.6212	13.2563	15.2521
7	Ru	13.9845	14.1218	13.1071
8	Ru	12.5713	13.3895	10.9286
9	Ru	12.545	11.7393	13.0055
10	Ru	12.6958	16.4737	13.1537
11	Ru	11.2048	14.0355	13.143
12	Ru	8.6255	13.999	12.922
13	Ru	9.7928	16.229	13.2824
14	Ru	9.8903	11.675	13.1349
15	Ru	11.0938	18.4395	12.8534
16	Ru	11.2385	14.0773	8.8049
17	Ru	10.0155	13.2035	11.0084
18	Ru	9.8132	13.363	15.2402
19	Ru	11.204	13.997	17.452
20	Ru	12.8067	16.4405	8.7422
21	Ru	11.1515	15.7245	11.1199
22	Ru	11.2483	15.6233	15.229
23	Ru	12.5208	16.3845	17.4304
24	Ru	12.7415	17.9138	10.9091
25	Ru	13.721	18.866	13.1271
26	Ru	12.2345	18.0348	15.2526
27	Ru	11.3882	9.4367	13.0616
28	Ru	12.599	11.887	8.6954
29	Ru	11.2588	11.0385	10.895
30	Ru	11.3165	10.8915	15.1772
31	Ru	12.6705	11.6828	17.3924
32	Ru	13.9215	14.0388	8.8429
33	Ru	13.9655	14.009	17.4385
34	Ru	15.3183	16.323	8.9071
35	Ru	15.3263	16.4532	13.1394
36	Ru	15.1825	16.427	17.3909
37	Ru	15.1963	17.919	11.0456
38	Ru	15.1405	18.042	15.236
39	Ru	14.033	9.5768	13.0809
40	Ru	12.9505	8.74	15.2264
41	Ru	15.2718	11.8888	8.7339
42	Ru	14.0005	11.0565	10.9182
43	Ru	13.922	11.0203	15.1453
44	Ru	15.2445	11.813	17.2736
45	Ru	16.564	14.123	8.7979
46	Ru	16.6318	14.1523	13.1326
47	Ru	16.521	14.2047	17.2944
48	Ru	16.62	15.6453	11.0448
49	Ru	16.6978	15.7905	15.3132
50	Ru	16.4898	9.5258	12.9748
51	Ru	16.6368	11.0455	10.9665
52	Ru	18.0625	11.61	13.1253
53	Ru	16.523	10.734	15.2789
54	Ru	17.947	13.4047	11.062
55	Ru	17.9548	13.293	15.2519
56	C	16.4213	6.5455	16.8119
57	C	15.7585	7.7763	16.2417
58	C	19.445	18.3073	12.9074
59	C	18.224	17.5623	13.3645
60	C	13.9365	9.21	5.5162
61	C	13.9573	10.1685	6.6768
62	C	7.9318	19.1433	15.7232
63	C	9.282	18.8142	15.1562
64	C	20.8305	13.7388	7.7451
65	C	19.554	13.6968	8.5457
66	C	7.746	16.7858	8.4016
67	C	8.9718	16.079	8.93
68	C	5.5018	10.9948	13.1846
69	C	6.8418	11.6765	13.0811
70	C	15.1558	12.5838	21.5597
71	C	14.9503	12.7333	20.0738
72	C	22.1983	12.126	14.6203
73	C	20.701	12.2595	14.4604
74	C	10.2583	6.98	9.608
75	C	10.776	8.1135	10.453
76	C	9.4468	16.537	20.6047
77	C	10.311	16.0608	19.4613
78	C	9.4865	9.072	18.843
79	C	10.3955	9.8288	17.9072
80	O	9.285	18.3838	13.9043
81	O	10.3208	18.95	15.8475
82	O	12.8373	10.7128	7.0075
83	O	15.0718	10.3988	7.2496
84	O	17.204	17.5313	12.5723

85	O	18.2408	16.9893	14.4963
86	O	16.5295	8.7315	15.8977
87	O	14.4768	7.759	16.1785
88	O	18.474	14.0273	7.9386
89	O	19.6123	13.3223	9.7625
90	O	9.3195	16.3632	10.1312
91	O	9.5715	15.276	8.1344
92	O	7.873	10.9535	12.9007
93	O	6.863	12.9565	13.201
94	O	15.6815	11.9875	19.3138
95	O	14.088	13.559	19.6487
96	O	20.0895	12.973	15.3239
97	O	20.1695	11.653	13.4662
98	O	10.9883	7.89	11.6935
99	O	10.9395	9.252	9.8813
100	O	11.2323	16.8525	19.0663
101	O	10.0563	14.9065	18.9719
102	O	11.4768	10.306	18.4083
103	O	10.0473	9.9618	16.692
104	H	8.1548	15.799	13.039
105	H	11.3303	19.8085	13.6484
106	H	12.4118	18.079	17.0742
107	H	11.612	12.7652	18.5432
108	H	8.3395	13.7958	11.134
109	H	8.206	13.4925	15.2727
110	H	9.8023	13.1612	9.2531
111	H	11.2788	15.8465	9.3886
112	H	12.5217	14.8133	18.3716
113	H	12.2638	19.4238	11.9322
114	H	14.7803	19.4995	11.8799
115	H	13.2038	19.507	14.6869
116	H	10.0645	10.1735	12.0643
117	H	11.237	12.6655	7.7667
118	H	13.619	10.4878	9.3418
119	H	11.2738	8.8888	14.8619
120	H	14.081	17.1435	7.7979
121	H	13.9165	17.0695	18.4246
122	H	13.9828	10.5198	17.6054
123	H	15.3035	19.1935	13.9058
124	H	15.5208	15.113	18.5263
125	H	15.7928	18.028	9.3704
126	H	15.4888	18.154	16.9671
127	H	11.171	12.507	16.3935
128	H	12.888	8.1485	13.631
129	H	16.8858	11.2885	9.1538
130	H	15.3935	9.913	10.4967
131	H	16.8528	11.011	16.991
132	H	18.3907	14.8843	15.5568
133	H	18.3148	15.1708	11.1852
134	H	18.035	13.2845	17.0123
135	H	18.3635	13.5018	13.4779
136	H	18.342	9.9405	12.9958
137	H	18.4318	11.5935	11.3701
138	H	18.1685	11.476	14.9635
139	H	15.9135	5.641	16.4559
140	H	16.3228	6.5745	17.9075
141	H	17.4853	6.5225	16.5565
142	H	16.633	18.5973	15.3761
143	H	20.1892	18.3565	13.7075
144	H	19.1615	19.3185	12.5866
145	H	19.8738	17.7908	12.0357
146	H	9.5445	14.9625	15.7474
147	H	14.7983	8.5363	5.5604
148	H	13.9928	9.7883	4.582
149	H	12.9973	8.6455	5.505
150	H	13.6893	18.3557	16.1359
151	H	8.0252	19.51	16.7495
152	H	7.3005	18.2435	15.703
153	H	7.4393	19.898	15.0943
154	H	9.6163	13.2733	17.0404
155	H	21.698	13.57	8.3907
156	H	20.9158	14.7058	7.2327
157	H	20.7948	12.9603	6.9698
158	H	10.844	16.453	16.6668
159	H	7.38	16.298	7.4927
160	H	8.0103	17.828	8.1708
161	H	6.9665	16.8028	9.1728
162	H	9.339	11.674	14.872
163	H	4.7008	11.6592	12.843
164	H	5.3178	10.7485	14.2412
165	H	5.5048	10.0608	12.6126
166	H	12.6198	14.8438	7.7347
167	H	14.6358	13.3788	22.1026
168	H	16.229	12.6013	21.789
169	H	14.7665	11.6065	21.8798
170	H	12.266	18.0818	9.1915
171	H	22.6025	11.4068	13.9012
172	H	22.4322	11.8125	15.646
173	H	22.6668	13.1075	14.462
174	H	17.111	15.938	9.2932
175	H	10.4743	7.1545	8.5488
176	H	9.1657	6.928	9.7347
177	H	10.6808	6.026	9.9424
178	H	15.2845	8.2665	12.7803
179	H	8.6467	15.8193	20.8114
180	H	9.0213	17.519	20.3601
181	H	10.07	16.6653	21.5004
182	H	16.1197	12.9445	7.5478
183	H	8.783	8.451	18.2796
184	H	8.9198	9.796	19.4459
185	H	10.0803	8.4585	19.5312
186	H	16.9805	16.2237	17.0768

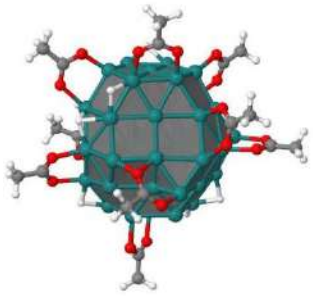

Domain 27 – $Ru_{55}(CH_3COO)_{10}(H)_{10}$

1	Ru	14.9639	13.5165	15.9732
2	Ru	15.0676	13.4069	11.6413
3	Ru	15.0385	11.9094	13.8631
4	Ru	13.5686	15.6981	15.9412
5	Ru	13.5311	15.6811	11.5794
6	Ru	12.2372	13.3137	15.89
7	Ru	13.6941	14.1801	13.7962
8	Ru	12.3495	13.3067	11.6872
9	Ru	12.299	11.6991	13.7757
10	Ru	12.1975	16.45	13.7578
11	Ru	10.9858	14.047	13.7183
12	Ru	8.3795	13.9776	13.6254
13	Ru	9.527	16.1781	13.7726
14	Ru	9.5685	11.5952	13.8079
15	Ru	10.6712	18.4826	13.6587
16	Ru	10.9731	13.8664	9.5606
17	Ru	9.7767	13.1155	11.7065
18	Ru	9.6128	13.2659	15.752
19	Ru	10.8443	14.0759	17.8889
20	Ru	12.2904	16.3391	9.5262
21	Ru	10.8265	15.5147	11.5934
22	Ru	10.8329	15.5372	15.8091
23	Ru	12.0763	16.4033	17.9066
24	Ru	12.1273	17.8508	11.6606
25	Ru	13.3715	18.7828	13.6816
26	Ru	12.0579	17.9555	15.8785
27	Ru	11.1178	9.4281	13.8998
28	Ru	12.4195	11.7712	9.5533
29	Ru	11.067	10.9936	11.6508
30	Ru	11.0271	11.0195	15.8278
31	Ru	12.2618	11.8263	17.9178
32	Ru	13.6239	14.023	9.5794
33	Ru	13.5108	14.0959	18.0634
34	Ru	14.8136	16.2799	9.5141
35	Ru	14.9121	16.6101	13.8337
36	Ru	14.62	16.5029	18.0715
37	Ru	14.6785	17.9445	11.7012
38	Ru	14.4688	18.023	15.9611
39	Ru	13.8599	9.5982	13.8438
40	Ru	12.5169	8.8328	15.7744
41	Ru	15.0155	11.714	9.667
42	Ru	13.7352	11.07	11.6908
43	Ru	13.6588	11.0203	15.9446
44	Ru	14.8659	11.9065	17.9603
45	Ru	16.1754	14.3019	9.5262
46	Ru	16.4047	14.1942	13.8631
47	Ru	16.0458	14.468	18.0426
48	Ru	16.1798	15.7002	11.6494
49	Ru	16.2043	15.8247	16.014
50	Ru	16.3426	9.6927	13.9726
51	Ru	16.3677	11.1243	11.7986
52	Ru	17.7077	11.9227	13.8449
53	Ru	16.3042	11.2531	15.9342
54	Ru	17.6067	13.5651	11.718
55	Ru	17.5419	13.4112	16.0821
56	C	5.188	11.036	13.641
57	C	6.541	11.6967	13.6595
58	C	14.3289	12.6617	22.2158
59	C	14.3159	12.8156	20.7172
60	C	20.192	13.5883	8.1032
61	C	18.9972	13.6177	9.0182
62	C	7.6008	16.4784	8.7021
63	C	8.8133	15.8528	9.3377
64	C	9.5653	21.4385	16.6953
65	C	10.2041	20.2721	15.9911
66	C	19.0409	18.4715	14.03
67	C	17.7644	17.7609	14.387
68	C	15.8995	6.0418	15.6803
69	C	14.8773	7.071	15.2944
70	C	13.7741	9.791	5.9374
71	C	13.7446	10.4747	7.2758
72	C	21.732	12.2896	15.5355
73	C	20.2557	12.4635	15.3009
74	C	8.9543	7.2371	10.8133
75	C	9.7473	8.3182	11.4948
76	O	6.5634	12.9832	13.6354
77	O	7.577	10.9458	13.6926
78	O	13.6825	13.7986	20.2154
79	O	14.9402	11.9132	20.0323
80	O	17.8583	13.898	8.4678
81	O	19.1622	13.392	10.2553
82	O	9.1182	16.2267	10.5185
83	O	9.464	14.9693	8.6646
84	O	10.9944	19.5299	16.6793
85	O	9.939	20.0896	14.7552
86	O	16.7621	17.8651	13.6038
87	O	17.7493	17.0597	15.4624
88	O	13.8008	7.1618	15.9639
89	O	15.144	7.8408	14.278
90	O	14.8603	10.7525	7.8324
91	O	12.5974	10.7255	7.805
92	O	19.6096	13.2111	16.1171
93	O	19.7192	11.8457	14.3164
94	O	10.021	8.1529	12.7392
95	O	10.1039	9.3404	10.8184
96	H	5.2834	9.9495	13.7267
97	H	4.6705	11.2911	12.7056
98	H	4.5773	11.4269	14.4659
99	H	15.2512	12.1678	22.5422
100	H	13.4803	12.0269	22.5131
101	H	14.2131	13.6358	22.7027
102	H	21.0271	13.0623	8.5764
103	H	20.4984	14.6235	7.8907
104	H	19.9284	13.119	7.1478
105	H	7.5479	16.2335	7.6367
106	H	7.6253	17.5654	8.848
107	H	6.699	16.1001	9.2061
108	H	8.5914	21.6678	16.2498
109	H	10.2128	22.3212	16.5819
110	H	9.464	21.2258	17.7652
111	H	19.7354	18.4772	14.8764
112	H	18.8255	19.4956	13.7007
113	H	19.5072	17.9429	13.1852
114	H	16.5062	5.7488	14.8168
115	H	15.4132	5.1694	16.1302
116	H	16.5677	6.4841	16.436
117	H	12.7764	9.7743	5.4877
118	H	14.1294	8.7585	6.0696
119	H	14.4863	10.2994	5.2752
120	H	17.9393	15.3233	11.8457
121	H	16.4309	10.6464	10.0624
122	H	13.5502	17.0737	8.4602
123	H	10.9091	15.5496	18.9627
124	H	11.5752	17.9388	9.9145
125	H	13.3377	17.2052	19.0495
126	H	9.1822	13.5532	17.4936
127	H	18.1305	11.7253	12.063
128	H	22.194	11.7356	14.7129
129	H	21.8851	11.745	16.478
130	H	22.2072	13.2729	15.6475
131	H	17.7862	14.0408	17.7464
132	H	8.8787	7.4299	9.7392
133	H	7.9469	7.1998	11.2529
134	H	9.4235	6.261	10.9936
135	H	8.9807	17.8875	13.5047

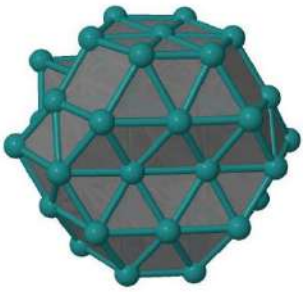

Domain 1 – Ru_{55}

1	Ru	11.0177	9.5196	8.7214	29	Ru	17.4431	11.6471	4.4877
2	Ru	12.3433	11.7107	8.7628	30	Ru	16.2502	10.9666	6.5890
3	Ru	12.2477	7.1318	8.7968	31	Ru	17.6195	11.8606	8.7913
4	Ru	13.5503	13.9180	8.7740	32	Ru	16.2719	10.9841	10.9529
5	Ru	13.5412	9.4002	4.6399	33	Ru	17.4632	11.6387	13.0537
6	Ru	12.2754	8.6542	6.7043	34	Ru	17.4657	13.1897	6.6635
7	Ru	13.5666	9.4493	8.7722	35	Ru	17.4157	13.2236	10.9227
8	Ru	12.2215	8.7222	10.7934	36	Ru	16.3458	4.9111	8.8718
9	Ru	13.5420	9.4426	12.8963	37	Ru	14.9490	4.2148	10.7713
10	Ru	14.8758	11.7085	4.6093	38	Ru	17.4277	7.1342	4.6019
11	Ru	13.5620	10.9475	6.6584	39	Ru	16.2454	6.3757	6.6962
12	Ru	14.9422	11.7665	8.7781	40	Ru	17.6339	7.1759	8.8008
13	Ru	13.5627	10.9654	10.8637	41	Ru	16.2300	6.3522	10.9235
14	Ru	14.8537	11.7023	12.9068	42	Ru	17.5436	7.1844	12.9169
15	Ru	14.8603	13.2041	6.7012	43	Ru	18.7591	9.4625	4.5305
16	Ru	16.1952	14.0318	8.7306	44	Ru	17.5634	8.6645	6.5702
17	Ru	14.8608	13.2387	10.8360	45	Ru	19.0139	9.4922	8.7783
18	Ru	13.5838	4.9205	8.8022	46	Ru	17.6067	8.7693	10.9589
19	Ru	14.8748	7.1414	4.6440	47	Ru	18.7203	9.4748	13.0719
20	Ru	13.5816	6.3891	6.6991	48	Ru	18.8033	10.9258	6.6441
21	Ru	14.8712	7.1135	8.7751	49	Ru	18.8180	11.0079	10.9071
22	Ru	13.5912	6.3992	10.8269	50	Ru	18.7820	4.9084	8.7935
23	Ru	14.8978	7.1291	12.9477	51	Ru	18.8300	6.3916	6.7084
24	Ru	16.1593	9.4286	4.5482	52	Ru	20.1957	7.1782	8.7551
25	Ru	14.8992	8.6943	6.6393	53	Ru	18.8657	6.4239	10.8632
26	Ru	16.2686	9.4567	8.7912	54	Ru	20.1026	8.6538	6.6619
27	Ru	14.8805	8.6479	10.9447	55	Ru	20.0936	8.6539	10.9216
28	Ru	16.1363	9.3995	13.0018					

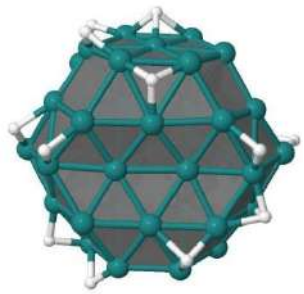

Domain 2 – $Ru_{55}(H)_{17}$

1	Ru	17.5321	8.7095	11.0068	5	Ru	16.1417	10.9699	6.6506
2	Ru	17.5076	8.6472	6.5918	6	Ru	14.7497	8.5814	10.9445
3	Ru	17.5916	7.1514	8.8106	7	Ru	16.2198	9.4179	8.8062
4	Ru	16.1266	10.8793	10.9981	8	Ru	14.8835	8.5481	6.6838

9	Ru	14.8377	7.0298	8.8327
10	Ru	14.7967	11.6666	8.7891
11	Ru	13.4650	9.3088	8.7281
12	Ru	10.9423	9.4479	8.6740
13	Ru	12.1542	11.5826	8.7994
14	Ru	12.1338	6.9729	8.6376
15	Ru	13.3911	13.8073	8.8575
16	Ru	13.5385	9.3204	4.5935
17	Ru	12.2167	8.5251	6.6046
18	Ru	12.1264	8.6543	10.7720
19	Ru	13.5079	9.3459	12.9464
20	Ru	14.7315	11.6540	4.6166
21	Ru	13.4757	10.9015	6.7116
22	Ru	13.4148	10.8331	10.8450
23	Ru	14.7018	11.6363	12.9271
24	Ru	14.7253	13.2019	6.8248
25	Ru	16.1772	14.0626	8.8744
26	Ru	14.6851	13.1189	10.8784
27	Ru	13.6550	4.8038	8.8877
28	Ru	14.9219	7.1083	4.6336
29	Ru	13.5857	6.2953	6.6927
30	Ru	13.3561	6.3511	10.8092
31	Ru	14.8232	6.9274	12.9458
32	Ru	16.0814	9.4809	4.5823
33	Ru	16.0774	9.2642	13.0541
34	Ru	17.4442	11.6255	4.5987
35	Ru	17.4660	11.8634	8.8849
36	Ru	17.2424	11.6682	13.0779
37	Ru	17.3572	13.2081	6.7697
38	Ru	17.2028	13.2246	11.0911
39	Ru	16.2815	4.8412	8.9463
40	Ru	14.8469	4.5552	11.3856
41	Ru	17.4936	7.1734	4.5795
42	Ru	16.2510	6.3155	6.7339
43	Ru	16.2924	6.3652	10.8866
44	Ru	17.5780	7.1446	12.9738
45	Ru	18.6670	9.4612	4.5505
46	Ru	18.9188	9.4857	8.7900
47	Ru	18.6572	9.4573	13.0969
48	Ru	18.7222	11.0226	6.7458
49	Ru	18.7053	11.0031	10.9176
50	Ru	18.7696	4.9135	8.6253
51	Ru	18.9020	6.4342	6.6804
52	Ru	20.1749	7.1268	8.8402
53	Ru	18.8297	6.3894	10.9196
54	Ru	20.0690	8.7559	6.7154
55	Ru	20.0796	8.7412	10.8796
56	H	11.6729	13.3685	8.8501
57	H	13.3022	10.8858	3.7628
58	H	10.7433	7.7890	7.6769
59	H	11.6473	6.6719	10.4698
60	H	16.1092	14.6353	7.1443
61	H	17.1264	14.8170	10.2054
62	H	13.8123	5.7191	5.0105
63	H	14.7044	8.3692	14.1298
64	H	14.6599	5.0603	13.0937
65	H	18.7333	12.7569	5.7193
66	H	14.9821	3.6239	9.7557
67	H	18.6623	8.0774	3.4366
68	H	18.8906	6.0767	4.9023
69	H	18.8652	7.9664	14.0213
70	H	19.1425	11.2516	12.7556
71	H	21.3922	7.9471	9.9062
72	H	19.9803	5.2399	9.8883

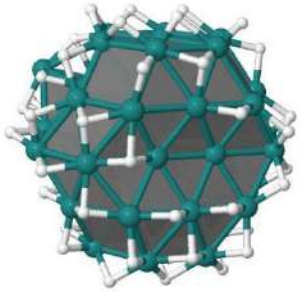

Domain 3 – $Ru_{55}(H)_{53}$

1	Ru	17.5999	8.6522	11.0012
2	Ru	17.7265	8.5796	6.6207
3	Ru	17.7054	7.1060	8.8309
4	Ru	16.1687	10.9548	11.0508
5	Ru	16.2435	11.0443	6.5750
6	Ru	14.8227	8.6577	10.8934
7	Ru	16.3381	9.4580	8.7803
8	Ru	14.9459	8.6618	6.5513
9	Ru	15.0192	7.1426	8.7146
10	Ru	14.9170	11.7891	8.8078
11	Ru	13.6645	9.4390	8.7218
12	Ru	10.9227	9.4530	8.5585
13	Ru	12.2078	11.6552	8.7135
14	Ru	12.0915	6.9603	8.6689
15	Ru	13.4861	13.8821	8.7621
16	Ru	13.6479	9.3514	4.5145
17	Ru	12.3840	8.4996	6.6855
18	Ru	12.2308	8.5609	10.6625
19	Ru	13.4542	9.2489	12.9188
20	Ru	14.9232	11.7155	4.5276
21	Ru	13.5968	10.9396	6.6556
22	Ru	13.5057	10.9193	10.8410
23	Ru	14.7622	11.6622	13.0367
24	Ru	14.8961	13.2668	6.6369
25	Ru	16.1004	14.1994	8.8528
26	Ru	14.8246	13.2400	10.9628
27	Ru	13.5557	4.7045	8.8102
28	Ru	15.0448	7.1009	4.5639
29	Ru	13.6509	6.3341	6.6954
30	Ru	13.5688	6.4124	10.6698
31	Ru	14.8617	6.9621	12.9137
32	Ru	16.3055	9.4058	4.4691
33	Ru	16.0853	9.3291	13.1043
34	Ru	17.5718	11.7858	4.5682
35	Ru	17.5590	11.8395	8.8800
36	Ru	17.3476	11.6119	13.1570
37	Ru	17.4429	13.2650	6.7474
38	Ru	17.3721	13.2043	10.9853

39	Ru	16.3074	4.7372	8.9741
40	Ru	14.6777	4.2834	11.1645
41	Ru	17.6335	7.2037	4.5495
42	Ru	16.4062	6.2553	6.6980
43	Ru	16.2282	6.3535	10.8754
44	Ru	17.4295	7.0754	13.0141
45	Ru	18.9377	9.5012	4.6078
46	Ru	18.9807	9.5981	8.9092
47	Ru	18.7515	9.3382	13.1327
48	Ru	18.9071	11.0788	6.8020
49	Ru	18.7968	11.0506	11.0290
50	Ru	18.8131	4.8630	8.7820
51	Ru	19.0518	6.3950	6.6249
52	Ru	20.3569	7.0637	8.8130
53	Ru	18.9326	6.3997	10.9691
54	Ru	20.2537	8.8291	6.8125
55	Ru	20.1345	8.6764	10.9676
56	H	9.3149	9.4925	8.5644
57	H	12.6919	3.4571	9.3736
58	H	10.4803	11.1240	8.8598
59	H	12.0985	13.2078	9.6916
60	H	10.6862	7.9121	7.6875
61	H	11.7737	8.9645	12.3347
62	H	13.1522	11.1640	4.8163
63	H	12.2152	13.1932	7.7042
64	H	11.9960	8.8589	4.9709
65	H	13.0016	11.0371	12.6645
66	H	14.5709	13.4030	4.8449
67	H	14.6898	14.8285	7.7221
68	H	14.2493	13.3082	12.6814
69	H	13.7183	7.8378	3.5806
70	H	12.8286	4.7450	7.1979
71	H	13.8701	5.7824	5.0101
72	H	11.9156	5.1346	9.1057
73	H	13.8150	5.4437	12.4390
74	H	14.9452	10.1437	3.4153
75	H	14.7006	10.0197	14.1102
76	H	16.2967	12.4906	3.5920
77	H	16.0616	12.5128	13.9854
78	H	17.4342	14.7205	7.8216
79	H	17.8607	13.4567	4.9726
80	H	19.2262	12.7693	7.1400
81	H	17.3918	14.6984	9.9892
82	H	16.3809	5.8345	4.8030
83	H	15.1175	4.8987	7.6613
84	H	16.3452	4.5079	11.1949
85	H	16.0897	6.3722	14.0675
86	H	17.7236	10.2368	3.4532
87	H	18.7398	7.8621	14.0853
88	H	20.5929	10.5889	7.0980
89	H	19.1870	12.7824	10.9821
90	H	17.6713	3.5651	9.1055
91	H	19.0459	6.1082	4.8619
92	H	17.8277	5.0712	6.7574
93	H	20.5475	5.3525	8.4227
94	H	18.5528	5.7146	12.5684
95	H	19.5038	4.6637	10.3099
96	H	20.6065	9.0688	5.0760
97	H	20.7949	7.0711	6.9733
98	H	20.8350	8.7636	9.1678
99	H	20.7762	6.8834	10.5554
100	H	10.4608	8.5416	9.9059
101	H	14.5262	14.7977	9.9538
102	H	13.3659	7.7074	13.7567
103	H	17.4422	9.9734	14.2467
104	H	14.9505	3.5252	9.4698
105	H	18.9349	8.0458	3.5995
106	H	19.3577	11.3275	5.0244
107	H	19.1822	11.1809	12.8338
108	H	20.4518	9.0152	12.6977

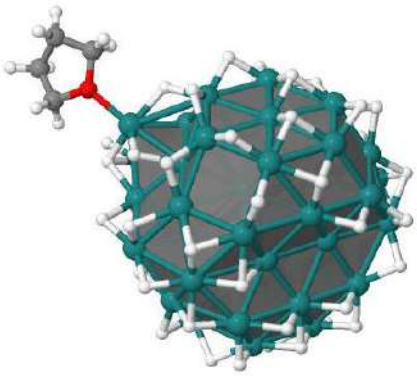

Domain 46 – $Ru_{55}(THF)(H)_{53}$

1	Ru	15.4913	13.8912	15.3175
2	Ru	15.5934	13.8135	10.9563
3	Ru	15.5760	12.3287	13.1687
4	Ru	14.0255	16.1608	15.3913
5	Ru	14.0826	16.2654	10.9073
6	Ru	12.6965	13.8562	15.2477
7	Ru	14.1983	14.6758	13.1157
8	Ru	12.8142	13.8640	10.8917
9	Ru	12.9015	12.3452	13.0583
10	Ru	12.7722	16.9922	13.1519
11	Ru	11.5251	14.6250	13.0665
12	Ru	8.7914	14.6169	12.8980
13	Ru	10.0576	16.8364	13.0549
14	Ru	10.0037	12.1615	13.0183
15	Ru	11.3188	19.0774	13.1284
16	Ru	11.5142	14.5612	8.8504
17	Ru	10.2396	13.7118	11.0074
18	Ru	10.1050	13.7417	15.0196
19	Ru	11.3320	14.4545	17.2648
20	Ru	12.7771	16.9344	8.8727
21	Ru	11.4450	16.1367	11.0013
22	Ru	11.3651	16.1149	15.1845
23	Ru	12.6257	16.8753	17.3802
24	Ru	12.7129	18.4654	10.9949
25	Ru	13.9439	19.4233	13.1796
26	Ru	12.6899	18.4427	15.3034

27	Ru	11.4443	9.9106	13.0817
28	Ru	12.9103	12.3239	8.8892
29	Ru	11.5500	11.5548	11.0374
30	Ru	11.4837	11.5848	15.0204
31	Ru	12.7681	12.1882	17.2753
32	Ru	14.1782	14.6360	8.8062
33	Ru	13.9678	14.5482	17.4430
34	Ru	15.4180	17.0185	8.9084
35	Ru	15.3981	17.0796	13.2118
36	Ru	15.2137	16.8454	17.4862
37	Ru	15.2872	18.4979	11.0999
38	Ru	15.2099	18.4195	15.3233
39	Ru	14.1586	9.9558	13.3167
40	Ru	12.5967	9.4649	15.5622
41	Ru	15.5024	12.4461	8.8794
42	Ru	14.2921	11.4866	11.0293
43	Ru	14.1110	11.5797	15.2115
44	Ru	15.3367	12.2928	17.3297
45	Ru	16.8021	14.7450	8.9461
46	Ru	16.8393	14.8344	13.2424
47	Ru	16.6294	14.5771	17.4623
48	Ru	16.7596	16.3223	11.1393
49	Ru	16.6608	16.2793	15.3582
50	Ru	16.6696	10.0842	13.0754
51	Ru	16.9368	11.6481	10.9402
52	Ru	18.2269	12.2733	13.1390
53	Ru	16.8163	11.6036	15.2846
54	Ru	18.1228	14.0765	11.1542
55	Ru	18.0133	13.9030	15.2962
56	C	11.4797	6.4381	15.5848
57	C	10.5771	7.7465	17.4014
58	C	10.1663	6.2916	17.5738
59	C	10.2409	5.7506	16.1371
60	O	11.5387	7.7368	16.2844
61	H	7.1812	14.6592	12.8823
62	H	10.6283	8.5259	13.1544
63	H	8.3417	16.2908	13.1993
64	H	9.9471	18.3744	14.0582
65	H	8.5945	13.0619	12.0239
66	H	9.6523	14.1390	16.6991
67	H	11.0085	16.3700	9.1612
68	H	10.0408	18.4012	12.0779
69	H	9.8582	14.0695	9.2899
70	H	10.8684	16.2411	17.0181
71	H	12.3831	18.6091	9.2048
72	H	12.5068	20.0306	12.0763
73	H	12.0999	18.5157	17.0237
74	H	11.6028	13.0505	7.8950
75	H	10.6398	9.9390	11.5867
76	H	11.7706	10.9978	9.3425
77	H	9.8688	10.3265	13.6281
78	H	11.8115	10.6218	16.8848
79	H	12.8139	15.3704	7.7560
80	H	12.5876	15.2278	18.4548
81	H	14.1248	17.7304	7.9402
82	H	13.9144	17.7367	18.3191
83	H	15.2225	20.0017	12.1053
84	H	15.6943	18.6868	9.3141
85	H	17.0863	18.0175	11.4334
86	H	15.2302	19.9184	14.3268
87	H	14.2502	11.0645	9.1568
88	H	12.9830	9.8563	11.9988
89	H	14.2588	9.7322	15.4449
90	H	14.0265	11.6352	18.4282
91	H	15.5899	15.4767	7.7882
92	H	16.6190	13.1196	18.4263
93	H	18.4511	15.8539	11.3936
94	H	17.0271	18.0276	15.3160
95	H	15.5484	8.7726	13.3345
96	H	16.9224	11.3245	9.2004
97	H	15.7433	10.3064	11.0791
98	H	18.4274	10.5649	12.7795
99	H	16.5122	10.9912	16.9567
100	H	17.3248	9.8399	14.6102
101	H	18.4665	14.3001	9.4125
102	H	18.6775	12.3207	11.2993
103	H	18.6595	14.0084	13.4612
104	H	18.6499	12.0997	14.8821
105	H	8.3583	13.6777	14.2472
106	H	12.3636	20.0011	14.3107
107	H	11.2702	12.8926	18.1014
108	H	15.3231	15.1976	18.5818
109	H	12.8596	8.7001	13.9783
110	H	16.8191	13.2876	7.9437
111	H	17.2105	16.5701	9.3570
112	H	17.0527	16.4165	17.1570
113	H	18.3290	14.2358	17.0247
114	H	11.4452	6.6537	14.5107
115	H	12.4064	5.8979	15.8293
116	H	10.3275	4.6573	16.0970
117	H	9.3500	6.0472	15.5646
118	H	9.1644	6.2017	18.0122
119	H	10.8759	5.7624	18.2261
120	H	11.0893	8.1869	18.2654
121	H	9.7353	8.3907	17.1070

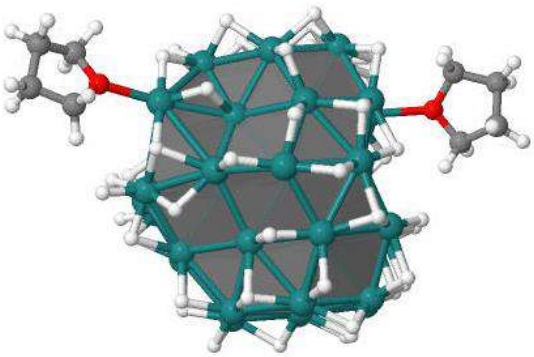

Domain 49 – $Ru_{55}(THF)_2(H)_{53}$

1	Ru	14.9092	13.4406	15.1112
2	Ru	14.9951	13.3712	10.7258
3	Ru	14.9413	11.8661	12.9514
4	Ru	13.4942	15.6796	15.1909
5	Ru	13.5285	15.8490	10.7427
6	Ru	12.1222	13.4114	15.0643
7	Ru	13.6452	14.2466	12.9028
8	Ru	12.2229	13.4696	10.6811
9	Ru	12.3023	11.9355	12.8346
10	Ru	12.2349	16.5652	12.9940
11	Ru	10.9602	14.2234	12.8705
12	Ru	8.2112	14.2670	12.7048
13	Ru	9.5232	16.4440	12.9371
14	Ru	9.3438	11.7195	12.7879
15	Ru	10.8212	18.6638	13.0170
16	Ru	10.9127	14.2068	8.6713
17	Ru	9.6464	13.3210	10.8343
18	Ru	9.5316	13.3190	14.7867
19	Ru	10.7590	13.9589	17.0772
20	Ru	12.2227	16.5687	8.7270
21	Ru	10.8753	15.7557	10.8267
22	Ru	10.8081	15.6655	15.0309
23	Ru	12.0895	16.3598	17.2073
24	Ru	12.1935	18.0641	10.8581
25	Ru	13.4490	18.9789	13.0109
26	Ru	12.2433	17.9762	15.1712
27	Ru	10.8408	9.4546	12.7916
28	Ru	12.2739	11.9406	8.6772
29	Ru	10.9320	11.1732	10.8274
30	Ru	10.8691	11.1843	14.7385
31	Ru	12.1486	11.6857	17.0672
32	Ru	13.5667	14.2328	8.6024
33	Ru	13.3918	14.0396	17.2467
34	Ru	14.8460	16.6173	8.7425
35	Ru	14.8779	16.6313	13.0431
36	Ru	14.6981	16.3781	17.2987
37	Ru	14.7824	18.0574	10.9432
38	Ru	14.6715	18.0076	15.1731
39	Ru	13.4811	9.5302	13.0338
40	Ru	11.8585	9.1600	15.5342
41	Ru	14.8745	12.0284	8.6415
42	Ru	13.6535	11.0654	10.7989
43	Ru	13.5027	11.0984	14.9942
44	Ru	14.7391	11.7710	17.0981
45	Ru	16.1993	14.3200	8.7112
46	Ru	16.2823	14.2816	13.0048
47	Ru	16.0346	14.0421	17.2645
48	Ru	16.1992	15.8461	10.9444
49	Ru	16.1630	15.7194	15.1199
50	Ru	15.9922	9.5990	12.8146
51	Ru	16.2974	11.1509	10.7012
52	Ru	17.5974	11.7724	12.8950
53	Ru	16.2024	11.0932	15.0355
54	Ru	17.5244	13.5772	10.9011
55	Ru	17.4306	13.3367	15.1074
56	C	10.3598	6.3159	15.3922
57	C	9.7195	7.5597	17.3566
58	C	9.3314	6.1023	17.5437
59	C	9.2100	5.6065	16.0936
60	C	18.8848	17.0000	16.2476
61	C	18.6434	17.4958	13.9073
62	C	20.1163	17.3066	14.2234
63	C	20.1706	17.6279	15.7242
64	O	17.9419	17.0357	15.1166
65	O	10.5666	7.5643	16.1552
66	H	6.6039	14.3513	12.7623
67	H	10.0360	8.0712	12.7091
68	H	7.7817	15.9515	12.9379
69	H	9.4475	18.0023	13.9436
70	H	7.9914	12.7175	11.8101
71	H	9.0813	13.6820	16.4752
72	H	10.4256	16.0036	9.0063
73	H	9.5431	17.9815	11.9454
74	H	9.2551	13.7329	9.1307
75	H	10.3167	15.7640	16.8573
76	H	11.8070	18.2384	9.0879
77	H	11.9573	19.6110	11.9234
78	H	11.5599	18.0156	16.8404
79	H	10.9700	12.7017	7.7010
80	H	10.0665	9.5073	11.3000
81	H	11.1101	10.6435	9.1110
82	H	9.2635	9.8963	13.3870
83	H	11.6787	9.8346	17.1740
84	H	12.2183	15.0116	7.5743
85	H	12.0074	14.7051	18.2755
86	H	13.5825	17.3687	7.7859
87	H	13.3910	17.1538	18.2068
88	H	14.7123	19.5777	11.9270
89	H	15.1832	18.2691	9.1599
90	H	16.5639	17.5439	11.2375
91	H	14.7466	19.4871	14.1498
92	H	13.6034	10.6702	8.9125
93	H	12.2495	8.8477	11.8911
94	H	13.5026	9.4237	15.7309
95	H	13.4133	11.2795	18.2613
96	H	14.9796	15.0853	7.5927
97	H	16.0405	12.5920	18.2074
98	H	17.8899	15.3344	11.1768
99	H	15.2491	18.0233	16.8856
100	H	14.8117	8.3225	13.1018
101	H	16.3211	10.9260	8.9523
102	H	15.0846	9.8583	10.7200
103	H	17.7183	10.0705	12.4129
104	H	15.9434	10.5086	16.7262
105	H	16.6906	9.3606	14.3382
106	H	17.8617	13.8638	9.1551
107	H	18.0363	11.8197	11.0299
108	H	18.1599	13.4305	13.3806
109	H	18.0414	11.4908	14.6091
110	H	7.7749	13.3248	14.0514
111	H	11.8765	19.5545	14.1826
112	H	10.6421	12.3901	17.8895
113	H	14.7201	14.7829	18.3653
114	H	12.0152	8.3873	13.8943
115	H	16.1923	12.8621	7.7097
116	H	16.6555	16.1020	9.1692
117	H	16.4719	15.8564	16.9800
118	H	17.7338	13.6546	16.8459
119	H	10.1588	6.6028	14.3532
120	H	11.3008	5.7493	15.4447
121	H	9.2927	4.5157	16.0071
122	H	8.2461	5.9123	15.6614
123	H	8.3986	5.9945	18.1115
124	H	10.1245	5.5577	18.0764
125	H	10.3154	7.9930	18.1682
126	H	8.8488	8.2031	17.1567
127	H	18.4171	17.5426	17.0796
128	H	19.0163	15.9448	16.5319
129	H	21.0537	17.2083	16.2227
130	H	20.1698	18.7154	15.8868
131	H	20.7562	17.9623	13.6200
132	H	20.4158	16.2646	14.0366
133	H	18.2673	16.8989	13.0682
134	H	18.3770	18.5534	13.7541

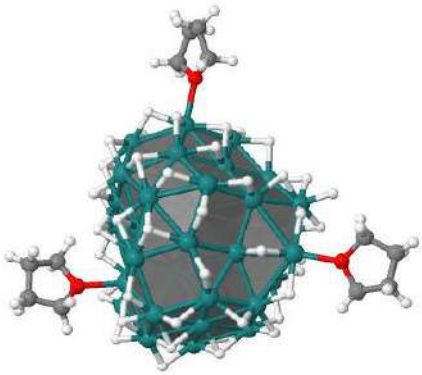

Domain 52 – $Ru_{55}(THF)_3(H)_{53}$

1	Ru	14.7763	13.6443	15.8379
2	Ru	14.8945	13.6624	11.4539
3	Ru	14.8419	12.1042	13.6512
4	Ru	13.3337	15.8818	15.9641
5	Ru	13.3870	16.1178	11.5166
6	Ru	11.9740	13.5811	15.7815
7	Ru	13.5037	14.4697	13.6593
8	Ru	12.1145	13.7288	11.4015
9	Ru	12.1930	12.1521	13.5161
10	Ru	12.0751	16.7785	13.7742
11	Ru	10.8237	14.4269	13.5921
12	Ru	8.0716	14.4272	13.4174
13	Ru	9.3538	16.6203	13.6871
14	Ru	9.2424	11.9155	13.4536
15	Ru	10.6257	18.8429	13.8208
16	Ru	10.8016	14.5117	9.3953
17	Ru	9.5383	13.5635	11.5245
18	Ru	9.3959	13.4676	15.4838
19	Ru	10.5976	14.0734	17.7986
20	Ru	12.0942	16.8670	9.5019
21	Ru	10.7374	16.0059	11.5824
22	Ru	10.6380	15.8239	15.7821
23	Ru	11.8961	16.4938	17.9803
24	Ru	12.0475	18.3257	11.6641
25	Ru	13.2352	19.2046	13.8559
26	Ru	12.0257	18.1451	15.9817
27	Ru	10.7717	9.6551	13.4094
28	Ru	12.1517	12.2492	9.3649
29	Ru	10.8407	11.4205	11.4835
30	Ru	10.7649	11.3491	15.3970
31	Ru	12.0339	11.8285	17.7545
32	Ru	13.4705	14.5530	9.3487
33	Ru	13.2323	14.1932	17.9783
34	Ru	14.7233	16.9586	9.5587
35	Ru	14.7255	16.8728	13.8505
36	Ru	14.5067	16.5488	18.0945
37	Ru	14.6043	18.3404	11.7610
38	Ru	14.4669	18.2113	15.9986
39	Ru	13.4173	9.7779	13.6630
40	Ru	11.7598	9.3194	16.1480
41	Ru	14.7813	12.3498	9.2766
42	Ru	13.5609	11.3682	11.4638
43	Ru	13.3866	11.2986	15.6630
44	Ru	14.6220	11.9467	17.7992
45	Ru	16.1015	14.6757	9.4805
46	Ru	16.1516	14.5392	13.7919
47	Ru	15.8669	14.2320	18.0190
48	Ru	16.0601	16.0871	11.7449
49	Ru	16.0089	15.9436	15.9239
50	Ru	15.9195	9.8549	13.4996
51	Ru	16.1941	11.4428	11.3945
52	Ru	17.4857	12.0248	13.6128
53	Ru	16.0911	11.2913	15.7466
54	Ru	17.4097	13.8654	11.6693
55	Ru	17.2856	13.5501	15.8674
56	C	10.0092	6.6076	16.0395
57	C	9.5532	7.9049	18.0185
58	C	9.0169	6.4971	18.2177
59	C	8.8094	6.0198	16.7716
60	C	18.7002	17.2837	17.0698
61	C	18.4736	17.7491	14.7202
62	C	19.9451	17.7859	15.1014
63	C	19.8938	18.1042	16.6026
64	C	15.0425	10.0499	6.9142
65	C	14.9842	12.2728	6.0242
66	C	14.9160	11.2959	4.8620
67	C	15.5461	10.0318	5.4706
68	O	14.7106	11.4509	7.1983
69	O	17.7789	17.2651	15.9255
70	O	10.3789	7.8140	16.8070
71	H	6.4623	14.4812	13.4763
72	H	9.9837	8.2660	13.2603
73	H	7.6292	16.1233	13.6776
74	H	9.1857	18.1624	14.6714
75	H	7.8792	12.9408	12.4404
76	H	8.9315	13.7912	17.1819
77	H	10.3066	16.2920	9.7439
78	H	9.4358	18.1317	12.6613
79	H	9.1414	14.0307	9.8311
80	H	10.1357	15.8762	17.6125
81	H	11.6194	18.5186	9.9165
82	H	11.7331	19.8469	12.7780
83	H	11.3760	18.1627	17.6691
84	H	10.8683	13.0171	8.3939
85	H	10.0101	9.7333	11.9126
86	H	10.9737	10.9660	9.7260
87	H	9.1831	10.0835	14.0103
88	H	11.6661	9.9663	17.8149
89	H	12.1321	15.3442	8.3248
90	H	11.8363	14.8034	19.0116
91	H	13.4528	17.7113	8.6043
92	H	13.1883	17.2824	19.0108
93	H	14.4441	19.8581	12.7419
94	H	15.1237	18.5932	10.0276
95	H	16.1322	17.6625	12.6839
96	H	14.5520	19.6955	14.9809
97	H	13.5135	10.9993	9.6253
98	H	12.1883	9.0214	12.5510
99	H	13.4172	9.5639	16.2534
100	H	13.3084	11.3941	18.9372
101	H	14.8798	15.4349	8.3634
102	H	15.8797	12.7603	18.9430
103	H	17.7679	15.6050	11.9930
104	H	15.0460	18.2069	17.7106
105	H	14.7342	8.5507	13.6289
106	H	16.2545	11.2012	9.6801
107	H	14.9864	10.1696	11.3110
108	H	17.6750	10.3333	13.1762

109	H	15.8119	10.6710	17.4157
110	H	16.5744	9.5932	15.0594
111	H	17.7688	14.2337	9.9486
112	H	17.9368	12.1000	11.7573
113	H	18.0109	13.6907	14.1417
114	H	17.9076	11.7239	15.3486
115	H	7.6537	13.3914	14.7021
116	H	11.6471	19.7427	15.0128
117	H	10.4950	12.4825	18.5687
118	H	14.5350	14.9324	19.1263
119	H	11.8017	8.5358	14.5342
120	H	16.2108	13.1814	8.5521
121	H	16.5196	16.4328	9.9647
122	H	16.2948	16.0531	17.7880
123	H	17.5769	13.8717	17.6047
124	H	9.8080	6.9272	15.0100
125	H	10.8832	5.9402	16.0550
126	H	8.7750	4.9264	16.6835
127	H	7.8721	6.4253	16.3643
128	H	8.0919	6.4886	18.8078
129	H	9.7606	5.8714	18.7325
130	H	10.2031	8.2767	18.8190
131	H	8.7517	8.6359	17.8292
132	H	18.1522	17.7120	17.9186
133	H	18.9704	16.2413	17.3008
134	H	20.8122	17.8216	17.1335
135	H	19.7173	19.1774	16.7664
136	H	20.4994	18.5341	14.5209
137	H	20.4106	16.8040	14.9300
138	H	18.2294	17.0612	13.9023
139	H	18.0678	18.7462	14.4904
140	H	15.7899	9.7188	7.6479
141	H	14.1175	9.4705	7.0539
142	H	15.2541	9.1132	4.9465
143	H	16.6426	10.1046	5.4447
144	H	15.4593	11.6616	3.9811
145	H	13.8708	11.1145	4.5729
146	H	14.2283	13.0678	6.0112
147	H	15.9836	12.7268	6.1318

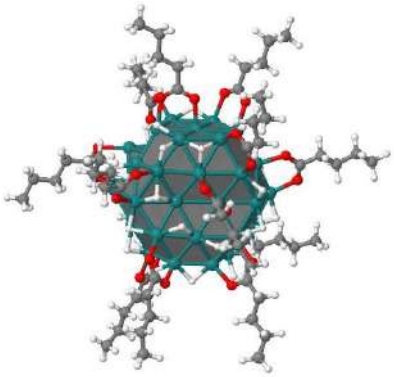

Domain 63 – $Ru_{55}(C_4H_9COO)_{14}(H)_{14}$

1	Ru	18.9684	16.8127	19.6028
2	Ru	19.1944	16.7301	15.2396
3	Ru	19.0906	15.2357	17.4502
4	Ru	17.6404	19.0447	19.5640
5	Ru	17.7244	19.1168	15.2442
6	Ru	16.2808	16.6237	19.4781
7	Ru	17.7982	17.5351	17.4055
8	Ru	16.4834	16.7505	15.2508
9	Ru	16.3115	15.0590	17.3351
10	Ru	16.3419	19.8524	17.3739
11	Ru	15.1056	17.4510	17.2819
12	Ru	12.4823	17.4309	17.1766
13	Ru	13.6764	19.5858	17.3561
14	Ru	13.5789	14.9989	17.3584
15	Ru	14.8380	21.9381	17.3439
16	Ru	15.1750	17.4317	13.1359
17	Ru	13.9121	16.6057	15.2352
18	Ru	13.6389	16.6458	19.2626
19	Ru	14.7883	17.3857	21.4338
20	Ru	16.4856	19.7957	13.1804
21	Ru	15.0105	18.9824	15.2071
22	Ru	14.9323	18.9044	19.3896
23	Ru	16.0862	19.7693	21.6053
24	Ru	16.3613	21.3193	15.3084
25	Ru	17.6221	22.1024	17.4016
26	Ru	16.1188	21.3075	19.5584
27	Ru	15.1197	12.7830	17.3797
28	Ru	16.4425	15.2558	13.1231
29	Ru	15.0979	14.4805	15.1475
30	Ru	15.0369	14.3331	19.4296
31	Ru	16.3097	15.1036	21.5366
32	Ru	17.8198	17.5507	13.1929
33	Ru	17.4875	17.4763	21.6746
34	Ru	19.0040	19.8767	13.2057
35	Ru	19.0676	19.8900	17.5126
36	Ru	18.7103	19.8149	21.7176
37	Ru	18.9374	21.4249	15.4416
38	Ru	18.5451	21.4401	19.5860
39	Ru	17.9200	12.9352	17.3699
40	Ru	16.5210	12.0869	19.1490
41	Ru	19.0434	15.2816	13.1095
42	Ru	17.8436	14.4284	15.2560
43	Ru	17.6452	14.3412	19.5073
44	Ru	18.8157	15.2299	21.5942
45	Ru	20.4177	17.7072	13.2467
46	Ru	20.4744	17.4892	17.5367
47	Ru	20.0416	17.7029	21.7401
48	Ru	20.3817	19.0192	15.3428
49	Ru	20.3093	19.0211	19.6859
50	Ru	20.3681	12.9869	17.6314
51	Ru	20.4341	14.4743	15.4635
52	Ru	21.7638	15.1785	17.5380
53	Ru	20.2801	14.5426	19.5650
54	Ru	21.7379	16.8470	15.3923
55	Ru	21.5547	16.6389	19.8107
56	C	14.4229	20.4110	26.0587

57	C	13.8982	20.5753	27.4871
58	C	14.2789	21.9244	28.0999
59	C	14.0499	19.0685	25.4298
60	C	14.5266	18.8753	24.0034
61	C	18.7332	14.8174	26.4831
62	C	18.4766	14.7287	27.9907
63	C	19.2133	13.5667	28.6575
64	C	17.9823	15.9823	25.8427
65	C	18.1134	16.1302	24.3398
66	C	21.4288	23.1649	23.9889
67	C	22.2306	24.2998	24.6309
68	C	22.5881	24.0183	26.0909
69	C	21.0630	23.4506	22.5332
70	C	20.2238	22.3857	21.8616
71	C	12.8111	25.7447	19.6024
72	C	12.3244	26.9957	20.3376
73	C	11.2000	27.7137	19.5893
74	C	13.9267	25.0110	20.3461
75	C	14.4370	23.7623	19.6589
76	C	24.5661	17.6938	10.6435
77	C	25.9629	18.0061	10.0958
78	C	25.9761	18.3053	8.5969
79	C	24.6088	17.3966	12.1396
80	C	23.2878	17.1742	12.8450
81	C	21.0144	23.5331	10.8062
82	C	21.3662	24.8261	10.0667
83	C	21.4491	24.6325	8.5518
84	C	20.9225	23.7143	12.3223
85	C	20.4123	22.4988	13.0677
86	C	26.2708	15.6641	20.7514
87	C	27.6928	15.1468	20.9886
88	C	28.3307	15.6993	22.2631
89	C	25.6659	15.0939	19.4709
90	C	24.2338	15.4802	19.1737
91	C	23.0735	22.8353	16.8276
92	C	24.3189	23.7194	16.7231
93	C	24.2864	24.6483	15.5088
94	C	23.1166	21.9060	18.0388
95	C	21.8903	21.0430	18.2425
96	C	12.1972	11.5462	22.4214
97	C	11.6734	10.4365	23.3372
98	C	10.4580	9.7100	22.7610
99	C	13.4027	12.2696	23.0185
100	C	14.1126	13.2342	22.0941
101	C	19.7755	8.3194	17.1337
102	C	20.3605	6.9060	17.1659
103	C	20.7625	6.4047	15.7777
104	C	19.4130	8.8444	18.5323
105	C	18.7011	10.1747	18.5041
106	C	11.4646	21.4500	12.8643
107	C	10.2609	22.0806	12.1604
108	C	9.8948	23.4524	12.7285
109	C	11.8309	20.0788	12.2906
110	C	13.0229	19.4216	12.9497
111	C	19.0424	13.6784	8.5036
112	C	18.9126	13.1591	7.0691
113	C	20.2653	12.8995	6.4047
114	C	17.6840	13.9408	9.1504
115	C	17.7211	14.4161	10.5854
116	C	8.1527	15.6229	15.8723
117	C	6.8595	14.8915	15.5011
118	C	5.7752	15.8278	14.9664
119	C	9.2238	14.6733	16.4084
120	C	10.5617	15.3061	16.7360
121	C	12.2734	11.2752	12.8647
122	C	11.2082	10.3138	12.3302
123	C	10.6411	10.7420	10.9763
124	C	12.8217	10.8390	14.2226
125	C	13.7765	11.8074	14.8863
126	O	14.2167	11.4891	16.0476
127	O	14.0818	12.8900	14.2798
128	O	11.5535	14.5137	16.8684
129	O	10.6197	16.5865	16.8672
130	O	16.5877	14.5618	11.1749
131	O	18.8540	14.6433	11.1371
132	O	13.7086	18.5905	12.2406
133	O	13.2818	19.7111	14.1632
134	O	17.6438	10.3244	19.2042
135	O	19.1667	11.0999	17.7240
136	O	15.0467	13.9508	22.6320
137	O	13.8123	13.2742	20.8618
138	O	21.9046	20.2454	19.2499
139	O	20.9087	21.1391	17.4347
140	O	23.7107	14.9466	18.1307
141	O	23.6146	16.2813	19.9543
142	O	20.1094	22.6593	14.3125
143	O	20.2765	21.4008	12.4453
144	O	23.3553	16.7878	14.0580
145	O	22.1879	17.4142	12.2208
146	O	15.2034	22.9898	20.3465
147	O	14.0921	23.5398	18.4539
148	O	19.8271	22.6347	20.6581
149	O	19.9484	21.3220	22.4990
150	O	17.4840	17.1046	23.8081
151	O	18.8343	15.2787	23.6940
152	O	14.2319	17.7741	23.4245
153	O	15.1848	19.8359	23.4646
154	H	22.0966	18.6180	15.6272
155	H	19.2879	13.2270	15.0422
156	H	17.6810	20.6922	12.2264
157	H	14.3517	19.1764	21.1323
158	H	15.5864	21.3401	13.7213
159	H	17.4177	20.5865	22.5851
160	H	13.2856	16.5295	21.0613
161	H	22.2034	15.0320	15.7019
162	H	13.4942	13.3299	17.8930
163	H	21.7341	17.1062	21.5446
164	H	17.9263	13.9123	13.4963
165	H	19.3406	18.5557	12.0147
166	H	16.1700	22.9062	16.4778
167	H	13.1888	21.3513	17.3865
168	H	14.4566	18.2282	26.0176
169	H	12.9572	18.9185	25.4284
170	H	14.0363	21.2272	25.4283
171	H	15.5186	20.5237	26.0505
172	H	14.2869	19.7589	28.1198
173	H	12.8002	20.4649	27.4901
174	H	13.8889	22.0312	29.1221
175	H	15.3719	22.0454	28.1444
176	H	13.8803	22.7575	27.5011
177	H	16.9009	15.9076	26.0492
178	H	18.2921	16.9443	26.2845
179	H	19.8133	14.9222	26.2934
180	H	18.4321	13.8751	25.9987
181	H	17.3918	14.6282	28.1679
182	H	18.7735	15.6781	28.4689
183	H	19.0027	13.5214	29.7354
184	H	18.9146	12.6030	28.2183
185	H	20.3025	13.6624	28.5341
186	H	20.5084	24.3994	22.4418
187	H	21.9681	23.5853	21.9165
188	H	22.0011	22.2255	24.0451
189	H	20.5075	22.9899	24.5671
190	H	21.6521	25.2374	24.5663
191	H	23.1531	24.4728	24.0505
192	H	23.1589	24.8460	26.5350
193	H	21.6825	23.8725	26.6989
194	H	23.1965	23.1059	26.1814
195	H	14.7999	25.6714	20.4914
196	H	13.6117	24.7189	21.3604
197	H	11.9647	25.0565	19.4473
198	H	13.1629	26.0187	18.5957
199	H	13.1715	27.6870	20.4871
200	H	11.9781	26.7177	21.3477
201	H	10.8555	28.6054	20.1316
202	H	11.5317	28.0362	18.5908
203	H	10.3322	27.0515	19.4497
204	H	25.2418	16.5215	12.3561
205	H	25.0885	18.2337	12.6780
206	H	23.8907	18.5429	10.4548
207	H	24.1351	16.8349	10.1043
208	H	26.6365	17.1584	10.3092

209	H	26.3801	18.8665	10.6472
210	H	26.9907	18.5385	8.2435
211	H	25.6096	17.4460	8.0158
212	H	25.3326	19.1650	8.3573
213	H	21.8984	23.9921	12.7555
214	H	20.2450	24.5451	12.5801
215	H	20.0523	23.1483	10.4319
216	H	21.7564	22.7534	10.5732
217	H	22.3253	25.2214	10.4432
218	H	20.6093	25.5953	10.2986
219	H	21.6873	25.5730	8.0350
220	H	22.2254	23.8992	8.2862
221	H	20.4951	24.2614	8.1474
222	H	26.2647	15.3798	18.5894
223	H	25.6919	13.9905	19.4855
224	H	25.6311	15.4035	21.6094
225	H	26.2743	16.7644	20.7031
226	H	28.3235	15.4011	20.1194
227	H	27.6734	14.0442	21.0343
228	H	29.3473	15.3065	22.4077
229	H	28.3981	16.7970	22.2305
230	H	27.7395	15.4311	23.1515
231	H	23.9818	21.2238	17.9874
232	H	23.2560	22.4816	18.9698
233	H	22.1731	23.4671	16.8800
234	H	22.9628	22.2360	15.9098
235	H	25.2196	23.0834	16.6789
236	H	24.4182	24.3200	17.6437
237	H	25.1823	25.2835	15.4595
238	H	24.2336	24.0722	14.5723
239	H	23.4075	25.3099	15.5401
240	H	13.1344	12.8199	23.9340
241	H	14.1684	11.5384	23.3357
242	H	12.4745	11.1217	21.4442
243	H	11.3956	12.2738	22.2154
244	H	11.4187	10.8595	24.3242
245	H	12.4844	9.7103	23.5203
246	H	10.1241	8.8962	23.4203
247	H	9.6109	10.3987	22.6246
248	H	10.6881	9.2713	21.7782
249	H	18.7716	8.1333	19.0715
250	H	20.3321	8.9688	19.1319
251	H	20.4885	9.0112	16.6597
252	H	18.8747	8.3257	16.4979
253	H	19.6222	6.2166	17.6090
254	H	21.2365	6.8855	17.8361
255	H	21.1513	5.3773	15.8173
256	H	19.9043	6.4102	15.0886
257	H	21.5439	7.0413	15.3362
258	H	10.9817	19.3803	12.4016
259	H	12.0376	20.1325	11.2113
260	H	12.3348	22.1220	12.7821
261	H	11.2615	21.3511	13.9416
262	H	9.3940	21.4025	12.2425
263	H	10.4734	22.1726	11.0814
264	H	9.0320	23.8892	12.2057
265	H	9.6408	23.3840	13.7968
266	H	10.7344	24.1576	12.6343
267	H	17.1165	14.6973	8.5816
268	H	17.0536	13.0360	9.1314
269	H	19.6053	12.9522	9.1116
270	H	19.6392	14.6041	8.5137
271	H	18.3387	13.8848	6.4681
272	H	18.3174	12.2300	7.0708
273	H	20.1455	12.5218	5.3796
274	H	20.8654	13.8203	6.3541
275	H	20.8484	12.1565	6.9693
276	H	8.8731	14.1785	17.3315
277	H	9.4212	13.8546	15.6983
278	H	8.5426	16.1531	14.9878
279	H	7.9422	16.4018	16.6216
280	H	6.4784	14.3508	16.3844
281	H	7.0830	14.1173	14.7470
282	H	4.8630	15.2767	14.6972
283	H	5.4990	16.5852	15.7152
284	H	6.1192	16.3621	14.0680
285	H	11.9993	10.6829	14.9419
286	H	13.3325	9.8638	14.1551
287	H	13.0993	11.3615	12.1408
288	H	11.8472	12.2871	12.9534
289	H	10.3883	10.2381	13.0652
290	H	11.6344	9.2993	12.2487
291	H	9.8669	10.0455	10.6243
292	H	10.1881	11.7431	11.0353
293	H	11.4292	10.7816	10.2097

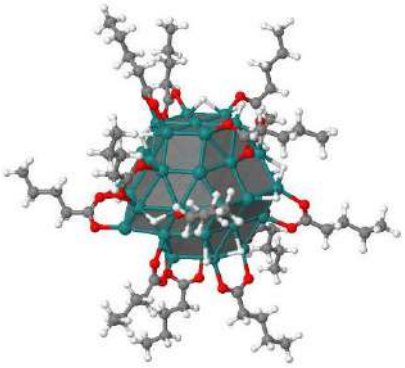

Domain 64 – $Ru_{55}(C_4H_9COO)_{14}(H)_{31}$

1	Ru	14.97085	12.82586	15.61492
2	Ru	15.20918	12.73741	11.25826
3	Ru	15.10525	11.26771	13.49558
4	Ru	13.65591	15.04448	15.63677
5	Ru	13.76181	15.18018	11.25643
6	Ru	12.29270	12.65460	15.53487
7	Ru	13.79939	13.61449	13.38859
8	Ru	12.44654	12.75418	11.27812
9	Ru	12.36305	11.10236	13.33626
10	Ru	12.39551	15.86326	13.38767

11	Ru	11.06700	13.43036	13.29836
12	Ru	8.46717	13.47038	13.31857
13	Ru	9.63125	15.63222	13.38578
14	Ru	9.62977	11.09582	13.31275
15	Ru	10.84006	17.91626	13.31798
16	Ru	11.21038	13.44118	9.13531
17	Ru	9.84180	12.60581	11.24509
18	Ru	9.61867	12.72801	15.34424
19	Ru	10.81844	13.50582	17.53990
20	Ru	12.53715	15.82251	9.10774
21	Ru	11.02537	14.98290	11.25234
22	Ru	10.95796	14.96986	15.39288
23	Ru	12.16326	15.82959	17.61807
24	Ru	12.27303	17.33061	11.31270
25	Ru	13.53097	18.11340	13.45936
26	Ru	12.15346	17.35756	15.63556
27	Ru	11.13010	8.83659	13.35114
28	Ru	12.53203	11.36571	9.07064
29	Ru	11.15770	10.44856	11.19777
30	Ru	10.93752	10.33843	15.45045
31	Ru	12.20742	11.05152	17.57176
32	Ru	13.84420	13.56103	9.18723
33	Ru	13.52044	13.49991	17.67480
34	Ru	15.13041	15.85555	9.18678
35	Ru	15.02391	16.00250	13.53523
36	Ru	14.76432	15.82597	17.80785
37	Ru	15.06021	17.40775	11.35615
38	Ru	14.69918	17.41959	15.69002
39	Ru	13.96306	8.88934	13.31566
40	Ru	12.51394	8.18919	15.24498
41	Ru	15.18804	11.28300	9.09550
42	Ru	13.83088	10.41534	11.17328
43	Ru	13.64915	10.32249	15.45660
44	Ru	14.84984	11.25011	17.64977
45	Ru	16.45622	13.67120	9.23666
46	Ru	16.42474	13.57399	13.53135
47	Ru	16.14761	13.51499	17.73908
48	Ru	16.36193	15.14384	11.27468
49	Ru	16.27273	15.10459	15.66069
50	Ru	16.39318	9.03577	13.53624
51	Ru	16.50792	10.51660	11.32819
52	Ru	17.78879	11.24108	13.44856
53	Ru	16.33253	10.59052	15.60417
54	Ru	17.75935	12.91380	11.45950
55	Ru	17.65175	12.66407	15.79747
56	C	10.48901	16.68080	22.09197
57	C	9.94596	16.84657	23.51406
58	C	10.33838	18.18128	24.14893
59	C	10.09709	15.34187	21.46910
60	C	10.58935	15.10330	20.05534
61	C	14.49773	10.90296	22.50392
62	C	14.32161	10.85909	24.02389
63	C	15.09970	9.71620	24.67751
64	C	13.71523	12.04456	21.85413
65	C	13.86189	12.15467	20.34941
66	C	17.43275	19.18499	20.20288
67	C	18.21579	20.33284	20.84618
68	C	18.59459	20.05145	22.30069
69	C	17.06330	19.47381	18.74962
70	C	16.24874	18.40162	18.05843
71	C	8.84194	21.78053	15.51665
72	C	8.26969	22.96978	16.29248
73	C	7.13041	23.66879	15.54928
74	C	9.97842	21.08493	16.26473
75	C	10.54508	19.85803	15.58175
76	C	20.70134	14.01579	6.88384
77	C	22.08000	14.11193	6.22562
78	C	22.00106	14.28103	4.70758
79	C	20.78186	13.84852	8.40162
80	C	19.44796	13.67123	9.09735
81	C	16.64460	19.59885	6.48319
82	C	17.22795	20.81787	5.76324
83	C	17.49558	20.56253	4.27961
84	C	16.38926	19.86818	7.96498
85	C	15.82798	18.70961	8.76224
86	C	22.27022	11.47465	16.71963
87	C	23.71885	11.02939	16.93747
88	C	24.34528	11.64411	18.18972
89	C	21.65019	10.85434	15.46909
90	C	20.21982	11.25882	15.17983
91	C	19.04293	18.93624	12.90059
92	C	20.28950	19.81206	12.75287
93	C	20.24413	20.69905	11.50758
94	C	19.09104	18.04049	14.13750
95	C	17.86751	17.17220	14.34916
96	C	8.40358	7.20986	18.32510
97	C	7.66788	6.26587	19.27944
98	C	6.33813	5.76743	18.71202
99	C	9.74738	7.68083	18.88921
100	C	10.46381	8.70682	18.03486
101	C	15.68690	4.32082	13.08507
102	C	16.14070	2.85900	13.07467
103	C	16.69682	2.42597	11.71718
104	C	15.15056	4.76825	14.45119
105	C	14.51689	6.13970	14.44692
106	C	7.48658	17.50412	8.94044
107	C	6.30503	18.14990	8.21293
108	C	5.93037	19.51511	8.79162
109	C	7.85520	16.13688	8.36308
110	C	9.05442	15.47729	9.00623
111	C	15.04069	9.58972	4.48507
112	C	14.88059	9.12338	3.03584
113	C	16.22064	8.91097	2.33057
114	C	13.69866	9.80507	5.18176
115	C	13.78029	10.30829	6.60704
116	C	4.21578	11.57875	11.85708
117	C	2.94402	10.82796	11.45315
118	C	1.83164	11.75755	10.96674
119	C	5.31786	10.63606	12.33814
120	C	6.63184	11.29465	12.70403
121	C	8.03085	7.40586	8.95359
122	C	7.04966	6.38359	8.37285
123	C	6.56474	6.75081	6.97013
124	C	8.50050	7.02638	10.35629
125	C	9.46842	7.99209	11.00654
126	O	9.92755	7.66093	12.15681
127	O	9.78083	9.07011	10.40513
128	O	7.64190	10.52142	12.83796
129	O	6.65441	12.56987	12.86425
130	O	12.65605	10.47961	7.21978
131	O	14.92195	10.53828	7.11583
132	O	9.63684	14.54171	8.34462
133	O	9.43097	15.88223	10.15551
134	O	13.50531	6.34436	15.20053
135	O	15.00839	7.03304	13.65113
136	O	11.18146	9.57448	18.63679
137	O	10.32068	8.65470	16.75984
138	O	17.95092	16.26488	15.25614
139	O	16.82279	17.38972	13.65898
140	O	19.67802	10.74260	14.13756
141	O	19.64356	12.07958	15.97478
142	O	15.53967	18.92828	9.98597
143	O	15.67904	17.57585	8.17706
144	O	19.46507	13.23892	10.30338
145	O	18.38176	13.94998	8.45550
146	O	11.34120	19.12959	16.28716
147	O	10.20932	19.61445	14.37750
148	O	15.95344	18.61161	16.82301
149	O	15.88634	17.37136	18.70921
150	O	13.58398	13.28256	19.81390
151	O	14.23714	11.11615	19.69832
152	O	10.24187	14.00704	19.50125
153	O	11.31188	16.00871	19.50454
154	H	9.17404	17.38241	12.98197
155	H	12.53046	14.39921	7.99691
156	H	8.56240	13.28924	10.50414
157	H	9.46329	11.11309	16.08298
158	H	13.64870	18.70411	11.79380
159	H	14.52887	18.91140	14.71213
160	H	12.45713	9.38818	10.60447
161	H	10.80591	11.91174	18.24485
162	H	13.56253	9.85574	17.28196

163	H	16.75502	16.87341	11.07427
164	H	12.56894	7.98758	12.67185
165	H	16.53880	12.09496	8.32495
166	H	16.62687	10.28700	9.54756
167	H	16.31312	11.89026	18.45467
168	H	16.59689	15.28232	17.47915
169	H	18.18402	12.96049	14.13263
170	H	17.04743	8.91275	15.15830
171	H	17.71613	14.67323	12.32227
172	H	15.21566	9.20252	11.60342
173	H	13.11119	16.62393	7.82524
174	H	10.37517	15.21041	17.15261
175	H	12.21767	17.49561	9.46010
176	H	13.44049	16.79067	18.43112
177	H	9.13701	13.17039	17.01085
178	H	18.29762	11.09632	11.67446
179	H	9.66655	9.42463	14.18655
180	H	17.87176	13.10625	17.49061
181	H	14.24158	9.85907	9.51728
182	H	15.73085	14.72095	7.94740
183	H	10.86634	18.50310	11.65947
184	H	10.45935	16.92587	14.82201
185	H	10.47125	14.50117	22.07782
186	H	9.00132	15.21851	21.45063
187	H	10.12210	17.50265	21.45669
188	H	11.58645	16.77450	22.09827
189	H	10.31039	16.01711	24.14437
190	H	8.84637	16.75398	23.49911
191	H	9.93578	18.27896	25.16705
192	H	11.43209	18.28516	24.21096
193	H	9.96026	19.02895	23.55785
194	H	12.63478	11.93150	22.05512
195	H	13.99676	13.01972	22.28038
196	H	15.56772	11.00828	22.26026
197	H	14.18052	9.94598	22.06211
198	H	13.24894	10.76177	24.26472
199	H	14.64386	11.82104	24.45829
200	H	14.96127	9.70341	25.76783
201	H	14.77337	8.74036	24.28751
202	H	16.17834	9.80613	24.47902
203	H	16.48360	20.40921	18.66959
204	H	17.96349	19.64064	18.13504
205	H	18.02342	18.25643	20.25458
206	H	16.51603	18.99082	20.78188
207	H	17.61642	21.25799	20.79274
208	H	19.12861	20.52926	20.25788
209	H	19.15485	20.88802	22.74171
210	H	17.69960	19.88618	22.91915
211	H	19.22151	19.15072	22.38042
212	H	10.82199	21.77762	16.42966
213	H	9.66066	20.77174	17.27234
214	H	8.04037	21.05240	15.31314
215	H	9.20092	22.11389	14.53059
216	H	9.07534	23.69461	16.50115
217	H	7.91066	22.62445	17.27731
218	H	6.73074	24.51502	16.12576
219	H	7.46948	24.05669	14.57700
220	H	6.29893	22.97470	15.35499
221	H	21.40604	12.98294	8.67512
222	H	21.27347	14.72206	8.86512
223	H	20.10789	14.91184	6.64448
224	H	20.14647	13.16629	6.45408
225	H	22.66295	13.20624	6.46593
226	H	22.63874	14.95693	6.66372
227	H	23.00068	14.34081	4.25459
228	H	21.47325	13.43551	4.24131
229	H	21.45608	15.19799	4.43758
230	H	17.32005	20.17569	8.47306
231	H	15.69581	20.71441	8.10199
232	H	15.70410	19.29376	5.99754
233	H	17.32813	18.74169	6.37834
234	H	18.16518	21.12124	6.26114
235	H	16.53778	21.67208	5.87266
236	H	17.90949	21.45255	3.78508
237	H	18.21254	19.73936	4.14116
238	H	16.57088	20.28625	3.75133
239	H	22.23829	11.10497	14.57004
240	H	21.66628	9.75275	15.52350
241	H	21.66312	11.21029	17.59986
242	H	22.22640	12.57268	16.64459
243	H	24.32108	11.29800	16.05251
244	H	23.75738	9.92865	17.00697
245	H	25.38342	11.31083	18.32806
246	H	24.35192	12.74286	18.13163
247	H	23.78159	11.36557	19.09269
248	H	19.96562	17.37064	14.11738
249	H	19.20606	18.64718	15.05309
250	H	18.14491	19.57183	12.94558
251	H	18.92125	18.30868	12.00271
252	H	21.18795	19.17218	12.71833
253	H	20.40140	20.44315	13.65139
254	H	21.14492	21.32297	11.42107
255	H	20.16889	20.09227	10.59239
256	H	19.37248	21.37024	11.53057
257	H	9.62885	8.11893	19.89107
258	H	10.43039	6.82131	19.01025
259	H	8.56604	6.71574	17.35505
260	H	7.76889	8.08664	18.11579
261	H	7.49015	6.78343	20.23767
262	H	8.31568	5.40430	19.51609
263	H	5.82199	5.10136	19.41779
264	H	5.66182	6.60646	18.48943
265	H	6.49086	5.20964	17.77592
266	H	14.39885	4.06424	14.83687
267	H	15.96760	4.78465	15.19443
268	H	16.52039	4.97466	12.78570
269	H	14.90265	4.46291	12.32337
270	H	15.28899	2.21314	13.34808
271	H	16.90398	2.70248	13.85586
272	H	16.99160	1.36729	11.72100
273	H	15.94996	2.56123	10.92058
274	H	17.58218	3.01863	11.44248
275	H	7.01354	15.42967	8.47242
276	H	8.05419	16.19560	7.28162
277	H	8.36253	18.17061	8.88686
278	H	7.25692	17.39953	10.01191
279	H	5.43223	17.47587	8.25925
280	H	6.54879	18.25691	7.14194
281	H	5.08403	19.96444	8.25288
282	H	5.64763	19.43218	9.85164
283	H	6.77604	20.21662	8.73135
284	H	13.07934	10.53074	4.62708
285	H	13.10405	8.87629	5.20033
286	H	15.63477	8.85410	5.05039
287	H	15.62018	10.52588	4.51241
288	H	14.28303	9.86488	2.47810
289	H	14.29779	8.18642	3.01347
290	H	16.08337	8.57795	1.29213
291	H	16.80841	9.84096	2.30848
292	H	16.82558	8.15149	2.84832
293	H	4.98661	10.07415	13.22929
294	H	5.54482	9.86955	11.57988
295	H	4.58581	12.16598	11.00128
296	H	3.98555	12.30988	12.64747
297	H	2.58137	10.23436	12.30999
298	H	3.18791	10.09854	10.66171
299	H	0.93216	11.19484	10.67970
300	H	1.54208	12.47392	11.74989
301	H	2.15487	12.33941	10.09040
302	H	7.64345	6.93133	11.04472
303	H	8.98282	6.03488	10.35783
304	H	8.90275	7.50580	8.28753
305	H	7.56056	8.40173	8.98096
306	H	6.18303	6.28440	9.04930
307	H	7.52904	5.38970	8.34994
308	H	5.86191	6.00263	6.57714
309	H	6.05181	7.72418	6.96938
310	H	7.40615	6.82196	6.26486

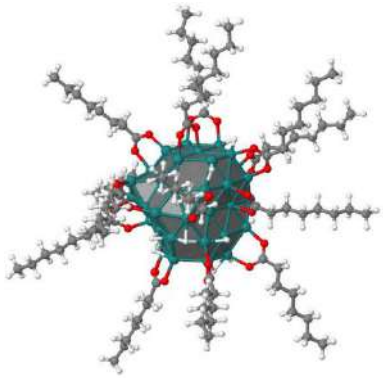

Domain 73 – $Ru_{55}(C_7H_{15}COO)_{14}(H)_{14}$

1	Ru	19.1127	16.9232	19.0664
2	Ru	19.1879	16.7932	14.7016
3	Ru	19.2164	15.3290	16.9275
4	Ru	17.7193	19.1054	19.0589
5	Ru	17.6543	19.1532	14.7336
6	Ru	16.4343	16.6600	19.0474
7	Ru	17.8488	17.5872	16.9033
8	Ru	16.4671	16.7561	14.8023
9	Ru	16.4334	15.0754	16.9143
10	Ru	16.3303	19.8605	16.9148
11	Ru	15.1596	17.4295	16.8879
12	Ru	12.5339	17.3545	16.8731
13	Ru	13.6707	19.5260	16.9965
14	Ru	13.6859	14.9468	17.0392
15	Ru	14.7630	21.9040	16.9339
16	Ru	15.0822	17.3693	12.7351
17	Ru	13.9047	16.5298	14.9049
18	Ru	13.7909	16.6031	18.9314
19	Ru	14.9912	17.3788	21.0523
20	Ru	16.3182	19.7714	12.7105
21	Ru	14.9403	18.9362	14.8012
22	Ru	15.0248	18.9001	18.9919
23	Ru	16.2304	19.7879	21.1693
24	Ru	16.2192	21.3079	14.8382
25	Ru	17.5470	22.1577	16.8577
26	Ru	16.1576	21.3228	19.0878
27	Ru	15.2914	12.7661	17.0101
28	Ru	16.3996	15.2356	12.6962
29	Ru	15.1517	14.4424	14.7834
30	Ru	15.2523	14.3336	19.0549
31	Ru	16.6008	15.1570	21.1077
32	Ru	17.7088	17.5663	12.6946
33	Ru	17.7000	17.5673	21.1890
34	Ru	18.8351	19.9297	12.6340
35	Ru	19.0543	19.9732	16.9426
36	Ru	18.8625	19.9363	21.1565
37	Ru	18.7996	21.4882	14.8730
38	Ru	18.5629	21.5263	19.0236
39	Ru	18.1080	12.9805	16.9082
40	Ru	16.7644	12.1383	18.7376
41	Ru	18.9843	15.3235	12.5855
42	Ru	17.8996	14.4638	14.7885
43	Ru	17.8620	14.4141	19.0270
44	Ru	19.1000	15.3543	21.0652
45	Ru	20.2942	17.7867	12.6477
46	Ru	20.5300	17.6259	16.9391
47	Ru	20.2499	17.8662	21.1517
48	Ru	20.3145	19.1266	14.7027
49	Ru	20.3999	19.1701	19.0712
50	Ru	20.5745	13.1247	17.0905
51	Ru	20.4941	14.5733	14.9009
52	Ru	21.8906	15.3563	16.9023
53	Ru	20.5054	14.6998	19.0020
54	Ru	21.7274	16.9939	14.7495
55	Ru	21.7141	16.8367	19.1709
56	C	9.2068	14.6201	16.9450
57	C	10.5892	15.2308	16.9004
58	C	18.4506	16.0507	25.3323
59	C	18.4880	16.2343	23.8313
60	C	24.2940	17.0478	11.1468
61	C	23.0809	17.0625	12.0529
62	C	11.5481	19.7931	12.0399
63	C	12.8300	19.2531	12.6329
64	C	13.6870	24.8073	20.0443
65	C	14.3204	23.6527	19.3048
66	C	23.0054	22.1757	17.2951
67	C	21.8629	21.2226	17.5523
68	C	20.1342	9.3621	18.7454
69	C	19.1545	10.4436	18.3596
70	C	17.5986	13.7093	8.7625
71	C	17.6104	14.3305	10.1416
72	C	25.8147	15.3664	18.8258
73	C	24.3967	15.7434	18.4727
74	C	12.9858	10.7490	13.8908
75	C	13.9328	11.7197	14.5566
76	C	14.3677	19.1039	25.0615
77	C	14.7642	18.8852	23.6180
78	C	13.9371	12.1748	22.7232
79	C	14.5113	13.1990	21.7706
80	C	6.2592	25.3357	11.8816
81	C	7.6265	24.8936	12.4047
82	C	8.0383	23.5014	11.9189
83	C	9.3965	23.0409	12.4533
84	C	9.8081	21.6490	11.9668
85	C	11.1478	21.1831	12.5405
86	C	2.4323	13.6421	13.5162
87	C	3.8387	14.2307	13.3951
88	C	4.6935	14.0096	14.6458
89	C	6.1055	14.5913	14.5410
90	C	6.9577	14.3418	15.7876
91	C	8.3686	14.9270	15.6937
92	C	11.7039	4.1538	10.2646
93	C	12.7710	5.0637	10.8749
94	C	12.1908	6.3345	11.5005
95	C	13.2414	7.2591	12.1222
96	C	12.6372	8.5310	12.7212
97	C	13.6614	9.4758	13.3555
98	C	13.7663	12.0744	2.3329
99	C	13.8097	12.9151	3.6098
100	C	15.0434	12.6393	4.4737
101	C	15.0859	13.4582	5.7663
102	C	16.3286	13.1931	6.6198

103	C	16.3355	13.9706	7.9386
104	C	9.1170	18.9523	30.6041
105	C	9.5049	18.4180	29.2247
106	C	10.8597	18.9378	28.7378
107	C	11.2474	18.4504	27.3392
108	C	12.6188	18.9564	26.8861
109	C	12.9852	18.5706	25.4506
110	C	20.0938	18.9485	32.2261
111	C	20.3349	19.0498	30.7192
112	C	19.5583	18.0055	29.9131
113	C	19.7644	18.1144	28.4002
114	C	19.0125	17.0431	27.6070
115	C	19.1672	17.1813	26.0906
116	C	14.2684	31.9253	22.7614
117	C	14.9997	30.7951	22.0351
118	C	14.1311	29.5500	21.8402
119	C	14.8362	28.4051	21.1089
120	C	13.9493	27.1703	20.9338
121	C	14.6278	26.0167	20.1907
122	C	8.2617	7.9326	25.5261
123	C	8.6159	9.0817	24.5805
124	C	10.1234	9.3229	24.4696
125	C	10.5082	10.4690	23.5296
126	C	12.0145	10.7364	23.5052
127	C	12.4419	11.8778	22.5776
128	C	30.1205	10.5166	22.9414
129	C	28.7080	10.9469	22.5434
130	C	28.6869	12.1184	21.5578
131	C	27.2762	12.5565	21.1556
132	C	27.2518	13.7391	20.1828
133	C	25.8342	14.1660	19.7947
134	C	31.3911	14.3315	10.0142
135	C	30.0563	14.1711	10.7433
136	C	29.0312	15.2491	10.3788
137	C	27.7034	15.1073	11.1267
138	C	26.6557	16.1562	10.7425
139	C	25.3648	16.0304	11.5553
140	C	26.9253	5.9257	17.9264
141	C	26.0168	7.0704	17.4761
142	C	24.6641	7.0860	18.1929
143	C	23.7466	8.2280	17.7499
144	C	22.3947	8.2385	18.4674
145	C	21.4764	9.3775	18.0161
146	C	25.0805	29.5731	17.3381
147	C	23.9399	28.5603	17.4469
148	C	24.3975	27.1090	17.2756
149	C	23.2611	26.0920	17.4058
150	C	23.7081	24.6358	17.2482
151	C	22.5590	23.6422	17.4293
152	C	22.8869	26.9808	28.6425
153	C	22.3458	25.7458	27.9209
154	C	22.2629	25.9154	26.4013
155	C	21.7053	24.6852	25.6819
156	C	21.6225	24.8345	24.1601
157	C	21.0076	23.6092	23.4797
158	C	20.9056	23.7515	21.9603
159	C	20.1933	22.6060	21.2711
160	C	21.3311	27.7177	5.1629
161	C	21.2700	26.3407	5.8265
162	C	21.0743	26.4092	7.3435
163	C	20.9966	25.0374	8.0186
164	C	20.8600	25.1125	9.5415
165	C	20.6976	23.7441	10.2112
166	C	20.5955	23.8571	11.7329
167	C	20.1605	22.6013	12.4584
168	O	10.6569	16.5214	16.8752
169	O	11.5951	14.4489	16.8938
170	O	17.8005	17.1848	23.3330
171	O	19.2213	15.4172	23.1498
172	O	21.9375	17.3143	11.5089
173	O	23.2524	16.8552	13.2960
174	O	13.1464	19.5966	13.8184
175	O	13.5239	18.4471	11.9033
176	O	15.1659	22.9267	19.9485
177	O	13.9863	23.4585	18.0899
178	O	20.8587	21.2513	16.7630
179	O	21.9380	20.4483	18.5739
180	O	18.0527	10.5106	18.9998
181	O	19.4399	11.2412	17.3790
182	O	18.7534	14.6345	10.6411
183	O	16.4952	14.4788	10.7568
184	O	23.7767	16.5535	19.2488
185	O	23.8670	15.1830	17.4486
186	O	14.4127	11.4134	15.7034
187	O	14.1980	12.8114	13.9400
188	O	15.3836	19.8595	23.0506
189	O	14.4793	17.7740	23.0587
190	O	14.1354	13.2239	20.5584
191	O	15.4305	13.9705	22.2560
192	O	19.7857	22.8144	20.0637
193	O	20.0257	21.5174	21.9051
194	O	19.9277	22.7278	13.7230
195	O	20.0082	21.5163	11.8191
196	H	9.3134	13.5362	17.0854
197	H	8.6957	15.0292	17.8323
198	H	18.8974	15.0781	25.5790
199	H	17.3904	16.0285	25.6315
200	H	24.7168	18.0684	11.1837
201	H	23.9523	16.8921	10.1138
202	H	11.6486	19.7672	10.9450
203	H	10.7583	19.0613	12.2912
204	H	12.7779	25.1020	19.5019
205	H	13.3956	24.4501	21.0440
206	H	23.8133	21.9449	18.0029
207	H	23.3800	21.9920	16.2752
208	H	19.6149	8.4008	18.5863
209	H	20.2724	9.4333	19.8370
210	H	17.7218	12.6218	8.9190
211	H	18.5044	14.0424	8.2360
212	H	22.0553	18.7683	14.9196
213	H	19.3405	13.2845	14.5815
214	H	17.4410	20.6796	11.6901
215	H	14.5001	19.1541	20.7549
216	H	15.4008	21.2952	13.2760
217	H	17.5625	20.6615	22.0695
218	H	13.4748	16.5215	20.7327
219	H	22.2536	15.1843	15.0637
220	H	26.3538	15.1119	17.9024
221	H	26.3029	16.2322	19.2960
222	H	13.6603	13.2439	17.5002
223	H	12.4794	11.2779	13.0719
224	H	12.2267	10.4683	14.6386
225	H	21.9421	17.3017	20.9034
226	H	14.4445	20.1818	25.2633
227	H	15.1442	18.6158	25.6774
228	H	17.9315	13.9200	13.0475
229	H	14.1789	12.4928	23.7472
230	H	14.5117	11.2462	22.5457
231	H	19.2381	18.6607	11.4292
232	H	5.9907	26.3382	12.2441
233	H	6.2442	25.3643	10.7814
234	H	5.4677	24.6419	12.2035
235	H	8.3941	25.6250	12.0995
236	H	7.6213	24.9043	13.5080
237	H	7.2640	22.7709	12.2140
238	H	8.0562	23.4923	10.8144
239	H	10.1714	23.7719	12.1625
240	H	9.3752	23.0474	13.5571
241	H	9.0225	20.9212	12.2384
242	H	9.8547	21.6467	10.8632
243	H	11.9378	21.9054	12.2769
244	H	11.1026	21.1720	13.6399
245	H	1.8412	13.8117	12.6049
246	H	2.4696	12.5563	13.6917
247	H	1.8837	14.0925	14.3573
248	H	4.3509	13.7879	12.5237
249	H	3.7707	15.3125	13.1885
250	H	4.1809	14.4514	15.5187
251	H	4.7602	12.9263	14.8518
252	H	6.6137	14.1604	13.6603
253	H	6.0413	15.6773	14.3526
254	H	6.4472	14.7663	16.6705

255	H	7.0236	13.2546	15.9701
256	H	8.8796	14.5196	14.8052
257	H	8.3154	16.0178	15.5539
258	H	12.1460	3.2508	9.8203
259	H	10.9765	3.8295	11.0243
260	H	11.1432	4.6743	9.4734
261	H	13.3373	4.5078	11.6414
262	H	13.5051	5.3442	10.1005
263	H	11.6265	6.8912	10.7313
264	H	11.4512	6.0541	12.2714
265	H	13.7962	6.7109	12.9037
266	H	13.9869	7.5337	11.3554
267	H	12.0852	9.0733	11.9330
268	H	11.8842	8.2534	13.4803
269	H	14.1889	8.9672	14.1779
270	H	14.4256	9.7531	12.6107
271	H	12.8737	12.2969	1.7309
272	H	14.6489	12.2625	1.7027
273	H	13.7514	10.9988	2.5660
274	H	13.7835	13.9867	3.3487
275	H	12.9009	12.7279	4.2066
276	H	15.0782	11.5635	4.7227
277	H	15.9537	12.8410	3.8812
278	H	15.0360	14.5335	5.5199
279	H	14.1822	13.2428	6.3633
280	H	16.3976	12.1120	6.8366
281	H	17.2321	13.4422	6.0356
282	H	16.2502	15.0509	7.7347
283	H	15.4515	13.7012	8.5362
284	H	8.1465	18.5559	30.9353
285	H	9.8655	18.6772	31.3627
286	H	9.0434	20.0504	30.5980
287	H	9.5269	17.3151	29.2469
288	H	8.7273	18.6905	28.4908
289	H	10.8475	20.0426	28.7446
290	H	11.6424	18.6418	29.4592
291	H	11.2369	17.3465	27.3166
292	H	10.4799	18.7759	26.6151
293	H	12.6448	20.0568	26.9799
294	H	13.3930	18.5780	27.5776
295	H	12.9624	17.4771	25.3259
296	H	12.2287	18.9749	24.7577
297	H	20.6699	19.7027	32.7809
298	H	19.0305	19.0967	32.4686
299	H	20.3842	17.9587	32.6098
300	H	20.0585	20.0584	30.3673
301	H	21.4125	18.9409	30.5082
302	H	19.8513	16.9956	30.2510
303	H	18.4815	18.0985	30.1412
304	H	19.4445	19.1146	28.0594
305	H	20.8426	18.0472	28.1718
306	H	19.3622	16.0443	27.9232
307	H	17.9389	17.0835	27.8650
308	H	18.7637	18.1510	25.7590
309	H	20.2374	17.1767	25.8241
310	H	14.9106	32.8078	22.8925
311	H	13.3749	32.2428	22.2026
312	H	13.9348	31.6047	23.7601
313	H	15.3490	31.1519	21.0510
314	H	15.9083	30.5195	22.5977
315	H	13.7841	29.1929	22.8264
316	H	13.2186	29.8289	21.2837
317	H	15.1750	28.7565	20.1185
318	H	15.7506	28.1245	21.6607
319	H	13.6181	26.8169	21.9264
320	H	13.0303	27.4585	20.3931
321	H	14.9470	26.3547	19.1913
322	H	15.5389	25.7055	20.7262
323	H	7.1746	7.7861	25.5992
324	H	8.7036	6.9846	25.1829
325	H	8.6412	8.1233	26.5416
326	H	8.2043	8.8768	23.5776
327	H	8.1264	10.0083	24.9252
328	H	10.5289	9.5295	25.4765
329	H	10.6165	8.3937	24.1327
330	H	10.1534	10.2444	22.5086
331	H	9.9810	11.3885	23.8397
332	H	12.3519	10.9585	24.5336
333	H	12.5444	9.8132	23.2091
334	H	12.2156	11.6283	21.5301
335	H	11.8656	12.7878	22.8134
336	H	30.1036	9.6769	23.6510
337	H	30.7025	10.1986	22.0630
338	H	30.6687	11.3437	23.4178
339	H	28.1722	10.0907	22.0994
340	H	28.1381	11.2244	23.4464
341	H	29.2227	12.9761	22.0025
342	H	29.2570	11.8431	20.6527
343	H	26.7447	11.7007	20.7026
344	H	26.7048	12.8207	22.0630
345	H	27.7808	14.5955	20.6363
346	H	27.8188	13.4768	19.2726
347	H	25.3079	13.3184	19.3258
348	H	25.2645	14.4289	20.7007
349	H	32.1009	13.5382	10.2890
350	H	31.2556	14.2934	8.9226
351	H	31.8617	15.2971	10.2541
352	H	29.6301	13.1781	10.5200
353	H	30.2270	14.1878	11.8333
354	H	29.4624	16.2447	10.5848
355	H	28.8458	15.2198	9.2903
356	H	27.2895	14.0995	10.9460
357	H	27.8918	15.1643	12.2133
358	H	27.0792	17.1664	10.8868
359	H	26.4317	16.0713	9.6644
360	H	24.9557	15.0121	11.4457
361	H	25.5861	16.1572	12.6256
362	H	27.8877	5.9392	17.3951
363	H	27.1392	5.9875	19.0044
364	H	26.4557	4.9480	17.7395
365	H	26.5263	8.0349	17.6437
366	H	25.8488	7.0029	16.3878
367	H	24.1536	6.1210	18.0251
368	H	24.8312	7.1530	19.2828
369	H	24.2561	9.1930	17.9186
370	H	23.5801	8.1610	16.6604
371	H	21.8861	7.2723	18.3004
372	H	22.5598	8.3094	19.5570
373	H	21.9777	10.3455	18.1889
374	H	21.3065	9.3108	16.9298
375	H	24.7203	30.6040	17.4647
376	H	25.8479	29.3920	18.1060
377	H	25.5757	29.5119	16.3570
378	H	23.4428	28.6685	18.4262
379	H	23.1691	28.7882	16.6909
380	H	24.8836	26.9941	16.2905
381	H	25.1772	26.8836	18.0252
382	H	22.7757	26.2158	18.3902
383	H	22.4816	26.3157	16.6565
384	H	24.1654	24.4957	16.2527
385	H	24.5038	24.4167	17.9821
386	H	22.0980	23.7893	18.4201
387	H	21.7679	23.8419	16.6900
388	H	22.9374	26.8246	29.7295
389	H	23.9003	27.2332	28.2952
390	H	22.2485	27.8589	28.4619
391	H	22.9817	24.8743	28.1526
392	H	21.3437	25.4999	28.3117
393	H	21.6334	26.7925	26.1672
394	H	23.2674	26.1500	26.0058
395	H	22.3274	23.8060	25.9265
396	H	20.6987	24.4605	26.0772
397	H	21.0253	25.7306	23.9137
398	H	22.6324	25.0213	23.7535
399	H	21.5941	22.7099	23.7231
400	H	20.0010	23.4299	23.8907
401	H	20.3780	24.6761	21.6784
402	H	21.9083	23.8336	21.5054
403	H	16.0374	22.9060	16.0159
404	H	21.4860	27.6386	4.0775
405	H	20.3990	28.2796	5.3262
406	H	22.1552	28.3208	5.5737

407	H	20.4504	25.7519	5.3808
408	H	22.1967	25.7833	5.6069
409	H	21.9015	26.9909	7.7890
410	H	20.1532	26.9772	7.5656
411	H	20.1421	24.4749	7.6030
412	H	21.8972	24.4517	7.7623
413	H	21.7402	25.6323	9.9604
414	H	19.9888	25.7421	9.7964
415	H	19.7935	23.2498	9.8236
416	H	21.5389	23.0862	9.9415
417	H	21.5486	24.1898	12.1772
418	H	19.8635	24.6333	12.0134
419	H	13.1316	21.2743	17.0196

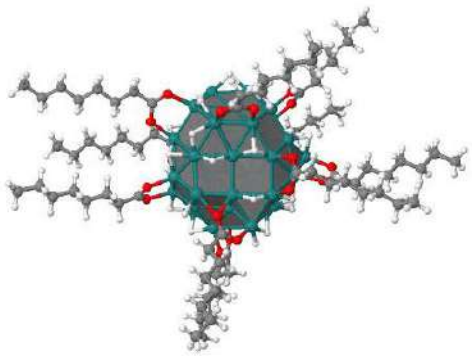

Domain 70 – $Ru_{55}(C_7H_{15}COO)_{10}(H)_{27}$

1	Ru	19.1566	17.9169	20.0149
2	Ru	19.2346	17.8192	15.6802
3	Ru	19.2461	16.3489	17.8697
4	Ru	17.6631	20.0473	20.0851
5	Ru	17.6218	20.1198	15.6492
6	Ru	16.3377	17.7373	19.9706
7	Ru	17.8199	18.5805	17.8535
8	Ru	16.4518	17.7230	15.7457
9	Ru	16.4567	16.1280	17.8556
10	Ru	16.3380	20.8548	17.8380
11	Ru	15.0917	18.4356	17.7847
12	Ru	12.4530	18.5108	17.6882
13	Ru	13.6056	20.6003	17.8531
14	Ru	13.5020	16.0500	17.8150
15	Ru	14.7735	22.8662	17.7995
16	Ru	15.0931	18.3162	13.6523
17	Ru	13.8565	17.5399	15.7831
18	Ru	13.7085	17.6953	19.8238
19	Ru	15.0451	18.3425	22.0244
20	Ru	16.4357	20.8012	13.5706
21	Ru	14.9576	19.9525	15.7003
22	Ru	14.9468	19.9675	19.8770
23	Ru	16.2607	20.6630	22.0817
24	Ru	16.2176	22.2950	15.7835
25	Ru	17.4461	23.1833	17.8938
26	Ru	16.1777	22.2999	19.9944
27	Ru	15.2943	13.7988	17.9399
28	Ru	16.5281	16.1917	13.6372
29	Ru	15.1984	15.3696	15.8033
30	Ru	14.9454	15.3979	19.8274
31	Ru	16.3482	15.9929	21.8952
32	Ru	17.7163	18.4485	13.6213
33	Ru	17.6656	18.4146	22.1414
34	Ru	18.9798	20.6752	13.5900
35	Ru	18.9787	21.0511	17.9240
36	Ru	18.7891	20.7932	22.1897
37	Ru	18.8268	22.3759	15.7828
38	Ru	18.6071	22.4147	20.1910
39	Ru	17.9809	13.9846	17.9701
40	Ru	16.6194	13.7134	20.4196
41	Ru	19.0953	16.3062	13.5504
42	Ru	17.9095	15.4630	15.7424
43	Ru	18.0141	15.5166	19.9480
44	Ru	19.0691	16.3160	22.1062
45	Ru	20.3357	18.6897	13.5716
46	Ru	20.4771	18.7002	17.8819
47	Ru	20.3238	18.6312	22.1126
48	Ru	20.3095	20.1996	15.7676
49	Ru	20.2839	20.2794	20.0570
50	Ru	20.4565	14.1026	17.9366
51	Ru	20.5387	15.5460	15.7313
52	Ru	21.8586	16.3146	17.8160
53	Ru	20.5471	15.7154	19.9613
54	Ru	21.7921	18.0771	15.7882
55	Ru	21.8012	17.9522	20.0023
56	C	9.1557	15.7339	18.3258
57	C	10.5151	16.3492	18.1004
58	C	17.8178	16.7517	26.2494
59	C	18.0215	16.9810	24.7702
60	C	24.5623	19.1492	12.5568
61	C	23.3195	18.7051	13.3009
62	C	11.6109	20.8296	12.9067
63	C	12.8712	20.2545	13.5104
64	C	13.7809	25.8360	20.8620
65	C	14.3672	24.6358	20.1553
66	C	22.9740	23.2309	18.2671
67	C	21.7809	22.3387	18.5368
68	C	19.7928	10.6270	20.2313
69	C	18.8230	11.6680	19.7269
70	C	17.6477	13.8558	10.1632
71	C	17.6953	14.6979	11.4199
72	C	25.7873	16.0892	19.7784
73	C	24.3576	16.4539	19.4389
74	C	12.9437	11.6847	14.9170
75	C	13.7473	12.7453	15.6348
76	C	7.4025	27.0057	11.2334
77	C	8.6916	26.4800	11.8667
78	C	8.7906	24.9518	11.8548
79	C	10.0877	24.4136	12.4636
80	C	10.1969	22.8872	12.4189
81	C	11.5055	22.3559	13.0068
82	C	2.9092	12.7960	14.9933

83	C	4.1860	13.6154	14.8046
84	C	4.9830	13.7995	16.0992
85	C	6.2905	14.5719	15.9098
86	C	7.0627	14.7987	17.2120
87	C	8.4143	15.4837	16.9988
88	C	21.0977	3.3432	22.2044
89	C	20.0778	4.3572	21.6853
90	C	20.6385	5.7778	21.5752
91	C	19.6238	6.7984	21.0528
92	C	20.1880	8.2156	20.9308
93	C	19.1772	9.2271	20.3843
94	C	32.7037	13.9328	17.2908
95	C	31.2039	13.9856	16.9963
96	C	30.3776	14.5369	18.1616
97	C	28.8831	14.6556	17.8517
98	C	28.0571	15.2397	19.0012
99	C	26.5906	15.4753	18.6300
100	C	13.3182	10.2771	4.9198
101	C	13.3564	11.1062	6.2042
102	C	14.7770	11.4415	6.6686
103	C	14.8197	12.2798	7.9488
104	C	16.2347	12.6357	8.4154
105	C	16.2414	13.4722	9.6973
106	C	32.1671	20.1583	12.4560
107	C	30.9404	19.7323	13.2635
108	C	29.6230	19.8702	12.4942
109	C	28.3994	19.4205	13.2977
110	C	27.0771	19.5325	12.5338
111	C	25.8706	19.0411	13.3398
112	C	6.6661	7.2930	14.7920
113	C	7.4599	8.3591	15.5480
114	C	8.7574	8.7619	14.8428
115	C	9.5512	9.8375	15.5887
116	C	10.8598	10.2256	14.8972
117	C	11.6372	11.3169	15.6377
118	C	30.0818	25.2994	20.3267
119	C	28.8715	24.4020	20.5880
120	C	27.7190	24.6295	19.6060
121	C	26.5118	23.7276	19.8731
122	C	25.3393	23.9453	18.9126
123	C	24.1584	23.0188	19.2107
124	C	19.5066	18.7859	33.4307
125	C	19.7092	19.1030	31.9482
126	C	18.9837	18.1248	31.0208
127	C	19.1702	18.4251	29.5312
128	C	18.4163	17.4528	28.6200
129	C	18.6064	17.7366	27.1282
130	C	8.2775	31.1875	21.0121
131	C	8.9078	30.0115	20.2651
132	C	10.1644	29.4609	20.9459
133	C	10.7790	28.2674	20.2115
134	C	12.0148	27.6794	20.8976
135	C	12.5759	26.4628	20.1578
136	O	10.6022	17.6267	18.0756
137	O	11.4989	15.5386	17.9204
138	O	17.7009	18.1115	24.2780
139	O	18.5206	16.0062	24.0840
140	O	22.1963	18.9266	12.7123
141	O	23.4311	18.1521	14.4418
142	O	13.2920	20.7358	14.6142
143	O	13.4523	19.2990	12.8768
144	O	15.0791	23.8228	20.8541
145	O	14.1484	24.4958	18.9058
146	O	20.8555	22.2785	17.6612
147	O	21.7490	21.6923	19.6466
148	O	17.7643	11.8941	20.3944
149	O	19.1265	12.2861	18.6239
150	O	18.8293	14.9317	11.9549
151	O	16.5795	15.1410	11.8886
152	O	23.7738	17.2963	20.2122
153	O	23.8126	15.9012	18.4234
154	O	14.2303	12.4485	16.7872
155	O	13.9171	13.8695	15.0566
156	H	13.0487	22.3076	17.7138
157	H	16.4266	19.2668	12.5284
158	H	12.2374	18.1780	15.8206
159	H	13.5226	16.1350	20.6258
160	H	17.5865	23.7909	16.2392
161	H	18.5850	23.8924	19.1635
162	H	16.4773	14.5576	14.8594
163	H	15.1515	16.8690	23.0072
164	H	16.2263	14.1771	22.1260
165	H	20.1218	21.9040	14.6498
166	H	16.6533	12.7666	17.6476
167	H	20.0515	17.3674	12.4099
168	H	20.7109	15.5400	13.9536
169	H	20.5856	16.9897	22.8157
170	H	20.6748	20.4299	21.9258
171	H	22.2852	18.1220	18.2282
172	H	21.2681	14.0354	19.4688
173	H	9.2914	14.7826	18.8604
174	H	8.5684	16.4143	18.9590
175	H	18.1010	15.7150	26.4769
176	H	16.7398	16.8602	26.4557
177	H	24.3796	20.1876	12.2339
178	H	24.6102	18.5630	11.6237
179	H	11.5521	20.4901	11.8627
180	H	10.7650	20.3616	13.4410
181	H	14.5999	26.5727	20.9556
182	H	13.5398	25.5311	21.8916
183	H	22.6100	24.2722	18.3240
184	H	23.2614	23.0801	17.2145
185	H	20.6584	10.5991	19.5556
186	H	20.1481	10.9767	21.2155
187	H	18.2714	12.9647	10.3432
188	H	18.1776	14.4260	9.3802
189	H	22.0549	19.8342	15.8137
190	H	19.3851	14.2996	15.4134
191	H	17.7065	21.5411	12.5600
192	H	14.4862	20.0959	21.7296
193	H	15.8001	22.3888	13.9954
194	H	17.5053	21.6185	23.0710
195	H	13.3147	18.1160	21.5078
196	H	22.2453	16.2484	15.9494
197	H	25.7429	15.3927	20.6345
198	H	26.2717	16.9988	20.1665
199	H	13.7452	14.3969	18.6916
200	H	12.7369	12.0463	13.9007
201	H	13.5793	10.7877	14.8360
202	H	22.0395	18.4051	21.7156
203	H	7.3598	28.1040	11.2525
204	H	7.3181	26.6875	10.1830
205	H	6.5153	26.6284	11.7641
206	H	9.5623	26.9021	11.3364
207	H	8.7675	26.8405	12.9067
208	H	7.9272	24.5270	12.3970
209	H	8.7000	24.5920	10.8144
210	H	10.9491	24.8542	11.9308
211	H	10.1728	24.7555	13.5097
212	H	9.3450	22.4424	12.9636
213	H	10.0982	22.5481	11.3724
214	H	12.3596	22.8133	12.4798
215	H	11.5990	22.6562	14.0612
216	H	2.3523	12.6910	14.0515
217	H	3.1381	11.7835	15.3594
218	H	2.2376	13.2675	15.7270
219	H	4.8283	13.1303	14.0501
220	H	3.9330	14.6073	14.3928
221	H	4.3530	14.3185	16.8430
222	H	5.2063	12.8082	16.5330
223	H	6.9332	14.0266	15.1956
224	H	6.0760	15.5474	15.4393
225	H	6.4481	15.4039	17.9010
226	H	7.2226	13.8303	17.7170
227	H	9.0451	14.8600	16.3447
228	H	8.2712	16.4441	16.4779
229	H	20.6671	2.3338	22.2710
230	H	21.9755	3.2876	21.5435
231	H	21.4571	3.6183	23.2078
232	H	19.7092	4.0369	20.6957
233	H	19.1954	4.3670	22.3477
234	H	21.0077	6.1009	22.5648

235	H	21.5219	5.7687	20.9120
236	H	19.2532	6.4687	20.0660
237	H	18.7429	6.8117	21.7184
238	H	20.5457	8.5554	21.9186
239	H	21.0773	8.1970	20.2759
240	H	18.8048	8.8840	19.4047
241	H	18.3026	9.2876	21.0499
242	H	33.2714	13.5363	16.4365
243	H	33.0981	14.9352	17.5158
244	H	32.9179	13.2916	18.1591
245	H	31.0258	14.6083	16.1028
246	H	30.8406	12.9763	16.7378
247	H	30.5232	13.8950	19.0487
248	H	30.7688	15.5313	18.4421
249	H	28.7515	15.2887	16.9567
250	H	28.4827	13.6630	17.5802
251	H	28.1169	14.5691	19.8770
252	H	28.5089	16.1959	19.3212
253	H	26.5370	16.1413	17.7538
254	H	26.1212	14.5303	18.3175
255	H	12.2864	10.0545	4.6123
256	H	13.8058	10.8087	4.0889
257	H	13.8411	9.3173	5.0494
258	H	12.7946	12.0442	6.0548
259	H	12.8306	10.5648	7.0096
260	H	15.3395	10.5039	6.8249
261	H	15.3048	11.9794	5.8612
262	H	14.2464	13.2104	7.7926
263	H	14.2975	11.7369	8.7566
264	H	16.8130	11.7078	8.5727
265	H	16.7556	13.1856	7.6111
266	H	15.6489	14.3875	9.5429
267	H	15.7300	12.9189	10.5012
268	H	33.0929	20.0452	13.0388
269	H	32.2732	19.5531	11.5434
270	H	32.0964	21.2121	12.1468
271	H	31.0590	18.6841	13.5871
272	H	30.8823	20.3294	14.1894
273	H	29.4917	20.9213	12.1802
274	H	29.6839	19.2822	11.5614
275	H	28.5432	18.3739	13.6192
276	H	28.3346	20.0151	14.2261
277	H	26.9164	20.5828	12.2324
278	H	27.1499	18.9564	11.5942
279	H	26.0274	17.9963	13.6490
280	H	25.7855	19.6210	14.2726
281	H	5.7442	7.0200	15.3252
282	H	6.3791	7.6465	13.7902
283	H	7.2587	6.3749	14.6603
284	H	6.8324	9.2558	15.6910
285	H	7.6986	7.9933	16.5611
286	H	9.3905	7.8670	14.7078
287	H	8.5225	9.1210	13.8247
288	H	8.9212	10.7370	15.7079
289	H	9.7717	9.4847	16.6118
290	H	11.4986	9.3307	14.7946
291	H	10.6435	10.5637	13.8683
292	H	11.0089	12.2182	15.7352
293	H	11.8699	10.9851	16.6619
294	H	30.8882	25.1108	21.0503
295	H	30.4927	25.1314	19.3194
296	H	29.8120	26.3638	20.3998
297	H	29.1802	23.3436	20.5430
298	H	28.5061	24.5658	21.6162
299	H	27.4047	25.6876	19.6513
300	H	28.0798	24.4654	18.5749
301	H	26.8296	22.6713	19.8212
302	H	26.1629	23.8858	20.9084
303	H	25.0082	24.9973	18.9706
304	H	25.6813	23.7906	17.8736
305	H	24.4874	21.9692	19.1477
306	H	23.8245	23.1655	20.2493
307	H	20.0319	19.5045	34.0758
308	H	18.4397	18.8146	33.7003
309	H	19.8811	17.7807	33.6773
310	H	19.3592	20.1281	31.7383
311	H	20.7869	19.0971	31.7120
312	H	19.3326	17.0982	31.2318
313	H	17.9053	18.1314	31.2610
314	H	18.8363	19.4562	29.3209
315	H	20.2465	18.3981	29.2846
316	H	18.7436	16.4213	28.8392
317	H	17.3397	17.4871	28.8637
318	H	18.2872	18.7639	26.8927
319	H	19.6777	17.6754	26.8747
320	H	7.3773	31.5564	20.4998
321	H	7.9849	30.8987	22.0331
322	H	8.9814	32.0296	21.0964
323	H	8.1680	29.1991	20.1650
324	H	9.1592	30.3188	19.2355
325	H	10.9148	30.2670	21.0348
326	H	9.9155	29.1645	21.9805
327	H	10.0156	27.4761	20.1074
328	H	11.0425	28.5681	19.1822
329	H	12.7960	28.4557	20.9804
330	H	11.7562	27.3963	21.9334
331	H	11.7856	25.7023	20.0506
332	H	12.8615	26.7470	19.1336

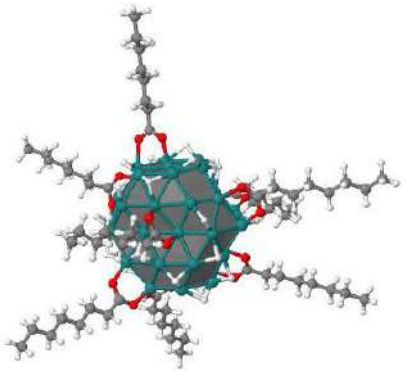

Domain 68 – $Ru_{55}(C_7H_{15}COO)_8(H)_{25}$

1	Ru	19.4873	17.002	19.8187
2	Ru	19.4838	16.8686	15.5182
3	Ru	19.5647	15.3762	17.7091
4	Ru	18.0597	19.1594	19.9033
5	Ru	17.9869	19.1888	15.4865
6	Ru	16.6218	16.8693	19.8497
7	Ru	18.1153	17.6736	17.7116
8	Ru	16.7664	16.8791	15.583
9	Ru	16.8172	15.2607	17.5986
10	Ru	16.7034	19.9679	17.6677
11	Ru	15.379	17.5381	17.6339
12	Ru	12.8125	17.6344	17.5309
13	Ru	13.9636	19.7351	17.6854
14	Ru	13.9157	15.1736	17.6746
15	Ru	15.1603	21.9933	17.6188
16	Ru	15.378	17.3831	13.4874
17	Ru	14.1785	16.6583	15.575
18	Ru	14.0448	16.8189	19.7345
19	Ru	15.3958	17.5147	21.8974
20	Ru	16.7699	19.8783	13.3992
21	Ru	15.2894	19.047	15.5275
22	Ru	15.3143	19.1191	19.7028
23	Ru	16.6481	19.7991	21.9053
24	Ru	16.5603	21.3854	15.5966
25	Ru	17.8871	22.2723	17.6533
26	Ru	16.5799	21.4435	19.7975
27	Ru	15.5589	12.9994	17.8157
28	Ru	16.7545	15.2145	13.5536
29	Ru	15.4963	14.5257	15.6002
30	Ru	15.4231	14.5677	19.6434
31	Ru	16.6828	15.1739	21.8084
32	Ru	18.024	17.5346	13.4345
33	Ru	18.018	17.5581	21.978
34	Ru	19.3162	19.6756	13.3722
35	Ru	19.3767	20.1593	17.7415
36	Ru	19.1905	19.8825	22.0144
37	Ru	19.1979	21.4242	15.557
38	Ru	18.9763	21.5068	20.0099
39	Ru	18.2322	13.0386	17.8823
40	Ru	16.9551	12.6511	20.1654
41	Ru	19.3141	15.3174	13.3906
42	Ru	18.2126	14.4974	15.5765
43	Ru	18.1314	14.6769	19.7536
44	Ru	19.4152	15.3892	21.9024
45	Ru	20.6377	17.5833	13.4168
46	Ru	20.7974	17.7779	17.7037
47	Ru	20.6633	17.6876	21.9298
48	Ru	20.644	19.2483	15.5117
49	Ru	20.6594	19.3372	19.8425
50	Ru	20.7589	13.153	17.6879
51	Ru	20.8562	14.7053	15.5628
52	Ru	22.1214	15.3262	17.7134
53	Ru	20.7974	14.7074	19.8522
54	Ru	22.0794	16.9901	15.6391
55	Ru	21.959	16.9225	19.7593
56	C	9.5991	14.7637	18.3096
57	C	10.9505	15.4102	18.117
58	C	18.2847	15.8498	26.0784
59	C	18.446	16.0867	24.5934
60	C	24.8581	18.3921	12.5276
61	C	23.6023	17.9641	13.2541
62	C	11.9217	19.957	12.7944
63	C	13.1964	19.3812	13.365
64	C	14.1509	24.9595	20.6726
65	C	14.7469	23.7664	19.9609
66	C	23.3611	22.309	18.1314
67	C	22.1575	21.4277	18.3892
68	C	20.4022	9.7513	20.0894
69	C	19.3995	10.8129	19.697
70	C	17.8049	12.8905	10.0462
71	C	17.8546	13.7305	11.3
72	C	7.7298	26.1181	11.0588
73	C	9.0104	25.6018	11.7162
74	C	9.1031	24.074	11.7367
75	C	10.3943	23.541	12.3624
76	C	10.5018	22.0143	12.3275
77	C	11.815	21.4826	12.9053
78	C	3.3268	11.984	14.8842
79	C	4.6204	12.7816	14.7139
80	C	5.4411	12.8884	16.0024
81	C	6.7403	13.6829	15.84
82	C	7.5331	13.8285	17.1421
83	C	8.8567	14.5796	16.9704
84	C	21.3826	2.4031	22.0676
85	C	20.4141	3.464	21.5428
86	C	21.0388	4.8587	21.4517
87	C	20.0816	5.9262	20.916
88	C	20.7193	7.3115	20.7806
89	C	19.7442	8.371	20.2622
90	C	13.5968	9.3604	4.7027
91	C	13.5993	10.1685	6.0005
92	C	15.0073	10.487	6.5106
93	C	15.0178	11.3078	7.8019
94	C	16.4206	11.6662	8.2969
95	C	16.4031	12.508	9.5746
96	C	32.4517	19.2532	12.289
97	C	31.2515	18.8384	13.1411
98	C	29.918	18.9581	12.3988
99	C	28.7063	18.5231	13.2264
100	C	27.3774	18.675	12.483
101	C	26.1657	18.2123	13.2959
102	C	30.4297	24.4122	20.2421
103	C	29.2383	23.4892	20.4991
104	C	28.097	23.6835	19.4976
105	C	26.8919	22.7787	19.7615
106	C	25.7299	22.9947	18.7884
107	C	24.535	22.0864	19.085
108	C	19.7964	17.8294	33.2996
109	C	20.0312	18.1773	31.8287
110	C	19.3295	17.2176	30.8646
111	C	19.5409	17.55	29.3846
112	C	18.8293	16.5708	28.4472
113	C	19.0218	16.8714	26.9582
114	C	8.5974	30.2512	20.8829
115	C	9.2309	29.0871	20.12
116	C	10.5049	28.5509	20.7796
117	C	11.1279	27.3697	20.0322
118	C	12.3676	26.7855	20.7155
119	C	12.9434	25.5805	19.9678
120	O	11.0145	16.6884	18.0662
121	O	11.956	14.6206	17.9762
122	O	18.1391	17.2267	24.1178
123	O	18.8825	15.0931	23.8892
124	O	22.498	18.0912	12.6238
125	O	23.702	17.5053	14.445
126	O	13.6339	19.8594	14.4655
127	O	13.7652	18.4286	12.7174
128	O	15.483	22.968	20.6514
129	O	14.5051	23.6142	18.7168
130	O	21.2328	21.3931	17.5147
131	O	22.1218	20.7662	19.4918
132	O	18.4202	11.0365	20.4602
133	O	19.5839	11.4223	18.5512
134	O	19.004	14.0301	11.7698
135	O	16.7461	14.1005	11.8382
136	H	13.4484	21.4652	17.5111
137	H	16.743	18.3638	12.344
138	H	12.4838	17.2032	15.7871
139	H	13.9626	15.1998	20.4606
140	H	17.9568	22.8428	15.9844
141	H	18.9252	22.9929	18.9806
142	H	15.4322	16.0755	22.8985
143	H	16.9047	13.3361	21.8844
144	H	20.5275	20.8992	14.4533
145	H	16.8028	11.8164	18.5227
146	H	20.524	16.2215	12.2972
147	H	20.4568	13.8926	14.1062
148	H	20.9083	16.0969	22.6822
149	H	21.0374	19.4852	21.73
150	H	22.2541	13.6378	18.5515
151	H	9.7493	13.7858	18.7884
152	H	9.002	15.3976	18.981

153	H	18.6267	14.8295	26.2994
154	H	17.2043	15.8921	26.2984
155	H	24.7118	19.4485	12.2422
156	H	24.8784	17.8399	11.5733
157	H	11.836	19.6224	11.7508
158	H	11.0905	19.4849	13.3488
159	H	14.9636	25.7016	20.7767
160	H	13.9066	24.6453	21.6986
161	H	23.0073	23.3541	18.1822
162	H	23.6568	22.1533	17.0813
163	H	21.2034	9.7139	19.3392
164	H	20.8495	10.0622	21.0481
165	H	18.4226	11.9963	10.2344
166	H	18.3456	13.4526	9.2653
167	H	22.0724	18.7096	16.5121
168	H	19.0999	13.0242	16.2626
169	H	18.0684	20.6637	12.4427
170	H	14.867	19.2945	21.5442
171	H	16.134	21.4757	13.8247
172	H	17.9291	20.7277	22.892
173	H	13.664	17.2407	21.4308
174	H	22.6919	15.2366	15.9563
175	H	14.2926	13.4327	16.6072
176	H	22.4347	17.5133	21.3466
177	H	7.692	27.2167	11.0506
178	H	7.6528	25.7747	10.0159
179	H	6.8359	25.7579	11.5906
180	H	9.8875	26.0089	11.1845
181	H	9.0783	25.9847	12.7487
182	H	8.2344	23.6632	12.2814
183	H	9.0178	23.6936	10.7028
184	H	11.2605	23.9764	11.8332
185	H	10.4706	23.891	13.4068
186	H	9.653	21.5737	12.8804
187	H	10.3943	21.6699	11.2835
188	H	12.6644	21.945	12.3754
189	H	11.9147	21.777	13.9608
190	H	2.7569	11.9322	13.9453
191	H	3.534	10.9515	15.205
192	H	2.6744	12.4401	15.6442
193	H	5.2392	12.3183	13.927
194	H	4.3827	13.797	14.3528
195	H	4.8223	13.356	16.7886
196	H	5.6777	11.8734	16.3685
197	H	7.3731	13.1943	15.0782
198	H	6.5069	14.686	15.4422
199	H	6.9101	14.3493	17.8906
200	H	7.7368	12.8268	17.5601
201	H	9.5046	14.0291	16.2691
202	H	8.6726	15.5684	16.5211
203	H	20.9108	1.4112	22.1144
204	H	22.2688	2.3198	21.4207
205	H	21.7357	2.6519	23.08
206	H	20.047	3.1675	20.5456
207	H	19.5234	3.5063	22.1922
208	H	21.4025	5.1611	22.45
209	H	21.9338	4.8129	20.8055
210	H	19.6956	5.607	19.9314
211	H	19.201	5.9931	21.5788
212	H	21.1152	7.6311	21.7609
213	H	21.5912	7.2471	20.1064
214	H	19.3253	8.0458	19.2953
215	H	18.8948	8.469	20.9552
216	H	12.5745	9.1525	4.356
217	H	14.118	9.9008	3.8977
218	H	14.1071	8.3941	4.8344
219	H	13.0491	11.1129	5.8489
220	H	13.0463	9.6191	6.781
221	H	15.56	9.5442	6.6697
222	H	15.5614	11.0334	5.7265
223	H	14.4428	12.2374	7.6453
224	H	14.4837	10.7524	8.5932
225	H	16.9978	10.7405	8.4708
226	H	16.9586	12.214	7.5028
227	H	15.8127	13.4225	9.4086
228	H	15.8851	11.9588	10.3766
229	H	33.3953	19.165	12.8459
230	H	32.5353	18.6249	11.3893
231	H	32.3589	20.2976	11.9538
232	H	31.3831	17.7982	13.4842
233	H	31.2144	19.4555	14.0551
234	H	29.7791	20.0036	12.0697
235	H	29.9625	18.3554	11.4743
236	H	28.8337	17.471	13.536
237	H	28.6699	19.1111	14.1606
238	H	27.2426	19.7323	12.1932
239	H	27.4222	18.1066	11.5369
240	H	26.2847	17.1539	13.5767
241	H	26.1135	18.7709	14.2434
242	H	31.2305	24.2568	20.979
243	H	30.8581	24.2403	19.2427
244	H	30.1298	25.4699	20.2943
245	H	29.5705	22.4375	20.471
246	H	28.8544	23.6568	21.5197
247	H	27.7725	24.7391	19.5188
248	H	28.4746	23.5039	18.4752
249	H	27.2111	21.7224	19.7183
250	H	26.5335	22.9429	20.7929
251	H	25.411	24.0513	18.8305
252	H	26.0799	22.8242	17.7548
253	H	24.8497	21.0319	19.0328
254	H	24.1959	22.246	20.12
255	H	20.3119	18.5315	33.9703
256	H	18.7247	17.8574	33.5488
257	H	20.1614	16.8175	33.5326
258	H	19.6847	19.2063	31.6328
259	H	21.1141	18.1773	31.6174
260	H	19.6805	16.1882	31.0586
261	H	18.2469	17.212	31.0842
262	H	19.1853	18.5759	29.1841
263	H	20.6223	17.5539	29.1604
264	H	19.1856	15.5474	28.6592
265	H	17.7496	16.5683	28.6783
266	H	18.6589	17.8836	26.7221
267	H	20.0967	16.8581	26.7124
268	H	7.6808	30.6068	20.3908
269	H	8.3304	29.9551	21.9089
270	H	9.289	31.1042	20.9556
271	H	8.5005	28.265	20.029
272	H	9.4612	29.4018	19.0879
273	H	11.2445	29.3671	20.8624
274	H	10.2743	28.2461	21.816
275	H	10.3709	26.5734	19.9206
276	H	11.3897	27.6822	19.0058
277	H	13.1415	27.5681	20.808
278	H	12.1079	26.4912	21.7476
279	H	12.1611	24.8126	19.8515
280	H	13.2293	25.8752	18.9468

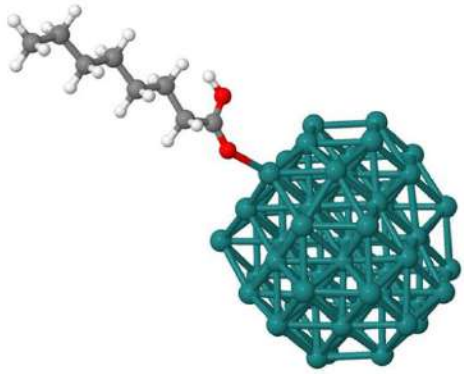

Structure 69, figure 4.11 (a) – $Ru_{55}(C_7H_{15}COOH)$

Ru	10.9363	10.4615	13.5803	Ru	17.4513	7.9740	17.6779
Ru	12.2670	12.6295	13.6531	Ru	18.6433	10.3963	9.3402
Ru	12.1330	8.0468	13.5972	Ru	17.4493	9.5733	11.3682
Ru	13.4927	14.8920	13.6490	Ru	18.9318	10.3363	13.5829
Ru	13.4205	10.3800	9.4767	Ru	17.5195	9.5947	15.7531
Ru	12.1623	9.6165	11.5349	Ru	18.6583	10.2480	17.8706
Ru	13.4740	10.3610	13.6092	Ru	18.7113	11.8218	11.4858
Ru	12.1358	9.6015	15.6252	Ru	18.7523	11.8272	15.7316
Ru	13.4785	10.2768	17.7289	Ru	18.6458	5.7575	13.5047
Ru	14.7805	12.6725	9.4762	Ru	18.6975	7.2853	11.4540
Ru	13.4738	11.8963	11.5294	Ru	20.0843	8.0223	13.5070
Ru	14.8685	12.6670	13.6438	Ru	18.7563	7.2353	15.6060
Ru	13.5030	11.8390	15.7212	Ru	19.9913	9.5343	11.4343
Ru	14.8110	12.5180	17.7700	Ru	20.0055	9.4510	15.7123
Ru	14.7933	14.1403	11.5895	C	11.4890	17.2755	12.9176
Ru	16.1325	14.9058	13.6425	C	5.4717	23.8730	14.0956
Ru	14.8085	14.1065	15.7152	C	6.3325	23.1253	13.0733
Ru	13.4435	5.8255	13.5468	C	7.1993	22.0353	13.7106
Ru	14.7378	8.1170	9.4292	C	8.0850	21.2482	12.7332
Ru	13.4463	7.3368	11.4800	C	8.9043	20.1825	13.4688
Ru	14.7525	8.0083	13.5580	C	9.8295	19.2965	12.6162
Ru	13.4835	7.2630	15.6044	C	10.5498	18.2895	13.5252
Ru	14.8173	7.9473	17.7271	O	12.0045	16.3915	13.6211
Ru	16.0362	10.3878	9.3691	O	11.7878	17.3268	11.6113
Ru	14.7870	9.6338	11.4598	H	11.3038	18.0648	11.1873
Ru	16.1745	10.3220	13.6120	H	4.8590	24.6493	13.6162
Ru	14.7915	9.5003	15.7531	H	4.7880	23.1888	14.6206
Ru	16.0680	10.2063	17.8165	H	6.0932	24.3663	14.8582
Ru	17.3513	12.5875	9.3408	H	5.6815	22.6740	12.3058
Ru	16.1600	11.8935	11.4358	H	6.9783	23.8443	12.5419
Ru	17.5540	12.7243	13.6448	H	7.8405	22.4945	14.4838
Ru	16.2080	11.8330	15.7927	H	6.5443	21.3265	14.2483
Ru	17.4258	12.4258	17.8955	H	7.4535	20.7750	11.9613
Ru	17.3998	14.0950	11.5471	H	8.7565	21.9435	12.2002
Ru	17.3837	14.0523	15.7911	H	9.5170	20.6790	14.2410
Ru	16.2200	5.7840	13.5983	H	8.2098	19.5223	14.0163
Ru	14.8198	5.0620	15.4775	H	9.2320	18.7708	11.8508
Ru	17.2895	8.0835	9.3733	H	10.5582	19.9343	12.0838
Ru	16.1097	7.2938	11.4577	H	11.1425	18.8285	14.2844
Ru	17.5248	8.0453	13.5665	H	9.8132	17.7098	14.1045
Ru	16.1223	7.1893	15.6744				

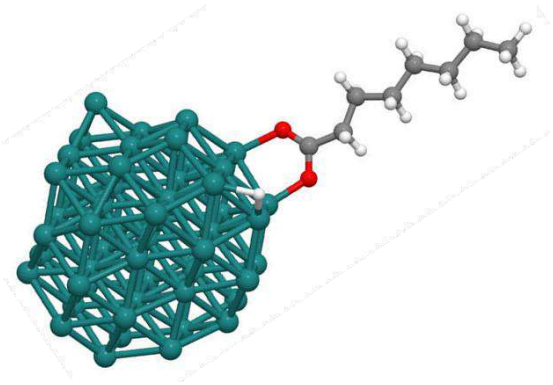

Structure 70, figure 4.11 (c) – $Ru_{55}(C_7H_{15}COO)(H)$

Ru	9.1549	12.9894	10.2290	Ru	15.9864	10.5022	13.6741
Ru	10.4571	15.1856	10.2726	Ru	16.5351	13.2875	5.4068
Ru	10.3874	10.6267	10.0131	Ru	15.4929	12.3566	7.4729
Ru	11.6397	17.4010	10.3155	Ru	17.1358	13.0596	9.6270
Ru	11.3354	13.1717	5.9226	Ru	15.8617	12.1805	11.8028
Ru	10.2308	12.2861	8.0458	Ru	17.1966	12.7003	13.9009
Ru	11.6899	12.9373	10.0537	Ru	16.7359	14.6121	7.6126
Ru	10.5314	12.0577	12.1335	Ru	17.0756	14.4526	11.8675
Ru	12.0280	12.7529	14.2685	Ru	16.9214	8.4866	9.3170
Ru	12.6398	15.5015	5.9528	Ru	16.8080	10.1056	7.3483
Ru	11.5001	14.5706	8.0326	Ru	18.3152	10.7676	9.3775
Ru	13.0515	15.2801	10.0817	Ru	17.1472	9.8634	11.4957
Ru	11.8341	14.3116	12.2385	Ru	18.0433	12.3584	7.3612
Ru	13.2551	15.0579	14.1590	Ru	18.3665	12.0849	11.6312
Ru	12.8164	16.8515	8.1102	C	12.0555	14.4164	16.7555
Ru	14.2822	17.5597	10.0831	C	12.5021	16.3936	25.4649
Ru	13.1358	16.6242	12.2181	C	11.9005	15.3395	24.5314
Ru	11.7391	8.4378	9.7476	C	12.2178	15.6036	23.0580
Ru	12.7062	10.9274	5.6616	C	11.6465	14.5830	22.0604
Ru	11.5595	10.0408	7.7711	C	12.0415	14.9723	20.6349
Ru	12.9983	10.6402	9.7717	C	11.5895	14.1113	19.4368
Ru	11.8986	9.7759	11.8698	C	12.1603	14.8262	18.2092
Ru	13.3348	10.4274	13.9227	O	11.6591	13.2889	16.3086
Ru	13.9288	13.2497	5.6162	O	12.5010	15.3662	15.9942
Ru	12.8512	12.3512	7.7428	H	17.1671	14.1253	15.0200
Ru	14.3745	12.9905	9.7969	H	12.2642	16.1865	26.5180
Ru	13.1911	12.0560	12.0280	H	13.5986	16.4295	25.3736
Ru	14.5832	12.7294	13.9891	H	12.1208	17.3993	25.2305
Ru	15.2256	15.4529	5.5994	H	12.2756	14.3413	24.8136
Ru	14.1842	14.6391	7.7339	H	10.8070	15.3060	24.6702
Ru	15.7318	15.4046	9.8851	H	11.8487	16.6096	22.7881
Ru	14.5430	14.3664	11.9977	H	13.3148	15.6489	22.9314
Ru	15.8911	14.9915	14.0924	H	12.0218	13.5743	22.3042
Ru	15.4019	16.8577	7.8632	H	10.5484	14.5414	22.1592
Ru	15.6821	16.6307	12.1153	H	11.6837	16.0026	20.4574
Ru	14.5076	8.4445	9.6144	H	13.1436	15.0422	20.5976
Ru	13.2440	7.6002	11.5352	H	11.9723	13.0826	19.5202
Ru	15.2402	10.9445	5.4356	H	10.4914	14.0465	19.3897
Ru	14.2190	10.0445	7.5508	H	11.8111	15.8711	18.2168
Ru	15.7594	10.7301	9.5782	H	13.2530	14.9183	18.3518
Ru	14.5187	9.7581	11.7583				

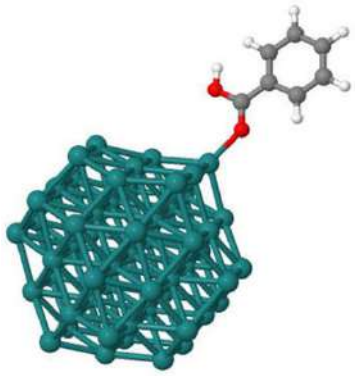

Structure 71, figure 4.11 (b) – $Ru_{55}(C_6H_5COOH)$

Ru	9.8358	12.0302	13.4472	Ru	15.1170	7.3535	13.4649
Ru	11.1648	14.1998	13.5304	Ru	13.7160	6.6305	15.3452
Ru	11.0313	9.6210	13.4685	Ru	16.1840	9.6585	9.2396
Ru	12.3867	16.4635	13.5959	Ru	15.0063	8.8653	11.3251
Ru	12.3218	11.9595	9.3509	Ru	16.4205	9.6140	13.4350
Ru	11.0605	11.1882	11.4028	Ru	15.0190	8.7560	15.5431
Ru	12.3710	11.9338	13.4794	Ru	16.3510	9.5368	17.5427
Ru	11.0348	11.1760	15.4963	Ru	17.5437	11.9620	9.2079
Ru	12.3780	11.8433	17.5999	Ru	16.3480	11.1428	11.2401
Ru	13.6757	14.2460	9.3525	Ru	17.8320	11.9043	13.4485
Ru	12.3713	13.4743	11.4059	Ru	16.4193	11.1598	15.6231
Ru	13.7723	14.2368	13.5273	Ru	17.5608	11.8183	17.7369
Ru	12.4058	13.4078	15.5958	Ru	17.6040	13.3938	11.3482
Ru	13.7178	14.0833	17.6454	Ru	17.6580	13.3863	15.5951
Ru	13.6788	15.7160	11.4873	Ru	17.5433	7.3248	13.3723
Ru	15.0345	16.4805	13.5062	Ru	17.5928	8.8575	11.3212
Ru	13.7250	15.6745	15.6044	Ru	18.9820	9.5890	13.3705
Ru	12.3408	7.3975	13.4163	Ru	17.6573	8.8025	15.4705
Ru	13.6330	9.6933	9.3007	Ru	18.8900	11.1073	11.3017
Ru	12.3438	8.9113	11.3482	Ru	18.9068	11.0178	15.5771
Ru	13.6518	9.5798	13.4272	C	10.3722	18.7190	13.0039
Ru	12.3810	8.8343	15.4723	C	8.8727	20.6862	12.5320
Ru	13.7173	9.5143	17.5971	C	7.8790	21.5755	12.9332
Ru	14.9388	11.9680	9.2440	C	7.3480	21.4948	14.2236
Ru	13.6878	11.2055	11.3308	C	7.8250	20.5245	15.1133
Ru	15.0738	11.8943	13.4826	C	8.8170	19.6310	14.7176
Ru	13.6900	11.0702	15.6231	C	9.3515	19.6935	13.4137
Ru	14.9705	11.7693	17.6896	O	10.8483	17.8623	13.7881
Ru	16.2500	14.1675	9.2183	O	10.8315	18.7113	11.7369
Ru	15.0520	13.4718	11.3126	H	10.3683	19.3840	11.2008
Ru	16.4532	14.2963	13.5156	H	9.1882	18.8715	15.4053
Ru	15.1138	13.3935	15.6699	H	7.4148	20.4650	16.1221
Ru	16.3285	13.9935	17.7679	H	6.5653	22.1883	14.5343
Ru	16.2995	15.6720	11.4252	H	7.5203	22.3343	12.2369
Ru	16.2845	15.6150	15.6731	H	9.2715	20.7978	11.5193

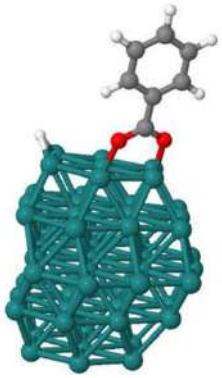

Structure 72, figure 4.11 (d) – $Ru_{55}(C_6H_5COO)(H)$

Ru	9.0307	13.3890	11.9200	Ru	14.3848	8.8338	11.3269
Ru	10.3398	15.5768	11.9899	Ru	13.1168	7.9883	13.2478
Ru	10.2625	11.0073	11.7021	Ru	15.1390	11.3435	7.1568
Ru	11.5287	17.7897	12.0531	Ru	14.1105	10.4413	9.2687
Ru	11.2240	13.5673	7.6385	Ru	15.6445	11.1230	11.3019
Ru	10.1168	12.6852	9.7497	Ru	14.3960	10.1395	13.4719
Ru	11.5705	13.3275	11.7621	Ru	15.8445	10.8775	15.4115
Ru	10.3930	12.4343	13.8242	Ru	16.4370	13.6853	7.1432
Ru	11.8355	13.0683	15.9130	Ru	15.3838	12.7515	9.1967
Ru	12.5438	15.8913	7.6705	Ru	17.0118	13.4497	11.3659
Ru	11.3935	14.9653	9.7526	Ru	15.7415	12.5630	13.5437
Ru	12.9325	15.6650	11.8154	Ru	17.0498	13.0637	15.6507
Ru	11.7083	14.6958	13.9573	Ru	16.6253	15.0073	9.3553
Ru	13.1100	15.3623	15.9429	Ru	16.9458	14.8278	13.6185
Ru	12.7020	17.2455	9.8459	Ru	16.8018	8.8773	11.0391
Ru	14.1650	17.9425	11.8342	Ru	16.6948	10.4968	9.0745
Ru	13.0020	16.9873	13.9677	Ru	18.1963	11.1575	11.1215
Ru	11.6168	8.8218	11.4496	Ru	17.0123	10.2420	13.2244
Ru	12.6040	11.3245	7.3723	Ru	17.9328	12.7463	9.1039
Ru	11.4443	10.4310	9.4726	Ru	18.2348	12.4695	13.3721
Ru	12.8720	11.0233	11.4790	C	11.7448	14.5800	18.4493
Ru	11.7608	10.1610	13.5725	C	10.7350	13.8273	20.6281
Ru	13.1840	10.7837	15.6226	C	10.5473	14.0065	21.9986
Ru	13.8258	13.6488	7.3367	C	11.1463	15.0863	22.6572
Ru	12.7368	12.7440	9.4546	C	11.9382	15.9900	21.9419
Ru	14.2580	13.3793	11.5222	C	12.1240	15.8215	20.5725
Ru	13.0735	12.4243	13.7184	C	11.5213	14.7405	19.9040
Ru	14.4343	13.0885	15.7097	O	11.3065	13.5265	17.8498
Ru	15.1265	15.8395	7.3333	O	12.3880	15.5192	17.8422
Ru	14.0740	15.0338	9.4630	H	17.0310	14.5063	16.7466
Ru	15.6125	15.7873	11.6360	H	12.7398	16.5157	20.0021
Ru	14.4028	14.7475	13.7465	H	12.4128	16.8288	22.4531
Ru	15.7350	15.3600	15.8431	H	10.9980	15.2238	23.7294
Ru	15.2880	17.2485	9.6197	H	9.9313	13.3025	22.5599
Ru	15.5490	17.0080	13.8713	H	10.2760	12.9868	20.1076

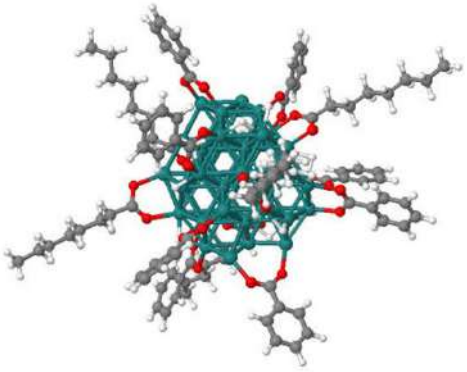

Structure 73, figure 4.12 (bottom right) – $Ru_{55}(C_7H_{15}COO)_5(C_6H_5COO)_8(H)_{13}$

Ru	19.6254	17.2457	19.6813	Ru	22.2350	17.1619	19.7962
Ru	19.7904	17.1233	15.2828	C	9.6949	15.2184	17.6615
Ru	19.7643	15.6826	17.4689	C	11.0846	15.7838	17.4844
Ru	18.2783	19.4740	19.6132	C	18.5960	16.3578	25.8906
Ru	18.3309	19.5052	15.2543	C	18.7615	16.5927	24.4064
Ru	16.9298	17.0562	19.5531	C	23.7623	17.4295	12.7709
Ru	18.4113	17.9388	17.4654	C	12.2469	20.2281	12.4403
Ru	17.0392	17.1410	15.3032	C	13.4952	19.6505	13.0660
Ru	16.9328	15.5213	17.4115	C	14.8442	23.9837	19.7793
Ru	16.9713	20.2069	17.4554	C	23.8047	22.2253	17.9067
Ru	15.7113	17.8939	17.3650	C	22.5507	21.4469	18.2375
Ru	13.1044	17.8454	17.3517	C	19.8966	10.7066	19.2230
Ru	14.3261	20.0313	17.3497	C	18.2915	13.3366	9.6707
Ru	14.1511	15.3310	17.4197	C	18.2808	14.1486	10.9447
Ru	15.5232	22.3797	17.4173	C	24.9156	16.0191	19.0939
Ru	15.7413	17.7221	13.1960	C	14.8243	11.9849	14.9591
Ru	14.4880	16.9527	15.3889	C	8.0523	26.4278	10.8226
Ru	14.3040	17.0308	19.3542	C	9.3517	25.8976	11.4304
Ru	15.4530	17.8552	21.5162	C	9.4660	24.3721	11.3712
Ru	17.0660	20.1179	13.1784	C	10.7609	23.8270	11.9782
Ru	15.6075	19.3568	15.2024	C	10.8682	22.3014	11.9158
Ru	15.5262	19.3802	19.4509	C	12.1620	21.7583	12.5257
Ru	16.7618	20.1915	21.7091	C	3.4954	12.0907	14.4651
Ru	16.8782	21.6388	15.3405	C	4.8274	12.7951	14.2029
Ru	18.1198	22.5076	17.3165	C	5.5798	13.1530	15.4869
Ru	16.8156	21.7634	19.5835	C	6.9283	13.8369	15.2471
Ru	15.8226	13.1906	17.4812	C	7.6533	14.2057	16.5435
Ru	17.0521	15.6014	13.1798	C	9.0279	14.8430	16.3258
Ru	15.7026	14.8349	15.2728	C	14.2536	9.4691	4.4097
Ru	15.6876	14.7895	19.4900	C	14.2279	10.3170	5.6820
Ru	16.9751	15.5447	21.6137	C	15.6195	10.7468	6.1543
Ru	18.3850	17.8720	13.2248	C	15.5946	11.5928	7.4291
Ru	18.1275	17.9021	21.7289	C	16.9781	12.0402	7.9089
Ru	19.6090	20.1509	13.1718	C	16.9161	12.8771	9.1886
Ru	19.7095	20.3047	17.4754	C	30.8084	24.6485	19.8349
Ru	19.3783	20.2350	21.7151	C	29.6455	23.7168	20.1794
Ru	19.4485	21.8190	15.4211	C	28.4758	23.8204	19.1968
Ru	19.2127	21.7884	19.5693	C	27.2949	22.9112	19.5459
Ru	18.5625	13.4341	17.3178	C	26.1363	23.0022	18.5494
Ru	17.3759	12.5231	19.1638	C	24.9346	22.1338	18.9322
Ru	19.6039	15.5956	13.1807	C	20.3480	18.2076	33.0897
Ru	18.4133	14.8714	15.2357	C	20.5715	18.5514	31.6161
Ru	18.3069	14.8067	19.5307	C	19.7878	17.6454	30.6633
Ru	19.4522	15.6776	21.6783	C	20.0009	17.9655	29.1811
Ru	20.9365	18.0890	13.2412	C	19.2068	17.0444	28.2522
Ru	21.1035	17.9364	17.5476	C	19.4116	17.3296	26.7620
Ru	20.7148	18.1593	21.7662	C	21.7177	8.9804	19.2912
Ru	20.9763	19.3914	15.3568	C	22.2206	7.7560	19.7278
Ru	20.9176	19.5265	19.7273	C	21.4626	6.9502	20.5838
Ru	20.9309	13.3649	17.8265	C	20.1955	7.3720	20.9998
Ru	21.0100	14.8208	15.5189	C	19.6840	8.5914	20.5591
Ru	22.3970	15.5898	17.5731	C	20.4425	9.4062	19.7013
Ru	20.9807	15.0460	19.6464	C	13.5568	11.2109	12.9398
Ru	22.3196	17.2094	15.4204	C	12.8207	10.2381	12.2648

C	12.5982	8.9895	12.8551
C	13.1171	8.7140	14.1246
C	13.8525	9.6830	14.8056
C	14.0757	10.9394	14.2173
C	24.9030	18.0304	10.6173
C	26.0644	18.2371	9.8738
C	27.3182	18.0190	10.4539
C	27.4088	17.5886	11.7820
C	26.2516	17.3811	12.5308
C	24.9897	17.6033	11.9529
C	13.2992	25.9524	19.7993
C	12.7095	27.0283	20.4604
C	13.0142	27.2803	21.8025
C	13.9115	26.4514	22.4845
C	14.5051	25.3743	21.8299
C	14.2027	25.1189	20.4807
C	26.9562	16.3180	20.5169
C	28.2864	16.0240	20.8139
C	29.0099	15.1444	20.0021
C	28.4000	14.5592	18.8874
C	27.0707	14.8498	18.5842
C	26.3396	15.7306	19.3991
C	14.6872	13.7774	22.1592
C	12.7594	12.2285	22.5319
C	11.9551	11.4628	23.3744
C	12.2100	11.4290	24.7496
C	13.2722	12.1672	25.2820
C	14.0783	12.9374	24.4449
C	13.8274	12.9714	23.0629
C	14.9071	19.4770	23.9396
C	13.0577	18.9883	25.5561
C	12.1951	19.3859	26.5772
C	12.3181	20.6580	27.1456
C	13.3138	21.5309	26.6944
C	14.1781	21.1397	25.6726
C	14.0521	19.8660	25.0928
C	20.9454	22.8206	13.0358
C	21.7453	23.8728	10.9137
C	22.1465	24.9899	10.1838
C	22.2500	26.2374	10.8087
C	21.9576	26.3634	12.1709
C	21.5566	25.2498	12.9070
C	21.4443	23.9964	12.2813
O	20.7985	21.7112	12.4216
O	20.6462	22.9881	14.2842
O	14.7521	18.3077	23.4373
O	15.7103	20.3698	23.4712
O	14.4488	13.7709	20.9084
O	15.6571	14.4500	22.6960
O	11.1997	17.0646	17.3888
O	12.0569	14.9567	17.4328
O	18.1212	17.5571	23.8735
O	19.5454	15.7887	23.7663
O	22.6220	17.6637	12.1965
O	23.8817	17.0837	13.9908
O	13.8112	20.0294	14.2451
O	14.1676	18.7934	12.3837
O	15.7094	23.2852	20.4223
O	14.5135	23.7472	18.5535
O	21.5257	21.6214	17.4960
O	22.5699	20.6464	19.2400
O	18.6830	10.9862	19.5538
O	20.6722	11.4339	18.5018
O	19.4119	14.5014	11.4392
O	17.1524	14.4442	11.4785
O	24.2810	16.8302	19.8627
O	24.3820	15.4264	18.0870
O	15.2800	11.7082	16.1241
O	14.9687	13.1329	14.3945
H	9.7735	14.3225	18.2943
H	9.0818	15.9656	18.1854
H	18.8939	15.3224	26.1075
H	17.5270	16.4712	26.1268
H	12.1987	19.8840	11.3982
H	11.3863	19.7830	12.9701
H	23.4986	23.2709	17.7405
H	24.1422	21.8639	16.9193
H	18.9630	12.4787	9.8427
H	18.7984	13.9482	8.9045
H	22.7133	18.9615	15.5240
H	19.8860	13.7174	14.7642
H	18.2784	20.8841	12.1342
H	15.0328	19.6231	21.2168
H	16.2088	21.6927	13.6980
H	18.1350	21.0203	22.6646
H	13.9664	16.9569	21.1590
H	22.7608	15.3537	15.7197
H	14.1022	13.5712	17.5826
H	22.4651	17.7180	21.4893
H	7.9957	27.5242	10.8782
H	7.9638	26.1429	9.7632
H	7.1740	26.0217	11.3470
H	10.2144	26.3459	10.9087
H	9.4298	26.2258	12.4811
H	8.6012	23.9231	11.8917
H	9.3889	24.0433	10.3194
H	11.6255	24.2748	11.4574
H	10.8383	24.1548	13.0297
H	10.0036	21.8532	12.4370
H	10.7910	21.9738	10.8638
H	13.0300	22.2001	12.0087
H	12.2414	22.0652	13.5798
H	2.9720	11.8493	13.5291
H	3.6462	11.1492	15.0150
H	2.8247	12.7205	15.0693
H	5.4678	12.1533	13.5742
H	4.6518	13.7137	13.6175
H	4.9439	13.8076	16.1091
H	5.7394	12.2356	16.0811
H	7.5724	13.1738	14.6432
H	6.7757	14.7472	14.6409
H	7.0206	14.8947	17.1305
H	7.7718	13.3001	17.1643
H	9.6803	14.1446	15.7775
H	8.9298	15.7453	15.7005
H	13.2406	9.1789	4.0957
H	14.7163	10.0179	3.5754
H	14.8336	8.5457	4.5586
H	13.6101	11.2159	5.5146
H	13.7299	9.7549	6.4905
H	16.2405	9.8488	6.3218
H	16.1183	11.3132	5.3477
H	14.9647	12.4843	7.2613
H	15.1001	11.0216	8.2349
H	17.6125	11.1520	8.0774
H	17.4727	12.6200	7.1093
H	16.2755	13.7579	9.0251
H	16.4277	12.2959	9.9869
H	31.6346	24.5492	20.5533
H	31.2098	24.4309	18.8337
H	30.4882	25.7018	19.8392
H	30.0031	22.6733	20.2073
H	29.2835	23.9395	21.1979
H	28.1289	24.8683	19.1553
H	28.8345	23.5814	18.1794
H	27.6428	21.8648	19.6043
H	26.9274	23.1641	20.5559
H	25.8133	24.0553	18.4628
H	26.4958	22.7131	17.5461
H	25.2478	21.0836	19.0387
H	24.5578	22.4377	19.9220
H	20.9201	18.8716	33.7533
H	19.2856	18.2985	33.3624
H	20.6559	17.1735	33.3071
H	20.2875	19.6017	31.4336
H	21.6469	18.4829	31.3793
H	20.0682	16.5935	30.8515
H	18.7111	17.7165	30.8999
H	19.7185	19.0151	28.9878
H	21.0761	17.8902	28.9413
H	19.4837	15.9957	28.4604
H	18.1317	17.1269	28.4908

H	19.1147	18.3645	26.5292
H	20.4811	17.2393	26.5095
H	18.6972	8.9289	20.8736
H	19.6038	6.7472	21.6702
H	21.8592	5.9932	20.9268
H	23.2081	7.4282	19.4000
H	22.3000	9.6169	18.6260
H	14.2562	9.4858	15.7984
H	12.9435	7.7410	14.5867
H	12.0176	8.2315	12.3266
H	12.4142	10.4552	11.2759
H	13.7329	12.1898	12.4944
H	26.3061	17.0544	13.5690
H	28.3860	17.4196	12.2364
H	28.2261	18.1870	9.8717
H	25.9927	18.5753	8.8391
H	23.9205	18.2055	10.1802
H	15.2060	24.7197	22.3473
H	14.1493	26.6470	23.5311
H	12.5524	28.1241	22.3175
H	12.0109	27.6755	19.9282
H	13.0737	25.7463	18.7533
H	26.5807	14.3994	17.7214
H	28.9626	13.8713	18.2548
H	30.0497	14.9126	20.2396
H	28.7605	16.4787	21.6849
H	26.3775	16.9956	21.1440
H	20.6544	14.2493	21.1528
H	14.9083	13.5181	24.8467
H	13.4725	12.1412	26.3542
H	11.5805	10.8269	25.4068
H	11.1264	10.8882	22.9580
H	12.5762	12.2642	21.4581
H	19.7816	22.0041	21.2203
H	14.9479	21.8151	25.3004
H	13.4096	22.5246	27.1346
H	11.6344	20.9716	27.9363
H	11.4156	18.7057	26.9236
H	12.9629	18.0072	25.0913
H	13.9830	20.2044	19.1414
H	21.3127	25.3373	13.9654
H	22.0342	27.3366	12.6580
H	22.5536	27.1128	10.2324
H	22.3715	24.8908	9.1208
H	21.6464	22.8973	10.4382

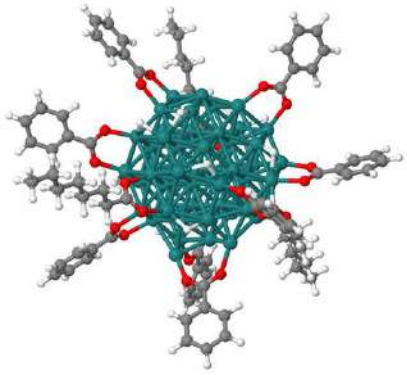

Structure 74, figure 4.12 (top right)– $Ru_{55}(C_7H_{15}COO)_3(C_6H_5COO)(H)_{11}$

Ru	19.5789	17.3288	19.6910
Ru	19.6997	17.3314	15.3174
Ru	19.6292	15.8093	17.4669
Ru	18.1799	19.5714	19.6476
Ru	18.2667	19.6278	15.2887
Ru	16.8289	17.1385	19.5848
Ru	18.2862	18.0359	17.5052
Ru	16.9691	17.2902	15.3191
Ru	16.8521	15.6373	17.4184
Ru	16.8979	20.3553	17.4584
Ru	15.6192	18.0361	17.3886
Ru	13.0546	18.0322	17.3678
Ru	14.3188	20.2710	17.4807
Ru	14.2796	15.5433	17.4469
Ru	15.4708	22.4891	17.4858
Ru	15.6580	17.9626	13.2210
Ru	14.3501	17.1542	15.4136
Ru	14.2052	17.1945	19.3946
Ru	15.3687	18.0187	21.5465
Ru	17.0032	20.2990	13.2612
Ru	15.5175	19.5523	15.2807
Ru	15.5338	19.4656	19.5575
Ru	16.7468	20.2686	21.7204
Ru	16.8777	21.8223	15.4136
Ru	18.1323	22.6310	17.4338
Ru	16.7411	21.8283	19.6220
Ru	15.6998	13.3433	17.4548
Ru	16.9567	15.7703	13.2036
Ru	15.6116	15.0021	15.2705
Ru	15.6329	14.8199	19.5368
Ru	16.9271	15.6264	21.6386
Ru	18.2949	18.0046	13.2798
Ru	18.0634	17.9644	21.7635
Ru	19.5782	20.2704	13.2186
Ru	19.6577	20.3125	17.4873
Ru	19.3330	20.2825	21.7249
Ru	19.4682	21.9221	15.5402
Ru	19.3235	21.7817	19.4845
Ru	18.4433	13.5555	17.3017
Ru	17.2903	12.6353	19.1562
Ru	19.5679	15.7145	13.2437
Ru	18.3295	15.0642	15.2632
Ru	18.2522	14.9101	19.5562
Ru	19.4192	15.7317	21.6574
Ru	20.8653	18.2315	13.2564
Ru	21.0635	18.0530	17.5695
Ru	20.6676	18.2063	21.7753
Ru	20.9547	19.5657	15.4261
Ru	20.8238	19.6281	19.7189
Ru	20.8510	13.5003	17.7376

Ru	20.9264	14.9777	15.5426
Ru	22.3144	15.6855	17.5961
Ru	20.8960	15.0903	19.6367
Ru	22.2335	17.3302	15.3973
Ru	22.1946	17.3654	19.6747
C	18.5774	16.3717	25.8895
C	18.7286	16.6180	24.4058
C	23.7340	17.6668	12.8195
C	12.1825	20.4670	12.4785
C	13.4305	19.8856	13.0990
C	14.9357	24.1752	19.8236
C	19.8098	10.8234	19.1044
C	18.2752	13.4390	9.7553
C	18.2567	14.2591	11.0236
C	24.8373	16.1340	19.1024
C	14.6208	12.2037	14.9299
C	7.9420	26.6168	10.8255
C	9.2463	26.1057	11.4384
C	9.3781	24.5814	11.3896
C	10.6753	24.0539	12.0073
C	10.7977	22.5295	11.9503
C	12.0892	21.9956	12.5733
C	14.1382	9.7155	4.4569
C	14.1421	10.5523	5.7363
C	15.5479	10.9360	6.2072
C	15.5496	11.7745	7.4872
C	16.9442	12.1787	7.9732
C	16.8947	13.0155	9.2535
C	20.2036	18.3637	33.0840
C	20.4218	18.6949	31.6068
C	19.6784	17.7475	30.6619
C	19.8892	18.0591	29.1778
C	19.1420	17.0972	28.2513
C	19.3391	17.3860	26.7607
C	21.6025	9.0693	19.0576
C	22.1366	7.8603	19.5000
C	21.4755	7.1190	20.4846
C	20.2721	7.5878	21.0218
C	19.7251	8.7882	20.5717
C	20.3891	9.5399	19.5873
C	13.2613	11.4832	12.9526
C	12.4722	10.5382	12.2987
C	12.2358	9.2914	12.8873
C	12.7963	8.9885	14.1327
C	13.5835	9.9301	14.7933
C	13.8188	11.1856	14.2080
C	24.9287	18.3814	10.7313
C	26.1093	18.6433	10.0372
C	27.3477	18.4243	10.6494
C	27.4044	17.9355	11.9589
C	26.2282	17.6705	12.6578
C	24.9815	17.8957	12.0485
C	13.4415	26.1832	19.8725
C	12.8763	27.2602	20.5533
C	13.1909	27.4849	21.8978
C	14.0763	26.6291	22.5622
C	14.6465	25.5517	21.8879
C	14.3313	25.3216	20.5369
C	26.8786	16.4541	20.5151
C	28.1953	16.1337	20.8414
C	28.8911	15.1771	20.0952
C	28.2671	14.5415	19.0164
C	26.9506	14.8572	18.6842
C	26.2468	15.8154	19.4342
C	14.6149	13.8858	22.1973
C	12.6156	12.4377	22.5837
C	11.7963	11.6903	23.4274
C	12.0934	11.5938	24.7911
C	13.2122	12.2529	25.3112
C	14.0321	13.0080	24.4738
C	13.7401	13.1026	23.1026
C	14.5764	19.8798	23.7042
C	12.6138	19.5453	25.2212
C	11.7067	20.0324	26.1606
C	11.8228	21.3427	26.6369
C	12.8547	22.1660	26.1736
C	13.7644	21.6857	25.2338
C	13.6481	20.3713	24.7493
C	20.8426	22.9960	13.1222
C	21.4943	24.1077	10.9822
C	21.8019	25.2514	10.2481
C	21.8880	26.4932	10.8868
C	21.6777	26.5865	12.2666
C	21.3728	25.4454	13.0074
C	21.2722	24.1987	12.3673
O	20.6613	21.9070	12.4816
O	20.6182	23.1247	14.3901
O	14.4523	18.6745	23.2823
O	15.4439	20.7060	23.2299
O	14.3767	13.8762	20.9456
O	15.6004	14.5467	22.7210
O	18.0535	17.5694	23.8853
O	19.5308	15.8445	23.7558
O	22.6047	17.9272	12.2394
O	23.8262	17.2477	14.0202
O	13.7715	20.2740	14.2642
O	14.0782	19.0022	12.4198
O	15.7936	23.4525	20.4478
O	14.5764	23.9415	18.6035
O	18.6095	11.0986	19.4819
O	20.5420	11.5419	18.3290
O	19.3859	14.5789	11.5510
O	17.1262	14.5961	11.5222
O	24.2196	17.0032	19.8233
O	24.2885	15.5129	18.1212
O	15.0712	11.9146	16.0974
O	14.8152	13.3367	14.3562
H	18.9303	15.3535	26.1045
H	17.5038	16.4269	26.1274
H	12.1331	20.1291	11.4341
H	11.3247	20.0142	13.0064
H	18.9197	12.5642	9.9439
H	18.8109	14.0322	8.9940
H	22.6579	19.0992	15.5673
H	18.2329	20.9151	12.1409
H	16.1617	21.8749	13.7743
H	18.1765	21.2079	22.6404
H	13.8215	17.1920	21.1596
H	22.6893	15.4700	15.7351
H	13.9291	13.8374	17.6199
H	22.3238	18.6955	20.8750
H	7.8730	27.7129	10.8727
H	7.8575	26.3228	9.7683
H	7.0676	26.2050	11.3523
H	10.1047	26.5601	10.9151
H	9.3192	26.4417	12.4868
H	8.5155	24.1260	11.9080
H	9.3105	24.2449	10.3394
H	11.5383	24.5091	11.4899
H	10.7420	24.3866	13.0580
H	9.9320	22.0745	12.4638
H	10.7336	22.1992	10.8984
H	12.9595	22.4465	12.0684
H	12.1546	22.2967	13.6299
H	13.1162	9.4578	4.1442
H	14.6138	10.2578	3.6257
H	14.6914	8.7741	4.5954
H	13.5513	11.4708	5.5792
H	13.6304	9.9987	6.5420
H	16.1413	10.0183	6.3675
H	16.0616	11.4922	5.4027
H	14.9470	12.6856	7.3242
H	15.0368	11.2139	8.2888
H	17.5511	11.2720	8.1441
H	17.4602	12.7451	7.1778
H	16.2800	13.9134	9.0837
H	16.3807	12.4477	10.0453
H	20.7475	19.0576	33.7406
H	19.1376	18.4191	33.3508
H	20.5486	17.3449	33.3179
H	20.0999	19.7313	31.4087
H	21.5003	18.6638	31.3763

H	19.9974	16.7095	30.8650
H	18.5981	17.7808	30.8916
H	19.5652	19.0940	28.9707
H	20.9684	18.0260	28.9470
H	19.4662	16.0633	28.4653
H	18.0635	17.1308	28.4850
H	18.9924	18.4040	26.5220
H	20.4129	17.3481	26.5133
H	18.7856	9.1600	20.9790
H	19.7579	7.0136	21.7939
H	21.8986	6.1761	20.8343
H	23.0729	7.4942	19.0763
H	22.1105	9.6576	18.2945
H	14.0200	9.7119	15.7677
H	12.6146	8.0160	14.5925
H	11.6119	8.5562	12.3766
H	12.0345	10.7763	11.3281
H	13.4483	12.4611	12.5094
H	26.2556	17.2984	13.6816
H	28.3696	17.7672	12.4388
H	28.2701	18.6385	10.1071
H	26.0648	19.0269	9.0170
H	23.9573	18.5582	10.2705
H	15.3368	24.8757	22.3919
H	14.3221	26.8039	23.6105
H	12.7454	28.3280	22.4285
H	12.1874	27.9283	20.0346
H	13.2048	25.9969	18.8254
H	26.4513	14.3676	17.8484
H	28.8092	13.7950	18.4341
H	29.9205	14.9260	20.3549
H	28.6811	16.6300	21.6829
H	26.3223	17.1944	21.0898
H	20.8795	14.5967	21.3360
H	14.9062	13.5267	24.8666
H	13.4459	12.1766	26.3741
H	11.4524	11.0046	25.4489
H	10.9227	11.1787	23.0210
H	12.3994	12.5192	21.5186
H	20.1856	21.8311	21.0239
H	14.5667	22.3187	24.8554
H	12.9453	23.1887	26.5427
H	11.1060	21.7243	27.3657
H	10.8997	19.3912	26.5180
H	12.5284	18.5312	24.8315
H	12.5483	19.7501	17.4512
H	21.1918	25.5071	14.0800
H	21.7410	27.5549	12.7647
H	22.1136	27.3899	10.3073
H	21.9639	25.1774	9.1717
H	21.4054	23.1366	10.4962

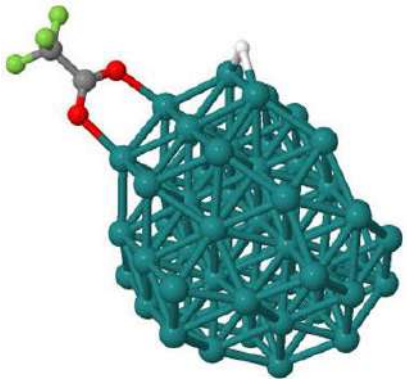

Domain 75, figure 4.18 (bottom) – $Ru_{55}(CF_3COO)(H)$

Ru	8.7884	13.5507	12.8993
Ru	10.0979	15.7412	12.9638
Ru	10.0214	11.1708	12.6830
Ru	11.2879	17.9542	13.0264
Ru	10.9729	13.7268	8.6141
Ru	9.8695	12.8461	10.7270
Ru	11.3292	13.4936	12.7348
Ru	10.1559	12.6050	14.8004
Ru	11.6096	13.2491	16.8791
Ru	12.2903	16.0525	8.6424
Ru	11.1454	15.1275	10.7244
Ru	12.6917	15.8282	12.7838
Ru	11.4728	14.8659	14.9264
Ru	12.8904	15.5584	16.8998
Ru	12.4559	17.4067	10.8167
Ru	13.9262	18.1084	12.7940
Ru	12.7706	17.1596	14.9299
Ru	11.3700	8.9847	12.4279
Ru	12.3513	11.4846	8.3456
Ru	11.1951	10.5924	10.4485
Ru	12.6261	11.1849	12.4519
Ru	11.5219	10.3246	14.5496
Ru	12.9481	10.9535	16.5984
Ru	13.5751	13.8099	8.3086
Ru	12.4894	12.9050	10.4275
Ru	14.0163	13.5404	12.4919
Ru	12.8343	12.5897	14.6927
Ru	14.2037	13.2559	16.6795
Ru	14.8748	16.0043	8.3031
Ru	13.8263	15.1950	10.4336
Ru	15.3719	15.9476	12.5996
Ru	14.1680	14.9131	14.7169
Ru	15.5081	15.5235	16.8107
Ru	15.0456	17.4087	10.5850
Ru	15.3184	17.1705	14.8313
Ru	14.1380	8.9957	12.2964
Ru	12.8765	8.1510	14.2198
Ru	14.8833	11.5021	8.1238
Ru	13.8610	10.6013	10.2387
Ru	15.4007	11.2834	12.2703
Ru	14.1521	10.3033	14.4416
Ru	15.6022	11.0402	16.3795
Ru	16.1833	13.8453	8.1066
Ru	15.1352	12.9095	10.1628

Ru	16.7689	13.6081	12.3306
Ru	15.5008	12.7247	14.5100
Ru	16.8191	13.2240	16.6113
Ru	16.3769	15.1655	10.3176
Ru	16.7090	14.9884	14.5782
Ru	16.5548	9.0361	12.0082
Ru	16.4437	10.6542	10.0404
Ru	17.9513	11.3160	12.0791
Ru	16.7702	10.4026	14.1915
Ru	17.6838	12.9045	10.0679
Ru	17.9954	12.6246	14.3338
C	11.4729	14.8243	19.3714
C	11.1274	14.9746	20.8764
O	11.0538	13.7567	18.8201
O	12.1521	15.7553	18.8367
F	9.7948	14.8540	21.0765
F	11.7467	13.9966	21.5859
F	11.5231	16.1622	21.3680
H	16.8026	14.6629	17.7093

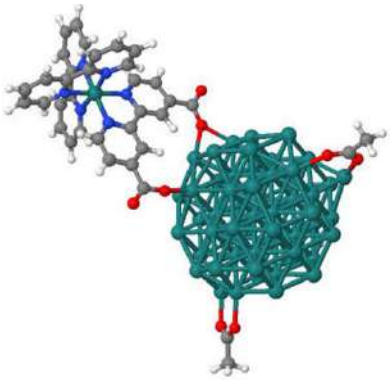

Domain 76, figure 5.4 (left) – $Ru_{55}(CH_3COO)_2(PS1)(H)_2$

Ru	11.1802	12.0506	18.9050
Ru	11.2141	11.9741	14.5236
Ru	11.3133	10.4882	16.7360
Ru	9.7191	14.2452	18.8471
Ru	9.8698	14.2003	14.5539
Ru	8.4347	11.8275	18.8309
Ru	9.8459	12.6975	16.7154
Ru	8.5673	11.8494	14.5652
Ru	8.6201	10.2736	16.6874
Ru	8.4280	14.9787	16.6197
Ru	7.1178	12.4734	16.6333
Ru	4.5965	12.4591	16.4841
Ru	5.8120	14.7229	16.5873
Ru	5.8640	10.1525	16.7069
Ru	6.8242	16.9757	16.5131
Ru	7.1887	12.5095	12.4685
Ru	5.9599	11.6463	14.5246
Ru	5.8312	11.7859	18.7031
Ru	7.0570	12.6011	20.7728
Ru	8.4136	14.8929	12.4830
Ru	7.1054	14.0174	14.5556
Ru	7.0545	14.0782	18.6829
Ru	8.2924	14.8794	20.8091
Ru	8.2851	16.3696	14.5257
Ru	9.5454	17.2840	16.5801
Ru	8.2124	16.4648	18.7131
Ru	7.3818	7.9990	16.7421
Ru	8.6300	10.3204	12.5517
Ru	7.3523	9.5020	14.6491
Ru	7.3037	9.4809	18.7074
Ru	8.5029	10.3489	20.8595
Ru	9.7581	12.6473	12.4907
Ru	9.6738	12.6842	20.8972
Ru	10.9377	14.9139	12.4138
Ru	11.0800	15.1610	16.6551
Ru	10.8466	15.0113	20.9328
Ru	10.8342	16.5478	14.5221
Ru	10.7658	16.5092	18.7679
Ru	10.1573	8.1527	16.7129
Ru	9.0161	7.4219	18.6825
Ru	11.1873	10.4695	12.4843
Ru	10.0140	9.6084	14.5699
Ru	9.9134	9.6491	18.8200
Ru	11.0399	10.5662	20.9333
Ru	12.3335	12.8310	12.4447
Ru	12.5672	12.8736	16.7301
Ru	12.2340	12.9149	21.0001
Ru	12.5073	14.3492	14.4935
Ru	12.2876	14.3526	18.8171
Ru	12.6062	8.2806	16.7051
Ru	12.5916	9.7509	14.6785
Ru	13.8600	10.5795	16.7850
Ru	12.5061	9.6788	18.8820
Ru	13.7793	12.0211	14.7098
Ru	13.6513	12.0414	18.8683
Ru	18.3955	14.6857	9.1532
N	19.7735	13.5951	10.2331
N	17.5121	15.3215	10.9287
N	17.2104	15.8331	7.9161
N	19.0134	14.0413	7.3003
N	19.9678	16.0070	9.2427
N	16.8626	13.3067	9.3199
C	12.4133	5.7008	20.9858
C	11.7123	6.7164	20.1076
C	5.2687	19.5831	19.6303
C	6.1162	18.5871	18.8863
C	17.4130	15.6508	6.5593
C	18.4053	14.6563	6.2186
C	16.2610	16.7133	8.3137
C	15.4978	17.4594	7.4288
C	15.7139	17.3026	6.0479
C	16.6711	16.3968	5.6223
C	18.7472	14.2845	4.9030
C	19.9500	13.0930	7.0581
C	19.7048	13.3114	4.6755
C	20.3255	12.7024	5.7822
C	19.9950	17.2481	8.7004
C	21.0924	15.5572	9.9132

C	21.0883	18.0948	8.7935
C	22.2301	17.6555	9.4893
C	22.2229	16.3875	10.0448
C	19.5894	12.3496	10.7317
C	20.9884	14.2193	10.4522
C	22.0138	13.5555	11.1541
C	21.8108	12.2776	11.6484
C	20.5652	11.6607	11.4363
C	17.8139	16.4078	11.6877
C	16.4530	14.5500	11.3315
C	15.6842	14.8812	12.4498
C	15.9617	16.0193	13.1948
C	17.0761	16.7879	12.8023
C	16.5107	12.3165	8.4555
C	16.1228	13.4311	10.4686
C	15.0700	12.5643	10.7511
C	14.6792	11.5829	9.8501
C	15.4446	11.4537	8.6736
C	13.4969	10.7055	10.1332
C	15.0675	16.4367	14.3416
O	5.8629	18.4005	17.6395
O	7.0187	17.9599	19.5401
O	12.3968	7.7577	19.8152
O	10.5062	6.4331	19.7660
O	14.0663	15.6276	14.5991
O	15.3105	17.4827	14.9532
O	12.7008	11.1635	11.1053
O	13.2945	9.6616	9.5171
H	11.8960	4.7365	20.9574
H	12.4144	6.0729	22.0214
H	13.4597	5.5896	20.6767
H	7.0386	14.0972	11.5933
H	5.7973	19.9578	20.5130
H	4.3501	19.0778	19.9666
H	4.9755	20.4071	18.9699
H	4.1797	10.5961	16.7008
H	16.8507	16.2532	4.5576
H	15.1369	17.8772	5.3239
H	14.7484	18.1475	7.8166
H	16.1284	16.8129	9.3902
H	18.2499	14.7672	4.0628
H	19.9700	13.0240	3.6582
H	21.0905	11.9373	5.6590
H	20.4021	12.6407	7.9397
H	19.0901	17.5532	8.1766
H	21.0452	19.0786	8.3288
H	23.1043	18.2983	9.5904
H	23.0942	16.0258	10.5890
H	22.9698	14.0540	11.3087
H	22.6027	11.7639	12.1929
H	20.3503	10.6611	11.8110
H	18.6151	11.9021	10.5398
H	18.6734	16.9908	11.3572
H	17.3405	17.6813	13.3676
H	14.8228	14.2752	12.7357
H	14.5478	12.6568	11.7101
H	17.1197	12.2368	7.5558
H	15.1952	10.6846	7.9430

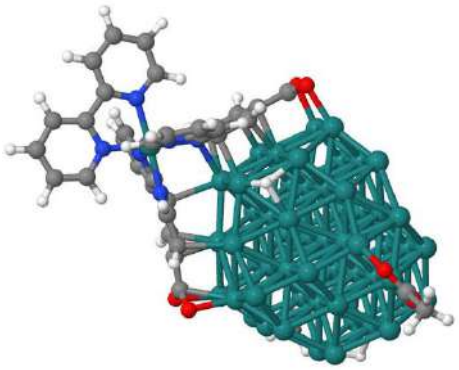

Domain 77, figure 5.4 (right) – $Ru_{55}(CH_3COO)_2(PS2)(H)_2$

Ru	16.5634	15.2789	18.5110
Ru	16.4719	14.6220	14.2254
Ru	16.8198	13.4700	16.5645
Ru	14.9165	17.3475	18.2562
Ru	14.9104	16.7308	13.9421
Ru	13.8862	14.8052	18.5505
Ru	15.1470	15.5135	16.2915
Ru	13.8211	14.2944	14.3088
Ru	14.0652	12.9854	16.5948
Ru	13.5386	17.6458	15.9960
Ru	12.4641	15.0968	16.3489
Ru	9.9218	14.9296	16.3301
Ru	10.9470	17.1742	16.1237
Ru	11.4073	12.6938	16.8091
Ru	11.7952	19.4914	15.6812
Ru	12.3856	14.5488	12.1783
Ru	11.2350	13.8754	14.3530
Ru	11.2479	14.5531	18.4884
Ru	12.4641	15.6169	20.4431
Ru	13.4075	17.1365	11.9745
Ru	12.1931	16.3664	14.0905
Ru	12.2808	16.9210	18.2421
Ru	13.4721	18.0201	20.1986
Ru	13.2729	18.8098	13.7566
Ru	14.4449	20.0182	15.7590
Ru	13.2202	19.3458	17.9128
Ru	13.0796	10.6269	17.1248
Ru	13.9926	12.4334	12.3733
Ru	12.8666	11.8916	14.6516
Ru	12.9660	12.4235	18.8080
Ru	14.0916	13.6358	20.7717
Ru	15.0085	14.9745	12.0708
Ru	15.0752	16.0600	20.4783
Ru	16.0402	17.4256	11.7756
Ru	16.1876	18.0014	15.9314
Ru	16.0798	18.4423	20.1616
Ru	15.7931	19.1052	13.6050
Ru	15.8716	19.6274	17.7911
Ru	15.8002	11.0797	16.8517
Ru	14.8062	10.5020	18.9777

Ru	16.5872	12.9018	12.3643
Ru	15.5205	12.2048	14.5163
Ru	15.5398	12.7895	18.7450
Ru	16.6808	14.0110	20.6767
Ru	17.7458	15.3375	12.1728
Ru	17.8360	15.8886	16.2300
Ru	17.6126	16.4712	20.4541
Ru	17.4458	17.1171	13.9100
Ru	17.4847	17.6369	18.1633
Ru	18.2016	11.3538	16.6621
Ru	18.0888	12.6399	14.4707
Ru	19.3527	13.7937	16.5134
Ru	18.1391	13.0282	18.7214
Ru	19.0660	14.9652	14.2049
Ru	19.0458	15.4213	18.4317
Ru	11.8757	11.3002	9.5088
N	10.9344	13.1085	9.2245
N	13.3885	12.5878	10.1693
N	13.0330	9.6970	10.0720
N	10.4293	10.0667	8.7756
N	11.3913	11.2084	11.5072
N	12.3698	11.2342	7.5184
C	13.3886	11.9095	6.9306
C	11.5706	10.4467	6.7196
C	10.4981	9.7617	7.4345
C	9.6080	8.8480	6.8522
C	9.4701	9.4586	9.5208
C	8.5660	8.5505	8.9907
C	11.8084	10.3312	5.3432
C	13.6643	11.8317	5.5728
C	12.8622	11.0231	4.7577
C	9.6838	13.2815	8.7308
C	9.1344	14.5252	8.4695
C	9.9167	15.6656	8.7205
C	11.1872	15.5107	9.2436
C	11.6987	14.2180	9.5259
C	8.6332	8.2326	7.6281
C	13.0207	13.9706	10.0862
C	14.7344	12.2176	10.2912
C	14.0984	14.9606	10.0121
C	15.8508	13.1501	10.2325
C	15.4891	14.5655	10.0182
C	13.6863	8.8223	9.2695
C	14.5877	7.8879	9.7520
C	14.1780	8.7389	11.9670
C	13.2391	9.6477	11.4291
C	12.4033	10.5293	12.2323
C	12.1568	10.1623	13.6187
C	10.4332	11.8600	12.1742
C	10.2843	11.8369	13.5968
C	14.8506	7.8627	11.1329
C	11.0658	10.8058	14.3002
C	10.8605	10.5233	15.7293
C	16.5420	15.6111	9.9614
C	18.4454	9.3013	21.2420
C	17.6285	10.1934	20.3301
C	10.2110	22.5043	18.3987
C	11.0440	21.3890	17.8272
O	10.7704	20.9956	16.6320
O	11.9561	20.8797	18.5620
O	18.2155	11.2438	19.9014
O	16.4217	9.8077	20.1038
O	11.5358	9.5508	16.3194
O	9.9821	11.2517	16.3796
O	16.2331	16.8708	9.7682
O	17.7899	15.2325	10.1153
H	13.9926	12.5237	7.5974
H	9.6901	8.6151	5.7912
H	9.4624	9.7272	10.5766
H	7.8237	8.0949	9.6451
H	13.0544	10.9393	3.6883
H	11.1616	9.7018	4.7333
H	14.4985	12.4011	5.1641
H	9.1266	12.3658	8.5326
H	8.1251	14.5980	8.0676
H	9.5303	16.6634	8.5129
H	11.8008	16.3848	9.4565
H	7.9426	7.5159	7.1852
H	14.9337	11.1793	10.0282
H	13.8729	15.9373	9.5757
H	16.7818	12.7930	9.7686
H	13.4726	8.9049	8.2039
H	15.0852	7.2093	9.0610
H	14.3823	8.7572	13.0364
H	12.5384	9.2175	14.0051
H	9.7237	12.4239	11.5671
H	9.2992	12.0921	13.9997
H	15.5771	7.1630	11.5464
H	18.0955	8.2649	21.1832
H	18.3157	9.6473	22.2787
H	19.5107	9.3686	20.9950
H	11.7448	16.3455	12.1942
H	15.3632	14.6111	21.8390
H	10.7366	22.9927	19.2255
H	9.2710	22.0811	18.7845
H	9.9544	23.2287	17.6169

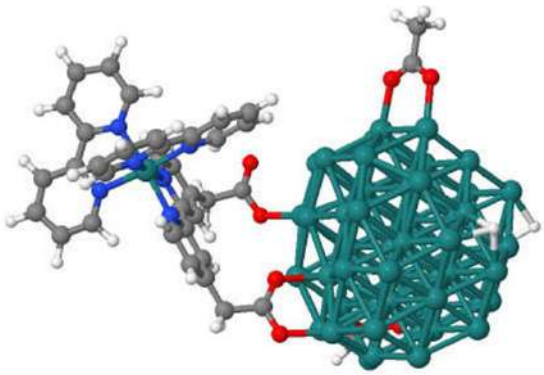

Domain 78, figure 5.5 (left) – $Ru_{55}(CH_3COO)_2(PS3)(H)_2$

Ru	11.5950	10.2017	13.7270
Ru	11.4161	10.1104	9.3826

Ru	11.6596	8.6144	11.5609
Ru	10.1042	12.3636	13.7293
Ru	10.0261	12.3517	9.3831
Ru	8.8300	9.9884	13.7759
Ru	10.1895	10.8284	11.5936
Ru	8.7974	9.9434	9.4834
Ru	8.9132	8.4123	11.6485
Ru	8.7157	13.0967	11.5611
Ru	7.4486	10.6571	11.5893
Ru	4.9117	10.5833	11.6025
Ru	6.0947	12.8719	11.5800
Ru	6.2155	8.2845	11.7423
Ru	7.2078	15.1783	11.5335
Ru	7.3602	10.5326	7.4925
Ru	6.1986	9.7286	9.5597
Ru	6.2080	9.9438	13.7077
Ru	7.4680	10.7317	15.7154
Ru	8.6012	12.9317	7.3751
Ru	7.2993	12.1745	9.5191
Ru	7.4264	12.2362	13.6528
Ru	8.7144	13.0192	15.7410
Ru	8.5087	14.4936	9.4756
Ru	9.8576	15.3837	11.4129
Ru	8.5674	14.6402	13.6678
Ru	7.6979	6.1262	11.7476
Ru	8.8302	8.4108	7.4682
Ru	7.6314	7.6152	9.6191
Ru	7.6842	7.6321	13.7094
Ru	8.9592	8.5392	15.8118
Ru	9.9553	10.7379	7.3548
Ru	10.1401	10.8306	15.7875
Ru	11.1962	12.9663	7.2563
Ru	11.4013	13.2721	11.5345
Ru	11.2170	13.2116	15.8025
Ru	11.1479	14.6225	9.4094
Ru	11.0920	14.6459	13.6441
Ru	10.4476	6.3037	11.6305
Ru	9.3789	5.5726	13.6541
Ru	11.4298	8.5686	7.3712
Ru	10.2399	7.7320	9.4799
Ru	10.2933	7.7887	13.7282
Ru	11.5093	8.6939	15.7481
Ru	12.5783	10.8155	7.2612
Ru	13.0057	10.9574	11.5097
Ru	12.6604	11.1920	15.8683
Ru	12.5368	12.4708	9.3854
Ru	12.6615	12.4846	13.6667
Ru	12.8742	6.3837	11.3641
Ru	12.8685	7.9743	9.4169
Ru	14.1608	8.6068	11.6957
Ru	12.8706	7.7368	13.6588
Ru	13.9963	10.1524	9.1960
Ru	14.0482	10.1177	13.6892
Ru	17.6784	17.1779	14.8576
N	17.1945	15.6333	16.1322
N	17.6200	15.5766	13.5644
N	15.7213	17.6101	14.3327
N	19.6685	16.9627	15.3559
N	17.9633	18.6049	13.4051
N	17.8810	18.6237	16.3122
C	16.9102	19.4588	16.7517
C	19.1520	18.7448	16.8570
C	19.4056	19.7028	17.8617
C	18.3984	20.5427	18.3004
C	17.1168	20.4224	17.7271
C	20.1355	17.8320	16.3303
C	20.5285	16.0565	14.8347
C	21.8599	15.9631	15.2100
C	22.3515	16.8533	16.1848
C	21.4859	17.7802	16.7379
C	15.5736	18.5538	13.3341
C	14.6114	17.0222	14.8343
C	13.3253	17.3351	14.4106
C	13.1623	18.3083	13.4103
C	14.2899	18.9125	12.8778
C	16.8108	19.1011	12.8197
C	16.8936	20.0511	11.7823
C	18.1255	20.5117	11.3483
C	19.2885	20.0153	11.9651
C	19.1590	19.0743	12.9749
C	17.8545	15.6326	12.2339
C	17.8086	14.5183	11.4119
C	17.2518	13.2030	13.3266
C	17.3110	14.3566	14.1188
C	17.0559	14.3905	15.5579
C	16.6638	13.2834	16.3200
C	16.5742	14.6837	18.2556
C	16.9659	15.7486	17.4603
C	17.5013	13.2604	11.9548
C	16.4047	13.4087	17.6886
C	15.8570	12.2643	18.4942
C	14.3551	12.1311	18.1343
C	17.4103	12.0466	11.0767
C	15.9782	11.6545	10.6979
C	12.7898	3.8720	15.9429
C	12.0651	4.8872	15.0831
C	5.5083	17.6163	14.6954
C	6.3768	16.6593	13.9248
O	6.1172	16.4931	12.6753
O	7.3012	16.0411	14.5562
O	12.7273	5.9474	14.8070
O	10.8621	4.5901	14.7454
O	15.8811	10.8732	9.6801
O	15.0235	12.0611	11.4205
O	13.5199	12.8817	18.6355
O	14.1544	11.2077	17.2131
H	16.9906	12.2498	13.7867
H	16.5152	12.3179	15.8363
H	18.0045	14.6347	10.3456
H	18.0908	16.6169	11.8332
H	17.0920	16.7465	17.8781
H	16.3821	14.8503	19.3153
H	14.7721	16.2735	15.6085
H	12.4722	16.8252	14.8662
H	12.1676	18.5760	13.0539
H	14.1870	19.6654	12.0977
H	15.9795	20.4194	11.3189
H	18.1890	21.2441	10.5437
H	20.2809	20.3522	11.6696
H	20.0342	18.6595	13.4735
H	15.9326	19.3290	16.2876
H	16.2925	21.0662	18.0295
H	18.5964	21.2841	19.0745
H	20.4041	19.7778	18.2899
H	21.8442	18.4748	17.4962
H	23.3937	16.8131	16.5014
H	22.4967	15.2097	14.7492
H	20.1124	15.3907	14.0794
H	17.9858	12.1790	10.1509
H	17.8333	11.1651	11.5878
H	16.3736	11.3269	18.2529
H	15.9454	12.4723	19.5673
H	12.2727	2.9073	15.9286
H	12.8218	4.2434	16.9782
H	13.8270	3.7608	15.6037
H	6.8366	12.3205	7.5550
H	6.0299	17.9828	15.5859
H	4.6025	17.0818	15.0211
H	5.1944	18.4484	14.0545
H	4.5690	8.7265	11.2740

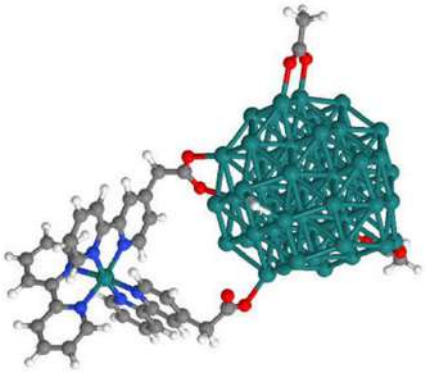

Domain 79, figure 5.5 (right) – $Ru_{55}(CH_3COO)_2(PS4)(H)_2$

Ru	11.6916	11.5882	19.3721	Ru	14.1680	11.5713	19.5109
Ru	11.9389	11.6223	14.9656	Ru	17.5420	15.1783	8.7784
Ru	12.0330	10.1115	17.1548	N	16.9653	15.8198	10.6510
Ru	10.1851	13.7368	19.3301	N	19.0806	16.5408	8.6046
Ru	10.5116	13.8573	15.0208	N	18.1625	14.8302	6.8419
Ru	8.9781	11.3140	19.1479	N	16.1845	16.6512	8.3013
Ru	10.4690	12.2537	17.1270	N	18.7062	13.6130	9.4383
Ru	9.3153	11.4784	14.8809	N	16.1645	13.6338	8.8343
Ru	9.2182	9.8160	16.9389	C	18.0634	12.3991	9.5749
Ru	8.9942	14.5172	17.0389	C	18.7533	11.2738	10.0589
Ru	7.7796	12.0620	16.8944	C	20.0981	11.3633	10.3840
Ru	5.2437	11.9675	16.6666	C	20.7495	12.5965	10.2180
Ru	6.3863	14.2284	16.8416	C	20.0228	13.6814	9.7516
Ru	6.6324	9.6570	16.8363	C	17.4028	15.3307	11.8360
Ru	7.4320	16.5557	16.9668	C	17.0311	15.8583	13.0605
Ru	8.0045	12.1922	12.7413	C	15.6481	17.5015	14.4214
Ru	6.6851	11.2317	14.7421	C	14.4352	16.6615	14.8174
Ru	6.3525	11.2193	18.8282	C	16.6580	12.4049	9.2072
Ru	7.4307	11.9800	20.9818	C	15.8359	11.2654	9.2084
Ru	9.1509	14.5260	12.8746	C	14.4930	11.3437	8.8487
Ru	7.7945	13.6286	14.8385	C	13.9951	12.6232	8.5177
Ru	7.5365	13.5552	18.9919	C	14.8476	13.7146	8.5215
Ru	8.6006	14.2360	21.2130	C	15.6905	17.4598	11.8936
Ru	8.9363	15.9907	14.9895	C	15.6226	17.3181	9.3730
Ru	10.0386	16.8011	17.1365	C	14.6502	18.3139	9.1660
Ru	8.6405	15.9609	19.1867	C	14.2573	18.6518	7.8810
Ru	8.0995	7.5168	16.8901	C	19.7160	16.5661	7.3712
Ru	9.3805	10.0111	12.8359	C	20.5443	18.2952	9.3821
Ru	8.1073	9.1072	14.7903	C	21.2068	18.3212	8.1383
Ru	7.9013	8.9308	18.9225	C	20.7881	17.4565	7.1436
Ru	8.9535	9.7304	21.0889	C	16.0855	16.8813	10.6754
Ru	10.6179	12.3810	12.8913	C	17.6556	13.9071	5.9903
Ru	10.0585	12.1362	21.3356	C	19.2071	15.6308	6.4007
Ru	11.7267	14.6374	12.9783	C	19.6971	15.4960	5.0837
Ru	11.6342	14.7160	17.2271	C	19.1589	14.5531	4.2271
Ru	11.2349	14.4453	21.4518	C	18.1135	13.7311	4.6940
Ru	11.5254	16.2302	15.1966	C	14.8510	17.9825	6.7966
Ru	11.2318	16.0225	19.3259	C	15.7957	17.0004	7.0513
Ru	10.8422	7.7668	17.0059	C	16.1567	16.9641	13.1070
Ru	9.6690	6.9359	18.9147	C	12.4858	10.3001	9.9023
Ru	11.9532	10.1901	12.8327	C	13.6006	10.1309	8.8447
Ru	10.7632	9.2773	14.8699	C	19.5030	17.3991	9.5636
Ru	10.5042	9.1857	19.1048	C	12.9951	5.2333	21.3308
Ru	11.5465	10.0067	21.3058	C	12.3097	6.2557	20.4477
Ru	13.1798	12.6223	13.0412	C	5.6650	19.0552	20.0517
Ru	13.2165	12.4417	17.3209	C	6.5091	18.0322	19.3418
Ru	12.6161	12.3646	21.5488	O	6.3194	17.8727	18.0778
Ru	13.1024	14.0198	15.2067	O	7.3524	17.3633	20.0302
Ru	12.7426	13.9296	19.4186	O	12.9812	7.3218	20.2234
Ru	13.2506	7.8990	17.0084	O	11.1331	5.9497	20.0317
Ru	13.3589	9.5190	15.0799	O	12.7863	9.7273	11.0532
Ru	14.5259	10.2466	17.3278	O	11.4770	10.9539	9.6376
Ru	13.1105	9.2308	19.2981	O	14.6574	15.4477	15.1167
Ru	14.4761	11.7628	15.1866	O	13.2803	17.2182	14.7282

H	18.2218	10.3320	10.1853
H	20.6342	10.4934	10.7627
H	21.8069	12.7190	10.4490
H	20.4886	14.6570	9.6197
H	18.0825	14.4819	11.7778
H	17.4012	15.4008	13.9771
H	16.4143	17.4004	15.2031
H	15.3505	18.5533	14.3387
H	16.2553	10.3006	9.4925
H	14.4835	14.7066	8.2578
H	12.9408	12.7581	8.2754
H	16.2710	16.4517	6.2393
H	14.9973	18.3011	11.8897
H	14.1977	18.8090	10.0237
H	13.4984	19.4169	7.7188
H	18.9714	17.3452	10.5128
H	20.5068	16.1409	4.7450
H	21.2864	17.4585	6.1751
H	20.8292	18.9596	10.1964
H	22.0337	19.0089	7.9607
H	16.8428	13.2982	6.3847
H	17.6613	12.9674	4.0633
H	19.5396	14.4490	3.2111
H	14.5827	18.2142	5.7668
H	14.1851	9.2254	9.0482
H	13.1056	10.0341	7.8677
H	12.4528	4.2827	21.3233
H	13.0323	5.6206	22.3597
H	14.0315	5.0873	21.0007
H	7.8850	13.7552	11.8098
H	10.1213	10.4861	22.4209
H	6.1774	19.4200	20.9484
H	4.7206	18.5829	20.3625
H	5.4221	19.8843	19.3771

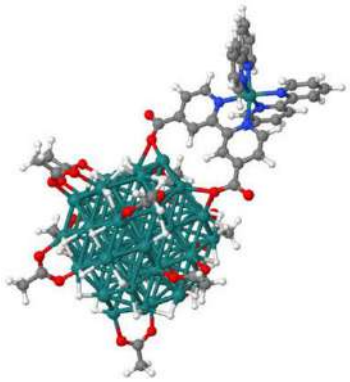

Domain 80, figure 5.6 (a) – $Ru_{55}(CH_3COO)_{10}(PS1)(H)_{27}$

Ru	14.7285	16.9586	15.9926
Ru	15.0521	16.8772	11.6192
Ru	14.7575	15.3768	13.8585
Ru	13.4304	19.1531	15.8949
Ru	13.5522	19.2333	11.5113
Ru	12.0071	16.8790	15.8582
Ru	13.5705	17.7212	13.6957
Ru	12.2697	16.8649	11.5785
Ru	12.0892	15.2370	13.6351
Ru	12.2063	19.9986	13.7036
Ru	10.8282	17.5894	13.5688
Ru	8.2480	17.7789	13.3660
Ru	9.4805	19.8489	13.6301
Ru	9.3243	15.3230	13.5425
Ru	10.7174	22.0825	13.5505
Ru	11.0563	17.5133	9.4095
Ru	9.6296	16.8065	11.4673
Ru	9.3964	16.9089	15.5966
Ru	10.5542	17.6529	17.8388
Ru	12.3899	19.9548	9.4271
Ru	10.8786	19.1381	11.5092
Ru	10.7096	19.1638	15.6646
Ru	11.9199	19.9783	17.9319
Ru	12.1986	21.4258	11.6045
Ru	13.4353	22.3383	13.7622
Ru	11.9941	21.4737	15.8221
Ru	10.8375	13.0030	13.7405
Ru	12.3518	15.4231	9.4206
Ru	10.9194	14.5905	11.5076
Ru	10.6522	14.5944	15.6788
Ru	11.8492	15.2444	17.8919
Ru	13.7037	17.6161	9.4742
Ru	13.2436	17.6071	18.0113
Ru	14.9613	19.9353	9.5646
Ru	14.8279	20.1095	13.8163
Ru	14.4774	19.9960	18.0313
Ru	14.7263	21.5154	11.6807
Ru	14.4364	21.4820	16.0382
Ru	13.5334	13.0279	13.9290
Ru	11.9535	12.5549	16.0415
Ru	14.9845	15.3249	9.5066
Ru	13.6072	14.4939	11.6249
Ru	13.3862	14.5562	15.8822
Ru	14.6192	15.4266	18.0959
Ru	16.3264	17.7933	9.6374
Ru	16.2094	17.6257	13.8591
Ru	15.9119	17.7310	18.0844
Ru	16.2341	19.1831	11.7470
Ru	16.0328	19.2177	15.9344
Ru	16.0511	13.1205	13.9781
Ru	16.2585	14.5621	11.8446
Ru	17.4508	15.2777	13.9663
Ru	15.9697	14.6483	15.9694
Ru	17.5992	17.0134	11.8188
Ru	17.3140	16.8584	16.0326
Ru	20.7359	9.3253	17.7693
N	21.8188	8.9569	16.0548
N	18.9818	9.4212	16.6773
N	19.8124	9.4942	19.6066
N	22.3628	9.4070	19.0305
N	20.8180	7.2670	17.7867
N	20.6057	11.3636	17.4355
C	4.8922	15.0494	13.6446
C	6.2852	15.6255	13.6199

C	13.3617	16.2011	22.2211
C	13.6115	16.3038	20.7367
C	20.5636	17.5061	8.6103
C	19.2479	17.3747	9.3350
C	7.5630	20.0264	8.6826
C	8.8344	19.4725	9.2679
C	9.8294	25.2030	16.4837
C	10.3683	23.9640	15.8219
C	18.9534	21.9278	14.0909
C	17.7020	21.1470	14.3880
C	13.6139	13.6606	5.6508
C	13.6377	14.2924	7.0185
C	8.3879	11.0791	10.6739
C	9.2973	12.0701	11.3526
C	9.9185	19.5309	21.7741
C	10.3392	19.2808	20.3493
C	10.8965	11.5251	20.1582
C	11.2970	12.4047	19.0005
C	20.6588	9.4640	20.7016
C	22.0676	9.4313	20.3833
C	18.4793	9.5944	19.8276
C	17.9188	9.6318	21.0949
C	18.7670	9.5577	22.2148
C	20.1337	9.4776	22.0092
C	23.1031	9.4528	21.3385
C	23.6648	9.4016	18.6570
C	24.4279	9.4453	20.9375
C	24.7162	9.4192	19.5602
C	20.2528	6.4507	18.7085
C	21.5154	6.6905	16.7379
C	20.3259	5.0679	18.6484
C	21.0176	4.4706	17.5777
C	21.6082	5.2883	16.6301
C	22.2851	9.8881	15.1880
C	22.0847	7.6238	15.7938
C	22.8553	7.2584	14.6719
C	23.3347	8.2253	13.8049
C	23.0350	9.5751	14.0655
C	18.1464	8.4012	16.3471
C	18.6014	10.6916	16.3211
C	17.3787	10.9307	15.6882
C	16.5213	9.8897	15.3512
C	16.9348	8.5875	15.6968
C	21.4851	12.3287	17.8135
C	19.5320	11.7507	16.6702
C	19.3772	13.0731	16.2401
C	20.2897	14.0546	16.6129
C	21.3629	13.6576	17.4388
C	20.1201	15.5025	16.2416
C	15.1884	10.1130	14.6861
O	15.0288	11.3013	14.0973
O	14.3288	9.2345	14.6941
O	19.0505	15.7984	15.4815
O	20.9026	16.3487	16.6647
O	6.3936	16.9007	13.7237
O	7.2614	14.8121	13.4806
O	13.2530	17.3847	20.1542
O	14.1523	15.2976	20.1568
O	18.2078	17.8366	8.7434
O	19.2462	16.8339	10.4911
O	9.2422	19.9590	10.3740
O	9.4261	18.5305	8.6243
O	11.0456	23.1550	16.5532
O	10.1410	23.7883	14.5769
O	16.7855	21.1226	13.4900
O	17.6115	20.5446	15.5118
O	14.7695	14.5551	7.5385
O	12.4976	14.5027	7.5828
O	9.7319	11.7578	12.5214
O	9.5857	13.1498	10.7439
O	11.0581	20.1893	19.7926
O	9.9770	18.1893	19.8003
O	11.5649	11.8042	17.8882
O	11.3172	13.6604	19.1892
H	8.9830	21.5742	13.4553
H	12.4123	18.3993	8.3511
H	8.0432	17.5393	11.5039
H	9.1972	15.3376	16.3879
H	14.2124	23.1462	12.4252
H	14.5845	22.9875	15.0049
H	12.2493	13.4116	11.1889
H	10.3505	16.0176	18.4761
H	13.3392	14.1462	17.7095
H	15.6088	21.5631	10.1587
H	12.1010	11.7895	14.3859
H	16.3469	16.1195	8.8090
H	16.4596	14.3952	10.0662
H	16.1137	16.1172	18.7988
H	16.3153	19.5090	17.8228
H	4.9141	14.0028	13.9657
H	4.4744	15.0939	12.6275
H	4.2465	15.6454	14.2996
H	13.9695	15.4044	22.6623
H	12.2985	15.9700	22.3840
H	13.5745	17.1615	22.7060
H	21.2614	16.7298	8.9425
H	20.9996	18.4876	8.8505
H	20.4127	17.4575	7.5262
H	7.5281	19.8587	7.6008
H	7.4696	21.0927	8.9172
H	6.7128	19.5026	9.1457
H	9.0638	25.6749	15.8599
H	10.6555	25.9133	16.6376
H	9.4236	24.9517	17.4715
H	19.6565	21.8665	14.9272
H	18.6948	22.9766	13.8897
H	19.4196	21.5247	13.1807
H	12.7697	14.0473	5.0678
H	13.4722	12.5754	5.7661
H	14.5608	13.8370	5.1302
H	17.9759	18.7550	11.9059
H	15.0359	13.3067	11.7150
H	13.7529	20.7973	8.5516
H	10.1710	19.3900	17.4300
H	11.7701	21.5651	9.8471
H	13.2324	20.9944	18.7341
H	8.8361	17.5181	17.1339
H	18.0098	15.1628	12.1658
H	9.3689	13.7447	14.5568
H	8.1523	11.4036	9.6558
H	7.4603	10.9836	11.2560
H	8.8660	10.0907	10.6560
H	17.6965	17.4953	17.6347
H	9.0305	18.9406	22.0224
H	9.7371	20.5991	21.9376
H	10.7413	19.2242	22.4372
H	13.9542	13.9709	9.8952
H	11.1600	12.0010	21.1088
H	11.3600	10.5362	20.0710
H	9.8043	11.3917	20.1332
H	15.1124	18.5068	8.4145
H	20.8112	9.4269	22.8605
H	18.3595	9.5685	23.2258
H	16.8382	9.7160	21.1996
H	17.8519	9.6342	18.9386
H	22.8544	9.4799	22.3985
H	25.2291	9.4626	21.6760
H	25.7408	9.4099	19.1910
H	23.8472	9.3821	17.5831
H	19.7188	6.9492	19.5165
H	19.8486	4.4711	19.4242
H	21.0854	3.3863	17.4915
H	22.1436	4.8498	15.7890
H	23.0715	6.2067	14.4891
H	23.9296	7.9433	12.9364
H	23.3756	10.3749	13.4099
H	22.0425	10.9225	15.4265
H	18.4791	7.4053	16.6368
H	16.2925	7.7385	15.4645
H	17.0734	11.9823	15.5344
H	18.5294	13.3480	15.6043
H	22.3130	11.9944	18.4372

H	22.0835	14.4004	17.7787

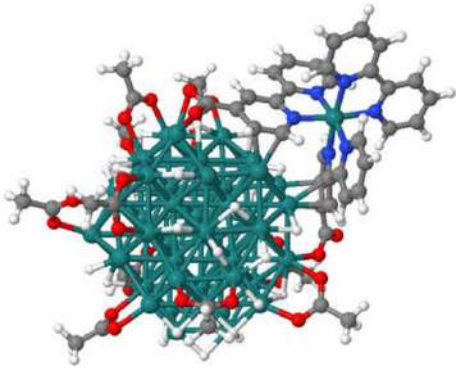

Domain 81, figure 5.6 (b) – $Ru_{55}(CH_3COO)_{10}(PS2)(H)_{27}$

Ru	15.0168	16.1249	16.3389
Ru	15.2673	16.0849	11.9811
Ru	15.0725	14.5971	14.2093
Ru	13.6797	18.3262	16.3149
Ru	13.7790	18.4126	11.9557
Ru	12.3229	15.9891	16.3108
Ru	13.8550	16.8855	14.1048
Ru	12.4627	16.0525	12.0205
Ru	12.3833	14.4151	14.1221
Ru	12.3898	19.1294	14.1746
Ru	11.1206	16.7353	14.0805
Ru	8.4979	16.7690	14.1036
Ru	9.6989	18.9588	14.1311
Ru	9.6676	14.3947	14.1511
Ru	10.9212	21.2336	14.0263
Ru	11.2248	16.7185	9.8901
Ru	9.8421	15.9490	12.0781
Ru	9.6882	16.0424	16.1530
Ru	10.9276	16.8455	18.3490
Ru	12.5370	19.1593	9.9432
Ru	11.0403	18.2869	12.0032
Ru	10.9719	18.3005	16.1421
Ru	12.2889	19.1580	18.3664
Ru	12.3115	20.6435	12.1347
Ru	13.7784	21.5292	14.1851
Ru	12.2630	20.6675	16.2763
Ru	11.1819	12.1488	14.1188
Ru	12.4848	14.6275	9.8367
Ru	11.1759	13.7582	11.9726
Ru	11.0787	13.6326	16.2543
Ru	12.3162	14.4759	18.3917
Ru	13.8635	16.8271	9.8922
Ru	13.6193	16.7924	18.4272
Ru	15.0858	19.1631	9.9772
Ru	14.9348	19.3170	14.1776
Ru	14.8698	19.1894	18.3502
Ru	14.8777	20.7527	12.0415
Ru	14.7308	20.6653	16.3787
Ru	13.9813	12.2551	14.1444
Ru	12.5832	11.4659	16.0718
Ru	15.1505	14.5492	9.8665
Ru	13.8466	13.7397	11.9644
Ru	13.7384	13.6935	16.2447
Ru	14.9915	14.6224	18.4315
Ru	16.5205	16.9910	9.9907
Ru	16.5123	16.7812	14.2066
Ru	16.2810	16.8997	18.3765
Ru	16.4517	18.4901	12.2731
Ru	16.3258	18.4742	16.1885
Ru	16.4526	12.2744	14.3870
Ru	16.4939	13.8097	12.1152
Ru	17.9571	14.5270	14.0766
Ru	16.4131	13.9094	16.2596
Ru	17.9130	16.3397	12.1320
Ru	17.7057	15.9824	16.3718
Ru	20.1886	11.3604	16.8830
N	20.5719	11.0992	14.8723
N	20.0272	13.3132	16.2096
N	19.5182	11.7746	18.7928
N	20.5487	9.4186	17.4761
N	18.1828	11.0734	16.6521
N	22.2071	11.4301	17.3095
C	23.0251	12.4957	17.1302
C	22.7524	10.2692	17.8153
C	21.8230	9.1528	17.9254
C	22.1606	7.8841	18.4242
C	19.6319	8.4213	17.5188
C	19.9169	7.1506	17.9989
C	24.1096	10.2037	18.1674
C	24.3742	12.4786	17.4561
C	24.9305	11.3097	17.9941
C	20.9963	9.9545	14.2833
C	21.1695	9.8316	12.9146
C	20.8846	10.9398	12.1014
C	20.4503	12.1156	12.6906
C	20.3040	12.1945	14.0911
C	21.2088	6.8742	18.4663
C	19.9345	13.4127	14.8004
C	19.9926	14.4347	16.9354
C	20.0335	14.6908	14.1362
C	19.8825	15.7534	16.3766
C	19.8077	15.8632	14.9372
C	20.2694	12.1633	19.8466
C	19.7343	12.4223	21.1015
C	17.5664	11.8889	20.2111
C	18.1615	11.6210	18.9639
C	17.4350	11.1928	17.7848
C	16.0555	10.8559	17.8000
C	17.5516	10.7126	15.4644
C	16.1550	10.3146	15.4209
C	18.3512	12.2871	21.2833
C	15.4280	10.3660	16.6682
C	13.9958	10.0086	16.7157
C	20.0453	17.1740	14.2256
C	5.2509	13.8896	14.0312
C	6.6094	14.5441	14.0536

C	14.0203	15.4987	22.6382
C	14.1529	15.5622	21.1369
C	20.6289	16.4777	8.6207
C	19.3698	16.3945	9.4486
C	7.6451	19.1476	9.3037
C	8.9558	18.6340	9.8347
C	10.1195	24.4240	16.8920
C	10.6107	23.1617	16.2374
C	19.4434	21.0420	14.3674
C	18.3120	20.0480	14.3293
C	13.7116	12.8635	6.0456
C	13.7613	13.4816	7.4189
C	8.5336	10.3410	11.1380
C	9.4850	11.2996	11.8054
C	10.2623	18.8462	22.2223
C	10.7038	18.5412	20.8139
C	10.1282	10.9105	19.6672
C	10.6003	12.0796	18.8435
O	6.6408	15.8249	14.1584
O	7.6339	13.7892	13.9551
O	13.7976	16.6486	20.5623
O	14.5879	14.5199	20.5312
O	18.3084	16.8984	8.9257
O	19.4303	15.8728	10.6059
O	9.4043	19.1430	10.9157
O	9.5447	17.7023	9.1769
O	11.3009	22.3536	16.9586
O	10.3298	22.9642	15.0070
O	17.8443	19.7582	13.1748
O	17.8886	19.6183	15.4627
O	14.9029	13.7517	7.9120
O	12.6341	13.6754	8.0154
O	9.9856	10.9428	12.9286
O	9.7412	12.4067	11.2253
O	11.4675	19.4074	20.2476
O	10.3135	17.4508	20.2853
O	10.1565	12.1962	17.6538
O	11.4573	12.8682	19.3791
O	13.2604	10.3411	17.7644
O	13.4063	9.4782	15.6734
O	19.5948	17.2495	12.9958
O	20.7056	18.0642	14.7786
H	22.5518	13.3853	16.7160
H	23.1720	7.6950	18.7811
H	18.6385	8.6768	17.1533
H	19.1320	6.3955	18.0089
H	25.9849	11.2640	18.2660
H	24.5178	9.2785	18.5718
H	24.9757	13.3710	17.2883
H	21.1903	9.1194	14.9553
H	21.5115	8.8861	12.4962
H	20.9940	10.8790	11.0185
H	20.1934	12.9797	12.0796
H	21.4641	5.8887	18.8556
H	20.0761	14.3158	18.0160
H	20.5318	14.8003	13.1723
H	20.2657	16.6060	16.9399
H	21.3375	12.2667	19.6563
H	20.3915	12.7301	21.9135
H	16.4879	11.7959	20.3252
H	15.4744	10.9374	18.7163
H	18.2366	10.3438	14.6971
H	15.8145	9.6055	14.6625
H	17.8924	12.4987	22.2490
H	9.2268	20.7116	13.9452
H	12.5143	17.6441	8.8329
H	8.3673	16.7368	11.9415
H	9.5842	14.4698	16.8748
H	14.6641	22.3754	12.9547
H	14.7191	22.2933	15.4924
H	12.5131	12.6878	11.3998
H	10.9427	15.2889	19.1647
H	13.7161	13.3016	18.0777
H	15.7323	20.7998	10.5015
H	12.5870	11.2878	13.4909
H	16.3090	15.5565	8.9808
H	16.6292	13.6249	10.2989
H	16.5274	15.2921	19.0940
H	16.6702	18.7094	18.1113
H	5.3297	12.8286	14.2896
H	4.8300	13.9774	13.0185
H	4.5728	14.4071	14.7202
H	14.6836	14.7348	23.0577
H	12.9818	15.2337	22.8873
H	14.2324	16.4801	23.0785
H	21.2983	15.6427	8.8554
H	21.1478	17.4125	8.8819
H	20.3935	16.5019	7.5511
H	7.5655	18.9664	8.2264
H	7.5330	20.2137	9.5309
H	6.8319	18.6058	9.8105
H	9.3487	24.9018	16.2792
H	10.9659	25.1168	17.0096
H	9.7342	24.2016	17.8946
H	20.0263	20.9156	15.2844
H	19.0160	22.0567	14.3446
H	20.0836	20.9093	13.4893
H	12.8478	13.2443	5.4882
H	13.5899	11.7749	6.1505
H	14.6423	13.0603	5.5034
H	17.7540	17.9361	11.1253
H	15.2162	12.5042	12.4432
H	13.8841	19.9800	8.9726
H	10.4827	18.5441	17.9127
H	11.9557	20.7752	10.3595
H	13.6282	20.1876	19.0865
H	9.2391	16.4492	17.8421
H	18.2608	14.2839	12.3624
H	9.7523	12.7296	15.0286
H	8.2620	10.6977	10.1397
H	7.6287	10.2448	11.7546
H	8.9943	9.3464	11.0744
H	18.0275	16.6698	17.9448
H	9.3746	18.2612	22.4843
H	10.0700	19.9195	22.3368
H	11.0784	18.5786	22.9102
H	14.3328	13.1047	10.3171
H	10.2131	11.1282	20.7373
H	10.7776	10.0540	19.4295
H	9.0985	10.6463	19.4017
H	15.2074	17.6909	8.8324

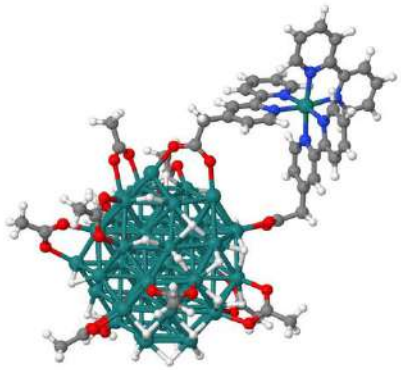

Domain 82, figure 5.6 (c) – $Ru_{55}(CH_3COO)_{10}(PS4)(H)_{27}$

Ru	14.0827	16.7832	15.9704	Ru	16.6743	16.9729	16.4115
Ru	15.0192	17.4119	11.7298	Ru	21.3622	9.8310	18.5449
Ru	14.7543	15.5839	13.7055	N	21.2278	11.8399	18.0704
Ru	12.4419	18.7547	15.9316	N	22.9925	9.9775	19.7938
Ru	13.2463	19.5129	11.7296	N	21.7281	7.8447	18.9533
Ru	11.4774	16.3063	15.3656	N	22.5777	9.9379	16.8896
Ru	13.1812	17.6592	13.6372	N	19.9337	9.8732	20.0265
Ru	12.3075	17.0455	11.2148	N	19.6404	9.5199	17.4542
Ru	12.1300	15.1222	13.0241	C	18.6261	9.7107	19.6025
Ru	11.4425	19.6980	13.7095	C	17.5643	9.7640	20.5250
Ru	10.5373	17.2174	13.0738	C	17.8160	9.9563	21.8733
Ru	8.0033	16.9739	12.5762	C	19.1500	10.0944	22.2970
Ru	8.8408	19.2216	13.1643	C	20.1616	10.0499	21.3503
Ru	9.5044	14.7534	12.5758	C	20.5152	12.7782	18.7381
Ru	9.7314	21.6136	13.5942	C	20.4129	14.0959	18.3247
Ru	11.3224	17.9062	9.0122	C	20.9359	15.9226	16.6340
Ru	9.7280	16.6721	10.7456	C	19.5233	16.1607	16.1005
Ru	8.9788	15.9871	14.7661	C	18.4657	9.5091	18.1769
Ru	9.6535	16.6164	17.2181	C	17.2310	9.3224	17.5303
Ru	12.2810	20.4322	9.6334	C	17.1590	9.1734	16.1498
Ru	10.6077	19.1032	11.2544	C	18.3717	9.1941	15.4329
Ru	9.8426	18.4097	15.2742	C	19.5654	9.3621	16.1123
Ru	10.6151	19.0672	17.7981	C	21.8082	13.5515	16.4596
Ru	11.5174	21.5183	11.9216	C	22.6228	11.1688	16.2572
Ru	12.4426	22.2204	14.3123	C	23.3318	11.3248	15.0509
Ru	10.7621	20.8657	15.9304	C	24.0166	10.2561	14.4964
Ru	11.3332	12.7333	12.5097	C	23.5024	8.7709	20.2527
Ru	12.9324	16.0502	8.8829	C	24.7026	11.1554	21.0215
Ru	11.3426	14.6817	10.6437	C	25.2176	9.9379	21.5111
Ru	10.6377	13.7914	14.7749	C	24.6133	8.7558	21.1235
Ru	11.3329	14.5030	17.1980	C	21.8838	12.2240	16.9192
Ru	13.8937	18.3010	9.5025	C	21.0090	6.7915	18.4989
Ru	12.2504	16.9305	17.7896	C	22.8130	7.5968	19.7817
Ru	14.7845	20.7229	10.1656	C	23.1713	6.2689	20.1015
Ru	13.9159	20.1771	14.2009	C	22.4297	5.2061	19.6186
Ru	13.1250	19.4661	18.2513	C	21.3122	5.4732	18.8022
Ru	14.0125	21.9183	12.3547	C	23.9935	9.0192	15.1667
Ru	13.1417	21.1638	16.5113	C	23.2685	8.9086	16.3427
Ru	14.0650	13.2163	12.9553	C	21.0724	14.5099	17.1464
Ru	12.6339	12.0091	14.5329	C	15.2767	10.4158	14.9896
Ru	15.5443	16.2424	9.4426	C	15.8371	9.0592	15.4487
Ru	13.9280	14.9825	11.0586	C	23.6023	11.1234	20.1795
Ru	13.2090	14.2201	15.2800	C	5.2549	13.7196	11.7675
Ru	13.9291	14.9872	17.8126	C	6.4871	14.5243	12.1001
Ru	16.4296	18.7816	10.1481	C	12.0449	15.0198	21.7914
Ru	15.8324	17.8484	14.1909	C	12.4403	15.3431	20.3705
Ru	14.8328	17.4445	18.2657	C	20.7953	19.2052	9.8213
Ru	15.8891	19.8454	12.4954	C	19.4259	18.7550	10.2665
Ru	15.0635	19.2051	16.2678	C	7.5546	19.9410	8.1508
Ru	16.2010	13.3046	14.0513	C	8.8189	19.4895	8.8315
Ru	16.4399	15.1563	11.8040	C	7.9344	24.1068	16.6917
Ru	17.3414	15.6921	14.1010	C	8.7326	23.0546	15.9696
Ru	15.7166	14.7519	15.9313	C	17.9533	22.4815	15.4547
Ru	17.4940	17.7703	12.2877	C	17.0238	21.3382	15.1140

C	15.0613	15.0731	5.2087
C	14.7662	15.4667	6.6338
C	9.4722	11.1057	8.8819
C	10.1174	12.0747	9.8405
C	8.0925	17.8689	21.1491
C	8.7680	17.8755	19.8014
C	9.9497	10.3504	17.6181
C	10.3299	11.6932	17.0412
O	6.3112	15.7522	12.4333
O	7.6180	13.9394	12.0071
O	12.0205	16.4470	19.8812
O	13.1516	14.4829	19.7417
O	18.4208	19.2311	9.6347
O	19.3474	17.9473	11.2568
O	9.0132	19.8624	10.0369
O	9.6216	18.7418	8.1654
O	9.3893	22.2163	16.6856
O	8.7270	23.0601	14.6915
O	16.7621	21.1820	13.8724
O	16.5593	20.6673	16.0988
O	15.7472	15.7935	7.3748
O	13.5335	15.4173	7.0105
O	10.4766	11.6171	10.9814
O	10.2763	13.2834	9.4679
O	9.4529	18.9214	19.5041
O	8.6389	16.8452	19.0633
O	10.2445	11.8356	15.7695
O	10.7046	12.6063	17.8484
O	14.0034	10.5010	15.0108
O	16.1288	11.2877	14.6132
O	18.7358	16.8705	16.8124
O	19.2178	15.5957	14.9987
H	16.5399	9.6590	20.1708
H	16.9943	10.0014	22.5875
H	19.4036	10.2377	23.3462
H	21.2065	10.1642	21.6369
H	20.0084	12.4355	19.6396
H	19.8064	14.7938	18.9025
H	21.1220	16.6469	17.4381
H	21.6504	16.1001	15.8188
H	16.3135	9.3143	18.1188
H	20.5138	9.3764	15.5776
H	18.3823	9.0956	14.3480
H	23.2117	7.9637	16.8818
H	22.3251	13.8319	15.5423
H	23.3323	12.2921	14.5506
H	24.5599	10.3744	13.5592
H	23.1690	12.0418	19.7846
H	24.0383	6.0857	20.7350
H	24.9943	7.8030	21.4889
H	25.1486	12.1126	21.2868
H	26.0769	9.9250	22.1813
H	20.1607	7.0402	17.8621
H	20.6872	4.6734	18.4082
H	22.7055	4.1816	19.8682
H	24.5255	8.1506	14.7813
H	15.0817	8.5851	16.0875
H	15.9338	8.4383	14.5429
H	8.1570	20.9123	13.1577
H	12.6387	19.1188	8.3351
H	8.0577	17.1231	10.6537
H	8.9983	14.2948	15.3027
H	13.3850	23.3519	13.3801
H	13.1407	22.8793	15.8252
H	12.8001	13.8880	10.0857
H	9.7299	14.9528	17.8008
H	12.9558	13.6021	17.0266
H	15.0699	22.3159	10.9777
H	12.9240	12.1728	11.9789
H	16.8600	17.3301	9.1091
H	16.9457	15.3190	10.0362
H	15.1185	15.8005	18.8835
H	15.0151	19.2964	18.2224
H	5.4456	12.6492	11.8985
H	4.9899	13.9011	10.7149
H	4.4109	14.0442	12.3871
H	12.7285	14.2834	22.2272
H	11.0293	14.5964	21.7862
H	12.0257	15.9342	22.3960
H	21.5564	18.4782	10.1239
H	21.0208	20.1674	10.3061
H	20.8158	19.3626	8.7370
H	7.6731	19.9238	7.0621
H	7.2720	20.9413	8.4979
H	6.7464	19.2464	8.4266
H	7.2037	24.5668	16.0188
H	8.6212	24.8842	17.0584
H	7.4359	23.6678	17.5642
H	18.4042	22.3294	16.4410
H	17.3639	23.4108	15.4790
H	18.7245	22.5918	14.6838
H	14.2465	15.3898	4.5475
H	15.1337	13.9764	5.1541
H	16.0159	15.5003	4.8842
H	17.6516	19.5043	12.2564
H	15.3345	13.7177	11.4726
H	13.6528	21.5039	9.0343
H	9.0645	18.3337	16.9445
H	11.4148	21.8931	10.1471
H	11.6401	20.1024	18.9175
H	8.1065	16.2051	16.2764
H	18.0364	15.9340	12.3513
H	9.6990	13.0079	13.2951
H	9.2579	11.5938	7.9262
H	8.5410	10.7217	9.3210
H	10.1386	10.2470	8.7233
H	16.6216	17.4899	18.1104
H	7.2628	17.1544	21.1627
H	7.7468	18.8759	21.4096
H	8.8325	17.5626	21.9041
H	14.7224	14.7249	9.4248
H	10.2715	10.2706	18.6616
H	10.3927	9.5462	17.0169
H	8.8576	10.2345	17.5674
H	15.2535	19.4950	8.8568

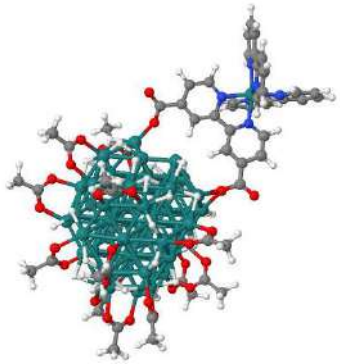

Domain 83, figure 5.8 (b) – $Ru_{55}(CH_3COO)_{14}(PS4)(H)_{31}$

Ru	15.1200	16.1570	16.2634	Ru	17.6602	16.0637	16.0955
Ru	15.0343	16.0611	11.8388	Ru	20.8225	8.2676	18.2283
Ru	15.0963	14.5987	13.9847	N	20.3890	8.9133	20.1432
Ru	13.7564	18.4686	16.2774	N	20.7289	10.2051	17.5560
Ru	13.6140	18.4150	11.9330	N	21.4150	7.4672	16.4232
Ru	12.4166	16.0156	16.2557	N	20.7747	6.2498	18.6492
Ru	13.7557	16.8767	14.0787	N	22.7100	8.3974	19.0466
Ru	12.3002	16.0608	11.9547	N	18.8715	8.3885	17.5859
Ru	12.3716	14.4498	14.1163	C	21.5119	6.0867	16.3843
Ru	12.3479	19.1851	14.0728	C	21.1368	5.4135	17.6063
Ru	11.1019	16.7454	14.0953	C	21.7089	8.1652	15.3000
Ru	8.4803	16.7981	14.2989	C	22.1249	7.5684	14.1205
Ru	9.6945	18.9683	14.1221	C	22.2530	6.1681	14.0771
Ru	9.6271	14.3612	14.2499	C	21.9432	5.4364	15.2111
Ru	10.8309	21.2282	14.1539	C	21.0925	4.0141	17.7682
Ru	10.8458	16.6719	9.9140	C	20.4079	5.6898	19.8262
Ru	9.6834	15.8924	12.2117	C	20.7054	3.4599	18.9759
Ru	9.7993	16.0212	16.2363	C	20.3608	4.3202	20.0353
Ru	11.0810	16.8639	18.3519	C	23.8759	8.1216	18.4137
Ru	12.3734	19.2233	9.8806	C	22.7617	8.7995	20.3715
Ru	10.9027	18.2744	11.9701	C	25.1170	8.2311	19.0206
Ru	11.0703	18.3205	16.1395	C	25.1824	8.6524	20.3625
Ru	12.4454	19.1305	18.4388	C	24.0016	8.9333	21.0277
Ru	12.0896	20.7336	11.9575	C	19.1581	9.2031	20.6290
Ru	13.4751	21.5350	14.1092	C	21.4806	9.0793	20.9776
Ru	12.3337	20.6446	16.1972	C	21.3007	9.5053	22.3090
Ru	11.2134	12.1097	14.2384	C	20.0336	9.7879	22.7899
Ru	12.3018	14.6215	9.7869	C	18.9342	9.6395	21.9253
Ru	11.0348	13.7070	12.0909	C	21.7776	11.0635	17.4831
Ru	11.1558	13.6608	16.3322	C	19.4992	10.6363	17.1065
Ru	12.4613	14.5206	18.3740	C	19.3472	11.9129	16.5497
Ru	13.6087	16.8913	9.7628	C	20.4365	12.7846	16.4566
Ru	13.7427	16.8933	18.3563	C	21.6769	12.3349	16.9529
Ru	15.0491	19.0761	9.7225	C	17.9788	7.3690	17.6017
Ru	14.9443	19.2238	14.0151	C	18.4324	9.6385	17.2084
Ru	15.1345	19.1225	18.3133	C	17.0670	9.8820	16.9791
Ru	14.8918	20.6365	11.8847	C	16.1495	8.8288	17.0355
Ru	14.9678	20.7398	16.1457	C	16.6388	7.5397	17.3084
Ru	13.9467	12.2044	14.0270	C	14.6655	8.9845	16.7911
Ru	12.9896	11.4464	16.1213	C	20.3704	14.1755	15.9050
Ru	14.9544	14.5790	9.6933	C	5.2212	13.9674	13.8800
Ru	13.6598	13.7347	11.8213	C	6.5878	14.5845	14.0320
Ru	13.8003	13.7519	16.2011	C	14.0648	15.4878	22.5642
Ru	15.1599	14.6673	18.3646	C	14.2068	15.5881	21.0649
Ru	16.2515	16.8640	9.6983	C	20.5399	16.7947	8.6895
Ru	16.4136	16.8874	14.0099	C	19.2503	16.6494	9.4579
Ru	16.4231	16.9489	18.2612	C	7.3086	19.2258	9.5500
Ru	16.2479	18.4393	11.7754	C	8.5941	18.5971	10.0220
Ru	16.3756	18.4902	16.0472	C	9.8903	24.0353	17.3797
Ru	16.2702	12.3380	14.0378	C	10.4473	22.8764	16.5983
Ru	16.3578	13.7790	11.8210	C	19.2002	21.6564	15.0654
Ru	17.7912	14.6337	13.9023	C	17.9617	20.9099	15.4941
Ru	16.4013	13.9147	16.1234	C	13.3383	12.3385	6.2363
Ru	17.6183	16.1683	11.9171	C	13.4449	13.1497	7.5011

C	8.4373	10.2055	11.4296
C	9.4273	11.1728	12.0287
C	9.9489	19.0127	22.0304
C	10.5942	18.6544	20.7157
C	10.1487	11.1573	19.9288
C	10.7542	12.1925	19.0123
C	15.8282	23.1341	8.3368
C	15.5338	21.9829	9.2654
C	16.2835	23.1095	19.6610
C	15.7554	21.9832	18.8067
C	12.3190	25.1276	11.8684
C	12.4659	23.6906	12.2978
C	12.9432	18.3916	5.6351
C	13.0106	18.2853	7.1374
O	6.6425	15.8692	14.0928
O	7.5939	13.7996	14.0724
O	13.7797	16.6509	20.5012
O	14.7232	14.5873	20.4534
O	18.1576	16.8236	8.8155
O	19.3261	16.3778	10.7018
O	9.1546	19.1055	11.0519
O	9.0280	17.5776	9.3808
O	11.2235	22.0625	17.2174
O	10.1365	22.7709	15.3624
O	16.8983	21.5779	15.7043
O	18.0573	19.6365	15.6012
O	14.5977	13.3474	7.9989
O	12.3434	13.5770	8.0166
O	9.9549	10.8504	13.1469
O	9.6719	12.2542	11.3954
O	11.3765	19.5223	20.1899
O	10.3386	17.5031	20.2250
O	10.2938	12.2828	17.8301
O	11.6949	12.9262	19.4853
O	15.3678	22.2231	10.4984
O	15.4521	20.8143	8.7177
O	15.9039	20.7916	19.2674
O	15.2159	22.2612	17.6942
O	11.9377	22.7963	11.5536
O	13.0849	23.4580	13.3924
O	12.7412	19.3503	7.8072
O	13.3115	17.1554	7.6451
O	19.1522	14.5625	15.4686
O	21.3477	14.9157	15.9121
O	14.1976	10.1925	17.0607
O	14.0006	8.0178	16.4201
H	22.0302	4.3508	15.2004
H	22.5853	5.6657	13.1690
H	22.3420	8.1904	13.2534
H	21.6054	9.2469	15.3733
H	21.3574	3.3690	16.9314
H	20.6653	2.3778	19.0993
H	20.0567	3.9359	21.0077
H	20.1374	6.3894	20.6164
H	23.7850	7.8045	17.3754
H	26.0148	7.9903	18.4532
H	26.1411	8.7576	20.8696
H	24.0257	9.2638	22.0653
H	22.1678	9.6190	22.9582
H	19.8945	10.1246	23.8170
H	17.9178	9.8626	22.2461
H	18.3290	9.0709	19.9358
H	22.7246	10.6862	17.8669
H	22.5408	12.9973	16.9151
H	18.3630	12.2199	16.1732
H	16.7153	10.8971	16.7699
H	18.3765	6.3939	17.8776
H	15.9519	6.6941	17.3072
H	9.0883	20.6284	13.9719
H	11.1491	18.2503	9.1394
H	8.2921	16.6218	11.7789
H	9.7187	14.4927	17.0393
H	15.0835	21.7344	13.2329
H	14.3035	22.2969	15.4047
H	12.2582	12.9057	11.0052
H	11.0894	15.3072	19.1673
H	13.8560	13.3673	18.0455
H	16.5982	20.2426	12.0679
H	12.5302	11.1310	13.6125
H	15.7952	15.5791	8.5078
H	16.6109	13.9488	10.0105
H	16.6447	15.3665	19.0536
H	16.8906	18.7150	17.8515
H	5.2481	12.9000	14.1209
H	4.8932	14.0902	12.8368
H	4.4980	14.4902	14.5177
H	14.7950	14.7829	22.9760
H	13.0544	15.1186	22.7953
H	14.1776	16.4769	23.0226
H	21.2909	16.0945	9.0730
H	20.9244	17.8154	8.8348
H	20.3696	16.6361	7.6195
H	7.0980	18.9457	8.5126
H	7.3611	20.3157	9.6565
H	6.4885	18.8646	10.1886
H	8.9922	24.4331	16.8960
H	10.6513	24.8292	17.4198
H	9.6748	23.7277	18.4096
H	20.0943	21.1977	15.5038
H	19.1273	22.7140	15.3392
H	19.2863	21.5825	13.9710
H	12.6007	12.7901	5.5615
H	12.9822	11.3286	6.4883
H	14.3139	12.2598	5.7463
H	17.7106	17.8443	12.7122
H	17.0422	12.1519	12.4859
H	13.4325	20.5499	10.5062
H	10.6880	18.6395	17.8917
H	11.2846	20.5283	10.2714
H	13.7906	19.6022	19.4227
H	9.2744	16.6167	17.7692
H	18.0922	14.3081	12.0499
H	9.7815	12.7156	15.1152
H	8.2300	10.4619	10.3859
H	7.5019	10.2536	12.0060
H	8.8206	9.1805	11.5061
H	18.1766	16.6928	17.6511
H	9.0149	18.4566	22.1651
H	9.7721	20.0928	22.0871
H	10.6365	18.7387	22.8446
H	14.9701	12.9826	10.8498
H	10.7352	11.0590	20.8478
H	10.0852	10.1930	19.4093
H	9.1239	11.4642	20.1826
H	15.9536	18.0987	8.4979
H	16.4489	22.8035	7.4964
H	16.3139	23.9495	8.8837
H	14.8760	23.5065	7.9299
H	11.3234	11.2217	15.8132
H	15.8223	24.0577	19.3658
H	17.3703	23.1862	19.5080
H	16.1066	22.9031	20.7232
H	9.9418	15.2543	10.4232
H	12.9688	25.7772	12.4629
H	11.2726	25.4371	12.0054
H	12.5545	25.2214	10.8010
H	16.1858	13.1436	17.6324
H	13.5455	17.6060	5.1671
H	13.2774	19.3839	5.3109
H	11.8959	18.2685	5.3203
H	13.8919	12.0296	12.2840

REFERENCES

[1] A. Züttel, A. Remhof, and L. Schlapbach, *Hydrogen as a Future Energy Carrier*. Darmstadt, Germany: John Wiley & Sons, 2011.

[2] N. S. Lewis, "Light work with water," *Nature*, vol. 414, no. 6864, pp. 589–590, 2001.

[3] J. K. Nørskov, F. Abild-Pedersen, F. Studt, and T. Bligaard, "Density functional theory in surface chemistry and catalysis," *Proc. Natl. Acad. Sci.*, vol. 108, pp. 937–943, 2011.

[4] Y. Li and G. A. Somorjai, "Nanoscale Advances in Catalysis and Energy Applications," pp. 2289–2295, 2010.

[5] J. Creus *et al.*, "Ligand-capped Ru nanoparticles as efficient electrocatalyst for the hydrogen evolution reaction," *ACS Catal.*, vol. 8, no. 12, pp. 11094–11102, 2018.

[6] J. De Tovar *et al.*, "Light-driven water oxidation using hybrid photosensitizer-decorated Co 3 O 4 nanoparticles," vol. 9, pp. 506–515, 2018.

[7] S. A. Grigoriev, P. Millet, and V. N. Fateev, "Evaluation of carbon-supported Pt and Pd nanoparticles for the hydrogen evolution reaction in PEM water electrolysers," *J. Power Sources*, vol. 177, no. 2, pp. 281–285, 2008.

[8] S. Liu, X. Mu, H. Duan, C. Chen, and H. Zhang, "Pd nanoparticle assemblies as efficient catalysts for the hydrogen evolution and oxygen reduction reactions," *Eur. J. Inorg. Chem.*, vol. 3, pp. 535–539, 2017.

[9] S. Drouet *et al.*, "A porous Ru nanomaterial as an efficient electrocatalyst for the hydrogen evolution reaction under acidic and neutral conditions," *hemical Commun.*, vol. 53, no. 85, p. 11713–11716., 2017.

[10] J. K. Nørskov *et al.*, "Trends in the Exchange Current for Hydrogen Evolution," *J. Electrochem. Soc.*, vol. 152, no. 3, pp. J23–J26, 2005.

[11] J. P. Wilcoxon and B. L. Abrams, "Synthesis, structure and properties of metal nanoclusters," *Chem. Soc. Rev.*, vol. 35, no. 11, pp. 1162–1194, 2006.

[12] C. Burda, X. Chen, R. Narayanan, and M. a. El-Sayed, *Chemistry and properties of nanocrystals of different shapes*, vol. 105, no. 4. 2005.

[13] G. Schmid, *Nanoparticles: From Theory to Applications*, 2nd ed. Weinheim, Germany: Wiley-VCH Verlag, 2010.

[14] J. D. A. Iii and R. G. Finke, "A review of modern transition-metal nanoclusters: their synthesis, characterization, and applications in catalysis," *J. Mol. Catal. A Chem.*, vol. 145, no. 1–2, pp. 1–44, 1999.

[15] R. Narayanan and M. A. El-sayed, "Catalysis with transition metal nanoparticles in colloidal solution: nanoparticle shape dependence and stability," *J. Phys. Chem. B*, vol. 109, pp. 12663–12676, 2005.

[16] B. H. Kim, M. J. Hackett, J. Park, and T. Hyeon, "Synthesis, Characterization, and Application of Ultrasmall Nanoparticles," *Chem. Mater.*, vol. 26, no. 1, pp. 59–71, 2013.

[17] T. Castro, R. Reifenberger, E. Choi, and R. P. Andres, "Size-dependent melting temperature of individual nanometer-sized metallic clusters," *Phys. Rev. B*, vol. 42, no. 13, pp. 8548–8557, 1990.

[18] G. Schmid, *Metal Nanocluster in Catalysis ad Materials Science: The Issues of Size Control*. Amsterdam, Netherlands: Elsevier, 2008.

[19] E. Roduner, "Size matters: why nanomaterials are different," *Chem. Soc. Rev.*, vol. 35, no. 7, pp. 583–592, 2006.

[20] L. Guczi, Z. Paszti, and G. Petö, *Metal Nanocluster in Catalysis ad Materials Science: The Issues of Size Control*. Amsterdam, Netherlands: Elsevier, 2008.

[21] R. Narayanan, Æ. C. Tabor, and M. A. El-sayed, "Can the observed changes in the size or shape of a colloidal nanocatalyst reveal the nanocatalysis mechanism type: homogeneous or heterogeneous?," *Top. Catal.*, vol. 48, no. 1–4, pp. 60–74, 2008.

[22] R. Tsybukh, "A comparative study of platinum nanodeposits on HOPG (0001), MnO(100) and MnOx/MnO(100) surfaces by STM and AFM after

heat treatment in UHV, O2 , CO and H2," Leiden, 2010.

[23] G. Schmid, N. Klein, B. Morun, A. Lehnert, and J.-O. Malm, "Two, four, five-shell clusters and colloids," *Pure Appl. Chem.*, vol. 62, no. 6, pp. 1175–1177, 1990.

[24] O. Rossell and M. Seco, "SACs o nuevos catalizadores formados por átomos metálicos aislados sobre un soporte," *An. Química*, vol. 3, no. 165–171, pp. 165–171, 114AD.

[25] G. Schmid, B. D. Alexander, J. Barthelmes, A. M. Mueting, and L. H. Pignolet, "Hexachlorododecakis (Triphenyl-Phosphine) Pentapentacontagold, Au55[P(C6H5)3]12Cl6," *Inorg. Synth.*, vol. 27, pp. 214–218, 1990.

[26] P. Serp and K. Philippot, *Nanomaterials in Catalysis*. Weinheim, Germany: Wiley-VCH, 2013.

[27] A. Roucoux, J. Schulz, and H. Patin, "Reduced transition metal colloids: a novel family of reusable catalysts?," *Chem. Rev.*, vol. 102, no. 10, pp. 3757–3778, 2002.

[28] W. Soutter, "Nanocatalysis: New Dimensions in Catalysis," 2012. [Online]. Available: https://www.azonano.com/article.aspx?ArticleID=3079. [Accessed: 21-Feb-2019].

[29] M. Zahmakıran and S. Özkar, "Metal nanoparticles in liquid phase catalysis; from recent advances to future goals.," *Nanoscale*, vol. 3, no. 9, pp. 3462–3481, 2011.

[30] K. Na, Q. Zhang, and G. A. Somorjai, "Colloidal metal nanocatalysts: synthesis, characterization, and catalytic applications," *J. Clust. Sci.*, vol. 25, no. 1, pp. 83–114, 2014.

[31] T. L. Tan, L.-L. Wang, J. Zhang, D. D. Johnson, and K. Bai, "Platinum nanoparticle during electrochemical hydrogen evolution: adsorbate distribution, active reaction species, and size effect.," *ACS Catal.*, vol. 5, no. 4, pp. 2376–2383, 2015.

[32] M. Risch *et al.*, "Atomic structure of cobalt-oxide nanoparticles active in light-driven catalysis of water oxidation," *Int. J. Hydrogen Energy*, vol. 37, no. 10, pp. 8878–8888, 2012.

[33] K. Balasubramanian, "Electronic structure of coinage metal clusters," *J. Mol. Struct. THEOCHEM*, vol. 202, no. 1, pp. 291–313, 1989.

[34] X. Gu, M. Ji, S. H. Wei, and X. G. Gong, "Au N clusters (N= 32, 33, 34, 35): Cagelike structures of pure metal atoms.," *Phys. Rev. B*, vol. 70, no. 20, p. 205401, 2004.

[35] E. M. Fernández, J. M. Soler, I. L. Garzón, and L. C. Balbás, "Trends in the structure and bonding of noble metal clusters," *Phys. Rev. B*, vol. 70, no. 16, p. 165403, 2004.

[36] D. Fedlheim and C. Foss, *Metal nanoparticles: synthesis, characterization and applications*. Base, Switzerland: Marcel Dekker AG, 2002.

[37] B. Corain, G. Schmid, and N. Toshima, *Metal Nanoclusters in Catalysis and Materials Science: The Issue of Size Control*. Amsterdam, Netherlands: Elsevier, 2008.

[38] R. S. Rawat, "Dense plasma focus-from alternative fusion source to versatile high energy density plasma source for plasma nanotechnology," *J. Phys. Conf. Ser.*, vol. 591, no. 1, p. 012021, 2015.

[39] B. H. K. Kammler, L. Mädler, and S. E. Pratsinis, "Flame Synthesis of Nanoparticles," *Chem. Eng. Technol. Ind. Chem. Equipment-Process Eng.*, vol. 24, no. 6, pp. 583–596, 2001.

[40] H. Bönnemann, W. Brijoux, R. Brinkmann, T. Joußen, B. Korall, and E. Dinjus, "Formation of colloidal transition metals in organic phases and their application in catalysis," *Angew. Chemie Int. Ed. English*, vol. 30, no. 10, pp. 1312–1314, 1991.

[41] T. Adschiri, "Supercritical hydrothermal synthesis of organic–inorganic hybrid nanoparticles," *Chem. Lett.*, vol. 36, no. 10, pp. 1188–1193, 2007.

[42] K. S. Suslick, J. W. Goodale, P. F. Schubert, and H. H. Wang, "Sonochemistry and sonocatalysis of metal carbonyls," *J. Am. Chem. Soc.*, vol. 105, no. 18, pp. 5781–5785, 1983.

[43] M. T. Reetz and S. A. Quaiser, "A new method for the preparation of nanostructured metal clusters," *Angew. Chemie Int. Ed. English*, vol. 34, no. 20, pp. 2240–2241, 1995.

[44] C. Amiens *et al.*, "Organometallic approach for the synthesis of nanostructures," *New J. Chem.*, vol. 37, no. 11, pp. 3374–3401, 2013.

[45] J. Fan, S. W. Boettcher, and G. D. Stucky, "Nanoparticle assembly of ordered multicomponent mesostructured metal oxides via a versatile sol–gel process," *Chem. Mater.*, vol. 18, no. 26, pp. 6391–6396, 2006.

[46] M. Artus *et al.*, "Synthesis and magnetic properties of ferrimagnetic CoFe2O4 nanoparticles embedded in an antiferromagnetic NiO matrix," *Chem. Mater.*, vol. 20, no. 15, pp. 4861–4872, 2008.

[47] S. Roginsky and A. Schalnikoff, "Eine neue methode der herstellung kolloider lösungen," *Kolloid-Zeitschrift*, vol. 43, no. 2, pp. 67–70, 1927.

[48] V. K. LaMer and R. H. Dinegar, "Theory, production and mechanism of formation of monodispersed hydrosols," *J. Am. Chem. Soc.*, vol. 72, no. 11, pp. 4847–4854, 1950.

[49] J. Turkevich, P. C. Stevenson, and J. Hillier, “A study of the nucleation and growth processes in the synthesis of colloidal gold,” *Discuss. Faraday Soc.*, vol. 11, pp. 55–75, 1951.

[50] B. J. Hornstein and R. G. Finke, “Transition-metal nanocluster kinetic and mechanistic studies emphasizing nanocluster agglomeration: Demonstration of a kinetic method that allows monitoring of all three phases of nanocluster formation and aging,” *Chem. Mater.*, vol. 16, no. 1, pp. 139–150, 2004.

[51] C. Besson, E. E. Finney, and R. G. Finke, “A Mechanism for Transition-Metal Nanoparticle Self-Assembly,” *J. Am. Chem. Soc.*, vol. 127, no. 22, pp. 8179–8184, 2005.

[52] T. W. Hansen, A. T. Delariva, S. R. Challa, and A. K. Datye, “Sintering of Catalytic Nanoparticles: Particle Migration or Ostwald Ripening?,” *Acc. Chem. Res.*, vol. 46, no. 8, pp. 1720–1730, 2013.

[53] C.-J. Jia and F. Schüth, “Colloidal metal nanoparticles as a component of designed catalyst,” *Phys. Chem. Chem. Phys.*, vol. 13, no. 7, pp. 2457–2487, 2011.

[54] L. S. Ott and R. G. Finke, “Transition-metal nanocluster stabilization for catalysis : A critical review of ranking methods and putative stabilizers,” *Coord. Chem. Rev.*, vol. 251, no. 9–10, pp. 1075–1100, 2007.

[55] F. Bonet, V. Delmas, S. Grugeon, R. H. Urbina, P. Y. Silvert, and K. Tekaia-Elhsissen, “Synthesis of monodisperse Au, Pt, Pd, Ru and Ir nanoparticles in ethylene glycol,” *Nanostructured Mater.*, vol. 11, no. 8, pp. 1277–1284, 1999.

[56] R. M. Crooks, M. Zhao, L. Sun, V. Chechik, and L. K. Yeung, “Dendrimer-encapsulated metal nanoparticles: synthesis, characterization, and applications to catalysis,” *Acc. Chem. Res.*, vol. 34, no. 3, pp. 181–190, 2001.

[57] C. M. Pleass and D. G. Schimmel, “Kinetics of the Deposition from Solutions of Nickel Onto Powder Surfaces of Dicyclopentadienylnickel,” *J. Catal.*, vol. 24, no. 3, pp. 424–433, 1972.

[58] M.-L. Tschan, O. Diebolt, and P. W. N. M. van Leeuwen, “Ruthenium Metal Nanoparticles in Hydrogenation: Influence of Phosphorus-Ligands,” *Top. Catal.*, vol. 57, no. 10–13, pp. 1054–1065, 2014.

[59] K. Philippot, P. Lignier, and B. Chaudret, “Organometallic Ruthenium Nanoparticles and Catalysis,” in *Ruthenium in Catalysis*, no. Topics in Organometallic Chemistry, Switzerland: Springer International Publishing, 2014, pp. 319–370.

[60] S. D. Solomon, M. Bahadory, A. V Jeyarajasingam, S. A. Rutkowsky, and C. Boritz, “Synthesis and Study of Silver Nanoparticles,” *J. Chem. Educ.*, vol. 84, no. 2, pp. 322–325, 2007.

[61] G. Salas *et al.*, “Influence of amines on the size control of in situ synthesized ruthenium nanoparticles in imidazolium ionic liquids,” *Dalt. Trans.*, vol. 40, no. 17, pp. 4660–4668, 2011.

[62] P. Rempp, J. Herz, G. Hild, and C. Picot, “Tailor-made networks: synthesis and properties,” *Pure Appl. Chem.*, vol. 43, no. 1–2, pp. 77–96, 1975.

[63] J. M. Thomas and W.-J. Thomas, *Principle and Practice of Heterogeneous Catalysis*. VCH, 1997.

[64] J. K. Nørskov, T. Bligaard, J. Rossmeisl, and C. H. Christensen, “Towards the computational design of solid catalysts,” *Nat. Chem.*, vol. 1, no. 1, pp. 37–46, 2009.

[65] A. Nilsson, L. G. M. Pettersson, and J. K. Nørskov, *Chemical Bonding at Surfaces and Interfaces*. Elsevier, 2008.

[66] B. H. L. B. Hammer, L. B. Hansen, and J. K. Nørskov, “Improved adsorption energetics within density-functional theory using revised Perdew-Burke-Ernzerhof functionals,” *Phys. Rev. B*, vol. 59, no. 11, pp. 7413–7421, 1999.

[67] P. Sautet and F. Delbecq, “Catalysis and surface organometallic chemistry: a view from theory and simulations,” *Chem. Rev.*, vol. 110, no. 3, pp. 1788–1806, 2009.

[68] G. Kresse and J. Furthmüller, “Efficient iterative schemes for ab initio total-energy calculations using a plane-wave basis set,” *Phys. Rev. B*, vol. 54, no. 16, p. 11169, 1996.

[69] G. Kresse and J. Furthmüller, “Efficiency of ab-initio total energy calculations for metals and semiconductors using a plane-wave basis set,” *Comput. Mater. Sci.*, vol. 6, no. 1, pp. 15–50, 1996.

[70] L. H. Thomas, “The calculation of atomic fields,” *Math. Proc. Cambridge Philos. Soc.*, vol. 23, no. 5, pp. 542–548, 1927.

[71] E. Fermi, “Zur Quantelung des idealen einatomigen Gases,” *Zeitschrift für Phys.*, vol. 36, no. 11–12, pp. 902–912, 1926.

[72] W. Kohn and L. J. Sham, “Quantum density oscillations in an inhomogeneous electron gas,” *Phys. Rev.*, vol. 137, no. 6A, p. A1697, 1965.

[73] J. P. Perdew, K. Burke, and M. Ernzerhof, “Generalized Gradient Approximation Made Simple,” *Phys. Rev. Lett.*, vol. 77, no. 18, pp. 3865–3868, 1996.

[74] A. Stroppa, K. Termentzidis, J. Paier, G. Kresse, and J. Hafner, “CO adsorption on metal surfaces: A hybrid functional study with plane-wave basis set,” *Phys. Rev. B*, vol. 76, no. 19, p. 195440, 2007.

[75] B. Hammer and J. K. Nørskov, “Theoretical Surface Science and Catalysis—Calculations and Concepts,” *Adv. Catal.*, vol. 45, pp. 71–129, 2000.

[76] S. T. Bromley, I. de P. R. Moreira, K. M. Neyman, and F. Illas, “Approaching nanoscale oxides: models and theoretical methods,” *Chem. Soc. Rev.*, vol. 38, no. 9, pp. 2657–2670, 2009.

[77] K. Philippot and B. Chaudret, “Organometallic approach to the synthesis and surface reactivity of noble metal nanoparticles,” *Comptes Rendus Chim.*, vol. 6, no. 8–10, pp. 1019–1034, 2003.

[78] G. Wang, M. A. Van Hove, P. N. Ross, and M. I. Baskes, “Monte Carlo simulations of segregation in Pt-Ni catalyst nanoparticles,” *J. Chem. Phys.*, vol. 122, no. 2, p. 24706, 2005.

[79] R. L. McGreevy, “Reverse Monte Carlo modelling,” *J. Phys. Condens. Matter*, vol. 13, no. 46, p. R877, 2001.

[80] K. Honkala *et al.*, “Ammonia synthesis from first-principles calculations,” *Science (80-.).*, vol. 307, no. 5709, pp. 555–558, 2005.

[81] F. Viñes *et al.*, “Methane activation by platinum: Critical role of edge and corner sites of metal nanoparticles,” *Chem. Eur. J.*, vol. 16, no. 22, pp. 6530–6539, 2010.

[82] L. Cusinato, L. M. Martínez-Prieto, B. Chaudret, I. del Rosal, and R. Poteau, “Theoretical Characterization of the Surface Composition of Ruthenium Nanoparticles in Equilibrium with Syngas,” *Nanoscale*, vol. 8, no. 21, pp. 10974–10992, 2016.

[83] E. A. Seddon and K. R. Seddon, *The chemistry of ruthenium*. Elsevier, 2013.

[84] M. Muhler, E. Rosowski, O. Hinrichsen, A. Hornung, and G. Ertl, “Ruthenium as Catalyst for Ammonia Synthesis,” *Stud. Surf. Sci. Catal.*, vol. 101, pp. 317–326, 1996.

[85] J. Zhang, M. Cui, Q. Qian, and B. Han, “Synthesis of acetic acid via methanol hydrocarboxylation with CO2 and H2,” *Nat. Commun.*, vol. 7, p. 11481, 2016.

[86] T. Weskamp, W. C. Schattenmann, M. Spiegler, and W. A. Herrmann, “A novel class of ruthenium catalysts for olefin metathesis,” *Angew. Chemie Int. Ed.*, vol. 37, no. 18, pp. 2490–2493, 1998.

[87] T. Naota, H. Takaya, and S. Murahashi, “Ruthenium-Catalyzed Reactions for Organic Synthesis,” *Chem. Rev.*, vol. 98, no. 7, pp. 2599–2660, 1998.

[88] Y. Nakao and K. Kaeriyama, “Preparation of noble metal sols in the presence of surfactants and their properties,” *J. Colloid Interface Sci.*, vol. 110, no. 1, pp. 82–87, 1986.

[89] G. Viau *et al.*, “Ruthenium Nanoparticles: Size, Shape, and Self-Assemblies,” *Chem. Mater.*, vol. 15, no. 2, pp. 486–494, 2003.

[90] F. Fiévet *et al.*, “The polyol process: a unique method for easy access to metal nanoparticles with tailored sizes, shapes and compositions,” *Chem. Soc. Rev.*, vol. 47, no. 14, pp. 5187–5233, 2018.

[91] C. E. Lee, P. B. Tiege, Y. Xing, J. Nagendran, and S. H. Bergens, “Hydrogenation of Ru (1, 5-cyclooctadiene)(η3-C3H5) 2 over Black Platinum. A Low-Temperature Reactive Deposition of Submonolayer Quantities of Ruthenium Atoms on Platinum with Real Time Control over Surface Stoichiometry,” *J. Am. Chem. Soc.*, vol. 119, no. 15, pp. 3543–3549, 1997.

[92] K. Kusada *et al.*, “Discovery of Face-Centered-Cubic Ruthenium Nanoparticles: Facile Size-Controlled Synthesis Using the Chemical Reduction Method,” *J. Am. Chem. Soc.*, vol. 135, no. 15, pp. 5493–5496, 2013.

[93] L. M. Martínez-Prieto and B. Chaudret, “Organometallic Ruthenium Nanoparticles: Synthesis, Surface Chemistry, and Insights into Ligand Coordination.,” *Acc. Chem. Res.*, vol. 51, no. 2, pp. 376–384, 2018.

[94] B. K. Pelzer, O. Vidoni, K. Philippot, B. Chaudret, and V. Colli, “Organometallic Synthesis of Size-Controlled Polycrystalline Ruthenium Nanoparticles in the Presence of Alcohols,” *Adv. Funct. Mater.*, vol. 13, no. 2, pp. 118–126, 2003.

[95] A. Duteil *et al.*, “Preparation of Organic Solutions or Solid Films of Small Particles of Ruthenium , Palladium , and Platinum from Organometallic Precursors in the Presence of Cellulose Derivatives,” *Chem. Mater.*, vol. 5, no. 3, pp. 341–347, 1993.

[96] K. M. Koczkur, S. Mourdikoudis, L. Polavarapu, and S. E. Skrabalak, “Polyvinylpyrrolidone (PVP) in nanoparticle synthesis,” *Dalt. Trans.*, vol. 44, no. 41, pp. 17883–17905, 2015.

[97] C. Pan *et al.*, “Ligand-Stabilized Ruthenium Nanoparticles: Synthesis, Organization, and Dynamics,” *J. Am. Chem. Soc.*, vol. 123, no. 31, pp. 7584–7593, 2001.

[98] P. Debouttière, Y. Coppel, A. Denicourt-nowicki, A. Roucoux, B. Chaudret, and K. Philippot, “PTA-Stabilized Ruthenium and Platinum Nanoparticles: Characterization and Investigation in Aqueous Biphasic Hydrogenation Catalysis,” *Eur. J. Inorg. Chem.*, vol. 8, pp. 1229–1236, 2012.

[99] J. García-Antón *et al.*, “Reactions of olefins with ruthenium hydride nanoparticles: NMR characterization, hydride titration, and r[1] J. García-Antón et al., “Reactions of olefins with ruthenium hydride nanoparticles: NMR characterization, hydride titration, and room-temperature ,” *Angew. Chemie Int. Ed.*, vol. 47, no. 11, pp. 2074–2078, 2008.

[100] P. Lara, O. Rivada-wheelaghan, S. Conejero, R. Poteau, K. Philippot, and B. Chaudret, "Ruthenium Nanoparticles Stabilized by N-Heterocyclic Carbenes: Ligand Location and Influence on Reactivity.," *Angew. Chemie*, vol. 123, no. 50, pp. 12286–12290, 2011.

[101] I. Favier, S. Massou, E. Teuma, K. Philippot, B. Chaudret, and M. Gómez, "A new and specific mode of stabilization of metallic nanoparticles w," *Chem. Commun.*, vol. 28, pp. 3296–3298, 2008.

[102] F. Novio, K. Philippot, and B. Chaudret, "Location and Dynamics of CO Co-ordination on Ru Nanoparticles: A Solid State NMR Study," *Catal. Letters*, vol. 140, no. 1–2, pp. 1–7, 2010.

[103] K. Pelzer *et al.*, "New Ru Nanoparticles Stabilized by Organosilane Fragments," *Chem. Mater.*, vol. 16, no. 24, pp. 4937–4941, 2004.

[104] I. Favier *et al.*, "Hydrogenation Processes at the Surface of Ruthenium Nanoparticles : A NMR Study," *Top. Catal.*, vol. 56, no. 13–14, pp. 1253–1261, 2013.

[105] F. Novio *et al.*, "Surface chemistry on small ruthenium nanoparticles: evidence for site selective reactions and influence of ligands," *Chem. Eur. J.*, vol. 20, no. 5, pp. 1287–1297, 2014.

[106] K. Tedsree, A. T. S. Kong, and S. C. Tsang, "Formate as a surface probe for ruthenium nanoparticles in solution 13C NMR spectroscopy," *Angew. Chemie Int. Ed.*, vol. 48, no. 9, pp. 1443–1446, 2009.

[107] F. Schröder *et al.*, "Ruthenium nanoparticles inside porous [Zn4O(bdc)3] by hydrogenolysis of adsorbed [Ru(cod)(cot)]: A solid-state reference system for surfactant-stabilized ruthenium colloids," *J. Am. Chem. Soc.*, vol. 130, no. 19, pp. 6119–6130, 2008.

[108] D. González-Gálvez, P. Nolis, K. Philippot, B. Chaudret, and P. W. van Leeuwen, "Phosphine-Stabilized Ruthenium Nanoparticles: The Effect of the Nature of the Ligand in Catalysis," *ACS Catal.*, vol. 2, no. 3, pp. 317–321, 2012.

[109] A. P. Serp *et al.*, "Hexakis [60] Fullerene Adduct-Mediated Covalent Assembly of Ruthenium Nanoparticles and Their Catalytic Properties," *Chem. Eur. J.*, vol. 23, no. 54, pp. 13379–13386, 2017.

[110] P. Lara, K. Philippot, and B. Chaudret, "Organometallic ruthenium nanoparticles: a comparative study of the influence of the stabilizer on their characteristics and reactivity," *ChemCatChem*, vol. 5, no. 1, pp. 28–45, 2013.

[111] I. C. Gerber and R. Poteau, "Nanomaterials in Catalysis," in *Transition Metal Particles: Where are we now?*, Weinheim, Germany: Wiley-VCH, 2013, pp. 443–471.

[112] L. A. Truflandier, D. Rosal, B. Chaudret, R. Poteau, and I. C. Gerber, "Where does Hydrogen Adsorb on Ru Nanoparticles? A Powerful Joint H MAS-NMR/DFT Approach," *ChemPhysChem*, vol. 10, no. 17, pp. 2939–2942, 2009.

[113] T. Gutmann *et al.*, "Hydrido-Ruthenium Cluster Complexes as Models for Reactive Surface Hydrogen Species of Ruthenium Nanoparticles . Solid-State 2H NMR and Quantum Chemical Calculations," *J. Am. Chem. Soc.*, vol. 132, no. 33, pp. 11759–11767, 2010.

[114] L. M. Martínez-Prieto *et al.*, "Zwitterionic amidinates as effective ligands for platinum nanoparticle hydrogenation catalysts," *Chem. Sci.*, vol. 4, no. 8, pp. 2931–2941, 2017.

[115] C. Taglang *et al.*, "Enantiospecific C-H Activation Using Ruthenium Nanocatalysts," *Angew. Chemie Int. Ed.*, vol. 54, no. 36, pp. 10474–10477, 2015.

[116] G. H. Woehrle, L. O. Brown, and J. E. Hutchison, "Thiol-functionalized, 1.5-nm gold nanoparticles through ligand exchange reactions: Scope and mechanism of ligand exchange," *J. Am. Chem. Soc.*, vol. 127, no. 7, pp. 2172–2183, 2005.

[117] E. C. Hurst, K. Wilson, I. J. Fairlamb, and V. Chechik, "N-Heterocyclic carbene coated metal nanoparticles," *New J. Chem.*, vol. 33, no. 9, pp. 1837–1840, 2009.

[118] J. C. Love, L. A. Estroff, J. K. Kriebel, R. G. Nuzzo, and G. M. Whitesides, "Self-Assembled Monolayers of Thiolates on Metals as a Form of Nanotechnology," *Chem. Rev.*, vol. 105, no. 4, pp. 1103–1170, 2005.

[119] L. O. Brown and J. E. Hutchison, "Controlled Growth of Gold Nanoparticles during Ligand Exchange," *J. Am. Chem. Soc.*, vol. 121, no. 4, pp. 882–883, 1999.

[120] R. De Palma *et al.*, "Silane ligand exchange to make hydrophobic superparamagnetic nanoparticles water-dispersible," *Chem. Mater.*, vol. 19, no. 7, pp. 1821–1831, 2007.

[121] R. A. Sperling and W. J. Parak., "Surface modification, functionalization and bioconjugation of colloidal inorganic nanoparticles," *Philos. Trans. R. Soc. A Math. Phys. Eng. Sci.*, vol. 368, no. 1915, pp. 1333–1383, 2010.

[122] M. Branca, M. Ibrahim, D. Ciuculescu, K. Philippot, and C. Amiens, "Water Transfer of Hydrophobic Nanoparticles: Principles and Methods," in *Handbook of Nanoparticles*, M. Aliofkhazraei, Ed. Switzerland: Springer International Publishing, 2016, pp. 1279–1311.

[123] M. S. Nikolic, M. Krack, V. Aleksandrovic, A. Kornowski, S. Förster, and H. Weller, "Tailor-Made Ligands for Biocompatible Nanoparticles," *Angew. Chemie Int. Ed.*, vol. 45, no. 39, pp. 6577–6580, 2006.

[124] I. Favier, E. Teuma, and M. Gomez, “Palladium and ruthenium nanoparticles: Reactivity and coordination at the metallic surface,” *Comptes Rendus Chim.*, vol. 12, no. 5, pp. 533–545, 2009.

[125] M. V. Escárcega-Bobadilla *et al.*, “Ruthenium and rhodium nanoparticles as catalytic precursors in supercritical carbon dioxide,” *Catal. Today*, vol. 148, no. 3–4, pp. 398–404, 2009.

[126] M. C. Schoenmaker-Stolk, J. W. Verwijs, J. A. Don, and J. J. F. Scholten, “The catalytic hydrogenation of benzene over supported metal catalysts: I. Gas-phase hydrogenation of benzene over ruthenium-on-silica.,” *Appl. Catal.*, vol. 29, no. 1, pp. 73–90, 1987.

[127] W. Chen, N. B. Zuckerman, X. Kang, D. Ghosh, J. P. Konopelski, and S. Chen, “Alkyne-Protected Ruthenium Nanoparticles,” *J. Phys. Chem. C*, vol. 114, no. 42, pp. 18146–18152, 2010.

[128] F. Zhang *et al.*, “Alkyne-Functionalized Ruthenium Nanoparticles: Impact of Metal–Ligand Interfacial Bonding Interactions on the Selective Hydrogenation of Styrene,” *ACS Catal.*, vol. 9, no. 1, pp. 98–104, 2018.

[129] D. Gonzalez-Galvez *et al.*, “NHC-stabilized ruthenium nanoparticles as new catalysts for the hydrogenation of aromatics,” *Catal. Sci. Technol.*, vol. 3, no. 1, pp. 99–105, 2013.

[130] D. Astruc, *Nanoparticles and catalysis*. John Wiley & Sons, 2008.

[131] L. M. Rossi and G. Machado, “Ruthenium nanoparticles prepared from ruthenium dioxide precursor: Highly active catalyst for hydrogenation of arenes under mild conditions,” *J. Mol. Catal. A Chem.*, vol. 298, no. 1–2, pp. 69–73, 2009.

[132] A. Gual *et al.*, “Diphosphite ligands derived from carbohydrates as stabilizers for ruthenium nanoparticles: promising catalytic systems in arene hydrogenation.,” *Chem. Commun.*, vol. 24, pp. 2759–2761, 2008.

[133] K. P. and B. L. M. Martínez-Prieto, C. Urbaneja, P. Palma, b J. Cámpora and Chaudret, “A betaine adduct of N-heterocyclic carbene and carbodiimide, an efficient ligand to produce ultra-small ruthenium nanoparticles,” *Chem. Commun.*, vol. 22, no. 51, pp. 4647–4650, 2015.

[134] E. Bonne *et al.*, “Tin-decorated ruthenium nanoparticles: a way to tune selectivity in hydrogenation reaction.,” *Nanoscale*, vol. 6, no. 16, pp. 9806–9816, 2014.

[135] L. M. Martinez-Prieto *et al.*, “Organometallic ruthenium nanoparticles as model catalysts for CO hydrogenation: A nuclear magnetic resonance and ambient-pressure X-ray photoelectron spectroscopy study.,” *ACS Catal.*, vol. 4, no. 9, pp. 3160–3168, 2014.

[136] S. H. Joo, J. Y. Park, J. R. Renzas, D. R. Butcher, W. Huang, and G. A. Somorjai, “Size Effect of Ruthenium Nanoparticles in Catalytic Carbon Monoxide Oxidation,” *Nano Lett.*, vol. 10, no. 7, pp. 2709–2713, 2010.

[137] A. J. Creus *et al.*, “Ruthenium Nanoparticles Supported onto Carbon Microfibers for Hydrogen Evolution Electrocatalysis,” *Eur. J. Inorg. Chem.*

[138] W. J. Parak, L. Manna, C. F. Simmel, D. Gerion, and P. Alivisatos, “Quantum Dots,” in *Nanoparticles: From Theory to Application.*, 2nd ed., W. VCH, Ed. 2005, pp. 3–47.

[139] M. Ismail, S. Gul, M. A. Khan, and M. I. Khan, “Plant Mediated Green Synthesis of Anti- Microbial Silver Nanoparticles — A Review on Recent Trends,” *Rev. Nanosci. Nanotechnol.*, vol. 5, no. January, pp. 119–135, 2016.

[140] T. K. Sau and A. L. Rogach, *Complex-shaped metal nanoparticles: bottom-up syntheses and applications.* 2012.

[141] H. Hosseini-Monfared, H. Meyer, and C. Janiak, “Dioxygen oxidation of 1-phenylethanol with gold nanoparticles and N-hydroxyphthalimide in ionic liquid,” *J. Mol. Catal. A Chem.*, vol. 372, pp. 72–78, 2013.

[142] G. Schmid, “Conclusions and Prespectives,” in *Nanoparticles: From Theory to Application.*, 2nd ed., W. VCH, Ed. 2005, pp. 513–515.

[143] L. Wang, J. Li, Q. Jiang, and L. Zhao, “Water-soluble Fe3O4nanoparticles with high solubility for removal of heavy-metal ions from waste water,” *Dalt. Trans.*, vol. 41, no. 15, pp. 4544–4551, 2012.

[144] P. D. Howes, R. Chandrawati, and M. M. Stevens, “Colloidal nanoparticles as advanced biological sensors,” *Science (80-.).*, vol. 346, no. 6205, 2014.

[145] S. K. Murthy, “Nanoparticles in modern medicine: state of the art and future challenges.,” *Int. J. Nanomedicine nanomedicine*, vol. 2, no. 2, pp. 129–41, 2007.

[146] J. Palomo and M. Filice, “Biosynthesis of Metal Nanoparticles: Novel Efficient Heterogeneous Nanocatalysts,” *Nanomaterials*, vol. 6, no. 5, p. 84, 2016.

[147] M. J. Yoon, “Surface modifications and optoelectronic characterization of TiO2-nanoparticles: Design of new photo-electronic materials,” *J. Chinese Chem. Soc.*, vol. 56, no. 3, pp. 449–454, 2009.

[148] E. Serrano, G. Rus, and J. García-Martínez, “Nanotechnology for sustainable energy,” *Renew. Sustain. Energy Rev.*, vol. 13, no. 9, pp. 2373–2384, 2009.

[149] C. Amiens, D. Ciuculescu-Pradines, and K. Philippot, “Controlled metal nanostructures: Fertile ground for coordination chemists,” *Coord. Chem.*

Rev., vol. 308, pp. 409–432, 2016.

[150] H. University, "Alloy noble metal nanoparticles and their structures." [Online]. Available: https://nanoparticle.hokkaido.university/en/research/alloynoble. [Accessed: 19-Feb-2019].

[151] M. Grasemann and G. Laurenczy, "Environmental Science Formic acid as a hydrogen source – recent developments and future trends," *Energy Environ. Sci.*, vol. 5, pp. 8171–8181, 2012.

[152] P. Mars, J. J. F. Scholten, and P. Zwietering, "The catalytic decomposition of formic acid.," in *Advances in Catalysis*, Academic Press, 1963, pp. 35–113.

[153] H. Häkkinen, "Atomic and electronic structure of gold clusters: understanding flakes, cages and superatoms from simple concepts.," *Chem. Soc. Rev.*, vol. 37, no. 9, pp. 1847–1859, 2008.

[154] I. Chorkendorff and J. W. Niemantsverdriet, "Surface Reactivity," in *Concepts of Modern Caralysis and Kinetics*, Wiley-VCH Verlag, 2005, pp. 215–266.

[155] L. Porri, P. Pertici, G. Vitulli, and M. Paci, "A New Synthetic Method for the Preparation of Cyclo-olefin Ruthenium Complexes," *J. Chem. Soc., Dalt. Trans.*, vol. 3, pp. 1961–1964, 1980.

[156] B. Chaudret, G. Commenges, and R. Poilblanc, "The use of (cyclo-octadiene)(cyclo-octatriene) ruthenium (0) as the starting material for the synthesis of mono-and poly-nuclear ruthenium polyhydride phosphine complexes.," *J. Chem. Soc. Chem. Commun.*, vol. 24, pp. 1388–1390, 1982.

[157] A. Kraynov and T. E. Müller, "Concepts for the stabilization of metal nanoparticles in ionic liquids," in *Applications of Ionic Liquids in Science and Technology*, Germany: InTech, 2011, pp. 235–260.

[158] O. Vidoni *et al.*, "Novel, Spongelike Ruthenium Particles of Controllable Size Stabilized Only by Organic Solvents," *Angew. Chemie Int. Ed.*, vol. 38, no. 24, pp. 3736–3738, 1999.

[159] A. Roucoux, A. Nowicki, and K. Philippot, "Rhodium and Ruthenium Nanoparticles in Catalysis," in *Nanoparticles and Catalysis*, Wiley-VCH Verlag, 2008, pp. 349–338.

[160] S. Li, Y. Wu, J. Wang, Q. Zhang, and S. Zhang, "Double-responsive polyampholyte as a nanoparticle stabilizer : application to reversible dispersion of gold nanoparticles," *J. Mater. Chem.*, vol. 20, no. 21, pp. 4379–4384, 2010.

[161] N. Liakakos *et al.*, "The Big Impact of a Small Detail: Cobalt Nanocrystal Polymorphism as a Result of Precursor Addition Rate during Stock Solution Preparation," *J. Am. Chem. Soc.*, vol. 134, no. 43, pp. 17922–17931, 2012.

[162] C. I. Lynch, "An overview of first-principles calculations of NMR parameters for paramagnetic materials," *Mater. Sci. Technol.*, vol. 32, no. 2, pp. 181–194, 2016.

[163] A. Badia, S. Singh, L. Demers, L. Cuccia, G. R. Brown, and R. B. Lennox, "Self-Assembled Monolayers on Gold Nanoparticles," *Chem. Eur. J.*, vol. 2, no. 3, pp. 359–363, 1996.

[164] X. Liu, M. Yu, H. Kim, M. Mameli, and F. Stellacci, "Determination of monolayer-protected gold nanoparticle ligand–shell morphology using NMR," *Nat. Commun.*, vol. 3, pp. 1182–1189, 2012.

[165] L. Foppa, K. Yamamoto, W. C. Liao, A. Comas-Vives, and C. Copéret, "Electronic Structure–Reactivity Relationship on Ruthenium Step-Edge Sites from Carbonyl 13C Chemical Shift Analysis," *J. Phys. Chem. Lett.*, pp. 3348–3353, 2018.

[166] I. Del Rosal, F. Jolibois, L. Maron, K. Philippot, B. Chaudret, and R. Poteau, "Ligand effect on the NMR , vibrational and structural properties of tetra- and hexanuclear ruthenium hydrido clusters : a theoretical investigation," *Dalt. Trans.*, vol. 12, pp. 2142–2156, 2009.

[167] M. Guerrero *et al.*, "Efficient Ruthenium Nanocatalysts in Liquid – Liquid Biphasic Hydrogenation Catalysis : Towards a Supramolecular Control through a Sulfonated Diphosphine – Cyclodextrin Smart Combination," *ChemCatChem*, vol. 5, no. 12, pp. 3802–3811, 2013.

[168] J. Durand *et al.*, "DOSY technique applied to palladium nanoparticles in ionic liquids," *Magn. Reson. Chem.*, vol. 46, no. 8, pp. 739–743, 2008.

[169] T. C. Farrar and E. D. Becker, *Pulse and Fourier transform NMR: introduction to theory methods*. Elsevier, 2012.

[170] Y. Cohen, L. Avram, and L. Frish, "Diffusion NMR Spectroscopy in Supramolecular and Combinatorial Chemistry : An Old Parameter — New Insights," *Angew. Chemie Int. Ed.*, vol. 44, no. 4, pp. 520–554, 2005.

[171] A. Herron, J. Scaranto, P. Ferrin, S. Li, and M. Mavrikakis, "Trends in Formic Acid Decomposition on Model Transition Metal Surfaces : A Density Functional Theory study," *ACS Catal.*, vol. 4, no. 12, pp. 4434–4445, 2014.

[172] B. Hammer and J. K. Nørskov, "Electronic factors determining the reactivity of metal surfaces," *Surf. Sci.*, vol. 343, no. 3, pp. 211–220, 1995.

[173] D. Mott, J. Luo, P. N. Njoki, Y. Lin, L. Wang, and C. Zhong, "Synergistic activity of gold-platinum alloy nanoparticle catalysts," *Catal. Today*, vol. 122, no. 3–4, pp. 378–385, 2007.

[174] S. J. Blanksby and G. B. Ellison, “Bond Dissociation Energies of Organic Molecules,” *Acc. Chem. Res.*, vol. 36, no. 4, pp. 255–263, 2003.

[175] B. Y. L. Leiserowitz, “Molecular Packing Modes. Carboxylic Acids,” *Acta Crystallogr. Sect. B*, vol. 32, no. 3, pp. 775–802, 1976.

[176] da S. Pereira *et al.*, “Elucidating the real-time Ag nanoparticle growth on a -Ag 2 WO 4 during electron beam irradiation: experimental evidence and theoretical insights,” *Phys. Chem. Chem. Phys.*, vol. 17, no. 7, pp. 5352–5359, 2015.

[177] P. Raveendran, J. Fu, and S. L. Wallen, “Completely ‘ Green ’ Synthesis and Stabilization of Metal Nanoparticles,” *J. Am. Chem. Soc.*, vol. 125, no. 46, pp. 13940–13941, 2003.

[178] P. Liu and J. K. Nørskov, “Ligand and ensemble effects in adsorption on alloy surfaces,” *Phys. Chem. Chem. Phys.*, vol. 3, no. 17, pp. 3814–3818, 2001.

[179] J. W. Hennel and J. Klinowski, “Magic-Angle Spinning : a Historical Perspective,” in *New techniques in solid-state NMR*, Springer Berlin Heidelberg, 2005, pp. 1–14.

[180] H. J. (University of W. Reich, “Relaxation in NMR Spectroscopy,” 2017.

[181] M. J. Duer, *Solid-State NMR Spectroscopy Principles and Applications*. Blackwell Science Ltd, 2001.

[182] G. R. Fulmer *et al.*, “NMR chemical shifts of trace impurities: Common laboratory solvents, organics, and gases in deuterated solvents relevant to the organometallic chemist,” *Organometallics*, vol. 29, no. 9, pp. 2176–2179, 2010.

[183] L. H. Jones and E. Mclaren, “Infrared Spectra of CH3COONa and CD3COONa and Assignments of Vibrational Frequencies,” *J. Chem. Phys.*, vol. 22, no. 11, pp. 1796–1800, 1954.

[184] K. Ito and H. J. Bernstein, “The vibrational spectra of the formate, acetate, and oxalate ions,” *Can. J. Chem.*, vol. 34, no. 2, pp. 170–178, 1956.

[185] H. Noma, Y. Miwa, I. Yokoyama, and K. Machida, “Infrared and Raman intensity parameters of sodium acetate and their intensity distributions,” *J. Mol. Struct.*, vol. 242, pp. 207–219, 1991.

[186] J. K. Wilmshurst, “Infrared Investigation of Acetic Acid and Acetic Acid-d Vapors and a Vibrational Assignment for the Monomeric Acids.,” *J. Chem. Phys.*, vol. 25, no. 6, pp. 1171–1173, 1956.

[187] J.-H. Zhong *et al.*, “Probing the electronic and catalytic properties of a bimetallic surface with 3 nm resolution,” *Nat. Nanotechnol.*, vol. 12, no. 2, p. 132, 2017.

[188] H. Cui, D. Li, and C. Wang, “Infrared Spectrum Analysis of Perfluoro Polyethers (PFPE) of Fluorocarbon-based Magnetic Fluid’s Base Liquid,” *Adv. Mater. Res.*, vol. 391, pp. 1311–1314, 2012.

[189] D. W. Mayo, F. A. Miller, and R. W. Hannah, *Course notes on the interpretation of infrared and Raman spectra*. John Wiley & Sons, 2004.

[190] H. Deng, Z. Shen, L. Li, H. Yin, and J. Chen, “Real-time monitoring of ring-opening polymerization of tetrahydrofuran via in situ Fourier Transform Infrared Spectroscopy,” *J. Appl. Polym. Sci.*, vol. 131, no. 15, pp. 1–7, 2014.

[191] L. Van Lokeren *et al.*, “Characterization of Titanium Dioxide Nanoparticles Dispersed in Organic Ligand Solutions by Using a Diffusion-Ordered Spectroscopy-Based Strategy,” *Chem. Eur. J.*, vol. 13, no. 24, pp. 6957–6966, 2007.

[192] G. Canzi, A. A. Mrse, and P. Kubiak, “Diffusion-Ordered NMR Spectroscopy as a Reliable Alternative to TEM for Determining the Size of Gold Nanoparticles in Organic Solutions,” *J. Phys. Chem. C*, vol. 16, no. 115, pp. 7972–7978, 2011.

[193] A. Lu, E. L. Salabas, and F. Schüth, “Magnetic nanoparticles: synthesis, protection, functionalization, and application,” *Angew. Chemie Int. Ed.*, vol. 46, no. 8, pp. 1222–1244, 2007.

[194] Y.-W. Zhang, *Bimetallic Nanostructures: Shape-Controlled Synthesis for Catalysis, Plasmonics, and Sensing Applications*. John Wiley & Sons, 2018.

[195] T. Ayvalı, P. Lecante, P. F. Fazzini, A. Gillet, K. Philippot, and B. Chaudret, “Facile synthesis of ultra-small rhenium nanoparticles,” *Chem. Commun.*, vol. 50, no. 74, pp. 10809–10811, 2014.

[196] I. Cano, M. J. L. Tschan, L. M. Martínez-Prieto, K. Philippot, B. Chaudret, and P. W. van Leeuwen, “Enantioselective hydrogenation of ketones by iridium nanoparticles ligated with chiral secondary phosphine oxides.,” *Catal. Sci. Technol.*, vol. 6, no. 11, pp. 3758–3766, 2016.

[197] W. Li, C. Stampfl, and M. Scheffler, “Insights into the function of silver as an oxidation catalyst by ab initio atomistic thermodynamics,” *Phys. Rev. B*, vol. 68, no. 16, p. 165412, 2003.

[198] K. Reuter and M. Scheffler, “Composition, structure, and stability of RuO 2 (110) as a function of oxygen pressure,” *Phys. Rev. B*, vol. 65, no. 3, pp. 1–11, 2001.

[199] K. Reuter, C. Stamp, and M. Scheffler, “ab initio atomistic thermodynamics and statistical mechanics of surface properties and functions,” in *Handbook of Materials Modeling*, Springer: Berlin, Heidelberg, 2005, pp. 149–194.

[200] I. Rosal, L. Tru, R. Poteau, and I. C. Gerber, “A density functional theory study of spectroscopic and thermodynamic properties of surfacic

hydrides on Ru (0001) model surface: The influence of the coordination modes and the coverage.," *J. Phys. Chem. C*, vol. 115, no. 5, pp. 2169–2178, 2010.

[201] A. Comas-Vives *et al.*, "Predictive morphology, stoichiometry and structure of surface species in supported Ru nanoparticles under H2 and CO atmospheres from combined experimental and DFT studies," *Phys. Chem. Chem. Phys.*, vol. 18, no. 3, pp. 1969–1979, 2016.

[202] L. Cusinato, I. Del Rosal, and R. Poteau, "Shape, electronic structure and steric effects of organometallic nanocatalysts: relevant tools to improve the synergy between theory and experiment," *Dalt. Trans.*, vol. 46, no. 2, pp. 378–395, 2017.

[203] N. Lopez *et al.*, "On the origin of the catalytic activity of gold nanoparticles for low-temperature CO oxidation," *J. Catal.*, vol. 223, no. 1, pp. 232–235, 2004.

[204] P. M. Arnal, M. Comotti, and F. Schüth, "High-temperature-stable catalysts by hollow sphere encapsulation," *Angew. Chemie Int. Ed.*, vol. 45, no. 48, pp. 8224–8227, 2006.

[205] E. Ramirez, S. Jansat, K. Philippot, P. Lecante, A. M. Masdeu-bulto, and B. Chaudret, "Influence of organic ligands on the stabilization of palladium nanoparticles," *J. Organomet. Chem.*, vol. 689, no. 24, pp. 4601–4610, 2004.

[206] A. Rodriguez, C. Amiens, B. Chaudret, P. Lecante, J. S. Bradley, and D. Mu, "Synthesis and Isolation of Cuboctahedral and Icosahedral Platinum Nanoparticles . Ligand-Dependent Structures," vol. 4756, no. 8, pp. 1978–1986, 1996.

[207] C. Pan *et al.*, "A New Synthetic Method toward Bimetallic Ruthenium Platinum Nanoparticles ; Composition Induced Structural Changes," no. 24, pp. 10098–10101, 1999.

[208] K. Kim, D. Demberelnyamba, and H. Lee, "Size-selective synthesis of gold and platinum nanoparticles using novel thiol-functionalized ionic liquids," *Langmuir*, vol. 20, no. 3, pp. 556–560, 2004.

[209] A. U. Nilekar, S. Alayoglu, B. Eichhorn, and M. Mavrikakis, "Preferential CO oxidation in hydrogen: reactivity of core− shell nanoparticles," *J. Am. Chem. Soc.*, vol. 132, no. 21, pp. 7418–7428, 2010.

[210] P. Sabatier, "How I Have Been Led to the Direct Hydrogenation Method by Metallic Catalysts," *Ind. Eng. Chem.*, vol. 18, no. 10, pp. 1005–1008, 1926.

[211] J. N. Bronsted, "Acid and Basic Catalysis.," *Chem. Rev.*, vol. 5, no. 3, pp. 231–338, 1928.

[212] M. G. Evans and M. Polanyi, "Inertia and driving force of chemical reactions," *Trans. Faraday Soc.*, vol. 34, pp. 11–24, 1938.

[213] A. A. Balandin, "Modern State of the Multiplet Theory of Heterogeneous Catalysis," in *Advances in Catalysis*, Academic Press, 1969, pp. 1–210.

[214] L. Wang and Q. Ge, "Studies of rhodium nanoparticles using the first principles density functional theory calculations," *Chem. Phys. Lett.*, vol. 366, no. 3–4, pp. 368–376, 2002.

[215] M. E. Gruner, G. Rollmann, P. Entel, and M. Farle, "Multiply twinned morphologies of FePt and CoPt nanoparticles," *Phys. Rev. Lett.*, vol. 100, no. 8, p. 87203, 2008.

[216] T. O. Wehling *et al.*, "Molecular doping of graphene," *Nano Lett.*, vol. 8, no. 1, pp. 173–177, 2008.

[217] I. Del Rosal, M. Mercy, I. C. Gerber, and R. Poteau, "Ligand-Field Theory-Based Analysis of the Adsorption Properties of Ruthenium Nanoparticles," *ACS Nano*, vol. 7, no. 11, pp. 9823–9835, 2013.

[218] M. T. Gorzkowski and A. Lewera, "Probing the Limits of d-Band Center Theory: Electronic and Electrocatalytic Properties of Pd-Shell-Pt-Core Nanoparticles," *J. Phys. Chem. C*, vol. 119, no. 32, pp. 18389–18395, 2015.

[219] J. K. Nørskov, T. Bligaard, J. Rossmeisl, and C. H. Christensen, "Towards the computational design of solid catalysts," *Nat. Chem.*, vol. 1, no. 1, p. 37, 2009.

[220] L. Cusinato, "Chimie de Surface de Nanoparticules de Ruthenium: Approches Théoriques," Université de Toulouse, 2016.

[221] R. F. W. Bader, "A Quantum Theory of Molecular Structure and Its Applications," *Chem. Rev.*, vol. 91, no. 5, pp. 893–928, 1991.

[222] H. Group, "Bader Charge Analysis," *The University of Texas at Austin*. .

[223] D. Lim and J. Wilcox, "Mechanisms of the Oxygen Reduction Reaction on Defective Graphene-Supported Pt Nanoparticles from First-Principles," *J. Phys. Chem. C*, vol. 116, no. 5, pp. 3653–3660, 2012.

[224] M. Okumura, Y. Kitagawa, T. Kawakami, and M. Haruta, "Theoretical investigation of the hetero-junction effect in PVP-stabilized Au13 clusters. The role of PVP in their catalytic activities," *Chem. Phys. Lett.*, vol. 459, no. 1–6, pp. 133–136, 2008.

[225] A. E. Reed, R. B. Weinstock, and F. Weinhold, "Natural population analysis," *J. Chem. Phys.*, vol. 83, no. 2, pp. 735–746, 1985.

[226] I. C. Gerber and R. Poteau, "Critical assessment of charge transfer estimates in non-covalent graphene doping," *Theor. Chem. Acc.*, vol. 137, no. 11, p. 156, 2018.

[227] S. Ghosh, M. Ghosh, and C. N. R. Rao, "Nanocrystals, Nanorods and other Nanostructures of Nickel, Ruthenium, Rhodium and Iridium prepared by a Simple Solvothermal Procedure," *J. Clust. Sci.*, vol. 18, no. 1, pp. 97–111, 2007.

[228] A. Ishiguro *et al.*, "Nanoparticles of Amorphous Ruthenium Sulfide Easily Obtainable from a TiO2-Supported Hexanuclear Cluster Complex [Ru6C(CO)16]2−: A Highly Active Catalyst for the Reduction of SO2 with H2," *Chem. Eur. J.*, vol. 8, no. 14, pp. 3260–3268, 2002.

[229] D. Lamey, I. Prokopyeva, F. Cárdenas-Lizana, and L. Kiwi-Minsker, "Impact of organic-ligand shell on catalytic performance of colloidal Pd nanoparticles for alkyne gas-phase hydrogenation," *Catal. Today*, vol. 235, pp. 79–89, 2014.

[230] M. Yamamoto, Y. Kashiwagi, and M. Nakamoto, "Size-controlled synthesis of monodispersed silver nanoparticles capped by long-chain alkyl carboxylates from silver carboxylate and tertiary amine," *Langmuir*, vol. 22, no. 20, pp. 8581–8586, 2006.

[231] N. Zheng, J. Fan, and G. D. Stucky, "One-step one-phase synthesis of monodisperse noble-metallic nanoparticles and their colloidal crystals," *J. Am. Chem. Soc.*, vol. 128, no. 20, pp. 6550–6551, 2006.

[232] A. Centrone *et al.*, "The role of nanostructure in the wetting behavior of mixed-monolayer-protected metal nanoparticles," *Proc. Natl. Acad. Sci.*, vol. 105, no. 29, pp. 9886–9891, 2008.

[233] A. M. Jackson, J. W. Myerson, and F. Stellacci, "Spontaneous assembly of subnanometre-ordered domains in the ligand shell of monolayer-protected nanoparticles," *Nat. Mater.*, vol. 3, no. 5, p. 330, 2004.

[234] T. J. Woehl, J. E. Evans, I. Arslan, W. D. Ristenpart, and N. D. Browning, "Direct in Situ Determination of the Mechanisms Controlling Nanoparticle Nucleation and Growth," *ACS Nano*, vol. 6, no. 10, pp. 8599–8610, 2012.

[235] N. T. Thanh, N. Maclean, and S. Mahiddine, "Mechanisms of nucleation and growth of nanoparticles in solution," *Chem. Rev.*, vol. 114, no. 15, pp. 7610–7630, 2014.

[236] R. H. Terrill *et al.*, "Monolayers in Three Dimensions: NMR, SAXS, Thermal, and Electron Hopping Studies of Alkanethiol Stabilized Gold Clusters," *J. Am. Chem. Soc.*, vol. 117, no. 50, pp. 12537–12548, 1995.

[237] U. S. S. of Commerce, "NIST Standard Reference Database Number 69," 2018. [Online]. Available: webbook.nist.gov.

[238] H. Bonnernann and B. Korall, "Ether-Soluble Ti0 and Bis (η6-arene) titanium (0) Complexes from the Reduction of TiCl4 with Triethylhydroborate," *Angew. Chemie Int. Ed. English*, vol. 31, no. 11, pp. 1490–1492, 1992.

[239] H. Bonnemann and W. Brijoux, "The preparation, characterization and application of organosols of early transition metals," *MRS Online Proc. Libr. Arch.*, vol. 351, pp. 1–5, 1994.

[240] E. Matito i Gras, P. S. Sedano, and J. Styszyński, "Benchmark calculations of metal carbonyl cations: Relativistic vs. electron correlation effects," *Phys. Chem. Chem. Phys.*, vol. 15, no. 46, pp. 20080–20090, 2013.

[241] S. Carenco, C. Boissière, L. Nicole, C. Sanchez, P. Le Floch, and N. Mézailles, "Controlled design of Size-tunable monodisperse nickel nanoparticles," *Chem. Mater.*, vol. 22, no. 4, pp. 1340–1349, 2010.

[242] C. Barrière *et al.*, "Ligand effects on the air stability of copper nanoparticles obtained from organometallic synthesis," *J. Mater. Chem.*, vol. 22, no. 5, pp. 2279–2285, 2012.

[243] W. W. Yu, Y. A. Wang, and X. Peng, "Formation and stability of size-, shape-, and structure-controlled CdTe nanocrystals: ligand effects on monomers and nanocrystals," *Chem. Mater.*, vol. 15, no. 22, pp. 4300–4308, 2003.

[244] M. J. Thrippleton, N. M. Loening, and J. Keeler, "A fast method for the measurement of diffusion coefficients: One-dimensional DOSY," *Magn. Reson. Chem.*, vol. 41, no. 6, pp. 441–447, 2003.

[245] Y. Zhao, Y. Luo, X. Yang, Y. Yang, and Q. Song, "Tunable preparation of ruthenium nanoparticles with superior size-dependent catalytic hydrogenation properties," *J. Hazard. Mater.*, vol. 332, pp. 124–131, 2017.

[246] C. J. Murphy *et al.*, "Anisotropic metal nanoparticles: synthesis, assembly, and optical applications," *J. Phys. Chem. B*, vol. 109, pp. 13857–13870, 2005.

[247] R. J. White, R. Luque, V. L. Budarin, J. H. Clark, and D. J. MacQuarrie, "Supported metal nanoparticles on porous materials. Methods and applications," *Chem. Soc. Rev.*, vol. 38, no. 2, pp. 481–494, 2009.

[248] R. B. Grubbs, "Roles of polymer ligands in nanoparticle stabilization," *Polym. Rev.*, vol. 47, no. 2, pp. 197–215, 2007.

[249] Y. Lin, H. Skaff, T. Emrick, A. D. Dinsmore, and T. P. Russell, "Nanoparticle assembly and transport at liquid-liquid interfaces," *Science (80-.).*, vol. 299, no. 5604, pp. 226–229, 2003.

[250] V. Subramanian, H. Zhu, and B. Wei, "Alcohol-assisted room temperature synthesis of different nanostructured manganese oxides and their pseudocapacitance properties in neutral electrolyte," *Chem. Phys. Lett.*, vol. 453, no. 4–6, pp. 242–249, 2008.

[251] H. Li *et al.*, "Ultrasound-assisted polyol method for the preparation of SBA-15-supported ruthenium nanoparticles and the study of their

catalytic activity on the partial oxidation of methane," *Langmuir*, vol. 20, no. 19, pp. 8352–8356, 2004.

[252] G. Arivazhagan, R. Shanmugam, and T. Thenappan, "Dielectric, FT-IR and UV-vis spectroscopic studies on the fluid structure of diisopropyl ether-caprylic acid mixture," *J. Mol. Struct.*, vol. 990, no. 1–3, pp. 276–280, 2011.

[253] S. Grimme, J. Antony, S. Ehrlich, and S. Krieg, "A consistent and accurate ab initio parametrization of density functional dispersion correction (dft-d) for the 94 elements H-Pu," *J. Chem. Phys*, vol. 132, p. 154104, 2010.

[254] S. Grimme, S. Ehrlich, and L. Goerigk, "Effect of the damping function in dispersion corrected density functional theory," *J. Comp. Chem.*, vol. 32, p. 1456, 2011.

[255] N. P. Markus Niederberger, *Metal Oxide Nanoparticles in Organic Solvents: Synthesis, Formation, Assembly and Application*. Springer Science & Business Media, 2009.

[256] M. Niederberger and G. Garnweitner, "Organic Reaction Pathways in the Nonaqueous Synthesis of Metal Oxide," *Chem. Eur. J.*, vol. 12, no. 28, pp. 7282–7302, 2006.

[257] M. Raymond and F. Rousset, "An exact test for population differentiation," *Evolution (N. Y).*, vol. 49, no. 6, pp. 1280–1283, 1995.

[258] G. D. Ruxton, "The unequal variance t -test is an underused alternative to Student's t -test and the Mann–Whitney U test," *Behav. Ecol.*, vol. 17, no. 4, pp. 688–690, 2006.

[259] E. Ramirez, L. Eradès, K. Philippot, P. Lecante, and B. Chaudret, "Shape Control of Platinum Nanoparticles," *Adv. Funct. Mater.*, vol. 17, no. 13, pp. 2219–2228, 2007.

[260] J. M. Asensio, S. Tricard, Y. Coppel, R. Andrés, B. Chaudret, and E. de Jesús, "Knight Shift in 13C NMR Resonances Confirms the Coordination of N-Heterocyclic Carbene Ligands to Water-Soluble Palladium Nanoparticles," *Angew. Chemie*, vol. 129, no. 3, pp. 883–887, 2017.

[261] L. E. Marbella and J. E. Millstone, "NMR Techniques for Noble Metal Nanoparticles," *Chem. Mater.*, vol. 27, no. 8, pp. 2721–2739, 2015.

[262] E. A. Baquero, S. Tricard, J. C. Flores, E. De Jesffls, and B. Chaudret, "Highly Stable Water-Soluble Platinum Nanoparticles Stabilized by Hydrophilic N-Heterocyclic Carbenes," *Angew. Chemie*, vol. 126, no. 48, pp. 13436–13440, 2014.

[263] B. M. R. D. Bank, "Octanoic Acid (C8 H16 O2)." [Online]. Available: http://www.bmrb.wisc.edu/metabolomics/mol_summary/show_data.php?id=bmse000502&whichTab=1. [Accessed: 27-Feb-2019].

[264] K. Tedsree *et al.*, "13C NMR guides rational design of nanocatalysts via chemisorption evaluation in liquid phase," *Science (80-.).*, vol. 332, no. 6026, pp. 224–228, 2011.

[265] J. A. Lopez-ruiz and R. J. Davis, "Decarbonylation of heptanoic acid over carbon-supported platinum nanoparticles," *Green Chem.*, vol. 16, no. 2, pp. 683–694, 2014.

[266] H. H. Lamb, L. Sremaniak, and J. L. Whitten, "Reaction pathways for butanoic acid decarboxylation on the (111) surface of a Pd nanoparticle," *Surf. Sci.*, vol. 607, pp. 130–137, 2013.

[267] Y. Coppel, G. Spataro, C. Pages, B. Chaudret, A. Maisonnat, and M. L. Kahn, "Full Characterization of Colloidal Solutions of Long-Alkyl-Chain-Amine- Stabilized ZnO Nanoparticles by NMR Spectroscopy: Surface State, Equilibria, and Affinity," *Chem. Eur. J.*, vol. 17, no. 18, pp. 5384–5393, 2012.

[268] T. Pradeep, "Noble metal nanoparticles for water purification : A critical review," *Thin Solid Films*, vol. 517, no. 24, pp. 6441–6478, 2009.

[269] K. A. Z. Nagashima *et al.*, "Stejskal – Tanner Equation Derived in Full," *Concepts Magn. Reson. Part A*, vol. 40, no. 5, pp. 205–214, 2012.

[270] D. Li, Q. He, Y. Yang, H. Mo, and J. Li, "Two-Stage pH Response of Poly (4-vinylpyridine) Grafted Gold Nanoparticles," *Macromolecules*, vol. 41, no. 19, pp. 7254–7256, 2008.

[271] A. Mene, B. N. Chichkov, and S. Barcikowski, "Influence of Water Temperature on the Hydrodynamic Diameter of Gold Nanoparticles from Laser Ablation," *J. Phys. Chem. C*, vol. 11, no. 46, pp. 2499–2504, 2010.

[272] M.-A. Neouze and U. Schubert, "Surface Modification and Functionalization of Metal and Metal Oxide Nanoparticles by Organic Ligands," *Monatshefte für Chemie-Chemical Mon.*, vol. 139, no. 3, pp. 183–195, 2008.

[273] C. B. Post, "Exchange-transferred NOE spectroscopy and bound ligand structure determination," *Curr. Opin. Struct. Biol.*, vol. 13, no. 5, pp. 581–588, 2003.

[274] M. P. Williamson, *Chapter 3 - Applications of the NOE in Molecular Biology*, 1st ed., vol. 65. Elsevier Ltd, 2009.

[275] J. W. Olesik, "Elemental analysis using ICP-OES and ICP/MS," *Anal. Chem.*, vol. 63, no. 1, p. 12A–21A, 1991.

[276] A. Desireddy *et al.*, "Ultrastable silver nanoparticles," *Nature*, vol. 501, no. 7467, p. 399, 2013.

[277] S. Park and K. Hamad-schifferli, "Evaluation of Hydrodynamic Size and Zeta-Potential of Surface-Modified Au Nanoparticle-DNA Conjugates via Ferguson Analysis," *he J. Phys. Chem. C*, vol. 112, no. 20, pp. 7611–7616, 2008.

[278] D. Tsai, T. J. Cho, F. W. Delrio, J. Taurozzi, M. R. Zachariah, and V. A. Hackley, "Hydrodynamic Fractionation of Finite Size Gold Nanoparticle Clusters," *J. Am. Chem. Soc.*, vol. 133, no. 23, pp. 8884–8887, 2011.

[279] H. L. Abbott *et al.*, "CO Adsorption on Monometallic and Bimetallic Au - Pd Nanoparticles Supported on Oxide Thin Films," *J. Phys. Chem. C*, vol. 114, no. 40, pp. 17099–17104, 2010.

[280] F. Vindigni, M. Manzoli, A. Chiorino, and F. Boccuzzi, "Catalytically active gold sites: nanoparticles, borderline sites, clusters, cations, anions? FTIR spectra analysis of 12 CO and of 12 CO-13 CO isotopic mixtures," *Gold Bull.*, vol. 42, no. 2, 2009.

[281] M. Walter *et al.*, "A unified view of ligand-protected gold clusters as superatom complexes," *Proc. Natl. Acad. Sci.*, vol. 105, no. 27, pp. 9157–9162, 2008.

[282] C. M. Aikens, "Electronic Structure of Ligand-Passivated Gold and Silver Nanoclusters," *J. Phys. Chem. Lett.*, vol. 2, no. 2, pp. 99–104, 2010.

[283] P. Kanninen, C. Johans, J. Merta, and K. Kontturi, "Influence of ligand structure on the stability and oxidation of copper nanoparticles," *J. Colloid Interface Sci.*, vol. 318, no. 1, pp. 88–95, 2008.

[284] D. Astruc, F. Lu, and J. R. Aranzaes, "Nanoparticles as recyclable catalysts: the frontier between homogeneous and heterogeneous catalysis," *Angew. Chemie Int. Ed.*, vol. 44, no. 48, pp. 7852–7872, 2005.

[285] K. Okitsu and Y. Mizukoshi, "Catalytic Applications of Noble Metal Nanoparticles Produced by Sonochemical Reduction of Noble Metal Ions," in *Handbook of Ultrasonics and Sonochemistry*, Singapore: Springer, 2016.

[286] T. Mokrane, A. Boudjahem, and M. Bettahar, "Benzene hydrogenation over alumina-supported nickel nanoparticles prepared by polyol method," *RSC Adv.*, vol. 6, no. 64, pp. 59858–59864, 2016.

[287] W. Alsalahi, W. Tylus, and A. M. Trzeciak, "Green Synthesis of Rhodium Nanoparticles that are Catalytically Active in Benzene Hydrogenation and 1-Hexene Hydroformylation," *ChemCatChem*, vol. 10, no. 9, pp. 2051–2058, 2018.

[288] E. T. Silveira *et al.*, "The Partial Hydrogenation of Benzene to Cyclohexene by Nanoscale Ruthenium Catalysts in Imidazolium Ionic Liquids," *Chem. Eur. J.*, vol. 10, no. 15, pp. 3734–3740, 2004.

[289] X. Liu, C. Meng, and Y. Han, "Substrate-mediated enhanced activity of Ru nanoparticles in catalytic hydrogenation of benzene," *Nanoscale*, vol. 4, no. 7, pp. 2288–2295, 2012.

[290] C. Hydrogenation, "Ru nanoparticles immobilized on montmorillonite by ionic liquids: a highly efficient heterogeneous catalyst for the hydrogenation of benzene," *Angew. Chemie*, vol. 118, no. 2, pp. 272–275, 2006.

[291] X. Cui *et al.*, "Highly selective hydrogenation of arenes using nanostructured ruthenium catalysts modified with a carbon–nitrogen matrix," *Nat. Commun.*, vol. 7, p. 11326, 2016.

[292] "Carboxylic Acids." [Online]. Available: https://crab.rutgers.edu/~alroche/Ch20.pdf. [Accessed: 28-Feb-2019].

[293] Sigma-Aldrich, "Cyclohexanemethanol."

[294] S. Meng, E. G. Wang, and S. Gao, "Water adsorption on metal surfaces: A general picture from density functional theory studies," *Phys. Rev. B*, vol. 69, no. 19, p. 195404, 2004.

[295] J. Nishigaki *et al.*, "A New Binding Motif of Sterically Demanding Thiolates on a Gold Cluster," *J. Am. Chem. Soc.*, vol. 134, no. 35, pp. 14295–14297, 2012.

[296] J. Y. Rempel, B. L. Trout, M. G. Bawendi, and K. F. Jensen, "Density functional theory study of ligand binding on CdSe (0001),(0001), and (1120) single crystal relaxed and reconstructed surfaces: implications for nanocrystalline growth," *J. Phys. Chem. B*, vol. 110, no. 36, pp. 18007–18016, 2006.

[297] F. H. B. Lima *et al.*, "Catalytic Activity - d-Band Center Correlation for the O2 Reduction Reaction on Platinum in Alkaline Solutions," *J. Phys. Chem. C*, vol. 111, no. 1, pp. 404–410, 2007.

[298] Z. D. Pozun *et al.*, "A Systematic Investigation of p-Nitrophenol Reduction by Bimetallic Dendrimer Encapsulated Nanoparticles," *J. Phys. Chem. C*, vol. 117, no. 15, pp. 7598–7604, 2013.

[299] A. J. Barker, B. Cage, S. Russek, and C. R. Stoldt, "Ripening during magnetite nanoparticle synthesis: Resulting interfacial defects and magnetic properties," *J. Appl. Phys.*, vol. 98, no. 6, p. 063528, 2005.

[300] S. Bian, I. A. Mudunkotuwa, T. Rupasinghe, and V. H. Grassian, "Aggregation and dissolution of 4 nm ZnO nanoparticles in aqueous environments: influence of pH, ionic strength, size, and adsorption of humic acid," *Langmuir*, vol. 27, no. 10, pp. 6059–6068, 2011.

[301] P. An *et al.*, "Fast synthesis of dopamine-coated Fe3O4 nanoparticles through ligand-exchange method," *Chinese Chem. Lett.*, vol. 23, no. 9, pp. 1099–1102, 2012.

[302] S. A. Difranco, N. A. Maciulis, R. J. Staples, R. J. Batrice, and A. L. Odom, "Evaluation of Donor and Steric Properties of Anionic Ligands on High

Valent Transition Metals," *Inorg. Chem.*, vol. 51, no. 2, pp. 1187–1200, 2011.

[303] P. Ranjan *et al.*, "Metallic Nanocrystal Ripening on Inorganic Surfaces," *ACS Omega*, vol. 3, no. 6, pp. 6533–6539, 2018.

[304] P. Fiurasek and L. Reven, "Phosphonic and Sulfonic Acid-Functionalized Gold Nanoparticles: A Solid-State NMR Study," *Langmuir*, vol. 23, no. 5, pp. 2857–2866, 2007.

[305] R. R. Allison, G. H. Downie, R. Cuenca, X. Hu, C. J. H. Childs, and C. H. Sibata, "Photosensitizers in clinical PDT," *Photodiagnosis Photodyn. Ther.*, vol. 1, no. 1, pp. 27–42, 2004.

[306] D. Bechet, P. Couleaud, C. Frochot, M.-L. Viriot, F. Guillemin, and M. Barberi-Heyob, "Nanoparticles as vehicles for delivery of photodynamic therapy agents," *Trends Biotechnol.*, vol. 26, no. 11, pp. 616–621, 2008.

[307] D. Kumar, L. Shan, and Y. Zhang, "Nanoparticles in photodynamic therapy: An emerging paradigm," *Adv. Drug Deliv. Rev.*, vol. 60, no. 15, pp. 1627–1637, 2008.

[308] P. Huang *et al.*, "Photosensitizer-conjugated magnetic nanoparticles for in vivo simultaneous magneto fluorescent imaging and targeting therapy," *Biomaterials*, vol. 32, no. 13, pp. 3447–3458, 2011.

[309] M. Lahav *et al.*, "Photoelectrochemistry with Integrated Photosensitizer-Electron Acceptor and Au-Nanoparticle Arrays," *J. Am. Chem. Soc.*, vol. 122, no. 46, pp. 11480–11487, 2000.

[310] R. Bakalova, H. Ohba, Z. Zhelev, M. Ishikawa, and Y. Baba, "Quantum dots as photosensitizers?," *Nat. Biotechnol.*, vol. 22, no. 11, pp. 1360–1361, 2004.

[311] S. Ferrere and B. A. Gregg, "Photosensitization of TiO2 by [FeII(2, 2'-bipyridine-4, 4 '-dicarboxylic acid)2(CN)2]: band selective electron injection from ultra-short-lived excited states," *J. Am. Chem. Soc.*, vol. 120, no. 4, pp. 843–844, 1998.

[312] S. M. Zakeeruddin *et al.*, "Design, synthesis, and application of amphiphilic ruthenium polypyridyl photosensitizers in solar cells based on nanocrystalline TiO2 films," *Langmuir*, vol. 18, no. 3, pp. 952–954, 2002.

[313] F. Number, "New photosensitizer. Tris (2,2'-bipyridine) ruthenium (II) chloride," *J. Am. Chem. Soc.*, vol. 93, no. 7, pp. 1800–1801, 1971.

[314] C. A. Bignozzi, C. Chiorboli, M. T. Indelli, M. A. R. Scandola, G. Varani, and F. Scandola, "Simple poly (pyridine) ruthenium (II) photosensitizer:(2, 2'-bipyridine) tetracyanoruthenate (II)," *J. Am. Chem. Soc.*, vol. 108, no. 24, pp. 7872–7873, 1986.

[315] G. Carrone, F. Gantov, L. D. Slep, and R. Etchenique, "Fluorescent Ligands and Energy Transfer in Photoactive Ruthenium-Bipyridine Complexes.," *J. Phys. Chem. A*, vol. 118, no. 45, pp. 10416–10424, 2014.

[316] S. M. Ponder *et al.*, "Surface chemistry and electrochemistry of supported zerovalent iron nanoparticles in the remediation of aqueous metal contaminants," *Chem. Mater.*, vol. 13, no. 2, pp. 479–486, 2001.

[317] A. Kathiravan and R. Renganathan, "Effect of anchoring group on the photosensitization of colloidal TiO2 nanoparticles with porphyrins," *J. Colloid Interface Sci.*, vol. 331, no. 2, pp. 401–407, 2009.

[318] R. M. O. Donnell, R. N. Sampaio, G. Li, P. G. Johansson, C. L. Ward, and G. J. Meyer, "Photoacidic and Photobasic Behavior of Transition Metal Compounds with Carboxylic Acid Group(s)," *J. Am. Chem. Soc.*, vol. 138, no. 11, pp. 3891–3903, 2016.

[319] E. Schzab, Franck W; Wichers, "Preparation of benzoic acid of high purity," *J. Res. Natl. Bur. Stand. (1934).*, vol. 25, pp. 747–757, 1940.

[320] M. A. Connell *et al.*, "Improving the accuracy of pulsed field gradient NMR diffusion experiments: Correction for gradient non-uniformity," *J. Magn. Reson.*, vol. 198, no. 1, pp. 121–131, 2009.

[321] C. Miller Cruickshank, "The Stokes-Einstein Law for Diffusion in Solution," *Proc. R. Soc. Lond. A*, vol. 106, pp. 724–749, 1924.

[322] J. T. Edward, "Molecular Volumes and the Stokes-Einstein Equation," *J. Chem. Educ.*, vol. 47, no. 4, pp. 261–270, 1970.

[323] E. ToolBox, "Benzene Liquid - Thermal Properties.," 2011. [Online]. Available: https://www.engineeringtoolbox.com/benzene-thermal-properties-d_1762.html.

[324] Engineering ToolBox, "Benzene - Dynamic and Kinematic Viscosity," 2018. [Online]. Available: https://www.engineeringtoolbox.com/benzene-benzol-dynamic-kinematic-viscosity-temperature-d_2073.html.

[325] B. Das, M. N. Roy, and D. K. Hazra, "Densities and viscosities of the binary aqueous mixtures of tetrahydrofuran and 1,2-dimethoxyethane at 298, 308 and 318 K," *Indian J. Chem. Technol.*, vol. 1, pp. 1–5, 1994.

[326] T. Zheng, P. Cherubin, L. Cilenti, K. Teter, and Q. Huo, "A simple and fast method to study the hydrodynamic size difference of protein disulfide isomerase in oxidized and reduced form using gold nanoparticles and dynamic light scattering," *Analyst*, vol. 141, no. 3, pp. 934–938, 2016.

[327] B. K. Teo and N. J. A. Sloane, "Magic Numbers in Polygonal and Polyhedral Clusters," *Inorg. Chem.*, vol. 24, no. 26, pp. 4545–4558, 1985.

[328] A. Radi, D. Pradhan, Y. Sohn, and K. T. Leung, "Nanoscale shape and size control of cubic, cuboctahedral, and octahedral Cu− Cu2O core− shell nanoparticles on Si (100) by one-step, templateless, capping-agent-free electrodeposition," *ACS Nano*, vol. 4, no. 3, pp. 1553–1560, 2010.

[329] S. V. Sokolov, C. Batchelor-McAuley, K. Tschulik, S. Fletcher, and R. G. Compton, "Are Nanoparticles Spherical or Quasi-Spherical?," *Chem. Eur. J.*, vol. 21, no. 30, pp. 10741–10746, 2015.

[330] P. E. Blöchl, "Projector augmented-wave method," *Phys. Rev. B*, vol. 50, no. 24, p. 17953, 1994.

[331] G. Kresse and D. Joubert, "From ultrasoft pseudopotentials to the projector augmented-wave method," *Phys. Rev. B*, vol. 59, no. 3, p. 1758, 1999.

[332] J. Hafner, "Ab-initio simulations of materials using VASP: Density-functional theory and beyond," *J. Comput. Chem.*, vol. 29, no. 13, pp. 2044–2078, 2008.

[333] H. J. Monkhorst and J. D. Pack, "Special points for Brillouin-zone integrations," *Phys. Rev. B*, vol. 13, no. 12, pp. 5188–5192, 1976.

[334] G. Henkelman, B. P. Uberuaga, and H. Jónsson, "A climbing image nudged elastic band method for finding saddle points and minimum energy paths," *J. Chem. Phys.*, vol. 113, no. 22, pp. 9901–9904, 2000.

[335] G. Henkelman and H. Jónsson, "Improved tangent estimate in the nudged elastic band method for finding minimum energy paths and saddle points minimum energy paths and saddle points," *J. Chem. Phys.*, vol. 113, no. 22, pp. 9978–9985, 2000.

[336] C. Adamo and V. Barone, "Optimization methods for finding minimum energy paths Optimization methods for finding minimum energy paths," *J. Chem. Phys.*, vol. 128, no. 13, p. 134106, 2008.

[337] C. J. Pickard and F. Mauri, "All-electron magnetic response with pseudopotentials: NMR chemical shifts," *Phys. Rev. B*, vol. 63, no. 24, p. 245101, 2001.

[338] N. Marzari and F. Mauri, "Spin and orbital magnetic response in metals: Susceptibility and NMR shifts," *Phys. Rev. B*, vol. 76, no. 16, p. 165122, 2007.

[339] M. J. Frisch *et al.*, "Gaussian 09 Revison D.01." Gaussian Inc. Wallingford CT, 2009.

[340] M. Dolg, U. Wedig, H. Stoll, and H. Preuss, "Energy-adjusted abinitio pseudopotentials for the first row transition elements," *J. Chem. Phys.*, vol. 86, no. 2, pp. 866–872, 1987.

[341] A. Bergner, M. Dolg, W. Küchle, H. Stoll, and H. Preuß, "Ab initio energy-adjusted pseudopotentials for elements of groups 13-17," *Mol. Phys.*, vol. 80, no. 6, pp. 1431–1441, 1993.

[342] K. L. Schuchardt *et al.*, "Basis set exchange: A community database for computational sciences," *J. Chem. Inf. Model.*, vol. 47, no. 3, pp. 1045–1052, 2007.

[343] D. Feller, "The role of databases in support of computational chemistry calculations," *J. Comput. Chem.*, vol. 17, no. 13, pp. 1571–1586, 1996.

[344] C. Adamo and V. Barone, "Toward reliable density functional methods without adjustable parameters: The PBE0 model," *J. Chem. Phys.*, vol. 110, no. 13, pp. 6158–6170, 1999.

[345] F. London, "Théorie quantique des courants interatomiques dans les combinaisons aromatiques," *J. Phys. Radium*, vol. 8, no. 10, pp. 397–409, 1937.

[346] R. McWeeny, "Theory for the Fock-Dirac Density Matrix," *Phys. Rev.*, vol. 126, pp. 1028–1034, 1962.

[347] R. Ditchfield, "Self-consistent perturbation theory of diamagnetism: I. A gauge-invariant LCAO method for NMR chemical shifts," *Mol. Phys.*, vol. 27, no. 4, pp. 789–807, 1974.

[348] J. L. Dodds, R. McWeeny, and A. J. Sadlej, "Self-consistent perturbation theory: Generalization for perturbation-dependent non-orthogonal basis set," *Mol. Phys.*, vol. 36, no. 4, pp. 1779–1791, 1977.

[349] K. Wolinski, J. F. Hinton, and P. Pulay, "Efficient implementation of the gauge-independent atomic orbital method for NMR chemical shift calculations," *J. Am. Chem. Soc.*, vol. 112, no. 23, pp. 8251–8260, 1990.

[350] M. W. Lodewyk, M. R. Siebert, and D. J. Tantillo, "Computational Prediction of 1H and 13C Chemical Shifts: A Useful Tool for Natural Product, Mechanistic, and Synthetic Organic Chemistry.," *Chem. Rev.*, vol. 112, no. 3, pp. 1839–1862, 2012.

[351] K. K. Baldridge and J. S. Siegel, "Correlation of empirical δ(TMS) and absolute NMR chemical shifts predicted by ab initio computations," *J. Phys. Chem. A*, vol. 103, no. 20, pp. 4038–4042, 1999.

[352] A. K. Jameson and C. J. Jameson, "Gas-phase13C chemical shifts in the zero-pressure limit: refinements to the absolute shielding scale for13C," *Chem. Phys. Lett.*, vol. 134, no. 5, pp. 461–466, 1987.

[353] H. Widjaja *et al.*, "DFT + U and ab initio atomistic thermodynamics approache for mixed transitional metallic oxides: A case study of CoCu2O3surface terminations," *Mater. Chem. Phys.*, vol. 201, pp. 241–250, 2017.

[354] K. Duanmu, J. Friedrich, and D. G. Truhlar, "Thermodynamics of metal nanoparticles: Energies and enthalpies of formation of magnesium clusters and nanoparticles as large as 1.3 nm," *J. Phys. Chem. C*, vol. 120, no. 45, pp. 26110–26118, 2016.

[355] F. Khorasheh, R. Radmanesh, and M. Kazemeini, “Mechanism discrimination in heterogeneous catalytic reactions: Fractal analysis,” *Ind. Eng. Chem. Res.*, vol. 37, no. 2, pp. 362–366, 1998.

[356] G. Ertl, “Reactions at well-defined surfaces,” *Surf. Sci.*, vol. 299, pp. 742–754, 1994.

[357] D. A. McQuarrie, *Statistical Mechanics*, 2nd ed. California, USA: University Science Books: Saulito, 2000.

[358] A. V. Marenich, C. J. Cramer, and D. G. Truhlar, “Universal solvation model based on solute electron density and on a continuum model of the solvent defined by the bulk dielectric constant and atomic surface tensions,” *J. Phys. Chem. B*, vol. 113, no. 18, pp. 6378–6396, 2009.

[359] J. Tomasi, Benedetta Mennucci, and Roberto Cammi, “Quantum mechanical continuum solvation models,” *Chem. Rev.*, vol. 105, no. 8, pp. 2999–3094, 2005.

[360] M. W. Chase Jr., C. A. Davies, J. R. Downey Jr., D. J. Frurip, R. A. McDonald, and A. N. Syverud, “JANAF Thermochemical Tables.” U.S. National Bureau of Standards, 1985.

[361] “VTST Tools - Dymanical Matrix.” [Online]. Available: http://theory.cm.utexas.edu/vasp/dymmat.html#dymmat.

[362] S. Maintz, V. L. Deringer, A. L. TchougrÃ©eff, and R. Dronskowski, “LOBSTER: A tool to extract chemical bonding from plane-wave based DFT,” *J. Comput. Chem.*, vol. 37, no. 11, pp. 1030–1035, 2016.

[363] V. L. Deringer, A. L. Tchougréeff, and R. Dronskowski, “Crystal orbital Hamilton population (COHP) analysis as projected from plane-wave basis sets,” *J. Phys. Chem. A*, vol. 115, no. 21, pp. 5461–5466, 2011.

[364] S. Maintz, V. L. Deringer, A. L. Tchougréeff, and R. Dronskowski, “Analytic projection from plane-wave and PAW wavefunctions and application to chemical-bonding analysis in solids,” *J. Comput. Chem.*, vol. 34, no. 29, pp. 2557–2567, 2013.

[365] R. W. F. Bader, *Atoms in Molecules: A Quantum Theory*. New York, USA: Clarendon Press, Oxford University Press, 1994.